ABSTRACT

FOULING AND AGING IN MEMBRANE FILTRATION: HYBRID AFM-BASED CHARACTERIZATION, MODELLING AND REACTIVE MEMBRANE DESIGN

by
Wanyi Fu

Membrane filtration has been extensively used in water and wastewater treatment, desalination, dairy making, and biomass/water separation. However, membrane fouling, aging and insufficient removal efficiency for dissolved organic matters remain major challenges for wider industrial applications. In order to tackle these challenges, this doctoral dissertation investigates mechanisms of membrane fouling and development of antifouling membrane filtration technologies. Specifically, four major research areas are explored: (i) nanoscale physicochemical characterization of the chemically modified polymeric membranes; (ii) quantitative modelling between membrane properties and membrane fouling and defouling kinetics; (iii) development of quantitative structure-activity relationships for membranes that undergo thermal and chemical aging treatments; and (iv) design of microwave-assisted reactive and antifouling membrane filtration system.

The first research study focuses on the development and validation of atomic force microscope (AFM) and hybrid AFM-IR techniques to acquire surface topography, hydrophobicity and chemical distribution at nanoscale on polymeric membranes. AFM is used to obtain the topography images that show the pore size, porosity and also surface roughness of the polymeric membranes. Moreover, the chemical force mode of AFM is applied to probe nanoscale hydrophobicity on modified membranes. Furthermore, the AFM-IR technique offers accurate chemical identifications and distribution of additives on modified membranes at nanoscale, which is not achievable by conventional FTIR due to

its low resolution or low sensitivity. The hybrid AFM techniques are believed to be critical for the nanoscale characterization for material properties in a wide spectrum of applications.

In the second work, predictive models for membrane fouling and defouling kinetics are developed. The models integrate membrane surface properties (i.e., hydrophobicity and surface charge) and filtration performances with protein, saccharides and natural organic matters (NOM) as model foulants. Positive correlations (R^2=0.74-0.99) are obtained between the fouling rates and the foulant deposition rates on different membrane-foulant interaction systems. This correlation could be used for further developing predictive models of membrane fouling.

In the third work, the chemical and thermal stability of surface chemically modified polyether sulfone (PES) membranes are investigated. The membranes' physical (i.e., pore size, roughness), mechanical (i.e., tensile strength) and chemical characteristics (i.e., IR spectrum, and hydrophobicity) are evaluated. The quantitative structure-activity relationships (QSAR) for membrane filtration after aging are developed.

Sustaining high flux and diversified pollutant rejection are two crucial benchmarks for membrane filtration. In the fourth work, a microwave-enhanced membrane filtration process that uses microwave (MW) to energize catalyst-coated ceramic membranes is designed. MW irradiation is selectively absorbed by catalysts and H_2O_2 to produce ‘‘hotpots” on membrane surface and promote generation of radicals and nanobubbles. The MW-Fenton-like reactions enhance chemical degradation of persistent organic pollutants (i.e., 1,4-dioxane) and significant mitigation of fouling. MW irradiation can effectively penetrate membrane modules and selectively promote surface reactions, which may open new avenues toward reactive and antifouling membrane filtration techniques.

FOULING AND AGING IN MEMBRANE FILTRATION: HYBRID AFM-BASED CHARACTERIZATION, MODELLING AND REACTIVE MEMBRANE DESIGN

by
Wanyi Fu

A Dissertation
Submitted to the Faculty of
New Jersey Institute of Technology
in Partial Fulfilment of the Requirements for the Degree of
Doctor of Philosophy in Environmental Engineering

John A. Reif, Jr. Department of Civil and Environmental Engineering

May 2019

APPROVAL PAGE

FOULING AND AGING IN MEMBRANE FILTRATION: HYBRID AFM-BASED CHARACTERIZATION, MODELLING AND REACTIVE MEMBRANE DESIGN

Wanyi Fu

Dr. Wen Zhang, Dissertation Advisor — Date
Associate Professor of Civil and Environmental Engineering, NJIT

Dr. Taha F. Marhaba, Committee Member — Date
Professor and Chair of Civil and Environmental Engineering, NJIT

Dr. Hsin-Neng Hsieh, Committee Member — Date
Professor of Civil and Environmental Engineering, NJIT

Dr. Somenath Mitra, Committee Member — Date
Professor of Chemistry and Environmental Science, NJIT

Dr. Ngai Yin Yip, Committee Member — Date
Assistant Professor of Earth and Environmental Engineering, Columbia University

BIOGRAPHICAL SKETCH

Author: Wanyi Fu

Degree: Doctor of Philosophy

Date: May 2019

Undergraduate and Graduate Education:

- Doctor of Philosophy in Environmental Engineering,
  New Jersey Institute of Technology, Newark, NJ, 2019

- Master of Science in Civil Engineering,
  Tsinghua University, Beijing, P. R. China, 2014

- Bachelor of Science in Mineral Processing Engineering,
  Central South University, Changsha, Hunan, P. R. China, 2011

Major: Environmental Engineering

Presentations and Publications:

1. Fu, W.; Wang, L.; Chen, F.; Zhang, X.; Zhang, W., Polyvinyl chloride (PVC) ultrafiltration membrane fouling and defouling behavior: EDLVO theory and interface adhesion force analysis. *J. Membr. Sci.* 2018, *564*, 204-210.

2. Fu, W.; Zhang, W., Measurement of surface wettability of engineered nanoparticles using atomic force microscope. *Phys. Chem. Chem. Phys.* 2018, *20*, 24434-24443.

3. Fu, W.; Zhang, W., Microwave-enhanced membrane filtration for water treatment. *J. Membr. Sci.* 2018, *568*, 97-104.

4. Wang, Y.; Fu, W.; Zhang, W.; Huang, H., Insight on the adsorption of acetaminophen on MWCNT by hyperspectral imaging. *Langmuir* 2018, *34*, 13210-13218.

5. Sun, S.; Yao, H.; Fu, W.; Hua, L.; Zhang, G.; Zhang, W., Reactive photo-Fenton ceramic membranes: synthesis, characterization and antifouling performance. *Water Res.* 2018, *144*, 690-698.

6. Zhang, W.; Fu, W., Hua, L., Membrane distillation apparatus and membrane for use therein, U.S. Patent application No. 62/727,107, 9/5/2018.

7. Zhang, W.; Fu, W., Antifouling membrane filtration system, U.S. Patent No. 2018/0104653/A1, 4/19/2018.

8. Fu, W.; Zhang, W., Hybrid AFM for nanoscale physicochemical characterization: recent development and emerging applications. *Small* 2017, *13.11*, 1603525.

9. Fu, W.; Hua, L.; Zhang, W., Experimental and modeling assessment of the roles of hydrophobicity and zeta potential in chemically modified polyethersulfone membrane fouling kinetics. *Industr. Engin. Chem. Res.* 2017, *56,* 8580-8589.

10. Fu, W.; Carbrello, C.; Wu, X.; Zhang, W., Visualizing and quantifying nanoscale hydrophobicity and chemical distribution of surface modified polyethersulfone (PES) Membranes. *Nanoscale* 2017, *9*, 15550-15557.

11. Lu, J.; Obara, S.; Liu, F.; Fu, W; Zhang, W., Shingo Kikuchi. Melt extrusion for a high melting point compound with improved solubility and sustained release. *AAPS Pharm. Sci. Tech.* 2017, 1-13.

12. Zhang, W.; Fu, W., Microfluidic cell for atomic force microscopy enabling in situ membrane filtration characterization, Patent application No. 62/554,122, 9/5/2017.

13. Fu, W., Microwave-enhanced membrane filtration for water treatment, AEESP student poster session, Princeton University, Oct. 8th, 2018.

14. Fu, W.; Zhang, W., Nanoscale hydrophobicity and chemical distribution of surface modified polyethersulfone (PES) membranes. NAMS 27th Annual Meeting, Lexington, KY, Jun. 11st, 2018.

15. Fu, W.; Zhang, W., Nanoscale imaging and quantifying chemically modified polymer membrane properties. MAST Center IAB Meeting, State College, PA, Apr. 23rd, 2018.

16. Fu, W.; Zhang, W., Probing nanoscale hydrophobicity and chemical distribution of surface modified membranes. ACS 255th Annual Conference, New Orleans, LA, Mar. 18th, 2018.

17. Fu, W.; Zhang, W., Probing functionalized nanomaterials on filtration membranes at nanoscale using hybrid AFM. 1st Pan American Congress of Nanotechnology. São Paulo, Brazil, Nov. 27th, 2017.

18. Fu, W.; Zhang, W., Probing nanoscale hydrophobicity and chemical distribution of surface modified polyethersulfone (PES) membranes, Eastern Analytical Symposium & Exposition, Plainsboro, New Jersey, Nov. 14th, 2017.

19. Fu, W.; Zhang, W., Experimental and modeling assessment of the roles of hydrophobicity and zeta potential in chemically modified polyethersulfone membrane fouling kinetics, AEESP student poster session, New Jersey Institute of Technology, Aug. 24th, 2017.

20. Fu, W.; Zhang, W., Characterization and antifouling performances study of chemically modified polyethersulfone (PES) membranes, Dana Knox Student Research Showcase, New Jersey Institute of Technology, April 19th, 2017.

21. Fu, W., Low cost ceramic membrane application on drinking water treatment, AEESP student poster session, Columbia University, Oct. 28th, 2016.

22. Fu, W., Nanoscale imaging and quantifying with hybrid AFM technology. ACS 252nd Annual Conference, Philadelphia, PA, Aug. 21st, 2016.

23. Fu, W., Nanoscale imaging and quantifying chemically modified polymer membrane properties. MAST Center IAB Meeting, Newark, NJ, Apr. 18th, 2016.

24. Fu, W., Low Cost ceramic membrane application on drinking water treatment, AWWA Annual Conference Student Poster Contest, Atlantic City, March 16th, 2016.

25. Fu, W., Low Cost Ceramic Membrane Application on drinking water treatment, NJEN annual poster session, Princeton University, March 1st, 2016.

To my dearest mom, dad and brother; your infinite love makes me happy every day.
To make you proud of me is my endless motivation toward success.

致我最爱的妈妈，爸爸和哥哥，你们的爱使我每天都很快乐．
让你们为我骄傲是我最大的奋斗动力．

ACKNOWLEDGEMENTS

Pursuing a Ph.D. degree really is a lot more about the journey than the end, and I could not have made through mine so joyfully without the support from many people. Here, I would like to mention those people who made this journey an unforgettable experience for me.

Words will never be enough to express my gratitude to my advisor, Dr. Wen Zhang, for his constant and precious guidance all the time and providing me the opportunities to expand my knowledge and experience. I am always grateful for his trust, his encouragement, believing in my potential and letting me explore the field of membrane technologies. I believe that he is the most reliable and helpful mentor and advisor that cares about students the most. He always keeps in mind my career goal as faculty and helps me build up critical skills for this profession. I have also been very fortunate to have had the opportunity to get involved in multiple research projects, attend numerous international and regional conferences, get involved in proposal writing and mentor students. What he taught me is not limited to the research studies but also how to be an independent researcher and mentor. It has been an honor and a pleasure to study under the supervision of such an individual of exceptional professional, teaching and personal qualities.

Special thanks go to my dissertation committee members, Dr. Taha F. Marhaba, Dr. Hsin-Neng Hsieh, Dr. Somenath Mitra, and Dr. Ngai Yin Yip. I want to especially thank them for finding time in their busy schedules to review this dissertation and provide considerate advice, important feedback, constructive, and critical comments.

I would like to acknowledge all of the financial support that made this dissertation possible, provided by the NSF Industry/University Cooperative Research Center for Membrane Science, Engineering and Technology (NSF Award IIP1034720), New Jersey

Water Resources Research Institute (NJWRRI) grant from USGS (Project Number: 2018NJ399B), Faculty Instrument Usage Seed Grant (FIUSG), and Undergraduate Research Innovation (URI) phase I and II grants.

My industrial mentors, Dr. Christina Carbrello (EMD Millipore Corporation), Dr. Derek Dehn (3M Corporation) and Dr. Xiaosong Wu (Pall Corporation) are highly appreciated for their support of membrane samples and valuable advice on the research. In particular, Dr Christina Carbrello also gave me the advice on career development and wrote the recommendation letters for my applications to the scholarships. Also, she gave me the valuable opportunity to visit the membrane research lab in Millipore at Boston and learn the membrane preparation procedures.

In addition, I received lots of help from the professors and students in NJIT. I want to thank Professor Kamalesh Sirkar and his PhD student Dr. Na Yao for allowing me trying their filtration system and inspiring me to fabricate my own filtration modules. In particular, Prof. Sirkar gave me lots of encouragement and support during the MAST project and my doctoral study. And many thanks to Prof. Zafar Iqbal, Dr. Mostafa Benchafia, Dr. Maocong Hu, Dr. Xiaoyang Xu, Tianyu Sun, Yung-hao Tsou and Zhenhua Yao for their help on ATR-FTIR measurement and BET test of membrane samples. Special thanks go to Dr. Mengyan Li (NJIT) and his students, Fei Li, Pham Dung, Daiyong Deng for their help on GC operation for 1,4-dioxane measurements. And thanks also go to Dr. Yuanwei Zhang and his student Xiangshan Liu (NJIT) for help with MS trial analysis on microplastics in bottle water. Dr. Siva Nadimpalli and his PhD student Mr. Subhajit Rakshit are also thanked for let me try their AFM instrument during my first semester here. Also, Prof. Rajesh Dave and his student Kai Zheng were appreciated for the tensile strength tests on

polymeric membrane samples. Moreover, I'd like to thank Dr. Xueyan Zhang and Dr. Jeong Shim for their training, help and advice on Raman, AFM, FTIR, XRD and SEM measurement and operation. In particular, I want to thank Dr. Taha Marhaba, our department chair, and Ms. Heidi Young, our previous chair assistant for providing a comfortable place for me to work and study. Also, Nasser and Steve are truly appreciated for their kind help on my research. Aristides and Andrew are gratefully thanked for their help on the membrane module fabrication as well.

Moreover, the collaborators and professors from other universities and institutes helped me a lot during my doctoral study. I appreciate the opportunity to learn the membrane fabrication technique in Dr. Yongsheng Chen's research group, and thank Chunyan Xu and Su Liu for teaching me the tricks of membrane fabrication. Thanks go to Dr. Ian Armstrong (Bruker), Dr. Ardavan Zandiatashbar (Park Systems Inc.), Dr. Xiao Tong (Brookhaven National Laboratory, BNL) and Dr. Dmytro Nykypanchuk (BNL) for the help of AFM topography and surface potential on PES membranes; Dr. Tom Tague (Bruker) for help of FTIR spectrum of PES membranes; Dr. Peng Wang (Bruker) and Dr. Wei Liu (WITec) for help of Raman spectrum of PES membranes; Dr. Marko Surtchev and Dr. Oleg Butyaev (NTMDT) for help of AFM-Raman characterization of PES membranes; Dr. Qichi Hu, Dr. Curtis Marcott and Mr. Jay Anderson from Anasys Instruments for help of AFM-IR characterization of PES membranes; Dr. Mark Pothecary (Malvern) for help of surface zeta potential measurement; Dr. Vinod Radhakrishnan and Mr. Edward Lim (Anton Paar Inc.) for the surface zeta potential measurements by SurPASS 3; Dr. Appala Raju Badireddy and his student, Yuxiang Zhang (University of Vermont) for the help with HIS measurements; Dr. Gerald R. Poirier, Dr. Wei Fan, Dr.

Jing Qu and Dr. Roddel Ansu Remy from the University of Delaware for their help on NanoIR2 instrument. It is specially my fortune to gratefully acknowledge Prof. Xihui Zhang for his continuous support and encouragement. Without his recommendation, I would not have this opportunity to meet Dr. Wen Zhang and get enroll as a PhD student in NJIT.

I also thank my current and previous group members, Xiaonan Shi, Chunzhao Chen, Likun Hua, Qingquan Ma, Ahmed K. Ahmed, Liyuan Kuang and all the students who worked in our lab. And they are: Dharani, Shaobin, Tengge, Tianhao, Ruichen, Kaiqin, Xinyuan, Ran, Han, Changzhou, Saloni and Mitali. I really appreciate their valuable help and support during the period of my research. I feel grateful to my current and former office mates: Mandeep Pokhrel, Anuruddha Jayasuriya, Abdullah Shabarek, Yuanyuan Fan, Di Zhang, Jin Fan and Abolfazl Bayat for providing a fun filled environment. Moreover, words fail me to express my appreciation to my dearest friends: Wei Yin, Chunzhao, Xiaonan, Ke, Fangqi, Peng, Fei Li, Wancheng, Pham, Ian, Dharali, Dr. Swati Patel, Dr. Jing Qu, Dr. Zuli Piya, and Honghao Lin for their generous care and encouragement, which made my stay in USA not lonely but enjoyable. Those lovely persons gave me lots of happiness and energy whenever I am up or down.

Lastly but the most importantly, I would not succeed in this endeavor without my parent's long-lasting support, understanding, encouragement, and patience, which accompany me through all the hardship during the research adventure. I also appreciate my brother's pushing me during my application at the beginning. Without that, I would not have had the chance to experience this 4-year wonderful journey. Making them proud of me is my endless motivation toward success.

TABLE OF CONTENTS

TABLE OF CONTENTS
(Continued)

TABLE OF CONTENTS
(Continued)

Chapter **Page**

TABLE OF CONTENTS
(Continued)

TABLE OF CONTENTS
(Continued)

TABLE OF CONTENTS
(Continued)

TABLE OF CONTENTS
(Continued)

TABLE OF CONTENTS
(Continued)

TABLE OF CONTENTS
(Continued)

Chapter **Page**

LIST OF TABLES

LIST OF TABLES
(Continued)

LIST OF FIGURES

LIST OF FIGURES
(Continued)

LIST OF FIGURES
(Continued)

LIST OF FIGURES
(Continued)

LIST OF FIGURES
(Continued)

LIST OF FIGURES
(Continued)

LIST OF FIGURES
(Continued)

LIST OF FIGURES
(Continued)

LIST OF FIGURES
(Continued)

LIST OF FIGURES
(Continued)

LIST OF FIGURES
(Continued)

LIST OF FIGURES
(Continued)

LIST OF FIGURES
(Continued)

LIST OF FIGURES
(Continued)

LIST OF FIGURES
(Continued)

LIST OF FIGURES
(Continued)

LIST OF FIGURES
(Continued)

LIST OF SYMBOLS

AAP	acetaminophen
AFM	atomic force microscopy
AOP	advanced oxidation process
ARB	antibiotic resistance bacteria
ARG	antibiotic resistance genes
ATR	attenuated total reflection
BFO	$BiFeO_3$
BSA	bovine serum albumin
CA	contact angles
CCD	charged coupled device
CFF	cross flow filtration
CNT	carbon nanotube
CPD	contact potential differences
DEX	dextran
DFM	dark field microscopy
DI	deionized
DLS	dynamic light scattering
DOM	dissolved organic matter
DSC	differential scanning calorimetry
EDLVO	extended Derjaguin–Landau–Verwey–Overbeek
EDS	energy dispersive X-ray spectroscopy
ED-HSI	enhanced dark-field hyperspectral imaging
EEMs	excitation–emission matrices

EL	electrostatic double-layer
ENP	engineered nanoparticles
EPS	expanded polystyrene
FITC	fluorescein isothiocyanate
FTIR	Fourier transform infrared spectroscopy
GC-MS	gas chromatography–mass spectrometry
HA	humic acid
HOPG	highly oriented pyrolytic graphite
HPLC	high performance liquid chromatography
HPMC	hydroxypropyl methylcellulose
HRT	hydraulic retention time
IEP	isoelectric point
IR	Infrared
JKR	Johnson-Kendall-Roberts
KPFM	Kelvin probe force microscopy
LA	lactic acid
LOD	limits of detection
MB	methylene blue
MBs	microbubbles
MICO	MW-induced catalytic oxidation
MLR	multiple linear regres
MPs	microplastics
MW	microwave
MWCO	molecular weight cut off
NBs	nanobubbles

NOM	natural organic matter
NPs	nanoparticles
• OH	hydroxyl radical
O-PTIR	optical photothermal infrared
PCM	photocatalytic ceramic membranes
PDPB	poly(diphenylbutadyine)
PE	polyethylene
PEG	polyethylene glycol
PES	polyethersulfone
PET	polyethylene terephthalate
PFOA	perfluorooctanoic acid
PHB	poly(hydroxybutyrate)
PI	polyisoprene
PMMA	polymethyl methacrylate
PTFE	polytetrafluoroetheylene
PTIR	photo-thermal induced resonance
PVC	polyvinylchloride
PVDF	polyvinylidene fluoride
PVP	polyvinylpyrrolidone
py-GC/MS	pyrolysis gas chromatography coupled with mass spectrometry
QA/QC	quality assurance/quality check
QCL	quantum cascade laser
QNM	quantitative nanomechanical
QSAR	Quantitative Structure-Activity Relationships

RFR	relative flux recovery
RMS	root-mean-square
SAMs	self-assembled monolayers
SEM	scanning electron microscopy
SERS	surface-enhanced Raman spectroscopy
SNR	signal-to-noise ratios
SZP	surface zeta potential
TEM	transmission electron microscopy
TERS	tip-enhanced Raman spectroscopy
TMP	transmembrane pressure
TOC	total organic carbon
vdW	van der Waals

CHAPTER 1

INTRODUCTION

1.1 Background and Challenges

During the last few decades, membrane filtration has been extensively used in water and wastewater treatment,[1, 2] desalination,[3, 4] dairy making,[5] and recovery of rare metals. However, membrane fouling is one of the major challenges in the industrial applications.[6] To mitigate the membrane fouling, three major methods were investigated: modification of membrane to obtain antifouling membranes;[7-9] periodic cleaning including hydraulic cleaning and chemical cleaning;[10-12] improvement of operation conditions including pretreatment[13-15] and additional force aided technology. Nevertheless, these methods still have a number of limitations. Their problems and challenges would be discussed below.

First, a comprehensive characterization platform is in need for the modified membranes. To mitigate the membrane fouling, chemical modification of membranes is a popular way to enhance antifouling properties and durability.[7-9] For the modification of membranes, hydrophilized polymer membranes are broadly manufactured for industrial applications as hydrophilic membranes are known to suffer less from membrane fouling in water treatment.[16, 17] Chemical modification of membrane surface chemistries are often achieved by cross-linking, adsorption or covalent grafting of charged ionic species, amphiphilic or hydrophilic additives.[18, 19] Even a small fraction of such chemical blending at a local scale or nanoscale lengths of materials may substantially alter surface characteristics, such as electric, mechanical, wetting properties and topography as well as the interfacial properties. These characteristics eventually play a complex interplay the

resulting filtration performance in terms of solute-membrane interactions, permeate flux, rejection selectivity, fouling/antifouling, and aging. Proper characterization is the key to accurately delineating and predicting the influences of chemical modification on membrane properties and filtration performances. However, traditional diffraction (*e.g.*, FTIR, Raman and XPS) based characterization tools has limited spatial resolution at several microns and no capability to resolve chemical features at nanoscale that potentially permits a molecule-level understanding of material property changes after modification. For instance, FTIR and contact angle measurements are often used to analyze surface functional groups and hydrophobicity, which are both a bulk scale measurement and have no indication of local scale material properties. Clearly, innovative combinations of different emerging analytical tools are needed to perform rapid, *in situ*, and possibly real-time imaging and quantification of both physical and chemical properties of membranes, which is crucial for unravel new information about material properties and novel membrane design.

Second, there still remains a challenge to better understand membrane aging mechanism in order to develop optimized cleaning protocols. It is well known that membrane filters undergo reversible and irreversible fouling. Reversible fouling could be reduced by hydraulic backwash while irreversible fouling, often involved in strong chemical binding between foulant and membrane surface, has to be chemically cleaned using harsh agents (*e.g.*, oxidant, acid and base).[20, 21] The intensity of backwash and the exposure of cleaning agents may have negative influence on the membrane life time.[22] For example, chemical cleaning can induce the polymer oxidation and thus compromise the material integrity of membranes. In most cases, membrane aging is reduced to polymer

aging and methods developed are based on the evaluation of polymer characterization. Until now, there is neither an established definition nor detailed elucidations of membrane aging in the literature. Therefore, in order to compensate for the lack of aging data and aging mechanism from the literature, there is a continuous need for investigation to elucidate the aging mechanisms.

Third, novel non-destructive membrane defouling processes are urgently needed to promote sustainable separation processes. Additional drawbacks of those periodic cleaning techniques are that they interrupt the continuous filtration process. Alternatively, pretreatments (*e.g.*, coagulation, adsorption, oxidation, biological treatment, and some integrated pretreatments) can in various degrees alleviate the fouling by improving the membrane filtration feed quality. But for these pretreatment technologies, multiple problems (*e.g.*, uncertainty on the membrane fouling, unfavorable by-products, scale problem and higher cost) emerged during the applications. Novel membrane filtration processes that exhibit robust antifouling properties are urgently needed to promote sustainable separation processes for producing value-added products (*e.g.*, clean water) or chemicals for drug, food, and pharmaceutical processing. The use of additional forces to aid filtration has gained increasing attention in recent years.[23-25] For example, the magnetically assisted filters, electrically assisted filters and ultrasonically enhanced filtration were investigated to mitigate membrane fouling. However, these methods suffer high energy consumption, membrane erosion and insufficient energy dissipation across membrane modules. Clearly, developing innovative membrane filtration processes that can efficiently filtrate water with strong antifouling characteristics is a pressing task.

1.2 Advances of Hybrid AFM for Nanoscale Physicochemical Characterization

Atomic force microscopy (AFM) has evolved to be one of the most powerful tools for characterization of material surfaces especially at nanoscale.[26, 27] AFM utilizes a cantilever with a sharp tip (radius of curvature is 5-10 nm) that oscillates over the surface of samples. The subtle changes in heterogeneity on local material surfaces induces sensitive changes in vibration amplitude and frequency of the cantilever tip.[28-30] Multiple physicochemical and electric properties can be mapped and quantified by AFM with nanometer resolutions. For example, characteristics such as, surface morphology,[31, 32] surface roughness,[33] stiffness,[34, 35] adhesiveness,[36, 37] viscosity,[38] hydrophobicity,[33] conductivity,[39] capacitance,[40, 41] magnetization,[42] surface potential[43] and work function[32] can be determined accurately. Additionally, analyses such as Kelvin probe force microscopy (KPFM), operated in the electric mode of AFM, could generate 3D mapping of the surface electric potential distribution and measure the local work functions (or Fermi energy levels).[44, 45] In particular, the surface electric potential measures the work function difference between the probe tip and sample surfaces brought into close proximity.[46] The surface electric potential is also highly sensitive to the samples' chemical compositions, electric states, local charges, doping levels, and dielectric properties.[47] Compared to other electron microscopies, such as scanning electron microscopy (SEM) and transmission electron microscopy (TEM),[48, 49] AFM has more characterization functions related to physicochemical properties. A few have been mentioned above.

More importantly, in AFM characterization, the original physiological states of samples can be well preserved. Samples can be placed in vacuum, gases, or aqueous environments with desirable conditions or chemistries, reducing potential artifacts on

samples from sample preparation. Thus, AFM characterization provides an attractive and non-destructive means for examining surface properties.

In addition to physical, mechanical and electric properties, probing chemical properties (*e.g.*, chemical identification and distribution) on sample surfaces is an indispensable aspect of material characterization, which can also be achieved by AFM. In fact, KPFM has proven to be a powerful mode that not only maps surface potential distribution but also identifies the chemical domain, based on the work function differences of different molecular moieties.[35, 50, 51] KPFM has been used to characterize morphology and determine the surface potentials of a broad spectrum of materials, including semiconductors,[52] inorganic films,[53] self-assembled monolayers (SAMs),[54] and polymer thin films.[55, 56] Particularly, the measured surface potentials could help identify and differentiate target materials from the background or surrounding components.[57]

Recent development of AFM has incorporated a suite of analytical techniques, including Raman spectroscopy, Infrared (IR) spectroscopy and confocal microscopy to further extend other capabilities such as revealing chemical composition and mapping the chemical distribution on sample surfaces.[58-60] For example, scanning microwave microscopy was designed for nanoscale electromagnetic properties measurements,[61, 62] mode synthesizing atomic force microscopy for characterization of low-density material,[63] and combined scanning electrochemical-atomic force microscopy for simultaneous topographical and electrochemical measurements with high spatial resolutions.[64] Likewise, traditional diffraction (*e.g.*, IR, Raman and Confocal Raman) has limited spatial resolution at several microns (*e.g.*, 3–30 μm), depending on the laser wavelength and instrumentation. By contrast, hybrid AFM techniques combined with IR and Raman demonstrated

simultaneous physical and chemical characterization of organic interfaces of bacteria and polymer blends at ~10 nm lateral resolution and monolayer sensitivity (over 100 times higher in spatial resolution compared to traditional FTIR and Raman).[59, 65-67] Clearly, hybrid AFM makes it possible to perform rapid, *in situ*, and possibly real-time imaging and quantification of both physical and chemical properties at a nanoscale level. This is crucial to unravel novel and revolutionary information about material properties.

The following literature review aims to deliver the current state of knowledge on hybrid AFM principles and applications with focuses on AFM-IR and AFM-Raman techniques. Basic concepts and principles pertaining to these two techniques and other relevant spectroscopy are presented first. These are followed by critical review and discussion of various major applications in different research fields or sample types to highlight the major achievement in the past. The current drawbacks and limitations of these two hybrid AFM techniques are discussed with extensive examples. These discussions shed new light on the future research requirements and further improvements in stability and reliability of characterizations.

1.2.1 Principles and Applications of AFM-IR

To increase spatial resolution and detection sensitivity, AFM-IR was first designed by Alexandre Dazzi and co-workers in 2005.[68] Within the last decade, the AFM–IR instrument facilitated many research fields in polymer material, biological structure and pharmaceutical development. In AFM-IR, a ZnSe prism is used as a sample holder with a pulsed tunable IR laser as the irradiation source. As shown in Figure 1.1,[69] when the laser wavelength matches an absorption band of the sample, the absorbed laser light causes a photothermal heating effect and a local material expansion. The rapid thermal expansion

excites resonant oscillations of the AFM cantilever, which are detected as a ringdown signal. The signal amplitude is then Fourier transformed to be a function of the laser wavenumber and directly reflects the IR absorption characteristics of materials. As the resonance frequency is correlated well with the conventional IR spectra,[70] the spectra obtained from AFM-IR can be searchable in existing databases.[71, 72]

Using an AFM tip to detect the local thermal expansion makes the IR absorption measurement below the conventional diffraction limit possible. Therefore, AFM-IR is also called photo-thermal induced resonance (PTIR) technique. To further enhance the measurement sensitivity, a laser source called quantum cascade laser (QCL) with a high pulsed frequency about 1000 times higher than that previous lasers used for AFM-IR.[73] As shown in Figure 1.1, by matching the repetition frequency of the mid-infrared QCL pulses with the resonant frequency of the AFM cantilever, the mechanical resonant enhancement of the cantilever deflection amplitude is achieved. This increases the detection sensitivity of the force on AFM tips due to the thermal expansion and gives rise to the IR sensitivity by several orders of magnitude.[73, 74]

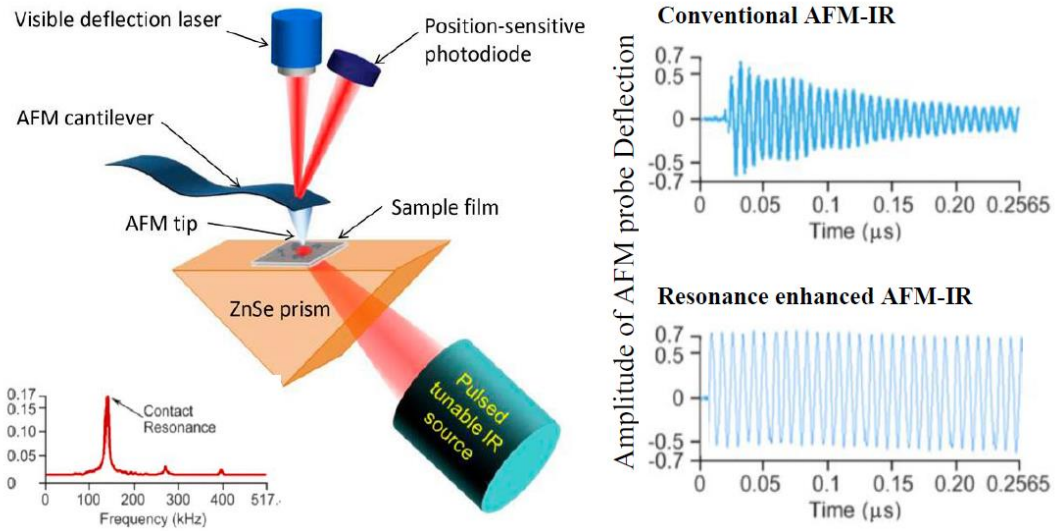

Figure 1.1 Schematics of the AFM-IR measurement.
Source: Ref.[69]

1.2.1.1 Applications in Polymer Characterization. Traditional IR spectroscopy of bulk polymers provides an average of all absorptions in the path of radiation. Variations within a sub-micrometer sample regions may not be detectable[75], which hampers the analysis of polymer (*e.g.*, fibers) with diameters smaller than the wavelength of infrared radiation. In addition, distortions may occur to IR spectral band shapes and limit detection sensitivity. In polymer characterization, Ghosh *et al*. applied AFM-IR and obtained infrared spectra and IR mapping images of poly(diphenylbutadyine) (PDPB) fibers at a high spatial resolution (~ 100 nm) (Figure 1.2).[71] Dazzi *et al*. applied resonance enhanced AFM-IR with QCL to study a polyurethane film with antioxidant and lubricant as additives. The results showed that AFM-IR successfully mapped out the distribution of additives on the surface (Figure 1.3),[65] which opens to the possibility of analyzing the additive loss. It is noted that leaching might affect the medical device biocompatibility. Besides, a "lightning rod" effect can be produced using the Au coated probes, which enhances the illumination on local sample surfaces and ultimately increases the detection sensitivity.[65] For example, imaging of self-assembled monolayers by resonance enhanced AFM-IR. This was reported by Lu *et al*., who indicated that the sensitivity was improved by several orders of magnitude and also pointed out that the spatial resolution of images can only be limited by the apex size of AFM tips.[73]

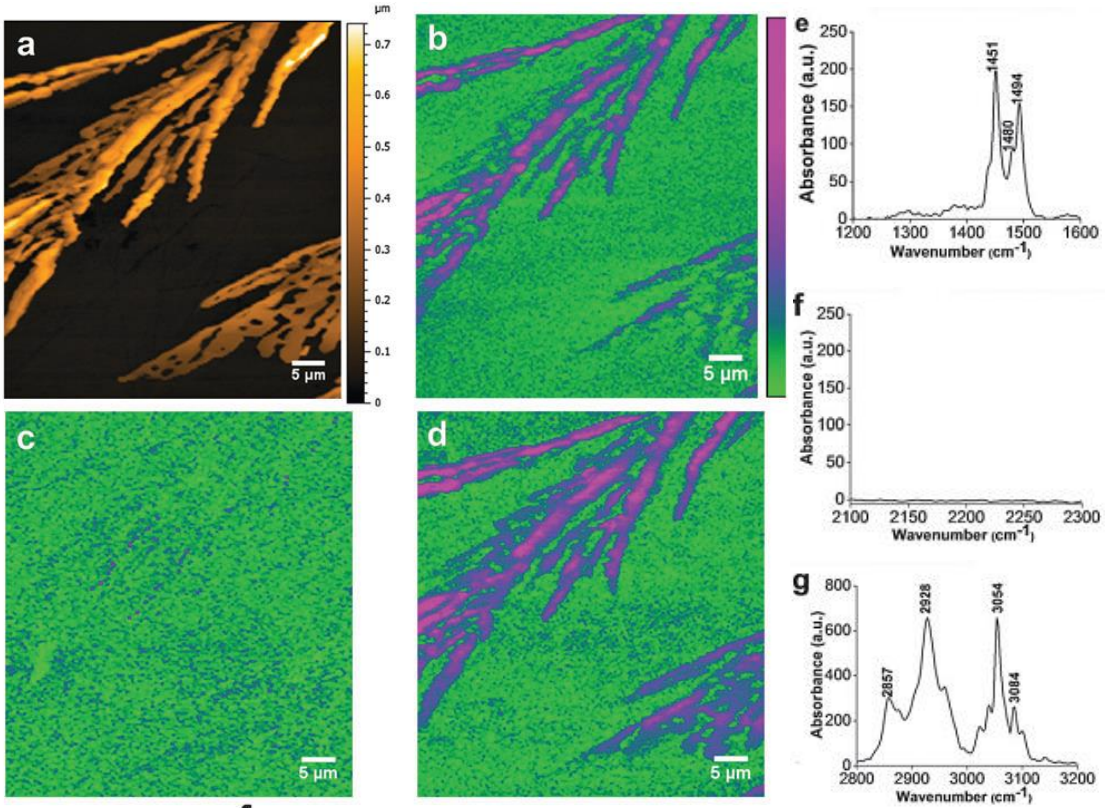

Figure 1.2 AFM image, IR mapping and infrared spectra of PDPB fibers by AFM-IR. (a) Topographic image of photosynthesized PDPB by conventional AFM (The color scale on the right shows the Z-height of the sample). (b-d) AFM-IR mappings of the photo-induced PDPB polymer nanostructures at different fixed wavenumbers (The color scale on the right shows the intensity of IR absorption signal): 1490 cm^{-1} (b) 2146 cm^{-1} (c) and 3054 cm^{-1} (d). (e–g) IR spectra recorded at three different spectral regions of the PDPB polymer.
Source: Ref.[71]

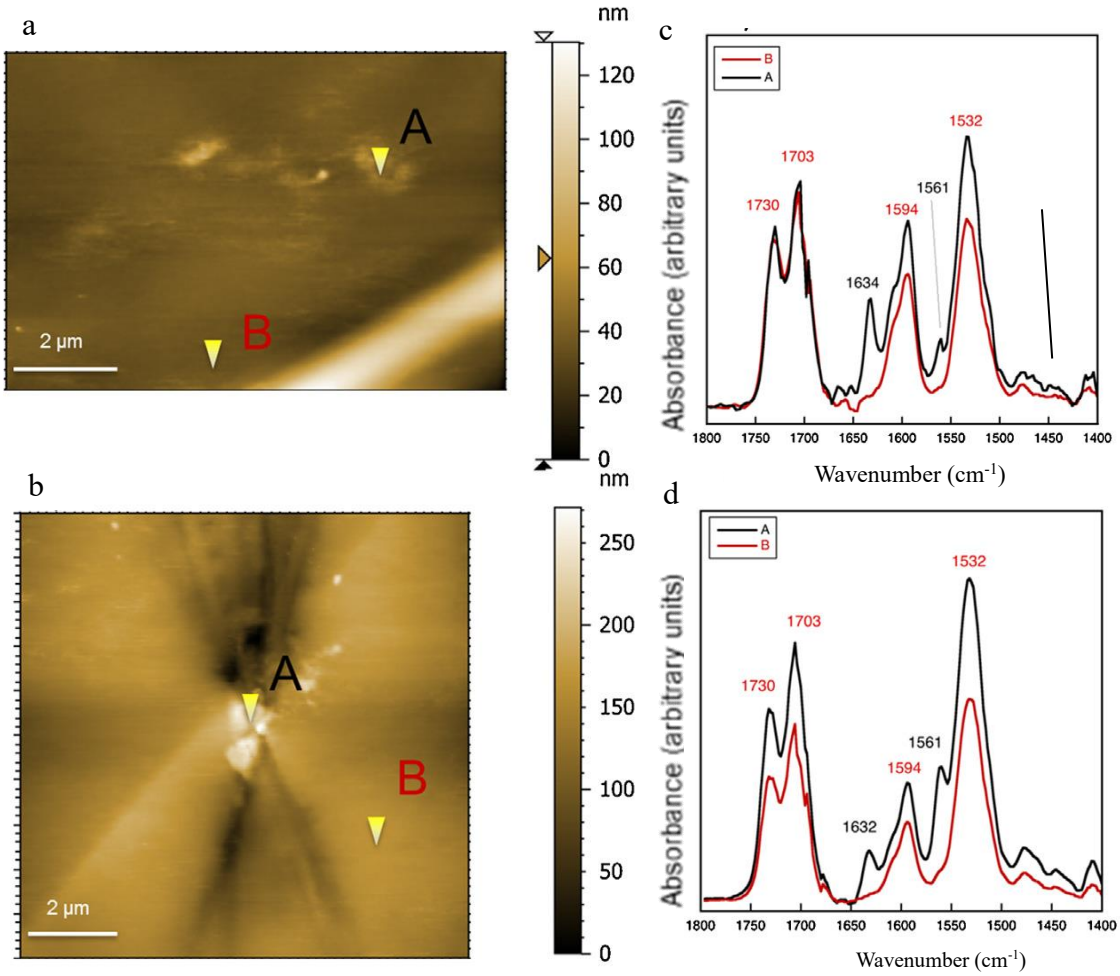

Figure 1.3 Height images and IR spectra of the lubricant deposits on the spincoated polyurethane film. (a) (b) height images; (c) (d) corresponding IR spectra for the deposit (A) and the film surface (B). The color scale on the left image shows the Z-height of the sample.
Source: Ref.[65]

With the unparalleled capabilities in local chemical mapping and identification, distribution and partitioning (or phase-separation) of multicomponent polymer blends can be examined using the AFM-IR technique, based on spectral fingerprints and variations. H. Cho *et al*. used AFM-IR to characterize a polymer blend of polystyrene (PS) and polymethyl methacrylate (PS/PMMA) and determined the spatial distribution on samples of polymer film (Figure 1.4).[76]

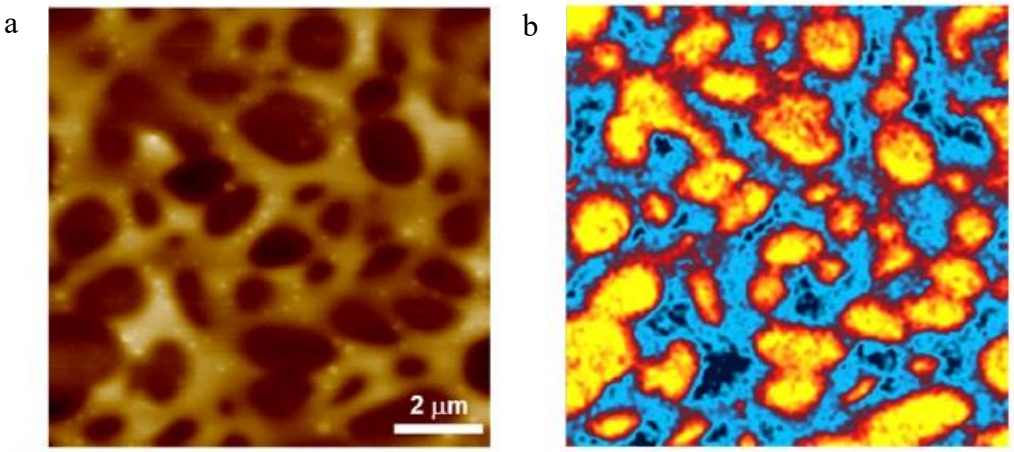

Figure 1.4 AFM topography image and IR chemical mapping of a polymer blend sample (PS/PMMA). (a) AFM topographic image; (b) AFM-IR chemical map at a fixed wavenumber of 3026 cm^{-1}.
Source: Ref.[76]

1.2.1.2 Applications in Pharmaceutical Industries. Determining the extent of miscibility of amorphous components is important for pharmaceutical engineering such as polymer-polymer blending. Van Eerdenbrugh *et al.* utilized AFM-IR to investigate a set of polymer blends comprised of poly(vinylpyrrolidone) (PVP) with dextran at a ratio of 50:50 (w/w) and gained spatially resolved insights into the morphology of the blend.[77] Figure 1.5 shows that molecular weights of polymer blends could vary the morphology or phases of polymer films according to the AFM mapping and local mid-IR spectra acquired at nanoscale. Hitesh *et al.* used AFM-IR for miscibility determination of amorphous solid dispersion (ASD) of itraconazole (ITZ) and hydroxypropyl methylcellulose (HPMC) in conjunction with differential scanning calorimetry (DSC).[78] As shown in Figure 1.6, the spectra from the discrete domains show the presence of a carbonyl peak (indicative of the ITZ-rich phase), whereas the continuous phase or drug-lean phase either lacks the carbonyl peak or has a low signal at 1700 cm^{-1}. The AFM results revealed that the ITZ-HPMC system was not uniformly mixed, but had a phase separation. Conversely, the DSC results

showed that the ASDs were miscible. Thus, miscibility evaluation in drug−polymer systems is one of the unique analytical capabilities of AFM-IR.

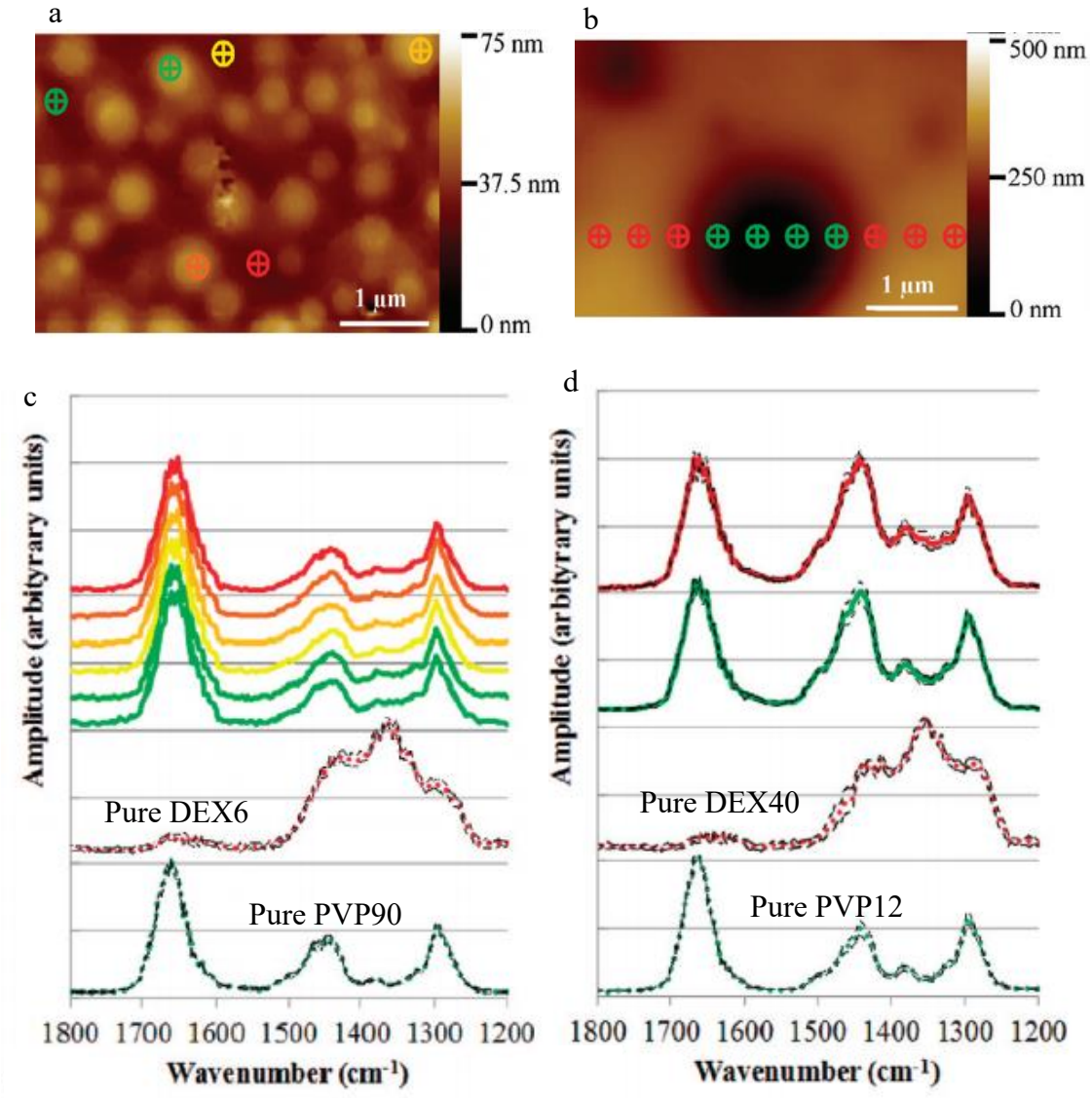

Figure 1.5 Localized nanoscale mid-IR spectra of a DEX6-PVP90 blend (Left column) and a DEX40-PVP12 blend (Right column). (a-b) Topographical images (the positions of the spectral measurements are marked). (c-d) Local nanoscale mid-IR spectra. (Dextrans molecular weights 6,000 (DEX6) and 40,000 (DEX 40); PVP grades K 12 (PVP12) and K 90 (PVP90)). The color scales on the upper images show the Z-height of the sample.
Source: Ref.[77]

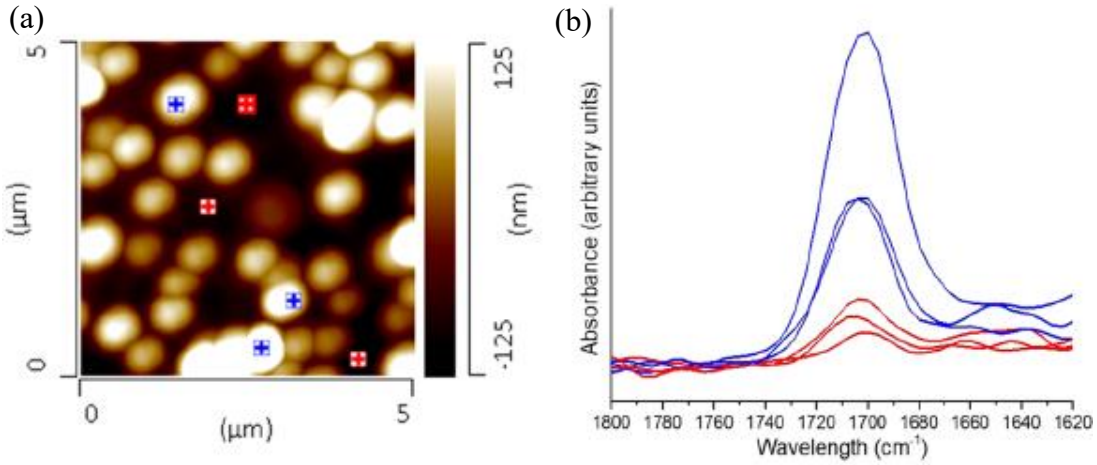

Figure 1.6 AFM topographic image and local scale IR spectra of the ITZ-HPMC ASD films. (a) AFM topographic image; (b) local scale IR spectra obtained from the points marked by blue and red cross. The color scale on the left image shows the Z-height of the sample.
Source: Ref.[78]

1.2.1.3 Applications in Biological Materials. Biopolymers, cells and other biological specimens have chemically distinct structures that are usually smaller than the diffraction limit of infrared wavelengths.[79] AFM-IR can provide subcellular chemical information and better illustrate cellular features of interest.[59] Kennedy *et al*. used the AFM-IR technique to characterize human epithelial cells and resolved membrane boundaries, and the nuclei was at a sub-50 nm resolution (Figure 1.7).[80] Vitry *et al*. used a combination of AFM-IR and mode synthesizing atomic force microscopy (MS-AFM) to estimate the size distribution of triglyceride vesicles (intracellular lipid) produced by *Streptomyces* bacteria. AFM-IR was used to detect the localization of the vesicles at a specific IR band of 1,740 cm^{-1}. In MS-AFM, mechanical actuators excite the probe and the sample at different frequencies to reveal the presence of vesicles and their sizes inside the cells (Figure 1.8).[81]

Similarly, AFM-IR successfully verified the location and sizes of poly(hydroxybutyrate) (PHB) produced by *Rhodobacter capsulatus* bacterium for energy storage.[82] PHB is a kind of bioplastics with similar mechanical and thermoplastic properties

with commercial polymers.[83] In this way, AFM-IR is an important tool for deciding the proper culture for PHB production. Baldassarre *et al*. studied the amide I absorption maps in human HeLa cells using AFM-IR. It has demonstrated that label-free chemical characterizations of biological samples with a higher lateral resolution than the diffraction limit of FTIR can be acheived.[84] Figure 1.9 shows that due to the inhomogeneous distribution of the protein density, comparison between the AFM-IR maps and the topography of human HeLa cells reveals the anomalies in the contour of the cell. This could not be detected by AFM topography imaging only. This study might indicate a potential application for medical diagnostics. Here AFM-IR could detect anomalies in the cell structure and even track exogenous molecules by comparing their IR spectra with those of the biochemical constituents in the cell.[84] The powerful AFM-IR nanoimaging of live cells may enable the studies of surface chemical heterogeneity at different cell growth stages or evolution conditions (*e.g.*, during carcinogenesis).[80]

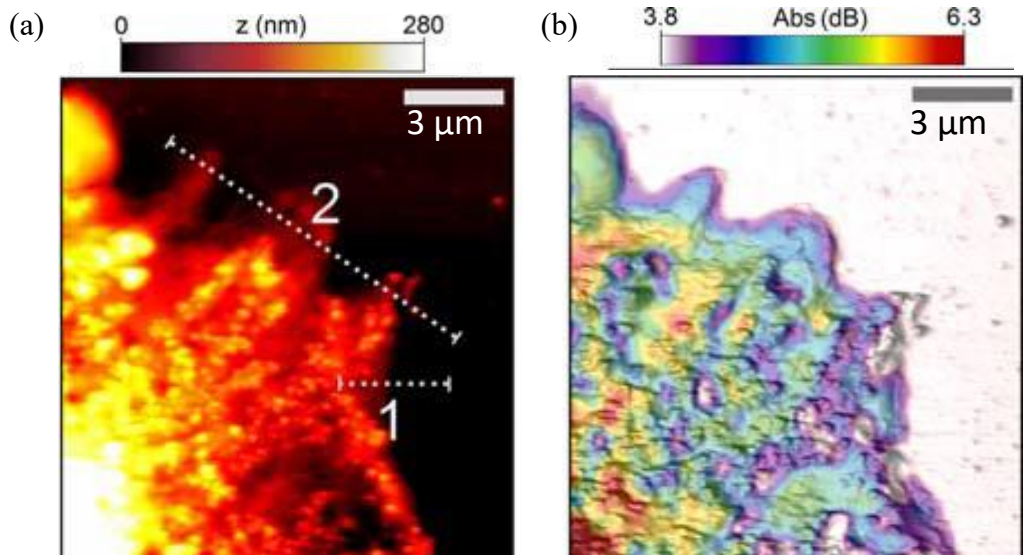

Figure 1.7 AFM topography and IR absorption images of the human epithelial cells. (a) AFM topography (The color scale on the top shows the Z-height of the sample). (b) AMF-IR absorption imaging (The color scale on the top shows the intensity of IR absorption signal).
Source: Ref.[80]

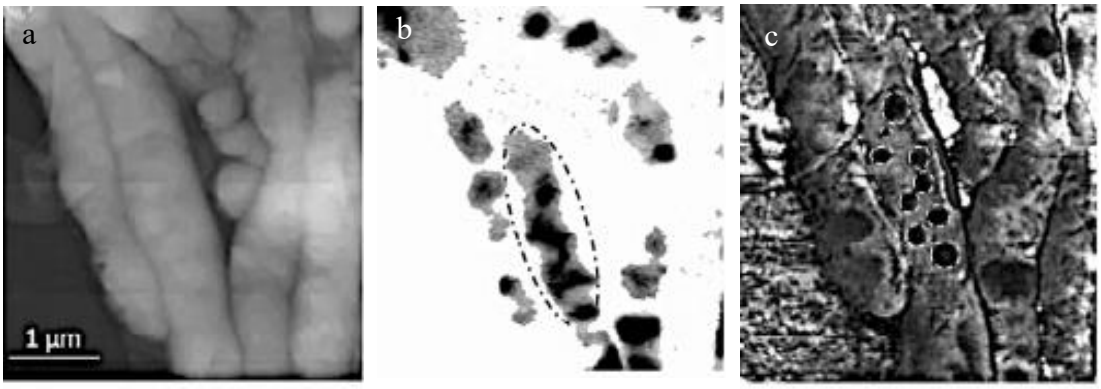

Figure 1.8 AFM topography, IR mapping and MS-AFM images of the vesicles inside the bacteria. (a) AFM topography; (b) AFM-IR chemical mapping at 1,740 cm^{-1}; (c) MS-AFM image at $\Delta f = 50$ kHz.
Source: Ref.[81]

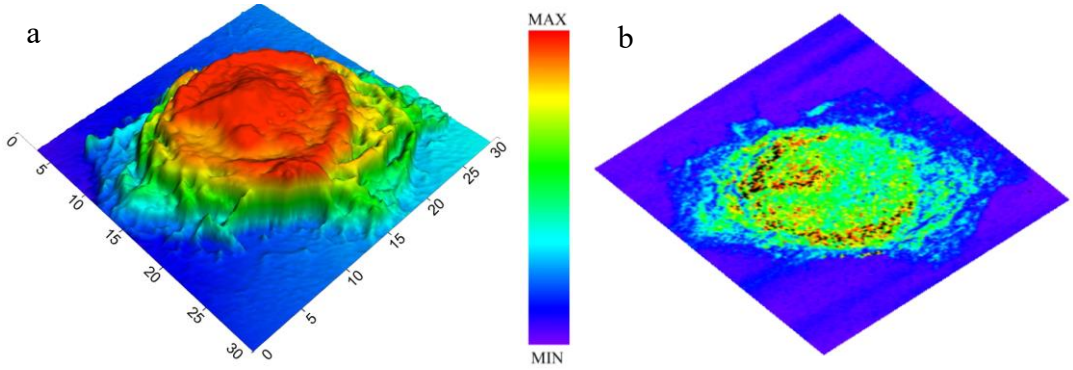

Figure 1.9 The AFM topography and IR mapping images of a single HeLa cell. (a) Three-dimensional morphology and (b) AFM-IR image at 1660 cm^{-1}. The inner part corresponds to the cell nucleus. In the AFM-IR image, the red-yellow dots mark the maximum of the amide I signal. Map size is 30 × 30 microns. The color scale in the middle shows the Z-height of the sample and the intensity of IR absorption signal.
Source: Ref.[84]

1.2.2 Limitations of AFM-IR

Several potential limitations are perceived from our polymer research and relevant literature survey and are herein discussed. They provide insight into the use and potential pitfalls of AFM-IR and other alternative solutions.

First, morphological variations (*e.g.*, sample height or roughness) may affect the characteristics of thermal expansion caused by the IR absorption, especially when the

thermal expansion scale is much smaller than the roughness of the sample surface. Consequently, the detection sensitivity may be reduced. To verify that the IR absorption mapping is not effected by the surface roughness, one should collect IR mapping with at least three different laser wavelengths, centered on the identified resonant wavelength. If no sample morphology-caused artifacts exist in AFM-IR images, the intensities of the domain polymer at the two non-resonant wavenumbers should be much lower than that obtained at the resonant wavenumber. Moreover, the contour of the height in morphological images, obtained at the two non-resonant wavenumbers, should be hardly distinguishable as compared to that obtained at the resonant wavenumber.[84]

Second, AFM-IR is also useful for characterizing multilayer films, which are applied commercially in the products from food packaging to adhesives.[59, 85] However, sample thickness should neither be too thin nor too thick. Ideally, a sample thickness between 100 nm to 1 μm could lead to optimal thermal expansion, and could be sensitively measured by the oscillating probes.[86] For samples thicker than hundreds of micrometers, a large amount of IR energy absorbed by the sample results in a low signal-to-noise ratios (SNR).[87] To improve spatial resolution, microtoming or drop casting films can usually be employed to reduce sample thickness to 0.1-1 μm. Multilayer films can be analyzed by examining their cross-sections using AFM-IR.[88] For thin samples (thickness smaller than 1 μm), the AFM-IR signal increases linearly with thickness.[86] According to the theory presented by Dazzi *et al*, the AFM-IR signal (S) is related to the absorbed energy per unit area (U_{abs}), the sample thickness (z), the sample thermal expansion coefficient (α_{exp}), and the sample thermal conductivity (η): $S \sim \frac{\alpha_{\exp}}{\eta} \cdot U_{abs} \cdot z^3$.[89, 90] Clearly, samples with high heat conductivity and thermal diffusion may limit detection sensitivity.

Third, due to the tip-sample interactions, sample surfaces may be structurally disturbed or dragged, which may limit the application in imaging soft and sticky materials. Recently, Anasys Instruments introduced the Tapping AFM-IR to complement the contact mode and mitigate the negative impacts from tip-sample interactions.[91] Highly porous samples or samples with large topographic variations are also not conducive for IR nanoimaging. This is due to steric constraints of the tip apex reaching all regions. Furthermore, despite the generally weak perturbing nature of IR radiation, sample heating, imposes a tradeoff on the IR intensity between the signal level and thermal load (leading to sample softening or local melting).[58]

Fourth, the high resolution mapping by AFM-IR requires a slow scanning rate (50 $nm \cdot s^{-1}$ –1000 $nm \cdot s^{-1}$) and renders the risk of low SNR. In order to eliminate the noise and enhance the SNR, extensive measurements (typically 256 measurements per wavenumber per pixel) are needed. This can take long acquisition times. Consequently, it usually takes several minutes to collect an IR spectrum at a fixed wavelength, and hours for two-dimensional IR absorption mapping. Recently, the cantilever transducer has been improved to increase the SNR of AFM-IR by a factor of six.[92] With the introduction of the wavelet transform windowing method, the AFM-IR measurement is sped up by 32-fold.[76]

Fifth, AFM-IR with contact mode has the limitation on samples with porous structure, high stickiness or rough surface. AFM-IR was tried on the CNT samples with sorption of AAP and the AFM-IR tip failed to detect the CNT. One reason was that the tip dragged the CNT around and the topography image was from the substrate without CNT. Second reason was that the CNT would adsorb on the tip and get the tip contaminated. Third reason for failure to detect the trace amount of AAP on the CNT was the small

amount of AAP was not able to cause effective thermal expansion. Consequently, the AFM-IR was not able to detect the AAP on the CNT.

Lastly, AFM-IR characterization is challenged by surface moistures and water content. Since the water molecule may strongly absorb the infrared light and the O-H vibrations are very strong and broad to affect the IR spectrum, the SNR of AFM-IR may significantly be reduced. For many sample tests, it is desirable to achieve *in situ* characterization (*e.g.*, in liquid), which has not been reported so far.

1.2.3 Principles and Applications of AFM-Raman

Raman spectroscopy, complementary to Infrared spectroscopy, is an indispensable tool for analyzing chemical species, surface defects, mechanical and thermal properties.[93-96] Raman spectroscopy is particularly useful for detecting molecular structures and symmetry.[97] In Raman spectroscopy, a sample is illuminated by a laser beam to induce scattered light. This scattered light has a frequency difference from the incident light, which is used to construct a Raman spectrum.[98] However, to produce strong Raman scattering, a large number of molecules or a big sample size is usually required. Furthermore, its resolution is limited to the micrometer scale due to the Abbe diffraction limit.[99] The integration of AFM with Raman offers a unique combination of acquiring the physical properties (AFM) and chemical composition (Raman) for samples. One of the combined AFM and Raman techniques is named co-localized AFM-Raman, which shuttle the sample between the AFM platform and the Raman spectrometry (Figure 1.10).[100] Raman measurements are made on the same sample spot as AFM images and are acquired by translating the sample with a high-accuracy positioning stage to ensure the high performance of both systems. Even though the spatial resolution of analysis is still diffraction-limited, the co-localized

AFM-Raman instrument has been used to study the material properties in different research fields such as semiconductors, graphene, carbon nanotubes, polycrystals and epoxy compound.[100-104]

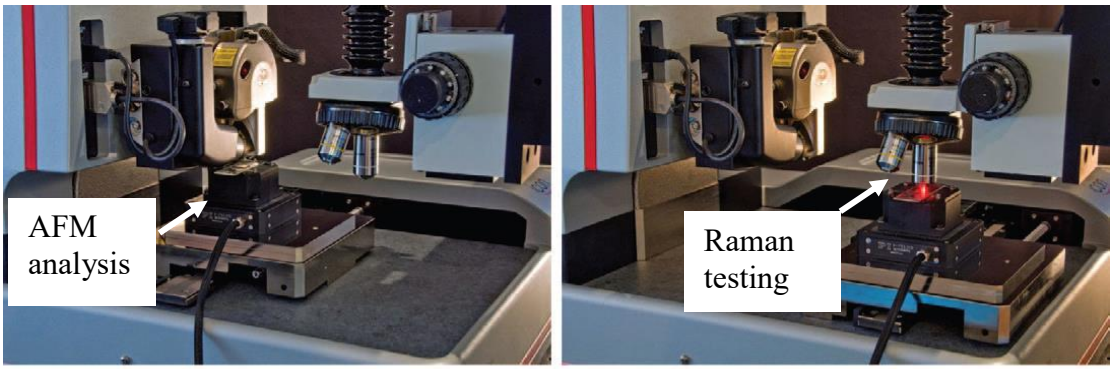

Figure 1.10 View of the co-localized AFM-Raman instrument (Dimension Icon AFM-Raman system, Burker). The stage shuttles the sample between the AFM head (left) and the Raman objective (right).
Source: Ref.[100]

In the 1970s, it was found that a roughened metal substrate usually made of gold or silver would produce intense Raman scattering from the sample on the substrate. Here the Raman signal could be intensified by factors up to 10^{14}-10^{15} (Figure 1.11a).[105] This discovery led to the development of surface-enhanced Raman spectroscopy (SERS).[106-110] In SERS, these roughened metal nanostructures are excited by laser and create a highly localized (plasmonic) light field, due to the resonant oscillation of the surface charges.[111, 112] When a molecule is placed close to the enhanced field at the surface, the Raman signal can be enhanced greatly. Based on the enhanced Raman signals, it is possible to detect lower concentrations (down to parts per trillion level) without the need for fluorescent labeling.[113] Because the SERS experiments were usually carried out at roughened metal surfaces and only coinage metal (Ag, Au, and Cu) substrates provide strong Raman enhancements, it is difficult to study atomically smooth, well-defined single-crystalline

surfaces.[99, 114] The integration of SERS and AFM overcame these obstacles and created a powerful chemical imaging tool known as tip-enhanced Raman spectroscopy (TERS).[99] In TERS, a sharp metal or metal-coated AFM tip is positioned at the center of a laser focus. This tip is typically coated with silver or gold (diameter of apex around 10-30 nm). Under the laser irradiation, a local electromagnetic field at the apex of the tip is enhanced. Then the SERS effect occurs within the vicinity of the tip-apex. Due to the localized surface plasmon resonance and the "lightning rod" effect,[65] TERS results in unparalleled spatial resolution and increased Raman signal intensity that is much higher than regular Raman and confocal Raman.

In fact, co-localized AFM-Raman technique is actually a simple combination of AFM and Raman spectroscopy without the enhancement of Raman signals and sensitivity. There is a strong misunderstanding of AFM-Raman and TERS techniques. AFM-Raman is a combination of AFM system with confocal Raman module. Such combination provides users with simultaneous measurements in AFM and Raman of the same point of interest, so you can overlay topography/electrical/mechanical maps (from AFM) with chemical distribution (from Raman). AFM-Raman is a very powerful system, but it doesn't give you nanometer spacial optical resolution. TERS is a technique based on combination of AFM and Raman. In order to perform TERS you need to have good and stable AFM-Raman system and most importantly, the TERS tip. If you use AFM-Raman with conventional cantilever you won't get any TERS signal. However, with special TERS tip, you might be able to achieve nanometer resolution. One more thing from the theory behind TERS technique is that TERS signal is: (1) Great from 1D material (quantum dotes); (2) Mediocre from 2D material (single nanotubes) – drops 10-100 times comparing to 1D samples; (3)

Low from 3D materials (thin films) – drops 10-100 times comparing to 2D materials. In practice, things are much more complicated, as not every sample works with TERS and you need a proper TERS tip, good substrate and stable system.

As shown in Figure 1.11b, the laser beam in TERS can be focused from below onto the AFM tip coated with SERS active metal or metal nanoparticles.[115] The enhanced Raman scattered light is collected in a backscattering mode with the same microscope objective where the laser beam is provided as illustrated in Figure 1.12a.[115] To perform the TERS measurement under this configuration, sample layers should be "transparent" so that the laser beam can effectively pass through sample layers and irradiate the TERS tip.[116, 117] Alternatively, following the similar illumination and scattering modes as SERS, a long working distance objective can be placed at a tilted angle above the sample surface (Figure 1.12b).[118] Finally, a parabolic mirror was reported to focus the laser onto a sample spot and direct the incident rays that are parallel to the axis of the mirror (Figure 1.12c).[119]

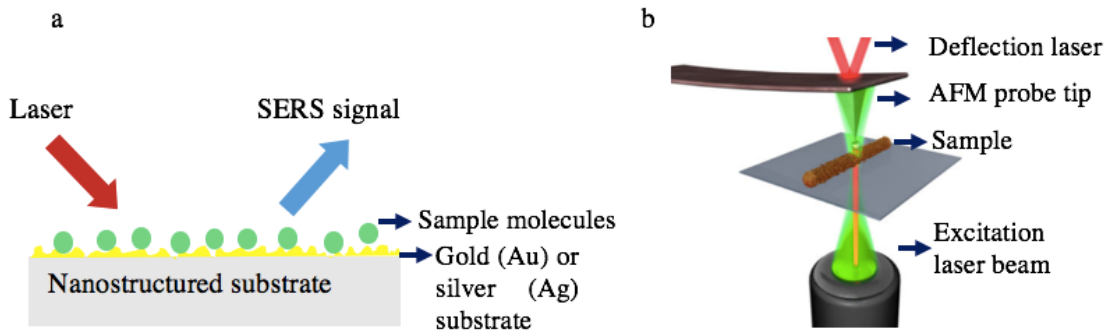

Figure 1.11 (a) Conceptual illustration of SERS and (b) schematic description of a TERS setup.
Source: Ref.[115]

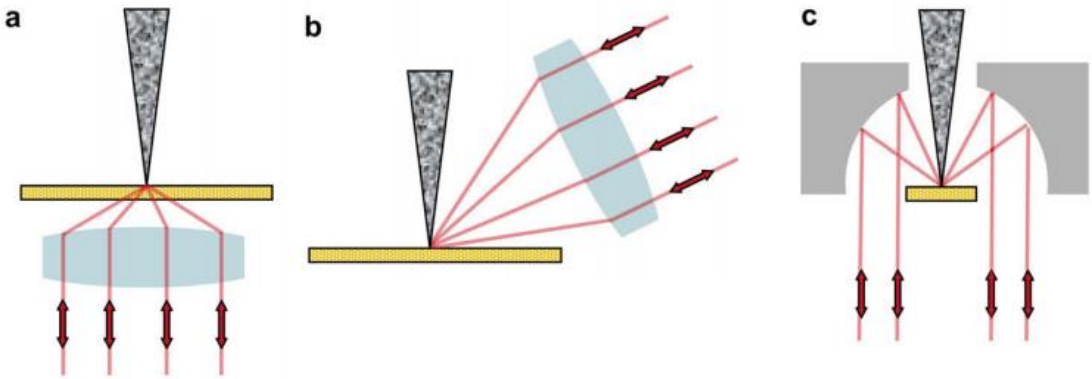

Figure 1.12 Three optical configurations of the illumination on the TERS tip. (a) Bottom illumination using an inverted microscope, (b) side illumination with a long working distance objective and (c) illumination with a parabolic mirror.
Source: Ref.[116]

1.2.3.1 Application in Material Characterization. In applications of polymer blend characterization, Yeo *et al*.[120] performed TERS on a mixed polyisoprene (PI)/polystyrene (PS) thin film to investigate the surface composition. The results show that the PI and PS were detected at the surface and subsurface, respectively, and the nanopores on the polymer film were resolved as well (Figure 1.13). A wealth of structural information with a nanometer spatial resolution outperforms the 2D chemical mapping by conventional analytical Raman spectroscopy. Moreover, TERS can analyze physical properties such as elasticity in materials. For example, Yano *et al*. employed pressure-assisted TERS with silver-coated AFM tip to investigate the mechanical properties of carbon nanotubes in contact mode. The results indicated that TERS is not only well suited for samples with different elastic properties but also achieves a super-high spatial resolution (4 nm).[121]

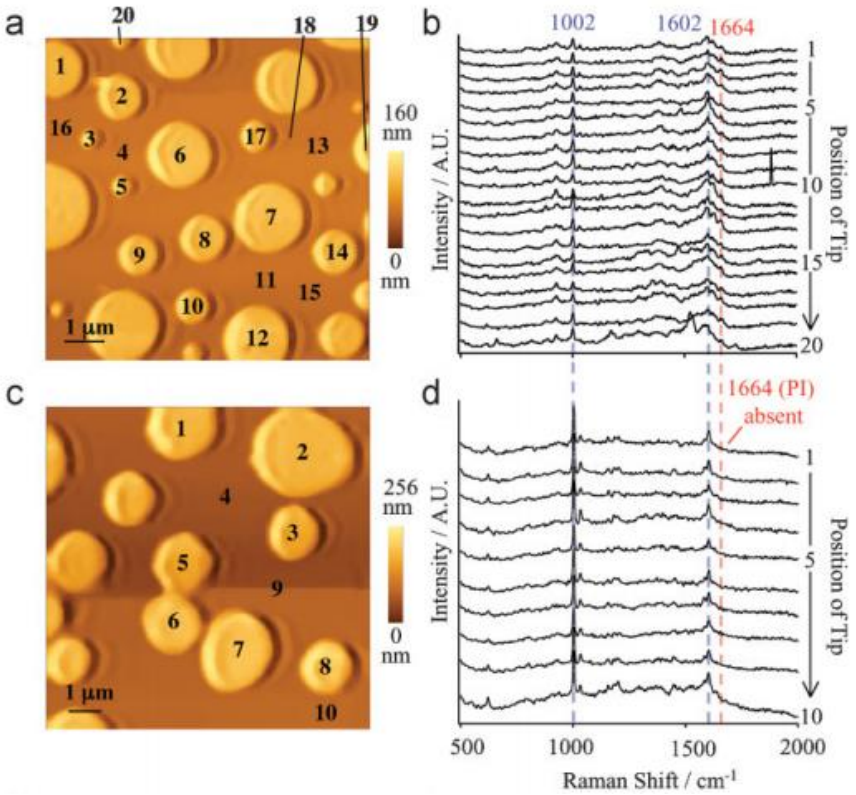

Figure 1.13 AFM topography images and TER spectra of a PI/PS film. (a) AFM topography image; (b) sequence of TER spectra collected from the positions depicted in (a); (c) AFM topography image of a hexane-washed PI/PS film; (d) sequence of TER spectra collected from the positions depicted in (c).
Source: Ref.[120]

1.2.3.2 Application in Biological Materials. TERS is an attractive technique for the label-free, real-time and high-resolution characterization of complex biological materials (*e.g.*, biomolecules, cells, viruses and bacteria).[115, 122-124] For example, Sweetenham applied TERS to investigate the topographical, mechanical, and chemical properties of lipid bilayers with high spatial resolution.[125] This study highlights a new avenue to study the complex heterogeneous cell surfaces *in situ*. Protein aggregates and macromolecules, such as DNA, RNA, amyloid and collagen fibrils, were also extensively studied by TERS.[126] For example, Figure 1.14 shows the high-quality Raman spectra of the nucleobases at different positions along the single-strand RNA chain using TERS.[123] Wood *et al*. used TERS to analyze hemozoin crystals in the digestive vacuole of a sectioned malaria parasite-

infected cell with a spatial resolution of less than 20 nm.[127] The AFM images clearly showed the location of the crystal and the TER spectra identified the characteristic bands of hemozoin (Figure 1.15).

Moreover, specially configured TERS can work with samples in the presence of water or moisture, which largely helps maintain the native physiological conditions of biological samples. Shmid *et al*.[128] demonstrated TERS experiments in liquid for the first time. As shown in Figure 1.16, the tip is mounted below a Teflon plate with a window, through which the laser goes through. A charge coupled device (CCD) camera is used for capturing images. The sample and AFM probe are immersed in a droplet of water, where a meniscus is formed between the sample substrate and the Teflon plate. This setup enabled the investigation of biological cells, cell membranes, or supported lipid bilayers in aqueous environments by TERS[116]. The water environment largely preserves the original state of samples and prevents their alternation from heat and the probe tip from carbon contamination.[129]

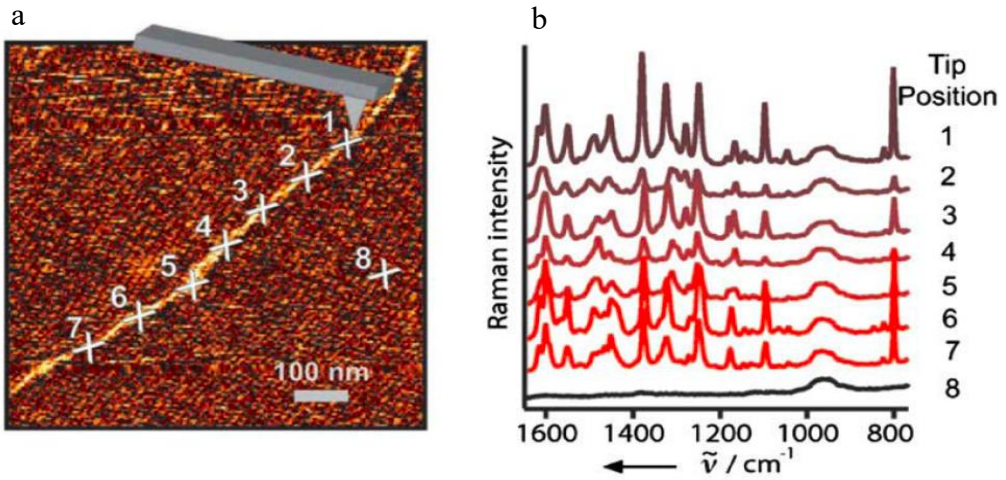

Figure 1.14 TERS experiment along an RNA strand. (a) Topography image showing seven adjacent spots corresponding to the positions of the TERS experiments and one additional spot for the reference measurement (position 8). (b) Raman spectra of the positions in (a).
Source: Ref.[123]

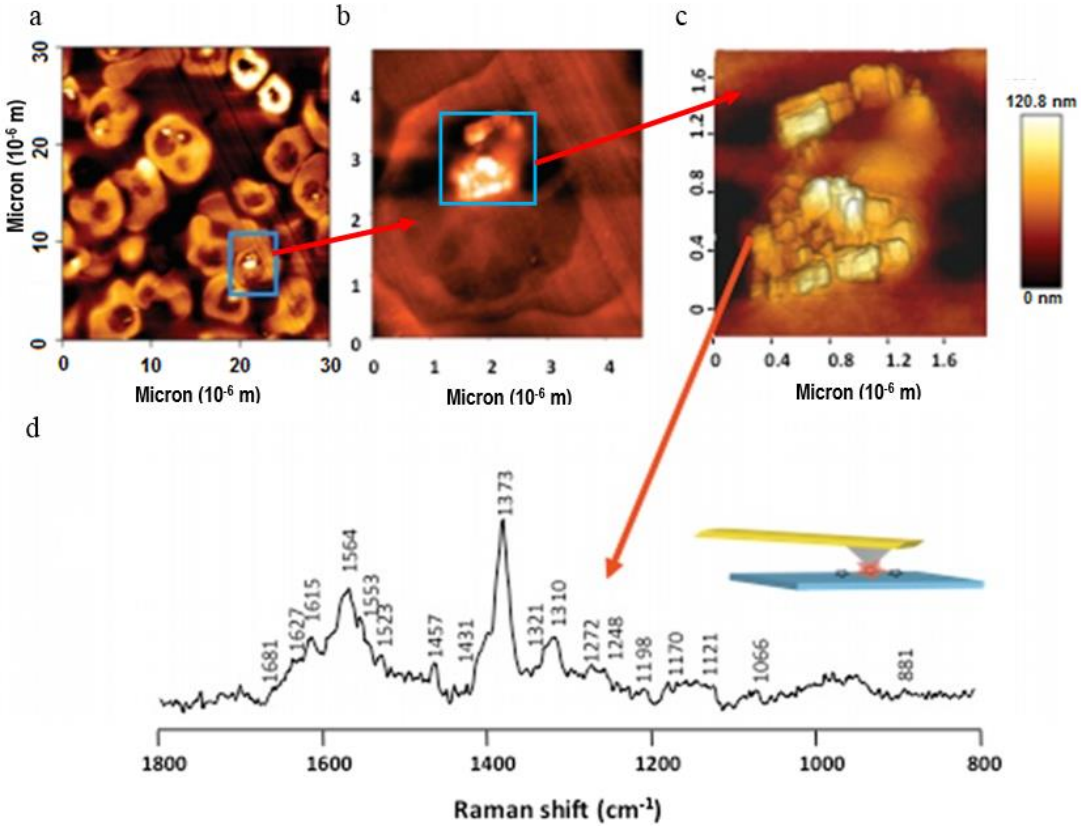

Figure 1.15 AFM images and TER spectrum of hemozoin crystals within a sectioned erythrocyte. (a-c) AFM images recorded of sectioned cells prior to TERS acquisition. (d) TER spectrum recorded of the edge of a hemozoin crystal.
Source: Ref.[127]

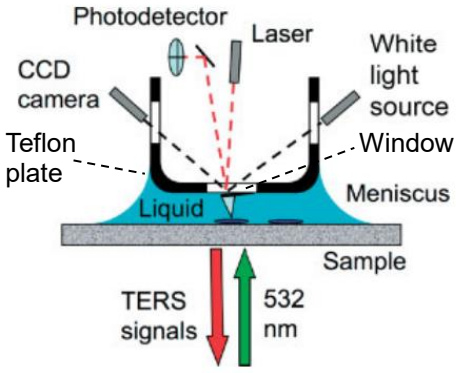

Figure 1.16 Schematic diagram of the TERS setup in aqueous conditions. Reprinted with permission.
Source: Ref.[128]

1.2.3.3 Application in Catalysis Research. TERS has proven to be useful for *in situ* chemical mapping of catalytic solids and surfaces, providing ample opportunities to elucidate reaction mechanisms.[130-134] Harvey *et al*. used AFM-TERS to analyze the photo-oxidation of rhodamine-6G (Rh6G) over Al_2O_3-supported Ag NPs.[131] The results showed that not only the local heterogeneities of NP size and shape were successfully resolved, but that the different chemical reactivity was identified at nanoscale. Additionally, this study demonstrated the capability of AFM-TERS to correlate material structures with catalytic activity in a heterogeneous catalysis. It also helped identify catalytically active sites.[135] The application of TERS for *in situ* photo-activated catalytic reaction was demonstrated by Van Schrojenstein Lantman *et al.*[130] Time-dependent Raman spectra collected during the reaction occurred at the nanoscale (Figure 1.17). This study also opened the door for the real-time measurements in heterogeneous catalysis research.

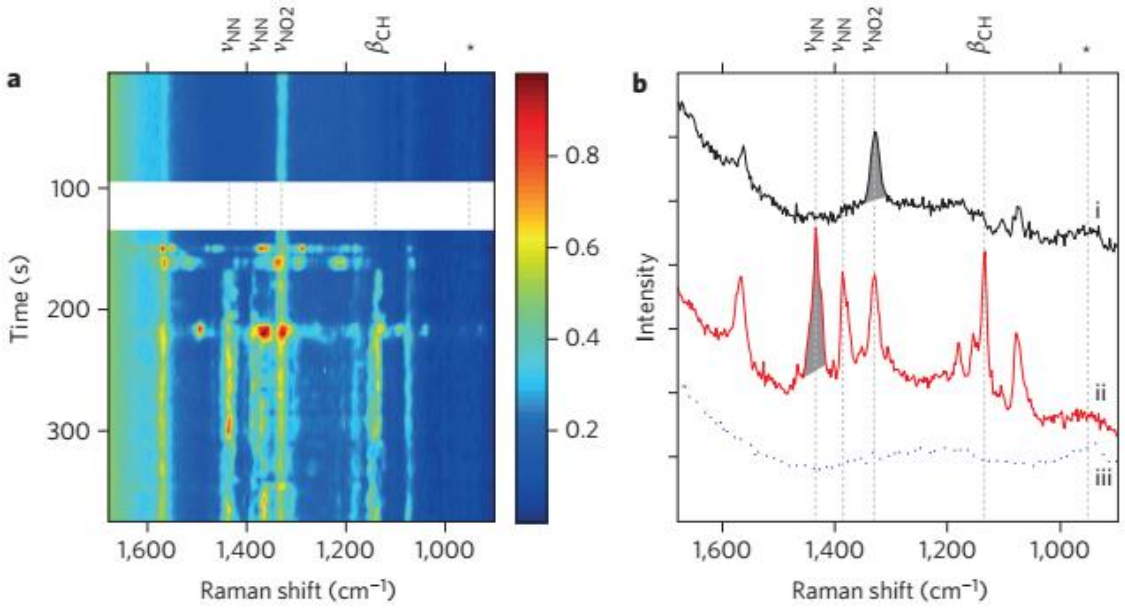

Figure 1.17 Time-dependent TERS measurements before and after reaction. (a) Time-dependent TER spectra shown before (top) and after (below the white band) illumination. (b) Two spectra from (a) are shown: spectrum (i) is taken at 90 s and spectrum (ii) at 265 s. Spectrum (iii) is the reference spectrum taken after the time-dependent spectra. Reprinted with permission.
Source: Ref.[130]

1.2.3.4 Application in Crystallization Studies. In the research of optical nanocrystallography, TERS was used to determine the ferroelectric order and intrinsic ferroelectric domains of barium titanate ($BaTiO_3$),[136] as shown in Figure 1.18. The selection of different transverse optical phonon modes is due to the versatility of the instrument. TERS can further probe crystals exhibiting polar phonon modes and identify crystallographic orientation of nanocrystals or the nanodomain topology of bulk materials.[99] AFM-Raman is generally applicable to most crystal classes. It is also useful for analysis of structural inhomogeneities, phase transitions, ferroelectric order and related finite-size effects occurring on nanometer length scales with simultaneous symmetry selectivity, nanoscale sensitivity and chemical specificity.[136]

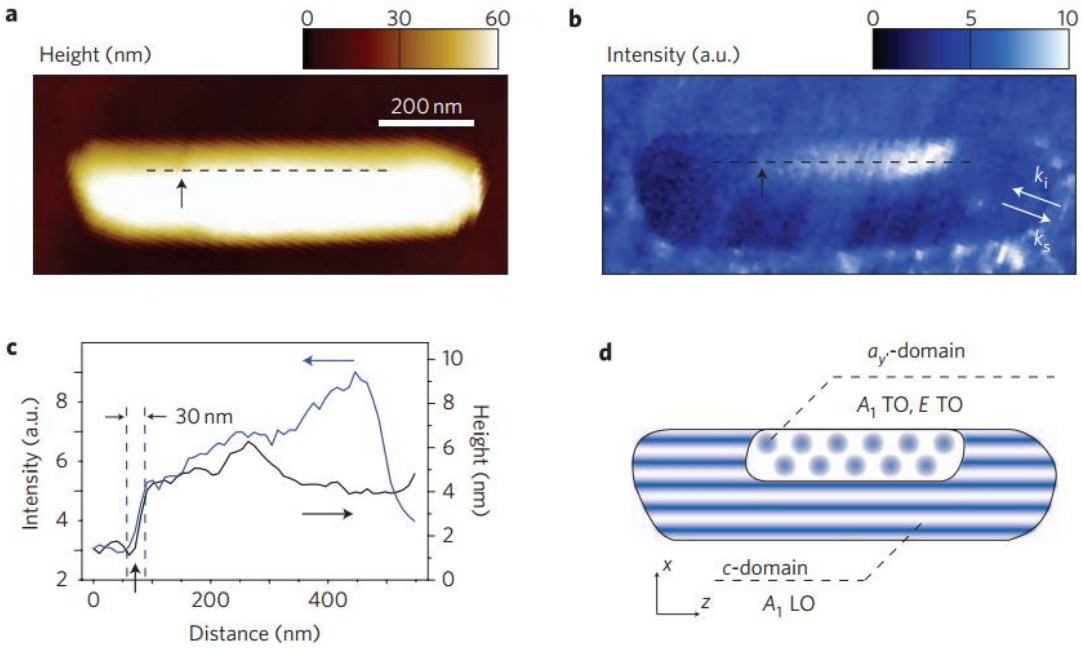

Figure 1.18 Spatially resolved TERS for ferroelectric domain imaging. (a) Topography of a $BaTiO_3$ nanorod. (b) The spectrally integrated TERS signal for ferroelectric domain imaging. (c) Lateral cross-section along the dashed lines in (a) and (b) of the region of high TERS signal (blue) and corresponding topography (black) on the rod. (d) Domain assignment based on the Raman selection rules for the TERS geometry used. Reprinted with permission.
Source: Ref.[136]

1.2.4 Limitations of AFM-Raman

Despite the advances, TERS still has many inherent challenges that hamper its use in many applications by various users. These challenges are largely related to its complex operation, requiring delicate handling by skilled personnel. Additional skills including the reproducibility of the Raman signal enhancement, durability and contamination of TERS probe tips are also required.[137] Moreover, functional TERS tips designed with precision-controlled geometry and surface coatings are essential for local amplification of the Raman signals and nanometer spatial resolution.[116] As universal TERS tips and excitation laser illumination conditions (intensity and wavelength) are not available for various samples, one must determine the optical selections on a case by case basis. Uncertainties such as tip degradation, tip damage, tip contamination, and even sample damage due to the local

heating by the excitation laser need to be considered as well.[116] Particularly, Ag-coated tips may get oxidized rapidly at ambient conditions; whereas, Au tips can be more chemically stable. Moreover, the metal coating (especially Au films) may peel off after several scans due to the weak adhesion of the coating to the tip.[138] To tackle this problem, an ultrathin (few nanometers) protective layer of alumina or silica was alternatively coated on gold and silver TERS tips to increase the tip stability.[133, 139] On the other hand, carbonaceous contaminants on the surface of the tip can enhance artifact Raman signals.[140] To reduce the tip contamination, we can decrease the laser power or reduce the tip scanning time, which may lower the quality spectra and increase the data acquisition time.

In the investigation of biomolecules, such as amino acids and lipids, TERS may be challenged because the vibrational bands produced are similar to those produced by different chemical structures and functional groups in Raman spectra.[141, 142] Moreover, AFM probes might degrade and get contaminated during the measurements, which limits the TERS imaging of large biological samples.[97] Consequently, to date, TERS has been applied only to a limited types of samples including carbon nanotubes,[143] grapheme,[144, 145] Si nanostructures,[146] polymers,[120] and thin molecular layers.[128, 147]

Another limiting factor is that the tip and biological samples may not be able to withstand high temperatures caused by the local heating effects,[148] and thus resulting in morphological changes, which are clearly artifacts (not true changes in chemical compositions).[116] The Raman laser power should be well controlled in order to prevent a significant heating of biological samples.[149] A study of TERS performed on a benzenethiol monolayer showed that roughness could result in a mismatch between the topography image and the Raman mapping image.[147] A possible reason is that the enhanced Raman

signal occurs primarily on the upper terrace of sample surface and not below the tip. This may not synchronize the morphology and TERS images. Thus, TERS is not suitable for samples with steep edges or steps.[116]

1.2.5 Summary and Outlook of Hybrid AFM Technology

The complete understanding of physical and chemical properties at materials interfaces with high spatial resolution will provide a foundation for nanoscience and nanotechnology. Hybrid AFM represents the fusion of physicochemical analysis, high spatial resolving powers, and the ability to operate in ambient conditions. A review of some of the latest developments, applications and limitations of hybrid AFM techniques has been presented in this work. This article critically reviewed the principles, recent developments and applications of the AFM-IR and AFM-Raman (TERS) techniques. Areas of research presented here include polymer, pharmaceutical, biological, catalysis, crystallization and life sciences.

AFM-IR and AFM-Raman are complementary techniques by measuring absorbed and scattered light respectively. However, chemical spectra and chemical images collected at specific IR wavenumbers could be affected by the material surface characteristics (*e.g.*, roughness and overlay of multiple components) and thus produce potential artifacts that AFM-Raman may be able to avoid. Due to the IR limitations, AFM-IR also encounters challenges for wet or moisturized samples. By contrast, AFM-Raman may allow sample analysis in aqueous environments. The challenges such as the reproducibility of the Raman signal enhancement, durability and contamination of TERS probe tips still remain. The operation of TERS requires experienced and skilled personnel. Moreover, materials with high thermal expansion coefficient and small thermal conductivity are good for AFM-IR

measurements. Sample materials with very low thermal expansion coefficient may better be analyzed by AFM-Raman. Particularly, AFM-Raman is especially useful for detecting inorganic and carbonaceous nanomaterials such as graphene and carbon nanotube (CNT).[121, 143, 150-153] Consequently, selecting the appropriate analytical techniques will be based on the sample specifications and the desired selectivity. For a better comparison between these two hybrid AFM techniques, an outlining table of key information of these two hybrid AFM techniques is provided in Table 1.1. On the other hand, a decrease in data acquisition time, the improvement of AFM probing accuracy and versatility and the automatic optimization of the AFM tip and sample interaction are important for high throughput and efficient characterization.

Table 1.1 Table Outlining the Principles, Applications, Advantages and Limitations of AFM-IR and AFM-Raman

Techniques	AFM-IR	AFM-Raman
Principles	• A ZnSe prism is used as a sample holder with a pulsed tunable IR laser as the irradiation source; • IR laser absorbed by the sample is converted to heat, causing a rapid thermal expansion pulse under the AFM tip, in turn exciting resonant oscillation of the AFM cantilever; • The amplitude of the cantilever oscillation is then Fourier transformed to be a function of the laser wavenumber and directly reflects the IR absorption characteristics of the material.[68]	• A sharp metal or metal-coated AFM tip is positioned at the center of a laser focus. This tip is typically coated with silver or gold (diameter of apex around 10-30 nm); • A sample is illuminated by a laser beam to induce scattered light. This scattered light has a frequency difference from the incident light, which is used to construct a Raman spectrum;[98] • The excitation laser light is focused onto the tip-apex to enhance the Raman signal within the vicinity of the tip-apex.[99]
Applications	• Polymer characterization • Pharmaceutical Industries • Biological Materials	• Material Characterization • Biological Materials • Catalysis Research • Crystallization Studies
Advantages	• Nanoscale spatial resolution; • User-friendly; • High reproducibility.	• High Raman signal intensity; • Allows sample analysis in aqueous environments;[128] • Especially useful for detecting inorganic and carbonaceous nanomaterials.[121, 143, 150-153]
Limitations	• Morphological variations may affect the characteristics of thermal expansion caused by the IR absorption;[84] • Sample thickness affects the signal-to-noise ratios greatly; [86, 87] • The tip-sample interactions result that sample surfaces may be structurally disturbed or dragged; • Slow scanning rate and long acquisition time for high resolution IR mapping; • Challenged by surface moistures and water content.	• Complex operation, requiring delicate handling by skilled personnel; • The reproducibility of the Raman signal enhancement, durability and contamination of TERS tips are the challenges; [116, 137] • Universal TERS tips and excitation laser illumination conditions (intensity and wavelength) are not available for various samples; • Carbonaceous contaminants on the surface of the tip can enhance artifact Raman signals;[140] • The tip and samples may not be able to withstand high temperatures caused by the local heating effects.[148]

To summarize, the past achievements in AFM-IR and AFM-Raman are primarily focused on above mentioned research or industrial applications. In fact, there are many potential areas or applications that benefit from the integrated AFM platforms. For example, the characterization of functional engineered nanomaterials, such as nanotubes, nanowires, graphene, and semiconductor, the identification of molecules in biological interfaces, as well as the detection of trace organic substances are important for the research in environmental applications, energy production and food safety.

1.3 Current Research on Membrane Fouling/Defouling Model Analysis

Membrane fouling has been a limiting factor for membrane filtration in diverse applications in separation and water treatment.[154-159] Membrane fouling is primarily attributed to membrane–foulant interactions followed by subsequent foulant–foulant interactions.[160-163] Interfacial properties of both membranes and foulants have important impacts on membrane fouling kinetics and fouling removal or defouling.[161-168] Therefore, the delineation of the membrane–foulant or foulant–foulant interaction mechanisms are critical to understanding their roles in membrane fouling and defouling processes.

Natural organic matter (NOM) and protein are common membrane foulants known to cause significant loss of membrane permeability and are often used as foulant models to analyze membrane fouling mechanism.[161, 162, 168-174] In aqueous solutions, NOM and protein usually bond together to form colloidal aggregates of tens or hundreds of nanometers in size.[160, 165, 167] Most previous studies examined bulk scale membrane fouling behavior and evaluations, such as membrane fouling index, membrane flux decline rate and flux resistance.[175-178] However, membrane characteristics, such as

hydrophobicity/hydrophilicity, surface charge, roughness, pore size and porosity, as well as foulants properties (*e.g.*, molecular weight distribution, zeta potential and particles size) have proven to impact membrane filtration performance.[158, 179-181] Particularly, the impacts of hydrophobicity and surface charge on membrane fouling during filtration have been reported previously.[158, 179, 182-185] The extended Derjaguin Landau Verwey Overbeek theory (EDLVO or XDLVO theory) is widely used to describe the contributions of surface properties of membranes or foulants to colloidal interactions and fouling potential on membrane filters.[186-188]

Atomic force microscopy (AFM) has been used as a versatile tool for the study and characterization of pristine and fouled membrane surfaces.[189-192] In addition to surface morphology mapping, quantification of interaction forces by AFM greatly provides aid in the understanding of membrane fouling mechanisms.[161, 193-200] For example, interaction forces were measured between polymeric membranes and AFM probes coated with foulants of humic acid (HA) and bovine serum albumin (BSA).[160, 165] Adhesion forces of membrane-foulant and foulant-foulant measured could indicate the fouling propensity.[195-200] Mi *et al*. observed a strong correlation between organic fouling and intermolecular adhesion force, indicating that foulant–foulant interaction plays an important role in determining the rate and extent of organic fouling.[200] Meng *et al*. reported that high membrane–HA interaction forces result in a rapid adsorption of the HA onto the surface or in the inner membrane pore surface, causing severe membrane pore blocking or narrowing and membrane flux decline in the initial filtration stage.[160] Nevertheless, many previous studies assessed membrane fouling or defouling behavior without sufficient examinations of microscale or nanoscale material properties and their contributions to membrane fouling

or defouling processes. For instance, flux decline, flux recovery, and flux resistance are commonly measured to characterize fouling or defouling.[178, 201-204] Clearly, further investigations of fouling formation, defouling processes, and contribution from interfacial forces will provide new insight into the prevention of membrane fouling and rationale design of antifouling membrane filtration processes.

1.4 Current Research on Membrane Aging

1.4.1 Concept of Aging

One of the drawbacks of membrane filtration is that during the filtration process, the membrane is subject to fouling. Consequently, periodic cleaning is required. In the short term fouling is treated with hydraulic cleanings (back pulsing) and in the long term fouling is treated by means of chemical cleaning. Although the cleaned membranes are considered suitable for continued use, they may have suffered damage, which is manifested as holes in the membrane skin.[205] Previous reports on the effect of hypochlorite treatment on UF membranes indicated a flux increase in NaOCl-treated membranes.[206,207] This increase was explained by Wolff and Zydney in terms of a direct relationship between membranes pore size and bleach treatment duration.[208] Qin *et al*. reported a five-fold increase in membrane flux and a narrowed pore size distribution after the hypochlorite treatment.[209] These studies indicated that the magnitude and number of back pulses, and the nature, exposure and concentration of the cleaning agent have an influence on the membrane life time.[22] The membrane aging problem has recently become a key issue.

No established definition of membrane aging can be found in the literature. Membrane aging must not be confused with membrane integrity. If the level of membrane

integrity can be determined, it is not possible to determine the aging of a membrane quantitatively with no reference to the initial state and properties of the membrane. Consequently, the aging study is a comparative study. Membrane aging corresponds to the aging of the materials which constitute the membrane. It depends on the operating conditions of both the production and cleaning/disinfection steps and results in a decrease of productivity, an increase in backwash or cleaning/disinfection step frequency, a modification of the physical-chemical properties of the membrane (elasticity/plasticity of the membrane, membrane surface zeta potential.), an alteration of the membrane selectivity and a loss of integrity.[210]

Even if aging can arise on macroscopic scale by several characteristic symptoms (increase of permeability, modification of mechanical properties), no quantitative criterion has been defined yet to delimit the boundaries of the aging field. Concerning the microscopic scale, the aging characterization remains mainly qualitative even if some quantitative studies have been recently published.[211] For instance, the surface roughness analysis is used as an aging parameter. This measurement has been applied on polyvinylchloride membrane (PVC) before and after chemical cleaning by Zhang *et al*.[212]

1.4.2 Simulation of Aging Process

In order to investigate the aging mechanism, the researchers simulated the aging process by accelerating test. The total dose (concentration × contact time, parameter "c × t") is a concept which suggests that aging generated by a high concentration during a short time equals to the one attributed to a low concentration during a long time. For example, aging experiments lasted for 150 days which would be equivalent to 10 years of use assuming that membranes are subjected to 1h cleaning per day.[213] Generally speaking, the reliability

of accelerated test may be legitimately questioned and a different innovative and representative approach must be used to study membrane aging in order to predict membrane lifetime in given conditions.[214] At water treatment facilities the addition of free chlorine is performed to either prevent the biofouling by back flushing of 1 min with 2–8 mg L^{-1} of NaClO, or to clean the membrane surface from foulants by soaking in 20–400 mg L^{-1} free chlorine for approx. 1 h. Although at treatment plant the membranes are most of the time in contact with water and just periodically with chlorine, the combined effect of oxidation can be expressed as total dose (concentration × contact time) of hypochlorite.

The researchers used aging solution immersion and UV irradiation for aging simulation. Hashim *et al.* investigated the stability of PVDF hollow fiber membranes after immersion into the sodium hydroxide (NaOH) aqueous solution. The effect of NaOH concentration, treatment time and temperature on mechanical properties, thermal properties and crystalline structure of the PVDF hollow fiber membranes were investigated through mechanical strength measurement, surface area analysis, XRD, FTIR and DSC analyses.[215] Antón *et al*. exposed six commercial polymeric UF membranes made of PES to 0.01, 0.1 and 1.0 M nitric acid (HNO_3) and sodium hydroxide (NaOH) solutions at 50 ^oC for 150 days. Water permeability, molecular weight cut-off curves, ATR-FTIR, SEM-EDS, AFM and contact angle measurements were employed to evaluate membrane aging.[213] Bégoin *et al*. made PES membranes age in chlorine industrial conditions at 200 ppm (pH = 9), at 50 ^oC, for a cumulated contact time corresponding to 15 years of use in a plant.[216] Antony *et al*. addressed the mechanistic aspect of hypochlorite attack on a commercial polyamide membrane and the oxidative degradation taking place under active (applied pressure with constant stirring) and passive (unpressurised and unstirred)

conditions.[217] Nystrom and Jarvinen modified hydrophobic polysulfone UF membranes with UV irradiation and hydrophilicity increasing agents and observed that UV irradiation increased flux and the hydrophilicity of the membranes.[218]

We will perform the accelerated membrane aging experiments using both filtration and immersion with the same level of CT. The only difference is that filtration enables the variations of hydraulic flux through the membrane, which may also contribute to aging kinetics.

1.4.3 Characterization of Aging

In most cases, membrane aging is reduced to polymer aging and methods developed are based on the evaluation of polymer characterization. The investigated membrane characteristics include the color change of membrane surfaces (by visual observation),[215] morphology of membrane surfaces (by SEM and AFM),[213] surface hydrophilicity (by contact angle),[213] crystal structure changes (X-ray diffraction),[215] surface charge (by dynamic light scattering), surface functional group composition (by Fourier Transform Infrared spectroscopy, ATR-FTIR and Raman spectroscopy),[213, 215, 217, 219, 220] and water flux and rejection performance[213, 221].

1.4.4 Mechanism of Aging

1.4.4.1 PVDF Membranes. PVDF is an excellent membrane material due to its outstanding thermal stability, mechanical strength, and also its distinction in chemical resistance against a wide range of harsh chemicals. Early investigations reported the observation of brownish discoloration of PVDF after its exposure to a sodium hydroxide (NaOH) solution. Zhang *et al*. observed some changes in the fingerprint region of the fluorocarbon stretching (1250-1000 cm^{-1}) by FTIR analysis after different NaClO exposure

intensity and found the loss of element F in aged membranes by XPS, indicating the defluorination of PVDF in alkaline solutions.[223] However, the detailed aging mechanism and FTIR spectrum were not presented in the paper. In the recent years of publications, the chemical reactions between PVDF and NaOH were explained as a phenomenon of dehydrofluorination[220], in which the carbon–carbon double are formed as a result of the elimination of hydrogen fluoride (HF) units from the polymer.[215, 224, 225, 226] The obtained results indicate that the reaction between PVDF and NaOH was initiated even at low concentrations of NaOH and was aggravated with the extended treatment time, resulting in the decrease in mechanical strength and crystallinity of PVDF hollow fiber membranes. The reaction was accelerated and intensified by increasing the concentration of NaOH and/or treatment temperature.[215]

1.4.4.2 PES/PVP Membranes. Membranes are generally polymerized from blends including several polymers to improve their performances or modify their properties. For instance, it has been underlined that poly (vinyl pyrrolidone) (PVP) consumption, most frequently used additive, can influence membrane transport properties and generate an increase in permeability, or induce a drop of tracer retention and a decrease of membrane hydrophilicity resulting in an increase in fouling.[227]

Winenk *et al*. were the first to study the effect of a treatment with sodium hypochlorite on a PES/PVP membrane. The immersion of the membrane, for pH included between 3.9 and 11.5, leads to a disappearance of PVP.[207] Roesink *et al*. proposed two mechanisms for the selective PVP elimination induced by the action of sodium hypochlorite according to pH: in a alkaline medium, the opening of a ring in the PVP molecules (Figure 1.19); in acid medium, a chain scission of PVP by hypochlorite (Figure

1.20).[228] But Roesink could not find direct evidence for these mechanism while Roesink presented the experiments to give more clarity on the mechanism of the reaction of PVP with sodium hypochlorite.

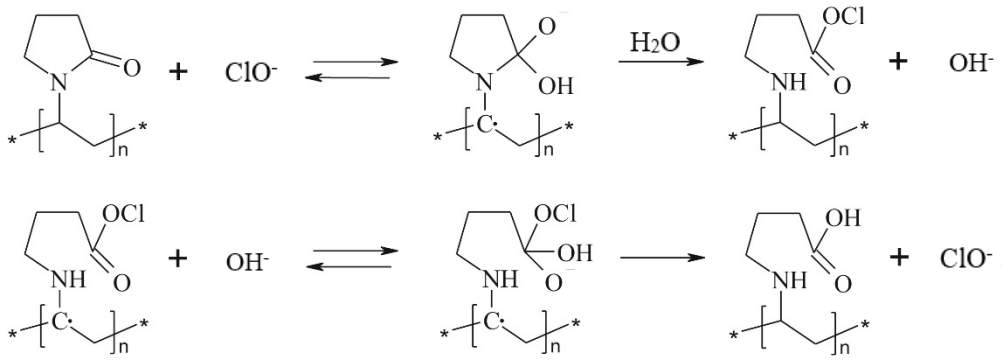

Figure 1.19 Reaction mechanism for the reaction of PVP with hypochlorite in alkaline solution. Ring-opening of PVP.[228]

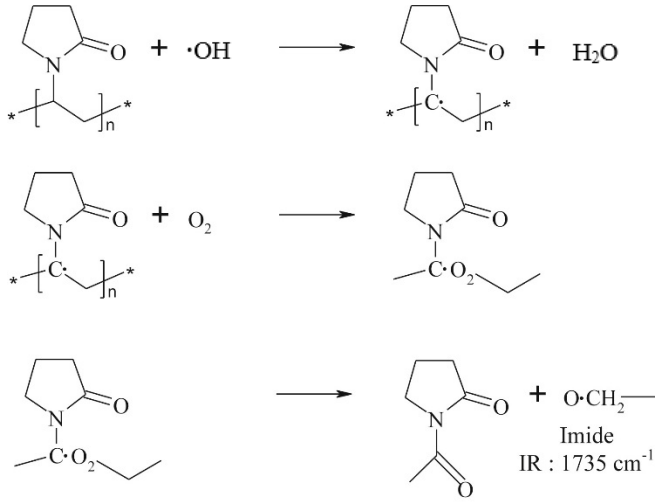

Figure 1.20 Reaction mechanism for the reaction of PVP with hypochlorite in acidic solution. Chain scission of PVP via radical reactions: (a) disproportionation and (b) oxidative degradation.[228]

1.4.4.3 PES Membranes. Yadav and Morison observed a decrease of the whey flux and an increase in the water flux resulting from an exposure of polyethersulfone (PES) membrane to chlorine.[229] The microscopic degradations were observed by ATR-FTIR and SEM-EDX analysis.[230-232] In terms of aging mechanism, two different degradation

mechanism of PES were proposed. The first mechanism shows the formation of sodium sulfonate (Figure 1.21), and the sulfonates groups become sulfonic acid end-groups.[233] Arkhangelsky *et al*. also concluded to the formation of a phenylsulfonate group.[234] It indicates that the chemical aging mechanism of PES membranes is a membrane oxidation leading to partial disruption of $((Ph\text{-}SO_2\text{-}Ph\text{-}O)_n)$ bonds. Another degradation mechanism of PES was proposed due to the sensitivity of $((Ph\text{-}SO_2\text{-}Ph\text{-}O)_n)$ bonds to photodegradation. This mechanism (Figure 1.22) shows that the chain breaking down leads to a group ended by a sulfonic acid and another one ended by a chlorinated phenylic group.[216, 230, 232]

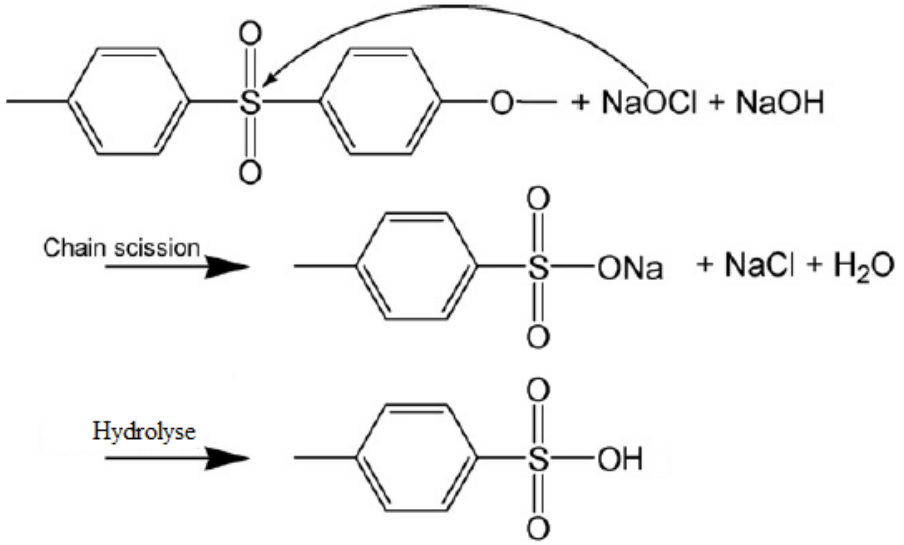

Figure 1.21 The mechanism of formation of sodium sulfonate in PES membrane by NaClO.[233, 234]

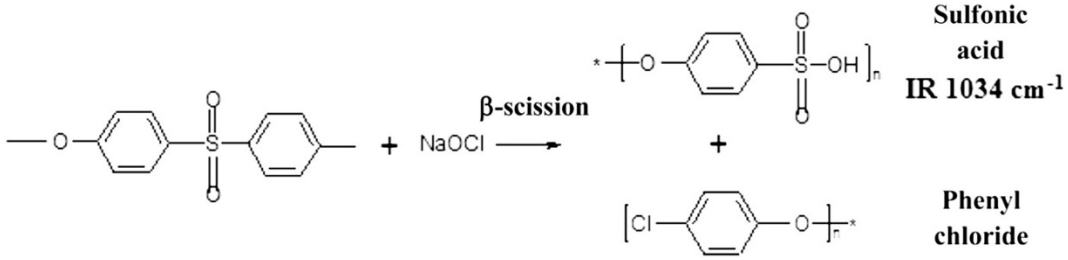

Figure 1.22 The mechanism of chain scission in PES membrane by hypochlorite.[216, 230, 232]

In general, there still remains a challenge to better understand membrane aging. To carry out the aging study, besides the parameters, methods and ways of characterization, another two things should be considered as well. First, as membrane materials evolve, as new processing applications develop, and as environmental and cost pressures drive further changes in the industry, there is a continuous need for investigation to elucidate the aging mechanisms and incorporate them into qualitative and quantitative models. Second, it is also essential for such studies to be conducted under conditions that mimic the industrial process and have sufficiently long run lengths and repeated periods to ensure the best match between the outcomes coming from the research activities and the needs of industrial practitioners. As the published researches show, the aging process should be simulated with filtration instead of immersion experiments.

1.5 Current Understanding of Microwave Irradiation and Nanobubbles

1.5.1 Microwave Technology

Microwaves are a form of electromagnetic radiation with wavelengths ranging from 1 m to 1 mm and frequencies between 300 megahertz (MHz) and 300 gigahertz (GHz) The microwave induces polar molecules such as water, fat, and other substances to rotate and produce thermal energy in a process known as dielectric heating.[235] The adsorbed energy are converted directly into atomic motion and then converted into heat. Many molecules (such as those of water) are electric dipoles, meaning that they have a partial positive charge at one end and a partial negative charge at the other, and therefore rotate as they try to align themselves with the alternating electric field of the microwaves.[236] Rotating molecules hit other molecules and put them into motion, thus dispersing energy.

Consumer microwave ovens usually use 2.45 GHz. While microwaves in this frequency range are not absorbed by most plastics, glass or ceramics, which means that microwaves might not impose direct damage on the polymeric or ceramic membranes. The microwave irradiation was shown to lead to hydrolyzation of starch to the monosaccharide and consequently may enhances surface organic foulants degradation and detachment.[237] Hefa and *et al*. also used the technologies of microwave-induced degradation through hydrophobic microporous mineral coupling adsorption to remove the organic pollutants from water efficiently.[238] Giancarlo and *et al*. utilized a microwaves-assisted, solvent-free method for soil decontamination, which marks a considerable advance in the search of more efficient, environment-friendly procedures for the degradative oxidation of persistent organic pollutants.[239] But its applications and underlying mechanisms of microwave irradiation in mitigating membrane fouling and cleaning membranes have not yet been reported thus far, which would be one focuse of research.

In recent years, microwave (MW) radiation has attracted great attention in environmental field. Interesting reports have appeared on the application of MW heating technology for regenerating activated carbon[240] and removal of ammonia from wastewater.[241, 242] MW radiation was also used to remediate soils contaminated by persistent organic pollutants[243-246] and heavy metals[247], and promising results were achieved. The microwave technology was introduced to couple with membrane distillation. A novel membrane module and device which are suitable for microwave vacuum membrane distillation were designed. The microwave irradiation significantly improved the mass transfer process of the vacuum membrane distillation. Correspondingly, some prior research showed that microwave irradiation could effectively induce uniform heating

in the radial direction of the membrane module, and significantly improve the mass transfer process of vacuum membrane distillation.[248] The effects of the microwave irradiation on membrane fouling and membrane properties were investigated as well.[248]

Huang and Yang[249] analyzed the effect of microwave photons on the chemical bonding and suggested that it was difficult for microwave to break the chemical bonds directly as the energy of microwave photons was much less than the bonding energy. But microwave could weaken some chemical bonds, which affected the stability of the substance. In the current study, the use of microwave irradiation weakened the chemical bonds and caused the detachment of the fouling layer from the membrane surface, therefore mitigated the fouling behavior. The increase of the permeation flux observed was also attributed to the effect of microwave on chemical bonding. With the fouling substances detached from the membrane surface, certain number of the blocked pores was recovered which led to an increased flux.

An advanced oxidation process (AOP) combining hydrogen peroxide and microwave heating was used for the solubilization of phosphate from secondary municipal sludge from an enhanced biological phosphorus removal process. The microwave irradiation is used as a generator agent of oxidizing radicals as well as a heating source in the process. This AOP process could facilitate the release of a large amount of the sludge-bound phosphorus from the sewage sludge. More than 84% of the total phosphorous could be released at a microwave heating time of 5 min at 170°C. This innovative process has the potential of being applied to simple sludge treatment processes in domestic wastewater treatment and to the recovery of phosphorus from the wastewater.

1.5.2 Nanobubbles

1.5.2.1 Concepts of Nanobubbles. Nanobubbles (NBs) are defined as gas bubbles <1 μm in diameter, which are also called ultrafine bubbles[250-253]. The first detection of NBs was in 2000, Lou *et al*.[254] measured NBs with atomic force microscopy (AFM). Since the early demonstrations of the presence of NBs using atomic force microscopy (AFM) supported strongly[255-257], many experimental studies have been conducted to elucidate the mechanisms of NBs' formation, factors involved, characterizations, and applications. There is a growing interest in nanobubble because of its wide range of potential applications (*e.g.*, detergent-free cleaning, water aeration, ultra-sound imaging and intracellular drug delivery, and mineral processing).[258-260]

Figure 1.23 shows the key differences among macrobubbles, microbubbles (MBs) and nanobubbles (NBs). MBs tend to gradually decrease in size and subsequently collapse due to long stagnation and dissolution of interior gases into the surrounding water, whereas NBs remains as such for months and do not burst out at once[261]. It has been revealed that the interface of NBs consists of hard hydrogen bonds similar to those found in ice and gas hydrates. This in turn leads to reduced diffusivity of NBs that helps to maintain adequate kinetic balance of NBs against high internal pressure.

NBs stay suspended for a long period because bubbles with diameter less than 5 μm do not rise due to the Brownian motion.[262] However, bubbles with diameter greater 1 mm rise fast and collapse on the surface[263-266]. NBs are highly stable and lasting for hours [254], days [267, 268], weeks [269], and even months [270]. The difference in the long life of the NBs is returned to the differences in the used procedure to generate the NBs, and the characterizations of the solutions and gases that have been used.

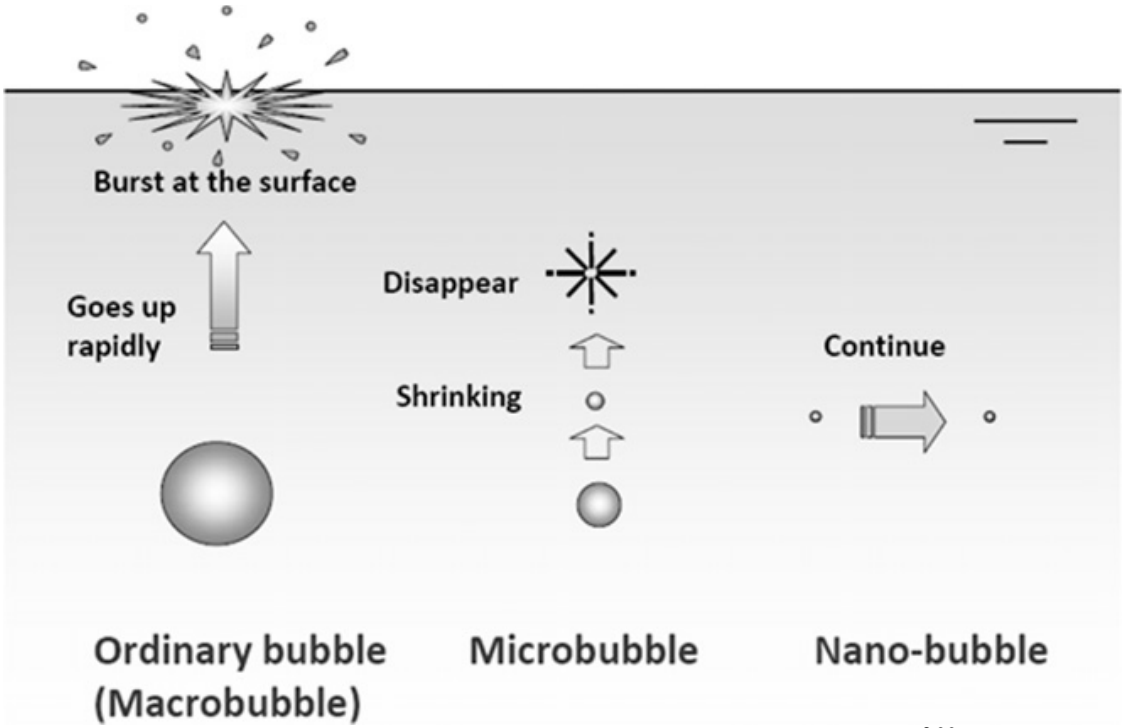

Figure 1.23 Schematic diagram showing macro, micro and nanobubbles.[266]

1.5.2.2 Characteristics of Nanobubbles. NBs have several special characteristics such as a long residence time in the solution due to their low buoyancy and stability against coalesces, collapse or burst, compared with bulk bubbles[264, 267]. Also, NBs have the ability to improve the efficiency of gas mass transfer as decreasing the bubbles' size is accompanied with the increasing in the internal pressure and improving the gas transfer efficiency[264, 271]. Furthermore, the high specific surface area of NBs increases the contact area between the liquid and gas[272]. This high specific surface facilitates mass transport, physical adsorption, and chemical reaction in the gas liquid interface. In the past few years, more and more attention has been given to the potential applications of the MBs and NBs for water treatment due to their ability to generate highly reactive free radicals.[272] It reported that the collapse of NBs creates the shock waves which in turn promote the formation of hydroxyl radicals[266, 273-275]. Due to pyrolytic decomposition that takes place within the collapsing bubbles, the radical hydroxyl radicals and shock waves can be

generated at the gas–liquid interface[276].

In particular, NBs have been applied for the prevention and removal of proteins adsorbed onto solid surfaces. It has been shown that adsorption of proteins onto various surfaces could be inhibited by NBs, thus preventing the surfaces from fouling. The nanobubbles act as antifouling agents.[277] Nanobubbles were produced on highly oriented pyrolytic graphite (HOPG) surfaces electrochemically and observed by atomic force microscopy (AFM). *In situ* observations indicate that nanobubbles can be used both for minimizing the fouling of a surface and cleaning an already fouled surface. The air–water interface of the nanobubble is responsible for the defouling action.[277] The other fouling removal mechanism was proposed recently in Figure 1.24 by Jie Zhu, *et al*., who demonstrated that nanobubbles can prevent the fouling of surfaces and also clean already fouled surfaces using bovine serum albumin (BSA) and lysozyme as model contaminants. The role of nanobubbles in preventing fouling is to provide a mechanical barrier to the adsorption of material on the surface.[278]

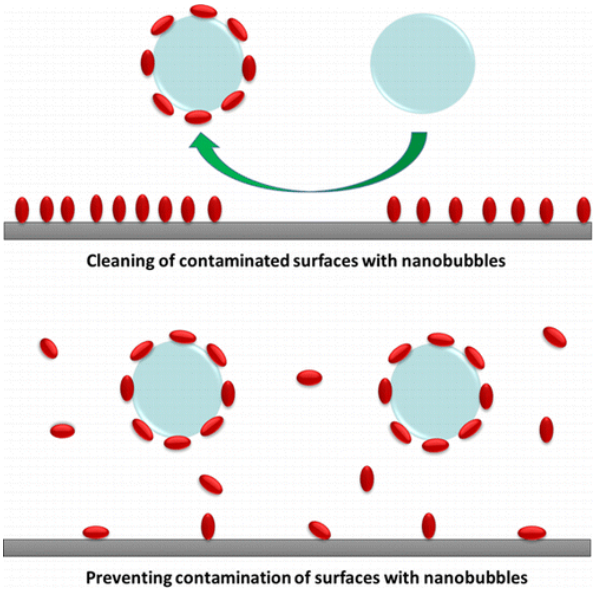

Figure 1.24 The schematic graph for the fouling removal mechanism proposed by Jie Zhu *et al*.

1.5.2.3 Generation Methods of Nanobubbles. In recent research, many methods have been investigated to generate NBs.[279-283] These methods mostly depend on these seven ways to generate NBs:[284]

(1) Dissolve the gas into the liquid by compressing air flow in the liquid, then release the mixed compressed flow through a NBs nozzle to create NBs by cavitation.

(2) Use ultrasound waves to stimulate cavitation at the standing points of these waves.[285]

(3) Inject low pressure gas, and break the gas bubbles with flow focusing, fluid oscillation, or mechanical vibrations.[286]

(4) Increase the temperature suddenly. In this way, the liquid is saturated with bubbling the gas at a low temperature, then the liquid temperature is increased rapidly to stimulate the gas bubbles formation.[287] This method controls the bubbles nucleation by the temperature rather than pressure, and it provides easier control for the laboratory works.[288]

(5) In the solvent-exchange method a solvent with higher gas solubility, generally ethanol, and then a solvent with lower gas solubility, such as water, is flushed through a fluid cell enclosed by a hydrophobic surface. This may create gas supersaturation during the solvent-exchange process, leading to the formation of nanobubbles on the solid surface.

(6) Generate nanobubbles by electrolysis of water.[289] Electrolysis is employed to produce surface nanobubbles on HOPG surface. Hydrogen (oxygen) nanobubbles are formed when the HOPG surface acts as a negative (positive) electrode.

(7) Microwave irradiation was used to generate interfacial nanobubbles.[290] Graphite has a strong microwave absorption ability, resulting in a dramatic temperature increase on the surface. The hot substrate may provide possibilities for interfacial nanobubble formation in an aqueous solution.

1.5.3 Microwave Irradiation and Nanobubbles

Recently, Wang *et al*. used microwave irradiation to generate interfacial nanobubbles.[290] AFM measurement showed that nanobubbles with diameters ranging from 200 to 600 nm were generated at a water-HOPG surface by applying microwave radiation to aqueous solutions with 9.0−30.0 mg L^{-1} dissolved oxygen. Graphite displays strong microwave absorption and transmits high thermal energy to the surface. The thermal and nonthermal effects of microwave radiation made contributions to decreasing the gas solubility, thus

facilitating nanobubble nucleation. The generation of nanobubbles could be well controlled by adjusting the gas concentration, microwave power, or irradiation time. The study provides a quick and convenient way to produce nanobubbles that may be useful for various applications.[290]

1.5.4 Challenges for Nanobubbles

More researches are needed on nanobubbles' interactions with hydrophobic and hydrophilic surfaces, solution matrixes such as electrolyte, NOM, and surfactants. The surface charge of nanobubbles affects greatly the interactions with other substances. This information could lead to transformative applications of NBs in the cleaning technology and water purification.

The presence of hydroxyl radical in NBs solutions is a controversial topic and needs more theoretical and experimental studies. For example, the reliable methods to measure •OH in NBs solutions, the mechanisms of •OH formation, the affected factors that control the •OH reactions in NBs solutions. The effects of •OH on pollutants during membrane fouling processes.

The study of the coalescence of NBs under different circumstances is necessary for better understanding of NBs behavior.[291] The NBs aggregation rate should be considered in the NBs applications to ensure the quality and quantity of effective NBs and doses applied to the treatment processes. Equally important is the formation of radicals and factors that are involved as reactive radicals are critical for achieving degradation of organic compounds in water. Thus, we need to understand what factors could influence the efficacy of radical formation and design optimal environments to boost the radical formation.

1.6 Research Objectives

According to the background and challenges about membrane filtration technology investigated in preliminary work, the research objectives of my research are as follows:

(1) Develop a comprehensive characterization platform, which offers new insights into novel membrane development, surface modification, membrane defouling and other related applications.

(2) Examine the membrane integrity and stability especially under the stress of repeated filtration and cleaning to provide new insight into the mechanisms of aging with the comprehensive characterization platform studied in previous section.

(3) Build models based on classic theories and comprehensive characterization of membrane and foulant properties to predict the membrane filtration performance and unravel the membrane fouling/defouling mechanisms.

(4) Design an innovative antifouling membrane filtration process and study the antifouling efficiency and mechanism.

The overview organization of this doctoral research is shown in Figure 1.25.

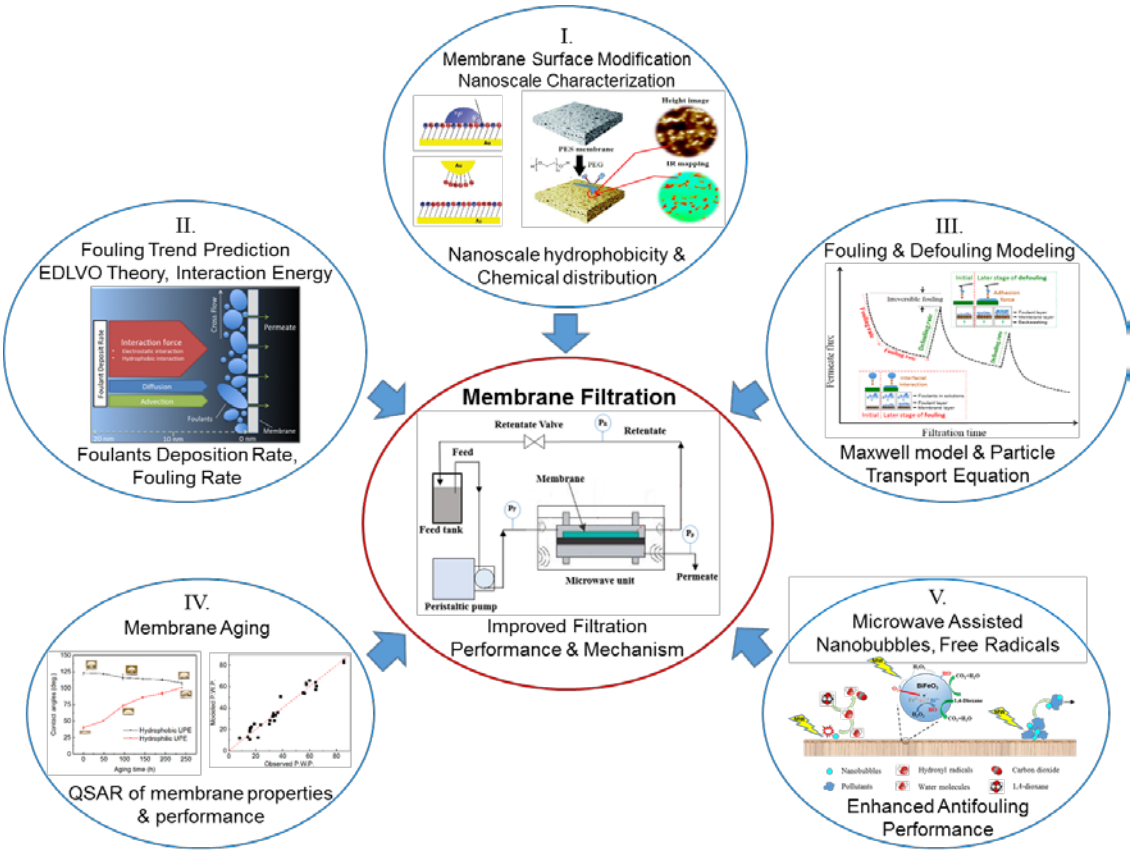

Figure 1.25 Overview schematic of this dissertation research.

1.7 Novel Contributions

This section briefly highlights key contributions in the dissertation. The main theme of this dissertation is membrane fouling and aging with the focus on the characterization, modelling and antifouling membrane design. **First, we apply the AFM for nanoscale hydrophobicity measurements and AFM-IR for nanoscale chemical mapping on chemically modified membranes**, which has not been done before. Next, **we provide new insight into the membrane fouling and defouling processes by developing based on particle transport equations and EDLVO theory**. These findings show the interaction force between the foulants and membranes dominate the fouling and defouling kinetics. Also, we notice that there are much less studies on membrane aging than membrane fouling and cleaning, so **we carry out the aging experiments to mimic the industrial aging process and study the effect of aging on membrane properties and performances with QSAR models**. The findings provide new insight into the membrane aging. In order to enable the antifouling and adequate removal of pollutants of the membranes, we also **pioneer a microwave-assisted membrane filtration process, which demonstrates high removal efficiency for 1,4-dioxane via MW-Fenton-like reactions and reduced the membrane fouling through nanobubbles generation and radical formation under microwave irradiation.** In summary, this dissertation on membrane fouling and aging provides tremendous new insight into the parameters dominating membrane filtration performance and also design antifouling membrane process to enable sustainable membrane filtration.

CHAPTER 2

NANOSCALE IMAGING AND QUANTIFYING CHEMICALLY MODFIED POLYMER MEMBRANE PROPERTIES

2.1 Introduction

During the last few decades, membrane filtration has extensively been used in water and wastewater treatment,[292, 293] desalination,[294] dairy making,[295] biomass/water separation,[296] and recovery of rare metals.[297-300] Hydrophilic membranes are ideal for water and wastewater treatment owing to the antifouling feature.[301-303] Many commercial polymeric membranes, such as poly (vinylidene fluoride) (PVDF) and polyethersulfone (PES), are hydrophobic, which reduces water interaction and causes fouling.[304, 305] Therefore, hydrophilized polymeric membranes are broadly manufactured to improve the water flux and mitigate membrane fouling.[306]

Chemical modification such as cross-linking, coating or covalent grafting of hydrophilic additives is a common way to engineer surface wettability and improve polymeric membranes filtration. For example, macromolecular additives such as poly (ethylene glycol) (PEG)[307-309] and polyvinylpyrrolidone (PVP)[309-311] are commonly used in membrane manufacturing industries. A small fraction of chemical blends may substantially alter the interfacial properties and the overall filtration performance.[293, 312, 313] For example, hydrophilization of membranes could lead to a heterogeneous distribution of surface functional groups or chemical domains and influence physical (pore size, porosity, and surface roughness),[314, 315] electric (zeta potential),[316] and mechanical (elasticity) properties.[317] These properties largely determine solute-membrane interactions, filtration flux, selectivity, fouling/antifouling, and chemical and mechanical stability.[318-320]

Many traditional analytical methods or instruments still suffer the limitations in the spatial resolution and/or chemical sensitivity in the acquisition of structural and chemical information of polymeric membrane surfaces. For regular hydrophobicity analysis, the water contact angle measurement only provides averaged hydrophobicity indication on bulk surfaces. Similarly, traditional diffraction (*e.g.*, Infrared, Raman and Confocal Raman spectroscopy) has limited spatial resolution at several microns (*e.g.*, 3–30 μm), depending on the laser wavelength and instrumentation. Therefore, developing novel methods to address the nanoscale characterization is of paramount importance to provide a more comprehensive understanding of modified membranes and guide design for high-performance membranes. Atomic Force Microscope (AFM) has evolved to be one of the most powerful tools for characterization of material surfaces especially at nanoscale.[321, 322] In addition to many physical properties (*e.g.*, morphology, electric and roughness) that can be probed by AFM, recent development of AFM has incorporated a suite of IR, Raman and confocal microscopy to further extend capabilities of chemical analysis.[58-60, 323]Such hybrid AFM techniques lead to simultaneous physical and chemical characterization of polymer blends and multilayer films at ~10 nm lateral resolution and monolayer sensitivity (over 100 times higher in spatial resolution compared to traditional FTIR and Raman).[59, 65-67] For example, AFM–IR replies on the detection of the local thermal expansion of samples under IR irradiation to make the IR absorption measurement that is far below the conventional diffraction limit possible. As the resonance frequency is correlated well with the conventional IR spectra,[70] the spectra obtained from AFM-IR can be searchable in existing databases.[71, 72] Clearly, hybrid AFM makes it possible to perform rapid, *in situ*, and possibly real-time imaging and quantification of both physical and chemical properties at

a nanoscale level. This is crucial to unravel novel and revolutionary information about material properties.

In this study, we applied AFM and AFM-IR to visualize and quantify the PVP additives on PES membranes and analyze the hydrophobicity and chemical compositions changes on modified membrane surfaces. Chemically modified PVP/PES membranes with different PVP blend levels were obtained from EMD Millipore Corporation. Specifically, (1) AFM was first used to probe local scale hydrophobicity of membrane surfaces, which has not yet been reported; and (2) AFM-IR was applied to spatially map the distribution of chemical additives on the base PES membrane. The goal of this work is to present a set of novel AFM-based approaches for unraveling surface properties of chemically modified membranes to support the design and development of functional and robust filtration systems.

2.2 Materials and Methods

2.2.1 Preparation of Chemically Modified Membranes

Figure 2.1a-c shows the photos of three kinds of flat sheet PES membranes obtained from Pall Corporation for testing: (1) pristine PES membrane; (2) PES membrane blended with 10% (w/w) PVP; (3) PES membrane cross-linked with 8% (w/w) PEG. The membrane preparation procedures of these three kinds of membranes were detailed by Wu *et al*.[306]

Eight kinds of PES membranes (Figure 2.1d and e) received from Millipore-Sigma Corporation are: (1) Pristine PES membrane and PES membrane dip-coated in 2%, 3% and 4% PEG solution with a nominal pore size of 20 nm; (2) Pristine PES membrane and PES membrane dip-coated in 2%, 3% and 4% PEG solution with a nominal pore size of 200

nm. The pristine PES membrane and chemically modified PES/PVP membranes were both prepared by the phase inversion method.[324] PVP solutions were prepared by dissolving different amounts (2, 3, and 4 wt.%) of PVP powder into deionized water. Then the PES membranes were dipped into the PVP solutions for certain times, exposed to an electron beam to cross-link the PVP, and dried in air. The chemically modified PES/PEG membranes were fabricated in the same method with PEG solutions. The modification process details are proprietary.

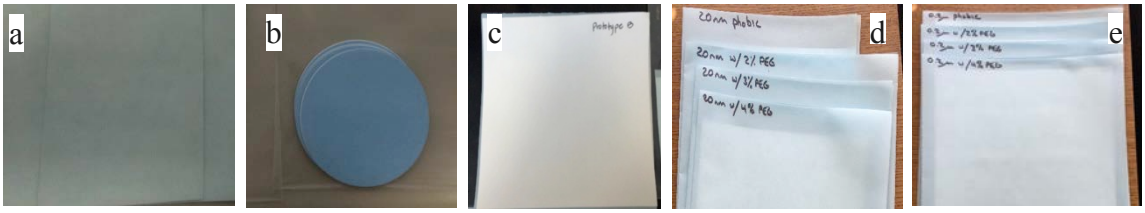

Figure 2.1 Polymeric membrane samples received from Pall Corporation: (a) PES membrane, (b) PES membrane blended with 10% PVP, (c) PES membrane cross-linked with 8% PEG; and samples from Millipore-Sigma Corporation: (d) PES membrane with 0%, 2%, 3%, 4% PEG, pore size 20 nm, (e) PES membrane with 0%, 2%, 3%, 4% PEG, pore size 200 nm.

2.2.2 Morphology of Membrane Surfaces

Morphology of membrane surfaces was examined by the Field Emission Scanning Electron Microscope (FESEM, LEO 1530 VP, Oberkochen, Germany) equipped with energy dispersive X-ray spectrometer (EDS) detector. These membrane samples were positioned on a metal holder, then sputter coated with carbon under vacuum for 3 min. The scanning was performed at an accelerating voltage of 10 kV.

The topography measurements were performed under ambient conditions with a Bruker PeakForce Tapping AFM (Pall membrane samples) and a Park XN20 AFM (Millipore-Sigma membranes). For Pall membrane samples, ScanAsyst-Air probes were used for tapping mode imaging and the scanning speed was 0.5 Hz. The images were

analyzed through the AFM Nanoscope software to obtain surface roughness measurements. The scanned topography images were analysed with ImageJ software to determine the porosity of the membrane surfaces semi-quantitatively based on the grey levels of the images. For Millipore-Sigma membranes, NCHV-A probes were used for tapping mode imaging and the scanning speed was 0.5 Hz. Likewise, the images were analyzed through the XEI software to obtain surface roughness measurements.

The roughness of the surface was determined by measuring the root-mean-square (RMS) roughness parameter, defined as the root-mean-square average of the height (Z) taken from mean data plane, expressed as Equation 2.1.

$$RMS = \sqrt{\frac{\sum_{i=1}^{N}(Z_i - Z_{ave})^2}{N}} \tag{2.1}$$

where Z_i is the current Z value and N is the number of points within the box cursor.

2.2.3 Bulk Scale Hydrophobicity Assessment by the Contact Angle Measurement

A drop of probe liquid (~5 μL) was placed on a dry membrane surface. At least three measurements of liquid drops at different locations were averaged to obtain contact angles for each membrane sample. The image of the liquid drop was taken within 10 s to determine the air–liquid–surface contact angles with the ImageJ software.

2.2.4 Nanoscale Hydrophobicity Assessment Using AFM

Previous studies indicated that the adhesion force measured by functionalized AFM tips is linearly correlated with local hydrophobicity of local material surface being probed by AFM tip.[325-330] Chemical force microscopy with hydrophobic, methyl-terminated tips has

been demonstrated for measuring the nanoscale surface hydrophobicity of bacteria and nanomaterials.[37, 328] Adhesion force can be deduced from the Johnson-Kendall-Roberts (JKR) model:

$$F_{\text{adh}} = 1.5\pi R W_{\text{adh}} \tag{2.2}$$

where R is the radius of curvature of the AFM tip (nm), which can be precisely measured under SEM. The work of adhesion in water, W_{adh} can be expressed as:

$$W_{\text{adh}} = \gamma_{sample.water} + \gamma_{tip.water} - \gamma_{tip,sample} = W_{tip,sample} - W_{sample,water} - W_{tip,water} + 2\gamma_{water} \tag{2.3}$$

where $\gamma_{sample.water}$, $\gamma_{tip.water}$ and $\gamma_{tip,sample}$ are the interfacial energy, $W_{tip,sample}$, $W_{sample,water}$ and $W_{tip,water}$ are the work of adhesion in vacuum, and γ_{water} is the surface energy. The term $W_{sample,water}$ can be deduced from the water contact angle using the Young's equation:

$$W_{sample,water} = \gamma_{sample} + \gamma_{water} - \gamma_{sample.water} = \gamma_{water}(1+\cos\theta) \tag{2.4}$$

Combining Equations (2.2 – 2.4) yields the following expression:

$$\frac{F_{\text{adh}}}{1.5\pi R} = W_{tip,sample} - W_{tip,water} - \gamma_{water}\cos\theta + \gamma_{water} \tag{2.5}$$

Assuming that $W_{tip,sample}$ and $W_{tip,water}$ values are similar, which seems reasonable because the CH_3-modified tip is involved only in dispersion interactions (London forces), Equation 2.5 becomes:

$$\frac{F_{\text{adh}}}{1.5\pi R} = \gamma_{water} - \gamma_{water}\cos\theta \tag{2.6}$$

This equation demonstrates that the measured adhesion forces could be linearly related to the cosine function of water contact angle. Since the AFM probe has a tip radius of 10-30 nm, the adhesion force measured can serve as a quantitative measure of the local surface hydrophobicity at nanoscale, which has not been well used for polymer membrane characterization.

A variety of thin organic films, polymer surfaces and fungal spores have been characterized using AFM tips functionalized with hydrophobically and hydrophilically terminated self-assembled monolayers (SAMs).[328, 330-332] SAMs are well-ordered structures and allow homogenous interactions at different microscopic scales. The measured adhesion forces between CH_3-terminated SAMs are typically 1-2 orders of magnitude larger than the forces observed for hydrophilic groups (COOH/COOH, OH/OH, COOH/OH, CH_3/OH).[330, 331] Moreover, substrate consisting of carboxylic acids and amine groups show pH-dependent behavior, while a nearly pH independent adhesion force was obtained from surface OH groups and CH_3 groups in the pH regime studied.[331, 333]

2.2.4.1 Self-assembled Monolayers (SAMs). In this study, adhesion forces were measured, under DI water, between AFM tips and gold substrate surfaces functionalized with alkanethiol SAMs terminated with OH and CH_3 groups.[328] Briefly, gold (111) substrate surfaces (Agilent, USA) were immersed for 14 h in ethanol solutions containing 1 mM $HS(CH_2)_{11}CH_3$ and $HS(CH_2)_{11}OH$ in various proportions (0:100, 10:90, 20:80, 30:70, 40:60, 50:50, 60:40, 70:30, 80:20, 90:10, and 100:0) and then rinsed with ethanol before use. In order to validate the quality and wettability of the surface modification, water contact angles were measured on the functionalized gold substrate surfaces.

2.2.4.2 Functionalization of AFM Cantilever Tips. Silicon nitride (Si_3N_4) cantilever tip (RC800PB, Asylum Research, USA) with Cr/Au (50/50) coating on the both reflex side and tip surface and a tip radius of <30 nm was used in the acquisition of force distance curves by AFM. Hydrophobic cantilever tips were obtained by coating with CH_3 groups by immersion in 1 mM $HS(CH_2)_{11}CH_3$ for 14 h and cleaning by ethanol before use.

2.2.4.3 Adhesion Force Measurement with AFM. An MFP-3D AFM (Asylum Research, Santa Barbara, CA, USA) was used to measure the adhesion forces between the functionalized probes and the sample surfaces in DI water. The SAMs-coated AFM tips and samples (gold substrate or membranes) immobilized on the sample holder were immersed in DI water and stabilized for 15 min before the adhesion force measurement. The adhesion force was obtained by recording the AFM cantilever deflection caused by the vertical movement of the AFM tip through the following three processes: first, the tip approaches the sample surface (noncontact region). Second, the tip makes contact with the surface, and is pushed against the surface (contact region). Third, the cantilever deflects until a preset cantilever deflection setpoint (0.8 V) is reached. Then, the cantilever is retracted and leaves the sample at some point, resulting in the adhesion dip (retract trace). A force-distance curve is obtained from the curve of deflection (V) versus piezo position (nm) (See example curve in Figure 2.2).[334] From the retrace curves the peak value of the adhesion dip was converted to the deflection of the cantilever in nanometers and the force applied to the cantilever was calculated in nanonewtons using Hook's law: $F = K_{sp}d$, where d is the cantilever deflection displacement (nm) and K_{sp} is the cantilever spring constant (54.84 ± 0.02 pN nm^{-1}).[335] The adhesion force was plotted with the water contact angles to establish a linear correlation or the standard calibration curve of adhesion force over

different hydrophobicity. This calibration curve will be used to quantify the sample surface hydrophobicity at nanoscale.

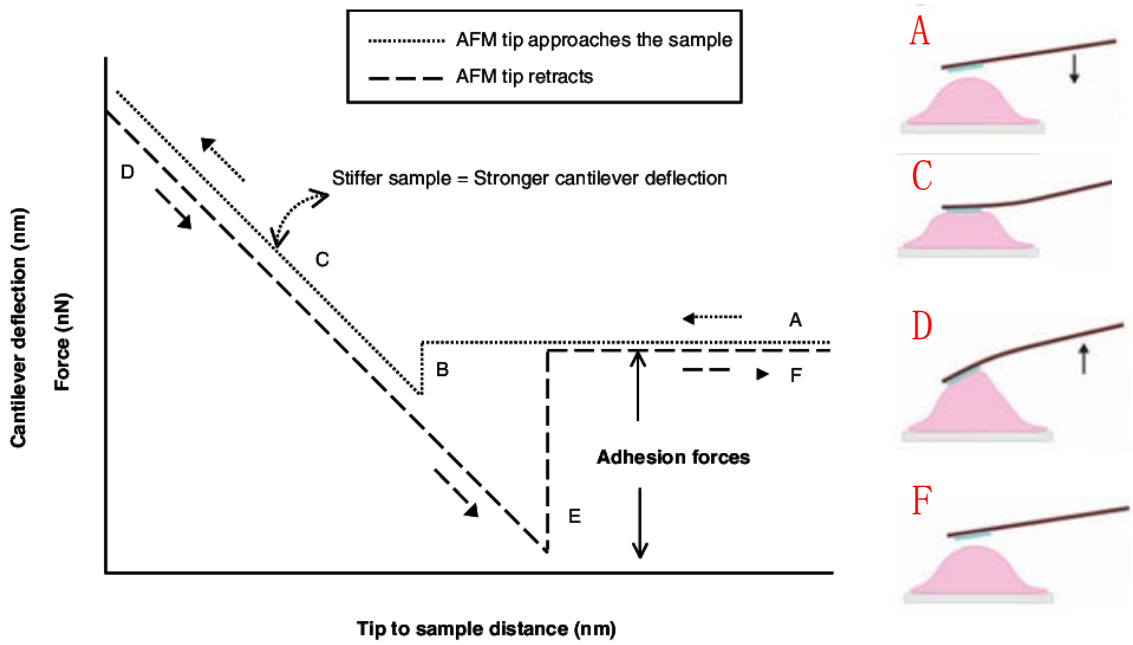

Figure 2.2 Schematic illustration of a force curve measured during the experiment. (A) the tip is approaching the sample surface (noncontact region); (B) the initial contact between the tip and the surface is mediated by the attractive van der Waals forces (contact) that lead to an attraction of the tip toward the sample; (C) the tip makes contact with the surface, and is pushed against the surface (contact region); (D) the cantilever deflects until a preset cantilever deflection setpoint (0.8 V) is reached and the cantilever is retracted and leaves the sample at some point, resulting in the adhesion dip (retract trace); (E) these adhesive forces can be taken directly from the force-distance curve; (F) the tip withdraws and loses contact with the sample upon overcoming the adhesive forces.[334] Solid line: approaching trace; dashed line: retract trace.

For the polymer membranes, at least 70 locations of sample surfaces were randomly selected to measure the adhesion force using the functionalized AFM tips. At least 3 force measurements were performed at each location. Based on the obtained adhesion forces, a histogram of adhesion force distribution was generated for each sample. For the membrane samples, adhesion force mapping was carried out to show the lateral distribution of the membranes hydrophobicity or hydrophilicity. The 2D adhesion force images were

collected through the force mapping mode and the force curves were performed pixel by pixel over an entire image frame of 500 nm × 500 nm. Each image was consisted with 4 pixels × 3 pixels. For each pixel, the tip moved into position, a force curve was acquired, and the tip was withdrawn and moved to next position. The scan rate was 500 nm s^{-1}. The adhesion maps were plotted by AFM offline software (Igor Pro 6.22A, WaveMetrics Inc., OR, USA) as gray-scale images.[336]

2.2.5 Membrane Surface Potential

The Kelvin Probe Force Microscopy (KPFM) set up used was a MFP-3D AFM (Asylum Research, USA). KPFM measurements were performed under ambient conditions using SCM-PIT-V2 silicon probes with a platinum-iridium coating, a spring constant of 3.0 N m^{-1} and a tip apex of around 25 nm. The tip used is 15 μm long. The cantilever used is 225 μm long, 35 μm wide and 2.8 μm thick. Surface potential was recorded in a dual-pass: the first pass is used to acquire topography of the surface; the second pass is used to measure contact potential differences (CPD) by lifting the tip up to a fixed distance above the surface.[337, 338] Images were obtained with a scan rate of 0.5 Hz and a scan size of 0.5 μm × 0.5 μm. All AFM images and data were analyzed by AFM offline software (Igor Pro 6.22A, WaveMetrics Inc., OR, USA).

2.2.6 Quality Assurance (QA)/Quality Check (QC) for AFM Measurements

2.2.6.1 Topography. After the measurement of each sample, the standard sample with known pattern on the surface will be scanned to check the integrity and intactness of the tips. The QC result should show that the variation of height or topographical measurement is within 5% of the known value. Otherwise, the AFM probes will be re-calibrated by thermal-K to determine the spring constant and resonant frequency. If the result after the

re-calibration still does not met the criteria, it indicates that the AFM probes may be either contaminated or broken or damaged during sweeping.

2.2.6.2 Surface Potential. The QC is conducted on a HOPG sample with fresh surface before and after certain numbers (5 or 10) of sample mapping to check the integrity of the conductive tips. A surface potential value of 5% of the HOPG's known work function is recommended. Otherwise, a new conductive tip should be used to replace the old tip that may be contaminated or damaged.

2.2.6.3 Adhesion Force. To verify the coating integrity of the functionalized tips during the force measurement, adhesion force measurements are carried out on the gold substrate surface functionalized with 100% CH_3- group after 10 or 20 force measurements on sample surfaces. The measured adhesion force values should have variations of less than 10% of that obtained with the newly prepared tips. Otherwise, the cantilever tip would be changed. Duplicate values are taken for each measurement point and the variation should be within 5% of the average. To avoid the artifacts from the tip engagement on membrane pores that could render no physical contact between the tip and membrane surface, the topographical images of polymer membranes were first obtained and then, the adhesion force measurements were conducted only on the membrane surfaces with at least 20 nm^2, which can be visualized and located from the topographical images.

2.2.7 Membrane Surface Chemistry

2.2.7.1 ATR-FTIR and AFM-IR Analysis. Functional group and chemical compositions of the membrane surfaces were first analyzed by attenuated total reflection - Fourier transform infrared spectroscopy (ATR-FTIR). ATR-FTIR spectra were recorded on a Nicolet spectrometer (model 560, Thermo Electron, Waltham, MA, USA) together

with a MIRacle attenuated total reflectance (ATR) platform assembly and a Ge plate. The scanning range was between 400 and 4000 cm^{-1}, and the scanning time was 32 s. Spectra were acquired at 4 cm^{-1} resolution. FTIR chemical imaging was performed using a Varian 670-IR spectrometer coupled with a Varian 620-IR microscope (Agilent Technologies, Santa Clara, CA, USA). A mosaic method was used to image area of 20 μm × 20 μm, employing a motorized stage to automate image collection. The spectral resolution was 8 cm^{-1}.

Nanoscale infrared analysis (AFM-IR) was performed on a NanoIR2 system (Anasys Instruments, Inc., Santa Barbara, CA, USA) operating with top-down illumination. All AFM topographic and IR mapping images were collected in contact mode at a scan rate of 0.1 Hz using a gold-coated silicon nitride probe (model: PR-EX-NIR2, 0.07–0.4 N m^{-1} spring constant, 13 ± 4 kHz resonant frequency, Anasys Instruments).[339] Analysis Studio software (version 3.11, Anasys Instruments, Inc., Santa Barbara, CA, USA) was used for data collection and analysis. For the collection of local spectra, the IR laser produced 10 ns pulses at a repetition rate of 1 kHz. The power levels of the incident IR radiation on the sample surface were set to *ca.* 50 μW.[340] Local spectra were collected over spectral ranges: 900–1800 cm^{-1}, using a data point spacing of 4 cm^{-1}.

The chemical structures of PES, PVP and PEG are shown in Figure 2.3. The functional groups assignments of these three polymers are shown in Table 2.1 as a reference for analysis of the spectrum obtained from the membrane samples.

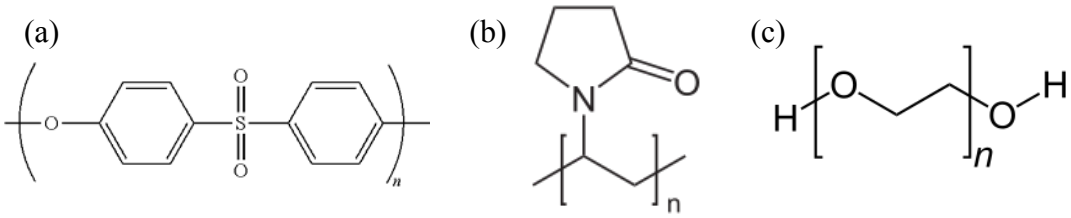

Figure 2.3 The chemical structures of (a) PES, (b) PVP, and (c) PEG.

Table 2.1 FTIR Assignments of PES, PVP and PEG Polymers

Materials	Functional groups	Wave number	References
PES	Aromatic bands Sulfone groups (S=O)	1486 cm^{-1}, 1578 cm^{-1} 1322 cm^{-1}, 1298 cm^{-1}	Zhang *et al.*[341]
PVP	CO stretching CH_2 bending C-N stretching	1650 cm^{-1} 1427 cm^{-1} 1293 cm^{-1}	Borodko *et al.*[342] Shahbaziniaz *et al.*[343]
PEG	Ether C-H; C-O-C	2891 cm^{-1} 1103 cm^{-1}	Castillo *et al.*[344]

2.2.7.2 Raman Spectroscopy and AFM-Raman Analysis. Raman spectroscopy is a powerful laser-based scattering technique that detects the chemical features of the specimen as well as identifying the structures of its molecules.[345, 346] The functional groups assignments of these three polymers are shown in Table 2.2 as a reference for analysis of the spectrum obtained from the membrane samples. Raman spectra and spectral mapping were taken using a DXR Raman microscope (Thermo Fisher Scientific, Madison, WI) with a 3 mW 532 nm laser line using a 50× objective, producing a laser spot with a diameter of ~0.7 μm on the sample. Acquisition time for a single spectrum was 30 s.

Table 2.2 Raman Assignments of PES, PVP and PEG Polymers

Materials	Functional groups	Wave number	References
PES	Phenyl-ring Symmetric C-O-C stretching	1580 cm^{-1}, 1662 cm^{-1} 1150 cm^{-1}	Sharma *et al.*[347]
PVP	Amide, C=O, C-N stretch CH_2 Wag, C-N stretch	1662 cm^{-1} 1296 cm^{-1}	Yuri *et al.*[342]
PEG	C-O-C bands	1280 cm^{-1}	Yahia *et al.*[348]

Integration of AFM with Raman can simultaneously generate topographical and chemical mapping of the same sample area at nanoscale. With AFM/Raman (NTEGRA Spectra, NTMDT, Russia), we expect to resolve the chemical distribution of composite membranes with a higher resolution and sensitivity than conventional Raman. The

AFM/Raman instrument was equipped with a 532 nm laser in upright configuration. A 100× objective (Numerical Aperture or N.A. 0.7) provided a laser spot size about 330 nm. The laser power was kept well below 1 mW for nondestructive Raman measurements.

2.2.8 Characterization of HA and BSA as Model Foulant and Pollutant

Natural organic matter (NOM) constitutes a complex mixture of organic compounds with varying molecular weights, charge densities, and hydrophobicity.[349] The presence of NOM in drinking water primary affects the aesthetic quality by creating taste, color, and odor problems.[350] Moreover, the presence of NOM has a great impact on the efficiency of nearly all treatment processes applied for drinking water production, as it can reduce the adsorption capacity of activated carbon for the removal of target pollutants,[351] it can provoke extensive membrane fouling,[352] it can increase the frequency for ion-exchange resin regeneration cycles,[353] it can increase the required coagulant and oxidant dosages,[354, 355] and it can favor the formation of carcinogenic disinfection by-products (DBPs).[356] Therefore, NOM composition and properties are considered nowadays as key parameters for the efficient design of any drinking water plant. Humic acid has been used to present the NOM in water.

The powdered HA (Sigma-Aldrich) was purchased to represent the humus-like substance in typical natural organic matters. The HA stock solution (0.1 g L^{-1}) was prepared by dissolving 0.1 g HA into 1000 mL deionized water. The solution pH was adjusted before carrying out the measurements or experiments by 0.1 mol L^{-1} HCl or 0.1 mol L^{-1} NaOH. The solid BSA (MW = 67 kDa, Sigma- Aldrich) was chosen to represent the protein-like substance in natural organic matter. The BSA stock solution (2 g L^{-1}) was

prepared by dissolving 2 g BSA into 1000 mL deionized water. The pH of the BSA solution was also adjusted with 0.1 mol L^{-1} HCl or 0.1 mol L^{-1} NaOH.

Contact angles of the HA and BSA were measured using the same way as described in Section 2.2.3. The HA and BSA coated surfaces were made by depositing the HA solutions and BSA solutions onto clean flat gold coated wafer and dried in the air.

Zeta potential and mean size of HA or BSA in the solution were determined by dynamic light scattering (DLS) with a Malvern Zetasizer, Nano ZS (Malvern Instruments Limited, UK). Zeta potential was calculated by the Smoluchowski equation.[357] Each data value was an average of five measurements and all the measurements were performed at 25 ± 1 ^{o}C. The concentrations of BSA and HA solutions were determined by UV absorbance measurement at 287 nm and 254 nm,[358, 359] respectively, using a UV–Vis Spectrophotometer (Evolution 201, Thermo Scientific, Waltham, MA, USA). A linear calibration curve with a coefficient of determination (R^2) greater than 0.99 between BSA or HA concentration and UV absorbance was obtained within the concentration range used in this study.

2.3 Results and Discussion

2.3.1 Morphology of Membrane Surfaces by SEM and AFM

Morphology of membrane surfaces were obtained by SEM as shown Figure 2.4 and compared with the ones obtained by AFM. The topographical images consistently show that the hydrophilic polymeric additives, PVP and PEG, increased pore sizes of the modified PES membranes, which agrees with the literature.[222] Surface roughness (*e.g.*, RMS) and porosity were also increased significantly after modification (Table 2.3).

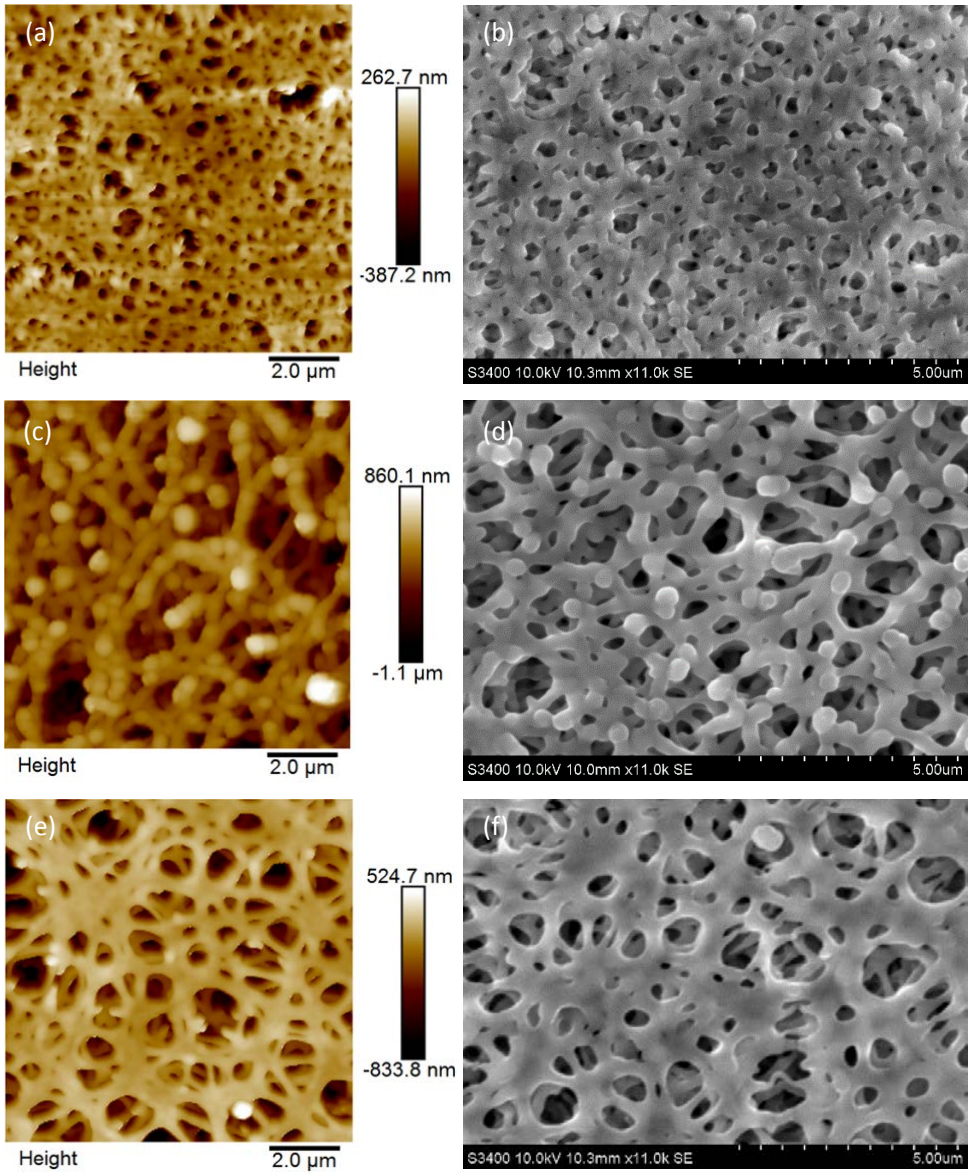

Figure 2.4 AFM (left column) and SEM (right column) topographical images of (a, b) PES membrane; (c, d) PES/PVP membranes; (e, f) PES/PEG membranes.

Table 2.3 The Porosity and Roughness of Three Membrane Samples

Membranes	Porosity (%)*	RMS (nm)	Mean pore diameter (nm)
PES	17	69.0±8.2	447.6±103.8
PES/PVP	32	172.0±40.7	1155.5±188.8
PES/PEG	36	187.0±18.7	1257.5±194.3

*Porosity was calculated based on the pore areas measured from the acquired 2D images.

2.3.2 Hydrophobicity and Hydrophilicity Analysis

Average contact angle measurements for the probe liquids on the three membranes (PES,

PES/PVP and PES/PEG) and the two model foulants (BSA and HA) are shown in Table 2.4. The hydrophobic/hydrophilic properties of chemically modified PES membranes were expected to vary as compared with the pristine PES membranes due to the presence of the hydrophilic functional groups such as hydroxyl groups and amino groups in PVP and ether groups in PEG. Table 2.4 shows that the pristine PES membrane displayed a water contact angle of 83.99 ± 1.06°, indicative of the highly hydrophobic nature of PES. After blending with PVP, the water contact angle reduced to 0°, a super-hydrophilic surface state. Similarly, the Pall PES membrane cross-linked with PEG showed a water contact angle of 7.52±0.63°, also a highly hydrophilic surface property. Increasing the blending ratio of PEG from 0% to 4% in PES gradually reduced the water contact angle from 71º to 27º.

Table 2.4 Average Contact Angles of Membranes and Two Model Foulants

Materials		Contact angle (º)		
		Water	**Formamide**	**Glycerol**
Pall Membranes	PES	84.0±1.1	59.4±8.9	58.1±8.9
	PES/PVP	0±0	46.6±2.5	77.4±5.2
	PES/PEG	7.5±0.6	26.1±3.7	24.2±2.4
Millipore Membranes Pore size: 200 nm	PES/0% PEG	71.3±12.3	12.1±3.5	42.4±7.4
	PES/2% PEG	39.3±6.9	15.0±6.4	38.8±9.6
	PES/3% PEG	42.7±8.5	12.1±4.9	43.9±9.8
	PES/4% PEG	27.4±2.9	0±0	52.5±14.5
Foulants	Bovine Serum Albumin	23.0±2.4	31.8±0.6	50.4±0.4
	Humic Acid	31.5±2.2	30.0±2.7	60.8±4.1

2.3.3 Membrane Nanoscale Hydrophobicity Probed by AFM

2.3.3.1 Water Contact Angles of SAM Surfaces. Water contact angle measurements for different SAMs are shown in Table 2.5. The surface hydrophobicity is shifting from

highly hydrophilic to hydrophobic when increasing the fraction of CH_3 groups. These contact angles measurements will be used to compare with and validate the model calculation of nanoscale "contact angles" converted from the adhesion force measurement in the following sections.

Table 2.5 Water Contact Angles for Various SAM Surfaces

SAMs	Molar fractions of CH_3 (%)										
	0	10	20	30	40	50	60	70	80	90	100
Contact angle (°)	25.7	31.0	33.8	40.3	45.7	55.1	58.7	63.0	65.5	75.3	83.0
SD (°)	8.1	5.7	4.0	3.4	2.2	6.8	6.1	5.8	7.7	5.7	4.0

2.3.3.2 Adhesion Force Measurement Between CH_3-coated Gold Tip and SAMs. Before applying the AFM method to probe the surface hydrophobicity of polymer membranes, we further verified the correlation between adhesion forces and water contact angles on SAM surface with well-controlled water angles. In this study, the bulk contact angles and the adhesion forces between the CH_3-coated gold tips and ten different SAM surfaces were measured and plotted versus the fraction of CH_3- (Figure 2.5a, b and c). Then, the adhesion forces were further plotted over -cosθ in Figure 2.5d, where θ is the water contact angle obtained above in Table 2.5. Linear regression reveals that water contact angles and adhesion forces follow a good linear relationship as reported:

$$F_{adh} = (6.21 \pm 0.62) - (6.85 \pm 0.79) \cdot \cos\theta \quad R^2 = 0.9449 \qquad (2.7)$$

According to the Equation 2.7, the adhesion would be negative when the contact angle is less than 24.98°. It means that repulsion occurs between the tip and sample surface and there will be no adhesion force that can be measured for hydrophilic surfaces, which

agrees with previous literature.[328] This equation will be used for the calculation of nanoscale "water contact angles" that are not or hard to measure experimentally at local material surfaces based on the measurement of adhesion force between the sharp tip of functionalized AFM cantilever probe and samples. The tip's integrity was verified by measuring the 100% CH_3 coated Au substrate for 10 times, the value should be similar as those obtained by new tips.

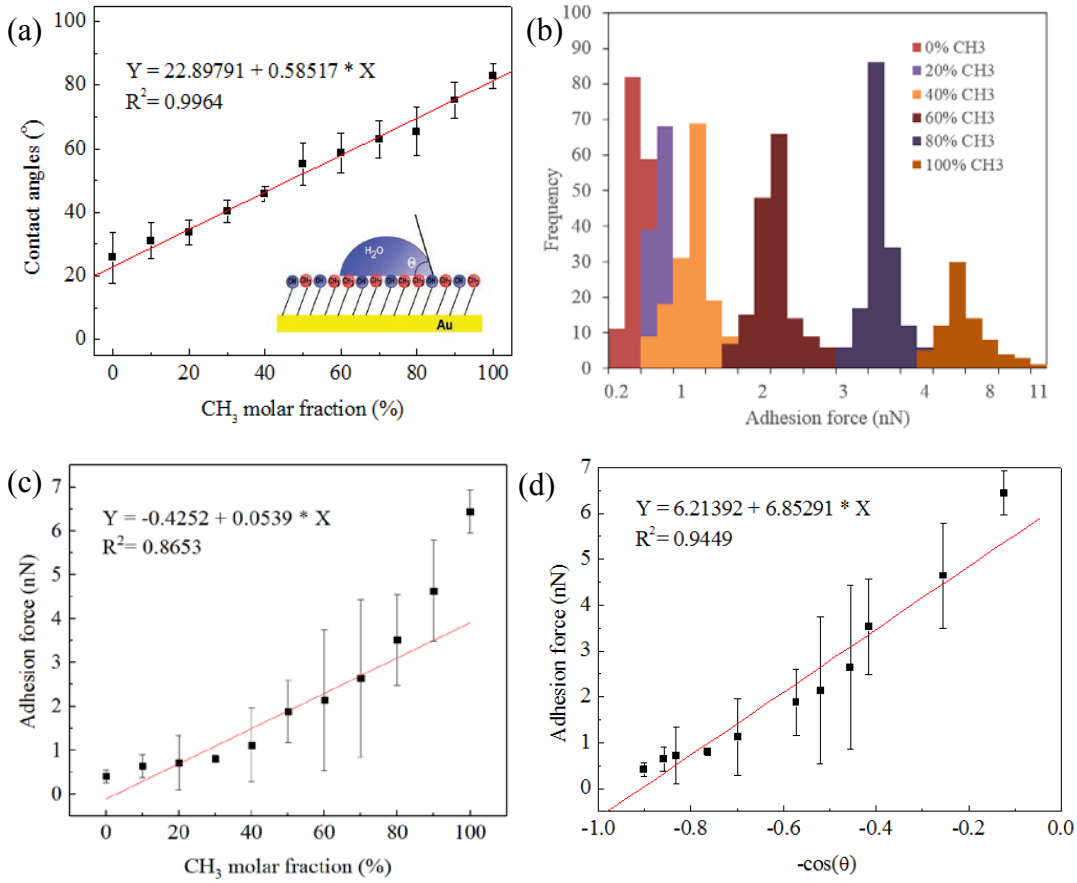

Figure 2.5 (a) Water contact angles values measured for SAMs as a function of the molar fraction of CH_3; (b) Histograms of adhesion forces between probes and different SAM surfaces; (c) Adhesion forces measured for SAMs as a function of the molar fraction of CH_3; (d) Adhesion forces versus the value of -cosθ for different SAM surfaces.

2.3.3.3 Adhesion Force Measurement between CH_3-coated Gold Tip and Different Membranes. The adhesion force curves were collected on the membrane surfaces at 70 different locations with CH_3-coated gold tip, and the histogram of the adhesion forces

are shown in Figure 2.6 and Figure 2.7. Spatially resolved force curves recorded with a hydrophobic, CH_3-coated gold tip yielded adhesion forces of pN to nN magnitude that were heterogeneously distributed on the membrane surfaces. In the previous studies, water contact angle measurements, partitioning in aqueous two-phase systems, and hydrophobic interaction chromatography were developed to analyse the surface hydrophobicity.[360] However, these methods had poor resolution since they provide averaged information obtained on bulk area. Therefore, this technique of hydrophobicity measurement with AFM demonstrated to be a powerful approach to the traditional methods, providing spatially resolved measurements of hydrophobicity on membranes.[328]

2.3.3.4 Membrane Nanoscale Hydrophobicity Calculated by Adhesion Force. The average water contact angles for different membranes are shown in Figure 2.8. The calculated contact angles using Equation 2.7 are compared with the bulk water contact angles. The calculated contact angles appear slightly smaller than the bulk ones especially for the hydrophobic membranes. The difference between the nanoscale and bulk scale water contact angles may be caused by the inhomogeneous hydrophilicity distribution on the membrane surfaces. The adhesion forces were measured on the real membrane surfaces by avoiding the membrane holes. This might induce the calculated contact angles different from the bulk water contact angles, which were affected by the roughness and pores of membrane surface.

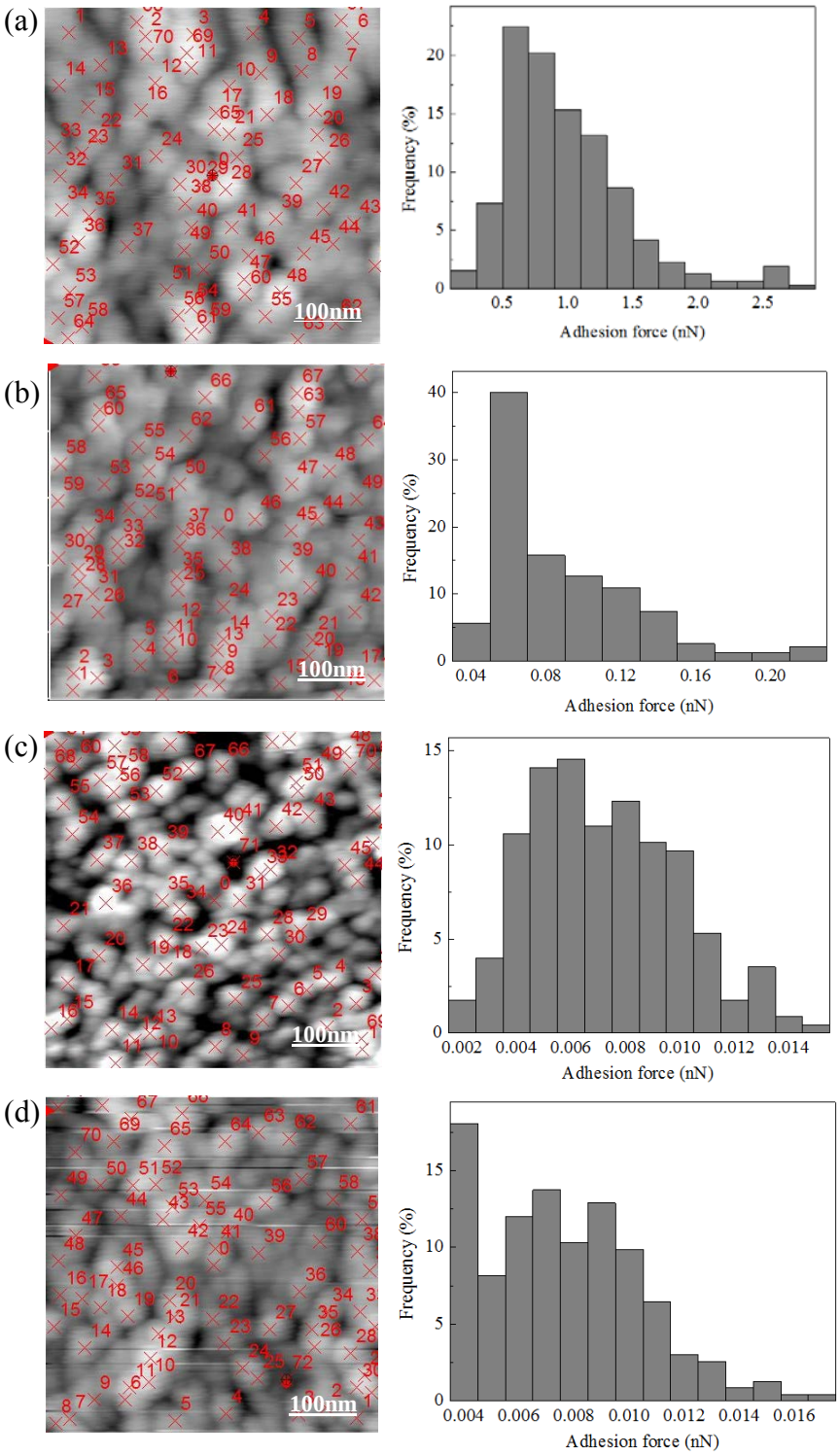

Figure 2.6 Adhesion force curve collection positions on the AFM height image (500 nm × 500 nm) (left column) and histogram (n = 210) of adhesion forces (right column) recorded on the membrane surface using AFM with a hydrophobic CH_3 tip. The samples are PES membranes with 0% PEG (a), 2% PEG (b), 3% PEG (c) and 4% PEG (d).

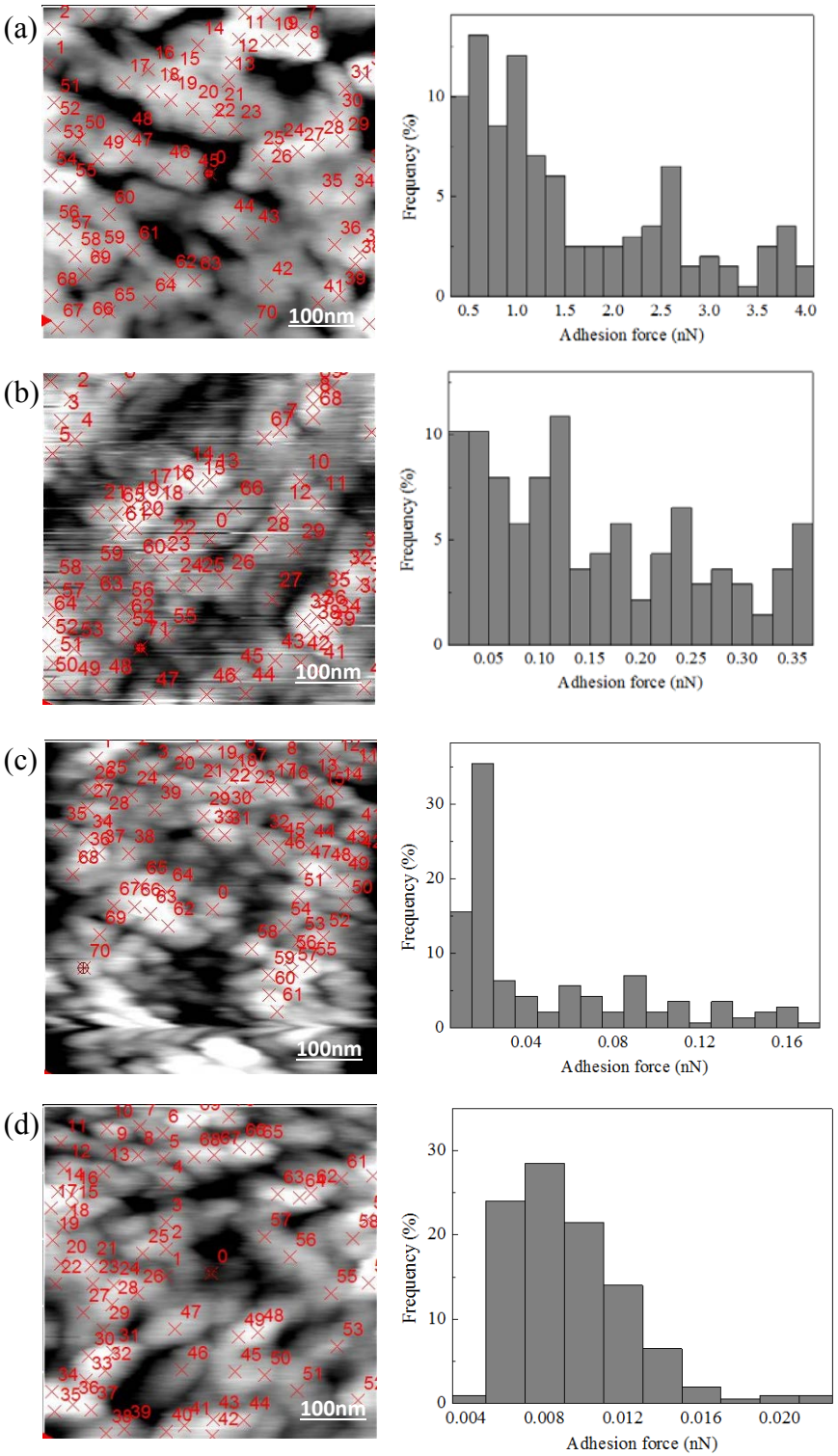

Figure 2.7 Adhesion force curve collection positions on the AFM height image (500 nm × 500 nm) (left column) and histogram (n = 210) of adhesion forces (right column) recorded on the membrane surface using AFM with a hydrophobic CH_3 tip. The samples are PES membranes with 0% PVP (a), 2% PVP (b), 3% PVP (c) and 4% PVP (d).

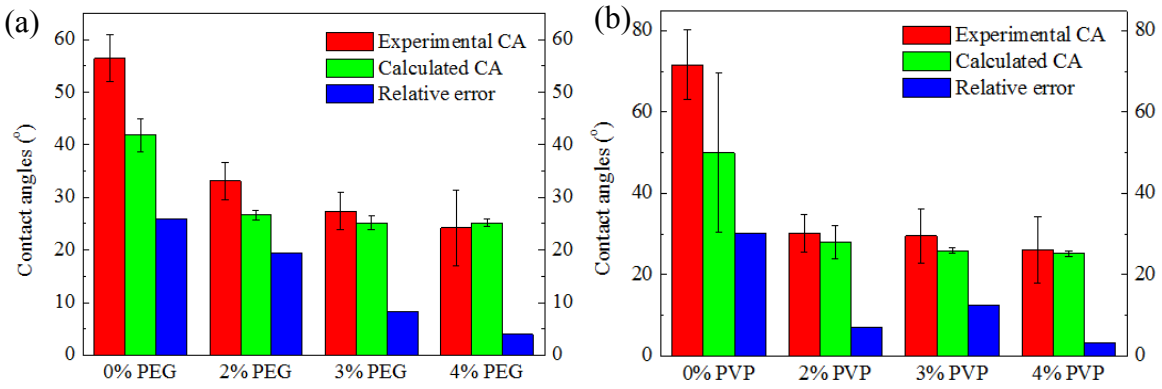

Figure 2.8 Comparison between contact angles calculated and measured experimentally for PES membrane modified with different amount of PEG (a) and PVP (b), pore size: 20 nm.

In the previous studies, water contact angle measurements, partitioning in aqueous two-phase systems, and hydrophobic interaction chromatography are commonly used to analyse the surface hydrophobicity.[360] However, these methods yield poor resolution and reveal no nanoscale information. Conversely, this AFM technique has proven to be a powerful approach that can not only quantitatively measure local scale hydrophobicity but also perform spatial mapping of surface hydrophobicity distribution.[328]

Different from SAMs, membranes are porous material and the surface roughness is heterogeneous at nanoscale. Due to the rough surfaces, the contact angles might be measured in two different models (Figure 2.9b). And the contact angles measurements (Figure 2.9a) of membrane surfaces are affected by the membrane pores. Clearly, water contact angle measurement is unable to capture this nanoscale contact angle especially for the membranes with nanoscale pore sizes. While AFM tip radius is around 20 nm (Figure 2.9c), which could avoid the membrane pores and probes on "real" membrane surface to obtain the force curves (Figure 2.9d). Then the nanoscale hydrophobicity of the membrane surfaces could be measured.

Nur Hashimah Aliasa *et al.* did not adopted contact angle measurement as an informative characterization of hydrophobicity in their study on nanofiber membranes,[361] because Cassie effect resulting from large air pocket and micron-range roughness in nanofiber has a significant contribution on water contact angle of nanofiber meshes.[362] As a result, a contact angle of nanofiber mesh does not indicate hydrophilicity or hydrophobicity of nanofibers. Fortunately, the hydrophobicity measured by AFM could overcome this limitation.

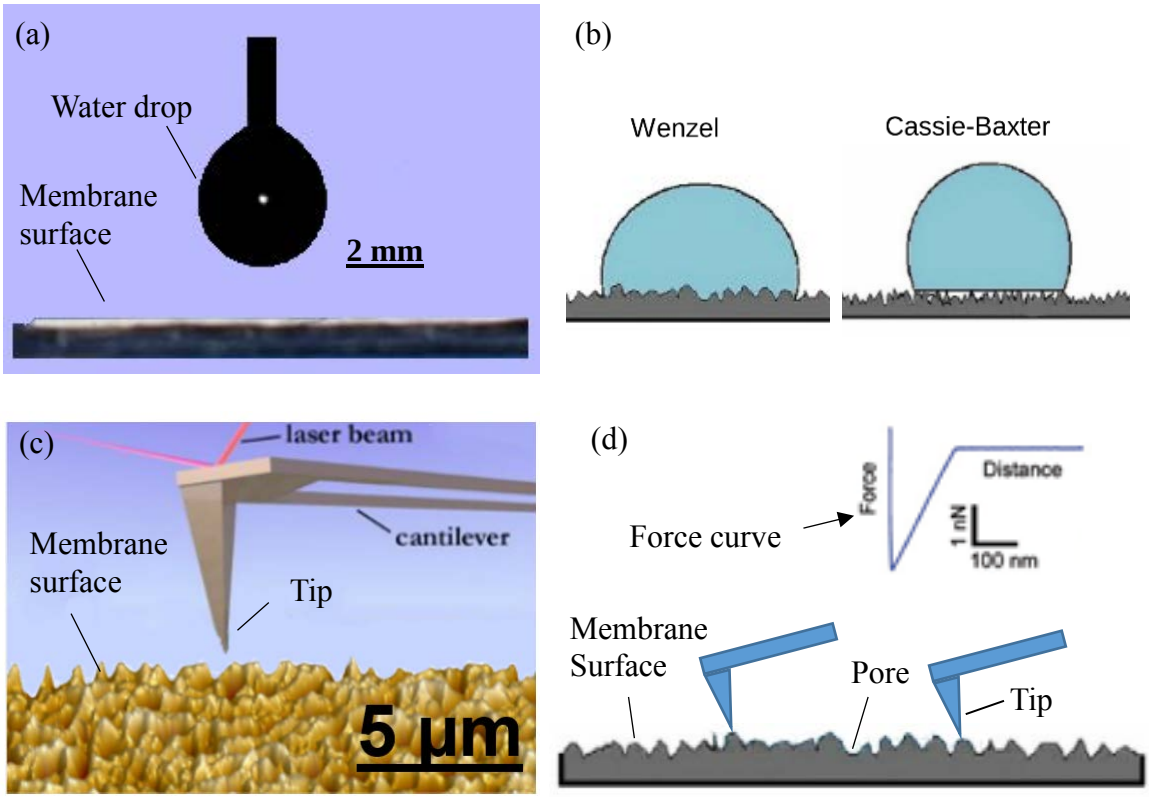

Figure 2.9 Comparison of bulk water contact measurement and AFM adhesion force measurement and its conversion into nanoscale hydrophobicity. (a) Bulk water contact measurement, (b) two wetting models of water drop on rough surface, (c) AFM adhesion force measurement and (d) AFM tip probing on membrane surface avoiding the membrane pores.

2.3.4 Membrane Surface Potential Measurement by KPFM

Different from surface zeta potential, Figure 2.10 shows the surface electric potential (CPD values) of different membranes surfaces as another sensitive approach to prob chemical homogeniety and distribution on membranes. Clearly, PVP and PEG additives (hydrophilic polymers) changed surface electric potential of the PES membranes. Again, the contrast in surface potential mapping is due to the difference in the work functions of probed membrane surfaces and AFM probes. The PES membrane had a homogenous surface that led to almost identical or even distribution of surface potential (approximately -7.92 V or -8.38 V) across the tested region. By contrast, the surface potential mapping of PES/PVP and PES/PEG membranes revealed a few spots with subtiantial contrast and differnet surface potentials at levels of -1.16 V to 4.92 V indicating the presence of foreign chemicals over the base PES polymer.

Figures 2.10 (d-i) shows the surface electric potential of PES membranes surfaces with different concentrations of PEG and PVP additives. Similarly to the results on Pall Membranes, PVP and PEG additives (hydrophilic polymers) changed surface electric potential of the Milipore's PES membranes. The PES membrane had a homogenous surface that led to almost identical or even distribution (approximately -8.70 V or -8.38 V) of surface potential across the tested region. By contrast, the surface potential mapping of PES/PVP and PES/PEG membranes had reduced surface potentials at levels of -6.43 to 1.92 V. Based on the surface potential difference, we may not only be able to detect chemical blends on polymer membranes but also possibly quantify the blend level or concentrations with well calibrated measurement.

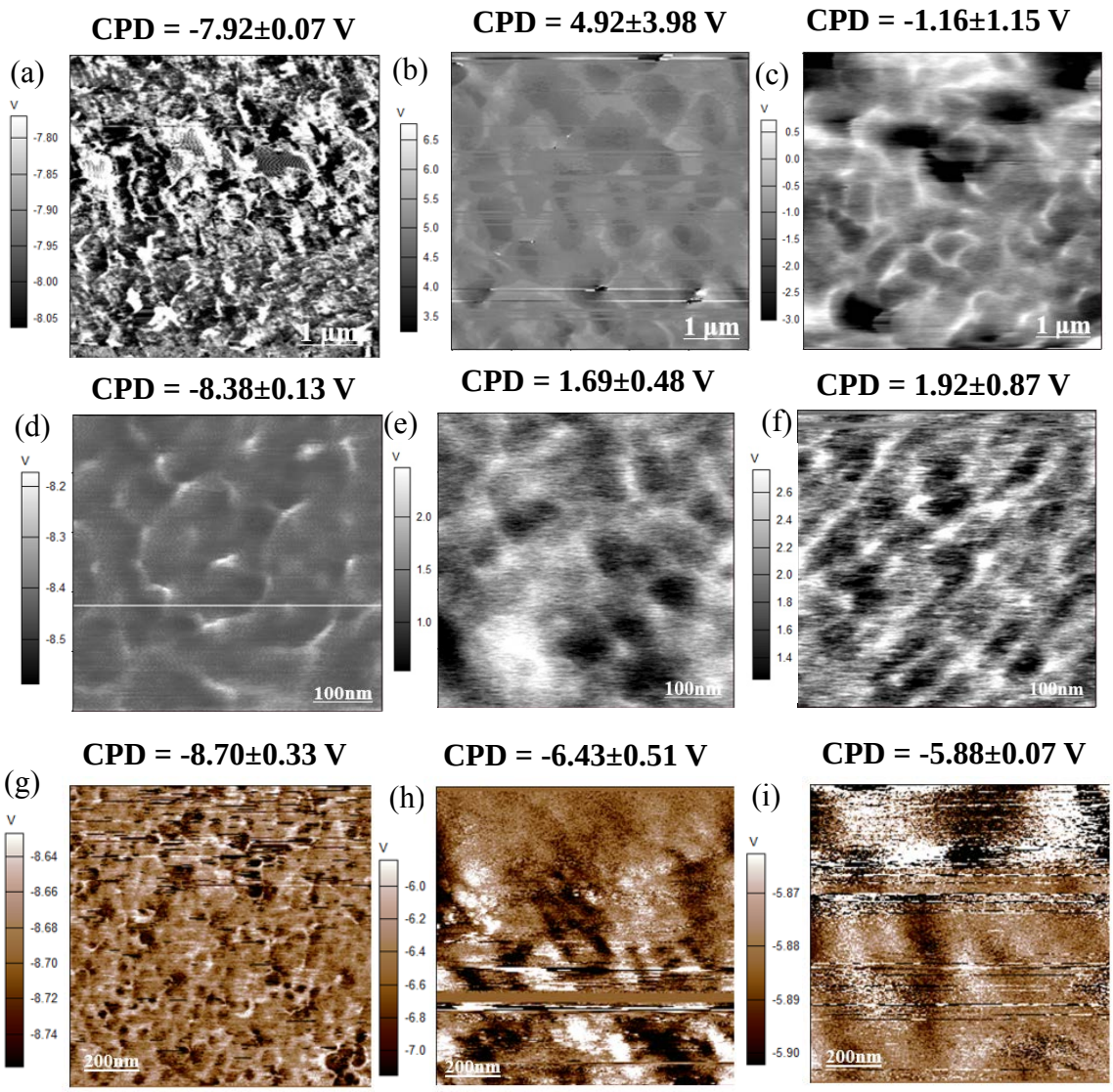

Figure 2.10 The surface potential images of three membrane samples. Pall membranes: (a) PES membrane, (b) PES/PVP membranes, (c) PES/PEG membranes; Millipore membranes (pore size is 20 nm): (d) PES/0%PEG membrane, (e) PES/2%PEG membranes, (f) PES/3%PEG membranes; (g) PES/0%PVP membrane, (h) PES/2%PVP membranes, (i) PES/4%PVP membranes.

KPFM provides a noncontact and noninvasive mapping of the local surface electric potential or surface potential, which is the contact potential differences (CPD) due to the difference in work functions (or Fermi energy levels) between sample surface and AFM probe. Work function, usually measured in eV, is the energy difference of an electron between the vacuum level and the Fermi level, which is the minimum energy needed to

liberate an electron from the surface of semiconductors.[363, 364] The local mechanical and electromagnetic properties, such as surface charges, doping levels, or dielectric constants, significantly affect the work function. Many previous studies show that KPFM could detect polymeric identities based on their unique surface potential or work function.[35, 50, 365] KPFM has been used to characterize morphology and determine surface potentials of a broad spectrum of materials, including semiconductors,[52] inorganic films,[53] self-assembled monolayers (SAMs),[54] and polymer thin films.[55, 56] Therefore, KPFM was used as an alternative tool that may sensitively probe chemical distribution of polymer membranes at nanoscale.

2.3.5 Membranes Surface Chemistry Measured by ATR-FTIR and AFM/IR

2.3.5.1 PES/PVP Membranes. First, we tried FTIR and AFM-IR on the PES/PVP membranes provided from Pall Corporation. For the PVP additives, Figure 2.11a shows that a small band at 1664 cm^{-1} that may indicate the presence of PVP (C=O stretching) in PES membrane. However, other characteristics bands of PVP such as 1466 cm^{-1}, 1293 cm^{-1} (C-N stretching) were not detected. The results were verified by AFM-IR spectrum that yielded similar findings as shown in Figure 2.11b, where AFM-IR spectra for the pure PES membranes and PES/PVP membranes were compared and the band at 1664 cm^{-1} was attributed to the additives of PVP.

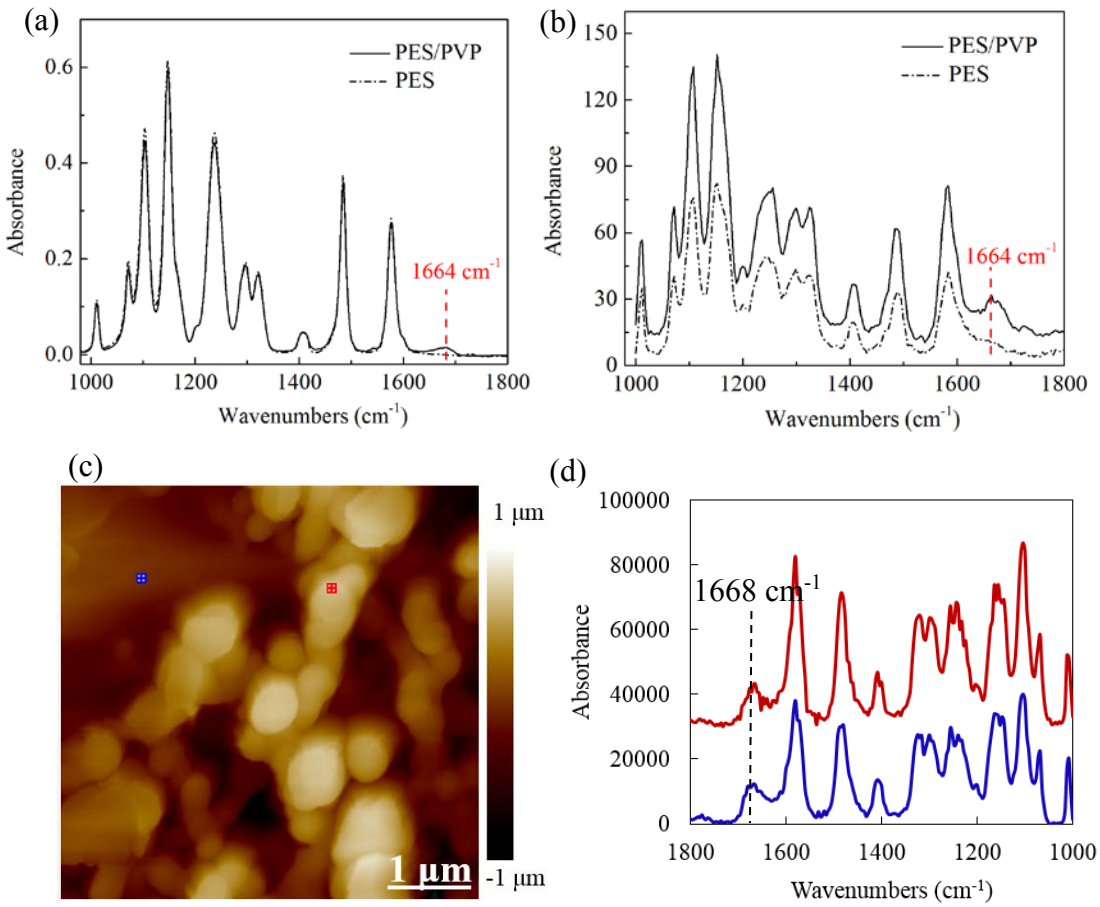

Figure 2.11 FTIR (a) and AFM-IR (b) spectra range for PES membrane and PES/PVP membrane. AFM image (c) and AFM-IR spectrum (d) for PES/PVP membranes. The spectra in red and blue colors were collected from the two locations labeled with red and blue "+".

In Figure 2.12a, the PES/PVP membrane was sectioned using microtom to achieve high spatial resolution chemical mapping of inner part of the sample. AFM-IR spectra collected from a number of locations are overlayed and appear to be almost identical, which indicates the sample had well mixed or even distribution of polymer species. In Figure 2.12b, the PES component was detected consistently across the scanned region of PES/PVP membrane. The IR absorption image was collected at 1152 cm^{-1} to show the chemical distribution of PES (Figure 2.12c-d). However, the IR mapping image was highly

consistent with the height image. It is thus speculated that the rougness of the membrane surface caused the artifacts in the IR absorption mapping.

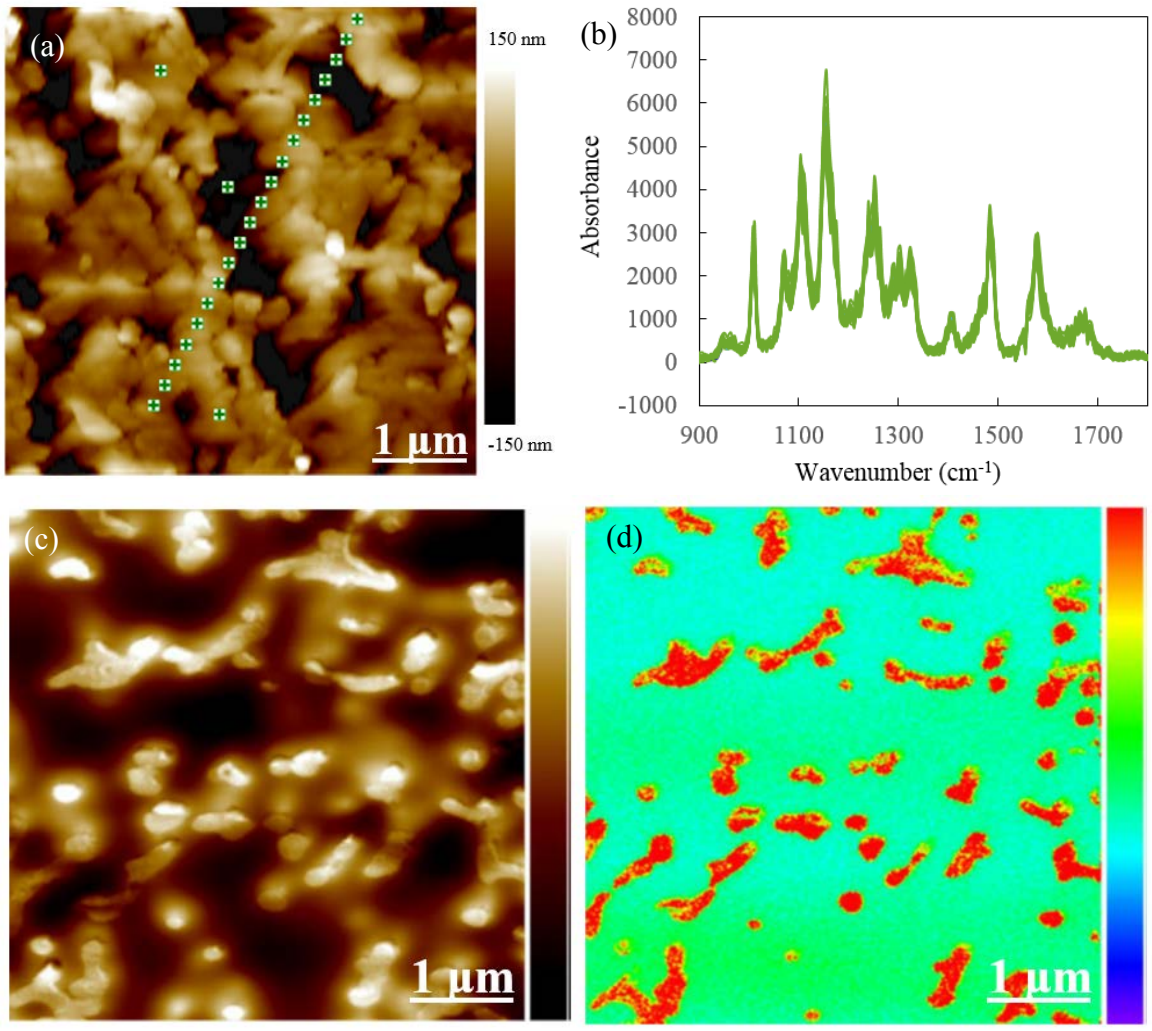

Figure 2.12 AFM image (a) and AFM-IR spectrum (b) for microtomed PES/PVP membranes. And AFM image (c) and IR absorption mapping at 1152 cm^{-1} (d) for PES/PVP membranes with cross-section.

Compared with the spectra obtained from microtomed membranes (Figure 2.12b), the AFM-IR spectra collected from non-microtomed membrane surfaces (Figure 2.11b) showed a sign of saturation, especially for the bonds at 1100-1200 cm^{-1}. The saturation issue happened probably because the membrane samples were too thick (140 µm) and the incident radiation at a particular wavenumber (*e.g.*, 1102 cm^{-1} and 1152 cm^{-1}) could be

totally absorbed by the sample well before the thermal diffusion limiting depth. Therefore, the spectra in Figure 2.11b show similar IR signal intensities for different absorbance peaks. Since the main purpose of this study is to resolve the surface chemical compositions on membrane samples, the saturation at 1152 cm^{-1} did not affect our objective for detection of modifier and its chemical distribution. In addition, because the membranes must be embedded in the epoxy or resin for microtoming, which might cause the surface contamination or damage or material distortion after the microtoming. That is why microtoming was not used to obtain thin samples or to measure cross sections. Since the characteristic band at 1668 cm^{-1} did not show significant signs of saturation, the AFM-IR spectra were directly collected from the pristine membrane samples without microtoming.

Based on the results above for PES/PVP membranes, it indicates that both of FTIR and AFM/IR successfully identified PVP on PES base membrane and their distribution could be mapped by AFM/IR as well. In this section, we expect that AFM-IR could also detect and map the distribution of additives on PES/PVP membranes with different PVP ratio. As shown in Figure 2.13, the band at 1668 cm^{-1} indicated the presence of PVP in PES membrane and the high amount of PVP blend in the membranes resulted in increased signal of the peak. Figure 2.13c shows the spectra acquired on the top and bottom surfaces of PES/PVP membrane, which appeared to be almost identical with the PVP C=O stretching carbonyl group band peak at 1668 cm^{-1}. This means that the PES/PVP membrane had homogenous chemical distribution.

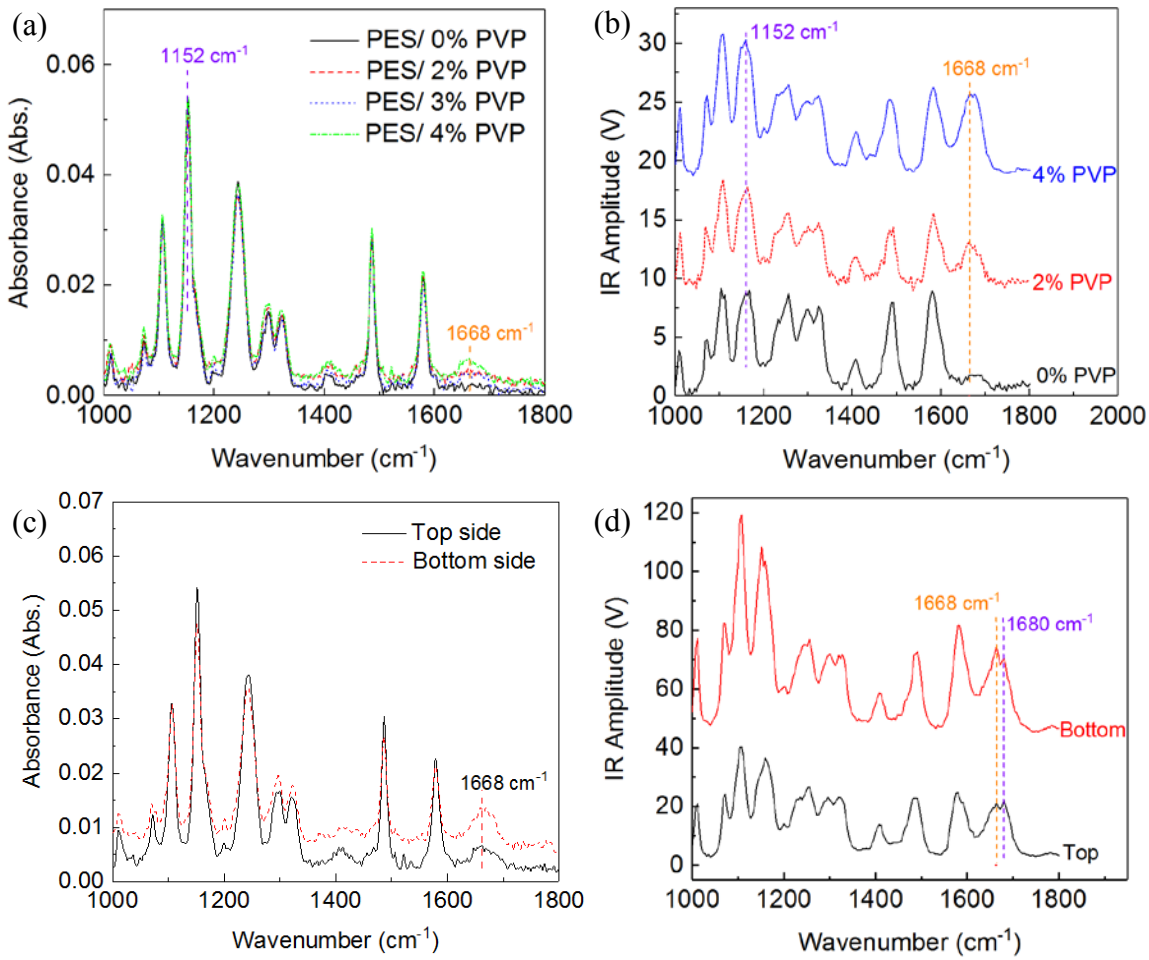

Figure 2.13 The spectrum collected with FTIR (a) and AFM-IR (b) from PES membranes (pore size is 200 nm) with different amount of PVP on the top (shiny) side; and comparison between the spectrum collected with FTIR (c) and AFM-IR (d) from top and bottom sides of PES membranes with 4% PVP.

Figure 2.14 shows the AFM-IR mapping that resolves the chemical distribution of PES and PVP on the membrane surfaces. For the PES/0%PVP membranes (Figure 2.14a), the PVP signal was quite weak (no red spots), indicating there was rare or no PVP in the PES/0%PVP membrane. For PES/2%PVP membranes (Figure 2.14b), there were some signals of PVP (red spots on the membrane surface) and the PES distribution signal was much stronger than those of PVP. Compared with PES/2%PVP membrane, PES/4%PVP membrane (Figure 2.14c) has a bigger area of PVP distribution signal. The results reveal

that the PES membranes dipped in the high concentration of PVP solutions were dip-coated with more PVP amount on the surface.

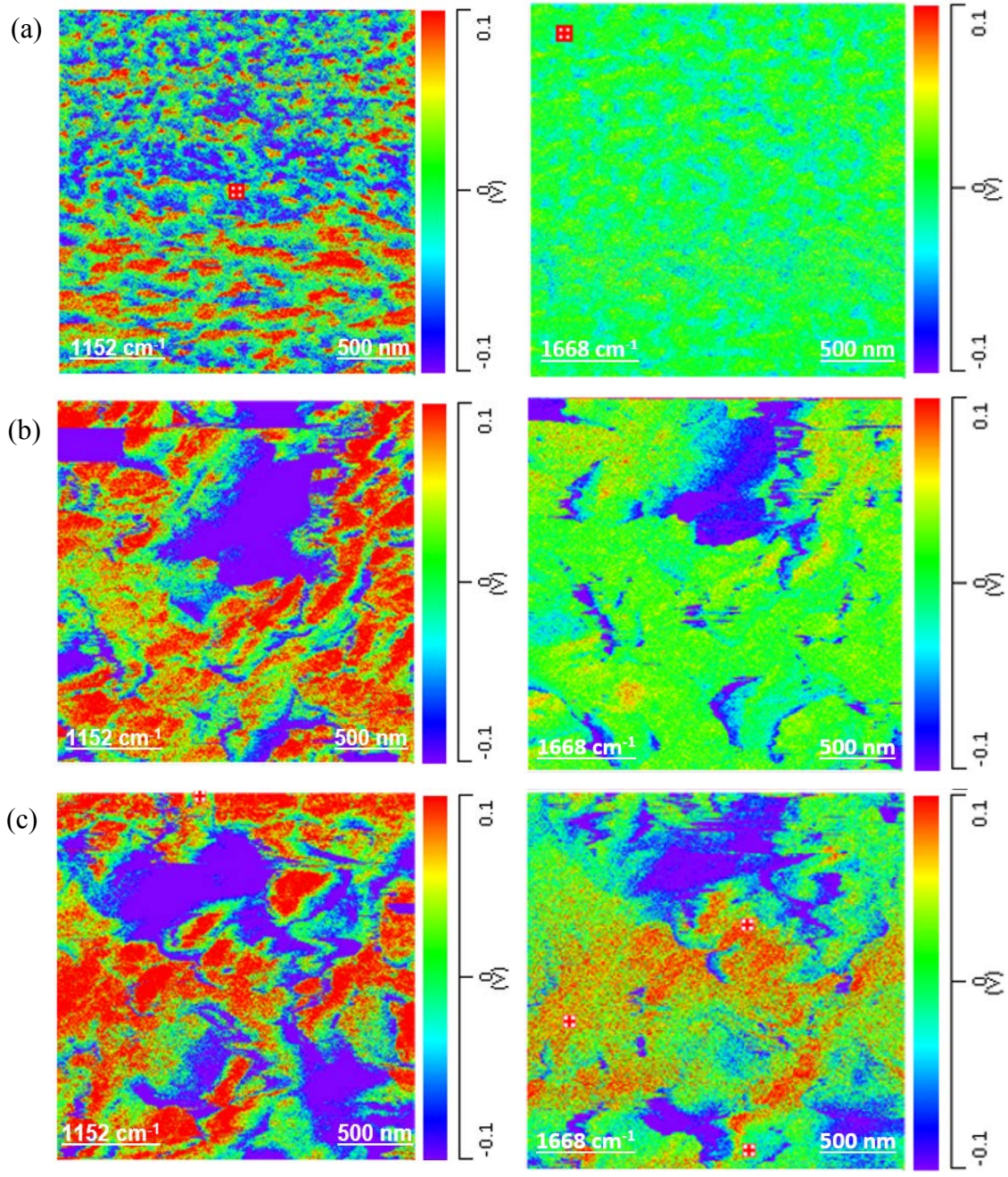

Figure 2.14 The IR mapping collected with AFM-IR at 1152 cm^{-1} (left) and 1668 cm^{-1} (right) for the distribution of PES and PVP, respectively, in PES (a), PES/2% PVP (b) and PES/4% PVP (c) membranes. Millipore PES membranes (pore size is 200 nm).

2.3.5.2 PES/PEG Membranes. For the PES membranes with PEG additives, FTIR was not able to identify PEG on PES base membrane with ATR-FTIR, probably because of the low content of PEG and the sensitivity limitation of ATR-FTIR. As shown in Figure 2.15, all spectra obtained for the different PEG blended PES membranes were the same. To better resolve the chemical speciation, a Varian 670-IR coupled with a Varian 620-IR microscope (Agilent Technologies – Santa Clara, CA, USA) was applied to collect the IR spectrum from PES and PES/2%PEG membranes (Figure 2.16a). The results show that an obvious band at 2888 cm^{-1} that may indicate the presence of PEG (Ether C-H) in PES membrane. However, other characteristics bands of PEG such as C-O-C band at 1103 cm^{-1} might be overlapped by PES peak at 1107 cm^{-1} because of the limited resolution of 8 cm^{-1}. IR mapping images at 1486 cm^{-1} and at 2888 cm^{-1} were collected to demonstrate the spatial distribution of PES (Figure 2.16b) and PEG (Figure 2.16c), respectively. AFM/IR was not able to identify PEG on PES base membrane (thus results were not shown here), probably because of the low content of PEG additives as well as the high solubility of PEG in water.[366]

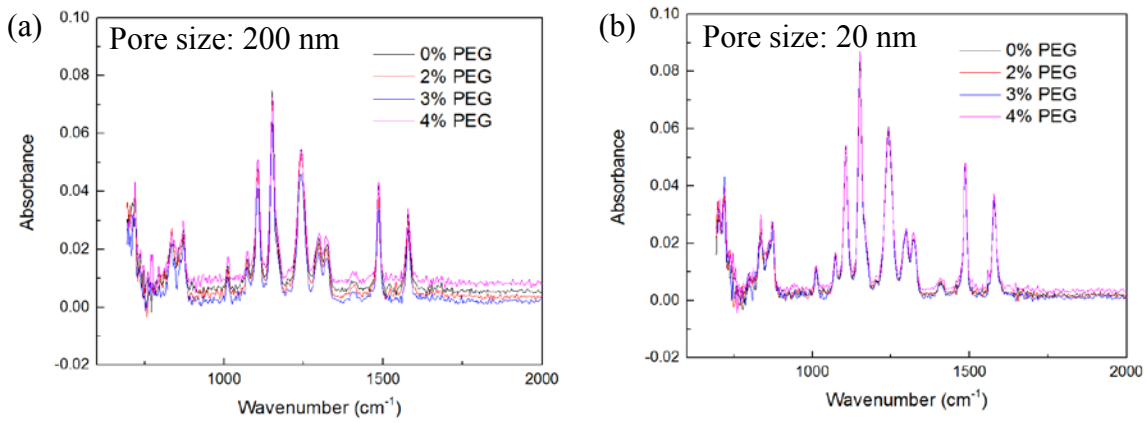

Figure 2.15 ATR-FTIR spectra for PES membranes with different PEG amount, pore size (a) 200 nm; (b) 20 nm.

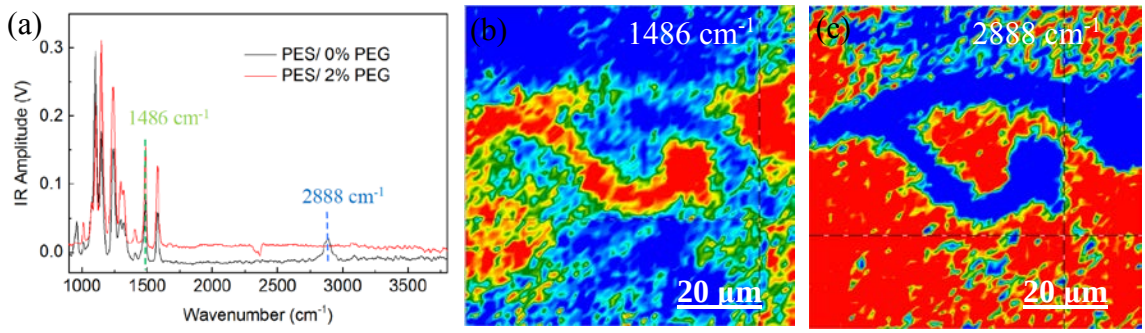

Figure 2.16 IR spectra (a) for PES membranes with different PEG amount (pore size is 20 nm); chemical distribution of PES (b) and PEG (c) for PES/2% PEG membrane.

2.3.5.3 Verify AFM-IR Method on Various Modified Membranes. The AFM-IR method was verified with application on various modified membranes (*i.e.*, hydrophilic UPE membrane, hydrophilic PVDF membrane and hydrophilic PES membranes without known modifiers). From the AFM-IR spectrum collected in Figure 2.17-2.19, the modifier hydrophilic groups were successfully detected. With the fixed wavelength, the IR mapping images of membrane backbone material and modifier material on the membrane surface were obtained. For the hydrophilic UPE membranes cross-linked with amide group, the spectrum (Figure 2.17a) has the peaks at 1469, 1668 (C=O stretching vibration of the amide group), 2848 & 2916 cm^{-1} (characteristic band of UPE, the asymmetric and symmetric stretching vibration peak of C–H). Then IR mapping of PVDF at 974 cm^{-1} (Figure 2.17b) and hydroxyl group at 3528 cm^{-1} (Figure 2.17c) were obtained. For the hydrophilic PVDF membranes cross-linked with hydroxyl group, the spectrum (Figure 2.18a) has the peaks at 974 &1284 (characteristic α-phase and β-phase bands of PVDF, symmetric stretching of C-F bonds), 1728 and 3448 cm^{-1} (stretching vibration of hydroxyl group). Then the IR mapping of PVDF at 974 cm^{-1} (Figure 2.18b) and hydroxyl group at 3528 cm^{-1} (Figure 2.18c) were obtained. For the hydrophilic PES membranes cross-linked with amide group,

the spectrum (Figure 2.19a) has the peaks at 1108, 1152 (the SO stretching band in PES), and 1664 cm^{-1} (the C=O stretching carbonyl group). IR mapping of PES at 1152 cm^{-1} (Figure 2.19b) and amide group at 1664 cm^{-1} (Figure 2.19c) were obtained. All the backbone material characteristic bands were detected and the modifier hydrophilic groups bands were detected as well, which was in agreement with the FTIR spectrum.

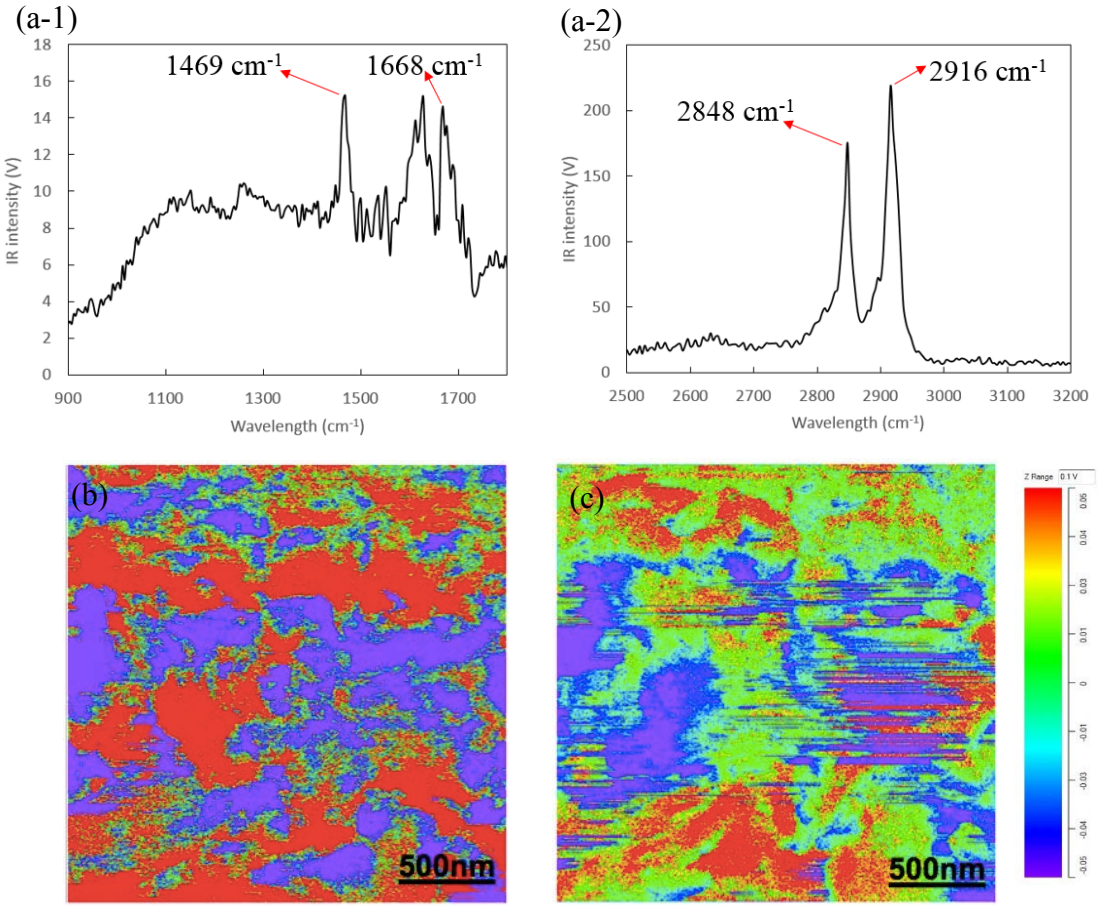

Figure 2.17. AFM-IR spectrum (a) and IR mapping of UPE at 2916 cm^{-1} (b) and amide group at 1668 cm^{-1} (c).

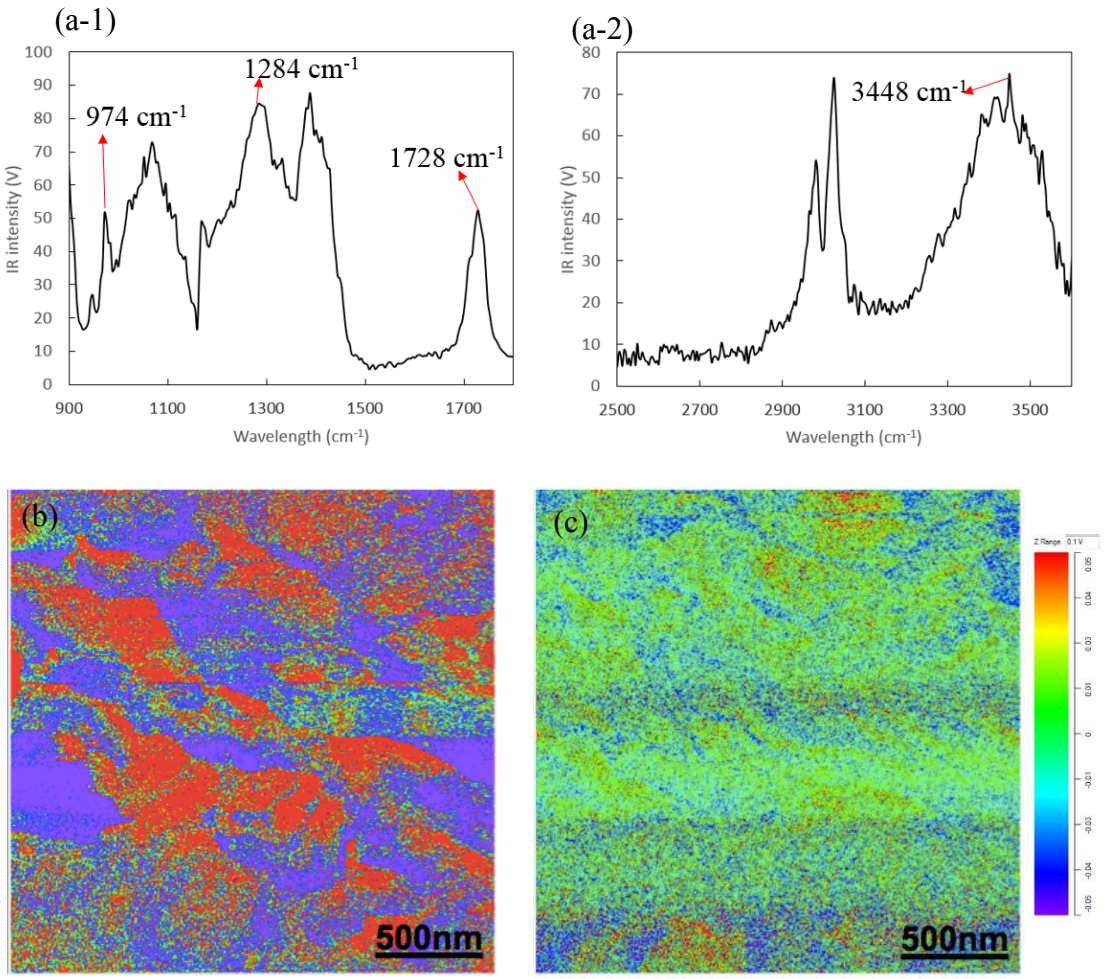

Figure 2.18. AFM-IR spectrum (a) and IR mapping of PVDF at 974 cm^{-1} (b) and hydroxyl group at 3528 cm^{-1} (c).

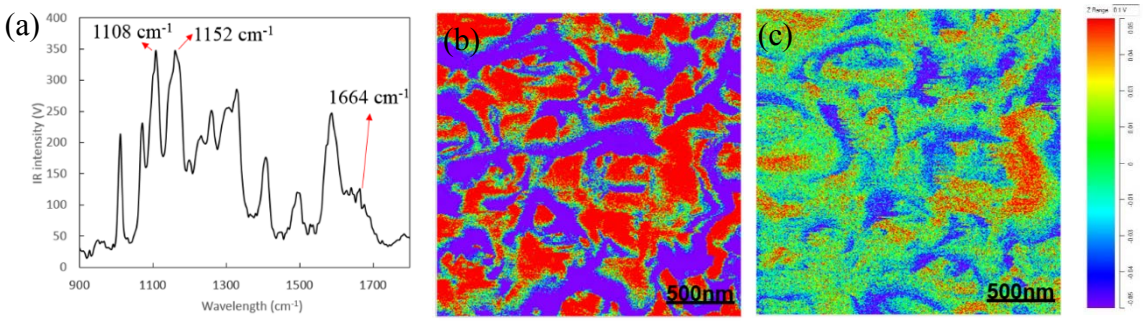

Figure 2.19. AFM-IR spectrum (a) and IR mapping of PES at 1152 cm^{-1} (b) and amide group at 1664 cm^{-1} (c).

In addition, we verified the feasibility of bigger scanning size and the reliability of AFM-IR techniques. Figure 2.20 shows the IR mapping of hydrophilic modifiers (amid I bonds in PVP) on PES membranes. We scanned twice bigger scanning size and the results showed that the IR mapping was representative and with high repeatability.

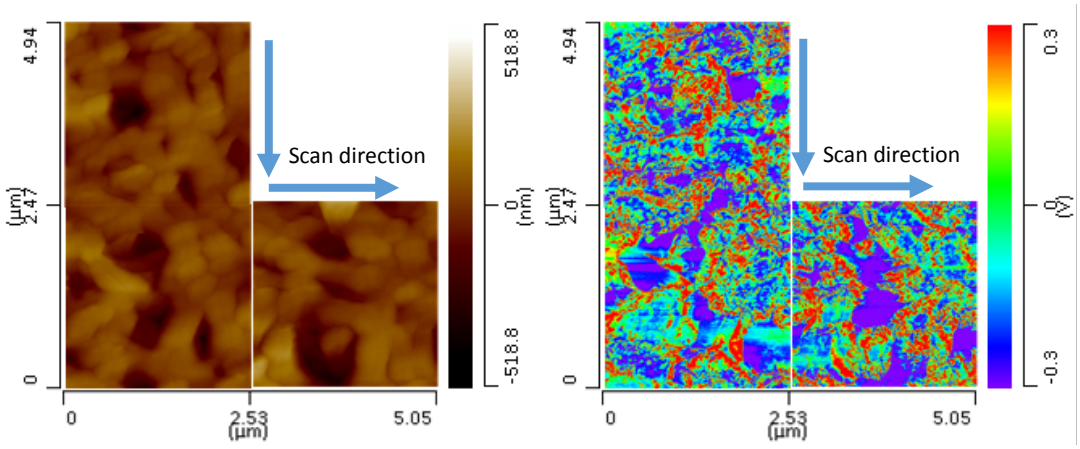

Figure 2.20. Modifier distribution area on hydrophilic membrane surface with PVP additives. The figures are IR mapping at 1664 cm^{-1}.

2.3.6 Membrane Surface Functional Group Measured by Raman and AFM/Raman

Figure 2.21 shows the Raman spectra of the three polymer membranes from Pall Corporation. Comparison of the spectra indicated that no PVP and no PEG band were detected in PES/PVP and PES/PEG membranes. The reason might be the low sensitivity of regular Raman spectroscopy. AFM/Raman was either not able to identify PEG on PES base membrane (thus data not shown), probably because of the low content of PEG additions. By contrast, Figure 2.22b shows that a very weak PVP peak around 2960 cm^{-1} at some sample regions. Most of the Raman detection results were similar with what we found with the conventional Raman spectroscopy data shows (Figure 2.21a).

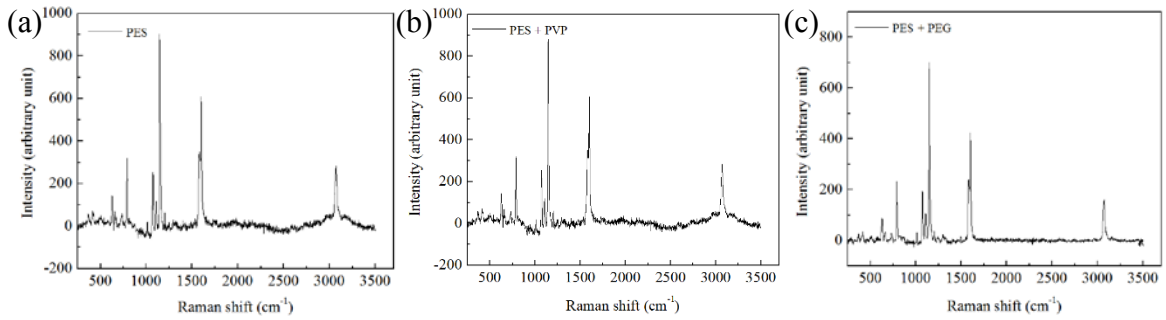

Figure 2.21 Raman spectra for (a) PES, (b) PES/PVP and (c) PES/PEG membranes from Pall Corp.

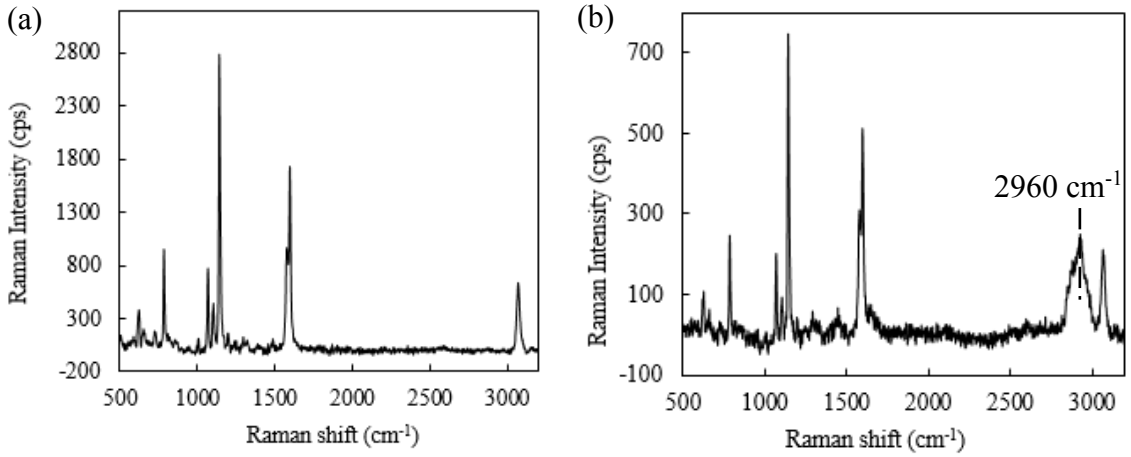

Figure 2.22 AFM-Raman spectra for (a) PES membrane and (b) PES/PVP membranes from Pall Corporation.

2.3.7 Potential Application of Optical Photothermal Infrared Spectroscopy on Surface Characterization of Surface Modified Membranes

As discussed in Section 2.3.5.1, the saturation issue of AFM-IR signal happened due to the high thickness of membrane samples. Ultramicrotome has been used widely in the preparation of very thin, frozen samples of biological tissue and this technique could be used to obtain thinner polymer membranes suitable for AFM-IR measurements.

Besides, for the thick membranes, another state-of-the-art technique named optical photothermal infrared (O-PTIR) spectroscopy, released in 2018 by Photothermal Spectroscopy Corp. might be able to overcome the problem. Similar to AFM-IR, O-PTIR

utilizes a mid-IR pulsed, tunable laser to heat the sample and the surface adsorption occurs when the IR laser excites a molecular vibration in the sample at a wavelength and thereby creates photothermal effects including thermal expansion. Different from AFM-IR, which uses AFM to detect the thermal expansion, O-PTIR use a visible probe laser, focused to 0.5 μm spot size to measure the thermal expansion via the scattered light, as shown in Figure 2.23. The component of the reflected visible laser signal that is modulated at the IR pump laser repetition rate is directly proportional to the absorption coefficient of the sample at that wavenumber. By operating in reflection mode, the need for thin samples is also eliminated, leading to dramatically easier sample preparation. Thus, with 0.5 μm spatial resolution, O-PTIR technique is a promising tool for the nanoscale characterization of polymeric membranes.

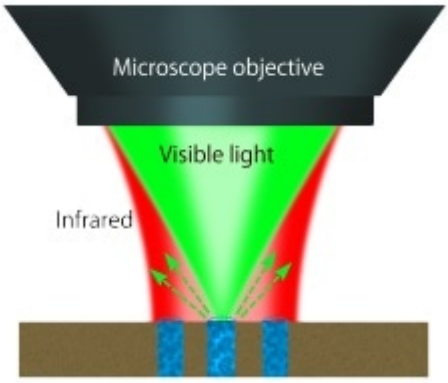

Figure 2.23 A pulsed tunable, IR source is focused on sample. Absorbed IR light causes sample to heat up, creating a photothermal response in the sample. A visible laser probe measures the photothermal response due to IR absorption. Figure was cited from website: https://www.photothermal.com/technique/.

2.4 Conclusion

In this study, we demonstrate that both AFM and AFM-IR are powerful techniques for analyzing the nanoscale surface properties of polymer membranes. Particularly, the

heterogeneous surface hydrophobicity and chemical distribution can be resolved at higher spatial resolutions compared to the water contact angle measurement and FTIR. The measured adhesion force between functionalized AFM tips and membrane surfaces was linearly correlated with "nanoscale" water contact angles (R^2= 0.9449). The contact angles calculated from adhesion force were smaller (3.9%-25.9%) than the bulk water contact angles, indicative of the potential discrepancies between local and bulk surface hydrophobicity. The AFM-IR nanoimaging at 1152 cm^{-1} and 1668 cm^{-1} was used to differentiate PES and PVP, which could not be resolved by regular FTIR spectroscope due to the diffraction limitation. The modified membranes dip-coated with higher concentration PVP solutions presented a stronger level of PVP IR signals. The AFM and hybrid AFM-IR technologies may bring a promising way to revolutionize the characterization of membrane surfaces, which is critical for functional membrane design and manufacturing as well as investigations of membrane fouling and weathering processes.

Moreover, these new methods are likely important for investigations of surface contamination or fouling process,[367] material weathering process, and antifouling surface design (*e.g.*, eye contact lenses[368] and sanitary coating[369]). nanobubbles production and stability investigation on specific substrate,[370] anti-fouling surface modified stainless steel for food processing,[371] biomolecular manipulation,[372] nanotopography release of nanoparticles from food package into environments[373] and any related nanotechnology and science research. For example, the anti-fouling coatings on ship hull in marine shipping filed for biofouling prevention was investigated with AFM for nanoscale topography and module values,[367] but AFM also can be used as a powerful tool for the nanoscale hydrophobicity analysis for those coatings instead of contact angle measurement method.

Another example, clean and contaminated membranes were analyzed and compared with AFM by Zhang *et al*,[374] but AFM force curve could be used to analyze the hydrophobicity change after the fouling, and AFM-IR could be used to investigate the fouling components distribution on membrane surface and in member pores, for further understanding of fouling mechanism.

CHAPTER 3

EXPERIMENTAL AND MODELING ASSESSMENT OF POLYMERIC MEMBRANE FOULING/DEFOULING KINETICS

3.1 Introduction

During the last few decades, membrane filtration has extensively been used in water and wastewater treatment,[292, 293] desalination,[294] dairy production,[295] biomass/water separation,[296] and recovery of rare metals.[297, 298, 300] Membrane fouling is still a major issue during the application of membrane filtration. Membrane fouling is commonly caused by cake formation, pore blocking, particle deposition, and concentration polarization, which results in the increase of membrane resistance, filtration failure and high operational cost.[375] Development of effective anti-fouling membrane materials is critical for economic viability and sustainability of membrane filtration processes.

Membrane characteristics, such as hydrophobicity/hydrophilicity, surface charge, roughness, pore size and porosity, etc., have been proven to impact on membrane filtration performance, especially on membrane fouling.[158, 179-181] Chemical modification such as cross-linking, adsorption or covalent grafting of charged ionic species and hydrophilic additives is a common way to engineer surface wettability and improve polymer membranes filtration. For example, macromolecular additives such as poly (ethylene glycol) (PEG)[307-309] and polyvinylpyrrolidone (PVP)[309-311] are widely used in membrane manufacturing industries. After the hydrophilization process, membrane properties (especially at nanoscale) could significantly differ from the pristine materials besides hydrophobicity or hydrophilicity. A small fraction of chemical blends may substantially alter the interfacial properties and the overall filtration performance.[293, 312, 313] Moreover,

the characteristics and performances of these chemically modified membranes may change sensitively with the concentrations and the molar ratios of chemical blends or additives.[319, 376, 377] For example, hydrophilization of membranes could lead to a heterogeneous distribution of surface functional groups or chemical domains and influence physical (pore size, porosity, and surface roughness),[314, 315] electric (zeta potential),[316] and mechanical (elasticity) properties.[317] These properties largely determine their bulk behavior such as solute-membrane interactions, filtration flux, selectivity, fouling/antifouling, and aging. For instance, Torrestiana-Sanchez *et al.* reported that water permeability and protein rejection were influenced by the addition of PVP and PEG during PES membrane.[319] Besides, molecular weight cut off (MWCO) of PES membrane could be changed by the addition of PVP.[320]

Particularly, the impacts of hydrophobicity and surface charge on membrane fouling during microfiltration have largely been reported previously.[179] However, most studies investigated the effects of hydrophobicity and surface charge of either membrane or foulants separately.[378-381] Only a few reports considered two factors together,[382-384] but none of them analyzed these interfacial properties of membranes and foulants at the same time.[186] Further, the interfacial properties of membranes, though playing a pivotal role in solute-membrane and foulant-membrane interactions,[385, 386] are largely overlooked probably due to the inadequate analytical approaches.

AFM has evolved to be one of the most powerful tools for characterization of material surfaces especially at nanoscale.[26, 27] Multiple physicochemical and electric properties can be mapped and quantified by AFM with nanometer resolutions. For example characteristics such as, surface morphology,[31, 32] roughness,[33] stiffness,[34, 35] adhesiveness,[36,

[37] viscosity,[38] hydrophobicity,[33] conductivity,[39] capacitance,[40, 41] magnetization,[42] surface potential[43] and work function[32] can be determined accurately. Compared to other electron microscopies, such as scanning electron microscopy (SEM) and transmission electron microscopy (TEM),[48, 49] AFM offers more characterization functions and more importantly, the original physiological states of samples can be well preserved. Samples can be placed in vacuum, gases, or aqueous environments with desirable conditions or chemistries, reducing potential artifacts on samples from sample preparation. Recent development of AFM has incorporated a suite of analytical techniques, including Raman spectroscopy, Infrared (IR) spectroscopy and confocal microscopy to further extend capabilities of chemical analysis and mapping on sample surfaces.[58-60] Traditional diffraction (*e.g.*, IR, Raman and Confocal Raman) has limited spatial resolution at several microns (*e.g.*, 3–30 μm), depending on the laser wavelength and instrumentation. By contrast, hybrid AFM techniques combined with IR and Raman demonstrated simultaneous physical and chemical characterization of polymer blends and multilayer films at ~10 nm lateral resolution and monolayer sensitivity (over 100 times higher in spatial resolution compared to traditional FTIR and Raman).[59, 65-67] Clearly, hybrid AFM makes it possible to perform rapid, *in situ*, and possibly real-time imaging and quantification of both physical and chemical properties at a nanoscale level. This is crucial to unravel novel and revolutionary information about material properties.

In this study, the effects of those macromolecular additives (PVP and PEG) on membrane properties and the filtration performances (*e.g.*, filtration flux, foulant rejection, and fouling) of the resulting PES membranes were systematically investigated. The hypothesis to verify is that different amounts of PVP and PEG additives may yield

heterogeneous surface properties (*e.g.*, hydrophobicity, surface charge) and significantly different filtration performances. A suite of analytic techniques such as AFM, ATR-FTIR, Raman, scanning electron microscopy (SEM), X-ray photoelectron spectroscopy (XPS) and dynamic light scattering (DLS) were employed to perform comprehensive characterization to reveal surface morphology, hydrophobicity, surface zeta potential, chemical binding and distribution of chemical additives on the base PES membrane matrix. These surface characteristics were further used to interpret the observed filtration performances (*e.g.*, foulant rejection and antifouling). Bovine serum albumin (BSA) and Aldrich humic acid (HA) were used as model foulants, representative of proteins and humic substances, respectively. Finally, the interfacial properties were integrated into the extended Derjaguin–Landau–Verwey–Overbeek (EDLVO) theory to derive a new correlation with membrane fouling kinetics. This correlation may enable quantitative prediction of membrane fouling to aid fouling mitigation and prevention. The study also aims to offer new insights into the novel membrane development, surface modification, antifouling design, and other related filtration separation applications.

3.2 Materials and Methods

3.2.1 Preparation of Chemically Modified Membranes

Three kinds of flat sheet PES membranes obtained from Pall Corporation for testing: (1) pristine PES membrane; (2) PES membrane blended with 10% (w/w) PVP; (3) PES membrane cross-linked with 8% (w/w) PEG. Another four kinds of PES membranes received from Millipore-Sigma Corporation are: Pristine PES membrane and PES membrane dip-coated in 2%, 3% and 4% PVP solution with a nominal pore size of 200 nm.

3.2.2 Bulk Scale Hydrophobicity Assessment by the Contact Angle Measurement

3.2.2.1 Probe Liquids. To determine the surface tension components of membrane surfaces, we performed the contact angle measurements using three probe liquids with well-known surface tension properties.[188] The probe liquids selected for this investigation are deionized (DI) water (18.2 MΩ cm at 25 ºC, Direct-Q® UV3 System, EMD Millipore, Bedford, MA, USA), glycerol (CAS NO. 56-81-5), and formamide (CAS NO. 75-12-7). Surface tension components (γ^{LW}, γ^{+}, and γ^{-}), polar energy component ($\gamma^{AB} = 2\sqrt{\gamma^{+}\gamma^{-}}$)[387] and the total free energy component (γ^{TOT}) of each probe liquid are shown in Table 3.1.

Table 3.1 Surface Tension Properties of Probe Liquids[388-390]

Probe liquids	Apolar energy component γ^{LW}	Electron-donor interaction components γ^{+}	Electron-acceptor interaction components γ^{-}	Polar energy component γ^{AB}	Total free energy component γ^{TOT}
Water	21.8	25.5	25.5	51.0	72.8
Formamide	39.0	2.3	39.6	19.0	58.0
Glycerol	34.0	3.9	57.4	30.0	64.0

3.2.2.2 Contact Angle Measurement Procedure. A drop of probe liquid (~5 μL) was placed on a dry membrane surface. At least three measurements of liquid drops at different locations were averaged to obtain contact angles for each membrane sample. The image of the liquid drop was taken within 10 s to determine the air–liquid–surface contact angles with the ImageJ software.

3.2.3 Measurement of Membrane Surface Zeta Potential and Its Principle

The membrane surface charge or surface zeta potential was measured by a surface zeta potential cell equipped on a dynamic light scattering (DLS) instrument (Malvern

Instruments ZetaSizer Nano ZS). The membrane samples were cut into 4 mm × 5 mm pieces and attached by double coated adhesive tapes (Tedpella) to the cell as shown in Figure 3.1. The cell was placed in a standard 12 mm^2 polystyrene cuvette (Fisher Scientific Co, Pittsburgh, PA) filled with the dispersant (*i.e.*, 1 mM NaCl solution within the pH range 4–10)[391] and tracer particles (300 nm carboxylated latex particles). The cuvette and cell were then placed in the temperature controlled ZetaSizer instrument at a temperature of 25± 1 ˚C. The pH was measured using a pH-meter (Orion model 420A, Boston, MA, USA) and adjusted by addition of NaOH and HCl solutions.

The distance between the tracer particle electrophoretic mobility measurement position and the membrane surface was varied by a height adjustable sample holder to change the roles of electrophoresis and the electro-osmosis in the movement of tracer particles. The measured electrophoretic mobility varied as a function of distance from the membrane surface. By plotting the reported mobility, or zeta-potential, as a function of displacement from the surface, the relationship can be used to derive the membrane surface zeta potential.[392, 393]

Figure 3.1a shows a charged surface in an electrolyte with an external electric field, *E* applied. The zeta potential of the surface in the electrolyte, the applied electric field and the presence of hydrated ionic species within the electrolyte cause electroosmotic fluid motion along the surface slipping plane.[357, 392] When the electric field is applied the tracers will move under electrophoresis and electro-osmosis. The measurements of tracer motilities at various points (position A – E in Figure 3.1b) can then be extrapolated to the intercept to yield the tracer mobility at the surface. Then the zeta potential can be calculated by the tracer particle mobility using the Henry's function:[394]

$$U_E = \frac{2\varepsilon z f(Ka)}{3\eta} \tag{3.1}$$

where U_E is the mobility, ε is the dielectric constant, z is the zeta potential, f(Ka) is Henry's function, and η is the viscosity. Henry's function generally has value of either 1.5 or 1.0. For measuring zeta potential in aqueous solutions of moderate electrolyte concentration, a value of 1.5 is used and this is referred to as the Smoluchowski approximation.[395] Then the surface zeta potential is indicated by the tracer electroosmotic mobility at the surface, which is calculated by the mobility at the surface subtract the electrophoretic mobility of tracer measured in the position far from the sample surface.

The surface zeta potential measurement strategy consisted of five measurements in the region 125–625 μm (position A – E in Figure 3.1b and blue dots in Figure 3.1d) in 125 μm steps and a further measurement at 1000 μm (red dots in Figure 3.1d) in order to estimate the tracer velocity, or tracer particle zeta potential ζ_{particle}. The measured electrophoretic mobility varied as a function of distance from the membrane surface. By plotting the reported mobility, or zeta-potential, as a function of displacement distance between the position where the mobility of tracer measured (marked as A, B, C, D or E in Figure 3.1b) and the sample surface, the relationship can be extrapolated back to the intercept, or zero displacement and obtain $\zeta_{\text{intercept}}$. The membrane surface zeta potential ζ_{membrane} was calculated using the equation:[392, 393]

$$\zeta_{\text{membrane}} = -\zeta_{\text{intercept}} + \zeta_{\text{particle}} \tag{3.2}$$

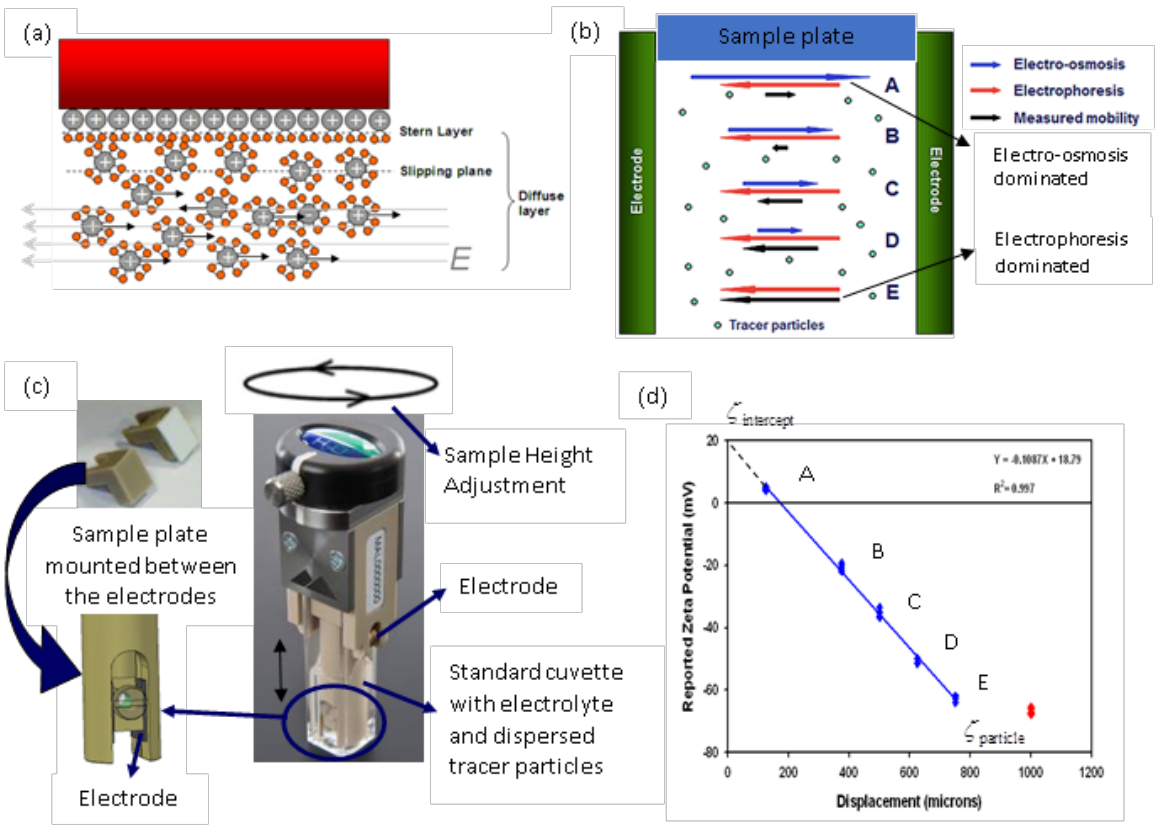

Figure 3.1 The basis of the surface zeta potential measurement technique. (a) The schematic of the surface zeta potential explanation; (b) the diagram with electro-osmosis, electrophoresis, resulting mobility; (c) schematics of the sample preparation procedure; (d) a typical measurement plot of zeta potential reported by the particle velocity against the displacement from the surface.

3.2.4 Characterization of HA and BSA as Model Foulant and Pollutant

The powdered HA (Sigma-Aldrich) was purchased to represent the humus-like substance in typical natural organic matters. The HA stock solution (0.1 g L^{-1}) was prepared by dissolving 0.1 g HA into 1000 mL deionized water. The solution pH was adjusted before carrying out the measurements or experiments by 0.1 mol L^{-1} HCl or 0.1 mol L^{-1} NaOH. The solid BSA (MW = 67 kDa, Sigma- Aldrich) was chosen to represent the protein-like substance in natural organic matter. The BSA stock solution (2 g L^{-1}) was prepared by

dissolving 2 g BSA into 1000 mL deionized water. The pH of the BSA solution was also adjusted with 0.1 mol L^{-1} HCl or 0.1 mol L^{-1} NaOH.

Contact angles of the HA and BSA were measured using the same way as described in Section 3.2.2.2. The HA and BSA coated surfaces were made by depositing the HA solutions and BSA solutions onto clean flat gold coated wafer and dried in the air. Zeta potential and mean size of HA or BSA in the solution were determined by dynamic light scattering (DLS) with a Malvern Zetasizer, Nano ZS (Malvern Instruments Limited, UK). Zeta potential was calculated by the Smoluchowski equation.[357] Each data value was an average of five measurements and all the measurements were performed at 25 ± 1 ^{o}C. The concentrations of BSA and HA solutions were determined by UV absorbance measurement at 287 nm and 254 nm,[358, 359] respectively, using a UV–Vis Spectrophotometer (Evolution 201, Thermo Scientific, Waltham, MA, USA). A linear calibration curve (Figure 3.7) with a coefficient of determination (R^2) greater than 0.99 between BSA or HA concentration and UV absorbance was obtained within the concentration range used in this study.

3.2.5 Static Adsorption of BSA and HA

To determine the adsorption kinetics and surface interaction of BSA toward polymer membrane, static adsorption experiments were conducted batchwise for up to 2 h at room temperature with a stirring rate of 100 rpm in a 50 mL beaker.[396] The beaker was filled with 8 mL of the BSA solution with an initial concentration of 100 mg L^{-1} and pH=6.25. Three square membrane pieces (0.25 cm^2 each) were used in the static adsorption reaction. At 20 minutes intervals, 2 mL of liquid samples were taken to analyze the solution BSA concentration. The concentration of BSA in the medium was determined spectrophotometrically at 287 nm using a calibration curve as shown Figure 3.7. The

amount of BSA adsorbed from membranes was calculated with the initial and final concentrations of BSA in the medium. After determination of the mass adsorbed, the membranes were discarded. A fresh membrane was used for each measurement. The static adsorption of HA toward polymer membranes were also carried out following the procedure described above, but the adsorption amount was too small to be analyzed. Therefore, the relative data was not presented in this study and the fouling caused by the adsorption of HA on membranes was assumed to be negligible.

3.2.6 Fabrication of Flat Membrane Cell

The flat membrane cell was designed in AutoCAD 2016 by Autodesk (San Rafael, CA). Schematic diagrams of the flat membrane cell can be seen in the Figure 3.2. The cell has an outer width and length of 4 inches, making the effective membrane area approximately 9.6 cm^2. The cell was manufactured with polytetrafluoroetheylene (PTFE) due to its strong chemical resistance and microwave transparence. The screws and nuts used to seal the cell were also made from PTFE.

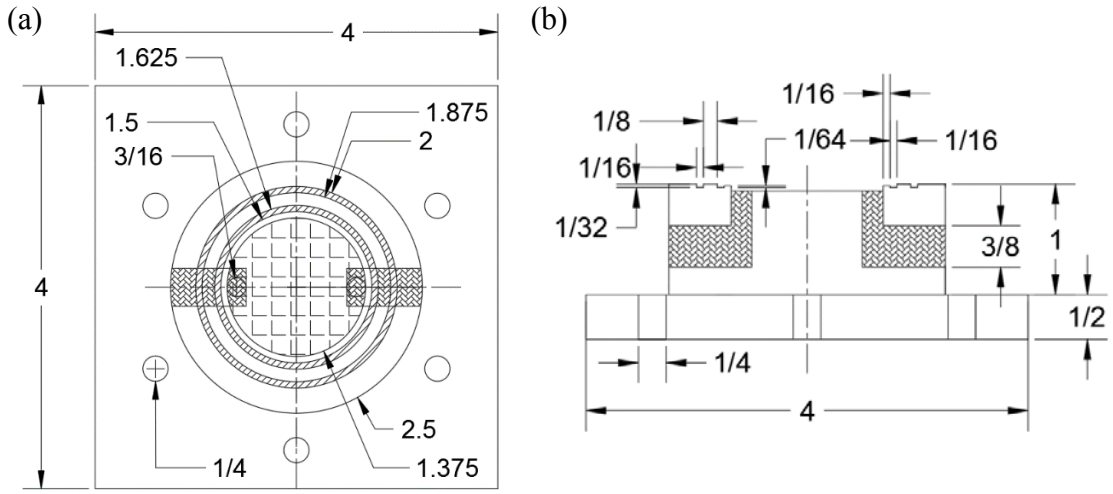

Figure 3.2 Top view (a) and side view (b) schematic of the flat membrane cell or module with dimensions in inches.

3.2.7 Cross-flow Filtration Performance

Figure 3.3 illustrates the schematic diagram for the bench scale filtration devise. The effective membrane area approximately 9.6 cm^2. As mentioned above, all parts of the filtration cell are made from Teflon (PTFE), including the O-ring, screen, screws and nuts. Cross-flow filtration (CFF) mode was used in the study, in which the feed solution passes tangentially along the surface of the membrane. A pressure difference across the membrane filter drives aqueous components that are smaller than the pores through the membrane. The solution that passes along the membrane surface and back to the feed tank is the retentate, whereas the solution that passes through the membrane is called permeate. This solution is usually pumped back to the feed tank and recirculated.

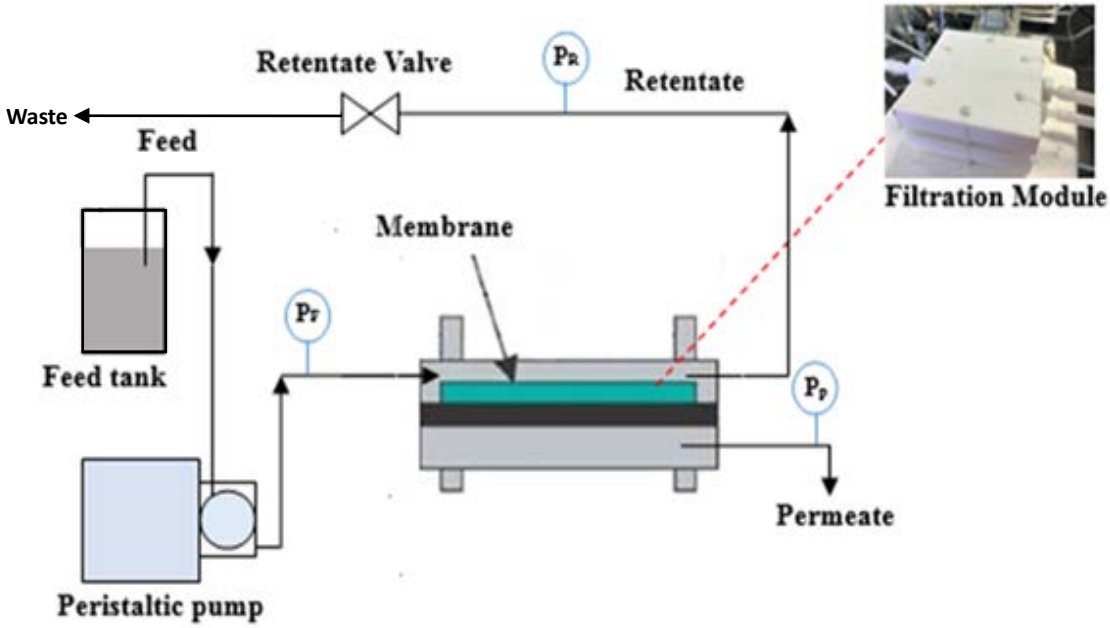

Figure 3.3 The schematic of the cross-flow filtration setup.

Liquid pressure and flow rates are essential factors for controlling and monitoring a cross-flow filtration process. Hydraulic pressure was monitored in the feed stream (P_F), the retentate stream (P_R) and the permeate stream (P_p). TMP represents the driving force

for transfer of material across the filter, and is calculated as shown in Equation 3.3. TMP was used to control the flux. The sum of the flow rates out of the filter on the retentate and permeate sides is equal to the flow rate of feed into the filter. The retentate flow rate is also known as the cross-flow rate or recirculation rate. The permeate flow rate is known as the flux. Flux is commonly expressed in units of liters per m^2 of membrane per hour (L m^{-2} h^{-1}, LMH).

$$TMP = \frac{P_F + P_R}{2} - P_P \tag{3.3}$$

The volume of the permeat was then measured and the flux was calculated using Equation 3.4:

$$J = \frac{V}{A \cdot t} \tag{3.4}$$

where J is the flux (LMH), V is the permeate volume (L), A is the effective surface area of the membranes (m^2) and t is the time of the permeate collection (h).

3.2.7.1 Compaction and Pure Water Permeability Measurement. All experiments were carried out by using the cross-flow cell filtration system (Figure 3.3) connected to a reservoir and pressurized by a peristaltic pump. Before the pure water permeability tests, the membranes were all pre-compressed at 5 psi (34.5 kPa) for 30 min to achieve a steady flux and to minimize the compaction effect. The pure water flux was otained by recording the volume of permeate over the time of 30 min under TMP of 34.5 kPa.

3.2.7.2 Membrane Fouling in BSA/HA Filtration. BSA was selected as the model protein foulant and HA as the model natural orgainc matters foulant in this study. For each filtration experiment, DI water was pumped at a TMP of 34.5 kPa through the filtration cell as a feed to determine the pure water flux (J_0). Then, the foulant solution (200 mg L^{-1} BSA solution and 10 mg L^{-1} HA solution) was subjected to the membrane cell under a TMP of 34.5 kPa and a cross-flow rate of 25 mL min^{-1} to observe the fouling accumulation. The TMP and flux were recorded every 5 min for 120 min. After that, the membranes were taken out, rinsed by immersion in 500 mL pure water and shaked for 1 min for removing the loosely-attached foulants on the membrane surface. Pure water fluxes before and after filtration were measured at the same pressure (34.5 kPa). The cleaning efficiency was indicated by the relative flux recovery (RFR) in Equation 3.5:[309, 397]

$$RFR(\%) = \frac{J}{J_0} \times 100 \tag{3.5}$$

During filtration of foultant (BSA and HA) solution, foulant concentrations in feed and permeate solutions were measured to detemrine the rejection rate:

$$\text{Rejection } (\%) = \frac{C_0 - C}{C_0} \times 100 \tag{3.6}$$

where C_0 and C are the concentrations of foulant in feed and permeate solutions, respectively.

3.2.8 Modelling of Membrane Fouling with BSA and HA Solutions

3.2.8.1 EDLVO Theory Analysis. The membrane-foulant interactions were modeled as particle–surface geometry.[398] In our calculation, the total interaction energies, U_{Total}, between membrane and foulants (BSA and HA) are equal to:

$$U_{Total} = U_{vdW} + U_{EL} + U_{AB} \tag{3.7}$$

where U_{vdW}, U_{EL}, and U_{AB} are the Lifshitz–van der Waals (vdW), electrostatic double-layer (EL) and polar or Lewis acid–base (AB) energy (k_BT), respectively.[188, 399, 400] To determine the individual contributions from van der Waals, electrostatic and Lewis acid–base interactions to the overall interaction energy, we first determined the surface energy, Hamaker constants, and zeta potentials of interacting entities as detailed in the following subsection.

First, U_{vdW} and U_{EL} can be calculated by the following equations:[166]

$$U_{132}^{vdW} = -\frac{A_{132}}{6}\left[\frac{a}{h} + \frac{a}{h+2a} + \ln\left(\frac{h}{h+2a}\right)\right] \tag{3.8}$$

$$U_{132}^{EL} = \pi\varepsilon_0\varepsilon\left(\xi_1^2 + \xi_2^2\right)\left[\frac{2\xi_1\xi_2}{\xi_1^2 + \xi_2^2}\ln\frac{1+\exp(-\kappa h)}{1-\exp(-\kappa h)} + \ln\left\{1-\exp(-2\kappa h)\right\}\right] \tag{3.9}$$

Although surface hydrophobicity changes may induce the changes to van der Waals, electrostatic and steric interaction energies, to simplify the EDLVO calculation, the effect of surface hydrophobicity changes is only attributed to the change of acid-base interaction energy in this study:[401]

$$U_{132}^{AB} = \pi a \lambda \Delta G_{132,D_0}^{AB} \exp\left(\frac{h_0 - h}{\lambda}\right) \tag{3.10}$$

$\Delta G_{132,D_0}^{AB}$ can be estimated by following equations:[402, 403]

$$\Delta G_{132,D_0}^{AB} = -\frac{K_{132}}{2\pi h_0 \lambda} \tag{3.11}$$

$$\log K_{132} = -7.0\left(\frac{\cos\theta_1 + \cos\theta_2}{2}\right) - 18.0 \tag{3.12}$$

where $\Delta G_{132,D_0}^{AB}$ is the standard polar or acid-base free energy (J m^{-2}) at the minimum equilibrium distance (h_0=0.157 nm) due to Born repulsion can be estimated by the hydrophobicity determination using water contact angles,[402, 403] K_{132} is the hydrophobic force constant (J). The contact angles (θ) were measured following the procedure described in Section 3.2.2.2.

The extended Young's equation is used to calculate the surface tension:[404]

$$(1 + \cos\theta) \cdot \gamma_L = 2(\sqrt{\gamma_i^{LW}\gamma_L^{LW}} + \sqrt{\gamma_i^{+}\gamma_L^{-}} + \sqrt{\gamma_i^{-}\gamma_L^{+}}) \tag{3.13}$$

where γ_L is the probe liquid surface energy (mJ·m^{-2}), which is known for the three probe liquids as shown in Table 3.1. γ_i^{LW} is the apolar part of surface tension of condensed material (i) caused by dispersion energy between molecules, and to γ_i^{+} or γ_i^{-} are the polar part of surface tension of condensed material (i) caused by dipole interaction included dipole moments and hydrogen bonds. According to Equation 3.13, γ_i^{LW} and the polar surface tension components: electron-acceptor (γ_i^{+}) and electron-donor (γ_i^{-}) can be solved

once the surface tension properties of probe liquids (γ_i^{LW} , γ_i^+ , and γ_i^-) and the contact angles (θ) of probe liquids on the samples surfaces are known, which are available in literature and shown in Table 3.1. The results of surface tension components (γ_i^{LW} , γ_i^+ and γ_i^-), polar energy component ($\gamma^{AB} = 2\sqrt{\gamma^+\gamma^-}$) and the total free energy component ($\gamma^{TOT} = \gamma^{LW} + \gamma^{AB}$) are shown in Table 3.4. The surface tension results are further used to compute the Hamaker constant for interaction between membrane and foulants in water using the method of van Oss:

$$A_{132} = 24\pi h_0^2 \left(\sqrt{\gamma_1^{LW}} - \sqrt{\gamma_3^{LW}}\right)\left(\sqrt{\gamma_2^{LW}} - \sqrt{\gamma_3^{LW}}\right) \tag{3.14}$$

where the subscript 1, 2, and 3 corresponds to membrane, foulant, and water, respectively. And all the parameters used in Equations 3.8-3.14 were explained in Table 3.2.

Table 3.2 Parameters Used in EDLVO Theory Equations

Parameters	Explanation	Remark
θ_1	the water contact angles of membranes	
θ_2	the water contact angles of foulants	
A_{132}	Hamaker constant for interacting subject 1 and subject 2 in the medium 3 (J).	
h_0	The minimum equilibrium distance due to the Born repulsion.	0.157 nm
h	The separation distance between the membrane and the foulants (nm).	
κ	The inverse Debye length (m^{-1}) defined as $\kappa = \left(N_A e^2 \sum c_i z_i^2 / \varepsilon_0 \varepsilon_r k_B T \right)^{1/2}$.	
N_A	Avogadro's number.	6.02×10^{23} mol^{-1}
e	Unit charge.	1.602×10^{-19} C
c_i	c_i is the molar concentration of one species ions (i), mol L^{-1}.	
ε_0	The dielectric permittivity of a vacuum	8.854×10^{-12} C V^{-1} m^{-1}
ε	The dielectric constant of water	78.5 (dimensionless)
z_i	The valence of the i^{th} ion.	
k_B	Boltzmann constant.	1.38×10^{-23} J K^{-1}.
T	The absolute temperature taken as 298 K.	
n	The molar concentration of ionic species in the medium (mol m^{-3}) multiplied by Avogadro's number (# mol^{-1}).	
ξ_1	Surface zeta potential (mV) for membranes	
ξ_2	Zeta potential (mV) for foulants	

3.2.8.2 Mathematical Modelling of Dynamic Membrane Fouling. The phenomenon of permeation flux decline or transmembrane pressure increase with filtration time is commonly termed as "membrane fouling". Flux decline is a result of the increase of membrane resistance commonly due to pore blocking, particle deposition, concentration polarization and cake formation.[375] For example, as shown in Figure 3.4, in the boundary of the gel polarized layer, the concentration of solute or particles increases from the bulk value (c_b) to c_m at the surface of the gel layer. The concentration of particles in the gel layer,

c_g, is assumed equal to c_m. The concentration of solute or particles in the filtrate is defined as c_p. Flux is a subtle combination of the effects of interactions between the particles themselves, the particles and the membrane surface, as well as other effects such as the influence of hydrodynamic forces.[405]

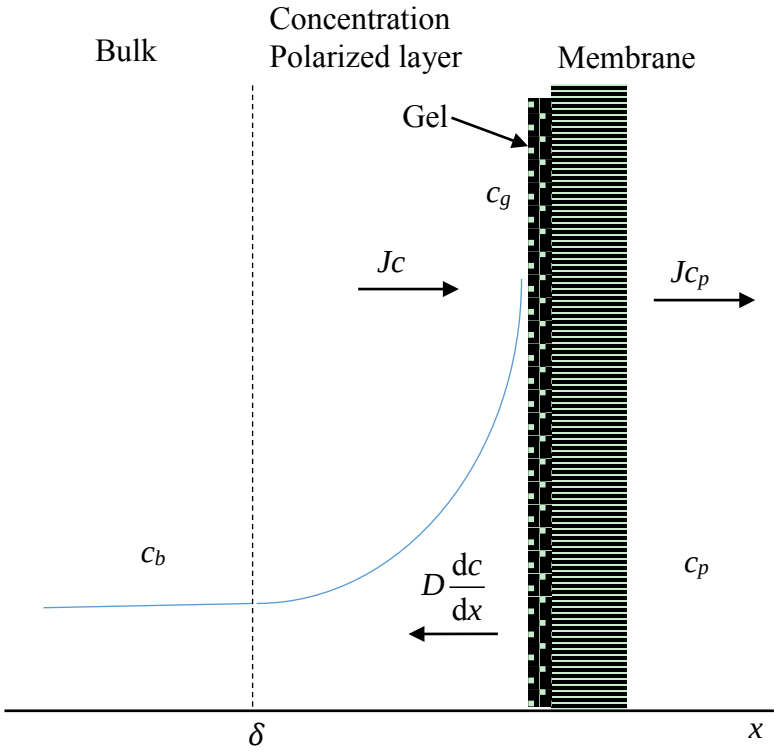

Figure 3.4 Schematic diagram of the concentration polarization and gel formation next to a membrane surface.[405]

In this study, a model of fouling dynamics in cross-flow filtration is developed based on the particle transport equation and the EDLVO theory.[406, 407]

$$J_x = -D_x \frac{\partial C}{\partial x} + u_x C + \frac{D_x F_x C}{k_B T} \tag{3.15}$$

where J_x is the particle flux (g m^{-2} s^{-1}) that is related to the particle deposition rate, D_x is the diffusion coefficient (cm^2 s^{-1}), C is the particle concentration (mg L^{-1}), u_x is the particle velocity components induced by the fluid flow (m s^{-1}), F_x is the component of the external force vector (N). T is the temperature (K), k_B is the Boltzmann constant, 1.38×10^{-23} J K^{-1}.

For the particle dispersion component, the particle deposition rate or flux is expressed as:

$$J_{x(disp)} = -D_x \frac{\partial C}{\partial x} = -D_x \frac{c_b - c_g}{h} \tag{3.16}$$

where c_b and c_g are the particle concentration (mg L^{-1}) in the bulk (feed) solution, and the gel layer, respectively; h is the separation distance between the foulants and the membrane (nm).

The particle deposition flux as a result of advection is expressed as:[408, 409]

$$J_{x(adve)} = u_x C = J c_b \tag{3.17}$$

where J is the pure water permeate flux, $J = \frac{Q}{A}$.

The particle deposition flux as a result of the interfacial force:

$$J_{x(force)} = \frac{D_x F_x C}{k_B T} = \frac{D_x c_b}{k_B T} \frac{\partial U_{mwf}^{TOT}(h)}{\partial h} \tag{3.18}$$

All parameters in this equation are described above. Thus, the overall particle deposition flux is expressed below:

$$J_x = -D_x \frac{c_b - c_g}{h} + Jc_b + \frac{D_x c_b}{k_B T} \frac{\partial U_{Total}(h)}{\partial h} \quad (3.19)$$

With the calculation result of overall particle deposition flux, we proposed that the particle deposition flux could be considered as the particle deposition rate, which is the growth rate of fouling layer on membrane surface as well. Then the positive correlations between the particle deposition rate and the flux decreasing rate might exist. The flux decreasing rate $\frac{\partial(J/J_0)}{\partial t}$ could be derived from slope of the flux changes with filtration time during the filtration time. It is assumed that the higher particle deposition rate calculated by Equation 3.19, the faster the flux decreasing rate will be. In this way, the fouling rate of the membrane could be indicated or predicted by calculation of particle deposition rate.

3.3 Results and Discussion

3.3.1 Hydrophobicity and Hydrophilicity Analysis

Average contact angle measurements for the probe liquids on the three membranes (PES, PES/PVP and PES/PEG) and the two model foulants (BSA and HA) are shown in Table 3.3. The hydrophobic/hydrophilic properties of chemically modified PES membranes were expected to vary as compared with the pristine PES membranes due to the presence of the hydrophilic functional groups such as hydroxyl groups and amino groups in PVP and ether groups in PEG. Table 3.3 shows that the pristine PES membrane displayed a water contact angle of 83.99 ± 1.06°, indicative of the highly hydrophobic nature of PES. After blending with PVP, the water contact angle reduced to 0°, a super-hydrophilic surface state. Similarly,

the Pall PES membrane cross-linked with PEG showed a water contact angle of 7.52±0.63°, also a highly hydrophilic surface property. Increasing the blending ratio of PEG from 0% to 4% in PES gradually reduced the water contact angle from 71° to 27°.

Table 3.3 Average Contact Angles of Membranes and Two Model Foulants

Materials		Contact angle (°)		
		Water	**Formamide**	**Glycerol**
Pall Membranes	PES	84.0±1.1	59.4±8.9	58.1±8.9
	PES/PVP	0±0	46.6±2.5	77.4±5.2
	PES/PEG	7.5±0.6	26.1±3.7	24.2±2.4
Millipore Membranes Pore size: 200 nm	PES/0% PEG	71.3±12.3	12.1±3.5	42.4±7.4
	PES/2% PEG	39.3±6.9	15.0±6.4	38.8±9.6
	PES/3% PEG	42.7±8.5	12.1±4.9	43.9±9.8
	PES/4% PEG	27.4±2.9	0±0	52.5±14.5
Foulants	Bovine Serum Albumin	23.0±2.4	31.8±0.6	50.4±0.4
	Humic Acid	31.5±2.2	30.0±2.7	60.8±4.1

Table 3.4 shows the calculated surface tension parameters and the free energy component for each of the membranes and foulants by Equation 3.13. The surface energy data show that PES membranes have high electron donor monopolarity, or high electron donor components (γ^-) and relatively low electron acceptor components (γ^+). By contrast, PES/PVP and PES/PEG membranes have high electron acceptor monopolarity. These results agree with previous studies reporting that original polymeric membranes typically have a high electron donor monopolarity.[410, 411] Specifically, the PES membrane has a low electron acceptor component, which translates into a low AB component. A high γ^{AB} component value of PES/PVP and PES/PEG membranes means that there is a higher degree of hydration on the surface or high hydrophilicity.

Table 3.4 Surface Energy Parameters of Seven Membranes, Two Model Foulants, and Three Probe Liquids [388, 389]

Materials		Polar surface tension components ($mJ \cdot m^{-2}$)	Polar surface tension components ($mJ \cdot m^{-2}$)		Polar energy component ($mJ \cdot m^{-2}$)	Total free energy component ($mJ \cdot m^{-2}$)
		γ^{LW}	γ^{+}	γ^{-}	γ^{AB}	γ^{TOT}
Pall membrane	PES	6.6±4.6	2.9±2.9	39.2±10.8	21.51	28.13
	PES/PVP	9.5±13.3	83.0±30.4	12.3±8.7	63.97	73.53
	PES/PEG	12.1±14.8	60.1±2.2	17.5±13.1	61.57	73.75
Millipore PES membrane	0%PEG	14.0±8.6	17.5±13.9	36.9±26.8	51.00	65.02
	2%PEG	10.4±14.6	30.4±19.3	21.9±29.6	51.70	62.10
	3%PEG	14.6±16.8	26.0±22.3	9.4±9.4	31.35	46.02
	4%PEG	31.4±13.8	7.16±5.37	33.0±4.2	30.78	62.27
Foulants	BSA	0.14±0.12	7.63±6.65	54.±3.6	40.67	40.81
	HA	19.8±8.7	12.7±12.5	17.6±9.9	29.96	49.84
Probe liquids	Water	21.8	25.5	25.5	51.0	72.8
	Formamide	39.0	2.3	39.6	19.0	58.0
	Glycerol	34.0	3.9	57.4	30.0	64.0

3.3.2 Membrane Surface Zeta Potential

Figure 3.5a shows the pH dependence of the surface zeta potentials (SZP) for the three membranes. All membrane surfaces were negatively charged over the entire pH range 4–11. The absolute SZP values increased (more negatively charged) with the increasing pH, which is consistent with literature.[391] The negative surface charges are because anions can approach more closely to hydrophobic surfaces (such as PES membrane).[412] The addition of PVP and PEG to PES obviously decreased the net surface charge of the PES membrane. With the addition amount of PEG, the net surface charge of PES was progressively reduced (Figure 3.5a).

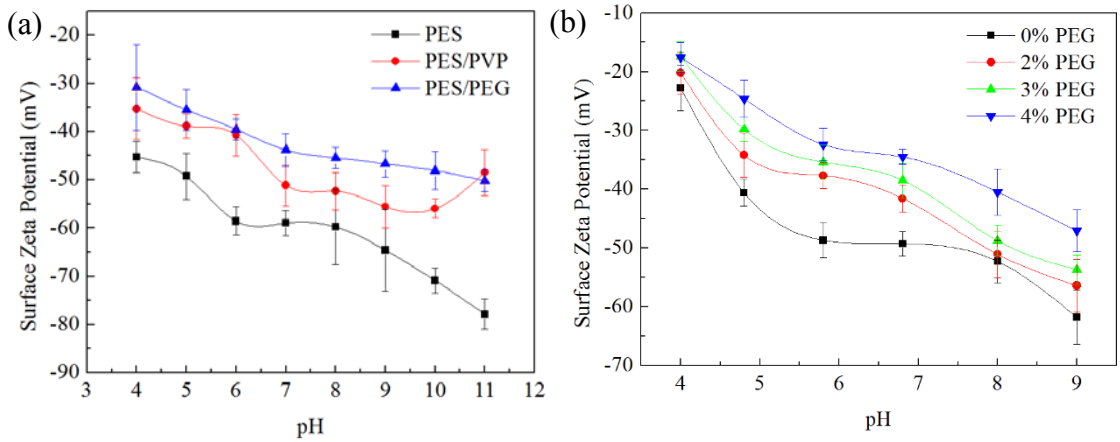

Figure 3.5 The surface zeta potential of membrane samples under different pHs. (a) Pall membranes; (b) Millipore membranes (pore size: 200 nm).

3.3.3 Effect of pH on the Physicochemical Properties of BSA and HA

Zeta potential of foulants, as a function of pH, is illustrated in Figure 3.6, which shows that the isoelectric point (IEP) of BSA was ~pH 4.7, consistent with the values reported in the literature.[413] When the pH was less than ~4.7, the basic residues and hydrogen ions on the BSA surface were completely associated, which is why the zeta potential was positive. When the pH value increased, amino acidic residues on the BSA surface gradually played a role in the solution, increasing the negative charge on the protein surface. When the amino acid residues on the surface completely dissociated, the zeta potential became stabilized.[413] The pH value changes the properties of the protein surface charge by affecting the degree of protonation of amino acid residues on the protein surface.[165]

Figure 3.6 shows that Zeta potential of HA molecules are negatively charged in the testing pH. The absolute values of zeta potential increases with pH increasing. This can be explained that large amounts of carboxylic and hydroxylic functional groups of HA molecular were protonated in acidic environment, which leads to the decrease of electrostatic repulsion and the molecular curls spherically. While the neutral and alkaline

conditions can deprotonate the functional groups of HA, which result in the increase of electronegative, so the molecular conformation stretch correspondingly.[397, 414]

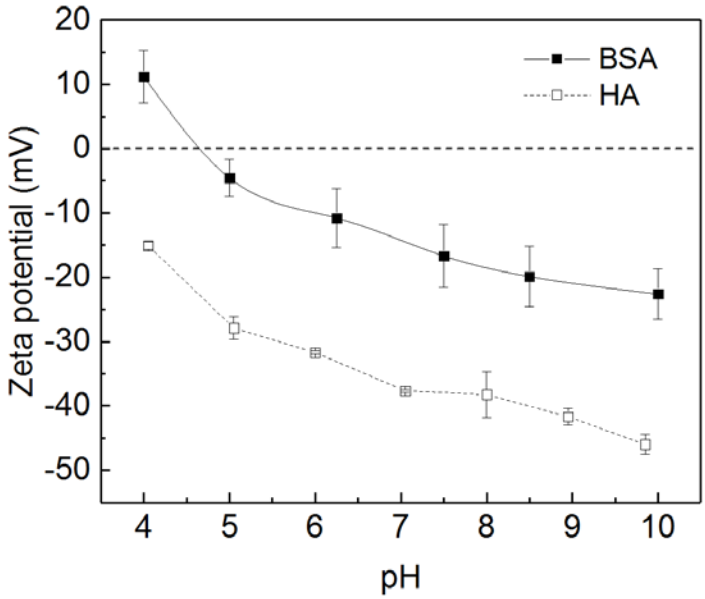

Figure 3.6 Effect of solution pH on zeta potential of BSA and HA. At least 3 replicate measurements were performed for each condition.

3.3.4 Effects of Membrane Surface Characteristics (Surface Charge and Hydrophobicity) on Static Adsorption of BSA and HA

The calibration curves for BSA and HA concentration measurements were obtained and shown in Figure 3.7. These calibration curves were used later as a means to determine the concentrations of BSA and HA in the solutions. The limits of detection (LOD) for BSA and HA were 3.08 mg L^{-1} and 0.39 mg L^{-1} respectively.

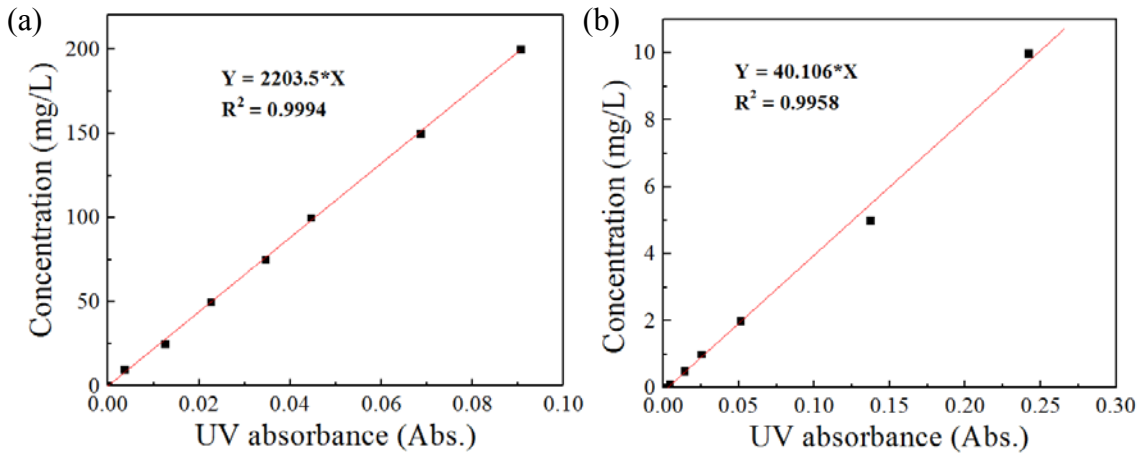

Figure 3.7 Calibration curves for BSA (a) and HA (b) based on the absorbance measurements at 287 nm and 254 nm respectively.

The dynamic adsorption of BSA on polymer membranes is given in Figure 3.8. Adsorption kinetics varied with membranes. PES had higher affinity toward the adsorption of BSA than PES/2%PEG membranes did. This is probably because of the strong adhesion force between the hydrophobic membrane and hydrophobic BSA, which is further analyzed below using the EDLVO theory.

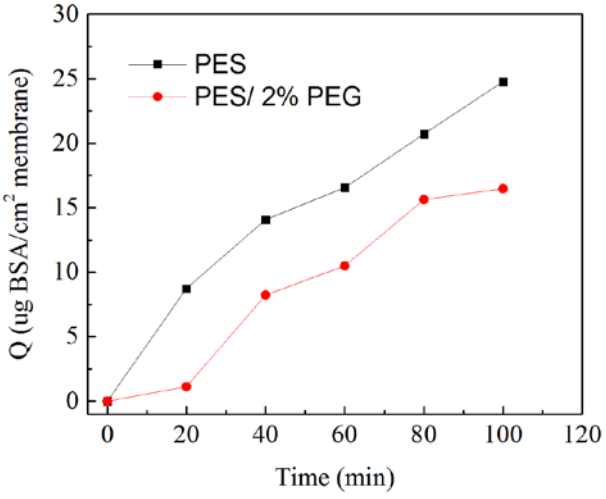

Figure 3.8 The dynamic adsorption of BSA onto PES and PES/2%PEG membranes at pH 6.25 with an initial BSA concentration of 100 mg·L^{-1}.

3.3.5 Evaluation of Filtration Performance

3.3.5.1 Membrane Compaction and Pure Water Permeability. Compaction is a common phenomenon during application of polymeric membranes, where the membrane structure is compressed under a transmembrane pressure difference. This compression may cause a decrease in membrane permeability due to mechanical deformation of the solid polymer.[415, 416] In this compaction study, the membranes were pressurized at high pressure (34.5 kPa) for 30 min. Table 3.5 shows the pure water permeability measured after 30 min of compaction. The membrane prepared with an additive showed the higher permeability those membrane made of pure PES. Especially, the PES membrane with pore size of 20 nm did not have any permeate through the membrane under the highest pressure shown by the pressure meter (200 kPa). In general, addition of a hydrophilic polymer (PVP or PEG) can facilitate the water through the membrane. But the higher amounts of PEG in the membranes did not obviously promote higher permeability than those with lower amounts.

Table 3.5 Pure Water Permeability Results

Membrane		**Water Permeability** ($L\ m^{-2}\ h^{-1}\ kPa^{-1}$)
Pall	PES	5.38 ± 0.22
	PES/PVP	28.25 ± 3.70
	PES/PEG	37.06 ± 0.57
Millipore 20 nm pore size	PES	0.41 ± 0.03
	PES/2%PEG	4.92 ± 0.24
	PES/3%PEG	4.03 ± 0.03
	PES/4%PEG	3.75 ± 0.07
Millipore 200 nm pore size	PES	3.95 ± 0.05
	PES/2%PEG	85.43 ± 0.20
	PES/3%PEG	97.57 ± 0.33
	PES/4%PEG	97.90 ± 0.35

3.3.5.2 Membrane Fouling During Filtration of BSA Solution. The effects of additives on membrane performance, fouling and pollutant rejection was investigated by

filtration of 200 mg L^{-1} BSA solutions. The results of flux changes over the filtration time (Figure 3.9) show that flux decreased for all membranes due to fouling or BSA clogging on pores. The presence of hydrophilic macromolecular additives clearly slowed down the decline rates of flux compared to pristine PES membrane. This is because water layer on hydrated membrane surface could hamper BSA adsorption and reduced membrane fouling. Figure 3.9b also indicates that when increasing PEG addition on PES, the fouling kinetics was significantly lowered.

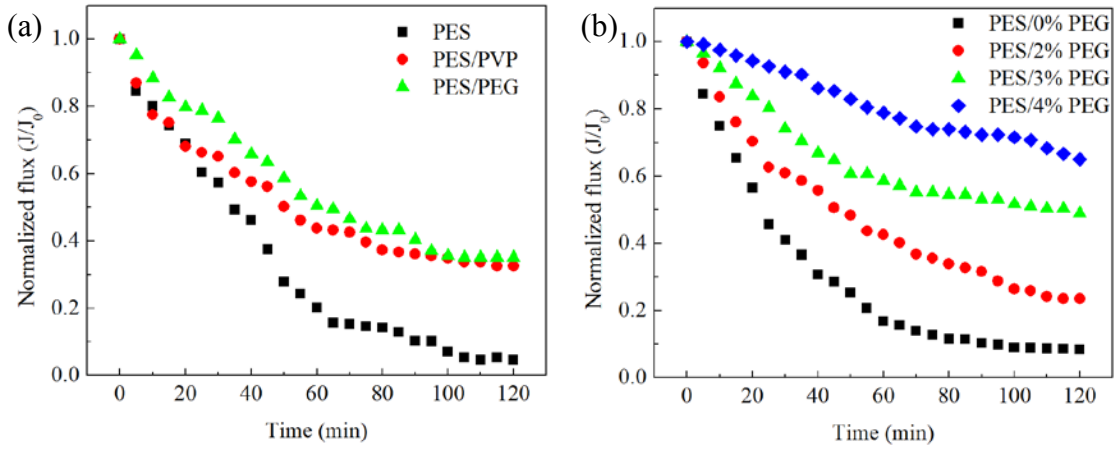

Figure 3.9 Flux decreasing in BSA filtration for PES, PES/PVP and PES/PEG membranes from Pall Corp. (a), and PES membranes with different PEG amounts from Millipore-Sigma Corp. (b), 200 mg L^{-1} BSA solution, pH =7.46.

The relative water flux recovery (RFR) was also used to assess the extent of cleaning efficiency and reversible fouling. Figure 3.10 shows that the pristine PES membrane had the highest flux recovery ratio although it suffered the fastest flux decline as shown in Figure 3.10. The possible reason is that the fouling mechanism for PES membranes could be dominated by the fast BSA adsorption on the shallow membrane pore surfaces. Therefore, the flux recovery on PES membrane could be easily obtained with water washing. For the modified membranes, however, the dominant fouling mechanism

might be the pore blockage because the modified membranes had bigger pore sizes and porosity, which increased the chances of BSA accumulation within the inner pores and surfaces. and the pore blocking that were not easily cleaned by water backwash.

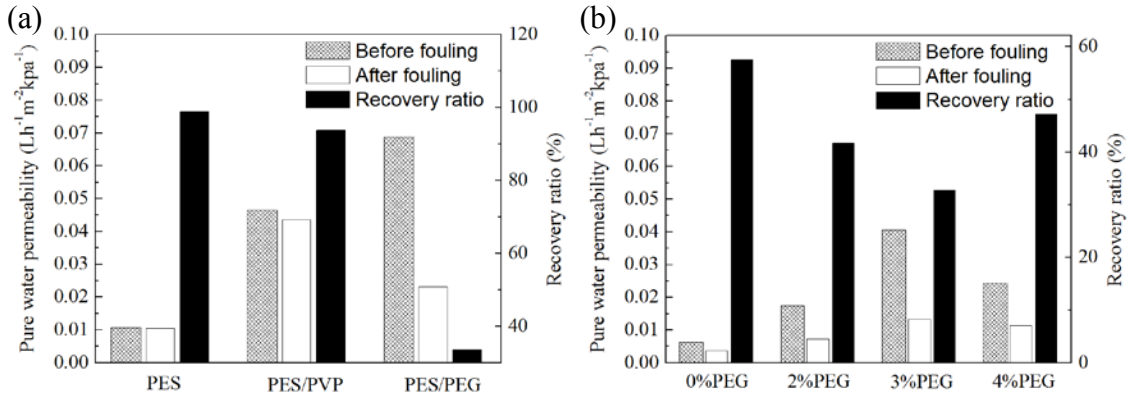

Figure 3.10 Relative flux recovery after filtration of BSA solution with PES, PES/PVP and PES/PEG membranes from Pall Corp. (a), and PES membranes with different PEG amounts from Millipore-Sigma Corp. (b), 200 mg L^{-1} BSA solution, pH =7.46.

Rejection data presented in Figure 3.11 shows that the PES membrane had the lowest protein rejection while modified membranes showed similar protein rejection for the Pall membranes without significant differences (p>0.05).

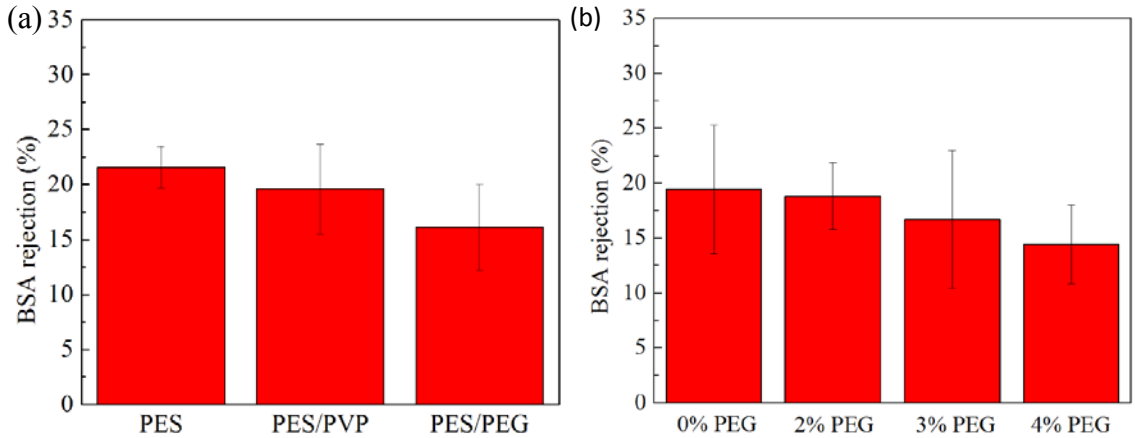

Figure 3.11 Protein rejection during the filtration of BSA solution with PES, PES/PVP and PES/PEG membranes from Pall Corp. (a), and PES membranes with different PEG amounts from Millipore-Sigma Corp. (b), 200 mg L^{-1} BSA solution, pH =7.46.

3.3.5.3 Membrane Fouling During Filtration of HA. During the filtration of 10 mg L^{-1} HA solutions, permeate flux also decreased with time for all membranes (Figure 3.12). Unlike the BSA filtration results, the presence of hydrophilic macromolecular additives did not decreased the flux decline rates significantly other than the PES/4%PEG membrane. The RFR in Figure 3.13 indicated that PES/PEG membrane showed higher resistance towards fouling and higher flux recovery compared to that of PES or PES/PVP membranes. Increasing the PEG amounts increased the RFR. Rejection data presented in Figure 3.14 shows that the PES membrane prepared without an additive had the lowest HA rejection while membranes prepared with an additive showed similar protein rejection. In general, performance test showed that the membrane prepared with addition of PEG as modifier agent for Pall Corp. and PES/4%PEG membranes for Millipore-Sigma Corp. showed the best performance, *i.e.*, the low flux decrease, high relative flux recovery and similar rejection could be obtained.

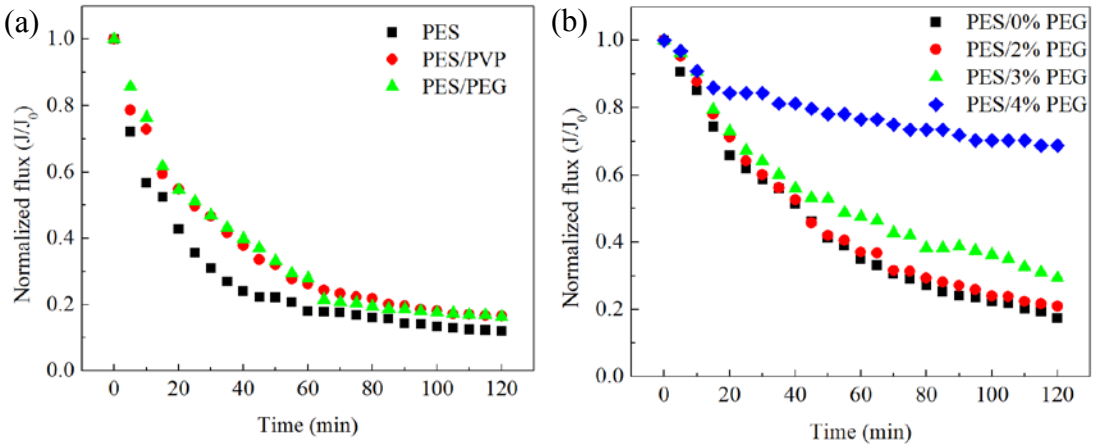

Figure 3.12 Flux decreasing in HA filtration for PES, PES/PVP and PES/PEG membranes from Pall Corp. (a), and PES membranes with different PEG amounts from Millipore-Sigma Corp. (b), 10 mg L^{-1} HA solution, pH =6.57.

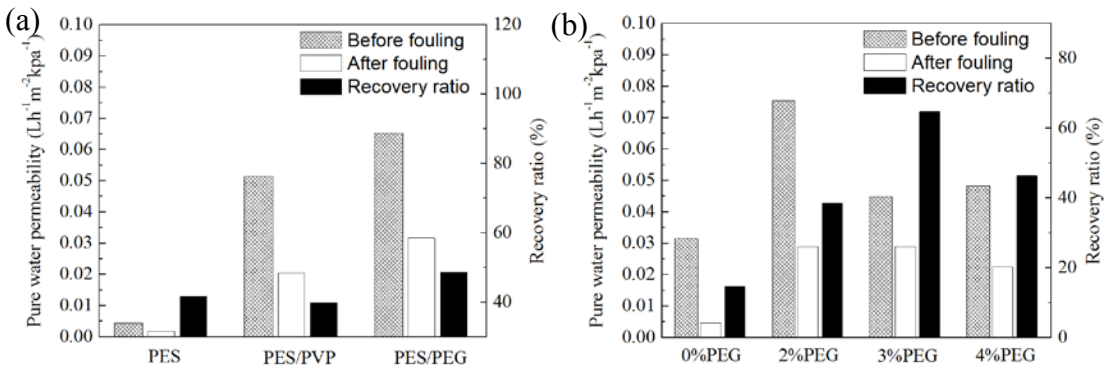

Figure 3.13 Relative flux recovery after filtration of HA solution with PES, PES/PVP and PES/PEG membranes from Pall Corp. (a), and PES membranes with different PEG amounts from Millipore-Sigma Corp. (b), 10 mg L^{-1} HA solution, pH =6.57.

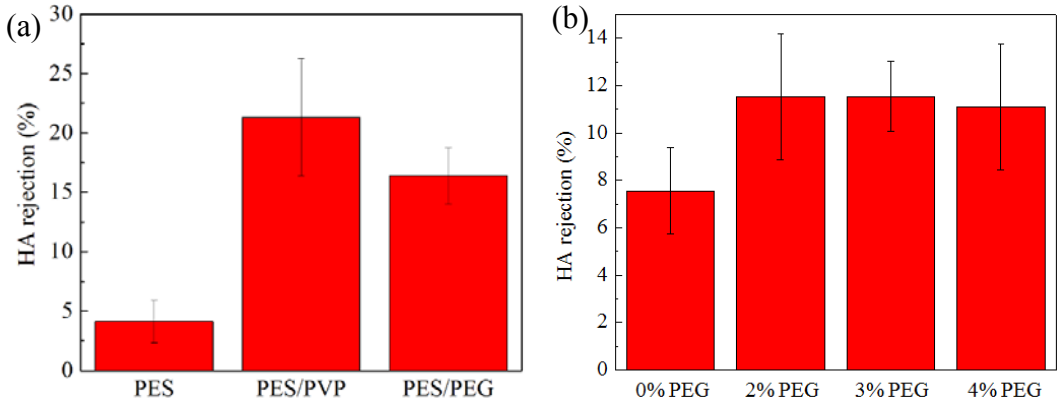

Figure 3.14 Humic acid rejection during the filtration of HA solution with PES, PES/PVP and PES/PEG membranes from Pall Corp. (a), and PES membranes with different PEG amounts from Millipore-Sigma Corp. (b), 10 mg L^{-1} HA solution, pH =6.57.

3.3.6 EDLVO Theory

Figure 3.15 shows the EDLVO interaction energy profiles for the two membrane–foulant interaction systems. For each membrane–foulant combination, Equations 3.8-3.9 were used to calculate the vdW, EL, and AB components of the interaction energies. These components were then added together according to their respective Equation 3.7 to obtain the total or net interaction energy profiles. The effects of zeta potential and hydrophobicity difference on the strength of energy barrier were compared. For all the seven membranes,

the total interaction was continually repulsive for the HA-membrane system due to the strong electrostatic repulsive force between HA and membrane surface according to the EDLVO theory. By contrast, the changes of surface hydrophobicity or hydrophilicity varied the order of magnitude of the AB interaction energy, which was less significant than the EL interaction energy. Therefore, increasing membrane surface charge might be more important than improving membrane surface hydrophilicity for membrane fouling control.[166]

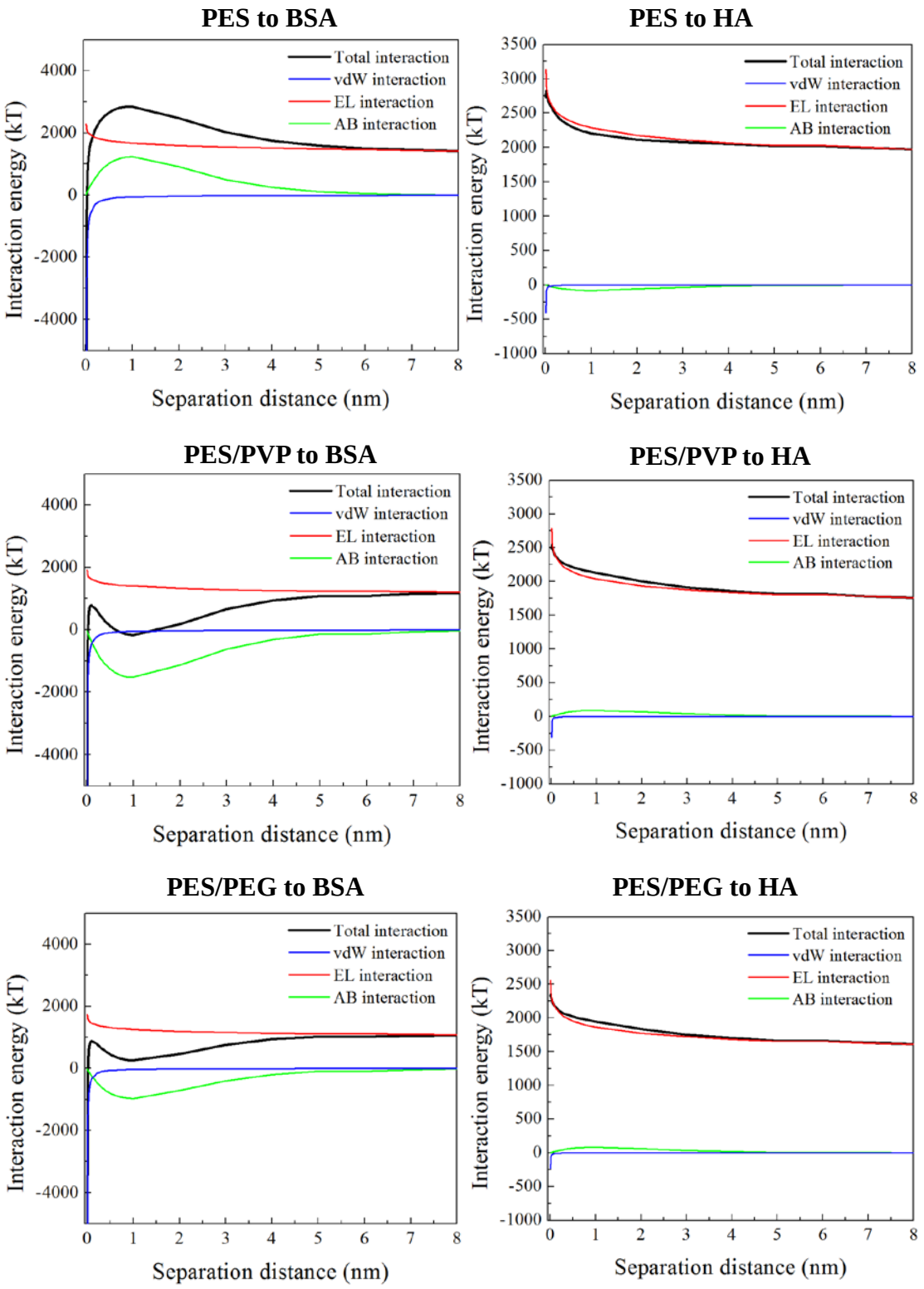

Figure 3.15 EDLVO interaction energy profiles for all the membrane–foulants combinations tested. (to be continued)

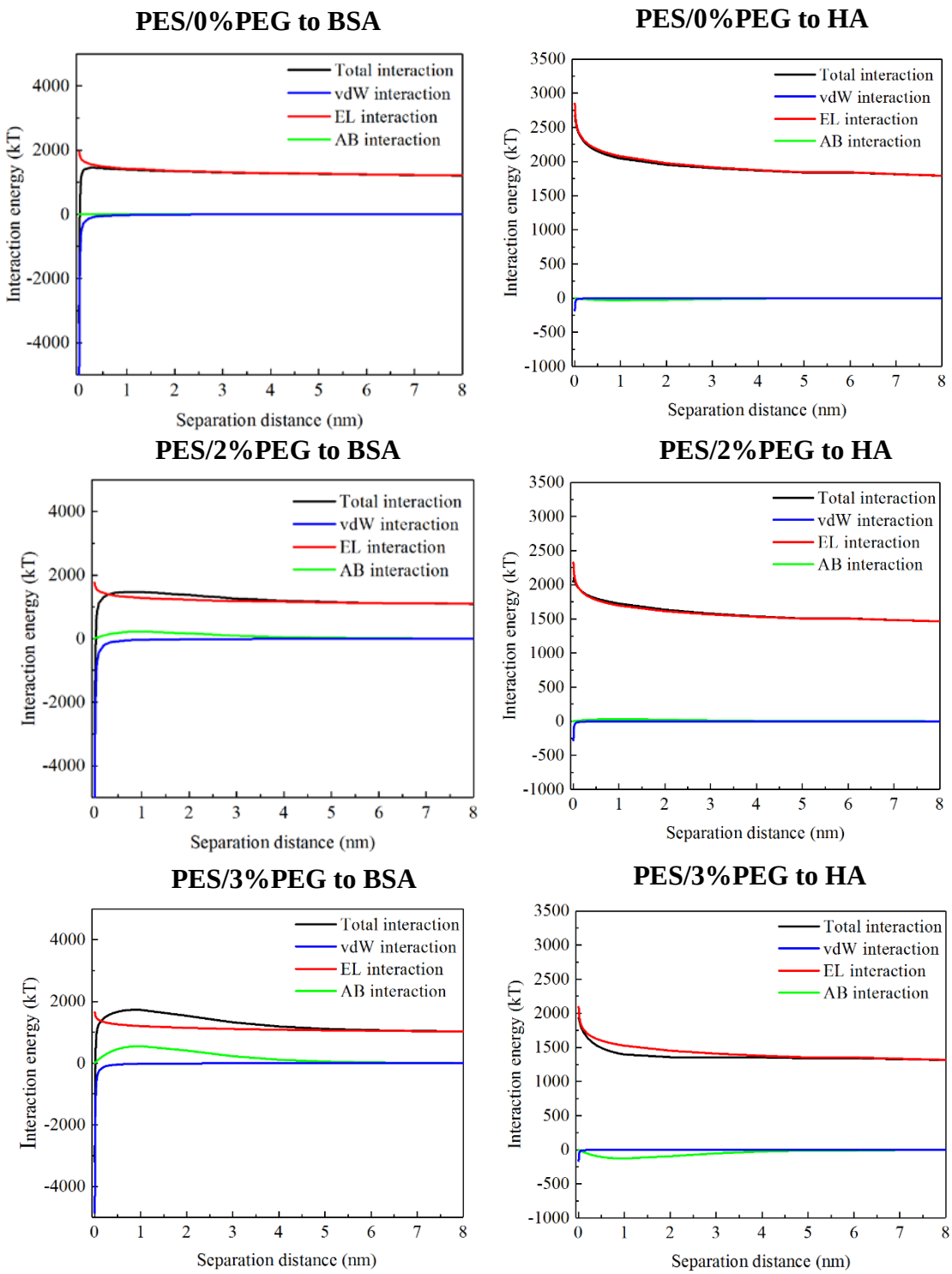

Figure 3.15 EDLVO interaction energy profiles for Millipore membrane–foulants combinations tested (to be continued).

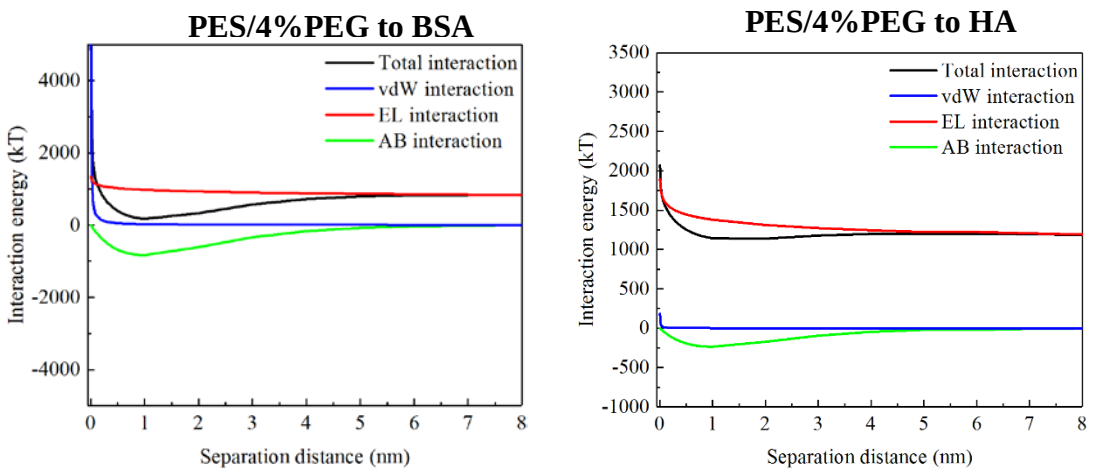

Figure 3.15 EDLVO interaction energy profiles for all the membrane–foulants combinations tested.

3.3.7 Mathematical Modelling of Dynamic Membrane Fouling

Previous studies have shown that the EDLVO theory can be used to predict membrane fouling in aqueous solutions.[188] Wang et al. found a positive correlation between the membrane–foulant adhesion force and the flux decline rate in the initial filtration stage.[161] However, the results only showed the propensity of fouling predicted by the EDLVO approach rather than a statistical correlation between the fouling rate and the interaction energies. In our study, we developed a mathematical model based on particle transport equation and the EDLVO theory aiming to quantitatively describe the interfacial energy's role in membrane fouling processes.

According to Section 3.2.8.2, the particle deposition rate is controlled by the joint effect of three components or fluxes (J), dispersion, advection, and deposition, as shown in Equation 3.20:

$$J_x = J_{x(disp)} + J_{x(adve)} + J_{x(force)} = -D_x \frac{c_b - c_g}{h} + Jc_b + \frac{D_x c_b}{k_B T} \frac{\partial U_{Total}(h)}{\partial h} \qquad (3.20)$$

where D_x is the diffusion coefficient ($cm^2\ s^{-1}$); c_b and c_g are the particle concentration (mg L^{-1}) in the bulk (feed) solution, and the gel layer, respectively; J is the pure water permeate flux; h is the separation distance between the foulants and the membrane (nm); k_B is the Boltzmann constant, 1.38×10^{-23} $J\cdot K^{-1}$; T is taken as 298 K; U_{Total} is the total membrane-foulant interaction energies.

For $J_{x(disp)}$, D_x=3.3×10^{-7} $cm^2\ s^{-1}$ for BSA solution,[417] D_x=5.9×10^{-7} $cm^2\ s^{-1}$ for HA solution,[418] c_b = 200 mg L^{-1} (BSA solution), c_b = 10 mg L^{-1} (HA solution), c_g is assumed to be 0 at the beginning of filtration, which is also the biggest point for the dispersion component. And h is assumed to be 0.157 nm, which is the nearest separation distance between the foulants and the membrane due to Borne repulsion.[419] Thus,

For BSA: $J_{x(disp)} = -3.3\times10^{-7}\,\frac{\text{cm}^2}{\text{s}}\times\frac{200\text{ mg L}^{-1}}{0.157\text{ nm}} = -42.04\,\frac{\text{g m}^{-2}}{\text{s}}$.

For HA: $J_{x(disp)} = -5.9\times10^{-7}\,\frac{\text{cm}^2}{\text{s}}\times\frac{10\text{ mg L}^{-1}}{0.157\text{ nm}} = -3.76\,\frac{\text{g m}^{-2}}{\text{s}}$.

For $J_{x(adve)}$, J is assumed to be $J_0 = \frac{5\text{ mL min}^{-1}}{9.6\text{ cm}^2}$ at the beginning of filtration, which is also the biggest point for the advection component. Thus,

For BSA: $J_{x(adve)} = 200\text{ mg L}^{-1}\times\frac{5\text{ mL min}^{-1}}{9.6\text{ cm}^2} = 1.74\times10^{-2}\,\frac{\text{g m}^{-2}}{\text{s}}$.

For HA: $J_{x(adve)} = 10\text{ mg L}^{-1}\times\frac{5\text{ mL min}^{-1}}{9.6\text{ cm}^2} = 8.68\times10^{-4}\,\frac{\text{g m}^{-2}}{\text{s}}$.

For J_x, $\frac{\partial U_{Total}(h)}{\partial h}$ is calculated from Figure 3.15, where the highest slope was taken when the foulants approaching the membrane surface. Table 3.6 summarized the values of $\frac{\partial U_{Total}(h)}{\partial h}$ for different interaction pairs.

Table 3.6 The Calculation of J_x

Foulants	Membrane	Pall			Millipore			
		PES	PES/PVP	PES/PEG	0% PEG	2% PEG	3% PEG	4% PEG
BSA	$\frac{\partial U_{Total}(h)}{\partial h}\times 10^{-18}$ (J m^{-1})	-1.34	-4.56	-4.68	-0.277	-0.419	-0.749	-1.43
	$J_{x(force)}$ (g m^{-2} s^{-1})	-2.15×10^{3}	-7.32×10^{3}	-7.51×10^{3}	-0.445×10^{3}	-0.672×10^{3}	-1.20×10^{3}	-2.30×10^{3}
	$J_{x(disp)}$ (g m^{-2} s^{-1})	42.04	42.04	42.04	42.04	42.04	42.04	42.04
	$J_{x(adve)}$ (g m^{-2} s^{-1})	1.74×10^{-2}	1.74×10^{-2}	1.74×10^{-2}	1.74×10^{-2}	1.74×10^{-2}	1.74×10^{-2}	1.74×10^{-2}
	J_x (g m^{-2} s^{-1})	-2.11×10^{3}	-7.28×10^{3}	-7.47×10^{3}	-0.403×10^{3}	-0.630×10^{3}	-1.16×10^{3}	-2.26×10^{3}
HA	$\frac{\partial U_{Total}(h)}{\partial h}\times 10^{-18}$ (J m^{-1})	-9.83	-10.6	-10.7	-8.00	-6.72	-9.14	-21.90
	$J_{x(force)}$ (g m^{-2} s^{-1})	-1.41×10^{3}	-1.52×10^{3}	-1.54×10^{3}	-1.15×10^{3}	-9.64×10^{2}	-1.31×10^{3}	-3.14×10^{3}
	$J_{x(disp)}$ (g m^{-2} s^{-1})	3.76	3.76	3.76	3.76	3.76	3.76	3.76
	$J_{x(adve)}$ (g m^{-2} s^{-1})	8.68×10^{-4}	8.68×10^{-4}	8.68×10^{-4}	8.68×10^{-4}	8.68×10^{-4}	8.68×10^{-4}	8.68×10^{-4}
	J_x (g m^{-2} s^{-1})	-1.41×10^{3}	-1.52×10^{3}	-1.54×10^{3}	-1.15×10^{3}	-9.64×10^{2}	-1.31×10^{3}	-3.14×10^{3}

According to Equation 3.19, the particle deposition rate is controlled by three components or fluxes (J): dispersion, advection, and deposition. The calculations of these three components showed that, compared with $J_{x(force)}$, the former two components ($J_{x(disp)}$ and $J_{x(adve)}$) are found to be substantially smaller by several orders of magnitude for both HA and BSA and thus can be negligible (see comparisons in Table 3.6). It is also interesting that these three transport components are all dependent on foulant concentration and $J_{x(force)}$ is always greater than $J_{x(disp)}$ and $J_{x(adve)}$ under our experimental conditions. For instance, the diffusion coefficients (D_x) for BSA and HA range from 5×10^{-7} cm^2 s^{-1} to 8×10^{-7} cm^2 s^{-1}.[417, 420] Our calculations show that only when the concentrations of BSA or HA reach above approximately 10^3 to 10^6 mg L^{-1}, $J_{x(disp)}$ and $J_{x(adve)}$ can reach similar orders of magnitude as $J_{x(force)}$ under normal filtration flux (40~100 LMH).[421] However, typical BSA or HA concentrations commonly used as model fouling agents are between 2.5 mg L^{-1} to 300 mg L^{-1}.[422-426]

3.3.8 Correlation between the Particle Deposition Rate and the Fouling Rate

To predict the fouling behavior of the PES membranes, a correlation between the particle deposition rate and the flux decline rate was developed. The flux decline rates, $\frac{\partial(J/J_0)}{\partial t}$, during the filtration of BSA and HA, could be derived by from the data in Figure 3.12 and are summarized in Table 3.7. $\frac{\partial(J/J_0)}{\partial t}$ and $J_{x(force)}$ (the dominant contribution for foulant deposition) for various membrane types were plotted in Figure 3.16, which elicits fairly satisfactory linear relationships (R^2=0.7~0.9). This linear relationship also suggests

that $J_{x(force)}$ or the interfacial forces between foulants and membrane surfaces play a decisive role in the membrane fouling kinetics, as opposed to diffusion or advection. Moreover, the linear correlation seems to shift from the two different membranes obtained from Pall Corporation and EMD Millipore Corporation. This shift implies that the different membrane fabrication procedures would greatly influence the correlation model. For example, molecular weight of polymers, membrane pore size, roughness and other possible membrane properties could vary the magnitude of hydrophobic and electrostatic interactions and consequently membrane fouling kinetics, which deserves further examinations.

Table 3.7 The Calculation of $\frac{\partial(J/J_0)}{\partial t}$

Membrane		PES	PES/ PVP	PES/ PEG	0%PEG	2% PEG	3%PEG	4%PEG
$\frac{\partial(J/J_0)}{\partial t}\times10^{-3}$ (min^{-1})	**BSA**	-12.7	-8.1	-7.9	-17	-9.3	-7.3	-3.6
	HA	-11.3	-10.8	-11	-10.4	-10.7	-9.1	-3.4

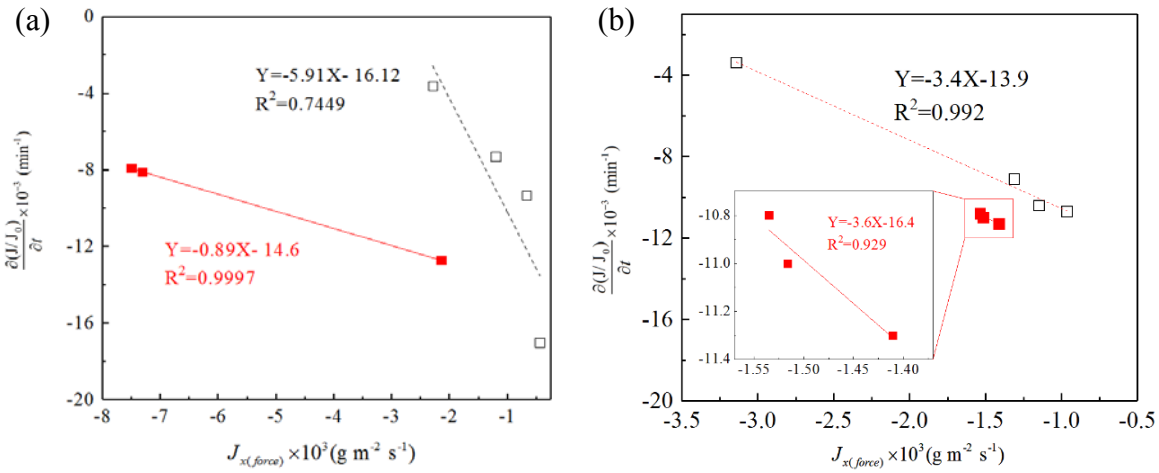

Figure 3.16 The positive correlation between the particle deposition rate and the flux decreasing rate during the filtration of BSA (a) and HA (b). Solid markers and line: Pall membranes; Hollow markers and dash line: Millipore membranes.

3.4 Conclusions

The filtration performance test generally showed that the membrane prepared with addition of PVP as modifier agent showed the best performance, *i.e.*, the low flux decrease rate, high relative flux recovery and similar rejection could be obtained. Moreover, the combined effect of membrane and foulant hydrophobicity and surface charge on membrane fouling during filtration was studied theoretically through EDLVO approach. The results showed that, though the EDLVO theory combined the effect of membrane and foulant hydrophobicity and surface charge on fouling during filtration, the statistical analysis of the results indicates that electrostatic interaction, rather than hydrophobic interaction, may be the predominant mechanism affecting fouling in this study. Fortunately, a positive correlation between the fouling rate (indicated by the flux decreasing rate during the filtration) and the particle deposition rate (derived from the EDLVO theory) were obtained, which could be used to predict membrane fouling during filtration.

The combined effects of hydrophobicity and surface charge of polymer membranes and foulants on membrane fouling was studied both experimentally and theoretically. Pristine PES membranes and their chemically modified forms were used for filtration experiments with BSA and HA as model foulants. The experimental results for different membrane–foulant systems showed that the hydrophilized membranes yielded smaller flux decline rates. Further, the EDLVO theory analysis indicated that the EL and AB components were both main contributors to the total interaction energy for BSA-membrane system, while the EL interaction energy was a primary contributor for HA-membrane system. Positive correlations (R^2=0.74-0.99) were obtained between the fouling rates and the particle deposition rates on different membrane-foulant systems. This correlation could

be further improved for developing predictive models of membrane fouling, which requires additional considerations of other factors such as membrane pore size, surface roughness, solute chemistry, and hydrodynamic conditions. Overall, the findings have important implications for future studies to elucidate or predict the structure−property−performance relationship of chemically modified membranes.

CHAPTER 4

POLYVINYL CHLORIDE (PVC) ULTRAFILTRATION MEMBRANE FOULING AND DEFOULING BEHAVIOR: EDLVO THEORY AND INTERFACE ADHESION FORCE ANALYSIS

4.1. Introduction

Membrane fouling has been a limiting factor for membrane filtration in diverse applications in separation and water treatment.[154-159] Membrane fouling is primarily attributed to membrane–foulant interactions followed by subsequent foulant–foulant interactions.[160-163] Interfacial properties of both membranes and foulants have important impacts on membrane fouling kinetics and fouling removal or defouling.[161-168] Therefore, the delineation of the membrane–foulant or foulant–foulant interaction mechanisms are critical to understanding their roles in membrane fouling and defouling processes.

Natural organic matter (NOM) and protein are common membrane foulants known to cause significant loss of membrane permeability and are often used as foulant models to analyze membrane fouling mechanism.[161, 162, 168-174] In aqueous solutions, NOM and protein usually bond together to form colloidal aggregates of tens or hundreds of nanometers in size.[160, 165, 167] Most previous studies examined bulk scale membrane fouling behavior and evaluations, such as membrane fouling index, membrane flux decline rate and flux resistance.[175-178] However, membrane characteristics, such as hydrophobicity/hydrophilicity, surface charge, roughness, pore size and porosity, as well as foulants properties (*e.g.*, molecular weight distribution, zeta potential and particles size) have proven to impact membrane filtration performance.[158, 179-181] Particularly, the impacts

of hydrophobicity and surface charge on membrane fouling during filtration have been reported previously.[158, 179, 182-185] The extended Derjaguin Landau Verwey Overbeek theory (EDLVO or XDLVO theory) is widely used to describe the contributions of surface properties of membranes or foulants to colloidal interactions and fouling potential on membrane filters.[186-188]

Atomic force microscopy (AFM) has been used as a versatile tool for the study and characterization of pristine and fouled membrane surfaces.[189-192] In addition to surface morphology mapping, quantification of interaction forces by AFM greatly provides aid in the understanding of membrane fouling mechanisms.[161, 193-200] For example, interaction forces were measured between polymeric membranes and AFM probes coated with foulants of humic acid (HA) and bovine serum albumin (BSA).[160, 165] Adhesion forces of membrane-foulant and foulant-foulant measured could indicate the fouling propensity.[195-200] Mi *et al*. observed a strong correlation between organic fouling and intermolecular adhesion force, indicating that foulant–foulant interaction plays an important role in determining the rate and extent of organic fouling.[200] Meng *et al*. reported that high membrane–HA interaction forces result in a rapid adsorption of the HA onto the surface or in the inner membrane pore surface, causing severe membrane pore blocking or narrowing and membrane flux decline in the initial filtration stage.[160] Nevertheless, many previous studies assessed membrane fouling or defouling behavior without sufficient examinations of microscale or nanoscale material properties and their contributions to membrane fouling or defouling processes. For instance, flux decline, flux recovery, and flux resistance are commonly measured to characterize fouling or defouling.[178, 201-204] Clearly, further investigations of fouling formation, defouling processes, and contribution from interfacial

forces will provide new insight into the prevention of membrane fouling and rationale design of antifouling membrane filtration processes.

In this study, we combined the experimental and theoretical assessment of polyvinyl chloride (PVC) ultrafiltration membrane fouling and defouling kinetics. Dextran (DEX), humic acid (HA) and bovine serum albumin (BSA) were used as model foulants, representative of polysaccharides, organic matters and proteins, respectively. Pristine and fouled PVC membranes were examined by confocal microscope and AFM-IR technique to reveal the foulant structural characteristics and chemical distribution. AFM was used to measure the interaction forces involved at the membrane–foulant and foulant–foulant interfaces. Surface interaction energies were calculated using the EDLVO theory to explain the contributions of factors such as surface hydrophobicity and charge to fouling kinetics. For the first time the fouling or defouling kinetics was analyzed separately for the initial and later stages of filtration, where foulant-membrane interactions and foulant-foulant interactions may jointly play a role. For example, we hypothesize that adhesion forces govern defouling propensity instead of fouling potential as reported previously, because adhesion only occurs when chemical bonds form between membrane and foulants. Therefore, adhesion forces were used to establish correlation with defouling kinetics based on Maxwell approach.[427]

4.2. Method and Materials

4.2.1 Organic Foulants

Commercial protein (BSA) (Beijing Jiangchen Biotech Co., M_w=66.45 kDa, China),

dextran (DEX) (Aladdin, M_w=70 kDa, China) and humic acid (HA) (Sigma Aldrich, USA) were used to prepare stock feed solutions. The concentrations of these stock solutions were: 1 g-BSA L^{-1}, 0.83 g-DEX L^{-1}, and 4.45 g-HA L^{-1}, respectively, which yield the same level of TOC at 280 mg L^{-1}. The HA solution was filtered with 0.45 μm membranes (cellulose nitrate membrane filters, Whatman) to remove the insoluble particles. All the solutions were stored at 4°C prior to use.

4.2.2 Ultrafiltration Membranes

Hollow fiber PVC membranes (MWCO, 50 kDa; manufacturer's reported pore sizes, 10 nm) were purchased from Hainan Litree Purifying Technology Co. Ltd. The membranes were filled into membrane modules as shown in Figure 4.1a. The effective membrane surface area was approximately 6.28 cm^2 per module. Prior to the experiment, virgin membranes were rinsed carefully to remove preservatives and soaked in deionized water for 24 h to remove impurities.[159, 428] The clean water tests were conducted to determine the filtration performance at different TMPs as shown in Figure 4.1b.

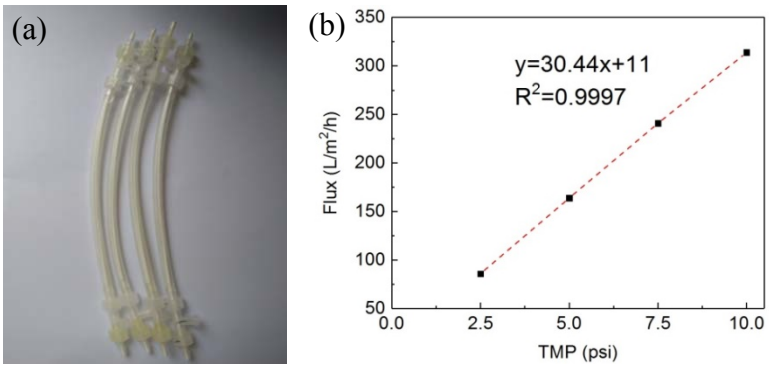

Figure 4.1 (a) The photo of PVC membrane module; (b) pure water permeate flux at different TMPs.

4.2.3 Filtration Experiments

A laboratory-scale filtration device (Figure 4.2) was assembled for membrane filtration

experiments. An electronic balance and computer were used to continuously monitor the permeate weight to calculate the permeate flux change. Filtration experiments generally consisted of the following steps. Firstly, the membrane was filtered with DI water under 7.0 psi TMP (84.2 ml min^{-1}) for 1h to reach a relatively stable flux. Then, the TMP was increased to 14.5 psi (14.2 ml min^{-1}) to establish a stable water permeate flux named J_0. Next, the fouling experiment was conducted at 14.5 psi (0.3 m s^{-1} of cross flow velocity) by filtering the stock solutions of BSA, DEX or HA, respectively. After every 15 minutes' filtration, the membrane was backwashed at 25 psi with 30 ml DI water for 5 minutes. The total filtration time was 150 min (10 cycles) and each filtration experiment was repeated for 3 times. The control group was carried out with the same method using DI water. Fouled membranes were collected for the following characterization.

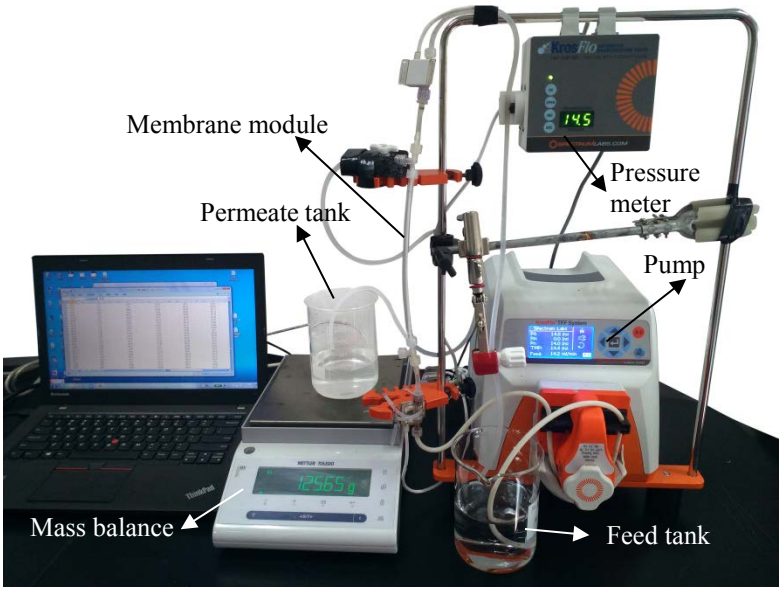

Figure 4.2 Bench top membrane filtration system.

The permeate flux data J ($L \cdot m^{-2} \cdot h^{-1}$) was calculated by Equation 4.1.

$$J = \frac{\Delta m}{\rho \cdot \Delta t \cdot A} \times 1000 \tag{4.1}$$

where J is the permeate flux ($L \cdot m^{-2} \cdot h^{-1}$, LMH); Δm (kg) is the mass of permeate measured in filtration duration time Δt (h); ρ is the density of permeate ($kg \cdot m^{-3}$); A is the filtration area (m^2).

The normalized flux J^* (dimensionless) is defined as the ratio of the actual flux J and the maximum or clean membrane flux J^0:

$$J^* = \frac{J}{J^0} \tag{4.2}$$

The flux decline rate was calculated by Equation 4.3 to indicate the fouling rate (min^{-1}):

$$\frac{\mathrm{d}J}{\mathrm{d}t} = \frac{J_n^* - J_{0,n}^*}{\Delta t_f} \tag{4.3}$$

where n is the cycle number; $J_{0,n}^*$ was the initial permeate flux of the n cycle; J_n^* was the permeate flux at the end of the n cycle; Δt_f is the filtration time in each cycle.

The flux recovery ratio was calculated with Equation 4.4:

$$\text{Flux recovery ratio (\%)} = \frac{J_{0,\mathrm{n+1}}^*}{J_{0,\mathrm{n}}^*} \times 100 \tag{4.4}$$

where n is the cycle number; $J_{0,\mathrm{n}}^*$ was the initial flux of the permeate of the n cycle; $J_{0,\mathrm{n+1}}^*$ was the initial flux of the permeate of the (n+1) cycle. The accumulative flux decline rate was calculated with Equation 4.5:

$$\text{Accumulative flux recovery ratio (\%)} = \frac{J_{0,n}^{*}}{J_{0,1}^{*}} \times 100 \tag{4.5}$$

where $J_{0,n}^{*}$ was the initial flux of the permeate of the *n* cycle; $J_{0,1}^{*}$ was the initial flux for the foulant at the first cycle.

The flux recovery rate (defouling rate) was calculated with Equation 4.6:

$$\text{Defouling rate } \frac{\mathrm{d}J^{d}}{\mathrm{d}t} = \frac{(J_{0,\mathrm{n}}^{*} - J_{15,n-1}^{*}) / J_{15,n-1}^{*}}{\Delta t_{b}} \tag{4.6}$$

where $J_{0,\mathrm{n}}^{*}$ was the initial flux of the permeate of the *n* cycle; $J_{15,n-1}^{*}$ was the flux before the backwashing at the n-1 cycle; Δt_{b} is the backwashing time during each cycle.

4.2.4 Characterization of Membranes and Foulants

4.2.4.1 Contact Angle Measurement. Contact angle measurement was conducted on an optical contact angle goniometer (JC2000DM, Powereach, Shanghai, China). Three probe liquids with well-known surface tension properties were used,[390] including DI water, diiodomethane, and formamide. A drop of probe liquid (~5 μL) was placed on a dry flat membrane surface. At least three measurements of liquid drops at different locations were averaged to obtain the contact angles for each membrane sample. The image of the liquid drop was taken within 10 s to determine the air–liquid–surface contact angles.

4.2.4.2 Measurement of Membrane Surface Zeta Potential. The membrane surface charge or surface zeta potential was measured by a surface zeta potential cell equipped on a dynamic light scattering (DLS) instrument (Malvern Instruments ZetaSizer Nano ZS), and this method was described in our previous work.[168] Briefly, the membrane samples

were cut into flat pieces with 4 mm × 5 mm area and attached by double coated adhesive tapes (Ted Pella, Inc.) to the surface zeta potential cell. The cell was placed in a standard 12 mm^2 polystyrene cuvette (Fisher Scientific Co., Pittsburgh, PA) filled with the dispersant (*i.e.*, 1 mM NaCl solution within the pH range 4–10) and tracer particles (300 nm carboxylated latex particles). The cuvette and cell were then placed in the temperature controlled ZetaSizer instrument at a temperature of 25 ± 1 ^oC. The pH was measured using a pH-meter (Orion model 420A, Boston, MA, USA) and adjusted by addition of NaOH and HCl solutions.

4.2.4.3 Characterization of BSA, DEX and HA. Contact angles of BSA, DEX and HA were measured using the same technique as described above on BSA, DEX and HA coated surfaces, which were made by depositing 1 mL stock solutions of BSA, DEX and HA onto pre-clean square glass slides (18×18mm, Fisher Scientific). The samples were dried and kept in a desiccator for contact angle measurement. Zeta potential and hydrodynamic diameter of BSA, DEX or HA were determined by the DLS instrument.[168] Each data value was an average of five measurements and all the measurements were performed at 25 ± 1 ^oC.

4.2.4.4 Chemical Mapping by AFM-IR. To obtain chemical distribution of foulants on PVC membranes at nanoscale, AFM-IR was performed on a NanoIR2 system (Anasys Instruments, Inc., Santa Barbara, CA, USA) operating with top-down illumination. All the tested membrane samples were cut into flat sheets and mounted onto AFM specimen disks (Ted Pella, 12 mm diameter) with adhesive tape (Ted Pella) (Figure 4.3). Then, the sample holder was placed on the NanoIR2 instrument sample stage for analysis. All AFM topographic and IR mapping images were collected in contact mode at a scan rate

of 0.1 Hz using a gold-coated silicon nitride probe (PR-EX-NIR2, 0.07–0.4 N m^{-1} spring constant, 13 ± 4 kHz resonant frequency, Anasys Instruments). Analysis Studio software (version 3.11, Anasys Instruments, Inc., Santa Barbara, CA, USA) was used for data collection and analysis. The power levels of the incident IR radiation on the sample surface were set to *ca.* 50 μW. Local spectra were collected over spectral ranges of 900-1800 cm^{-1} and the spectra resolution was 4 cm^{-1}.

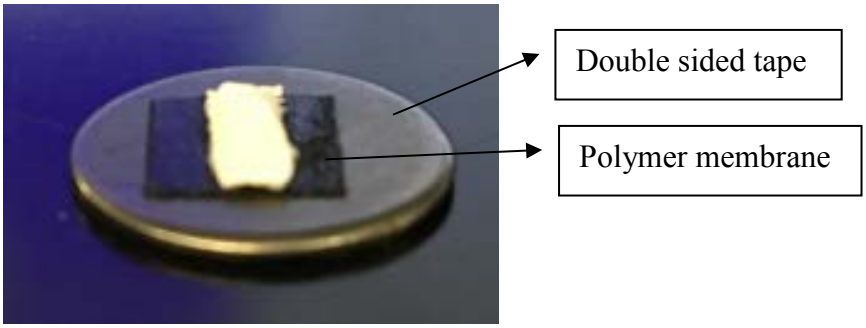

Figure 4.3 Photo of the mounted membrane samples on the AFM disks.

4.2.4.5 Foulant Layer Characterization by Confocal Microscopy. Confocal laser scanning microscopy (CLSM; Leica TCS SP8 Confocal Spectral Microscope Imaging System, GmbH, Germany) was employed to analyze the fouling distribution on PVC membranes at both inner surface and cross-section surfaces perspective. Fluorescein isothiocyanate (FITC) and calcofluor white were utilized to probe BSA and DEX content distributions, respectively.[429-432] There is no literature that applied confocal microscopy to evaluate HA distribution and thus we did not include HA in this study. For BSA-fouled membrane staining, the wet membrane fragments were placed in Eppendorf tubes. 0.1 M $NaHCO_3$ buffer solution was added into the tubes up to 1 mL with incubation of 30 min to keep the amine group in non-protonated form. 10 μL FITC solution (10 g L^{-1}) was added into the tubes with 2 hours of incubation in dark followed by DI water washing for twice to remove excess stain. For Dextran-fouled membrane staining, the same procedures with

BSA-fouled membrane staining were used except for that incubation time changed to 30 min after adding 10 μL calcofluor white solution. Then, the samples were immediately observed under the confocal microscope. Excitation at 488 nm and emission at 500–540 nm (green) were used to detect the FITC.[432] Calcofluor white was detected by excitation at 405 nm and from the emission width at 410–480 nm (blue). The results were analyzed using Leica confocal software and ImageJ software.

4.2.5 Interaction Energy Calculation Based on EDLVO Theory

In this study, the membrane-foulant interactions were modeled as surface–particle geometry and foulant-foulant interactions were particle-particle geometry. The total interaction energies (U_{Total}) of membrane-foulant and foulant-foulant systems are contributed by the Lifshitz–van der Waals (vdW), U_{vdW} , electrostatic double-layer (EL), U_{EL} and Lewis acid–base (AB) energy, U_{AB} , according to the EDLVO theory:[188, 400, 433]

$$U_{Total} = U_{vdW} + U_{EL} + U_{AB} \tag{4.7}$$

Equations for calculations of van der Waals, electrostatic and Lewis acid–base interaction energies are detailed in Chapter 3 Section 3.2.8.[168, 399]

4.2.6 Measurement of Foulant-Foulant and Foulant-Membrane Interaction Forces by AFM

4.2.6.1 Preparation of Foulant-coated Probes. The probe used in the AFM force measurements was commercial tipless silicon nitride probe (MLCT-O10, Bruker, America) with only one cantilever (E cantilever, marked spring constant 0.1 N m^{-1}). The AFM equipment (Bioscope Catalyst, Bruker, America) was used to first coat the free end of the

cantilever with a small drop of two-component epoxy resin (1:1) under an inverted microscope. Then, a polystyrene microsphere (10 μm diameter) was attached to the end of cantilever. The prepared probe was left at room temperature for at least 12 h. Figure 4.4 are the scanning electron microscopy (SEM) images that were acquired on the field emission scanning electron microscope (FESEM, LEO 1530 VP, Oberkochen, Germany) to show the AFM probe before and after attachment of microsphere. The foulant-coated colloidal probes were fabricated by immersing the prepared colloidal probes into BSA, DEX and HA solutions (identical to that in the corresponding fouling experiments) for 24 h at 4 ºC in order that adsorption equilibrium was reached.[160] Deflection sensitivity and spring constant were calibrated before use by the thermal noise and Sader methods.[434]

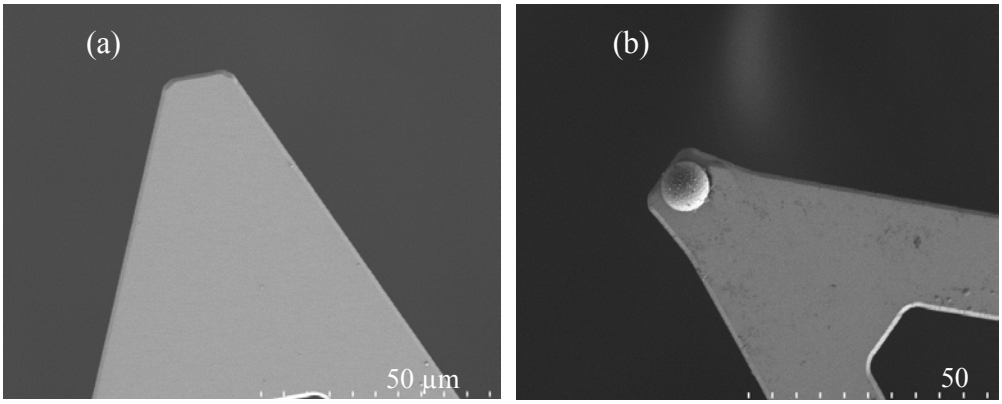

Figure 4.4 SEM images of (a) clean commercial probe and (b) modified colloidal probe.

4.2.6.2 Adhesion Force Measurements by AFM. All AFM measurements were carried out in a Petri dish with DI water using contact mode at the oscillation frequency of 1.03 Hz and the initial loading force of 5.0 nN. Each membrane sample was cut into flat sheets and then mounted onto a Petri dish bottom with double-sided adhesive tape. Each interaction force measurement was done at 15 spots and 20-30 curves depending on the repeatability of measurement results. QC was conducted between foulant-coated probe and pristine PVC membrane to make sure the adhesion forces were repeatable, which indicated no significant

loss or detachment of foulant coating occurred. Our QC result shows that when the adhesion force measurement times at one sample spot were above 50, the force peaks became significantly lower (1/2 smaller than that obtained from the first 30 curves).

4.3. Results and Discussion

4.3.1 Characterization of Membranes and Foulants

4.3.1.1 Hydrophobicity and Hydrophilicity Analysis. The contact angles of three probe liquids on the pristine PVC membranes and the three model foulants (BSA, DEX and HA) were measured and shown in Table 4.1. The hydrophobic/hydrophilic properties of fouled PVC membranes were expected to vary as compared with the pristine PVC membranes due to the presence of the functional groups such as hydroxyl groups and amino groups in BSA, DEX and HA.

Table 4.1 Average Contact Angles of Tested Membranes and Three Model Foulants

Materials	Contact angle (°)		
	Water	Diiodomethane	Formamide
Pristine PVC	72.0±2.4	13.3±1.6	39.8±2.1
Bovine Serum Albumin	33.4±1.6	54.2±1.4	31.8±2.4
Dextran	11.4±1.9	29.4±1.9	15.1±0.9
Humic Acid	23.4±2.3	45.1±2.5	26.4±4.2

Table 4.2 shows the calculated surface tension parameters and the free energy component for the PVC membrane and foulants. The surface energy data show that pristine PVC membrane had high electron donor components (γ^-) and relatively low electron acceptor components (γ^+). This result agrees with previous studies reporting that polymeric membranes are typically characterized by a high electron donor monopolarity.[435, 436] All foulants exhibited high electron donor monopolarity, *i.e.* high electron donor components

(γ^-) and negligible electron acceptor components (γ^+), as demonstrated in previous study.[435] These surface tension parameters will be used in the determination of Hamaker Constant for the EDLVO calculations.

Table 4.2 Surface Energy Parameters of PVC Membranes, Three Model Foulants, and Three Probe Liquids[390]

Materials		Apolar surface tension components ($mJ \cdot m^{-2}$)	Polar surface tension components ($mJ \cdot m^{-2}$)		Polar energy component ($mJ \cdot m^{-2}$)	Total free energy component ($mJ \cdot m^{-2}$)
		γ^{LW}	γ^+	γ^-	γ^{AB}	γ^{TOT}
Membranes	Pristine PVC	49.4±0.19	0.38±0.02	5.38±0.65	2.85	52.3
Foulants	Bovine Serum Albumin	31.9±0.45	2.71±0.09	48.4±0.26	22.9	54.8
	Dextran	34.0±1.45	2.24±0.39	50.6±0.15	22.1	56.1
	Humic Acid	36.9±0.77	0.91±0.06	52.6±0.30	13.8	50.7
Probe liquids	Water	21.8	25.5	25.5	51.0	72.8
	Formamide	39.0	2.3	39.6	19.0	58.0
	Diiodomethane	50.8	0.0	0.0	0.0	50.8

4.3.1.2 Surface Zeta Potential of Membrane and Foulants. The characteristics of foulants and membranes were summarized in Table 4.3. BSA and HA had mean hydrodynamic diameters of 266 and 213 nm respectively, which were greater than that of dextran. Zeta potentials of BSA and HA in their stock solution were also greater in magnitude than that of dextran.

Table 4.3 Characteristics of the Foulants and Tested Membrane

Foulant	pH value	Hydrodynamic diameter /nm	Zeta Potential/mV	Mass concentration/ g L^{-1}	Average Molecular weight/g mol^{-1}
BSA	8.0±0.1	266±20	-22.1±3.5	1	66,450
DEX	8.2±0.1	26±6	-16.4±3.1	0.83	70,000
HA	7.9±0.1	213±13	-39.1±1.8	4.45	4,100[a]
Pristine PVC membrane	/	/	-46.1±3.5[b]	/	/

[a]Chin *et al*. (1994).[437] According to previous literature, HA molecular weight range could be: 65% > 100 kDa[438]; 2-50 kDa[439, 440]; or 2-500 kDa.[441]
[b]Pristine PVC membrane was measured in 1 mM NaCl solutions with pH 8.0±0.1.

4.3.1.3 AFM-IR Results. Figure 4.5 shows the spectral shifts on PVC membranes before and after filtration of different foulant solutions. The pristine PVC membrane did not show those characteristic stretching assignments related to C-H bonds near Cl (1250 cm^{-1}) or C-C stretch bond (1099 cm^{-1}) in PVC.[442] The possible reason is that the expansion coefficient of PVC could be too low to generate detectable thermal expansion for AFM tip. By contrast, the fouled membranes exhibited characteristic bands of foulants. The characteristic bands around 1550 cm^{-1} related to amide II bonds (N-H bending vibration and C-N stretching vibration) in BSA.[443] The band around 1428 cm^{-1} was attributed to the carbonate stretching vibrations of aliphatic bonds in DEX and HA.[444, 445] Additionally, the fouled membranes showed stronger IR signals among the tested wavelength range and more visible spectrum peaks than pristine PVC membranes under the same laser power.

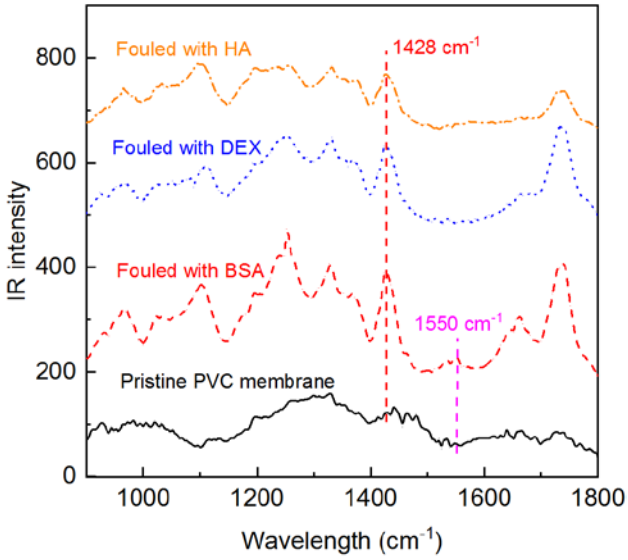

Figure 4.5 The IR spectra of the tested membranes.

Figure 4.6 shows the topography images and roughness of the pristine and fouled membranes. From the topography images, there is the obvious deposition of foulants on fouled membranes; while pristine membranes and membranes filtered DI water exhibited evenly and clear pores distribution. Some protein aggregates can be observed on the BSA-fouled membrane surface (as marked by the arrow), which increased the surface roughness. Similarly, Corbatón-Báguena *et al*. reported protein clusters and increased roughness on fouled membranes.[446] Compared with the BSA fouled membrane, the HA-fouled membranes shows that HA deposited on membranes much evenly as smooth layers and the roughness of the HA-fouled membrane was 96±12 nm, which was close to that of the pristine membrane. Yu *et al*. also used AFM to observe the morphological changes of fouled membrane surface and found that foulant materials could fill membrane pores and created an even and smooth layer over the original membrane.[447] That explains why the roughness for the BSA-fouled membrane was higher than the HA fouled membranes.

All of the IR mapping images in Figure 4.6e, h, k are shown with the colour scale

bar indicating signal intensities of BSA (1236 cm^{-1}), DEX (1428 cm^{-1}) and HA (1428 cm^{-1}). Areas with a high intensity of the foulants are shown in red, whereas areas with a reduced intensity in green or blue. The IR mapping images show that the foulants evenly distributed on the membrane surfaces.

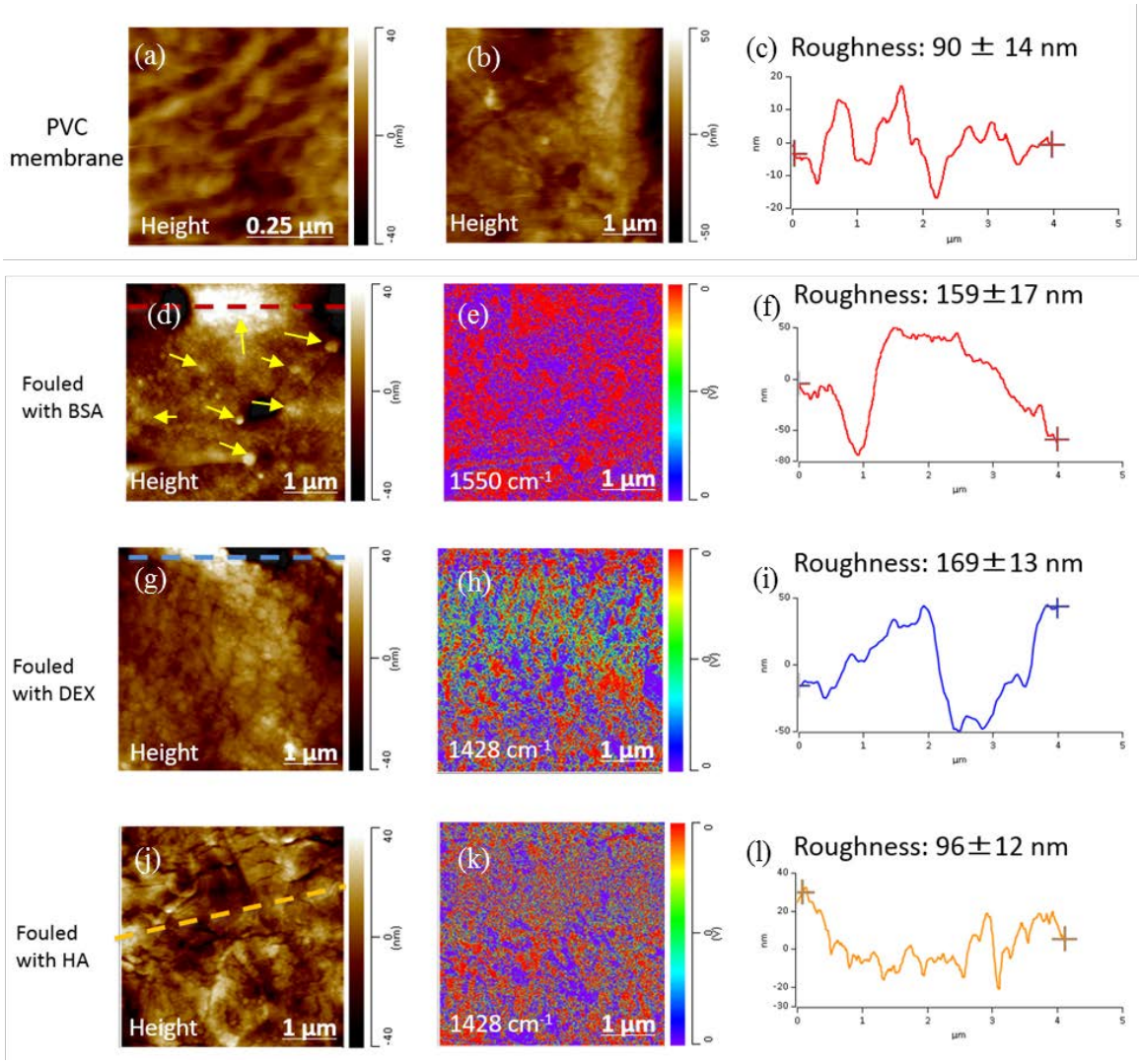

Figure 4.6 The topography image, IR mapping and roughness of (a-c) pristine PVC membranes and (d-l) fouled PVC membranes.

4.3.1.4 Confocal Microscopy Results. Figure 4.7 shows the fluorescence images of the PVC membranes fouled by DEX (blue) and BSA (green) through the staining method as mentioned above. Pristine membrane stained by FITC or calcofluor showed no

fluorescence and appeared completely dark in the graph (thus not shown). Figure 4.7a shows that membrane surface after 150 min filtration of DEX was covered by DEX, which is white colored and snowflakes like materials similar to AFM topography images in Figure 4.6g. By contrast, BSA (green dots) was homogeneously distributed on the surface of BSA-fouled membrane (Figure 4.7b).

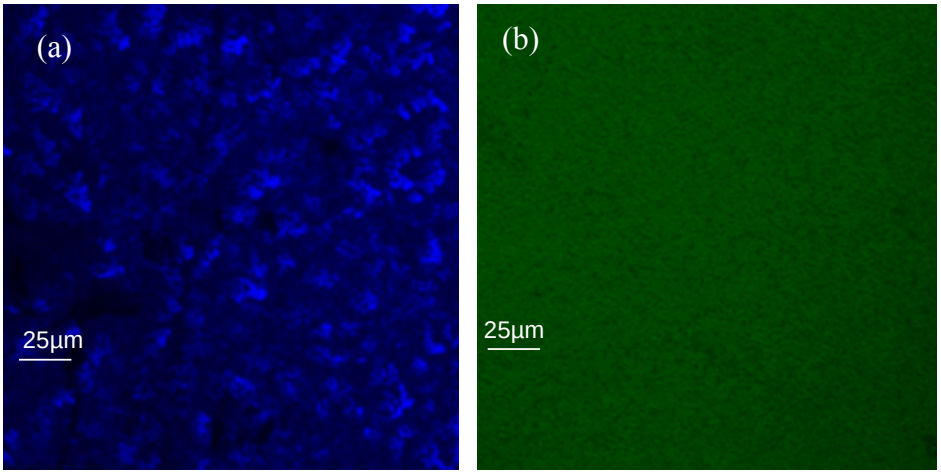

Figure 4.7 Confocal images of inner surfaces of (a) DEX-fouled and (b) BSA-fouled membranes.

To further analyze the morphology differences of DEX and BSA fouled membranes, the cross sections of both fouled membranes were observed with the CLSM. Figure 4.8 shows that the thickness of DEX-fouled layer was 22.17±2.69 µm, while that of BSA-fouled layer was 4.80±1.02 µm. Moreover, DEX was found in membrane pores (as marked by the arrow), whereas BSA was present only on the inner and outer surfaces as the green curves indicated. This means that the DEX may lead to membrane fouling through pore blocking due to the smaller size of DEX (25 nm) compare to BSA (>250 nm). BSA caused membrane fouling primarily through the formation of cake layer, which is a dominant mechanism for ultrafiltration when foulants size is larger than the membrane cut-off.[448, 449]

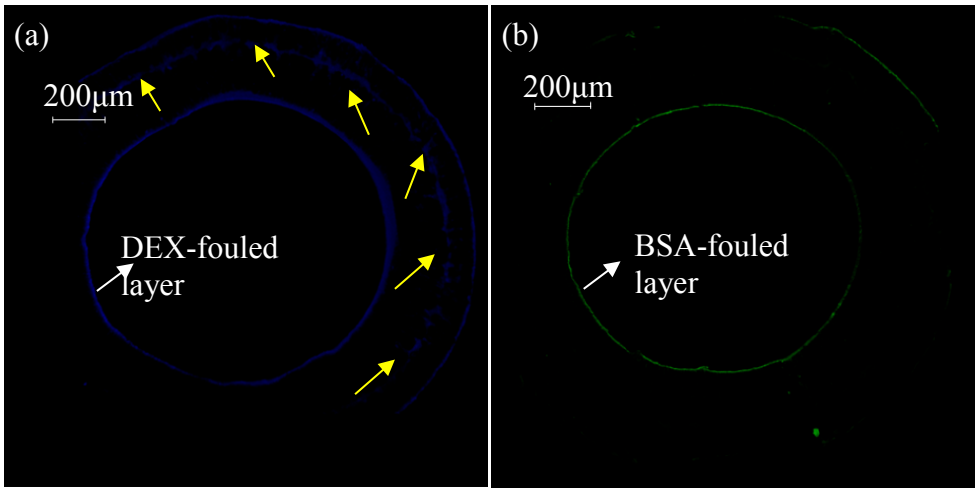

Figure 4.8 Confocal images of cross-section of (a) DEX-fouled and (b) BSA-fouled PVC membranes.

4.3.2 Fouling Kinetics for Different Foulants on PVC Membranes

Figure 4.9 shows the permeate flux changes during the filtration of BSA, DEX and HA solutions. Figure 4.9a shows the absolute fluxes for different foulants, which are normalized to the initial water fluxes (Figure 4.9b). The flux change in each filtration cycle was similar with a fast flux decrease in the first two minutes and a relatively slow decrease in the following time. Thus, the first filtration cycle in Figure 4.9b was extracted to better exhibit the potential turning point during fouling (Figure 4.9c), which was also used to analyze the fouling rates during filtrations of different foulants.

For those three foulants, the flux decline rates calculated by Equation 4.3 were different during the initial (the first two minutes in the cycle) and later filtration stages (after two minutes in the cycle). During the initial filtration period, the filtration flux decreased more rapidly and the flux decline rates (fouling kinetics) followed the order: BSA > HA > DEX. At the later filtration stage, the flux decline rate slowed down and generally followed the order: DEX > BSA > HA. Clearly, membrane fouling processes are

likely affected by various factors such as physicochemical properties of foulants and membranes and surface interaction characteristics (foulant-membrane and foulant-foulant),[160-163] which result in different fouling modes or fouling mechanisms.[450-452]

Because the cluster size of BSA is greater than the pore size, BSA molecules are trapped by membrane pores and accumulate on the membrane surface and subsequently form a cake layer as evidenced in Figure 4.6d and Figure 4.7b. The cake layer blocks the pores and reduces permeate flux sharply at the initial stage. In comparison, the permeate flux decline rate for DEX was relatively slower than that of BSA. As DEX has a particle size (26 ± 6 nm) and may pass through the membrane pore during the initial filtration stage, followed by the surface deposition on inner membrane pores and pore blocking as indicated by Figure 4.8a. This explains why at the initial filtration stage DEX led to a slower fouling rate than BSA. Additionally, BSA is more hydrophobic than DEX, and thus, the hydrophobic interactions could cause rapid binding and attachment of BSA on PVC membrane and thus a faster rate of fouling and flux decline than DEX in the beginning. Figure 4.9c shows that the fouling rate for the filtration of HA was between the rates of BSA and DEX. Since HA is not a homogeneous model organic matters, with molecular weights ranging from 2 kDa up to over 500 kDa,[438, 441] the fouling mechanism for HA could be a combination of pore blocking and a cake layer formation.[453] The large sized HA may deposit on the membrane surface and form a cake layer, whereas the small sized HA accumulates and blocks the pores. Figure 4.9d shows that the flux decline rate in each cycle during the 150 min filtration of DEX decreased slightly while decline rates of BSA and HA slowed down abruptly after two filtration cycles and then stayed at a slower rate level than DEX. This phenomena could be explained by the differences in the fouling modes of DEX

and HA and BSA. Fouling process could be affected by various factors such as physicochemical properties of foulants and membranes, operation conditions and solution chemistry.[450-452] Previous studies showed that the membrane-foulant and foulant-foulant interactions played an important role in the occurrence of membrane fouling and demonstrated that the EDLVO theory could partly explain membrane fouling behavior.[160-163] Therefore, both foulant-membrane and foulant-foulant interaction energies were calculated to predict the membrane behavior and fouling mechanism in the following sections.

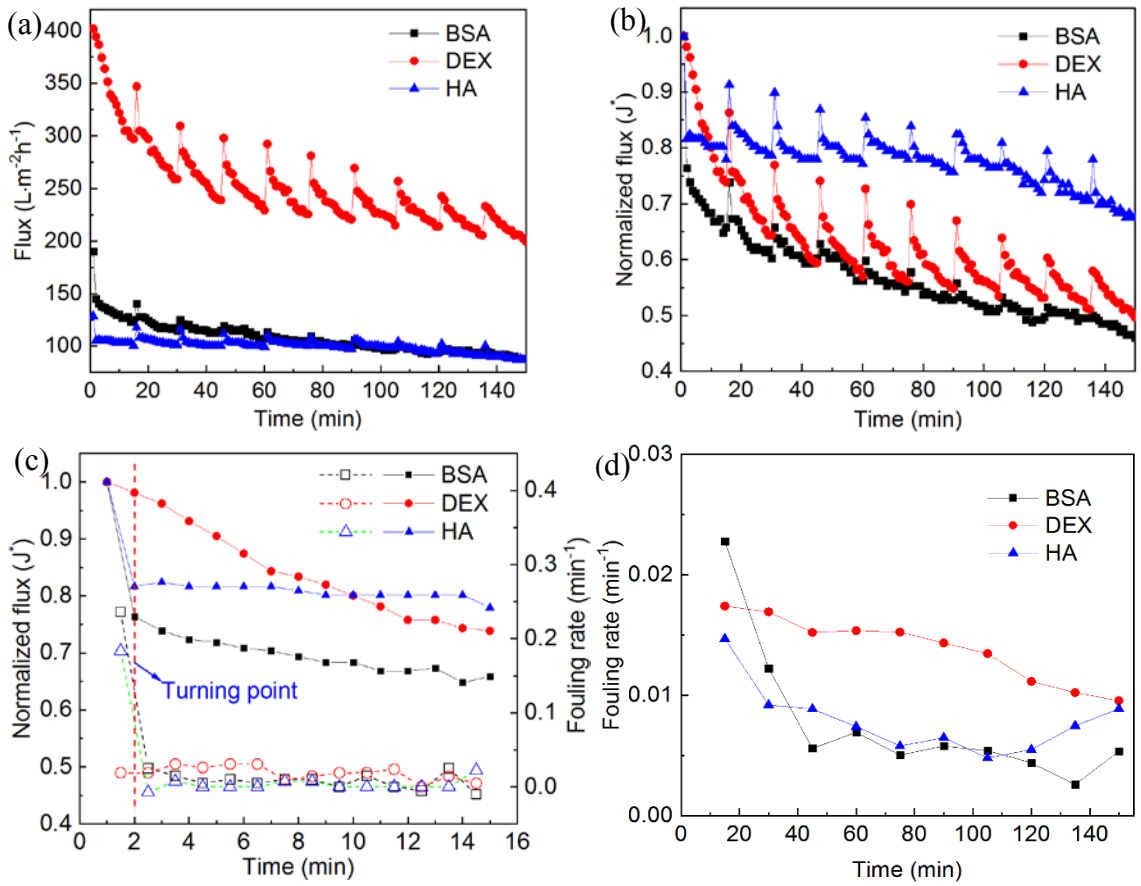

Figure 4.9 (a) Absolute flux changes and (b) normalized flux decline curves for BSA, DEX and HA (20℃, TMP=14.5 psi); (c) flux change with filtration time (solid dots) and the flux decline rate in different filtration stages (hollow dots) in the first cycle; and (d) Flux decline curves for BSA, DEX and HA in each cycle.

4.3.3 Interaction Energy for Membrane–Foulant and Foulant-Foulant Systems

Figure 4.10a shows the interaction energies between the PVC membranes and three foulants in DI water, which play decisive roles in the initial surface deposition (rate) of foulants on membrane. The energy barriers for the three foulant-membrane systems follow the order: HA > BSA > DEX. A lower magnitude of energy barriers usually lowers the repulsion of foulant-membrane interaction and causes rapid deposition of foulants on membrane surface.[167] The fouling rate for these three foulants should follow the order: DEX > BSA > HA, which partially agrees with the results of Figure 4.9c. DEX-membrane system actually had the slowest fouling rate although having the lowest energy barriers. This indicates that interaction energy analysis for fouling kinetics may not be valid for pore blocking and pore narrowing mechanisms by DEX or other colloids that have smaller sizes than pores.[428] Therefore, the fouling kinetics of DEX on PVC membranes was not further analyzed with EDLVO theory.

Figure 4.10b shows the interaction energies between foulants themselves, which were considered in the analysis of fouling kinetics in later filtration stage. Compared with the membrane-foulant interactions, the interaction energies were appreciably lower in magnitude for foulant-foulant interactions. The energy barriers followed the order: HA-HA > BSA-BSA > DEX-DEX, which is congruent with the fouling rate order (DEX > BSA > HA) during the later fouling stage (Figure 4.9c). HA had the highest inter-molecular repulsion, whereas DEX had the lowest. As a result, a lower inter-foulant energy barrier clearly promotes foulant-foulant interaction and formation of a relatively compact foulant layer, which increases the fouling tendency or rates (or a faster flux decline rate).

Figure 4.10 shows the EL interactions were always repulsive for all the three

foulants, and provided the repulsive force preventing foulant deposition on membrane surface or foulant layer. As the EL interaction stems from surface charge interactions, and the absolute surface potential of these foulants followed the order: HA > BSA > DEX. And the EL interaction was the dominant force when the foulants approaching the membrane surface. Meanwhile, the hydrophobicity of the three foulants follows the order: BSA>HA>DEX, which suggests the irrelevance of the hydrophobicity to the deposition tendency of foulants in the filtration system. Therefore, surface charge is a more important controlling factor rather than hydrophobicity of foulants or membranes in the membrane fouling. In order to further clarify the effect of interaction energy barrier on membrane fouling prediction, correlations between the fouling rate and the interaction energy were performed. The correlations were theoretically based on an EDLVO approach and the aggregation kinetics in the following section.

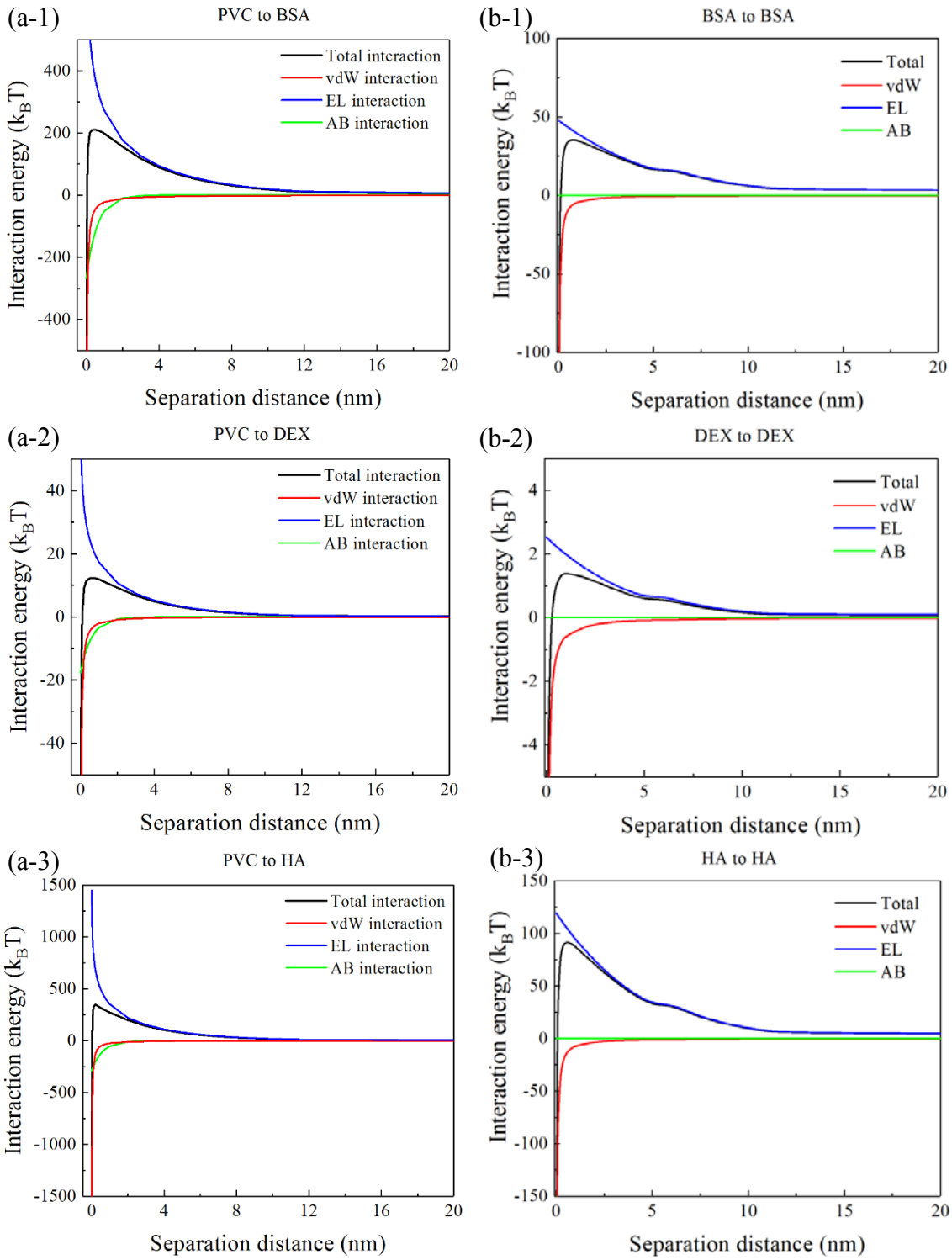

Figure 4.10 EDLVO interaction energy profiles for the membrane–foulant (a) and foulant-foulant combinations tested (b).

4.3.4. Fouling Resistance Analysis

The total filtration resistance R_T was determined by Equation 4.8 according to the Darcy's

law.[454]

$$R_T = \frac{\Delta P}{J \cdot \eta} \times 1000 \times 3600 \tag{4.8}$$

where ΔP was the TMP (Pa); J was the filtration flux ($L \cdot m^{-2} \cdot h^{-1}$); and η is viscosity of solution filtered (Pa·s). The total resistance (R_T) is generally the sum of the intrinsic resistance of the membrane (R_m) and resistance caused by the existence of foulant (R_f) brought by the feed solution.[178, 455] The foulant resistance can be divided into two parts: reversible resistance (R_{re}) caused by cake and irreversible resistance caused by pore blocking (R_{ir}). The fouling resistance values and the corresponding percentage values were calculated as follows:

$$R_{T,n+1} = \frac{\Delta P}{J_{T,n+1} \cdot \eta} \times 1000 \times 3600 \tag{4.9}$$

$$R_m = \frac{\Delta P}{J_0 \cdot \eta} \times 1000 \times 3600 \tag{4.10}$$

$$R_f = R_{T,\mathrm{n}} - R_m \tag{4.11}$$

$$R_{re} = R_{T,n} - R_{T,n+1} \tag{4.12}$$

$$R_{ir} = R_{T,n+1} - R_m \tag{4.13}$$

$$\text{Reversible resistance percentage } (\%) = \frac{R_{re}}{R_f} \times 100\% \tag{4.14}$$

$$\text{Irreversible resistance percentage } (\%) = \frac{R_{ir}}{R_f} \times 100\% \quad (4.15)$$

where $R_{T,n}$ was the total resistance before backwash followed by the filtration of (n+1) cycle; J_n was the filtration flux ($L \cdot m^{-2} \cdot h^{-1}$) before backwash followed by the filtration of (n+1) cycle; $R_{T,n+1}$ was the resistance just after backwash in the (n+1) cycle; ΔP was the trans membrane pressure (Pa); $J_{T,n+1}$ was the filtration flux ($L \cdot m^{-2} \cdot h^{-1}$) after backwash in the (n+1) cycle; J_0 was the DI water flux; and η is the viscosity of solution filtered (Pa·s).

As shown in Figure 4.11, The red part in the column represented the calculated percentage of irreversible fouling resistance in each cycle and the black part represented the percentage of reversible fouling resistance. We can see that for BSA, the irreversibile resistance is the main resistance for the whole filtration process, and the calculated average percentage of irreversibile resistance was 52.37%. For DEX and HA the reversible resistance accounted for most resistance, and the average percentage of reversibile resistance was 77.73% and 80.56%, respectively. The average irreversibile resistance percentage increased followed the order: BSA>DEX>HA. Considering the results that the accumulative defouling rate increasing in the following order: BSA<DEX<HA, it was obvious that for these three foulants, the larger irreversibile percentage, the lower was the defouling rate.

Figure 4.11 showed that the ratio of irreversible fouling was smaller than the reversible fouling for HA, compared with BSA. For BSA, the irreversible resistance is the main resistance for the whole filtration process, and the calculated average percentage of irreversible resistance was 52.37%. For HA, the reversible resistance accounted for most resistance, and the average percentage of reversible resistance was 80.56%. The

irreversible fouling resistance appeared to be correlated with the membrane-foulant adhesion force. The high adhesion forces between the membrane foulant led to a more severe irreversible fouling or higher irreversible resistance in the initial filtration stage.

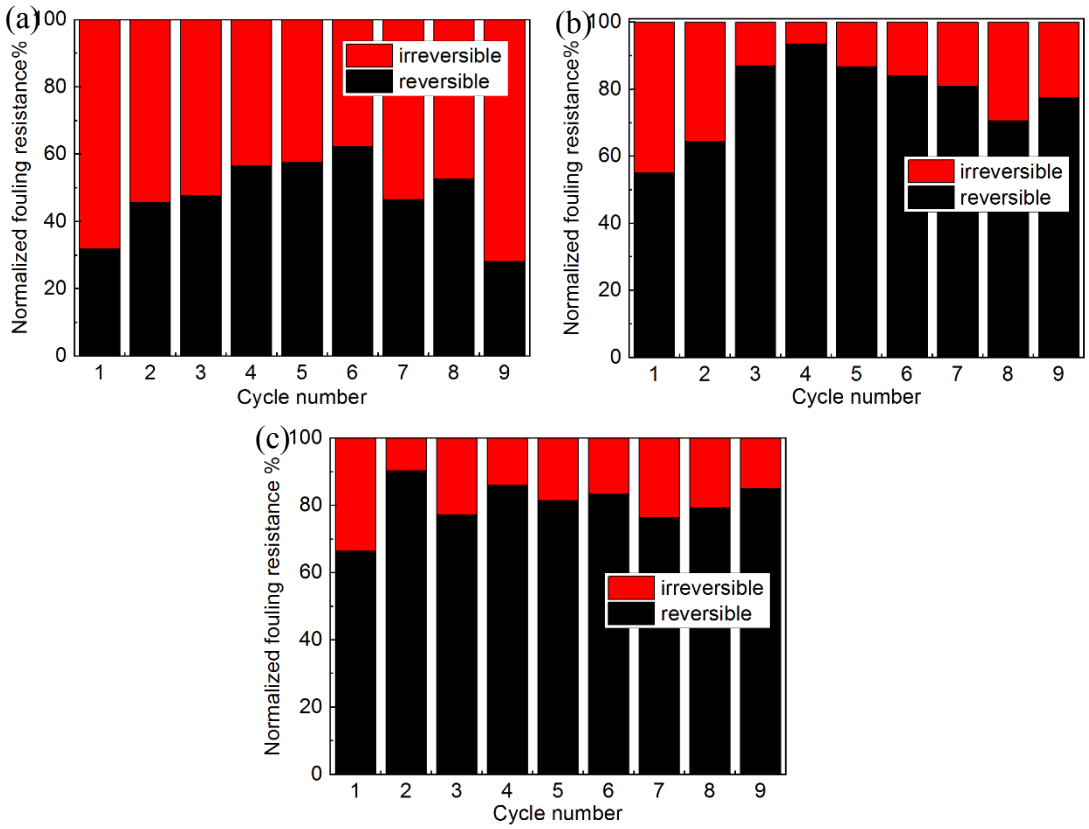

Figure 4.11 Reversibility of fouling during filtration experiment with different foulant: (a) BSA; (b) DEX; (c) HA.

4.3.5 Correlation Analysis Between Foulant Deposition Rate and Fouling Rate

Generally, a high interaction energy barrier reduces the tendency of colloidal interactions on membrane and thus prevents membrane fouling.[166] In Chapter 3, a fouling kinetics model that incorporated the EDLVO theory into the particle transport equation is established.[168] This model indicated that the gradient of attractive interaction energy mediated the fouling rates of BSA or HA on polymer membranes. To further explain the effect of interaction energy barrier on membrane fouling prediction, correlations between

the fouling rate and the interaction energy were performed based on an EDLVO approach and the irreversible aggregation kinetics in Smoluchowski's population balance equation:[456]

$$\frac{dn_k}{dt} = \frac{1}{2}\sum_{i+j=k}\alpha(r_i,r_j)\beta(r_i,r_j)n_i n_j - n_k\sum_{i=1}\alpha(r_i,r_k)\beta(r_i,r_k)n_i \tag{4.16}$$

where $\frac{dn}{dt}$ is the irreversible aggregation kinetics of particles (or surface deposition rate), $\alpha(r_i,r_j)$ is the collision efficiency, $\beta(r_i,r_j)$ is the collision frequency function, n_i is the number concentration of particles, r_i is the radii of particles.

In this study, the surface deposition process is assumed to occur in two sequential processes: (1) the deposition of foulant particles on the membrane surface in the initial filtration stage; and (2) foulant-foulant deposition in the later filtration stage. If the foulant detachment is ignored, the surface deposition rate can be approximated from the Smoluchowski's population balance equation:

$$\frac{dn}{dt} = \frac{1}{2}\alpha\beta n \tag{4.17}$$

The collision efficiency (α) can be solved with the Maxwell approach:[427]

$$\alpha = \delta \cdot \int_{E_b}^{\infty} e^{-E} E^{1/2} \mathrm{d}E \tag{4.18}$$

where δ is the hydrodynamic damping factor (also called the drag effect factor, dimensionless), which is simplified to 1. E_b is the interaction energy barrier (k_BT), obtained from the interaction energy profiles as shown in Figure 4.10, and E is the random kinetic

energy (k_BT) of foulants.

The collision frequency (β) of foulant particles against membrane surface is expressed as:[407, 456-458]

$$\beta = \frac{8k_BT}{3\mu}\left[2\int_0^{\infty}\lambda(u)\frac{\exp(U_{vwd}(h)/k_BT)}{(2+u)^2}\mathrm{d}u\right]^{-1} \tag{4.19}$$

$$\lambda(u) = \frac{6(u)^2+13(u)+2}{6(u)^2+4(u)} \tag{4.20}$$

$$u = h/r \tag{4.21}$$

where U_{vwd} is the van der Waals forces interaction energy calculated by the EDLVO theory equation (Equation 4.7); k_B is the Boltzmann constant; T is the absolute temperature; μ is the viscosity of the solution (1×10^{-3} Pa·s); r is the radius of foulants; h is separation distance between two particles (nm) or between particle and surface (nm); and $\lambda(u)$ is the correction factor for the diffusion coefficient, which is related to the separation distance by the Equation 4.20.

Particle number concentration (n) was approximated by the molar concentration of foulants (c_i, mol L^{-1}) times the Avogadro constant (N_A, 6.022×10^{23} # mol^{-1}). The molar concentration is equal to the mass concentration (C_i, mg L^{-1}) divided by molecular weight (MW, g mol^{-1}) of foulants (Table 4.3).

$$c_i = \frac{C_i}{MW} \tag{4.22}$$

$$n = c_i \cdot N_A \tag{4.23}$$

The calculated $\frac{dn}{dt}$ through Equation 4.17-4.23 is summarized in Table 4.4 using Matlab (the Matlab codes and instructions are detailed in the Appendix; also the results were verified by https://www.integral-calculator.com). Since the calculated values of $\frac{dn}{dt}$ and flux decline rates calculated from Figure 4.9c using Equation 4.2 have significant variations in order of magnitude, they were expressed in logarithm (Table 4.5).

Table 4.4 The Calculation of Deposition Rate ($\frac{dn}{dt}$)

Initial filtration stage: membrane-foulant interaction							
Foulant	E_b (J)	$-\frac{\lvert E_b \rvert}{k_B T}$ ($k_B T$)	α	β (m^3 s^{-1})	$n_{foulant}$ (# m^{-3})	$\frac{dn}{dt}$ (# s^{-1})	$\log\left(\frac{dn}{dt}\right)$
BSA	8.65E-19	-210.4	6.12E-91	6.60E-18	9.26E+21	1.87E-86	-85.7
HA	1.23E-18	-299.13	2.12E-129	6.79E-18	6.70E+23	7.10E-106	-105.1
DEX	5.08E-20	-12.34	1.60E-05	7.02E-18	7.14E+21	5.71E+16	16.8
Later filtration stage: foulant-foulant interaction							
Foulant	E_b (J)	$-\frac{\lvert E_b \rvert}{k_B T}$ ($k_B T$)	α	β (m^3 s^{-1})	$n_{foulant}$ (# m^{-3})	$\frac{dn}{dt}$ (# s^{-1})	$\log\left(\frac{dn}{dt}\right)$
BSA	1.09E-19	-26.6	1.47E-11	5.04E-18	9.26E+21	3.43E-7	-6.5
HA	3.76E-19	-91.54	1.69E-39	5.62E-18	6.70E+23	3.18E-33	-32.5
DEX	5.75E-21	-1.40	3.22E-06	5.49E-18	7.14E+23	6.31E-02	-1.2

Table 4.5 The Calculated Fouling Rate or Flux Decline Rate ($\frac{dJ}{dt}$)

Foulant	**Initial stage**		**Later stage**	
	$\frac{dJ}{dt}$ (min^{-1})	$\log\left(\frac{dJ}{dt}\right)$	$\frac{dJ}{dt}$ (min^{-1})	$\log\left(\frac{dJ}{dt}\right)$
BSA	0.23	-0.6	0.008	-2.1
HA	0.18	-0.7	0.003	-2.5
DEX	0.02	-1.7	0.017	-1.8

Table 4.4 showed that the deposition rates of BSA and HA at the initial filtration were the lowest, due to the small collision efficiency caused by the high energy barriers of BSA-membrane and HA-membrane interactions. The collision frequency of each foulant at either initial or later filtration stage is at the similar level (5.49-7.02×10^{-18} m^3 s^{-1}) as

shown in Table 4.4. Thus, the deposition rate at which foulant particles accumulate on a membrane surface or foulant layer is primarily determined by the collision efficiency α. According to Equation 4.18, foulants generally deposit fast onto the membrane/foulant layer surface when the interaction energy barrier is low. Table 4.5 showed the flux decline rate during the initial stage was much higher than that in the later stage, especially for BSA and HA. As discussed in above sections, BSA and HA were assumed to form foulant layer quickly at the initial filtration stage and caused an abrupt flux decline.

Our hypothesis to validate is whether the surface deposition rate ($\frac{dn}{dt}$) is correlated with the fouling rate. A linear regression between the deposition rate and the flux decline rate is established in Figure 4.12. The linear fitting to experimental data was shown with 95% prediction confidence limits. All the filtration data at the later filtration stage fitted the linear regression curve, indicating that the model may be suitable for the foulant-foulant interaction as the dominant fouling mechanism. Figure 4.12 shows that the filtration data of BSA and HA at the initial filtration stage did not fit the model prediction data. The actual flux decline rates were higher than that predicted by the linear fit. A schematic of foulant deposition processes presented in Figure 4.12b illustrate the BSA and HA foulants formed cake layer on the membrane surface and blocked the membrane pores, which caused the rapid flux decline within only 2 minutes (Figure 4.9c). The foulant-foulant interaction began to dominate the fouling process afterwards immediately. As a result, the flux decline rate was governed by foulant layer formation, whereas the contribution to fouling resistance and flux decline from membrane-foulant interaction remains constant.

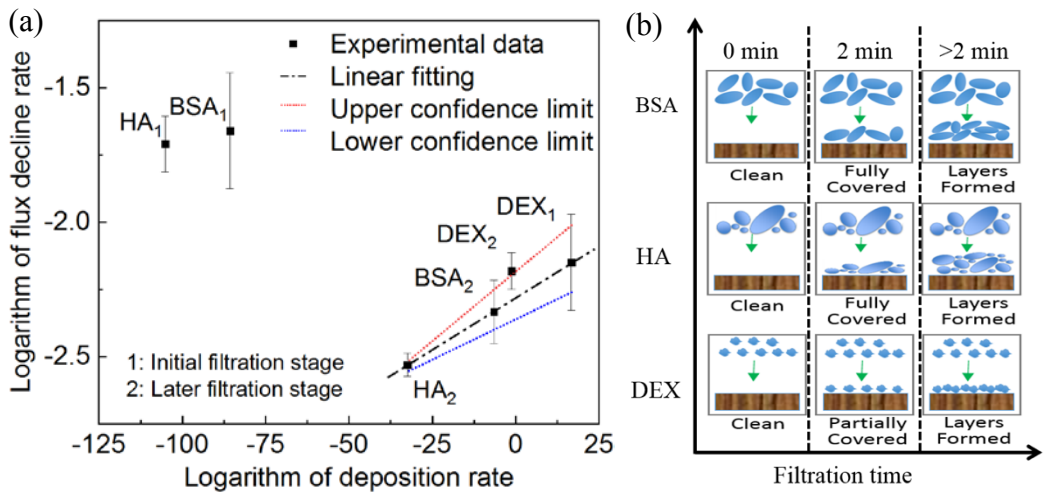

Figure 4.12 (a) The correlation between the logarithm of flux decline rate and the logarithm of deposition rate. The linear regression as well as the 95% prediction confidence are plotted; (b) the schematic of different foulant depostion processes of BSA, HA and DEX.

4.3.6 Defouling Kinetics for Different Foulant-Membrane Systems

Figure 4.13a shows the flux recovery ratio as defined in Equation 4.4 in each filtration/backwash cycle. The flux recovery ratio for all foulants was lowest at the first cycle of filtration after 15 min, which means that most irreversible fouling occurred in the first cycle. The flux recovery ratios for these three foulants were around 80% and stabilized after the third filtration cycle. Figure 4.13b shows that the accumulative recovery ratio followed the order: BSA (50.08%) < DEX (57.96%) < HA (77.94%), which means that the highest backwash cleaning efficiency was achieved on the HA-fouled PVC membranes.

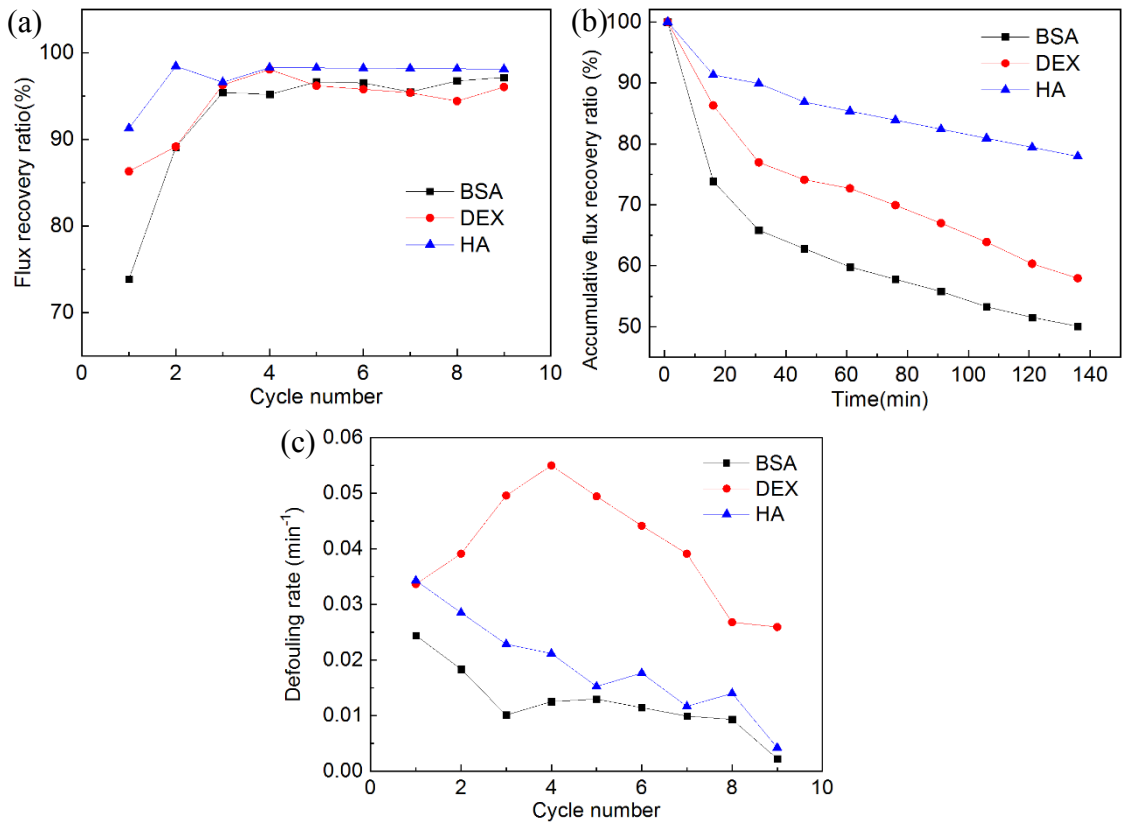

Figure 4.13 Flux recovery ratios for BSA, DEX and HA (a) in each cycle and (b) accumulative ratio; (c) Flux recovery rate (defouling rate) curve for BSA, DEX and HA in each cycle.

Figure 4.13c shows the defouling rate as defined in Equation 4.6 in each cycle as a measure of the flux recovery rate during the backwashing. DEX had a higher defouling rate than BSA and HA. Moreover, the defouling rate monotonically decreased with the filtration time for BSA and HA. However, DEX led to a peak of the defouling rate probably because DEX caused fouling through pore blocking or pore narrowing and backwash could remove the initial DEX deposit in pores more efficiently than remove BSA or HA foulant layers on membrane surfaces. Comparing the two cases it is observed that even though DEX fouling is more severe than the one caused by HA and BSA (Figure 4.9c), it is to a large extent reversible by backwashing. On the contrary, fouling caused by BSA is characterized by greater and increasing irreversibility, which is not remedied by the

periodic backwashing (Figure 4.11a).

Backwash was performed every 15 minutes to mitigate the membrane fouling. The flux decline rate after backwash followed the order: DEX > BSA > HA (Figure 4.9b). This result indicate that the filtration flux decline due to the pore blocking of DEX is hard to reverse by backwashing, compared with the cake layer formation of BSA and HA. It is possible that BSA formed a denser cake layer, whereas HA formed a looser cake layer, which led to different fouling and defouling rates for BSA and HA. Other factors (layer thickness, porosity, and compressibility) may also vary the flux resistance and fouling/defouling characteristics.

4.3.7 Adhesion Force Measurement for Foulant-Foulant and Foulant-Membrane Systems

During the defouling process, the detached foulant must overcome the adhesion force between the membrane and the foulants or between the foulants themselves. Adhesion force is also called rupture force that is used to break the adhesive bonds. Adhesion force can be measured by AFM through the typical force-distance curve as illustrated in Figure 4.14a or 4.14c. Figure 4.14b and 4.14d presented the relative frequency distributions and the average adhesion forces between BSA, DEX and HA and PVC membranes. The adhesion forces of membrane-foulant are stronger than the corresponding adhesion forces of foulant-foulant for each type of foulants used in this study.

The adhesion forces for PVC-BSA (3.8 nN) is greater than PVC-HA (0.03 nN), which supports the calculated defouling rate order (BSA < HA) in Figure 4.13c. Likewise, the adhesion forces between foulant and foulant followed the order: BSA-BSA > HA-HA, which coincided with the defouling rate in later filtration/backwash cycles. High membrane-foulant adhesion forces are likely to cause irreversible fouling and low flux

recovery ratio (Figure 4.13a) as reported previously.[165]

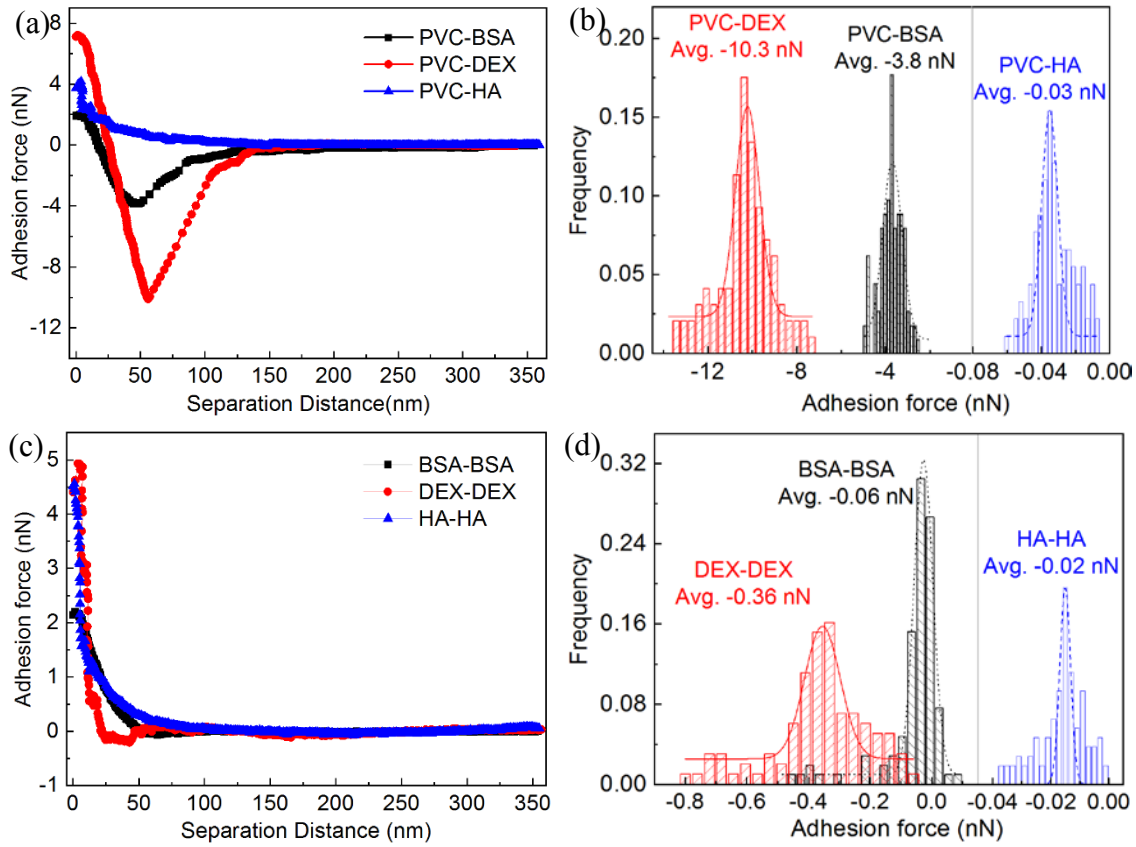

Figure 4.14 Representative force-distance curves and frequency distribution of (a-b) membrane-foulant and (c-d) foulant-foulant adhesion forces.

4.3.8 Correlation Analysis between Adhesion Force and Membrane Defouling Kinetics

A membrane defouling kinetics model was developed based on the particle transport equation that we employed previously:[406, 407]

$$J_x = -D_x \frac{\partial C}{\partial x} + u_x C + \frac{D_x F_x C}{k_B T} \tag{4.24}$$

where J_x is the particle flux or the particle detachment rate (g m^{-2} s^{-1}), D_x is the diffusion coefficient (cm^2 s^{-1}), C is the particle concentration (mg L^{-1}), u_x is the particle velocity components induced by the fluid flow (m s^{-1}), F_x is the component of the external force

vector (N). In our case, F_x is the adhesion force measured by AFM. T is the temperature (K), k_B is the Boltzmann constant, 1.38×10^{-23} J K^{-1}.

For the particle dispersion component, the particle detachment rate or flux is expressed as:

$$J_{x(disp)} = -D_x \frac{\partial C}{\partial x} = -D_x \frac{c_b - c_g}{h} = D_x \frac{c_g - c_b}{h} \tag{4.25}$$

where c_b and c_g are the particle concentration (mg L^{-1}) in the bulk (backwash) solution, and the gel layer (saturated concentration), respectively; h is the separation distance between foulants and membrane surface (nm).

The particle detachment flux as a result of advection driven by the fluid flow, is expressed as:[408, 409]

$$J_{x(adve)} = u_x C = J_b c_g \tag{4.26}$$

where J_b is the backwashing water flux (m^3 m^{-2} s^{-1}), $J_b = \frac{Q_b}{A}$, Q_b is the flowrate of the backwashing flow (6 mL min^{-1}); A is the membrane area (6.28 cm^2).

The particle detachment flux is dictated by the interfacial adhesion force:

$$J_{x(force)} = \frac{D_x F_x C}{k_B T} = \frac{D_x F_{adh} c_g}{k_B T} \tag{4.27}$$

where F_{adh} is the adhesion force measured by AFM. In the initial filtration stage, F_{adh} is the adhesion force between the membrane and foulant; in the later filtration stage, F_{adh} is thus approximated to be the sum of the adhesion force of membrane-foulant and foulant-foulant.

Thus, the overall particle detachment rate is expressed below:

$$J_x = D_x \frac{c_g - c_b}{h} + Jc_b + \frac{D_x F_{adh} c_b}{k_B T} \quad (4.28)$$

The detailed calculations of these three components are as follows: For $J_{x(disp)}$, D_x=3.3×10^{-7} cm^2 s^{-1} for BSA solution,[417] D_x=5.9×10^{-7} cm^2 s^{-1} for HA solution,[418] D_x=3.9×10^{-7} cm^2 s^{-1} for DEX solution, c_g = 40 mg L^{-1} (BSA solution), c_g = 1500 mg L^{-1} (HA solution), c_g = 30 mg L^{-1} (HA solution), c_b is assumed to be 0 for backwashing water, which yields the highest values of the dispersion component. And h is assumed to be 0.157 nm, which is the nearest separation distance between the foulants and the membrane due to Borne repulsion.[419] Thus,

For BSA: $J_{x(disp)} = 3.3\times10^{-7} \frac{\text{cm}^2}{\text{s}} \times \frac{40 \text{ mg L}^{-1}}{0.157 \text{ nm}} = 8.41\times10^{3} \frac{\text{g m}^{-2}}{\text{s}}$.

For HA: $J_{x(disp)} = 5.9\times10^{-7} \frac{\text{cm}^2}{\text{s}} \times \frac{1500 \text{ mg L}^{-1}}{0.157 \text{ nm}} = 5.64\times10^{3} \frac{\text{g m}^{-2}}{\text{s}}$.

For DEX: $J_{x(disp)} = 3.9\times10^{-7} \frac{\text{cm}^2}{\text{s}} \times \frac{30 \text{ mg L}^{-1}}{0.157 \text{ nm}} = 7.45\times10^{3} \frac{\text{g m}^{-2}}{\text{s}}$.

For $J_{x(adve)}$, J is assumed to be $J_b = \frac{6 \text{ mL min}^{-1}}{6.28 \text{ cm}^2}$. Thus,

For BSA: $J_{x(adve)} = 40 \text{ mg L}^{-1} \times \frac{6 \text{ mL min}^{-1}}{6.28 \text{ cm}^2} = 6.37\times10^{3} \frac{\text{g m}^{-2}}{\text{s}}$.

For HA: $J_{x(adve)} = 1500 \text{ mg L}^{-1} \times\times \frac{6 \text{ mL min}^{-1}}{6.28 \text{ cm}^2} = 2.39\times10^{5} \frac{\text{g m}^{-2}}{\text{s}}$.

For DEX: $J_{x(adve)} = 30 \text{ mg L}^{-1} \times\times \frac{6 \text{ mL min}^{-1}}{6.28 \text{ cm}^2} = 4.78\times10^{3} \frac{\text{g m}^{-2}}{\text{s}}$.

For $J_{x(force)}$, F_{adh} is taken from Figure 4.14 and Table 4.6 summarized the values of F_{adh} and $J_{x(force)}$ for different interaction pairs.

According to Equation 4.28, the particle detachment rate is controlled by three

components: dispersion, advection, and adhesion force. The calculations of these three components (see comparisons in Table 4.6) showed that, compared with $J_{x(force)}$, the former two components ($J_{x(disp)}$ and $J_{x(adve)}$) were found to be smaller. Particularly for BSA and DEX, $J_{x(disp)}$ and $J_{x(adve)}$ were substantially smaller by several orders of magnitude and thus could be negligible while the adhesion force for DEX was almost 100 to 300 times smaller than BSA and DEX, the three components for DEX were at the same order of magnitude. It is also interesting that these three components are all dependent on foulant saturated concentration c_g and $J_{x(force)}$ is always greater than $J_{x(disp)}$ and $J_{x(adve)}$ under our experimental conditions. Our calculations show that only when the backwashing flux of BSA or DEX reach above approximately 1.1×10^5 to 3.5×10^5 LHM, $J_{x(disp)}$ and $J_{x(adve)}$ can reach similar orders of magnitude as $J_{x(force)}$. However, typical backwashing flux commonly used for polymeric ultrafiltration membranes is between 7.5 LMH to 500 LHM.[459-463]

The defouling rate ($\frac{\mathrm{d}J^d}{\mathrm{d}t}$) is taken as the slope of the flux changes during the backwashing and calculated by Equation 4.6 using the data in Figure 4.13c. The calculated defouling rates are summarized in Table 4.7.

The particle detachment rate calculated in Equation 4.28 and the defouling rate were plotted in Figure 4.15, which elicits a linear relationship (R^2=0.845) for BSA and HA filtration system. However, the experimental flux decline rate for DEX was much higher than that predicted by the linear regressions. Since the colloidal size of DEX is smaller than HA and BSA, DEX might form pore narrowing or pore blockage to cause the flux decline.

During the backwash, the fouling caused by DEX foulants in the pores might be easier to be removed than the porous foulant layer on membrane surfaces. This also implies that our defouling kinetics model is primarily suitable for explaining the role of adhesion force in the cake layer fouling mechanism.

Table 4.6 The Calculation of J_x

System	Parameters	BSA	HA	DEX
Initial stage	F_{adh} (nN)	-3.81	-0.03	-10.33
	$J_{x(force)}$ (g m^{-2} s^{-1})	-1.22×10^{6}	-6.46×10^{5}	-2.94×10^{6}
	$J_{x(disp)}$ (g m^{-2} s^{-1})	8.41×10^{3}	5.64×10^{5}	7.45×10^{3}
	$J_{x(adve)}$ (g m^{-2} s^{-1})	6.37×10^{3}	2.39×10^{5}	4.78×10^{3}
	J_x (g m^{-2} s^{-1})	-1.21×10^{6}	1.57×10^{5}	-2.93×10^{6}
Later stage	F_{adh} (nN)	-3.87	-0.05	-10.69
	$J_{x(force)}$ (g m^{-2} s^{-1})	-1.24×10^{6}	-1.08×10^{6}	-3.04×10^{6}
	$J_{x(disp)}$ (g m^{-2} s^{-1})	8.41×10^{3}	5.64×10^{5}	7.45×10^{3}
	$J_{x(adve)}$ (g m^{-2} s^{-1})	6.37×10^{3}	2.39×10^{5}	4.78×10^{3}
	J_x (g m^{-2} s^{-1})	-1.23×10^{6}	-2.73×10^{5}	-3.03×10^{6}

Table 4.7 The Calculation of $\frac{\mathrm{d}J^d}{\mathrm{d}t}$

		BSA	HA	DEX
$\frac{\mathrm{d}J^d}{\mathrm{d}t}$ (min^{-1})	Initial stage	0.0244	0.0343	0.0337
	Later stage	0.0183	0.028	0.039

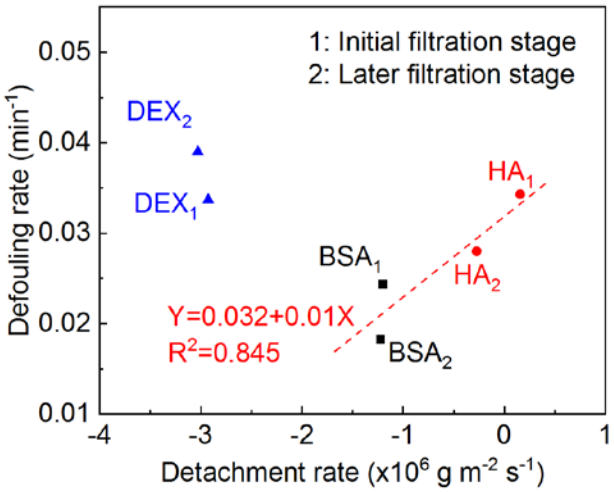

Figure 4.15 Linear correlations analysis between detachment rate and defouling rate.

4.4. Conclusions

Based on the evaluation of fouling and defouling kinetics of HA, BSA and DEX on PVC membrane during filtration, this study presented a universal toolset for analysis of membrane fouling and defouling kinetics using the combined EDLVO theory, Maxwell approach, and particle transport equation. A graphic summary of the main work done in this study was shown in Figure 4.16. In particular, membrane fouling and defouling performances were analyzed through monitoring the flux decline during filtration and flux recovery during backwash. The foulants distribution and morphology on PVC membrane were characterized using confocal microscopy and AFM-IR instrument. Physico-chemical properties (*e.g.*, hydrophobicity and surface charge) of PVC membrane and foulants were characterized, which were used in the EDLVO theory to calculate the interaction energies between membrane-foulant and foulant-foulant. The results showed that fouling kinetics is governed by interaction forces between foulant-membrane and foulant-foulant; the flux decline rate could be strongly correlated with the deposition rate (determined by the

interaction energy profile calculated by EDLVO) well at the later filtration stages.

Moreover, the adhesion forces of membrane−foulant and foulant−foulant were further measured by atomic force microscopy (AFM) with modified colloidal probes. The results showed that adhesion forces between the membrane and foulant and between foulants themselves dictated defouling rate and flux recovery. A correlation between the particle detachment rate (derived from particle transport rate with adhesion force) and the defouling rate was developed, which elicits fairly satisfactory linear relationships (R^2=0.845) for BSA and HA foulants filtration system. Moreover, DEX foulant filtration system was an outlier point in the correlation models for defouling kinetics prediction. This outlier implies that this correlation might be better suitable for cake layer fouling mode.

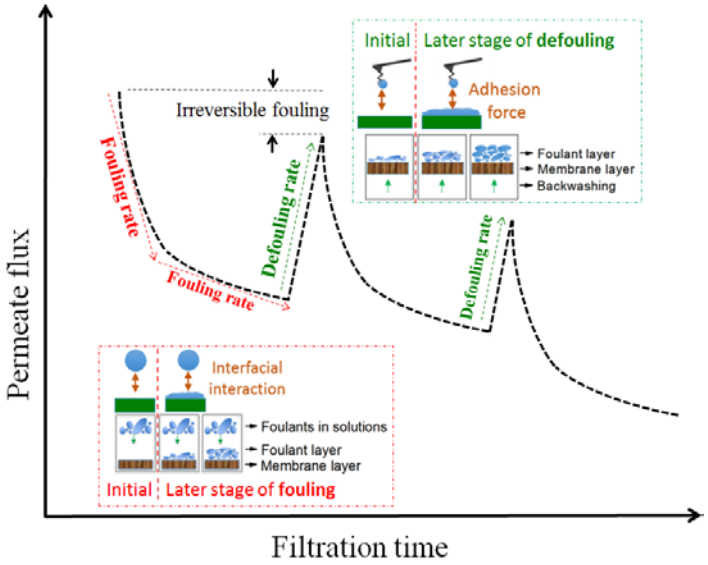

Figure 4.16 The graphic summary of this work.

4.5. Future Work and Recommendations

For further improvement of our modeling analysis, other important factors that could vary the fouling and defouling behavior, such as foulants colloidal sizes, membrane fouling

modes, fouling layer coverage ratio and foulant layer conformational change, deserve further examinations. Though the membrane fouling by polysaccharides, proteins and humic substances has been studied extensively, but this process is still complicated and has many problems to be solved. Most studies about fouling or defouling mechanism analysis were generally leading to the correlation fitting instead of developing specific models for universe membrane filtrations. The foulant deposition process seems to be generally rapid while the formation of foulant layer is usually accompanied with a structural change, such as the conformational change or rearrangement of the structure of the deposited foulants. Usually, the modeling has implicitly taken the foulant molecules as sphere colloids with homogeneous nature; whereas they actually bear structural flexibility and physicochemical heterogeneity.[464] The affecting factors are highly related to the physicochemical characteristics of foulants and membranes.[465] The development in instrumentation and instrumental techniques might help reveal the fouling behavior better. As such, modifications of the model are proposed for future work, including: (a) analyzing the role of interaction forces and adhesion forces for pore blocking fouling mechanisms, (b) giving consideration to the conformational change into the fouling kinetics, and further (c) developing feasible instrumental techniques for real-time fouling/defouling process observation.

CHAPTER 5

CHEMICAL AND THERMAL AGING OF CHEMICALLY MODIFIED POLYMERIC MEMBRANES: IMPACTS ON MEMBRANE PROPERTIES AND FILTRATION PERFOMRANCES

5.1 Introduction

Material aging is one of the major drawbacks that most polymer-based membranes have been suffering in water or chemical filtration processes.[227, 230, 233, 468, 469] Under physical, chemical or mechanical stresses, membrane materials may undergo physical damage and chemical degradation that leads to adverse impacts on the membrane filtration performances or stability.[22, 470] For example, after the hypochlorite treatment, a polysulfone ultrafiltration membrane began to have an increased flux increase and poor rejection against pollutants owing to the pore size increase.[206,] Wolff and Zydney analyzed and established the relationship between membranes pore size and bleach treatment duration.[208, 209] Hashim *et al.* investigated and revealed the dependence of mechanical properties, thermal properties and crystalline structure of the polyvinylidene fluoride (PVDF) hollow fiber membranes on the exposure to the sodium hydroxide (NaOH) solution as well as exposure conditions such as the NaOH concentration, exposure time and temperature.[215] Membrane aging is shown to not only affect membrane filtration performances but also contribute to possible emerging pollutions from the release of co-polymers,[469, 471] monomers,[472] fragments of membrane materials[470, 473] or microplastics/nanoplastics.

Besides chemical aging during the membrane cleaning, thermal aging investigations on polymer membranes show great importance as well for three main reasons. First, polymer membranes that used in fuel cells and batteries applications,

required high thermal safety and stability. For example, polyvinylidene fluoride (PVDF) membrane is used as a polymer separator in lithium-ion batteries because of its significant thermal stability.[474] While the perfluorosulfonic-acid (PFSA) membranes, the most widely used ionomer for polymer-electrolyte fuel cell (PEFC) applications,[475] are frequently subjected to high temperatures during operation, altering the properties of the polymer electrolyte. Second, thermal aging might change the membrane functional stability, such as hydrophilicity.[476-478] Third, the chemically modified polymer membranes (*e.g.*, PES membrane coated with PVP) might lose their surface hydrophilicity due to the loss of PVP additives on their surface.

Membrane aging occurs both on macroscopic and microscopic levels. In many studies, membrane aging is characterized by the changes of color or appearance,[215] permeability or rejection performance,[213, 221] morphology,[213] surface hydrophilicity,[213] crystal structures or crystallinity,[215] surface charge, and surface functional groups.[213, 215, 217, 219, 220] Besides, many studies also focused on the stability and distribution of chemical modifiers or additives during aging processes, which are shown to vary the bulk membrane properties and filtration performances.[222, 479-481] So far, no quantitative criterion has been proposed to classify the aging levels. Moreover, some research reports or findings are still debatable on the membrane characteristics that change during various aging processes.[482] For instance, several studies reported an increase in water permeability for aged membranes[472, 483-485] while a few studies have seen the opposite effect – decreasing permeability.[486-488] One of possible causes for this misinterpretation or debate is that lack of proper characterization tools and interrelationships between physicochemical and filtration characteristics. For example, the contact angel measurement is not only affected

by the surface chemical species but also affected by the surface roughness, which may depend on the pore sizes. Thus, it is difficult to attribute membrane surface hydrophobicity changes to one single factor (surface roundness or pore size). Nevertheless, many previous studies overlooked the interrelationships of these characterized membrane characteristics.

To address these knowledge gaps, this study first examined a suite of physicochemical characteristics (*e.g.*, surface hydrophobicity, surface charge, roughness, surface porosity) and filtration performance as a result of membrane aging, followed by a rigorous analysis of the quantitative structure-activity relationships between these membrane properties and filtration performance. We performed the accelerated membrane aging experiments on polyethersulfone (PES) membranes in both the filtration and immersion modes. The accelerated membrane aging was achieved under the same chemical treatment intensity (at a fixed exposure time to the hypochlorite solution). Hypochlorite solution was selected as the oxidant as it is widely used as a chemical cleaning agent to remove irreversible membrane foulants. [469, 489] In contrast to the immersion mode, aging tests via a filtration process may enable an inner membrane exposure to chemical oxidants and thus vary the membrane aging mechanisms or kinetics. Besides chemical aging, thermal aging was also studied these PES membranes as thermal stability or tolerance is also critical in many industrial applications.[490] Overall, this study holistically assessed the evolution of membrane properties during chemical/thermal aging treatment processes with a goal of establishing the relationship between these properties with membrane filtration performance. The degradation mechanisms of PES and PVP in the membranes were also analyzed to provide new insight into the development of anti-aging membrane materials.

5.2 Method and Materials

5.2.1 Membranes for Aging Tests

As shown in Table 5.1, PES membranes with different chemical modifications were prepared by a phase inversion method[324] and modified using UV-induced graft polymerization that a Rayonet photochemical chamber reactor system contained 300 nm UV lamps was used with the dip modification technique.[491] Briefly, the modifier solutions, including polyvinylpyrrolidone (PVP) as a hydrophilic modifier (for hydrophilic membranes) and fluoro-alcohols ($F(CF_2)_nCH_2CH_2OH$) as a hydrophobic modifier (for super-hydrophobic membranes),[492] were prepared in deionized (DI) water. Then, the pristine PES membranes were dipped into the modifier solutions for 30 min with stirring at 22 ^oC. For the double hydrophilic PES and double super-hydrophobic PES membranes, the dip-coating procedure was operated twice. After exposure to the modifier solution, the membranes were sealed in the photochemical chamber and irradiated in water-saturated N_2 (to minimize water evaporation from the modifier solution on the membrane surface) for 10 minutes. After modification, the membranes were washed rigorously and immersed in DI water for 24 h before use.

Table 5.1 The Information about the Polymeric Membrane Samples

Sample	Types	Modification groups
0.2 μm hydrophobic PES	None	None
0.2 μm hydrophilic PES	Crosslinked	Amide
0.2 μm Super-hydrophobic PES	Crosslinked	Fluorinated
0.2 μm Double hydrophilic PES	Double Crosslinked	Amide
0.2 μm Double Super-hydrophobic PES	Double Crosslinked	Fluorinated

In this study, the five PES membranes were used to study the stability of modifier additives on membrane surface through characterization with surface hydrophobicity,

AFM-IR and FTIR. Meanwhile, the hydrophobic PES and PVP-functionalized hydrophilic PES membranes were selected to study the changes in membrane properties such as surface morphology and pore geometry, surface hydrophilicity, surface charges, FTIR, tensile strength that jointly influence membrane permeability and pollutant rejection via QSAR models.

5.2.2 Aging Procedures

The chemical treatment intensity or dose is typically defined to be the chemical oxidant concentration × contact or exposure time ("c × t").[213] To accelerate the aging process in a relatively short duration (*e.g.*, a few hours or days), high concentrations of chemical oxidants are used to achieve the same equivalent chemical treatment intensity in longer exposure times such as months or years.

5.2.2.1 Static Immersion Chemical Aging with Sodium Hypochlorite. Accelerated aging tests were performed by soaking different polymer membranes in 4000 ppm NaClO solutions at pH 9 at 40 ^{o}C for different exposure times (1, 2, 5, and 10 days). The pH 9.0 as it was demonstrated that the pH range 8-9 of NaClO solutions leads to the most severe damage to polymer membranes.[493] The polyethylene flasks with membrane samples soaking in NaClO solutions were placed in a dark and thermostatized chamber under an orbital agitation of 150 rpm. The NaClO solution was decanted and replaced with new/fresh ones every day to maintain a constant NaClO concentration.[213] After each aging experiment, membrane samples were thoroughly rinsed with water to remove residual NaClO in the membrane,[215] then soaked in DI water for 24 h and finally dried at room temperature in a desiccator for 24 h.[230] The schematics of the static immersion aging

process is shown in Figure 5.1.[213, 494] In addition, control groups are those membranes that were immerged in DI water and subjected to the same soaking/rising procedures.[213]

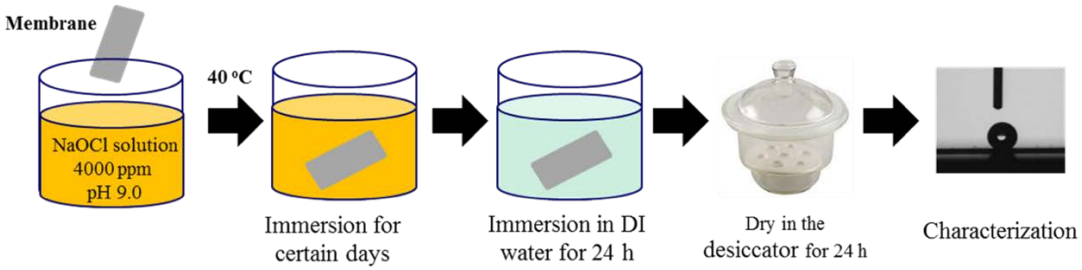

Figure 5.1 Schematics of the static immersion chemical aging process.

5.2.2.2 Chemical Aging via Dynamic and Continuous Filtration. To simulate the chemical aging that may occur during the chemical backwash on fouled membranes,[495] a continuous membrane filtration unit was assembled as shown in Figure 5.2. The chemical aging test via this filtration mode was performed with the same chemical treatment intensity. The only difference is that the treated membrane was continuously fed with the NaClO solution (4000 ppm and pH 9.0) for different times (1, 2, 5, and 10 days) at a flux of 150 $L \cdot m^{-2} \cdot h^{-1}$ (TMP varied with different membranes) in a dead-end mode.[495] The NaClO solution was freshly prepared and used in this test every 24 hours.

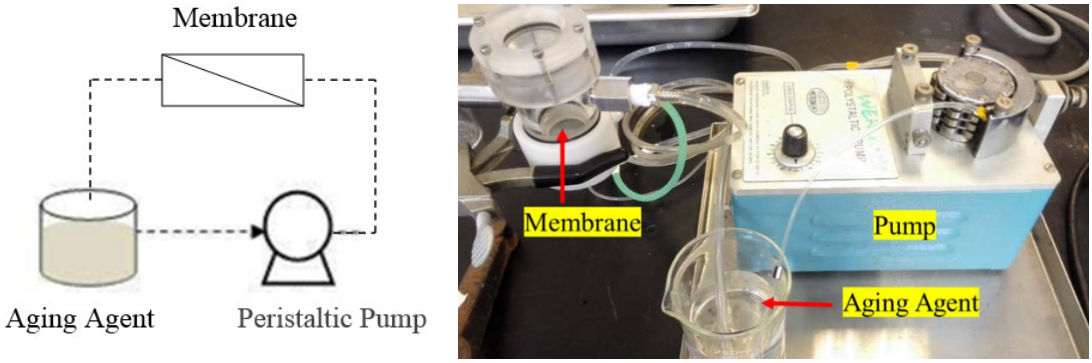

Figure 5.2 Experimental procedures for the dynamic chemical aging process.

5.2.2.3 Thermal Aging Tests. The thermal stability of these chemically modified membranes was examined by placing three identical pieces of membrane samples (2 cm × 2 cm) in an autoclave (Saniclave RS-SC-102, REVSCI, USA) with heating at 123 °C for

different hours (*i.e.*, 1 h, 2 h, 5 h and 10 h) and cooling for 40 min (Figure 5.3). After cooling, samples were thoroughly rinsed with DI water to remove any surface debris on the membrane and soaked in DI water for 24 h and then dried at room temperature in a desiccator for 24 h.

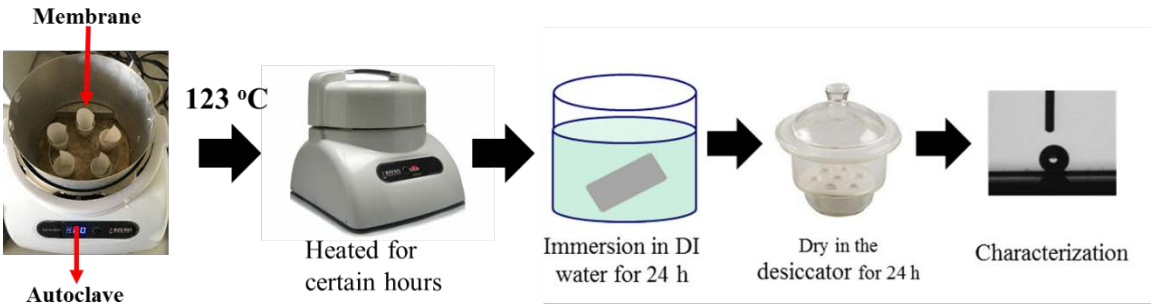

Figure 5.3 Schematics of the thermal aging process.

5.2.3 Characterization Techniques

A variety of characterizations were conducted to compare the changes of aged membranes as illustrated in Figure 5.4. According to many prior studies, it is imperative to study the changes in membrane properties such as surface morphology and pore geometry, surface hydrophilicity or charges that jointly influence membrane permeability and pollutant rejection.[222]

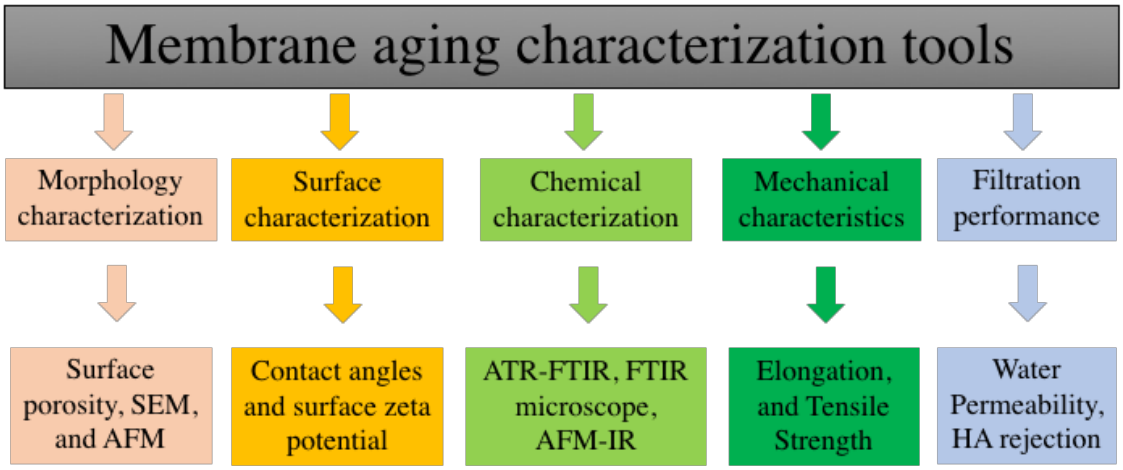

Figure 5.4 Membrane aging characterization tools used in this study.

5.2.3.1 Scanning Electron Microscope (SEM). The surface morphology of the membrane samples were examined by a Scanning Electron Microscope (SEM; JSM-5610LV, JEOL, Tokyo, Japan). These membrane samples were positioned on a metal holder, then sputter coated with 8-mm thick gold under vacuum. The micrographs of the membrane surfaces were taken at various magnifications and locations.[215]

5.2.3.2 Atomic Force Microscopy (AFM). Topography of membrane surfaces and Young's modulus were simultaneously acquired by a Bruker Dimension AFM using Peak Force quantitative nanomechanical analysis (PeakForce QNM) mode at room temperature. Images were acquired using ScanAsyst-air probes (silicon tips on silicon nitride lever, Bruker) at a scan rate of 1 Hz at a resolution of 256 pixels and 256 lines. The nominal spring constant of the cantilevers was 0.4 N m^{-1}. In all cases, the roughness and Young's modulus were measured repeatedly at three different scan areas with scan sizes: 5 μm × 5 μm and 10 μm × 10 μm. The first scan was always made at a large area (10 μm × 10 μm) and then zoomed into a small area (5 μm × 5 μm). Presented AFM topography images have been flattened with order 1 and analysed using the roughness analysis feature of Nanoscope Analysis 1.8. The RMS roughness (root-mean-squared roughness, R_q) was used to quantify the surface roughness.

Given that AFM images could be distorted by convolution between pore shape and cantilever tip shape and, the measurement of membrane pore size from AFM images is not always straightforward.[496] Moreover, the AFM mapping is often obtained on relatively small areas, which may not yield statistical representation of membrane pore geometry.[497] Thus, statistical analysis of morphological or pore size changes primarily relied on SEM images.

5.2.3.3 Contact Angle Measurements. To measure the water contact angle on membrane surface, a ~2.5μL drop of deionized water was placed onto the dried membrane surface with a 1 mL-syringe, and the air–water–surface contact angle was measured within 10s. At least three measurements of drops at different locations were averaged to obtain the mean and standard deviations of contact angles for one membrane sample.

5.2.3.4 Surface Zeta Potential for Membranes. The membrane surface charge was investigated by a surface zeta potential cell on the Zetasizer Nano instrument (Malvern Instrument, UK). The detailed procedure has been described elsewhere[498, 499] and in **Chapter 3 Section 3.2.3**.

5.2.3.4 ATR-FTIR Spectroscopy and FTIR Microscope. Attenuated Total Reflection Fourier Transform Infrared (ATR-FTIR) spectroscopy penetrates to greater depths (from <200 nm to >1 μm) depending on, among other factors, the incident wave number and the incident angle.[500] Although less quantitative than XPS, ATR-FTIR provides significant qualitative information about the types of functional groups. ATR-FTIR spectra and FTIR imaging were recorded on a FTIR spectrometer (Cary 660, Agilent Technologies, USA) coupled to an IR microscope (Agilent Cary 600). All spectra (64 scans at 4.0 cm^{-1} resolution and subtracted from the appropriate background spectra) were recorded at 25 ºC.

ATR-FTIR imaging has successfully been used to map the distribution of proteins and lipids in biological samples with a high spatial resolution.[501] Moreover, the ATR-FTIR imaging has also been used to determine the composition of the fouling layer on polypropylene (PP) and polytetrafluoroethylene (PTFE) membrane.[502] In our study, the ATR-FTIR imaging was obtained with a 64 by 64 pixels FPA detector. The Ge crystal in

the ATR accessory had a refractive index of 4 and numerical aperture 2.4. The depth of penetration was approximately 1.2 μm at 1000 cm^{-1} and the lateral resolution of 5 μm. Three 350 × 350 μm areas on each membrane were analyzed. The spectra were recorded with 64 scans and 4 cm^{-1} spectral resolution and analyzed in the range 950–4000 cm^{-1}.

5.2.3.5 AFM-IR. Nanoscale infrared analysis (AFM-IR) was performed on a NanoIR2 system (Anasys Instruments, Inc., Santa Barbara, CA, USA) operating with a top-down illumination. The detailed procedure has been reported by our prior study[503] and also in Chapter 2 Section 2.2.

5.2.3.6 Tensile Strength and Elongation. Tensile strength and elongation properties were analyzed for aged membranes, which were measured at the break of the prepared membranes using a Texture Analyzer (TA.XT2, Texture Technologies, Corp., New York) with a load cell of 1 kN at a constant elongation velocity of 5 mm min^{-1} at room temperature (20 ^{o}C). At least three sample fibers with 30 mm length and 10 mm width were tested and the average data was taken from each sample. Elongation at break (ε) was calculated from the experimental stress-strain curves.[215]

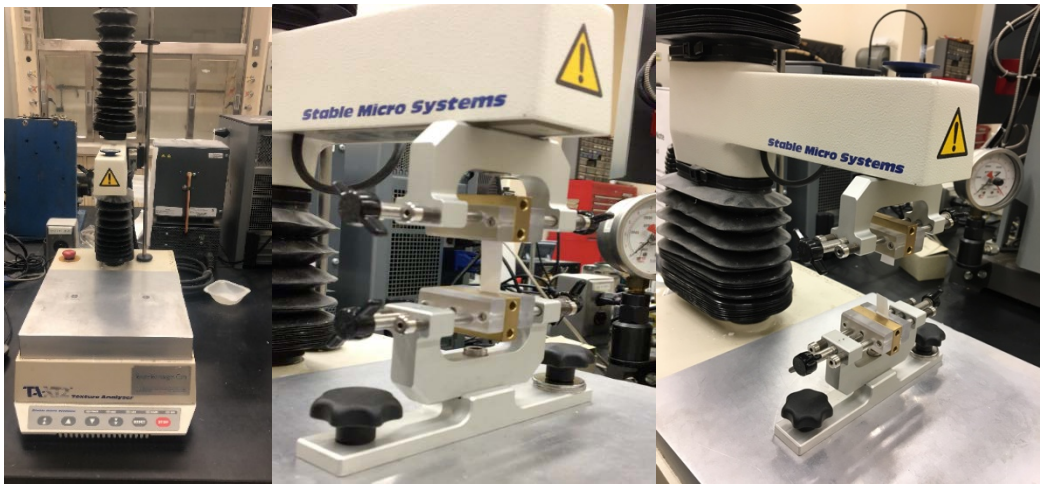

Figure 5.5 Tensile strength test on a Texture Analyzer.

5.2.3.7 Filtration Performances. A laboratory scale membrane module with a membrane surface are of 12 cm^2 was used to test the pure water permeability of pristine and aged membranes at controlled temperature of 20 ± 5 ^oC. To overcome the impact of membrane compaction, each tested module was first subjected to filtration of ultra-pure water at a maximum TMP of 0.14 MPa until pure water flux stabilized around 20 min. After membrane compaction, the TMP was operated ranging from 0.05 to 0.14 MPa to obtain the pure water flux. The pure water permeability at 20 ^oC in L h^{-1} m^{-2} kPa^{-1} was then taken as the slope of the linear regression between TMP and flux values according the Darcy law.[504] After dynamic aging (continuous filtration), pure water permeability was directly measured using the same filtration setup (Figure 5.3) by replacing the hypochlorite solution with DI water as the circulating feed solution.

Humic acid (HA), purchased from Sigma-Aldrich, was used as the model foulant in the rejection test for pristine and aged membranes. Fresh HA solution at a concentration of 5 mg L^{-1} was prepared by dissolving 5 mg HA in 1 L 0.1 M NaOH solution and filtered with 0.45 μm membranes (cellulose nitrate membrane filters, Whatman) to remove the insoluble particles. The molecular distribution of most HA substances was below the molecular weight cut-off (MWCO) of PES membranes. Membrane rejection was determined by assessing the removal rate of HA via membrane filtration. The HA concentration was measured on a UV spectrometer at 254 nm. The HA rejection ratio was calculated with the HA concentration in the permeate tank after 1 h filtration over the concentration in the feed.

5.2.3.8 Statistical Analysis. Statistical tests were used to determine if the characteristic changes on aged membranes were significantly different from those on the

pristine membranes. For the SEM images, at least three images at each magnification level of each membrane sample were obtained in randomly selected locations. Generally, the SEM images for all the membrane samples were all obtained by the same voltage and working distance conditions.

For the AFM topography images, at least three different regions of membrane surface were randomly selected, and the scanned areas were carried out over 5 μm × 5 μm, 2 μm × 2 μm, and 0.5 μm × 0.5 μm sample sections. Generally, the cantilever tips were regularly changed to avoid experimental artifacts and tip contamination. The force measurements within an AFM image were all completed by the same cantilever tip unless the reproducibility in force measurement became worse due to tip damage or contamination. The approach and retraction curves between the cantilever tip and the bare silicon wafer were always reproducible and thus easily averaged to check the status of cantilever tips. Finally, the reported roughness values for each membrane sample were averaged data from mean values from at least three AFM images, together with their standard deviations.

For the AFM-IR topography and IR mapping images, at least three different regions of membrane surface were randomly selected, and the scanned areas were carried out over 0.5 μm × 0.5 μm sample sections. At least three different locations were randomly selected to collect the spectrum on each IR mapping image. The modifier distribution area ratio on the IR mapping image was analyzed with ImageJ software and the results were presented with mean values ± standard deviation from at three IR mapping images. The same procedure was carried out for the IR amplitude ratio of characteristic bonds of modifier over the membrane matrix. For example, $I_{1736/1586}$ is the IR amplitude ratio of carbonyl

bond (hydrophobic modifier) at 1736 cm^{-1} over phenyl ring vibration band (backbone polymer PES) at 1586 cm^{-1}.

For the FTIR spectrum, at least three different samples were used for FTIR spectrum collection and one typical spectrum was selected for presentation. For FTIR imaging, at least three 350 × 350 μm areas on each membrane were analyzed and the spectra were recorded with 64 scans and 4 cm^{-1} spectral resolution and analyzed in the range 950–4000 cm^{-1}. The data was presented following the same procedure as described above for AFM-IR techniques.

5.2.4. Quantitative Structure-Activity Relationships (QSAR) for Water Permeability and HA Rejection by Membrane Aging Characteristics

To draw connections between the filtration performance of aged membranes and the aging descriptors, a QSAR model was developed using the multiple linear regression (MLR) model (fitlm function) in MATLAB.[505] The MLR model is a statistical technique that models the relationship between several explanatory variables and one response variables and predicts the level of effect of explanatory variables on the outcome of a response variable. The MLR assumes that each explanatory variable has a linear relationship with the response variable and creates a relationship that best approximates all the data points. In our study, a total of eight variables or descriptors were used as explanatory variables: surface porosity, S.P.; surface roughness, S.R.; surface hydrophobicity, S.H.; surface charge, S.C.; surface modifier spectrum intensity ratio, S.M.I.; tensile strength, T.S.; and elongation, EL.; and two variables were used as response/outcome variables: pure water permeability, P.W.P.; and HA rejection, HA.R. The data for each variable was obtained from previous sections and summarized together with the MATLAB codes and instructions of developing QSAR models detailed in Appendix.

5.3 Results and Discussions

5.3.1 Effects of the Aging Processes on Membrane Surface Porosity (Hydrophobic and Hydrophilic PES Membranes)

5.3.1.1 Chemical Aging. The pore structure of the pristine PES membranes was relatively homogeneous with the surface porosity of 35.0±0.2% for hydrophobic and 34.8±0.4% and hydrophilic membranes, as calculated from the SEM images with ImageJ software (Figure 5.6). After chemical aging treatment, apparent changes of pore structures were observed from the SEM images. For instance, after 2-day immersion in the NaClO solution, some polymeric fibers agglomerated due to degradation as pointed by the yellow arrows. Similarly, dynamic filtration with NaClO caused increased porosity from 35% to over 48% for hydrophobic membranes, indicating pore opening was one of the key changes to surface morphology of aged membranes. For the hydrophilic membranes, the SEM images in Figure 5.6b also revealed the same obvious damage to membrane morphology as visualized from the broken porous structures and fibrous debris. Figure 5.7 presents more zoom-out images of hydrophobic and hydrophilic membranes under two chemical aging modes, which further compares the destructive effects as discussed above.

Figure 5.8 plotted surface porosity versus the treatment times of two chemical aging modes. Clearly, surface porosity increased gradually with the exposure duration to NaClO agents. And the dynamnic filtraiton of NaClO solution yielded greater increase in porosity, which agrees with the SEM observitions of the apparent pore opening or perforation after dynamic filtration treatment.

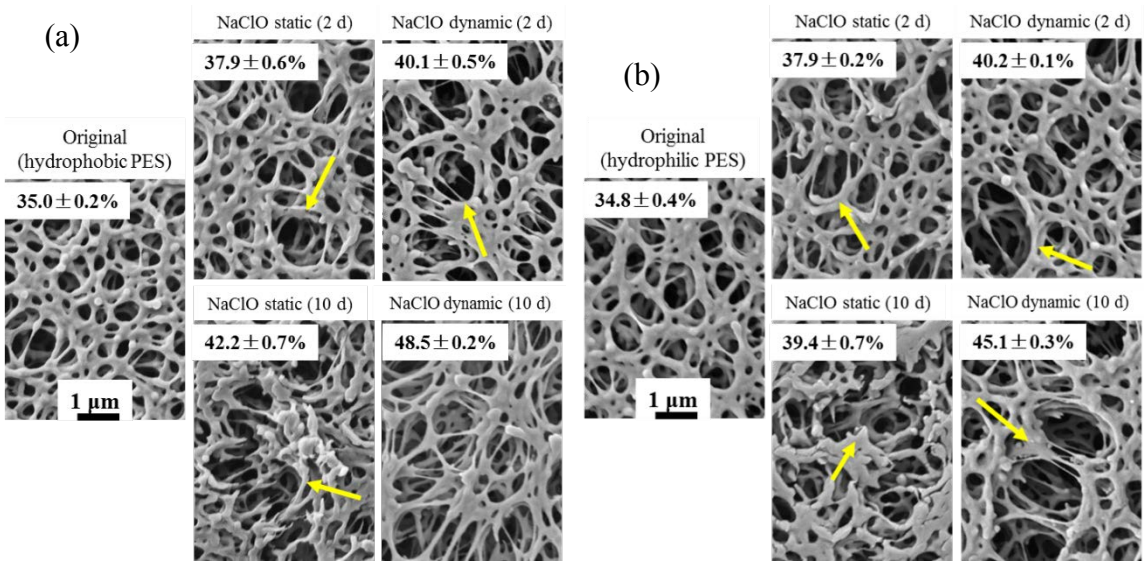

Figure 5.6 SEM image of (a) hydrophobic PES membrane and (b) hydrophilic membrane before and after chemical treatments.

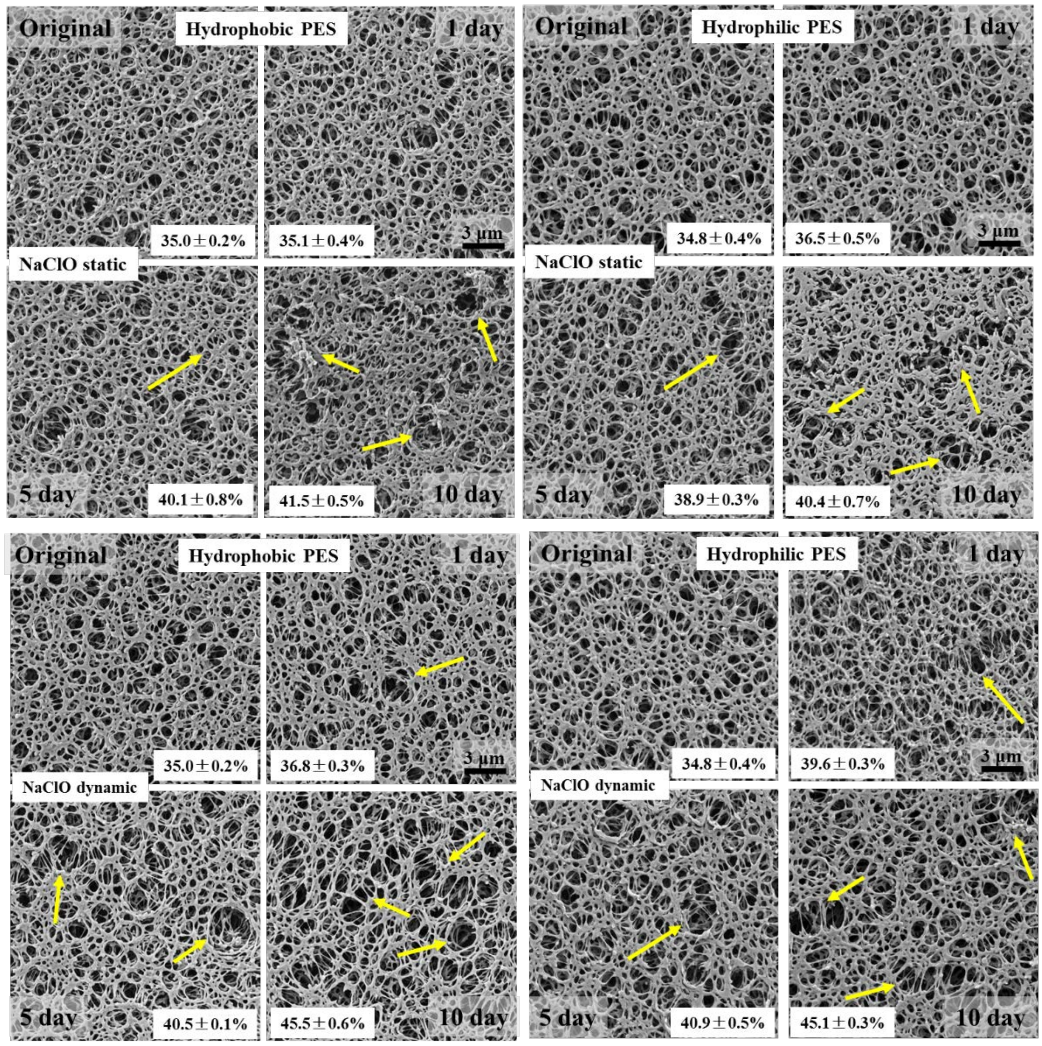

Figure 5.7 SEM micrographs of hydrophobic (left column) and hydrophilic (right column) membranes before and after static immersion and dynamic filtraion aging processes.

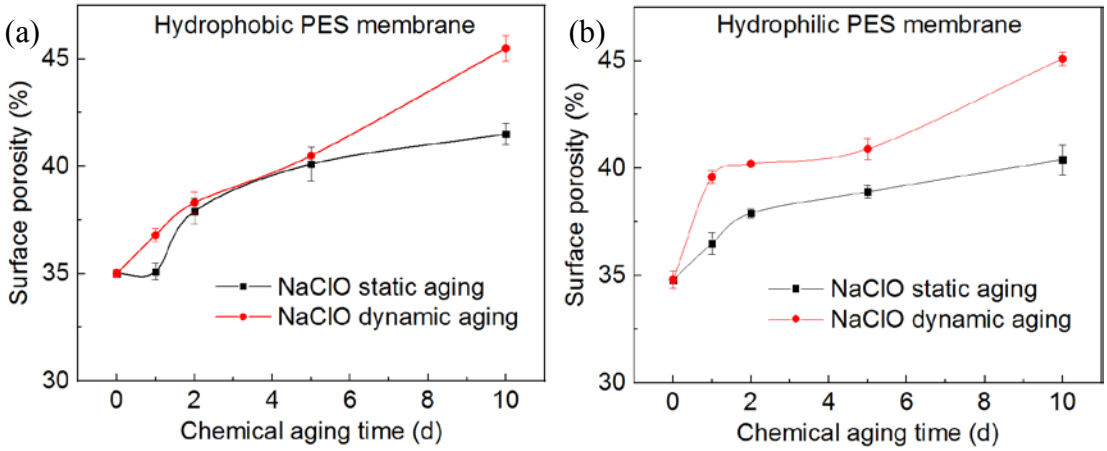

Figure 5.8 Surface porosity changes of (a) hydrophobic and (b) hydrophilic membranes in static immersion and dynamic filtraion processes.

5.3.1.2 Thermal Aging. Figure 5.9 and Figure 5.10 show that the surface porosity of both hydrophobic and hydrophilic PES membranes increased from 35% to 40%, respectively, after 10-h thermal treatment, with bigger pores appeared on the surface (see the yellow arrows). Besids, thermal aging at 123°C appeared to cause almost equivalent porosity increase for both hydrophobic and hydrophilic PES membranes and the porosity changed insignificantly after 2-day themal treatments (Figure 5.11). Thus, it is assumed that the porosity change might be attributed to the release of some loose residue left from the fabrication process but not by the degradation of PES or PVP polymers as during chemical aging process.

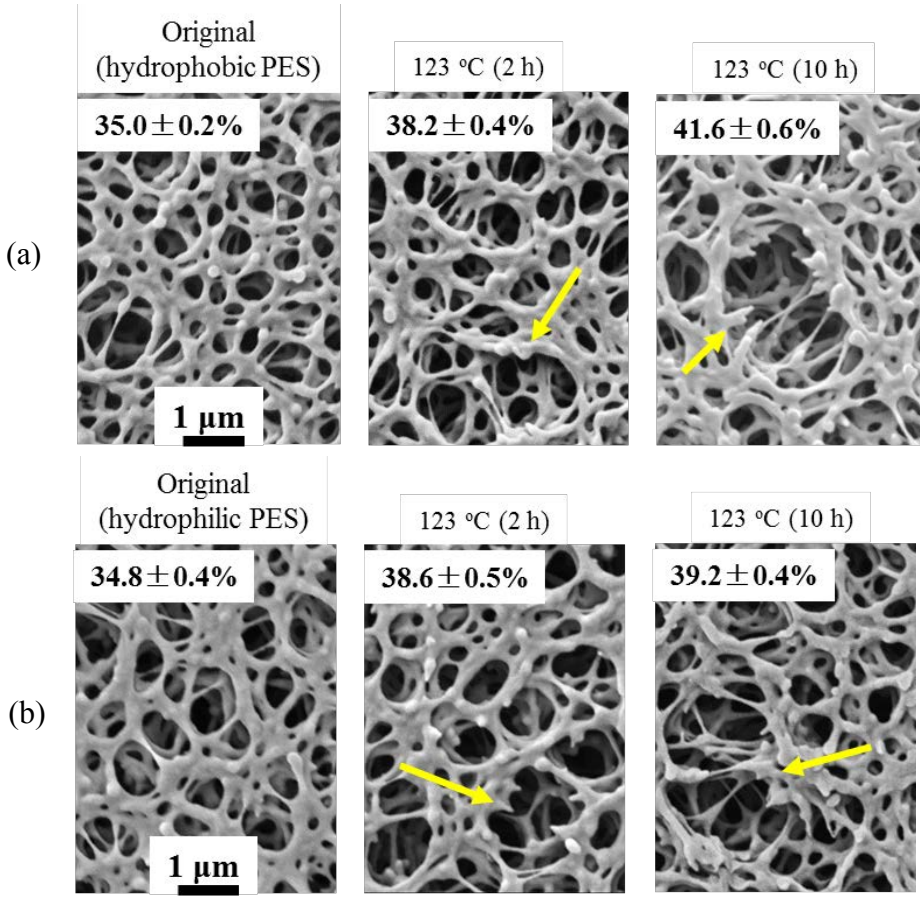

Figure 5.9 SEM image of (a) hydrophobic PES membrane and (b) hydrophilic membrane before and after thermal treatments.

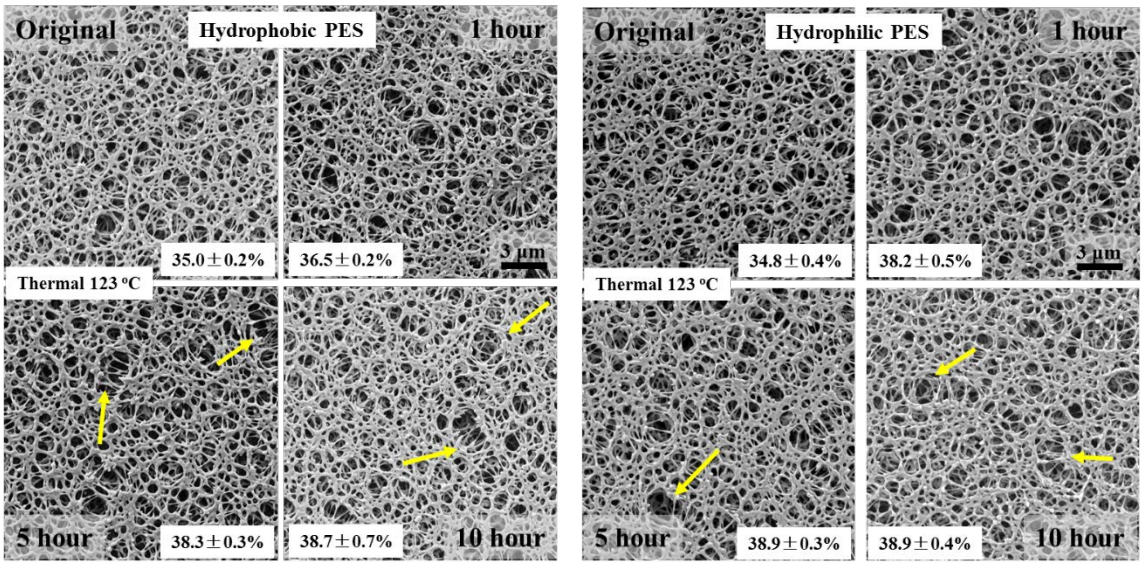

Figure 5.10 SEM micrographs of hydrophobic (left column) and hydrophilic (right column) membranes before and after thermal aging processes.

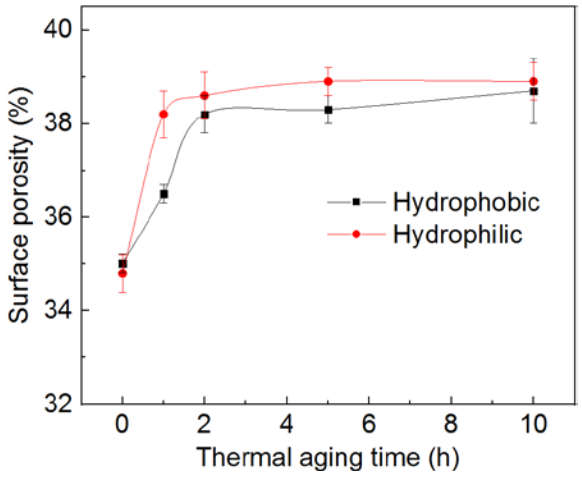

Figure 5.11 Surface porosity changes of hydrophobic and hydrophilic membranes during thermal aging processes.

5.3.2 Effects of the Aging Processes on Membrane Surface Roughness (Hydrophobic and Hydrophilic PES Membranes)

5.3.2.1 Chemical Aging. Figure 5.12 shows the AFM images of the hydrophobic and hydrophilic PES membranes before and after the aging processes. Different from SEM images, these AFM images were in fact three dimensional, which allows for the calculation of surface roughness, (RMS). Similar to what was observed on SEM images, hydrophobic

and hydrophilic membranes exhibited a homogeneous pore distribution with RMS roughness of 92 and 73 nm, respectively. After the aging with immersion in or filtration with the NaClO solution, there was an increase in roughness up to 130 nm, which is consistent with previous studies that found chemical aging treatment increased membrane roughness by 20%.[213] To statistically assess the changes in surface roughness, the scan size of AFM images was increased to 10 μm × 10 μm and the results are presented in Figure 5.13.

Figure 5.14 compares the changes of surface roughness for the hydrophobic and hydrophilic PES membranes before and after two different chemical aging processes. The roughness increased more significantly for the hydrophilic PES membranes, probably due to the release of PVP additives from the membrane surface. The error bars of the roughness calculated from three different AFM images for each membrane samples were higher after the aging treatment, probably due to the large variations of surface roughness that highly depends on the analyzed sample area.[213] Different from surface porosity changes, the hydrophobic and hydrophilic PES membranes generally had similar roughness increase and did not show strong dependence on the aging treatment modes. These membrane morphological changes are possibly connected with chemical characteristics and fingerprint changes as resolved by the FTIR analysis. Moreover, the ultimate impacts from these morphological properties permeability or water flux were also reported previously.[212]

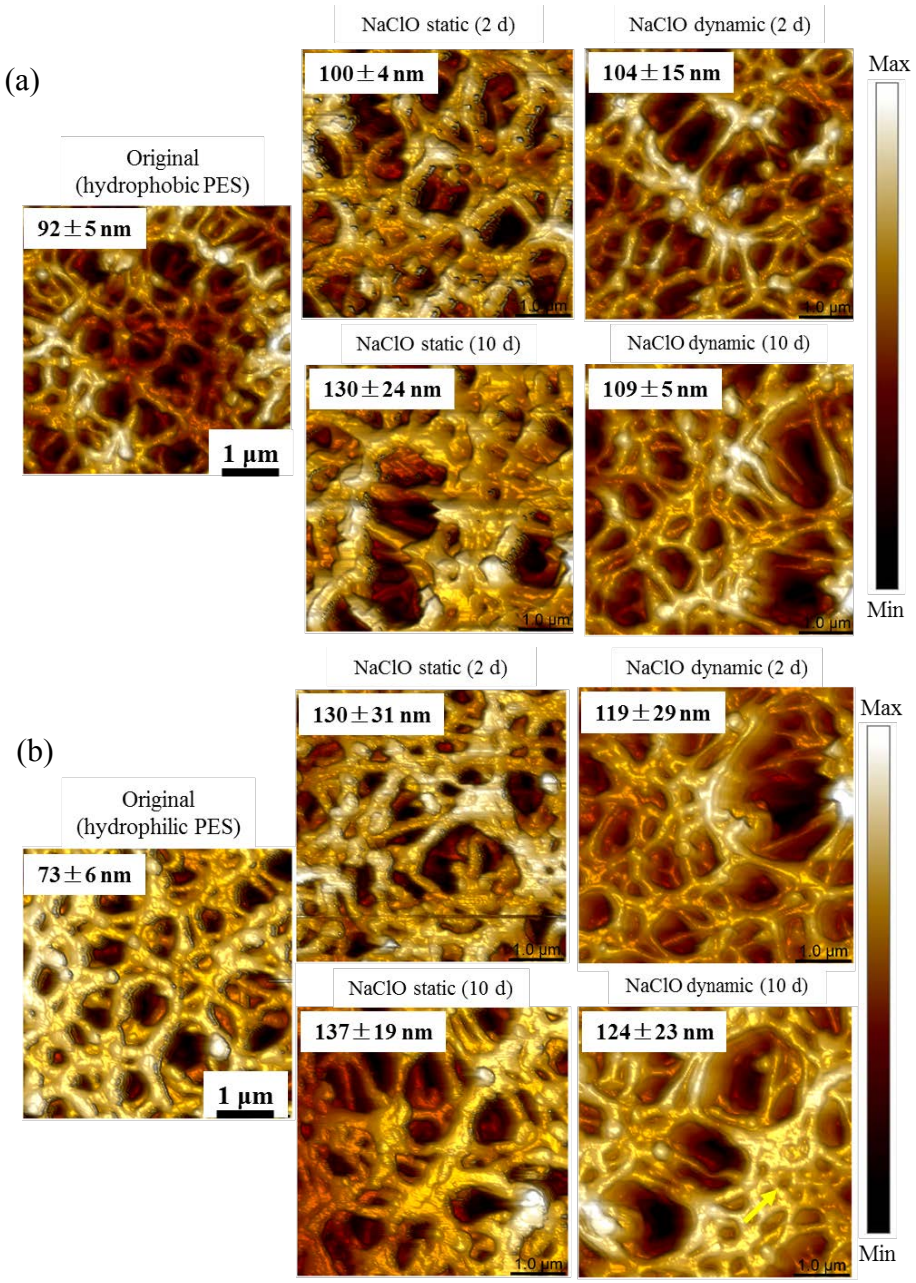

Figure 5.12 AFM topography images of hydrophobic (a) and hydrophilic (b) PES membranes before and after chemical treatments.

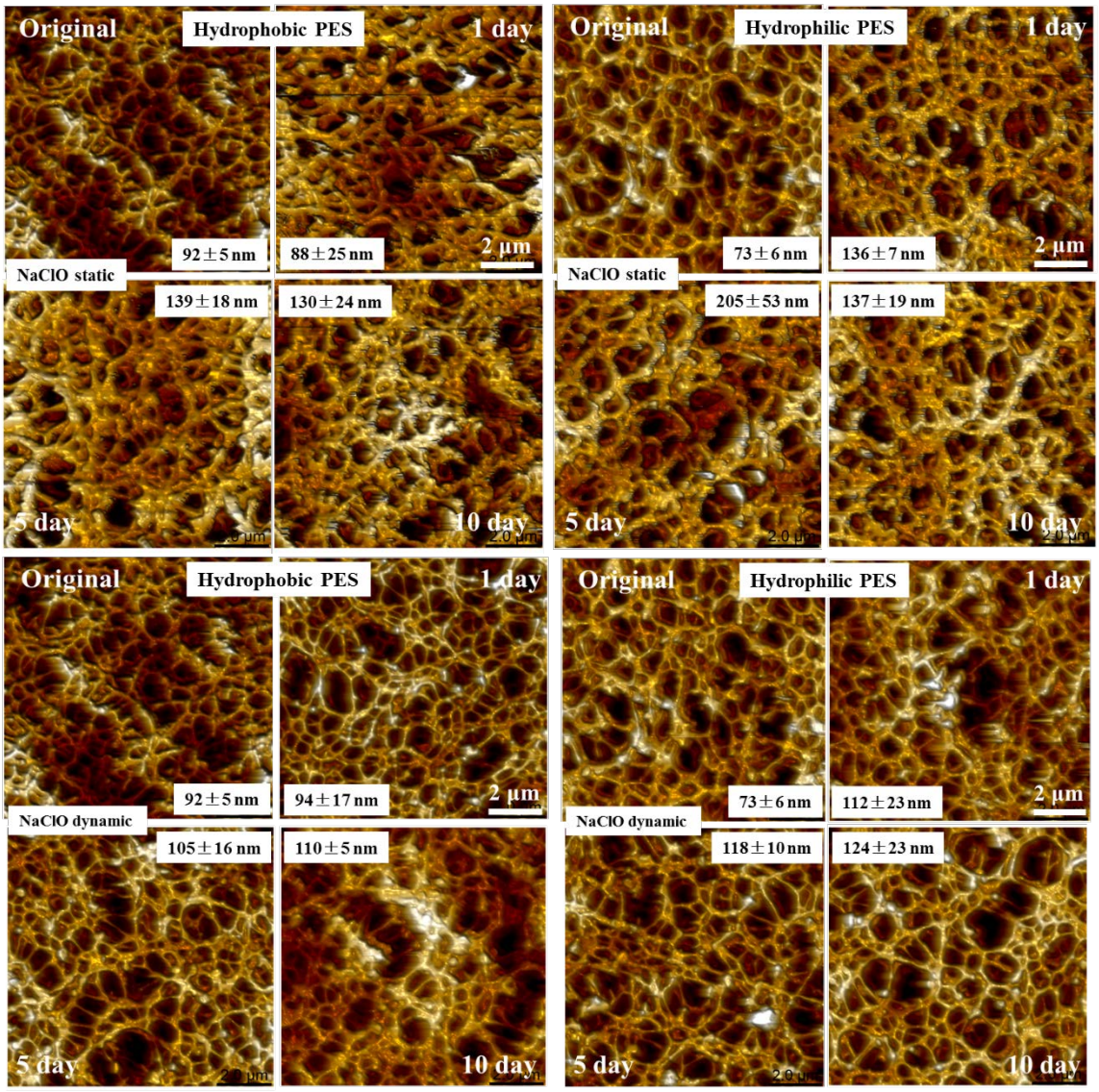

Figure 5.13 AFM images of the hydrophobic (left column) and hydrophilic (right column) membranes before and after the chemical aging. RMS roughness was calculated for the 10 μm × 10 μm scanned areas of the membranes.

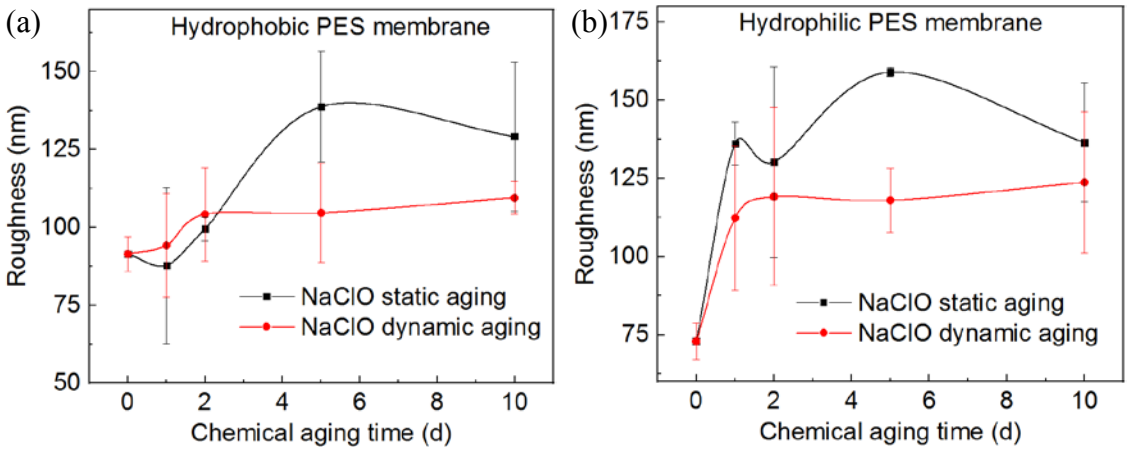

Figure 5.14 Surface roughness of (a) hydrophobic and (b) hydrophilic membranes before and after the aging under different exposure time and modes. RMS roughness was calculated for the 10 μm × 10 μm scanned areas of the membranes.

5.3.2.2 Thermal Aging. By contrast, the thermal aging under 123 ºC induced an increase in roughness up to 140 nm but the surface looks similar to the one in the original conditions. In Figure 5.15 and Figure 5.16, clearer and slightly bigger pores were observed after the thermal aging, which might induce the higher roughness. Both hydrophobic and hydrophilic membranes demonstrated a stabilization of roughness values and large error bars after 5-10 hour thermal aging (see Figure 5.17).

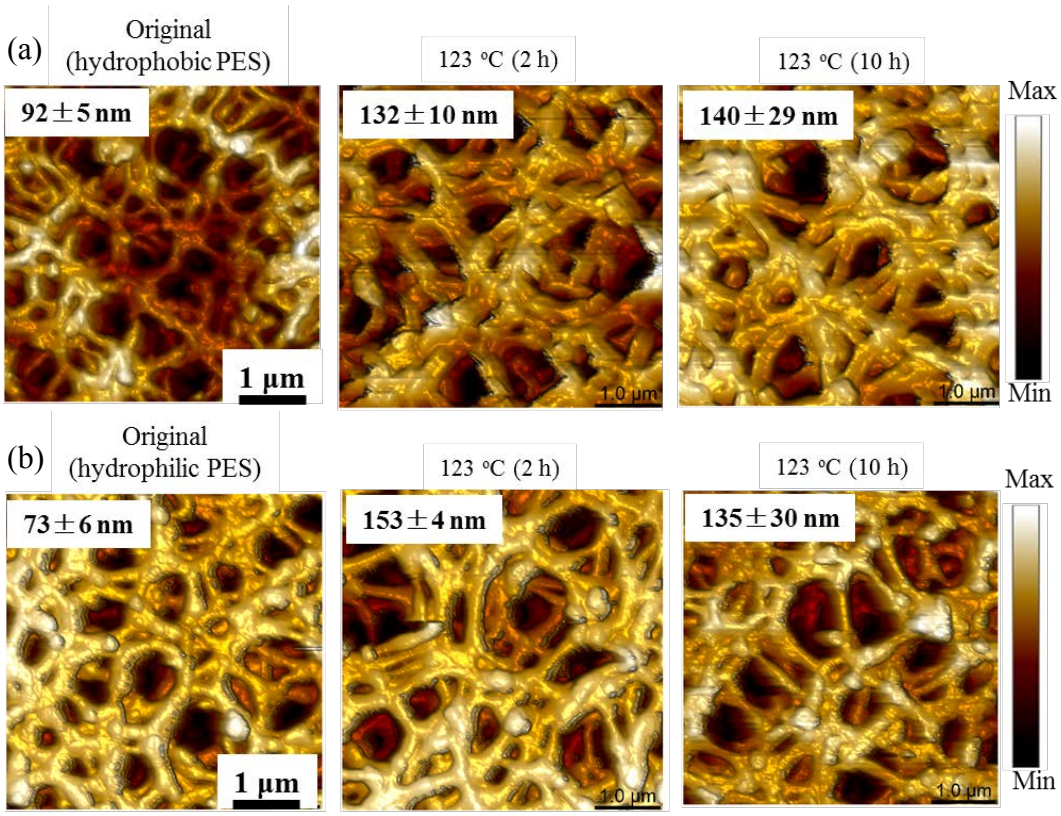

Figure 5.15 AFM topography images of (a) hydrophobic and (b) hydrophilic PES membranes before and after thermal treatments.

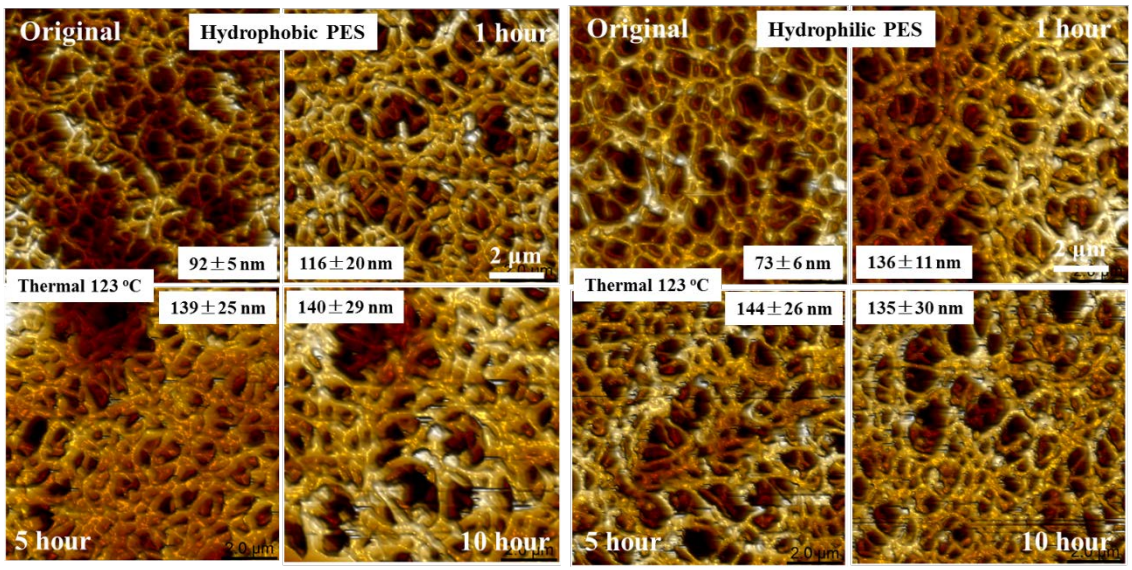

Figure 5.16 AFM images of the hydrophobic (left column) and hydrophilic (right column) membranes before and after the thermal aging. RMS roughness was calculated for the 10 µm × 10 µm scanned areas of the membranes.

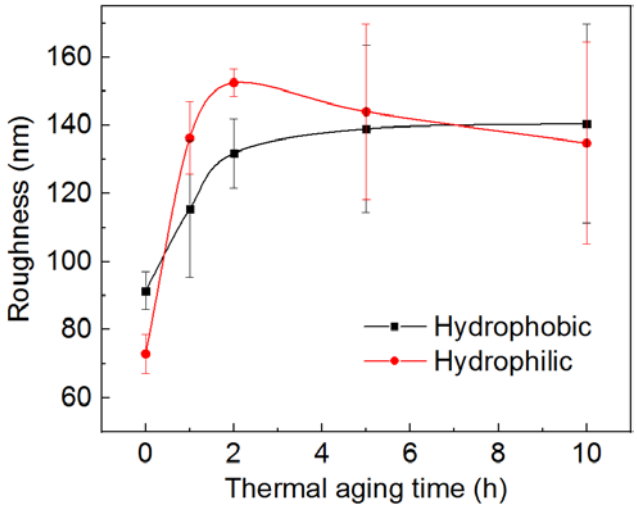

Figure 5.17 Surface roughness of hydrophobic and hydrophilic membranes before and after the thermal aging. RMS roughness was calculated for the 10 μm × 10 μm scanned areas of the membranes.

5.3.3 Effects of the Aging Processes on Surface Hydrophobicity

5.3.3.1 Chemical Aging.

a. Hydrophobic and Hydrophilic PES Membranes. Figure 5.18 compares the changes in surface hydrophobicity of hydrophobic and hydrophilic PES membranes after two different chemical aging treatments. For hydrophobic membranes, immersion in the NaClO solution caused the greater decline of CA than that from the dynamic filtration aging treatment. According to some previous works,[222, 469] under oxidative chemical attacks, the hydrophobic PES may undergo a chain scission of the backbone structure into sulfonic acid groups and phenyl chloride groups as illustrated in Figure 5.19.[469] The sulfonic acid was produced as a result of hydrolysis of sodium sulfonate. The sulfonic acid groups and phenyl chloride groups rendered the increasing hydrophilicity on the PES membranes. It is surprising that the dynamic filtration did not have the same impact as the immersion aging did. We suspected that under the influence of physical filtration pressures,

the surface structures of the hydrophobic PES membrane was damaged such as the pore size increase as shown in Figure 5.18a. The increased pores might result in the Cassie effect when measuring the water CA, where large void air pockets could exist on the membrane surface and repel water drops, which increases the measured values of water CA.[362]

However, for hydrophilic membranes, dynamic filtration of the NaClO solution caused the highest increase of CA among three aging treatments. Different from hydrophobic PES membranes that have no additives on the membrane surface, the PVP additives on the hydrophilic PES membrane surface are more vulnerable to the chemical oxidant attacks than the PES backbone. During the dynamic filtration aging process, the oxidant may permeate through membrane and oxidize PVP from the membrane surface. Compared to the static immersion, dynamic filtration results in faster removal of PVP because dynamic filtration of NaClO solution increased the oxidation rate of membrane materials as reported previously.[493]

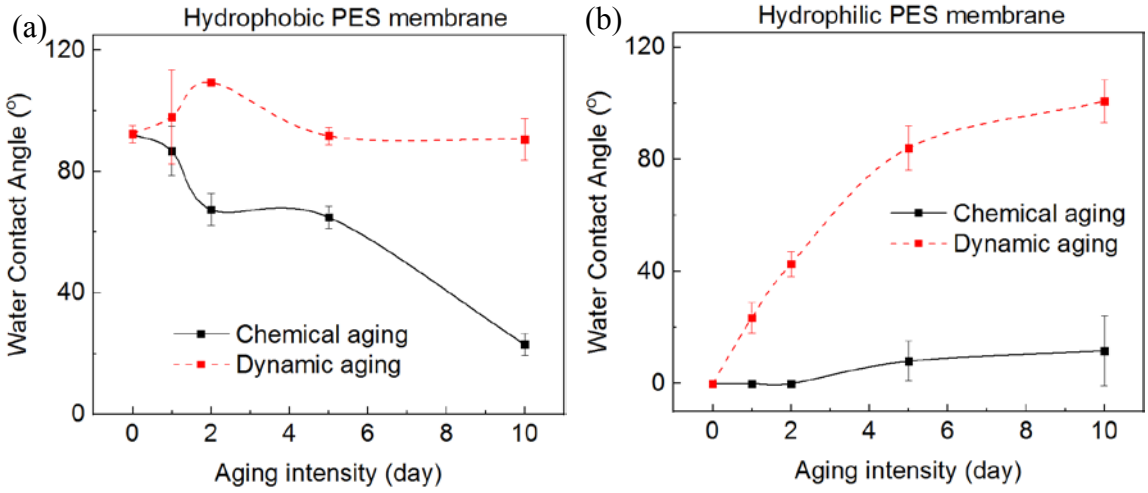

Figure 5.18 Membrane surface hydrophobicity evolution with different aging intensity: (a) hydrophobic PES membrane and (b) hydrophilic PES membranes.

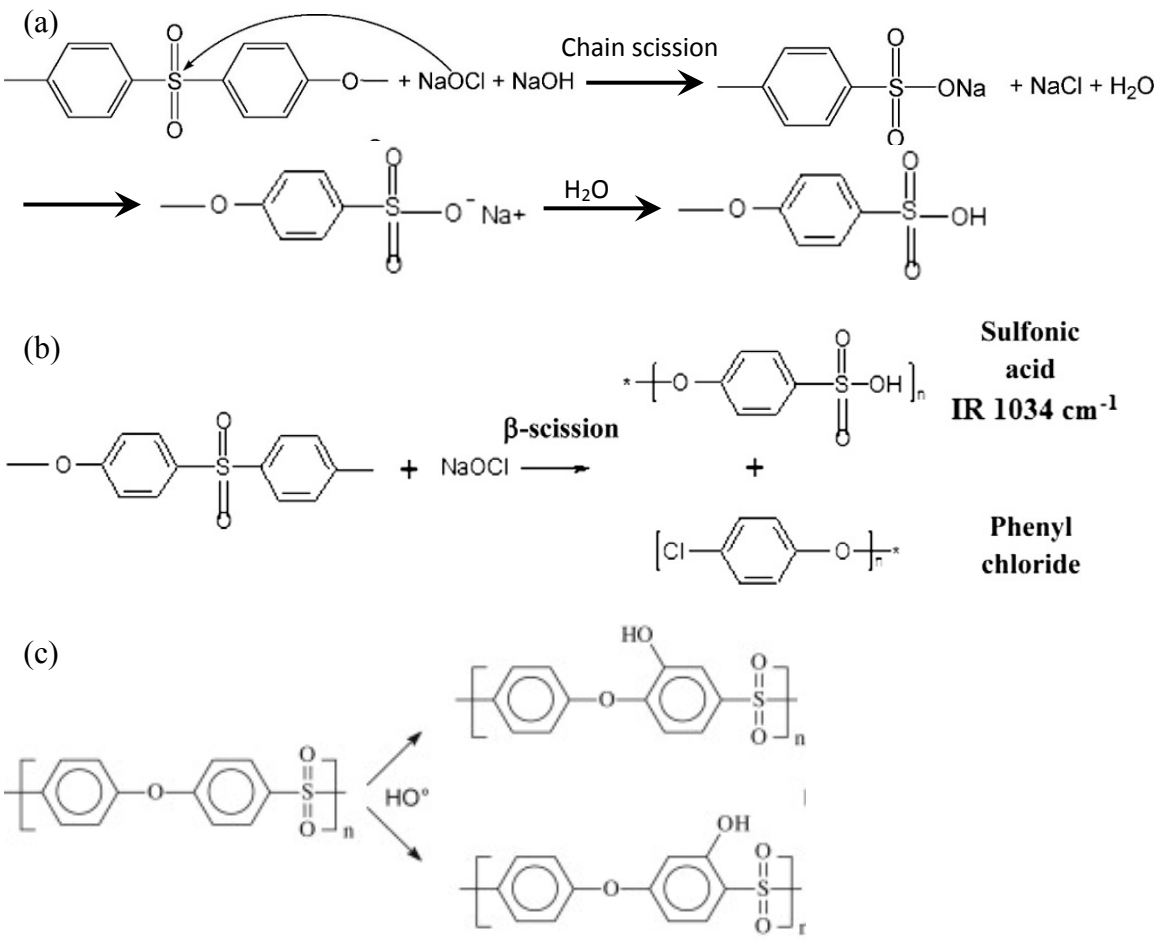

Figure 5.19 Three proposed PES degradation mechanisms: (a) the formation of sulfonic acid,[469, 506] the formation of sulfonic acid and phenyl chloride (b)[230] via chain scission and (c) radical-mediated degradation mechanism proposed by Prulho *et al*.[507]

b. Five Different Chemically Modified PES Membranes. The PES membranes with different chemical modifications exhibit different surface hydrophobicity as shown in Figure 5.20a. After the immersion chemical aging treatment, the hydrophobic PES membrane shifted to hydrophilic gradually (with the CA reducing from 90º to 25º). However, the super or double super hydrophobic PES membrane remained highly hydrophobic with slight decrease in CA (from 120º to 100º). By contrast, the hydrophilicity of the hydrophilic PES membrane did not have significant changes in CA. Pellegrin *et al*. also observed little changes in hydrophilicity for pristine PES/PVP membranes and those

aged ones after immersion in the NaClO solution.[484] Other studies indicated that the formation of charged groups such as COOH (carboxylic acid) or COO^- (carboxylate groups) derived from the PVP degradation[484] and ring opening[469] increased the hydrophilicity of aged PES/PVP membrane. Thus, the increased hydrophobicity on the aged hydrophilic membrane is not only ascribed to the formation of ionizable groups but also to the removal of the hydrophilic modifier (PVP) on membrane surface.

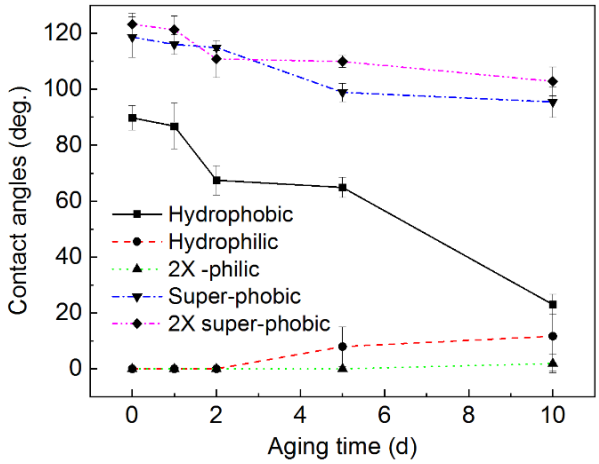

Figure 5.20 Hydrophobicity change measured by contact angle values for PES membranes (hydrophobic, hydrophilic, super hydrophobic, double-hydrophilic, and double-super hydrophobic, respectively) during (a) chemical and (b) thermal aging experiments.

5.3.3.2 Thermal Aging.

a. Hydrophobic and Hydrophilic PES Membranes. Since the PES backbone is thermally stable, as expected both the hydrophobic and hydrophilic PES membranes had negligible changes in hydrophobicity from the thermal treatment.

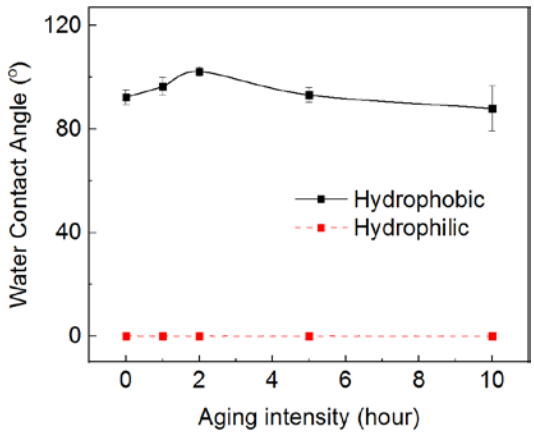

Figure 5.21 Membrane surface hydrophobicity evolution with different aging intensity.

b. Five Different Chemically Modified PES Membranes. Figure 5.22 shows the changes of surface hydrophobicity of various PES membranes were not significant after thermal aging, which is attributed to the high thermal stability of PES polymers.[508] The super-hydrophobic and double super-hydrophobic PES membranes had minor decrease in hydrophobicity after the thermal aging treatment, because the fluoro-alcohol additives on the PES membrane are thermally unstable and thus could be lost or degraded under thermal treatment.[509]

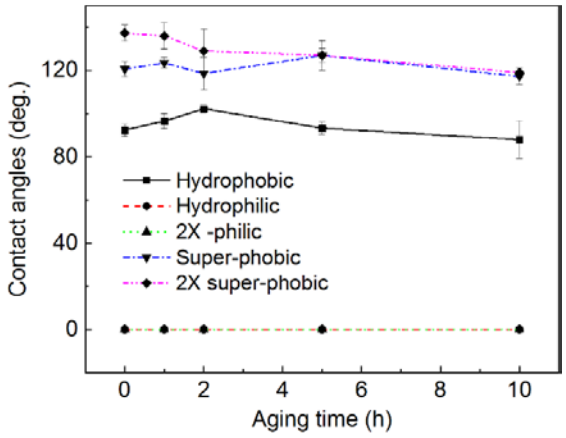

Figure 5.22 Hydrophobicity change measured by contact angle values for PES membranes (hydrophobic, hydrophilic, super hydrophobic, double-hydrophilic, and double-super hydrophobic, respectively) during thermal aging experiments.

5.3.4 Effects of the Aging Processes on Surface Charge (Hydrophobic and Hydrophilic PES Membranes)

5.3.4.1 Chemical Aging. The changes of surface functional groups on aged PES membranes are expected not only to change surface hydrophobicity but also surface charges. Figure 5.23 shows that for both hydrophobic and hydrophilic membranes, both chemical aging treatments rendered more negative surface charges as indicated by the surface zeta potential, which is probably owing to the formation of sulfonic acid and phenyl chloride groups on oxidized PES membranes as mentioned above[230] or the formation of carbonyl and carboxylate groups on oxidized PES.[510]

For the hydrophilic membrane, the increase of negative surface charges may be attributed to the ionization of weak acids groups due to the PVP degradation through a ring opening.[511] The FTIR data (Figure 5.25c) showed that most of the carbonyl group peak (1668 cm^{-1}) in the hydrophilic membranes disappeared due to the degradation of PVP. These surface charge changes on aged membranes likely influence filtration performances,[498, 499] which is discussed in the following section.

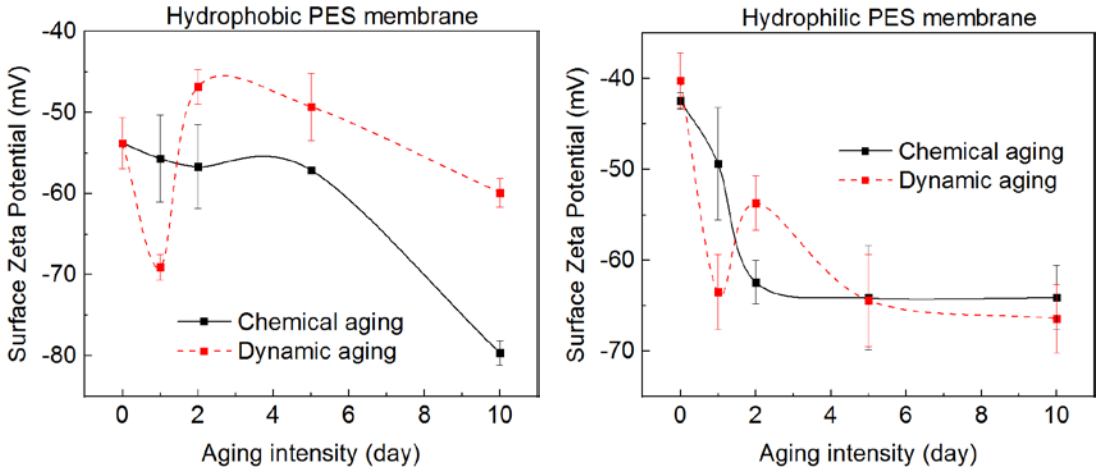

Figure 5.23 Membrane surface zeta potential evolution with different NaClO exposure intensity (4000 ppm): (a) hydrophobic PES membrane; (b) hydrophilic PES membranes. (pH=9, temperature = 25 ºC, ionic strength = 10 mM NaCl).

5.3.4.2 Thermal Aging. Figure 5.24 shows that for hydrophobic membranes, thermal aging treatments rendered less negative surface charges after 2-hour treatment while more negative surface charges after 5-hour and 10 hour treatments. While the hydrophilic membranes did not show much change on surface zeta potential after thermal treatment. This is in agreement with the discussion about surface porosity change after thermal aging that the change might be due to the release of residue left on the membrane surface during fabrication procedure instead of any chemical degradation.

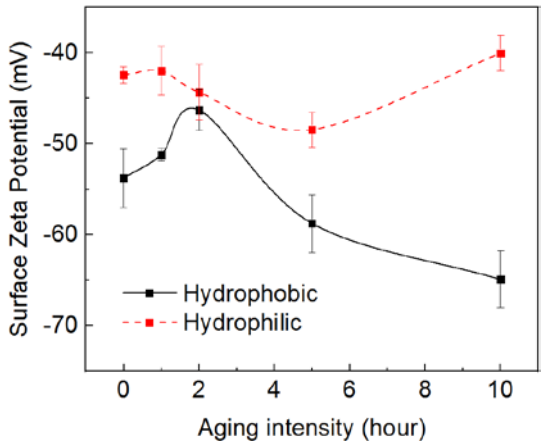

Figure 5.24 Membrane surface zeta potential evolution with different thermal aging intensity (123 ºC.

5.3.5 Effects of Different Aging Modes on Surface Functional Groups

5.3.5.1 Chemical Aging.

a. Hydrophobic and Hydrophilic PES Membranes. In this section, we compared the FTIR spectra evolution under different aging procedures with hydrophobic and hydrophilic PES membranes in Figure 5.25. It shows apparent changes in the characteristic peaks of PES and PVP after dynamic aging treatments. Compared to the NaClO static aging, the relative intensity decreased immediately after 1-day dynamic aging. For example, the peak at approximately 1660 cm^{-1} (assigned to C=O vibration of the PVP amide group

demonstrated significant decrease as compared to the pristine hydrophilic membrane. We believed that the peak representing carbonyl bond (C=O) is attributed by the additive PVP that is responsible for the hydrophilicity of the PES membranes. Therefore, the reduction in C=O peak intensity suggested a decline in hydrophilicity. This finding is in line with the contact angle measurement as the membrane was found to be more hydrophobic upon the dynamic aging process (Figure 5.14). This is further indicating that the chemical additive used to enhance the hydrophilic nature of the PES membranes may have been removed gradually during aging. Meanwhile, for the hydrophobic PES membranes, the characteristic band at 1240 cm^{-1} (assigned to C=O vibration of the PES backbone material) decreased gradually along with the dynamic aging duration. It is assumed that the dynamic aging might render the damage on PES material, which would be verified by the tensile tests in Section 5.3.6.

It is interesting to notice that a new peak around 1735 cm^{-1} (corresponding to the stretching vibration of carbonyl in ester groups, which is hydrophobic) was found on the aged hydrophilic membranes by dynamic aging. This new peak might from the succinimide groups (1700 cm^{-1}) formed by PVP degradation but shifted slightly.[511]

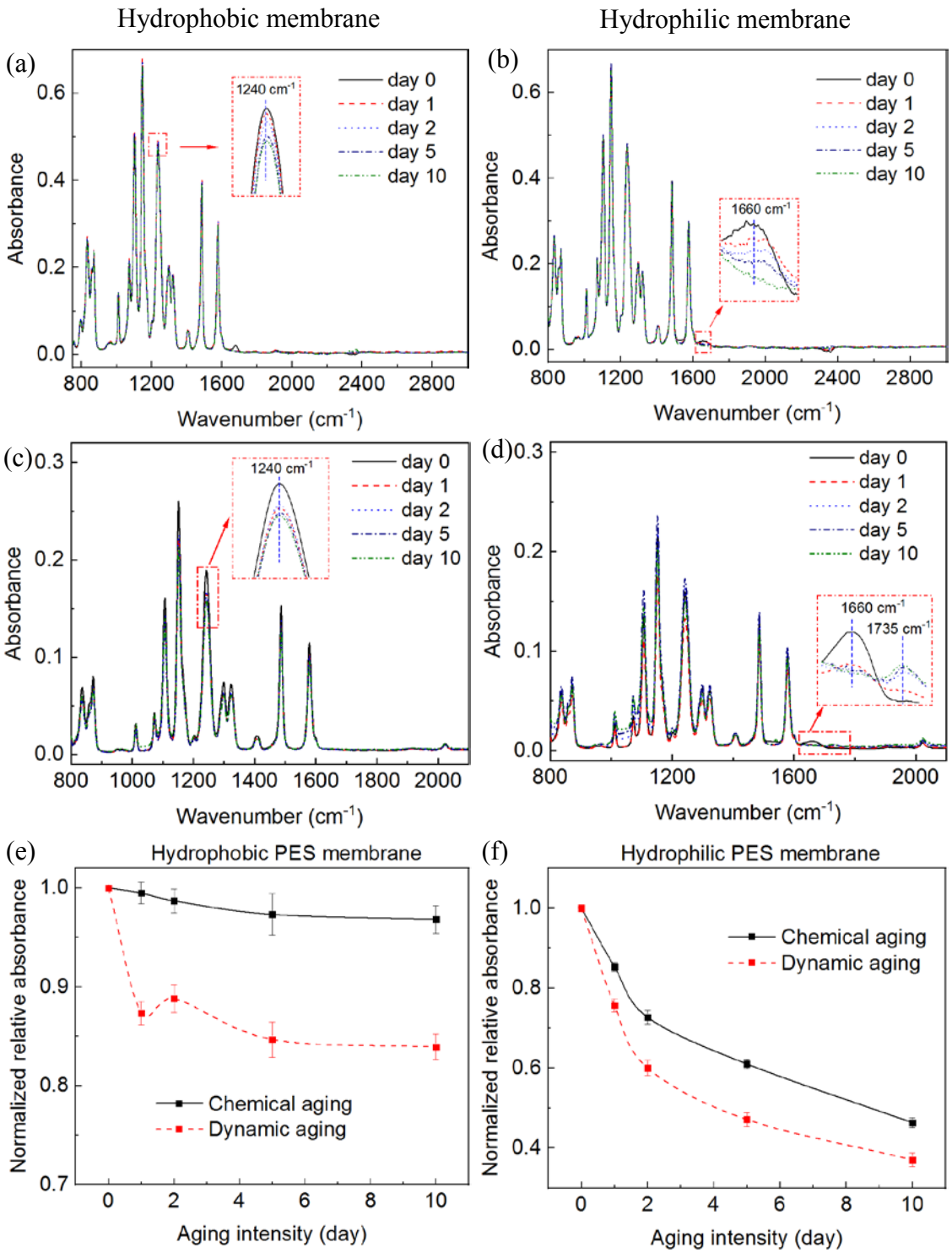

Figure 5.25 FTIR spectrum of dynamic NaClO treated hydrophobic PES membranes (left column) and hydrophilic PES membranes (right column); Normalized relative absorbance of the characteristic functional group bands measured on hydrophobic PES membranes (1240 cm^{-1}) and hydrophilic PES membranes (1660 cm^{-1}) aged under different chemical treatment modes.

b. Five Different Chemically Modified PES Membranes. The FTIR spectra of various membrane samples under chemical treatments (DI water immersion as a control) are depicted in Figure 5.26. There were no changes in both the peak heights and peak numbers, when the membranes were immersed in DI water only (spectra were same as the untreated samples). On the other hand, there were significant decreases in the peak intensities when sodium hypochlorite were used. It indicated that the chemical properties of the membrane surfaces deteriorated continuously as the absorbance of functional groups (*i.e.*, the height of peaks) decreased gradually, with an increase of the immersion duration in the sodium hypochlorite solution.

The pristine PES membrane had some characteristic stretching assignments related to aromatic bonds (1486 cm^{-1}) and to O=S=O symmetric stretching (1152 cm^{-1}).[341] Besides the assignments peaks of PES, PVP-modified membranes exhibited characteristic bands around 1668 cm^{-1} related to amide C=O stretching bonds in PVP.[342] And the higher PVP blend level on the PES membranes, the stronger signals found for the characteristic peaks at 1668 cm^{-1}. From Figure 5.20a, the characteristic bands of the PES functional groups were clearly observed in all the spectra, including absorption bands at 1323 cm^{-1} and 1297 cm^{-1} due to the SO_2 asymmetric stretching vibration and absorption band at 1151 cm^{-1} corresponding to the SO_2 symmetric stretching vibration. Aromatic bands at 1577 cm^{-1} and 1485 cm^{-1} and aromatic ether band at around 1240 cm^{-1} were also observed in the spectra. The obvious differences in the spectra of pristine and modified PES membranes were marked in the inserted figure.

The appearance of an absorption band at 1660 cm^{-1} was corresponding to the amide band from the hydrophilic modifier PVP. And it shows that the intensity of this peak was

higher in the double-modified hydrophilic PES membrane than the hydrophilic PES membrane. Another new absorption band at 1735 cm^{-1} corresponding to the stretching vibration of carbonyl in ester groups, which might be from the superhydrophobic modifier. Similarly, the absorption strength of the ester group showed a significant increase in the double modified superhydrophobic PES membrane. This indicated that the amount of ester groups coated onto the PES backbone after the second time of dip-coating into the modifier solutions.

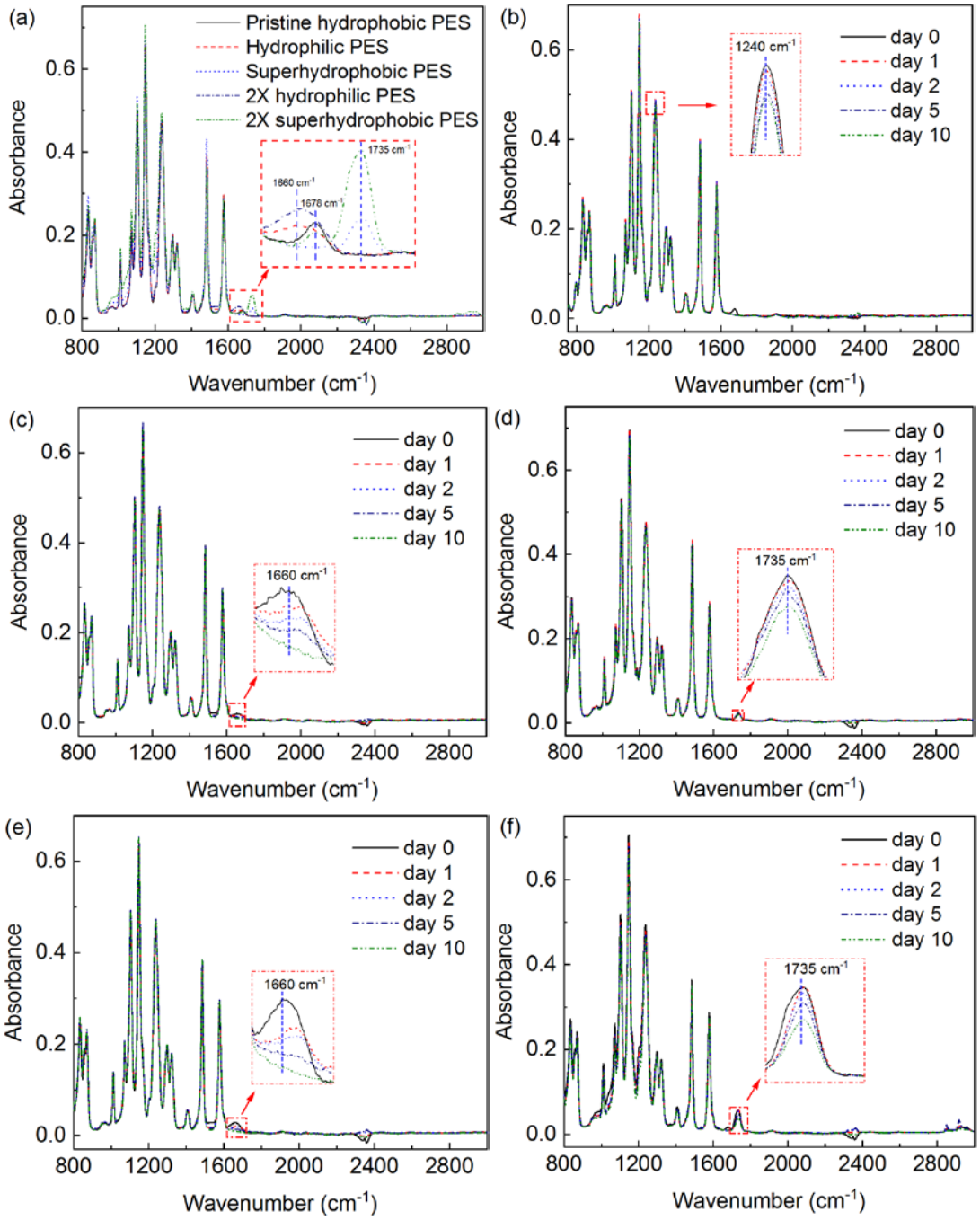

Figure 5.26 FTIR spectrum of untreated PES membranes (a) and sodium hypochlorite (4000 ppm, 45 ºC) treated PES membranes: (b) hydrophobic PES, (c) hydrophilic PES, (d) super hydrophobic PES, (e) double hydrophilic PES, and (f) double super hydrophobic PES.

These characteristic groups were recorded during the aging experiments. Figure 5.27 shows the relative absorbance of the amide band (1660 cm^{-1}), aromatic ether band

(1240 cm^{-1}) and carbonyl ester band (1735 cm^{-1}) decreased with an increase of the immersion duration in the sodium hypochlorite cleaning solution. It showed that the least relative absorbance change happened for the unmodified hydrophobic PES membrane, which indicated that PES material itself was chemical resistant. Meanwhile, the amide band in hydrophilic PES membranes and double modified hydrophilic PES membranes decreased to approximately 46% and 30% of its initial value after NaClO treatment, respectively. It demonstrates that PVP present in the membrane material was dislodged from PES matrix after the aging treatment. However, the absolute absorbance intensity at 1660 cm^{-1} for double modified hydrophilic PES membrane was still higher than the hydrophilic PES membrane. On the other hand, for the super hydrophobic PES membrane and double modified super hydrophobic PES membrane, the ester band at 1735 cm^{-1} decreased to 82% and 68%, respectively. It indicated that the detachment of those hydrophobic modifiers was not as severe as that of hydrophilic PES membranes.

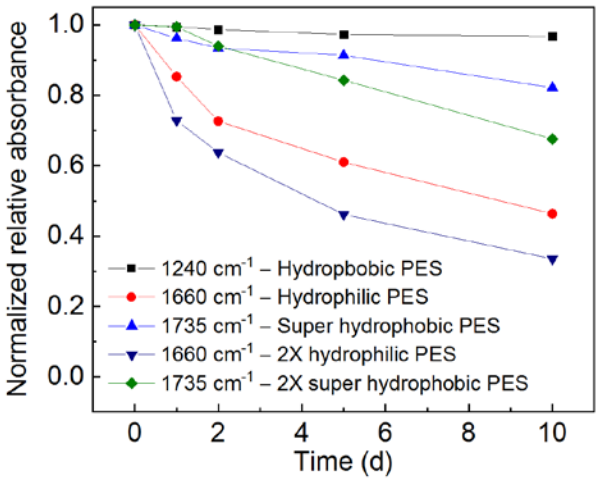

Figure 5.27 Normalized relative IR absorbance of the characteristic functional group bands measured on membrane exposed to sodium hypochlorite (4000 ppm, pH=9, 45 ^{o}C) at different immersion duration.

As shown in Figure 5.26c and Figure 5.26e, FTIR spectrum showed the appearance

of a band around 1700 cm^{-1} that can be attributed to succinimide groups,[511] formed by PVP radical attack from NaClO according to Figure 5.28 below. Indeed, Prulho *et al*. showed that hydroxyl radicals formed in bleach solution provoke PVP radical oxidation after a sufficiently long exposure time, leading to the formation of succinimide groups.[507]

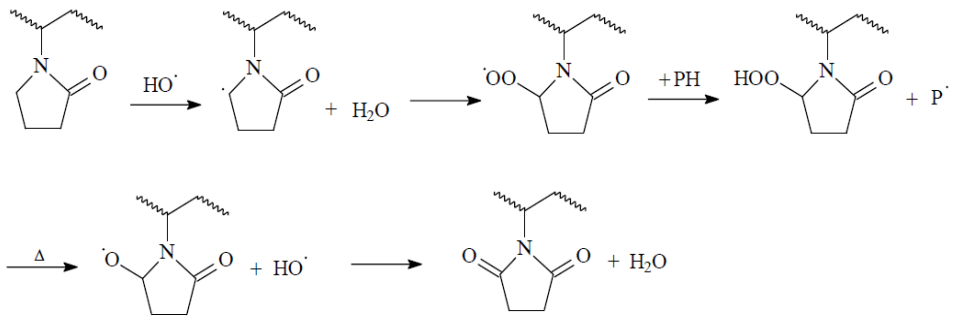

Figure 5.28 Succinimide formation mechanism by PVP radical attack.[507]

5.3.5.2 Thermal Aging.

a. Hydrophobic and Hydrophilic PES Membranes. As shown in Figure 5.29, no significant changes were observed for the hydrophobic PES membranes after thermal aging, indicating that PES material was thermal resistant. By contrast, hydrophilic PES membranes shows gradual decrease of functional group band signal with the increasing thermal aging time, indicating the release or dislodgement of PVP additives from the PES membrane surface.

We hypothesized the cross-linking process of PVP on PES matrix as well as the release processes of PVP from PES membrane surface through two different processes in Figure 5.30. The PES membranes was sulfonated[512] and dipped into the PVP solution to load the amide groups on the PES membrane surfaces. As shown in Figure 5.30a, PVP was assumed to be crosslinked onto sulfonated PES by hydrogen bonding. During the thermal aging treatment, the hydrogen bonding between PVP and PES might be broken and the

PVP released from the membrane surface (Figure 5.30b), inducing the decrease of IR absorbance for the amide group.

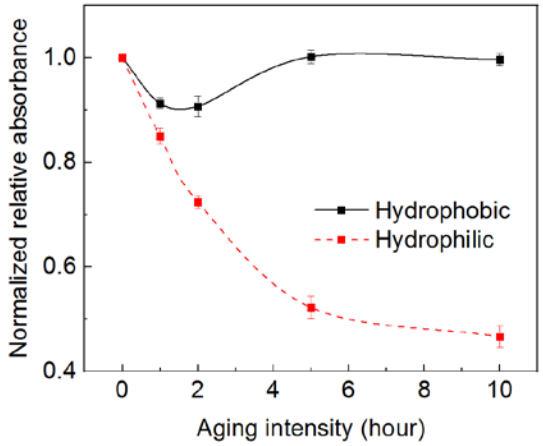

Figure 5.29 Normalized relative absorbance of the characteristic functional group bands measured on hydrophobic PES membranes (1240 cm^{-1}) and hydrophilic PES membranes (1660 cm^{-1}) aged thermally.

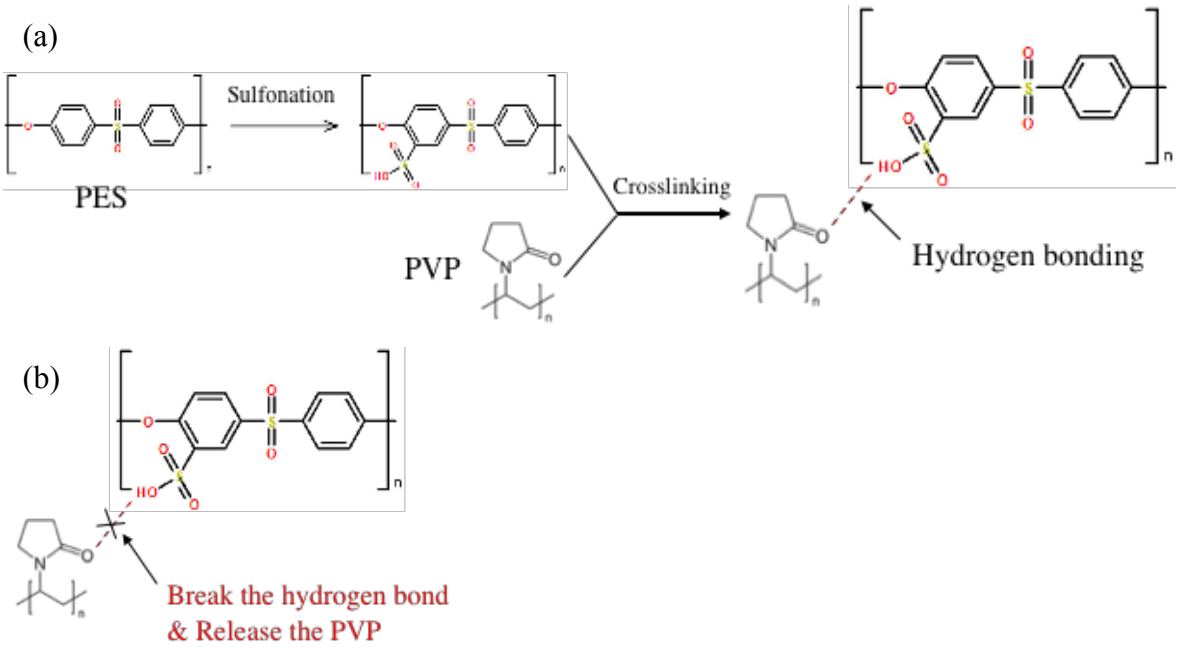

Figure 5.30 The hypothesized (a) cross-linking processes of hydrophilic membranes and (b) dislodgement process of PVP from PES matrix during thermal aging.

b. Five Different Chemically Modified PES Membranes. The thermos-stability of macromolecular additive in polymer membrane matrix was examined by being heated in

an autoclave (see Figure 5.2). The FTIR spectra of various membrane samples under thermal treatments are depicted in Figure 5.31. There were different levels of decreases in the peak intensities after the thermal aging treatment. It indicated that the chemical properties of the membrane surfaces deteriorated continuously as the absorbance of functional groups (*i.e.*, the height of peaks) decreased gradually, with an increase of the heating duration in the autoclaves. These characteristic groups were recorded during the aging experiments. Different from the chemical aging results, there was no new peaks around 1700 cm^{-1} (succinimide groups[511] formed by PVP degradation) were found, which indicated that the thermal aging might induced only physical detachment of PVP from PES matrix instead of chemically degradation. This is in line with the findings reported in the work of Hassouna *et al.*,[490] where the thermos-degradation results show that the PVP did not show any degradation.

Figure 5.32 shows the relative absorbance of the amide band (1660 cm^{-1}), and carbonyl ester band (1735 cm^{-1}) decreased with an increase of the heating duration in the autoclave at 123 ^{o}C. It showed that the least relative absorbance change happened for the unmodified hydrophobic PES membrane, which indicated that PES material itself was thermal resistant. Meanwhile, the amide band in hydrophilic PES membranes decreased seriously after 10-hour thermal treating while the absorbance of double-hydrophilic membrane only decreased to 50% of its initial value. It demonstrates that PVP present in the membrane material was dislodged from PES matrix after the thermal aging treatment. However, the absolute absorbance intensity at 1660 cm^{-1} for double modified hydrophilic PES membrane was still higher than the hydrophilic PES membrane. On the other hand, for the super hydrophobic PES membrane and double modified super hydrophobic PES

membrane, the ester band at 1735 cm^{-1} decreased to 10% and 40%, respectively. It indicated that the detachment of those hydrophobic modifiers was as severe as that of hydrophilic PES membranes.

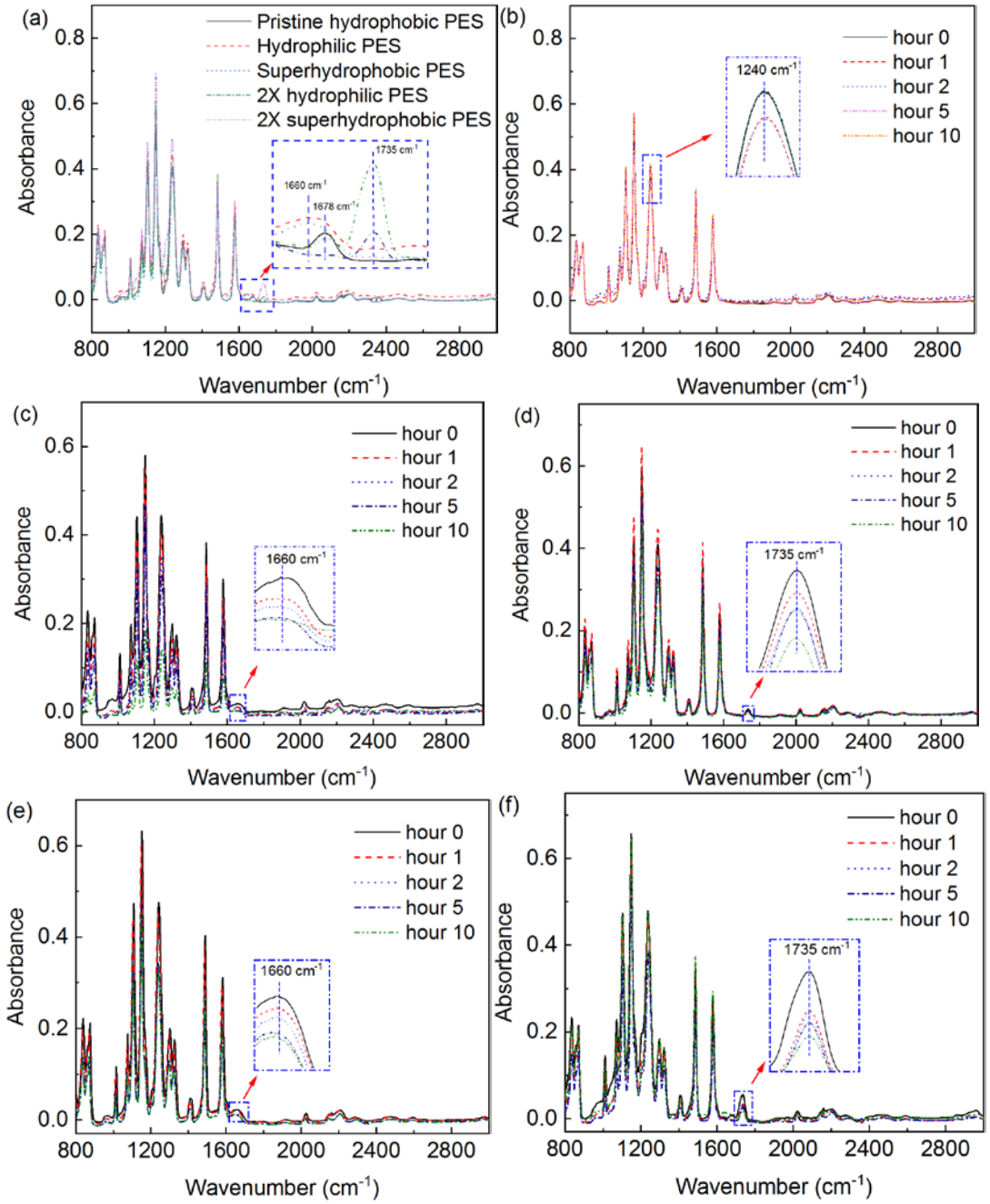

Figure 5.31 FTIR spectrum of untreated PES membranes (a) and thermally aged (123 ºC) PES membranes: (b) hydrophobic PES, (c) hydrophilic PES, (d) super hydrophobic PES, (e) double hydrophilic PES, and (f) double super hydrophobic PES.

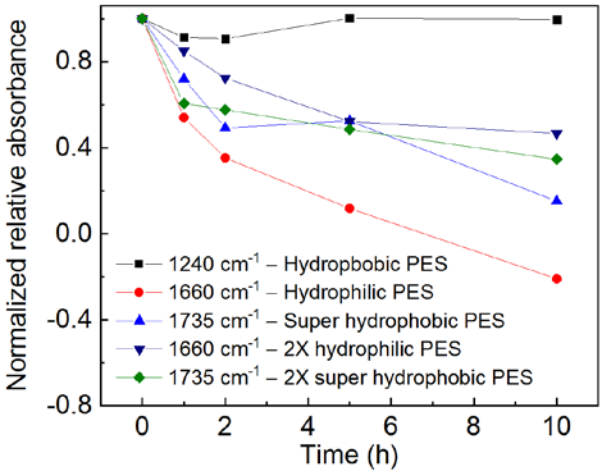

Figure 5.32 Normalized relative absorbance of the characteristic functional group bands measured on membrane exposed to high temperature (123 ºC) at different treatment duration.

5.3.6 Analysis of Aging Mechanisms

5.3.6.1 Chemical Aging. The degradation mechanisms of PES/PVP membranes have been analyzed or proposed in previous studies as summarized in Table 5.2.[513] Typically, four kinds of mechanisms were proposed: (1) The formation of sodium sulfonate from the chain scission at the sulfone groups of the PES as shown in Figure 5.19c.[506] The sodium sulfonate hydrolyses with water and become sulfonic acid end-groups. HClO could further attack the C-S bond and convert the SO_2 groups into SO_3 groups. The second mechanism is that the chain scission of the PES backbone resulted in the formation of sulfonic acid groups and phenyl chloride groups as shown in Figure 5.19b as proposed by Yadav *et al*.[230] The third degradation mechanism (Figure 5.19c) indicated that the radical oxidation of the aromatic rings of PES and later sulfonic acid groups led to the generation of phenol groups as proposed by Prulho *et al*.[507]

PVP was most frequently used as hydrophilic additive that can influence membrane filtration properties. PVP is a polymer soluble in water and it has the polar amid group

which gives it hydrophilic properties. The degradation mechanisms of PVP degradation related to the filtration membranes:

(1) An opening mechanism of PVP cycle under the action of hypochlorite ion in alkaline medium was proposed by Roesink *et al*.[514] As shown in Figure 5.33a, the breaking chains of PVP was resulted from a macroradical rearrangement induced by hydroxyl radicals. The ring opening of the PVP component is typically accompanied by the formation of carboxylic acid groups.

(2) Chain scission of PVP under the action of hydroxyl radicals in acid medium was proposal by Roesink *et al*. as well.[514] Smaller PVP chains and non-cyclic imide groups were formed.

(3) PVP β-scission with NaClO was proposed by Hassouna *et al*. through two ways (see Figure 5.34).[490] Oxidation involving secondary carbon leads to oxidation products of the pyrrolidone nucleus with some cyclic imides with no chain scission. Oxidation on tertiary carbon leads to non-cyclic imids and unsaturated products with macromolecular chain scission.

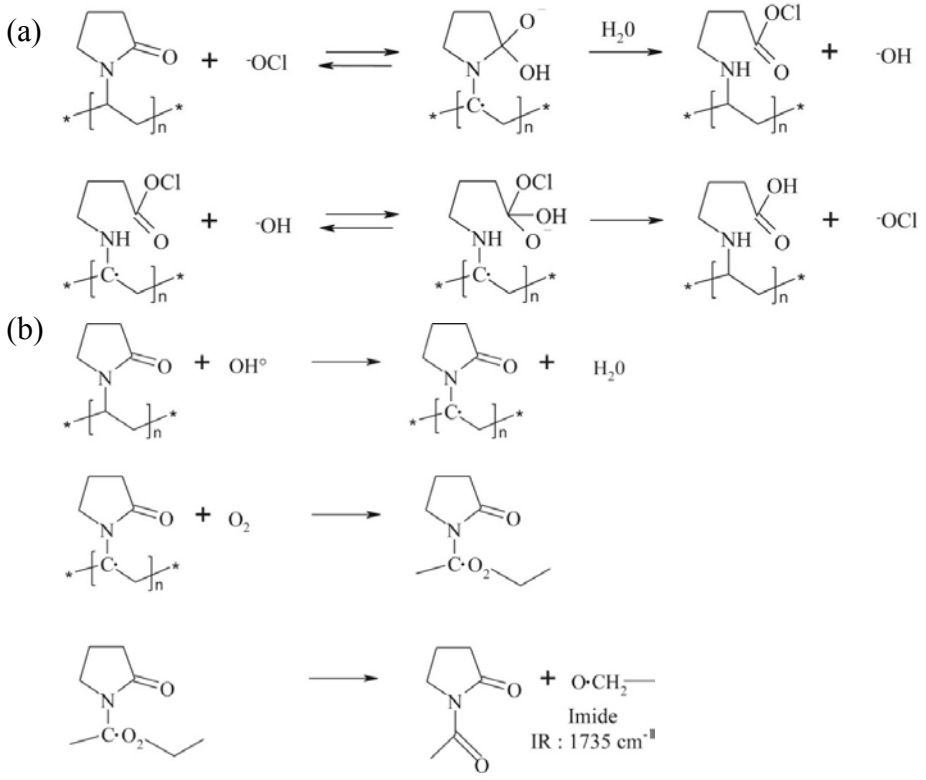

Figure 5.33 PVP degradation mechanism by NaClO in (a) alkaline condition and (b) acidic condition proposed by Roesink *et al*.[514]

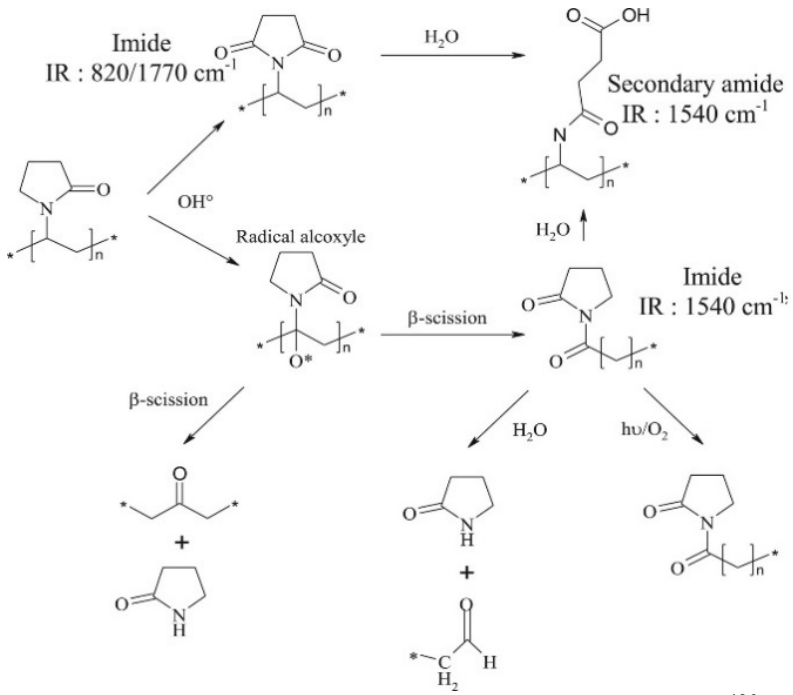

Figure 5.34 PVP degradation mechanism proposed by Hassouna *et al*.[490]

It is difficult to compare these previous studies because the experiments were not performed under identical conditions. Especially, the pH of NaClO solution was not consistent. Particularly, HClO and ClO^- components predominant under different pH of the NaClO solution: pH 6.0 (HClO predominance), 8.0 (coexistence of HClO and ClO^-) and 11.5 (ClO^- predominance) as shown in Figure 5.35.[515] Hanafi *et al*. concluded HClO and ·OH to be the responsible species for PES chain-scission and HClO was identified to have a greater impact than that of the free radicals.[511]

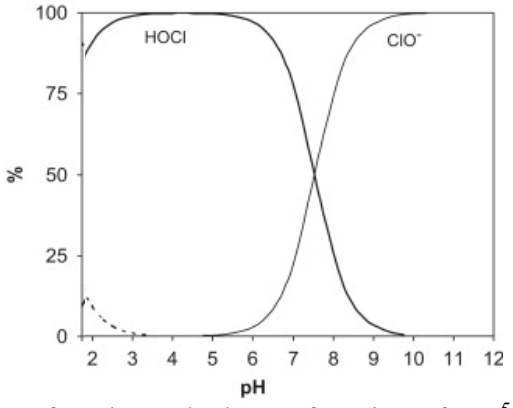

Figure 5.35 Concentration of HClO and ClO^- as function of pH.[515]

5.3.6.2 Thermal Aging. PES was analyzed under the pyrolysis temperatures from 500 °C to 700 °C.[516] It was indicated that phenol as a pyrolysis product is preferentially generated over SO_2 during the pyrolysis. In our study, the thermal aging was operated under 123 °C, where the pyrolysis process might not happen.

It was found that the vinyl pyrrolidone is the main volatile products of the thermal degradation of PVP under the temperature at more than 395 ^oC.[517] That is to say, the predominant mechanism during thermal degradation of this polymer is the depolymerization to monomer of the polymeric main chain. However, it was also evident that simultaneous reactions may be involved yielding oligomers: Peniche *et al*. concluded

that the obtained spectra strongly suggest the formation of pyrrolidone as the main product of the thermal degradation of PVP.[518] In contrast, Bianco *et al*. claimed that the very intense absorption band at 1748 cm^{-1} was apparently associated with ester formation as consequence of the scission of the N–C=O bond.[519]

Nevertheless, Loria-Bastarrachea *et al*. performed thermal degradation of PVP using a Perkin Elmer Thermogravimetry coupled with Fourier Transform Infrared Spectroscopy (TG/FTIR) system under high temperatures from 50 to 600 ºC. The results showed that PVP exhibited only one mass loss which started at 395 ºC and its maximum rate decomposition temperature was located at 480 ºC.[517] It indicated that thermal decomposition might not happen in our study, where the temperature was set at no more than 123 ºC.

Table 5.2 Summary of Previous Works on Degradation of PES/PVP Membranes by NaClO.[513]

Membrane materials	NaClO conc.	pH	Characterization tools	Main findings	Refs.
PES	0.4 wt%	9 and 11.5	SEM-DEX and ATR-FTIR	• Breakage of C-S bond, Cl-S bond formation • PES degradation	Begoin *et al.*[232]
PES	/	8	IR, SEC, and tensile tests	• PES degradation • Chain scissions localized at the sulfone group	Thominette *et al.*[506]
PES	150 ppm	7.2	XPS, ATR-FTIR, AFM	• Chain scission of the PES polymer (formation of phenyl sulfonate). • Decrease in mechanical strengths of the membranes and loss in membrane integrity	Arkhangelsky *et al.*[469]
PES	700 ppm	9 and 12	ATR-FTIR, SEM, TGA, and XPS	• Surface pitting and cracking was observed • Chain scission of the PES polymeric backbone into two parts (terminated by a sulfonic acid group and a phenyl chloride group)	Yadav *et al.*[230]
PES	700 ppm	9, 10, 11 and 12	Water flux, proteins rejection and SEC	• Scission and pitting of PES polymer • Increased water flux and reduced protein rejection	Yadav *et al.*[483]
PES & PES/PVP	3000 ppm	3.6, 6.9 and 11.5	NMR, IR and GPC	• Decrease in molecular weight of PVP • PES resistant to NaOCl treatment	Wienk *et al.*[520]
PES/PVP	4000 ppm	/	SEM and flux change	• Removal of PVP • Five times membrane flux increment • Narrower pore size distribution	Qin *et al.*[521]
PES/PVP	350 ppm	8	XPS, ATR-IR, SEC and AFM	• Degradation of PES/PVP membrane as a result of a radical induced PVP degradation	Pellegrin *et al.*[472]
PES/PVP	4000 ppm	8 and 12	UV visible spectra, FTIR and SEC	• Formation of phenol groups, as a result of the radical oxidation of the aromatic rings of PES	Prulho *et al.*[507]
PES/PVP	400 ppm	8	Streaming current and ATR-FTIR	• Formation of first phenol groups and later sulfonic acid groups on the surface of the membranes	Hanafi *et al.*[522]
PES/PVP	200 ppm	6.8 and 11.5	Flux, Streaming current, XPS and ATR–FTIR	• Degradation of PVP at all chosen pH values. • HClO and ·OH found to be responsible for PES chain-scission	Hanafi *et al.*[511]

SEC: steric exclusion chromatography; XPS: X-ray photoelectron spectroscopy; NMR: Nuclear magnetic resonance; GPC: gel permeation chromatography; TGA: thermal gravimetric analysis.

5.3.7 Effects of the Aging Processes on Bulk Distributions of Surface Modifier (Four Different Chemically Modified PES Membranes)

Based on the FTIR spectrum obtained for the five different PES membranes in Figure 5.25a, the characteristic band assignments are summarized in Table 5.3. The C=C stretch at 1260 cm^{-1} is assigned to v(C-O), which was present in all PES membrane samples. The amide I band was identified by the bands of 1668 cm^{-1}, which was present in the hydrophilic and double hydrophilic membranes. The C=O stretch at 1742 cm^{-1} is assigned to the fluorinated group present in the super-hydrophobic and double super-hydrophobic membranes. FTIR spectra of the membrane with the intensity ratio values of the absorbance at 1736 cm^{-1} (carbonyl bond) over that at 1580 cm^{-1} (phenyl ring vibration band) (*i.e.*, $I_{1736/1580}$) for super hydrophobic membranes and the absorbance at 1665 cm^{-1} (amide bond) over that at 1580 cm^{-1} (phenyl ring vibration band) (*i.e.*, $I_{1665/1580}$) for hydrophilic membranes were calculated to quantify the aging effects on functional groups.

Table 5.3 Assignment of IR Bands on PES Membranes

Peak position (cm^{-1})	Assignment	Present in membranes
1260	*v*(C-O)	All PES membranes
1660	Amide I	Hydrophilic, double hydrophilic membranes
1745	*v*(C=O)	Super-hydrophobic, double super-hydrophobic

5.3.7.1 Chemical Aging. Figure 5.36a shows that the super-hydrophobic membranes had a homogenous distribution of modifiers on the surface and higher absorbance intensity than the aged membranes by chemical aging. Meanwhile, a heterogeneous surface distribution of super-hydrophobic modifiers in the double super-hydrophobic membranes with almost 10 times higher of absorbance intensity than super-hydrophobic membranes and areas at high modifiers concentration reaching hundreds of μm^2. The dislodgement of

the hydrophobic modifiers in these areas could reasonably lead to the formation of modification defects. After the aging treatment, the distribution of modifiers obviously decreased indicating that the *ν*(C=O) is physically or chemically detached from the PES membrane surface during the aging.

For the hydrophilic membranes, the amide I bands were present on the surface as depicted in Figure 5.36b. In contrast to the double super-hydrophobic membranes, the double hydrophilic membranes demonstrated higher but still homogenous distribution of modifiers on the surface after twice dip-coating process. The hydrophilic PES membrane cleaned with NaClO for 10 days contained much less bands that could be assigned to Amide I suggesting that the NaClO might degraded the hydrophilic modifiers on the membrane surfaces.

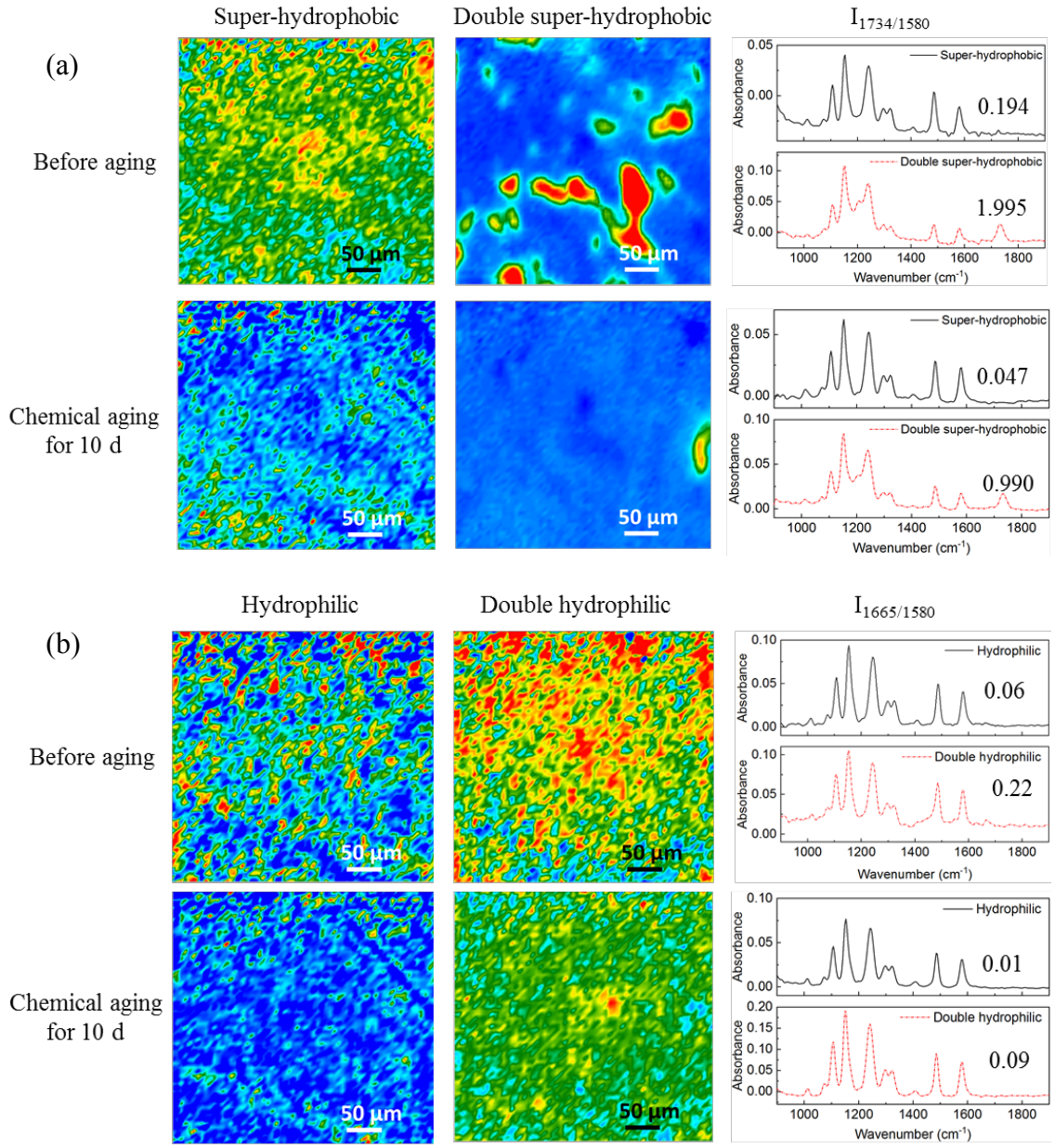

Figure 5.36 Representative modifier distribution images of (a) super-hydrophobic and (b) hydrophilic PES membranes before and after chemical aging treatment. The left two panels shows the corresponding 2D FTIR imaging map, where the intensity of the absorbance at 1734 cm^{-1} (carbonyl bond) for super hydrophobic membranes or 1665 cm^{-1} (amide band) for hydrophilic membranes was imaged in the chromatic maps. The right panel shows the FTIR spectra of the membrane with $I_{1736/1580}$ and $I_{1665/1580}$. The chromatic scale of the maps qualitatively shows the increasing intensity of the band as follows: blue < green < yellow < red.

The quantitative analysis of the IR images are summarized in Table 5.4 by modifier distribution area ratio and the specific band intensity ratio. When comparing the area ratios

of the modifier groups (amide I: 1660 cm^{-1}, fluorinated: 1745 cm^{-1}) to the membrane (PES: 1260 cm^{-1}), the ratios for the NaClO treated membranes were almost half of the pristine ones, thus giving the indication that the chemical aging procedure caused obvious aging to these PES membranes. It is in agreement with the findings on contact angles (Figure 5.18) and normalized absorbance changes (Figure 5.25) as shown in above sections.

Table 5.4 Modifier Distribution on the PES Membranes after Different Aging Procedures

Modifiers	Membranes	Pristine		Chemical aging (10 day)	
		Area (%)	Intensity	Area (%)	Intensity
Amide I*	hydrophilic	14	0.06	2.2	0.01
	double hydrophilic	48	0.22	8.1	0.09
v(C=O)**	super-hydrophobic	20	0.19	3.0	0.05
	double super-hydrophobic	8.0	1.99	1.1	0.99

* The intensity was calculated with the ratio of I_{1660}/I_{1520}.
** The intensity was calculated with the ratio of I_{1734}/I_{1520}.

5.3.7.2 Thermal Aging. Figure 5.37 shows that super-hydrophobic membranes lost a majority of additives on the surface after 10-hour thermal aging while double super-hydrophobic membranes remained half of the additives. The spectra intensity also showed similar results, which indicates that double dip-coating might help enhance the modifier stability for the super-hydrophobic membranes. In contrast, hydrophilic membranes did not show significant modifier loss after 10-hour thermal aging while double hydrophilic membranes had only half of the additives on the surface. And the intensity ratio of the double hydrophilic membranes decreased to half of the original value as well, which might due to the solubility of hydrophilic modifier after the second dip-coating and its release from the membrane surfaces during thermal aging process. The quantitative analysis of the

IR images are summarized in Table 5.5 by modifier distribution area ratio and the specific band intensity ratio. The results indicate that the thermal aging procedure caused severer aging to the super hydrophobic PES membranes than the hydrophilic ones and double dip-coating was more beneficial for super hydrophobic membranes.

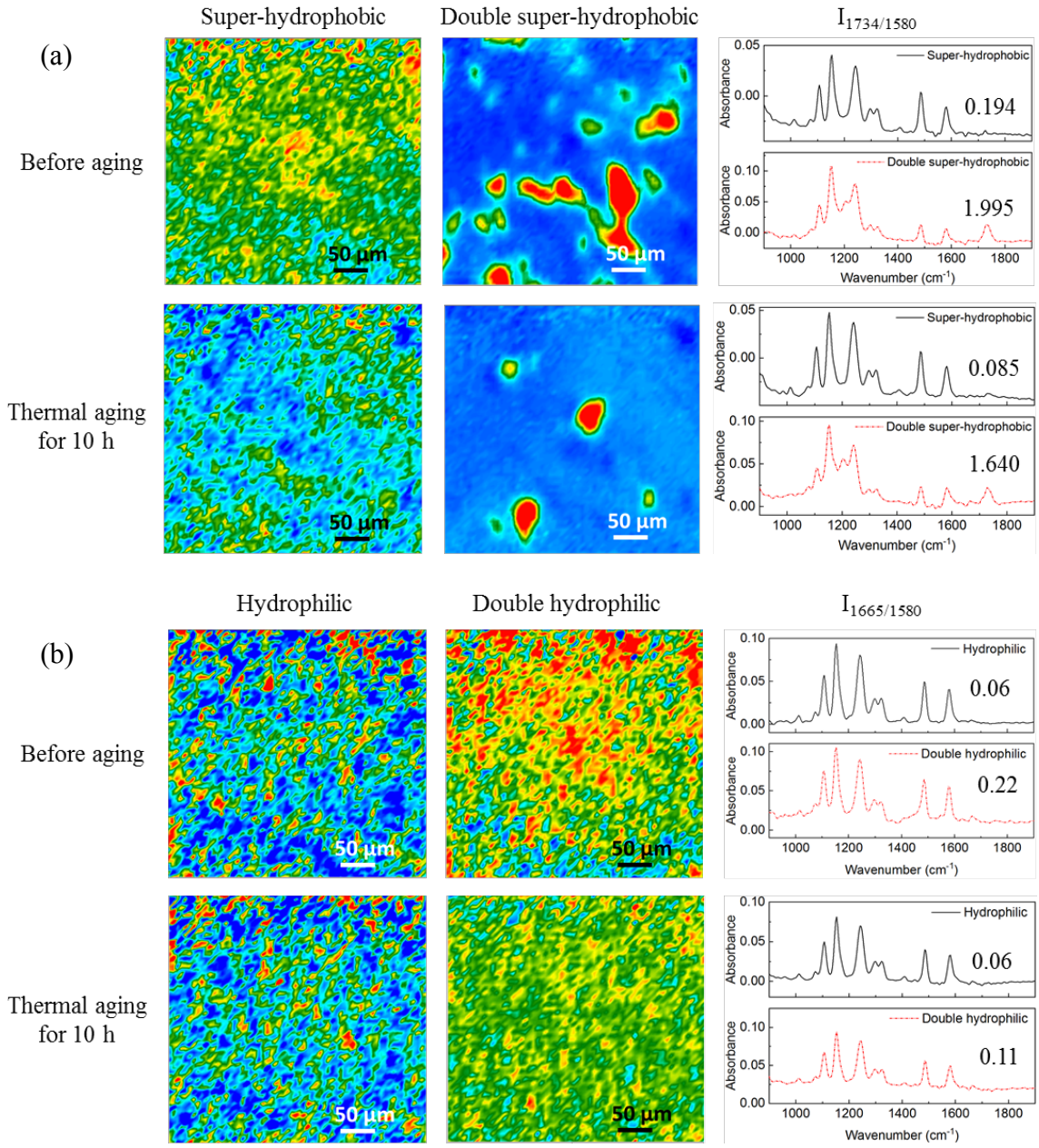

Figure 5.37 Representative modifier distribution images of (a) super hydrophobic membranes and (b) hydrophilic PES membranes before and after thermal aging treatment. The left two panels shows the corresponding 2D FTIR imaging map, where the intensity of the absorbance at 1734 cm^{-1} (carbonyl bond) for super hydrophobic membranes or 1665 cm^{-1} (amide band) for hydrophilic membranes was imaged in the chromatic maps. The right panel shows the FTIR spectra of the membrane with $I_{1736/1580}$ and $I_{1665/1580}$. The chromatic scale of the maps qualitatively shows the increasing intensity of the band as follows: blue < green < yellow < red.

Table 5.5 Modifier Distribution on the PES Membranes after Thermal Aging Procedures

Modifiers	Membranes	Pristine		Thermal aging (10 hour)	
		Area (%)	Intensity	Area (%)	Intensity
Amide I*	hydrophilic	14	0.06	11	0.06
	double hydrophilic	48	0.22	22	0.11
v(C=O)**	super-hydrophobic	20	0.19	3.1	0.09
	double super-hydrophobic	8.0	1.99	3.2	1.64

* The intensity was calculated with the ratio of I_{1660}/I_{1520}.
** The intensity was calculated with the ratio of I_{1734}/I_{1520}.

5.3.8 Effects of the Aging Processes on Nanoscale Distributions of Surface Modifier (Four Different Chemically Modified PES Membranes)

The changes in the functional groups of membranes caused by the aging solutions treatment are studied by AFM-IR as well. AFM-IR is a tool that reveals chemical composition of crucial nanostructures across a diverse range of applications, which has been summarized in Chapter 1. The procedures and application on nanoscale characterization of modified membrane surfaces have been elaborated in Chapter 2. This section aims to apply AFM-IR to investigate the modifier change at nanoscale for aged membranes.

5.3.8.1 Chemical Aging. Figure 5.38a shows the topography image, IR mapping image of modifier, and IR spectrum of super hydrophobic PES membranes. The spectrum was consistent with the FTIR spectrum obtained in ATR-FTIR. For the fluorinated modifiers used in the dip-coating process for the super-hydrophobic membranes, the characteristic spectrum peak of the modifier was assumed to be around 1736 cm^{-1}, which was assumed to be carbonyl bond in the fluorinated modifiers.[523] The IR mapping obtained by fixing the IR laser wavenumber at 1736 cm^{-1} showed the distribution of modifiers (15%, Figure 5.39). Compared with super-hydrophobic membrane, Figure 5.38e showed the

distribution area of the modifiers in the double super-hydrophobic membranes was slightly higher (21%, Figure 5.39). The normalized IR signal intensity by dividing with IR signal at 1586 cm^{-1} (phenyl ring vibration band in backbone polymer PES) to show the change of modifier signal. It showed that the normalized IR signal of modifier in double super hydrophobic membranes (0.76) was much stronger than that in super hydrophobic membranes (0.35). It indicated that more modifiers were dip-coated on the PES membranes.

After the immersion in NaClO solutions, the IR spectrum and IR mapping at 1736 cm^{-1} were checked again to observe the potential release of modifiers in the double super hydrophobic membranes. Compared with pristine double super-hydrophobic membranes, the modifiers IR mapping area ratio did not show obvious decrease after 2-day aging treatment, while the area ratio of modifier distribution decreased from 21% to 2.1% after 10-day aging treatment. The IR spectrum also showed that the modifier functional group normalized signal decreased from 0.75 to 0.6 in double super hydrophobic membranes after 10-day aging treatment while no obvious change was observed for the membranes after 2-day aging treatment.

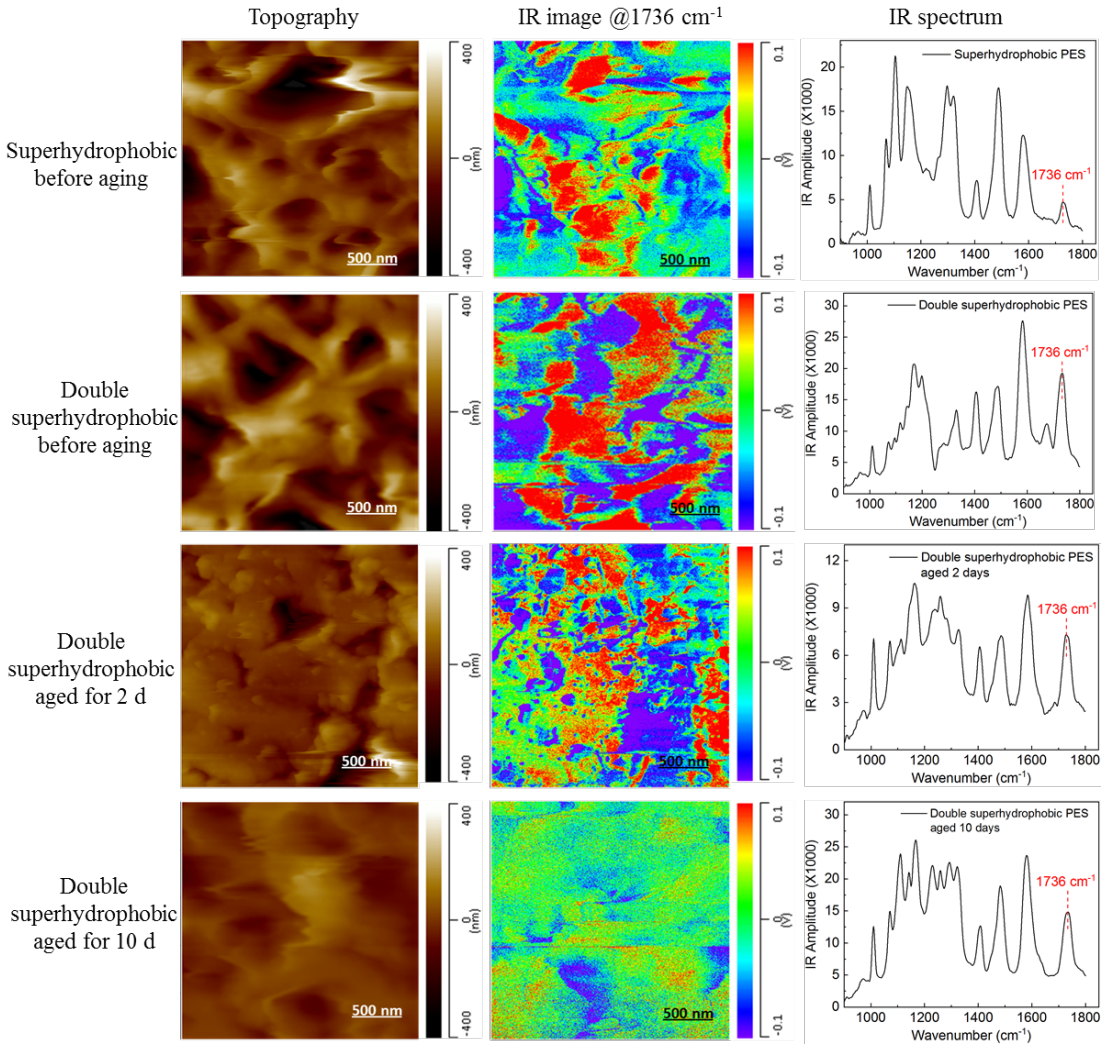

Figure 5.38 AFM topography, IR mapping images and IR spectra of (a-c) super-hydrophobic PES membrane, (d-f) double super-hydrophobic PES membrane, (g-i) double super-hydrophobic membrane aged for 2 days and (j-l) 10 days (4000 ppm NaClO, pH=9, 45 ºC).

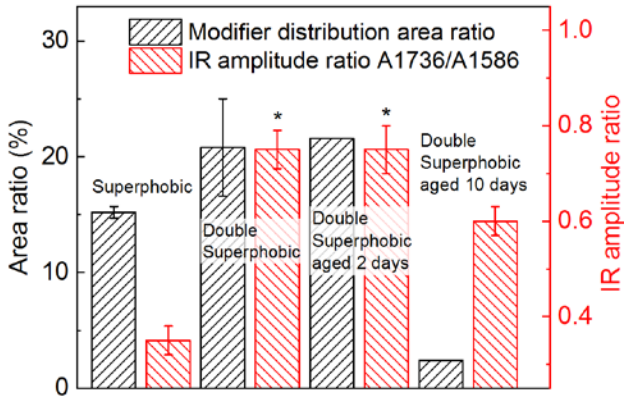

Figure 5.39 Modifier distribution area on modified membrane surface before and after aging treatment and the IR amplitude ratio at 1736 cm^{-1} to 1586 cm^{-1} (4000 ppm NaClO, pH=9, 45 ºC).

Figure 5.40a shows the topography image, IR mapping image of modifier, and IR spectrum of hydrophilic PES membranes. The characteristic spectrum peak of the modifier was assumed to be around 1664 cm^{-1}, which was assumed to be amide group in the hydrophilic modifiers, PVP. The IR mapping obtained by fixing the IR laser wavenumber at 1664 cm^{-1} showed the distribution of amide groups (14%, Figure 5.41). Compared with hydrophilic membrane, Figure 5.40e showed the distribution area of the modifiers was much higher (23%) in double hydrophilic membranes. The normalized IR signal intensity by dividing with IR signal at 1586 cm^{-1} was also calculated to show the change of modifier signal. It showed that the normalized IR signal of modifier in double hydrophilic membranes (0.69) was much stronger than that in hydrophilic membranes (0.35). It indicated that more PVP modifiers were dip-coated on the PES membranes.

After the chemical aging treatment, the IR spectrum and IR mapping at 1664 cm^{-1} were checked again to observe the potential release of modifiers in the double hydrophilic membranes. Compared with pristine double hydrophilic membranes, the PVP distribution area ratio showed slightly increase after 2-day aging treatment while the IR normalized signal decreased obviously from 0.69 to 0.28. The increase in the area ratio might be due to the measurement error and we did not measure the area ratio of PVP in aged membranes repeatedly due to the limited time and expense. On the other hand, the area ratio of modifier distribution decreased from 23% to 6.5% after 10-day aging treatment and the normalized IR signal decreased from 0.69 to 0.25 in double hydrophilic membranes after 10-day aging treatment. This results showed that the modifiers released seriously from the PES membranes after 10-day immersion in NaClO solutions.

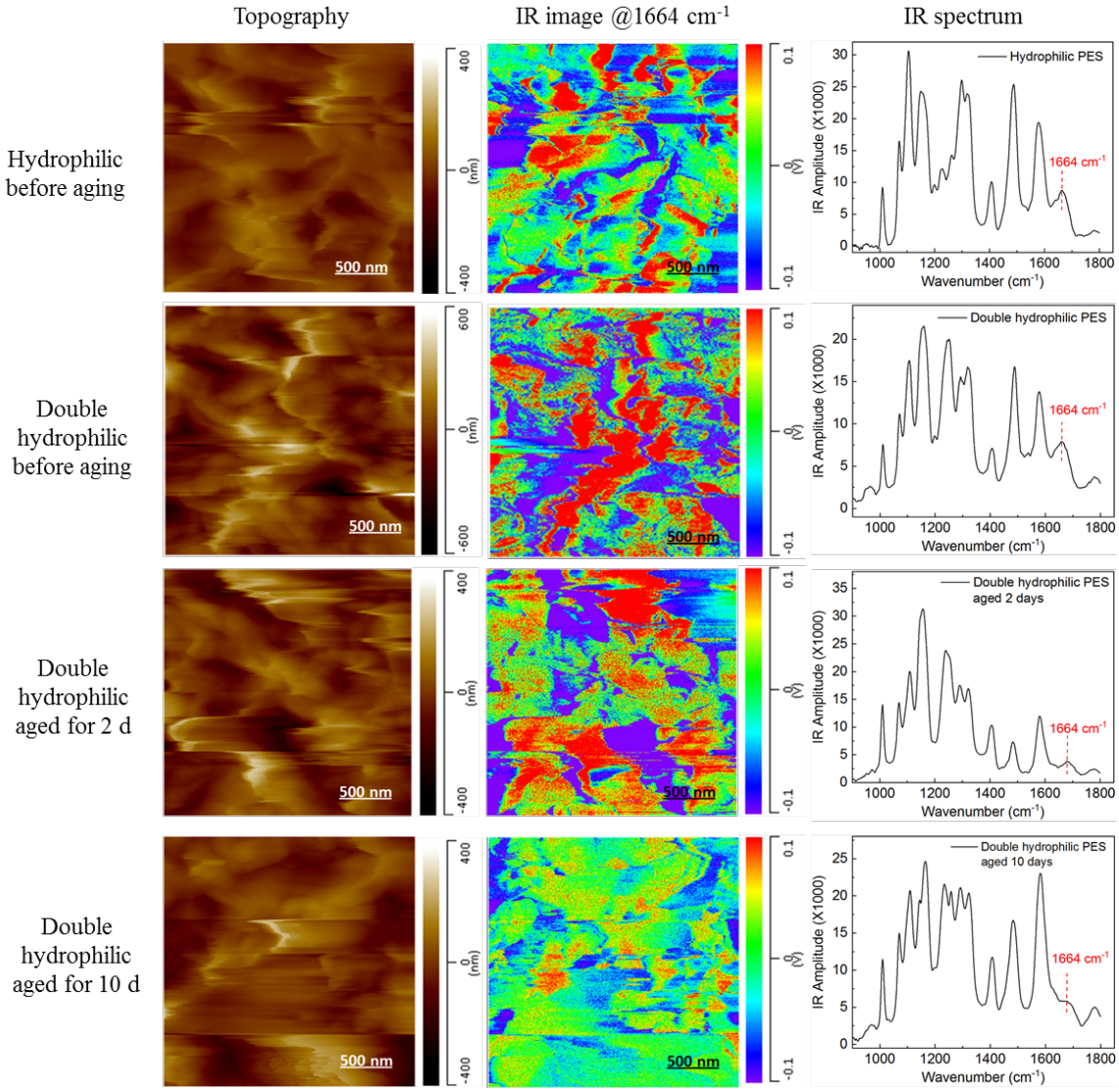

Figure 5.40 AFM topography, IR mapping images and IR spectra of (a-c) hydrophilic PES membrane, (d-f) double hydrophilic PES membrane, (g-i) double hydrophilic membrane aged for 2 days and (j-l) 10 days (4000 ppm NaClO, pH=9, 45 ºC).

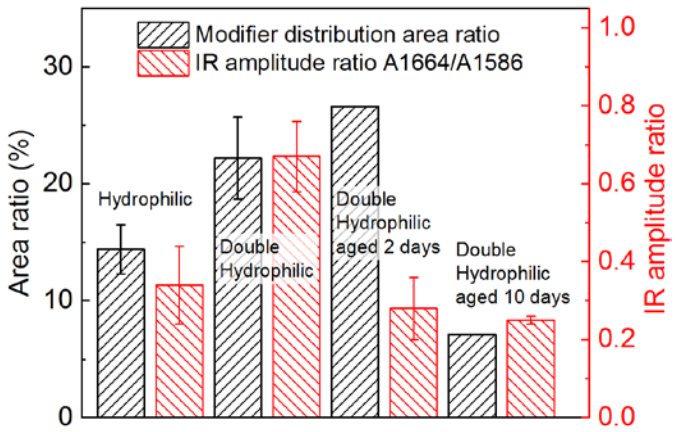

Figure 5.41 Modifier distribution area on modified membrane surface before and after aging treatment and the IR amplitude ratio at 1664 cm^{-1} to 1586 cm^{-1} (4000 ppm NaClO, pH=9, 45 ^{o}C).

5.3.8.2 Thermal Aging. Figure 5.42a-c shows the topography image, IR mapping image of modifier, and IR spectrum of super hydrophobic PES membranes. The spectrum was consistent with the FTIR spectrum obtained in ATR-FTIR. Since Millipore Corp. did not provide the information of the super hydrophobic modifier used in the modification process, the characteristic spectrum peak of the modifier was assumed to be around 1736 cm^{-1}, which was assumed to be carbonyl bond in the fluorinated modifiers. The IR mapping obtained by fixing the IR laser wavenumber at 1736 cm^{-1} showed the distribution of modifiers (area ratio 17%). Compared with super hydrophobic membrane, Figure 5.42e showed the distribution area of the modifiers was slightly higher (22%). The normalized IR signal intensity at 1736 cm^{-1} by dividing with IR signal at 1586 cm^{-1} (A1736/A1586) to show the change of modifier signal. The IR peak at 1586 cm^{-1} was assigned to be phenyl ring vibration band in backbone polymer PES. A1736/A1586 in double super hydrophobic membranes (0.76) was much stronger than that in super hydrophobic membranes (0.35). It indicated that more modifiers were dip-coated on the double super hydrophobic PES membranes.

After the aging treatment, the IR spectrum and IR mapping at 1736 cm^{-1} were checked again to observe the potential release of modifiers in the double super hydrophobic membranes. Compared with pristine double super hydrophobic membranes, the modifiers IR mapping area ratio did not show obvious decrease after 2-hour aging treatment or even 10-hour aging (Figure 5.43a). The IR spectrum also showed that the modifier functional group normalized signal did not show significant decrease after 10-hour.

Figure 5.43a-c shows the topography image, IR mapping image of modifier, and IR spectrum of hydrophilic PES membranes. The spectrum was consistent with the FTIR spectrum obtained in ATR-FTIR. The characteristic spectrum peak of the modifier was assumed to be around 1664 cm^{-1}, which was assigned to be amide group in the hydrophilic modifiers, PVP. The IR mapping obtained by fixing the IR laser wavenumber at 1664 cm^{-1} showed the distribution area ratio of amide groups was 10%. Compared with hydrophilic membrane, Figure 5.43e showed the distribution area ratio of the modifiers was slightly higher, 12% in double hydrophilic membranes. The normalized IR signal intensity of modifiers (A1664/A1586) in double hydrophilic membranes (0.69) was much stronger than that in hydrophilic membranes (0.35). It indicated that more PVP modifiers were coated on the PES membranes after second-time dip coating.

After the aging treatment, the PVP distribution area ratio in double hydrophilic membranes showed a slight increase after 2-hour aging treatment, but t-test showed that there was no significant difference between the aged and pristine ones (Figure 5.44b). Similarly, no significant changes were observed for the membranes after 10-hour treatments. This result showed that the thermal aging process did not result in obvious modifier release from the membrane surface as serious as that by NaClO treatments.

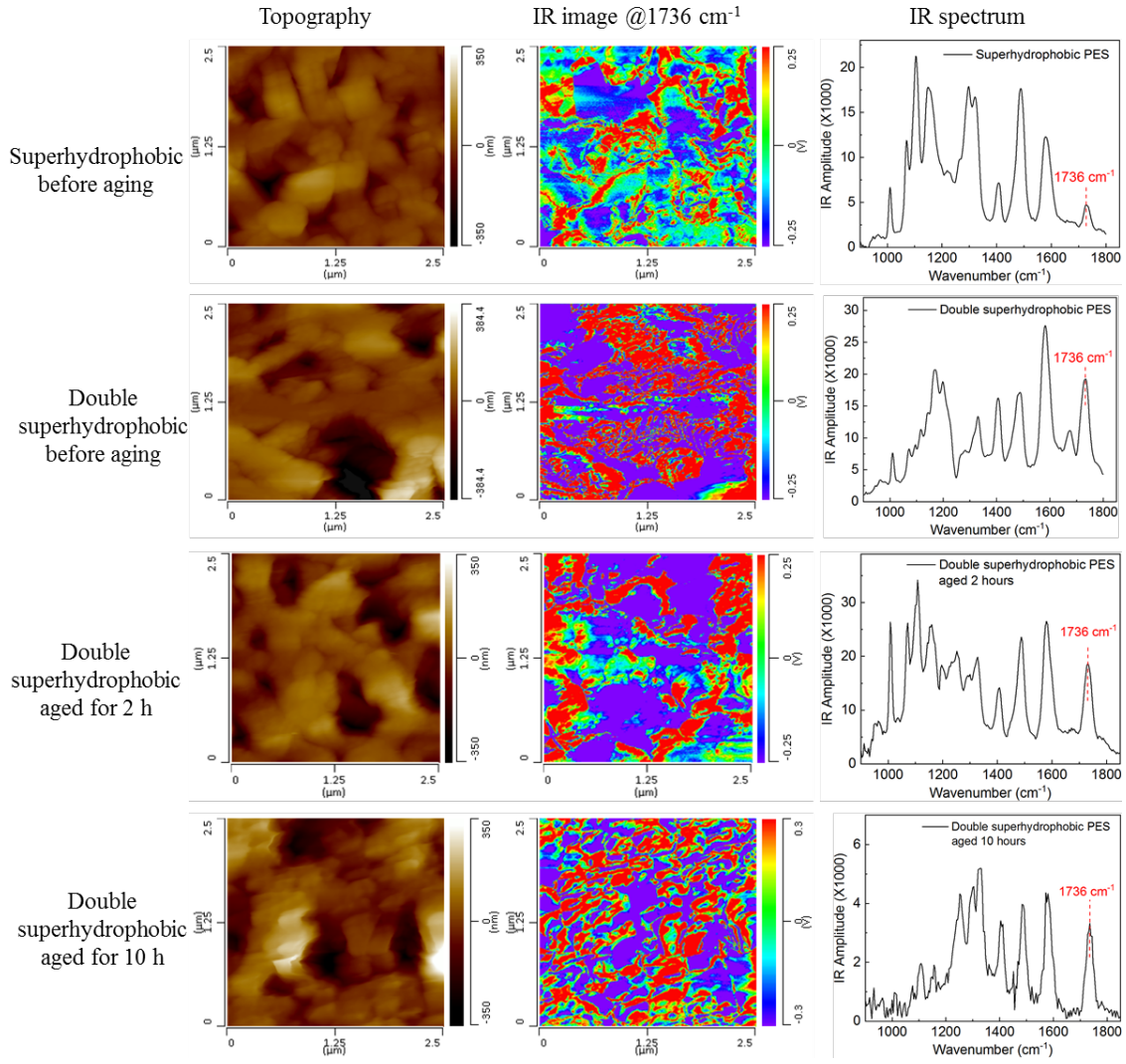

Figure 5.42 AFM topography, IR mapping images and IR spectra of (a-c) super-hydrophobic PES membrane, (d-f) double super-hydrophobic PES membrane, (g-i) double super-hydrophobic membrane aged for 2 hours and (j-l) 10 hours (123 ºC). The red region represents the distribution of hydrophobic chemical modifier (fluorinated groups).

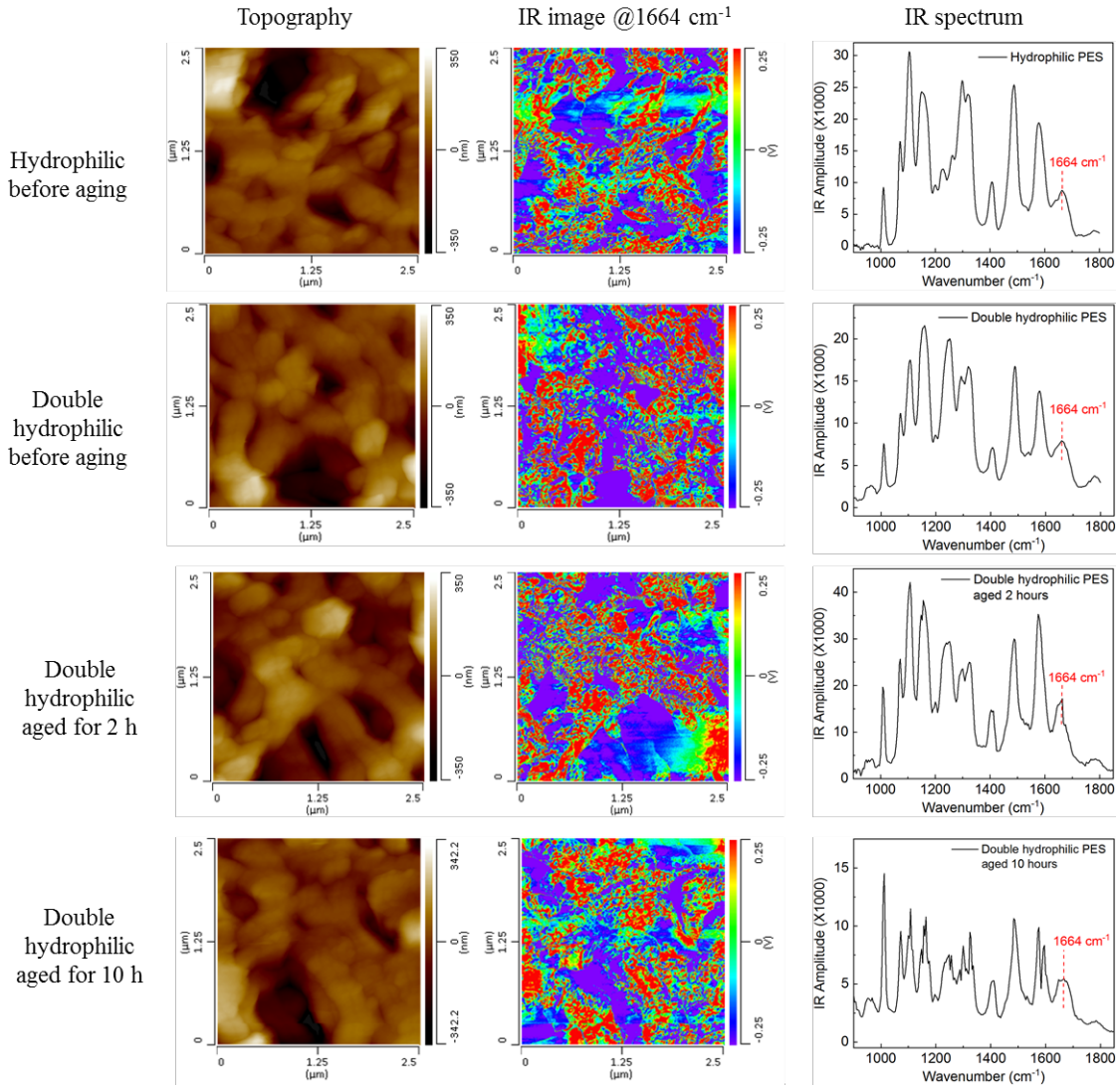

Figure 5.43 AFM topography, IR mapping images and IR spectra of (a-c) hydrophilic PES membrane, (d-f) double hydrophilic PES membrane, (g-i) double hydrophilic membrane aged for 2 hours and (j-l) 10 hours (123 ºC). The red region represents the distribution of hydrophilic chemical modifier (amide groups).

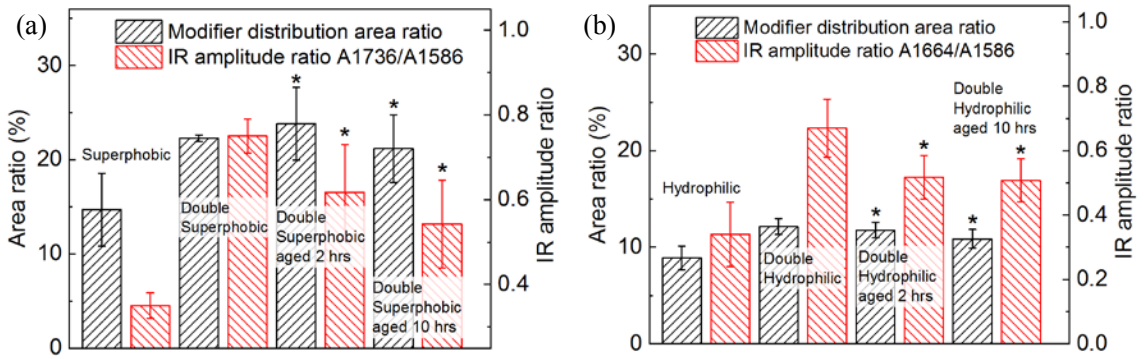

Figure 5.44 Modifier distribution area on modified membrane surface before and after aging treatment and the IR amplitude ratio at (a) 1736 cm^{-1} to 1586 cm^{-1} (hydrophobic chemical modified membrane) and (b) 1664 cm^{-1} to 1586 cm^{-1} (123 ^{o}C) (hydrophilic chemical modified membrane).

5.3.9 Effects of the Aging Modes on Tensile Strength and Elongation (Hydrophobic and Hydrophilic PES Membranes)

5.3.9.1 Chemical Aging. In this section, we evaluated the effect of aging modes on membrane mechanical properties: tensile strength and elongation. In Figure 5.45 we have reported the evolution of elongation at break and tensile strength of membrane samples versus aging time as a function of exposure modes. We found an obvious and sharp decrease in tensile strength and elongation after both the NaClO static and dynamic aging processes. The results indicate that contact with NaClO induced a significant decrease on membranes' mechanical strength, which is consistent with works already published.[472, 493]

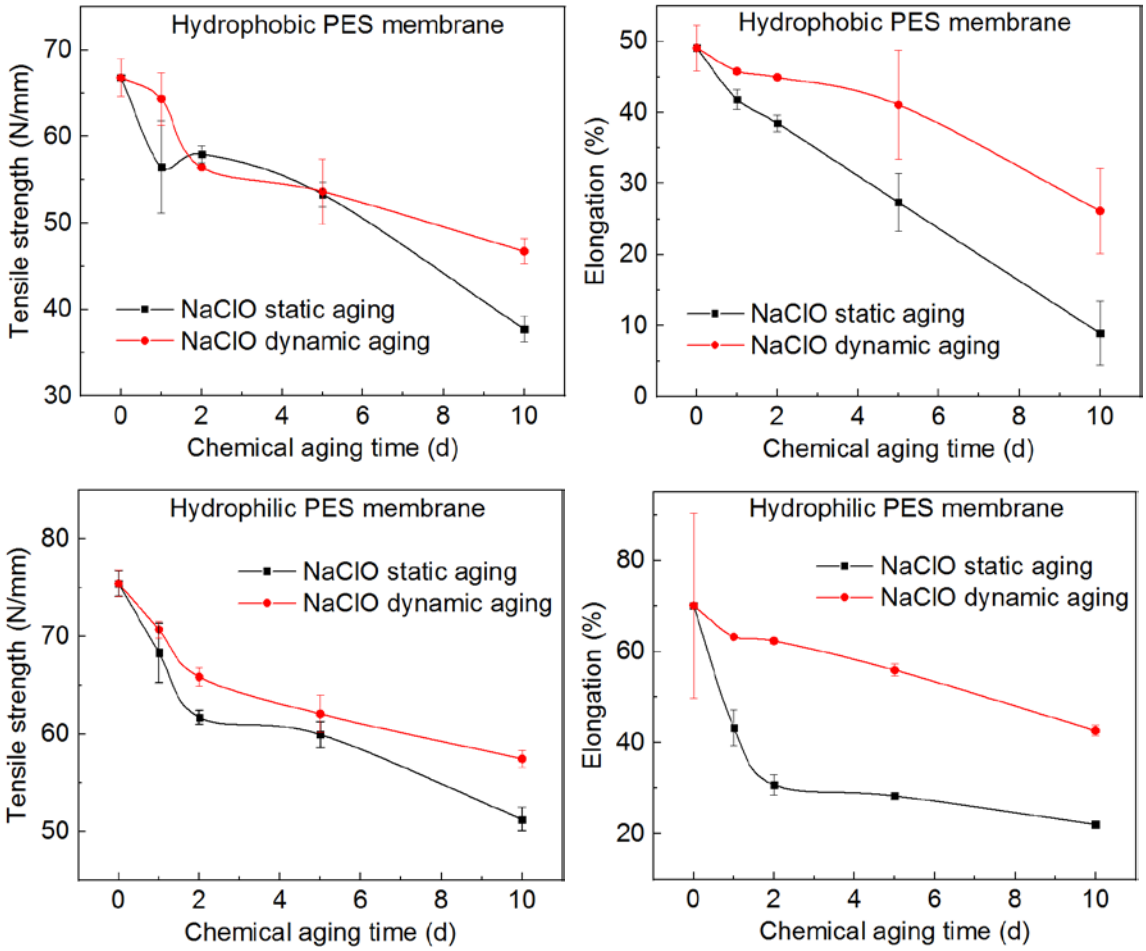

Figure 5.45 Tensile strength (left column) and elongation at break (right column) of membranes exposed to different aging modes versus aging time.

5.3.9.2 Thermal Aging. As shown in Figure 5.46 the thermal aging did not result in obvious evolution of mechanical properties. This result confirmed the thermal stability of PES and PVP polymers again.

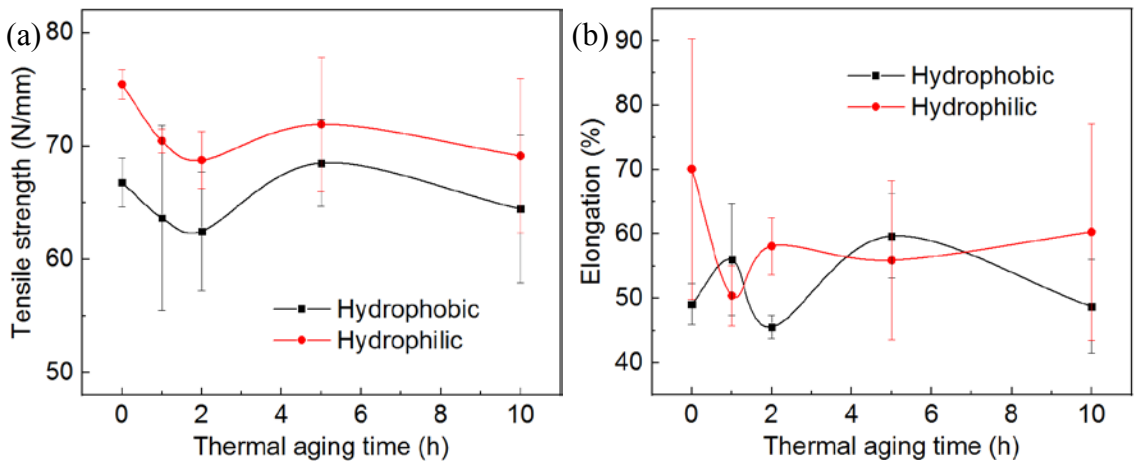

Figure 5.46 Tensile strength (a) and elongation at break (b) of membranes versus thermal aging time.

5.3.10 Effects of the Aging Modes on Membrane Filtration Performance (Hydrophobic and Hydrophilic PES Membranes)

5.3.10.1 Chemical Aging. As Figure 5.47 shows, when hydrophobic PES membrane interacted with NaClO solution, its water permeability increased significantly, then decreased and reached the stable stage (around 15 LMH kPa^{-1}), which could linked to the enhanced surface hydrophilicity and enlarged pore size. In addition, the HA rejection rate of hydrophobic membranes decreased obviously from 41% to 32% after exposure to NaClO while it also entered into a relative stable status in the region of 2-10 days for the static NaClO aging but kept decreasing for the dynamic NaClO aging. In consideration of the improved surface hydrophilicity and charges, the hydrophobic interaction between HA and membrane surface was weakened, and the electrostatic repulsion was enhanced. However, the aged membrane surface didn't play a positive effect in HA rejection. Therefore, we can only ascribe this decreased HA rejection to the pore enlargement, which was in agree with the SEM images (Figure 5.6).[524]

For the hydrophilic PES membranes, Figure 5.47 shows clearly that pure water

permeability decreased continuously along with the aging intensity. According to the previous studies, the enhanced hydrophilicity resulted in higher permeability. Considering the evolution on membrane surface properties such as membrane surface hydrophobicity, surface charge, and porosity during the aging processes, we proposed that the decreased hydrophilicity may have a dominant potential to decrease the membrane permeability. Meanwhile, the HA rejection was governed mainly by the pore size, hydrophilicity and electrostatic repulsion.[525] Therefore, the enhanced surface hydrophobicity, negative charges and porosity after the aging treatments resulted in the fluctuation of HA rejection for the hydrophilic membranes without a clear linear relationship.

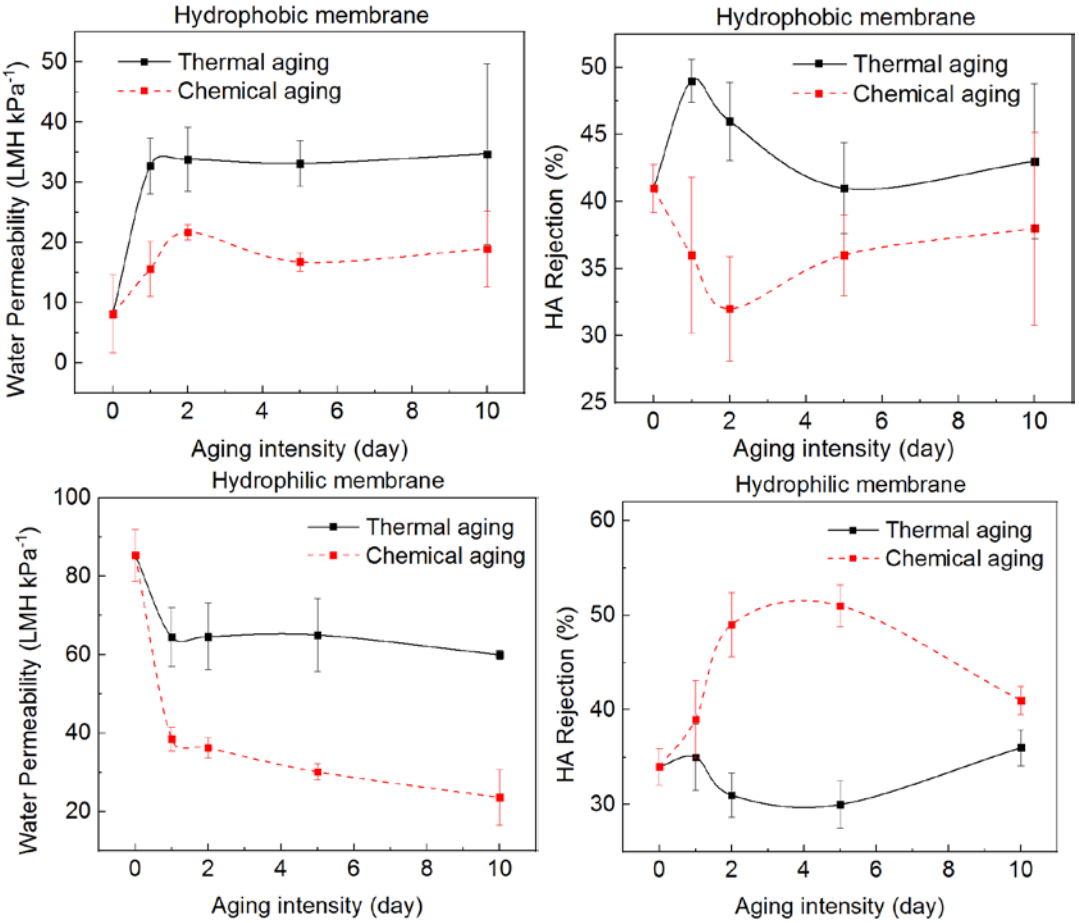

Figure 5.47 Membrane pure water permeability (left column) and HA rejection (right column) as a function of aging intensity.

5.3.10.2 Thermal Aging. Figure 5.48 summarized the membrane filtration performance after the thermal treatments. With the thermal aging treatments, the hydrophobic membranes demonstrated increasing water permeability and reached stable stage around 35 LMH kPa^{-1}; while hydrophilic membrane showed decreased water permeability and stopped around 60 LMH kPa^{-1}. This might due to the dwelling of membranes after the steaming in the autoclave heating. Similarly, HA rejection for both hydrophobic and hydrophilic membranes increased slightly and then decreased to the same level as pristine membranes. It indicated that the HA rejection might be related to the surface properties measured in the above sections, which did not show much change after the thermal aging treatments.

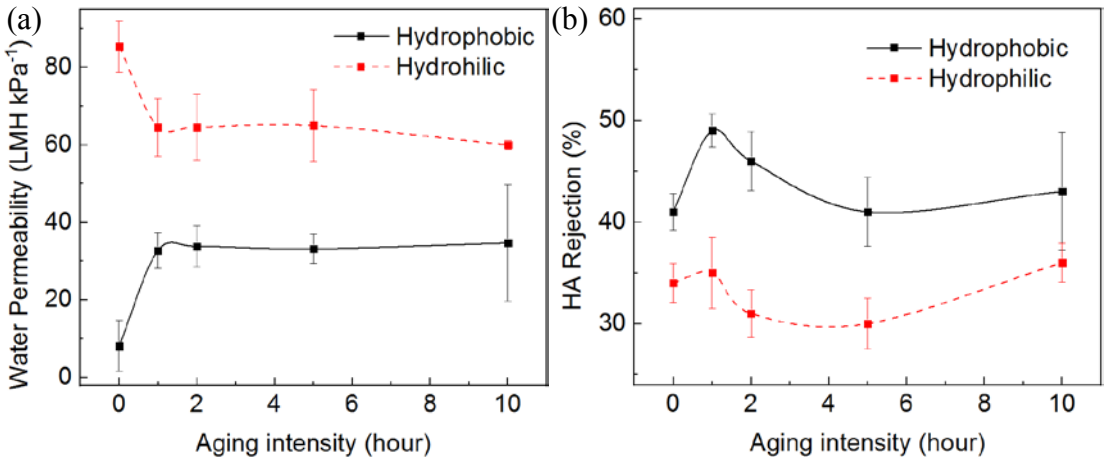

Figure 5.48 Membrane pure water permeability (a) and HA rejection (b) as a function of thermal aging intensity.

5.3.11 Development of Quantitative Structure-Activity Relationships (Hydrophobic and Hydrophilic PES Membranes)

Quantitative structure–activity relationships (QSARs) based on MLR models have been used to reveal the filtration performance (*i.e.*, pure water permeability, P.W.P.; and HA rejection, HA.R.) of pristine and aged membranes according to their physicochemical

characteristics of seven descriptors (*i.e.*, surface porosity, S.P.; surface roughness, S.R.; surface hydrophobicity, S.H.; surface charge, S.C.; surface modifier spectrum intensity ratio, S.M.I.; tensile strength, T.S.; and elongation, EL.). Particularly, QSAR for pure water permeability that may present the actual filtration performance by different aging intensities was developed as follows:

$$\begin{aligned} \text{P.W.P.} = & -55.705 + 2.2717 \cdot (\text{S.P.}) - 0.26925 \times (\text{S.R.}) + 0.07244 \times (\text{S.H.}) \\ & + 0.70522 \times (\text{S.C.}) + 3.1303 \times (\text{S.M.I.}) + 0.001249 \times (\text{T.S.}) \\ & + 0.00435 \times (\text{EL.}) \end{aligned} \quad (5.1)$$

In this model, we observed that positive coefficients for all these properties except roughness, indicating that surface porosity, charge, hydrophobicity, modifier intensity, tensile strength and elongation can increase the pure water permeability except surface roughness. Particularly, the two descriptors of S.H. and S.M.I. may influence each other in the QSAR because the surface hydrophobicity tends to decrease with increasing modifier intensity. Meanwhile, the larger surface roughness would result in less water permeability.

In addition, QSAR for HA rejection by different aging intensities was also developed as follows:

$$\begin{aligned} \text{HA.R.} = & 144.14 - 2.6579 \times (\text{S.P.}) + 0.2579 \times (\text{S.R.}) - 0.01696 \times (\text{S.H.}) \\ & - 0.14521 \times (\text{S.C.}) - 49.292 \times (\text{S.M.I.}) + 0.002145 \times (\text{T.S.}) \\ & - 0.001334 \times (\text{EL.}) \end{aligned} \quad (5.2)$$

In this model, we observed that the HA rejection were related positively with two descriptors: surface roughness and tensile strength. Increased HA rejection were likely related with decreasing surface porosity, hydrophobicity, surface charge, modifier intensity and elongation due to negative values.

From the developed QSARs (Equation 5.1 and 5.2), scatter plots between the developed QSARs versus the experimental permeability were shown with a reference line

in Figure 5.49. The majority of the permeability data were located near the reference line with the exception of hydrophilic membranes after 10-hour thermal aging treatment, which may demonstrate the meaning of considering statistical significances to develop more predictive QSARs.

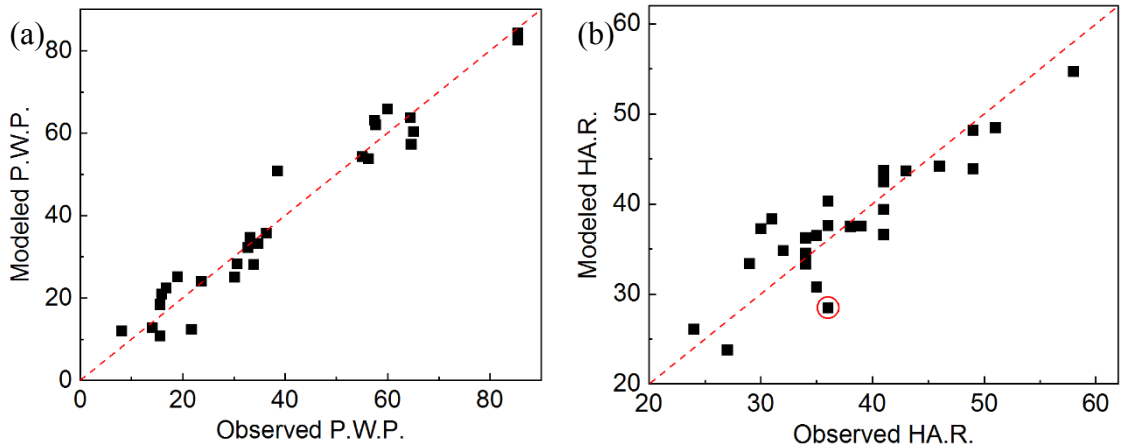

Figure 5.49 Relationship between observed and developed (a) P.W.P. and (b) HA.R. from the QSARs.

In QSAR results, the models showed the good relationships between seven descriptors of membrane characteristics and the filtration performances, which provide some insights on the effects of membrane properties on membrane filtration performances and moreover suggest roles of physicochemical descriptors on filtration processes during aging processes. However, membrane filtration performance would strongly be influenced by surrounding water chemistry conditions such as pH, ionic strength (IS), pollutants concentrations and hydraulic conditions. Therefore, there is a limitation to use our developed QSARs to predict membrane performance in different operation conditions. And other potential descriptors that may affect membrane filtration performance will be investigated in future research.

5.4 Conclusions and Future Prospects

To better understand the effect of thermal aging and chemical aging processes on filtration performance, physicochemical properties and mechanical strength of PES membranes, this study carried out detailed analysis using advanced characterization tools. The PES chain scission, PVP ring opening and radical oxidation degradation mechanism occurred when the PES membranes were exposed to NaClO solutions, and this has been discussed by summarizing previous studies about NaClO reaction with PES or PES/PVP membranes in the literature.

Particularly, modified PES membranes with different modification goals (*i.e.*, hydrophilic, super-hydrophobic, double hydrophilic and double super-hydrophobic) were investigated by thermal aging (heated in autoclave at 123 ^{o}C) and chemical aging treatments (soaking in or filtration with 4000 ppm sodium hypochlorite solutions). The membranes' physicochemical characteristics (*i.e.*, surface porosity, roughness, IR spectrum, modifiers distribution, surface charge and hydrophobicity) and mechanical properties (*i.e.*, tensile strength and elongation) were investigated comprehensively. The results indicate the aging mechanism and evolutions differed with the aging levels (chemical or thermal aging) and modes (static or dynamic). Furthermore, the distribution of modifiers on the membrane surface was analyzed with AFM-IR and FTIR microscopy with IR mapping images to present the modifier stability after the aging treatment. In addition, the water permeability and the foulant rejection of the aged membrane are also investigated by pure water filtration and humic acid (HA) filtration, respectively.

In terms of filtration performances, pore enlargement could be verified by the SEM images as well as the increased water permeability and the decreased HA rejection rate.

Moreover, the increased negative charge on aged PES membrane surface have a great impact on its rejection behavior for HA. It was confirmed that NaClO exposure induced PES degradation as well as PVP degradation and dislodgement from the PES matrix, leading to IR band intensity changes and mechanical strength decease. It was apparent that the filtration performance were affected by many different changes in characteristics and the given characteristics could impact performance in multiple ways. Thus, in order to elucidate the relationship between aging effects on membrane properties and the membrane filtration performances, the QSAR models were developed to highlight the linear relationship between the properties and performance whatever the aging mode. Thus, the membrane filtration performance could be predicted through their properties as membrane ages based on the models developed in the work.

However, there still remains a challenge to better understand membrane aging. It is essential for aging studies to be conducted under conditions that mimic the industrial process and have sufficiently long run lengths and repeated periods to ensure the best match between the outcomes coming from the research activities and the needs of industrial practitioners. As shown in this study, the aging process was simulated with filtration and immersion experiments in NaClO solutions and the dynamic aging mode rendered server degradation effects on the membranes. Furthermore, aging research must consider foulant effects in addition to interactions between membrane material and chemical aging agent in the practical applications. Thus, from a practical perspective, the future work about membrane aging will be suggested to be carried out in an industrial conditions.

CHAPTER 6

MICROWAVE-ASSISTED ANTIFOULING MEMBRANE FILTRATION TECHNOLOGY

6.1 Introduction

6.1.1 Membrane Fouling and Current Antifouling Methods

Membrane filtration finds many applications in chemical separation, water treatment, biopharmaceutical manufacturing and even clinical treatment systems (*e.g.*, point-of-care diagnostics and dialysis). However, membrane filtration technologies suffer from membrane fouling due to pore blocking, cake formation, concentration polarization, organic adsorption, inorganic precipitation and biological fouling.[526] Membrane fouling often results in the need for high-pressure pumps, increasing cost of maintenance, and shorter membrane lifetimes.

Investigation of membrane fouling has been a longstanding interest.[527-530] Membrane filters commonly undergo reversible and irreversible fouling. Reversible fouling could be removed by hydraulic backwash while irreversible fouling, often involved in strong chemical binding between foulant and membrane surface, has to be chemically cleaned using harsh agents (*e.g.*, oxidant, acid and base).[20, 21] The intensity of backwash and the exposure of cleaning agents may have negative influence on the membrane life time.[22] For example, chemical cleaning can induce the polymer degradation and thus compromise the material integrity of membranes. Additional drawbacks of those periodic cleaning techniques are that they interrupt the continuous filtration process and increase operational cost. Besides, periodically relax (a 30-minute production time followed by a 1-

minute relaxation), increasing cross-flow velocities, or a combination of the two were applied to increase flux.[531] The mechanical and bulk methods of reducing filter clogging are effective but time consuming, and in some instances, stopping operation to relax or flush the system is not favorable or even possible.[531] Alternatively, pretreatments (*e.g.* coagulation, adsorption, oxidation, biological treatment, and some combinations) can in various degrees alleviate the fouling by improving the membrane filtration feed quality. But for these pretreatment technologies, multiple problems (*e.g.* uncertainty on the membrane fouling, unfavorable by-products, scale problem and higher cost) emerge during the applications.

Other traditional antifouling techniques include the addition of magnetic or electric fields, ultrasonic perturbations and synthesis of functionalized nanocomposite membranes or modification of membrane surface for enhanced antifouling properties, ideally causing foulants to keep from attaching or to detach from the membrane surface.[532, 533] However, when handling potentially delicate products, chemical agents may harm the species targeted for collection or analysis and might damage the membranes themselves. So far, the membrane fouling mitigation strategies still came up with three categories: 1) coupling with pretreatments or external field, such as coagulation/electrocoagulation,[534] UV/chlorine pre-oxidation,[535] ozonation,[169, 536] granular activated carbon (GAC)[537, 538] and electric field;[539, 540] 2) surface modification of membranes including surface pattern by nanoimprint,[541] tailoring surface charge,[542] and special wettability;[543] 3) nanocomposite membranes, such as graphene oxide (GO)/multi-walled carbon nanotubes (MWCNTs).[544] Clearly, novel membrane filtration processes that exhibit robust antifouling properties are urgently needed to promote sustainable membrane filtration processes for water treatment.

6.1.2 Challenges in Water Treatment and Applications of AOPs

Besides the issue of membrane fouling, traditional membrane separations also suffer from inadequate removal of dissolved organic matters, especially for the trace emerging pollutants. For examples, 1,4-dioxane ($C_4H_8O_2$) was used as a model emerging organic pollutants.[545] The U.S. Environmental Protection Agency (USEPA) classified 1,4-Dioxane as a Group B2 Probable Human Carcinogen. In accordance with the New Jersey Ground Water Quality Standards rules at N.J.A.C. 7: 9C-1.7, the Department of Environmental Protection (DEP) has developed an interim specific ground water quality criterion of 0.4 μg L^{-1} and practical quantitation level (PQL) of 0.1 μg L^{-1} for 1,4-dioxane. 1,4-dioxane appears as a listed parameter in a published USEPA Method 522 entitled: "Determination of 1,4-dioxane in drinking water by solid phase extraction (SPE) and gas chromatography/ mass spectrometry (GC/MS) with selected ion monitoring (SIM)." However, sole membrane filtration could hardly reject 1,4-dioxane in the micropolluted water.

Advanced oxidation processes (AOPs) such as photocatalytic oxidation, photochemical oxidation, electrochemical oxidation, photochemical reduction, persulfate radical treatment, thermally induced reduction, and sonochemical pyrolysis have the potential to degrade recalcitrant pollutants or resistant microbes.[546] Combined membrane filtration–AOPs provides such complementary effect because the AOPs treatment assist in eliminating membrane fouling and remediation of organics in the concentrate via oxidation (mainly by free radicals) of the foulants, dissolve organic matters and organic compounds in the concentrate.[547-550] Three categories of AOP exist: (1) UV/O_3; (2) Photocatalysis (TiO_2 or other semiconductor particles under UV-vis illumination); (3) Fenton process (Fe^{2+} / H_2O_2), Photo Fenton process (Fe^{2+} / H_2O_2 / UV) and Photo-Fenton-like processes

of homogeneous nature (Fe^{3+}/ H_2O_2 / UV, Fe^{3+}/ APS / UV and Fe^{2+}/ APS / UV) and heterogeneous nature (Fe^0 / oxidants) (where APS is $(NH_4)_2S_2O_8$).[551] Combination of membrane filtration with AOPs holds potential to address emerging contaminant removal in drinking water. Some researchers combined membrane separation with chemical decomposition by integrating the membrane filtration with oxidants, such as ozone and hydrogen peroxide.[552-559] This combination is effective for decomposing organic contaminants and reducing membrane fouling. However, these oxidants are expensive, hazardous, and not sustainable or economically viable for large scale utilization. These oxidants attack polymeric membranes and shorten the lifetime of the membranes.

One potential solution to these problems is the introduction of photocatalytic ceramic membranes (PCMs).[560-564] Semiconducting inorganic materials, such as TiO_2 and ZnO, with a photocatalytic oxidation capability, have been fabricated in the form of water-permeable porous membranes. Along with the physical separation of contaminants in water through the porous structure of PCMs, the contaminants are chemically decomposed by reactive radical species generated on the PCMs under UV radiation. However, there are still some practical challenges when implementing the PCMs technology, including: (1) difficulty in providing effective UV illumination; (2) the reduced light penetration in tabular and spiral membrane surfaces; (3) the reduced active surface on catalyst and membranes accessible to chemicals and photons. Therefore, other than photo irradiation, an alternative irradiation source that can evenly pass through membrane modules and distribute energy to water, catalysts and membrane surface is highly needed.

Similarly, conventional disinfectants (*e.g.*, chlorine, chlorine dioxide, or ozone) can eliminate a wide spectrum of undesirable microorganisms; however, they also render the

rise of more than 600 different disinfection byproducts (DBP)[565-568] and increase microbial resistance to disinfectant chemicals.[569-571] Most DBPs (*e.g.*, trichloromethane, brominedichloromethane, dibromomethane and tribromomethane) are potentially carcinogenic.[572] Conventional disinfection methods are becoming less efficient due to the evolution of antibiotic-resistant strains or genes.[573, 574] UV irradiation is an effective, safe, and environmentally friendly disinfection method but the lack of persistent antibacterial capacity generally causes high risk of regrowth, particularly in poor sanitation. Thus, alternative irradiation source is in needed for effective disinfection.

6.1.3 Current Knowledge of Microwave Irradiation

Microwave irradiation (MW) has received increasing interest in organic synthesis due to remarkable enhancement of the rates of some reactions over conventional reactions.[576, 577] Microwave irradiation has long been used to improve or facilitate chemical reactions or digestion as it can selectively and uniformly distribute heat energy that may turn into reactive radicals or nanobubbles.[578, 579] MW irradiation also enhanced the processes of adsorption, desorption, and recycling because of the "hot spots" effect on the activated carbon adsorbents.[580]

Wang *et al*. used microwave irradiation to generate interfacial nanobubbles and found that surface nanobubbles (diameter 200-600 nm) may be formed by microwaving solutions containing dissolved oxygen, due to localized surface heating.[290] The principal cause behind cavitation, which is nucleation, growth, oscillations and transient collapse of small gas bubbles due to pressure variation or in general, energy dissipation in the system.[581] Surface fouling removal mechanism was proposed by Jie Zhu *et al*., who demonstrated that nanobubbles can prevent the fouling of surfaces and also clean the fouled

surfaces.[278] Others also reported the prevention of fouling using surface nanobubbles.[589-591] Nanobubbles provide a mechanical barrier or surface mask that prevents the adsorption of contaminants on the surface. The production of nanobubbles on a contaminated surface can also remove nearly all contamination. However, nanobubbles in these studies were prepared by electrolyzing water, with the resultant supersaturation of dissolved gas leading to the formation of surface nanobubbles. None of the previous research investigated nanobubbles formation on porous membranes under microwave irradiation.

MW irradiation alone is incapable of treating some organic pollutants, such as azo dyes, pesticides, pharmaceuticals. Combination methods with MW irradiation, such as MW-oxidant, MW-Fenton, MW-Fenton-Like, and MW-photo/electro/ultrasonic processes, have been studied. Recently, microwave irradiation was used to enhance the pollutant degradation (*e.g.*, pharmaceutical wastewater, RhB, 2-Nitrophenol, PFOA) in the Fenton-like reactions.[592-598] It showed that the microwave irradiation could widen the optimum pH range for Fenton reaction, and the localized MW superheating effect can also promote the generation of •OH in the Fenton-like process and enhanced the pollutant degradation.[599] For example, Li *et al*. synthesized Pb-doped $BiFeO_3$ (BFO) with decoration of reduced graphene oxide (rGO) to form a hybrid nanocomposite (Pb-BFO/rGO).[600] The Pb-BFO/rGO was successfully used as a heterogeneous catalyst in the microwave enhanced Fenton-like process that efficiently decomposes PFOA and shortened the reaction time. Gou *et al*. utilized ferric sulfate as catalyst, hydrogen peroxide as oxidant, with the assistant of microwave (MW) to study the efficiency of MW-Fenton-like process, which demonstrated increasing TOC removal and apparent reaction rate of TOC removal, reducing the catalyst dose and oxidant dose, shortening the reaction time.[595] These studies

inspired us to consider microwave as an alternative source of irradiation for photo-Fenton reactions, especially in a modulated membrane filtration process, where light illumination on tabular and spiral membrane surfaces could be practically difficult. Unlike photo irradiation or ultrasonic wave, microwave can evenly pass through membrane modules and distribute energy by exciting water and converting to heat or reactive radicals.

Reactive membranes worked as a support to prevent aggregation of catalytic nanoparticles and avoids the need to separate catalysts from the reaction mixture; the membrane geometry allows for continuous-flow reactions and results in rapid convective mass transport of reactants to immobilized catalyst nanoparticles. It would be difficult to immobilize nanoparticles in commercially available ceramic membranes because binding mediums on the membrane may be required to form bonds between nanoparticles and membrane support. Many attempts have been made to find appropriate organic binders or connection molecules for nanoparticles. Most importantly, however, the permeate water quality should be considered as nanoparticles are immobilized on the membrane for use in water treatment plants because release of nanoparticles from the membrane may raise environmental safety concerns. Dipping the Al_2O_3 membrane support into hydroxyapatite (HAP) solution as a binder has been explored by Ma *et al*. for stabilizing TiO_2 nanoparticles on the Al_2O_3 composite ceramic membranes.[601] Lv *et al*. modified a ceramic membrane surface by embedding amino groups on the membrane surface to form covalent bonds with silver atoms on the silver nanoparticles at the membrane surface.[602] Karnik *et al*. also fabricated $Al_2O_3/ZrO_2/TiO_2$ composite ceramic membranes with Fe_2O_3 nanoparticles by using phytic acid as an organic binder instead of cationic polyelectrolyte solution.[603] Xiangli *et al*. prepared polydimethylsiloxane (PDMS)/ceramic composite membrane with

PDMS deposited uniformly on the surface of tubular nonsymmetric ZrO_2/Al_2O_3 porous ceramic supports.[604]

Besides, microwave disinfection has been studied over the past few decades primarily in the field of sludge digestion with the goals of effectively removing pathogens in biosolids, or sludge.[605] As microwaves pass through sewage sludge, the water molecules within the sludge begin to rotate and align themselves with the frequency and electric field. This molecular movement causes vibrations, which produces frictional heat and water boiling. Water molecules inside pathogens and other microorganisms are also excited, causing the cells to expand and explode. Low microwave frequencies (<=2.45 GHz) are capable of denaturing DNA molecules and disassociating organic chemical bonds. These lower frequencies will allow for a more targeted application leading to a more cost effective treatment.[605] The thermal and non-thermal effects (*i.e.*, polarization, superheating, dielectric properties) on pollution degradation were demonstrated.[599, 606, 607] Microwave-based disinfection reduces the reaction time, decreases the activation energy and improves the speed of the reaction, reduces the equipment size necessary for treatment, reduces the waste product, and increases the yield and purity of products.[606]

6.1.4 Hypothesis of This Study

There has been no demonstration on coupling microwave irradiation with membrane filtration processes, although microwave-assisted flow-through reactors have been designed and utilized in chemical synthesis or conversion. A continuous flow process is essentially ideal for microwave irradiation, which has limited penetration depths.[609-611] The penetration depth generally used at 2.45 GHz is in the order of a few centimeters, depending on the dielectric properties of the absorbing materials. However, in membrane

filtration systems, irradiating microwaves to a reactant solution flowing through a membrane filtration (*e.g.*, capillary channels) should solve this penetration depth problem. Additionally, microwave can efficiently penetrate non-polar membrane casing materials or membrane modules without loss of microwave energy and highly selectively distribute energy to membrane surface-coated catalysts for chemical degradation or fouling removal through localized heating, radical formation or nanobubble formation. Microwave induced a highly frequent vibration of the molecules, and thus affecting the membrane fouling behavior and dislodging the attachment between the fouling layer and the membrane surface and the nanobubble may efficiently remove surface foulant while detaching from membrane surfaces (Figure 6.1).

The hypothesis to be tested include (1) nanobubbles and radicals may reduce or prevent the deposition of organic pollutants (*e.g.*, humic acid) on the membrane surfaces; (2) pollutants will be rapidly removed via degradation by the radicals and separated by the membrane. MW was selectively adsorbed by catalysts and H_2O_2 to produce ‘‘hotpots” on membrane surface that promoted the generation of •OH and enhanced the degradation of pollutants and further prevented the membrane fouling. The non-thermal effect of MW (such as the electrical effect, magnetic effect, and chemical effect) greatly increased the formation of •OH due to the excitation of H_2O_2 molecules to higher vibrational and rotational energy levels.[599] The thermal and nonthermal effects of microwave radiation also made contributions to decreasing the gas solubility and facilitating nanobubbles formation. The nanobubbles may interact with pollutants and made them less attracted to the membrane surfaces but stabilized in solution for further degradation.

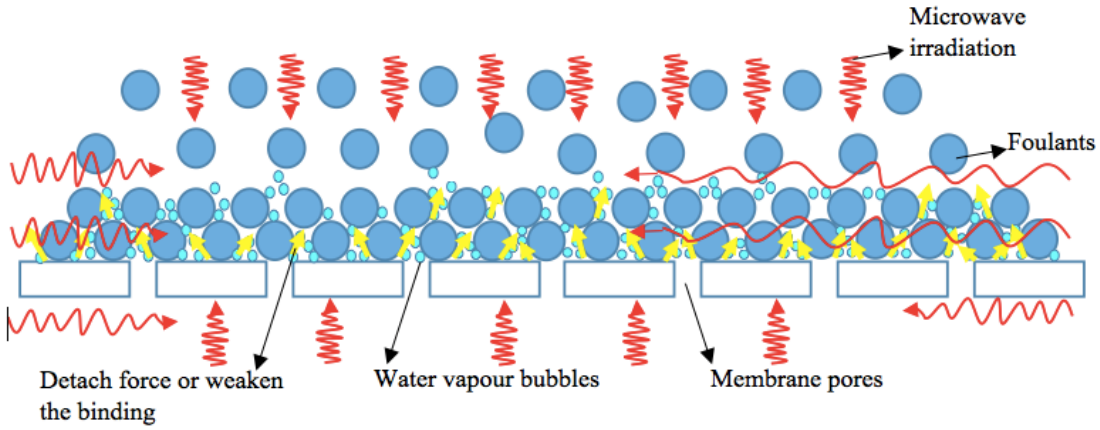

Figure 6.1 The schematic graph for the effect of microwave on membrane fouling.

This study aims to address these knowledge gaps and deliver insightful information for future industrialization and rationale design of microwave-assisted membrane filtration systems. The specific tasks are to systematically evaluate the microwave impacts on membrane filtration including microwave energy, time of exposure, membrane integrity and antifouling and filtration performances. The ultimate goals are (1) to upgrade passive membrane filtration to the next-generation reactive membranes that proactively degrade water contaminants and prevent surface fouling; and (2) to broaden membrane applications such as disinfection and/or virus inactivation for water reuse and decentralized point-of-use (POU) devices in small drinking water systems. The long-term goal is to establish a "greener" or chemical-free antifouling strategy for high flux membrane filtration processes. The research will lead to transformative applications of novel membrane filtration processes that enhance membrane filtration flux with longer stability and operation time, which will promote economically viable and sustainable practices of water/wastewater treatment and other industrial membrane separation applications.

6.2 Materials and Methods

6.2.1 Preparation and Characterization of Catalyst Coated Ceramic Membranes

A flat-sheet ceramic membrane (47N014, Sterlitech Corporation, US) was used as a base support for catalyst functionalization. This planar membrane is made of a zirconia/titania (Zr/TiO_2) coating on an alumina (α-Al_2O_3) supported with pore size of 140 nm and an effective surface area of 17.34 cm^2. The ceramic membrane was soaked into BFO solution (2 g L^{-1}) and placed in a vacuum oven at 80 °C for 24 h (Figure 6.2). In this way, the functionalized ceramic membranes remained high permeate flux. The stability of BFO on membrane surface will be analyzed after the filtration experiments.

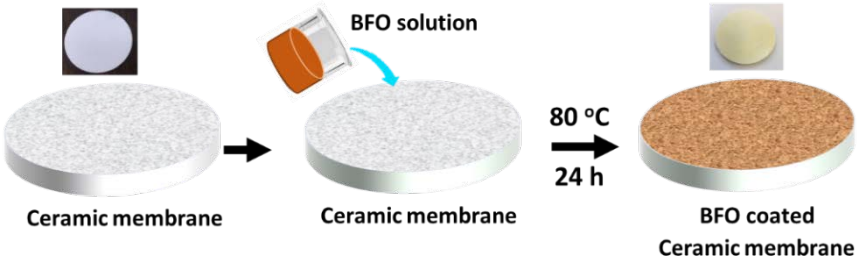

Figure 6.2 Schematic representation of the BFO-coated ceramic membrane preparation.

The membrane surface morphology were studied by a scanning electron microscope coupled to an energy dispersive spectrometer (SEM-EDS, JEOL JSM-6700F). The crystalline phase was examined by a X-ray diffraction analyzer (XRD, Rigaku, RXIII) on a D/MAX-2500 unit with Cu Ka radiation (k = 1.54056 Å). Fourier Transform infrared (FTIR) spectra were obtained (Perkin Elmer Spectrum BS-III) at a resolution of 4.0 cm^{-1}. The integrity of the membranes was investigated after exposure to microwave under different conditions to visualize possible damage on the membrane surface.

The overall membrane porosity (ε) was determined by a gravimetric method, as defined in the following equation:[612]

$$\varepsilon = \frac{m_w - m_d}{\rho A L} \tag{6.1}$$

where m_w is the weight of the wet membrane (after immersed in water for 24 hours); m_d is the weight of the dry membrane; A is the membrane surface area (m^2), ρ is the water density (1×10^6 g·m^{-3}), and L is the membrane thickness (m).

To determine the changes of mean pore radius (r_m) of membranes, the Guerout–Elford–Ferry equation was employed:[466]

$$r_m = \sqrt{\frac{(2.9 - 1.75\varepsilon)\times 8\eta L Q}{\varepsilon A \Delta P}} \tag{6.2}$$

where η is the water viscosity (8.9×10^{-4} Pa s), Q is the volume of permeate water per unit time ($m^3\cdot s^{-1}$), and ΔP is the operation pressure (3.5×10^4 Pa).

At the beginning, a binder medium, Bis-(3-[triethoxysilyl]-propyl)-tetrasulfide (BIS) was tried to link the BFO on ceramic membranes. To prepare the silane solution, 85 mL deionized water was taken into a 100 mL beaker and mixed with 5 mL Bis-(3-[triethoxysilyl]-propyl)-tetrasulfide (BIS). Then a certain amount (0.03 g) of BFO particles were added in the silane solution and ultrasonic dispersed for 10 min. The ceramic membrane was soaked into the suspension for 20 min, taken out, and solidified in a vacuum oven at 100 °C for 1 h. In this way, BFO catalyst was decorated onto ceramic membranes. However, the prepared ceramic membranes through the above procedure showed superhydrophobic properties. The pure water cannot penetrate the membrane pores even at TMP of 30 psi.

6.2.2 Assessment of Formation of Nanobubbles and Hydroxyl Radicals (•OH) Under Microwave Irradiation

6.2.2.1 Size Distribution and Zeta Potential of Nanobubbles. Measure the size distribution and zeta potential of the water before and after the microwave radiations under different modes. 8 mL DI water sample was filtered (Whatman, Anotop 25 plus, 0.02 μm) for twice to remove the possible particles or bubbles in the water. Then the sample was measured with DLS to get the size distribution and zeta potential without the microwave irradiation. Another 8 mL DI water sample filtered for twice was placed into the microwave oven and heated for 30 seconds, measured the temperature, cooled the sample down in the room naturally to 30 ^{o}C, heated the sample for another 30 seconds and measured the size distribution and zeta potential. Another two microwave irradiation modes were the same procedure as described but 15 seconds for 4 times and 10 seconds for 6 times respectively. The particle size distribution and zeta potential of MW-irradiated water were obtained from the dynamic light scattering (DLS, Zetasizer Nano ZS, Malvern Instruments Ltd., Worcestershire, UK).[613] Each zeta potential and size measurement were obtained corresponded to the mean values calculated from 90 measurements.

It is assumed that the decreasing solubility of gas in the water and/or the water vapor due to the high temperature caused by MW are likely responsible for the formation of Nanobubbles. In order to investigate the nanobubble formation mechanism, a further test was performed. 8 mL DI water sample was filtered (Whatman, Anotop 25 plus, 0.02 μm) for twice to remove the possible particles or bubbles in the water, boiled at 100 ^{o}C in the oven for 1 minutes. Then this DI water sample was taken as a sample to measure particle size distribution and zeta potential. It is assumed that boiled water is degassed. Then another 8 mL DI water sample was filtered twice, heated in oven at 100 ^{o}C for 1 minutes,

irradiated with MW for 30 s, took as a sample to check the particle size distribution and zeta potential.

6.2.2.2 Analysis of Hydroxyl Radicals (•OH) Formed Under Microwave Irradiation.

The formation of hydroxyl radicals (•OH) on the surface of BFO-coated membranes is detected by a photoluminescence (PL) technique with terephthalic acid as a probe molecule. Terephthalic acid readily reacts with •OH to produce highly fluorescent product, 2-hydroxyterephthalic acid.[614, 615] The intensity of the PL peak of 2-hydroxyterephtalic acid is in proportion to the amount of •OH radicals produced in water. This method relies on the PL signal at 425 nm of the hydroxylation of terephthalic acid with •OH generated at the water/BFO interface under microwave irradiation. Experimental procedures are as follows:[616] 5 mg of BFO powder sample is dispersed in a 30 mL of the 5×10^{-4} M terephthalic acid aqueous solution with a concentration of 2×10^{-3} M NaOH in a glass tube. Put into microwave oven and irradiate for 2 min. PL spectra of the generated 2-hydroxyterephthalic acid are measured on a Hitachi fluorescence spectrophotometer. After microwave irradiation every 30 s, the reaction solution was filtrated to measure the increase in the PL intensity at 425 nm excited by 315 nm light.

6.2.3 Preparation of a Filtration System Under Microwave Irradiation

A commercial MW oven (1250 W, 2.45 GHz, Panasonic Co., Shanghai) with different power setting was used to incorporate a membrane filtration system. The filtration cell was placed and radiated in the MW oven (Figure 6.3). The filtration cell (membrane housing) is made of Teflon (PTFE), including an O-ring, screens, screws and nuts (see the CAD design and illustrations in Figure 3.2). Teflon is a nonpolar material that does not absorb microwaves (transparent to microwaves), which allow microwaves to pass through

membrane housing and irradiate catalysts coated on membrane surface. Details of the novel MW-assisted membrane filtration system are provided in our provisional patent (62/409,431). The temperature of the filtration cell and solutions in the feed tank and pipes were measured with a Raytek MiniTemp MT4 non-contact infrared thermometer equipped with a laser pointer (Raytek Corporation Santa Cruz, CA, USA).

To determine the maximum heating area at the anti-nodes and minimal heating area at the nodes, cheese powder was placed on the tray and heated with 1250 Watt for 1 minute. As shown in Figure 6.4, the anti-nodes and nodes of the microwave are indicated by the melt or unmelt parts of the cheese powder. Measuring the distance between centers of those anti-nodes spots gives the possible wavelength of MW of approximately 10 cm, which is close to the reported wavelength of 12.2 cm (4.80 in) on consumer MW ovens with 2.45 gigahertz (GHz). In the following experiments, the filtration cell was placed in the anti-nodes area to allow efficient absorption of MW irradiation.

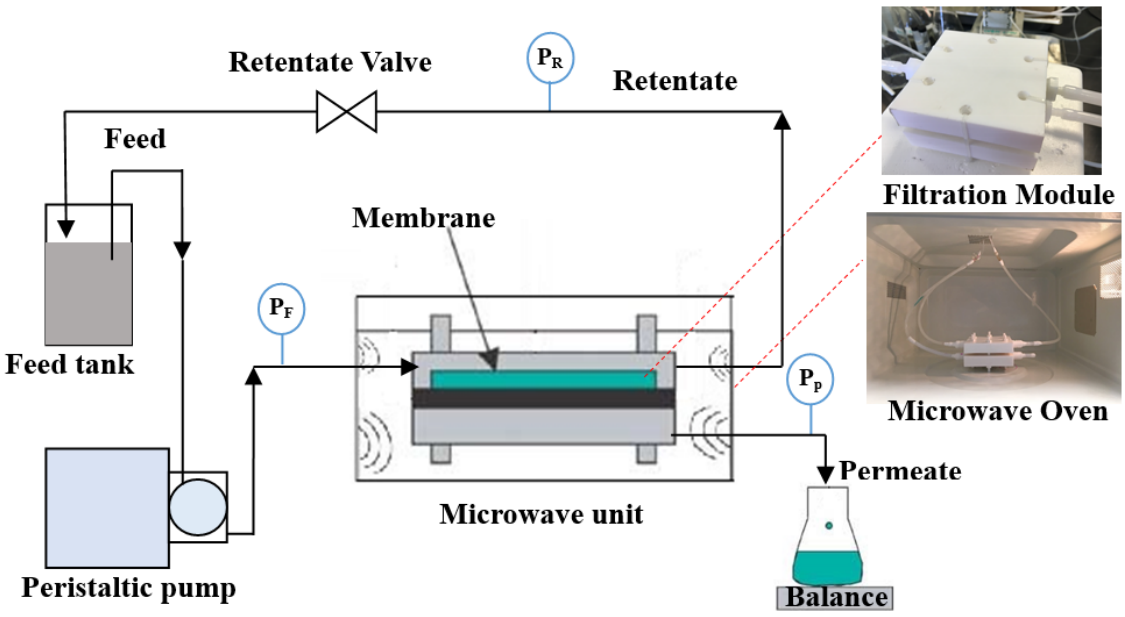

Figure 6.3 Experimental set-up for microwave-assisted membrane filtration system.

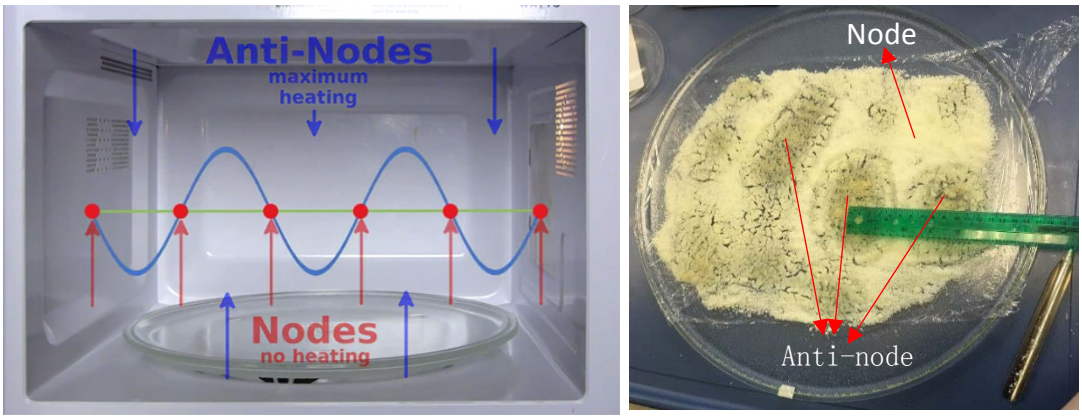

Figure 6.4 The anti-nodes and nodes arrangement of microwave and location of anti-nodes by melting cheese powder.

6.2.4 Pure Water Permeability with and without MW Irradiation Using Pristine and Catalyst-coated Ceramic Membranes

Clean water permeability experiments were performed at a microwave power level of 0, 125 or 250 W. DI water was pumped at a TMP of 34.5 kPa and a constant cross-flow velocity (25 mL min^{-1}) through the filtration cell as a feed to determine the pure water permeability. Before applying MW, the filtration system was run for 30 min to get stable water flux. The variation in permeate flux of the membranes was monitored under various experimental conditions to determine the variations of the permeability coefficient (K_w) by Equation 6.1. To avoid temperature effects, the K_w was normalized to 20 °C.[617, 618]

$$K_w = J_T \times \frac{101.37}{TMP} \times \frac{\mu_{20}}{\mu_T} \tag{6.3}$$

where K_w is the permeability coefficient (L m^{-2} h^{-1} kPa^{-1}) at 34.5 kPa and 20 °C, J_T is the permeate flux (L m^{-2} h^{-1}) at T °C, TMP is the transmembrane pressure (34.5 kPa), μ_{20} and μ_T are the dynamic viscosity of permeate at 20 °C and T °C (Pa s), respectively. Since temperature changes may alter liquid viscosity and influences membrane flux, all fluxes

J_T measured at temperature T were corrected to J_{25} values at temperature 25°C using the following equation:[619]

$$J_{25} = J_T \times 1.025^{25-T} \quad (6.4)$$

where J_{25} is the flux value at temperature 25 °C (L m^{-2} min^{-1}) and T is the temperature when flux J_T is determined (°C).

6.2.5 Filtration of Simulated Pollution Water with and without MW Irradiation Using Pristine and Catalyst-coated Ceramic Membranes

200 mg L^{-1} BSA solution and 10 mg L^{-1} HA solution were used as model foulants and subjected to the membrane filtration w/o MW irradiation under a TMP of 34.5 kPa and a cross-flow velocity of 25 mL min^{-1} to observe the membrane fouling processes. The TMP and flux were recorded every 5 min for 120 min. Membrane permeate and retentate were returned to the feed tank during the filtration process. The feed tank of the filtration system was cooled with ice bag at 23 ^{o}C. When microwave was used the temperature of the membrane cell was recorded every 10 minutes with a Raytek MiniTemp MT4 non-contact infrared thermometer equipped with a laser pointer (Raytek Corporation Santa Cruz, CA, USA).

6.2.6 Removal Performance of Methylene Blue (MB) by MW-assisted Membrane Filtration

Analytical grade methylene blue and hydrogen peroxide (30%) were used for the experimental study. A stock MB solution containing 100 mg L^{-1} was prepared and concentrations of 1, 3 and 5 mg L^{-1} MB solutions were prepared by successive dilutions. A UV–visible spectrophotometer was utilized to measure the MB concentrations in

aqueous samples at 664 nm. All the experiments were conducted in batch mode with a liquid volume of 25 mL in a 40 mL glass tube. Hydrogen peroxide coupled with microwave irradiation was employed to degrade synthetic dye wastewater containing different concentrations of MB (1, 3, and 5 mg L^{-1}). 100 µL or 200 µL of hydrogen peroxide was added and subsequently irradiated with different microwave powers. The H_2O_2 solution acts as an oxidizing agent and also for the generation of hydroxyl radicals using microwave energy. The MB solutions were irradiated at different power levels (125, 250 and 375 W) and for different irradiation times. The kinetic study was carried out at different concentrations of MB for a fixed microwave output power of 125W using 100 µL of H_2O_2. The MB concentration in the samples was determined using a spectrophotometer and the absorbance was measured at 664 nm.

The removal ratio of MB was calculated by:

$$R_{MB}(\%) = \frac{C_0 - C}{C_0} \times 100\% \tag{6.5}$$

where R_{MB} is the removal rate of MB, C_0 and C are initial and instantaneous concentrations of MB (mg L^{-1}), respectively. The energy input for decomposition of MB was calculated:

$$Q = \frac{P \times t}{3600} \tag{6.6}$$

where Q is the energy consumed (W h), P is the microwave power (W), and t is the microwave irradiation time (s).

6.2.7 Assessment of Degradation and Removal Performances of Emerging Organic Pollutants by MW-assisted Membrane Filtration with/without H_2O_2

6.2.7.1 Reagents and Apparatus. Analytical grade 1,4-dioxane (10^4 mg L^{-1}, Sigma-Aldrich) and hydrogen peroxide (30%) were used for the experimental study. Concentrations of 1,4-dioxane were measured using a gas chromatograph (GC, Trace 1300, Thermo Scientific, US) using a TG-624 capillary column (Thermo Scientific, 30 m length×0.25 mm ID×1.4 μm film) equipped with a flame ionization detector (FID) and an auto sampler (Thermo Scientific, A11310, US). The samples were filtered through 0.22-μm syringe filters (Waltham, MA) and the injection amount was 1 μL of the filtered via an auto-sampler.[620]

6.2.7.2 Batch Experiments. The experiments were conducted in batch mode with a working volume of 30 mL 1,4-dioxane solutions (10 mg L^{-1}) in a 40 mL glass vial. Sole hydrogen peroxide (30 mM), sole BFO (1 g L^{-1}), sole MW irradiation (125 W, 60 s), and correspondingly, hydrogen peroxide and/or BFO coupled with microwave irradiation were employed to analyze the degradation mechanism. pH was not varied in our experiments, and instead, the measured pH of 7.5 ± 0.5 in the 1,4-dioxane solutions was the influent pH value for all experiments. In addition, water bath heating at 70 °C was performed to analyze the influence of the high temperatures. Concentrations of 1,4-dioxane were measured by a gas chromatograph (GC, Trace 1300, Thermo Scientific, US) using a TG-624 capillary column (Thermo Scientific, 30 m length×0.25 mm ID×1.4 μm film) equipped with a flame ionization detector (FID) and an auto sampler (Thermo Scientific, A11310, US). The samples were filtered through 0.22-μm syringe filters (Waltham, MA) and the injection amount was 1 μL of the filtered via an auto-sampler [620]. Total organic carbon (TOC) was analyzed by a Sievers 900 portable TOC analyzer.

6.2.7.3 Filtration Experiments. Ceramic membrane coated with BFO was used in a dead-end filtration mode. Microwave was provided at 125 watts with 10 min-on/5min-off cycles. The 1,4-dioxane concentration in the feed tank was 10 mg L^{-1} and the feed pump rate was 5 mL min^{-1}. The H_2O_2 solution (2 w/w.%) was pumped into the filtration cell at 1.75 mL min^{-1}. TMP and temperature (near the permeate outlet port) were recorded during the 120-min filtration process. The permeate samples were taken during each cycle to measure the 1,4-dioxane concentrations. The removal ratio of 1,4-dioxane was calculated by:

$$R\ (\%) = \frac{C_0 - C}{C_0} \times 100\% \tag{6.7}$$

where R is the removal rate of 1,4-dioxane, C_0 and C are initial and instantaneous concentrations of 1,4-dioxane (mg L^{-1}), respectively.

6.2.7.4 Stability Test. The stability of the modified membrane was investigated through five consecutive filtration cycles (60 min per filtration cycle) to study potential membrane fouling and pollutant degradation decline with 10 ppm 1,4-dixoane solution and 5-min hydraulic cleaning (immersing the membrane in DI water and stirring at 200 rpm for 5 min[621]). The transmembrane pressure (TMP) and the 1,4-dixoane removal rate were measured to evaluate the stability of the modified membranes.

6.2.8 Assessment of Microbial Inactivation by MW-assisted Membrane Filtration with/without H_2O_2

6.2.8.1 Bacterial Cultivation and Preparation. The lethal effects of microwave irradiation, hydrogen peroxide and MW-Fenton-like process on bacterial viability were examined and compared. Antibacterial activity was assessed by exposing an *E. coli* (ATCC

25922) to the H_2O_2 or catalyst or their combination with appropriate controls. *E. coli* were incubated in a 15-mL Bertani (LB) medium at 37 °C at a shaker (200 rpm) for 16 h. The suspension was then centrifuged (5810R, Eppendorf AG, Hamburg, Germany) at 2500×g for 15 min, and the supernatant was removed. The remaining cell residue was re-suspended in 15 mL 1X GibcoTM phosphate buffer saline (PBS) solution (Fisher Scientific, Pittsburgh, PA). This procedure of centrifugation and re-suspension in PBS media was repeated twice to remove the remaining LB growth medium.

6.2.8.2 Antibacterial Assessment. 15 mg BFO powder w/o 25 µL H_2O_2 (30 w/w%) sample was added to 30 mL of the bacterial suspension in PBS (~10^4 CFU mL^{-1}) , where there was 0.5 g L^{-1} BFO w/o 10 mM H_2O_2, respectively. A control group was also prepared by adding 25 µL sterile DI water to the bacterial suspension. Bacterial suspensions were then subjected to MW irradiation (30 s at 125 W). Another identical set of samples was kept in the dark for the same exposure time without MW irradiation. Each sample was tested in triplicates. The samples were then serially diluted using 1X PBS, 100 µL samples were pipetted and grown on LB agar plates, incubated for 12-16 h at 37 ºC, and finally the bacterial colony was counted to determine the survival rates. The logarithmic cell removal (Log) was calculated to indicate the antibacterial activity of different conditions. N is the number of *E. coli* removed and N_0 is the initial number of *E. coli* per mL solutions.

6.2.9 Quantum Yield Efficiency Calculation

The quantum yield for a microwave degradation reaction is approximated similar to the common calculation used in photocatalysis.[623]

$$\phi = \frac{\text{rate of reaction induced by photon absorption}}{\text{flux of absorbed photons}} = \frac{\#\text{ molecules decomposed per second}}{\#\text{ photons absorbed per second}} \tag{6.8}$$

The rate of molecules decomposition can be calculated by

$$\#\text{ molecules decomposed per second} = \frac{N_A \cdot V \cdot (C_0 - C_t)}{t} \tag{6.9}$$

where N_A is Avogadro constant (6.02×10^{23} mol^{-1}), V is the solution volume, t is the reaction time (s), C_o is the initial molecules concentration (mol L^{-1}) and C_t is the molecules concentration after the reaction (mol L^{-1}).

The flux of photons absorbed can be calculated by:

$$\#\text{ photons absorbed per second} = \frac{Q - Q_H}{E_P} \tag{6.10}$$

where Q is the microwave power used in the experiment (W), Q_H is the energy converted to heat (W), and E_P is the energy in joules per photon for the microwave, which can be calculated by Planck's equation (Eq. 6.9).

$$E_p = h \times \upsilon \tag{6.11}$$

where h is Planck's constant (6.626×10^{-34} J s), υ is the frequency of the microwave (2.45 GHz, 2.45×10^{9} s^{-1}).

Thus, $E_P = (6.626\times10^{-34}\ \text{J}\cdot\text{s})\times(2.45\times10^{9}\ \text{s}^{-1}) = 1.62\times10^{-24}\ \text{J photon}^{-1}$.

6.2.10 Microwave Heating Efficiency Calculation

Heating efficiency is a measure of how well the microwave oven converts electricity energy source to heat. Efficiency (η) was calculated by the following equations,

$$Q = \frac{m \cdot C_p \cdot (T_s - T_f)}{t} \tag{6.12}$$

$$\eta = \frac{Q}{E} = \frac{Q}{P \cdot t} \tag{6.13}$$

where Q is the heat transferred to the water (joules), m is the mass (weight) of the object (kg), C_p is the specific heat of the object material (J kg^{-1} $^oC^{-1}$), T_s is the starting temperature (^oC), T_f is the final temperature (^oC), P is the power rating of the microwave oven (watt), E is the electrical energy used by the microwave oven within a specific time (joules), t is the time the microwave oven was turned on for (seconds).

6.3 Results and Discussion

6.3.1. Characterization of Functionalized Ceramic Membranes

6.3.1.1 Morphology of BFO Coated Ceramic Membrane. The morphologies of ceramic membrane, BFO and BFO/Ceramic membrane are compared in Figure 6.5. It can be observed that the surface of pristine ceramic membranes contains pores with hundreds nanometer, which is consistent with the reported pore size of 140 nm by the manufacture. The EDX data also showed that the pristine ceramic membrane exhibits a uniform three-dimensional structure with a thin zirconia/titania (Zr/TiO_2) coating on the top surface (Figure 6.5c). Figure 6.5d shows that BFO has a bead structure with a dimension of 5-20

μm while the magnified image showed that these spheres were consisted with numbers of cubic particles (Figure 6.5e). For the BFO/Ceramic membrane in Figure 6.5f, the holes of the ceramic membrane coexist with many irregularly shaped particles. The EDX spectra (Figure 6.5i) also confirmed the existence of titanium, zirconium, oxygen, bismuth and iron elements in BFO/Ceramic membranes, indicating that the ceramic membranes have been coated with BFO particles on the membrane surface.

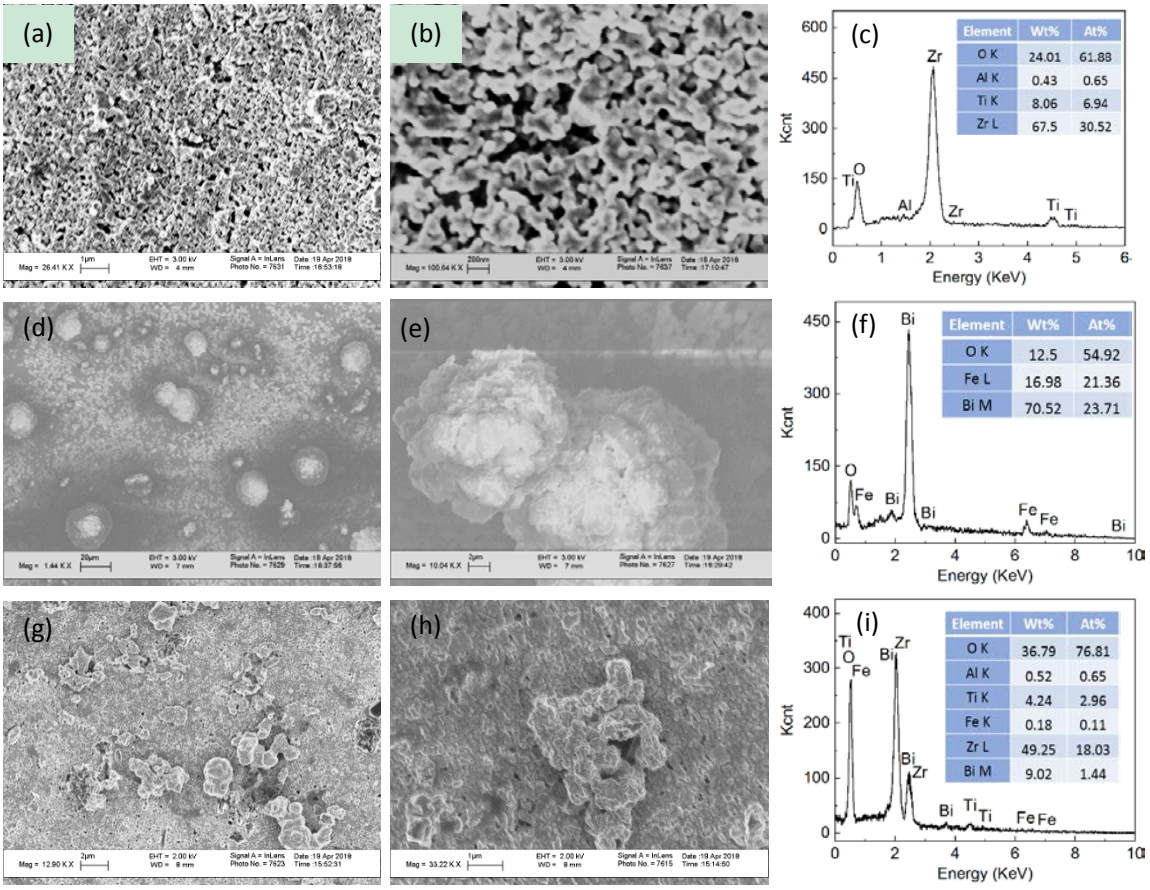

Figure 6.5 Morphology and EDX analysis of (a-c) pristine ceramic membrane, (d-f) BFO catalysts and (g-i) BFO/Ceramic membrane.

6.3.1.2 Crystallinity of BFO/Ceramic Membrane. Figure 6.6 shows that the XRD characteristic peaks of BFO and TiO_2/ZrO from the ceramic membrane surface. The XRD pattern of BFO can be indexed to the standard pattern of $BiFeO_3$, which is in good

agreement with the reported data (JCPDS No. 84-7214). Three observed peaks with 2θ values of 22.4°, 32.1°, 39.5°, 45.7° and 57.1° correspond to the (012), (110), (202), (024) and (300) diffraction peaks of crystalline bismuth iron oxide, respectively. The peaks at 60.5° marked as (▲) confirmed the existence of γ-Al_2O_3 on unmodified ceramic membrane. The XRD peaks at 30.3° and 50.4° match with the reported data (JCPDS No. 70-7301) for Zirconium oxide ZrO_2, and peaks at 27.6°, 54.7° and 63.0° match with the reported data (JCPDS No. 04-005-6161) for Titanium oxide TiO_2, which indicated the presence of ZrO_2 and TiO_2 on the ceramic membrane, respectively.

The XRD patterns of BFO coated ceramic membrane was almost the exact combination of XRD patterns of BFO and ceramic membrane composites, suggesting that the crystal structure of ceramic membrane was not modified by BFO coating. Meanwhile, all the characteristic peaks of BFO were detected on the surface of BFO-coated ceramic membrane, indicating that BFO has been successfully coated on ceramic membrane.

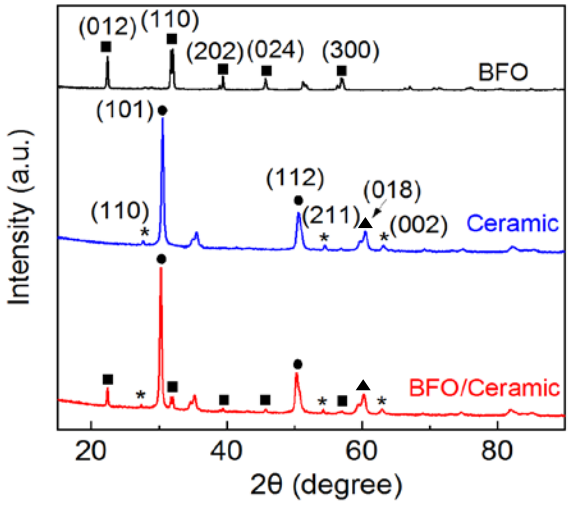

Figure 6.6 X-ray diffraction patterns of BFO, pristine ceramic membrane and BFO coated ceramic membrane. The symbols on the blue curve of the modified ceramic membrane denotes the major peaks of BFO (■), γ-Al_2O_3 (▲), TiO2 (*) and ZrO (●).

6.3.2 Nanobubbles Formation under Microwave Irradiation

Figure 6.7 shows the results of the hydrodynamic diameter distribution of bubbles produced in DI water under different treatment conditions. Without the microwave irradiation, no positive signals were detected as there was only one peak at 10 nm or smaller with a very low zeta potential value of -3.7 mV, which might be attributed to the instrumental noise. It should be noted that most measurements were aborted since there was no nanobubbles detected in pure water before microwave irradiation. After the microwave irradiation, bubbles of different sizes were detected as indicated by the multiple peaks that randomly involved. Some were in greater sizes like 1 μm or larger, which were clearly micro-bubbles, whereas some were tens to hundreds of nanometers. These peaks indicate the formation of micro-bubbles or nanobubbles also because of the pronounced level of negative zeta potentials, which is close to the reported values of air nanobubbles (-17 to -20 mV at neutral pHs) in water.[267] For example, the average particle diameter was 70 nm for the DI water treated with 125 W MW for 15 s and 4 times. 200 nm for the sample treated with MW for 30 s and 2 times; and 400 nm for the sample treated with MW for 10 s and 6 times. Yusuke *et al*. also reported the generation of nanobubbles in pure water by microwave irradiation.[624] Figure 6.8a shows size and temperature profiles in water during and after microwave irradiation for irradiation time until 90 °C. Closed and open symbols indicate sizes during and after microwave irradiation, respectively, and lines indicate the temperature profile. The bubble size in water increased during microwave irradiation and the bubble size was a maximum around the time the microwave was turned off. Figure 6.8b showed that longer irradiation time is more effective for attaining maximum bubble size in water because it takes more time for lower power to reach designated temperature. Figure

6.8a shows that temperature increased with irradiation time and dropped gradually after irradiation. But nanobubbles have high energy because the pressure and temperature are too high theoretically. Moreover, free radicals, which are important for chemical reaction, are generated after the collapse due to the self-pressurizing effect of nanobubbles (bubble contraction). However, bubble size profiles in water could not be explained only by irradiation time.[624] Figure 6.7 also shows that MW irradiation for 30s with 2 times had the biggest bubble size than shorter irradiation time with more times, which is consistent with this previous study.

Wang *et al*. also generated nanobubbles via microwave irradiation and observed the numbers and sizes of nanobubbles via AFM measurement.[290] It showed that nanobubbles with diameters ranging from 200 to 600 nm with irradiation time from 60 to 120s by 200 W microwave treatment.[290] However, it did not investigate the specific nanobubbles size distribution under different irradiation time. Further investigation of nanobubbles formation on ceramic membranes is be carried out with the AFM liquid cell.

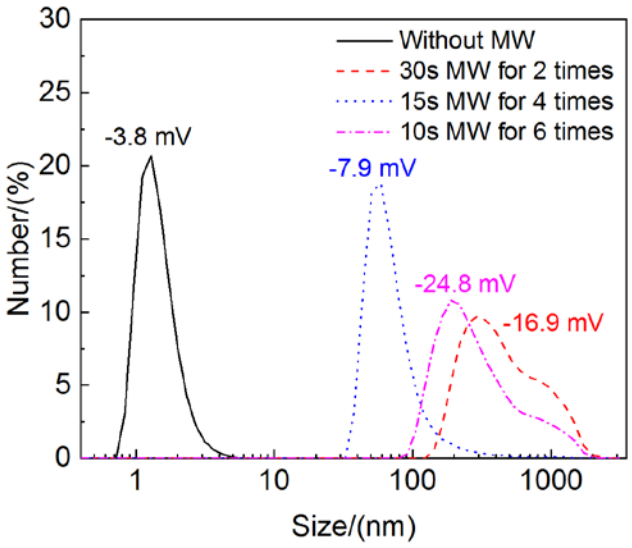

Figure 6.7 The size distribution and zeta potential measurement of DI water samples.

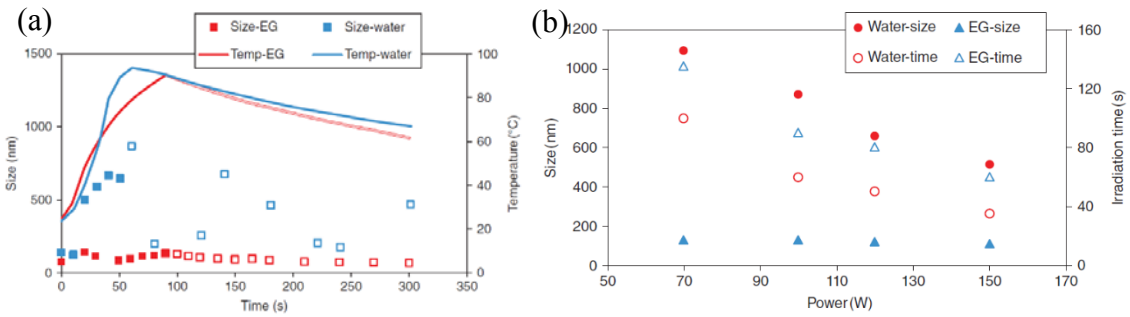

Figure 6.8 (a) Size and temperature profiles for water and ethylene glycol during and after microwave irradiation; (b) maximum size and irradiation time versus irradiation power during and after microwave irradiation (90 °C).[624]

6.3.3 Analysis of Hydroxyl Radicals (•OH)

The fluorescence spectra of 2-hydroxyterephthalic acid were used as indicators for the amounts of •OH generated during microwave irradiation processes. Figure 6.9a shows no obvious PL increase was observed in the absence of H_2O_2 samples (sole MW irradiation or BFO/MW system). This suggests that the fluorescence is caused by chemical reactions of terephthalic acid with •OH formed by H_2O_2. Figure 6.9a shows that the amount •OH generated in the BFO/H_2O_2/MW system was lower than that in the H_2O_2/MW system. The amounts of •OH generated were related to the degradation capabilities, the generation of •OH was larger, the more pollutant molecules could be degraded, which implied the superior performance of microwave irradiation system.

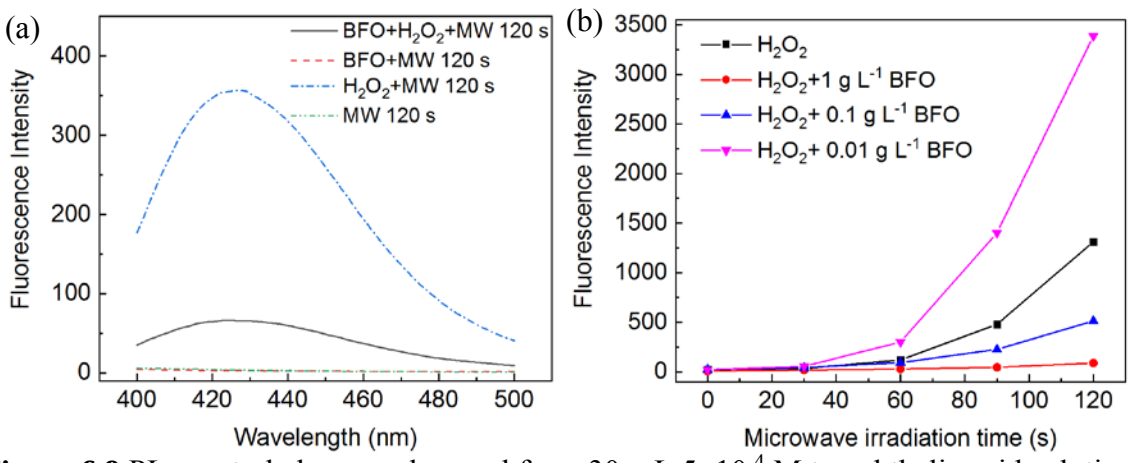

Figure 6.9 PL spectral changes observed from 30 mL 5×10^{-4} M terephthalic acid solution in 2×10^{-3} M NaOH: (a) under different conditions with 120 s MW; and (b) under different microwave irradiation time with 3 mM H_2O_2 and different BFO dosages. Each fluorescence spectrum was recorded with excitation wavelength at 315 nm.

Since H_2O_2 is a possible reaction intermediate, the effect of H_2O_2 on the •OH production was investigated. Before the irradiation, 10 μL of H_2O_2 solution (30%) was added into the 30 mL of terephthalic acid aqueous solution, which corresponds to the H_2O_2 concentration of 3 mM in the test suspension. It can be seen from Figure 6.9b that a gradual increase in PL intensity at about 425 nm is observed with increasing microwave irradiation time, indicating that microwave irradiation possibly increased the •OH generation by H_2O_2, which is consistent with previous studies.[625] It also showed the BFO/H_2O_2/MW system with less BFO generated more radicals under the same irradiation time, the specific reason for this phenomena might be due to the blockage by the BFO nanoparticles in the solution for the fluorescence detection. Besides, it is reported that extremely high temperatures can cause the elimination of the oxidative species. It indicated that the addition of an excess of BFO might cause extremely high temperature or lots of "hot-spots" and have a negative effect on the generation of hydroxyl radicals. Thus, even though higher temperature is beneficial for increasing the reaction rate constant, the temperature should be maintained

at an optimum level by means of various cooling technologies that use pulse MW irradiation, condensers, heat exchangers and cooling coils, etc.

Usually, a catalyst or a suitable MW absorbent was used to accelerate the treatment process (*i.e.*, to shorten the treatment time) in MW-H_2O_2 system.[626] The catalyst, BFO in this study, has been used in many wastewater treatment processes as a photocatalyst or microwave-catalyst.[625, 627-629] Under MW irradiation, the "hot spots" effect may be able to promote the catalytic capacity of the catalyst via the high temperature and enhance the •OH generation.

Figure 6.10 showed the temperature changes under different irradiation time, it showed that the three systems achieved the same level of high temperature after 120 s MW irradiation, indicating that the enhanced generation of radicals by MW irradiation is not due to the high temperature but the non-thermal effects of MW irradiation. It is reported that the non-thermal effect of MW greatly increased the formation of •OH due to the excitation of H_2O_2 molecules to higher vibrational and rotational energy levels, and then the chemical bond of H_2O_2 molecules could be weakened and broken to generate •OH.[599]

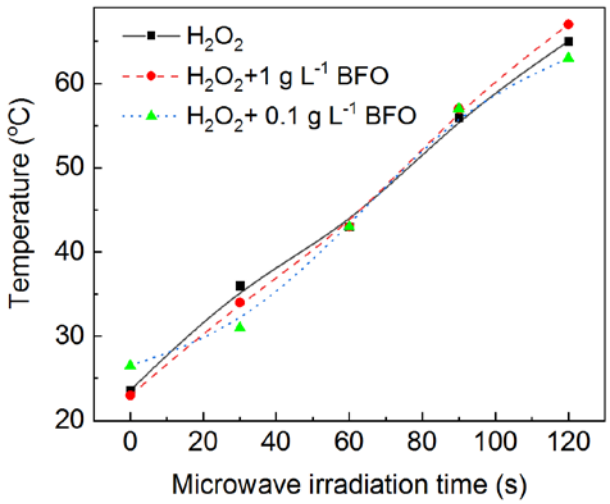

Figure 6.10 Temperature changes observed from 30 mL 5×10^{-4} M terephthalic acid solution in 2×10^{-3} M NaOH: 125 W microwave irradiation, 3 mM H_2O_2 and 1 g L^{-1} or 0.1 g L^{-1} BFO.

Furthermore, it is reported that an excess of H_2O_2 could cause the side reactions (Equation 6.10), which indicated obvious elimination of oxidative species, leading to a significant decrease of organic degradation efficiency. Thus, optimum H_2O_2 concentration should be determined with batch experiments.[599] In this study, 3 mM H_2O_2 was used to avoid this negative effect.

$$H_2O_2 + \bullet OH \rightarrow \bullet HO_2 + H_2O \quad (6.14)$$

$$\bullet OH + \bullet HO_2 \rightarrow H_2O + O_2 \quad (6.15)$$

It also showed the BFO/H2O2/MW system with less BFO generated more radicals under the same irradiation time in Figure 6.11, and the specific reason for this phenomena might be due to the blockage by the BFO nanoparticles in the solution for the fluorescence detection. Besides, it is reported that extremely high temperatures can cause the elimination of the oxidative species. It indicated that the addition of an excess of BFO might cause extremely high temperature or lots of "hot-spots" and have a negative effect on the generation of hydroxyl radicals. Thus, even though higher temperature is beneficial for increasing the reaction rate constant, the temperature should be maintained at an optimum level by means of various cooling technologies that use pulse MW irradiation, condensers, heat exchangers and cooling coils, etc.

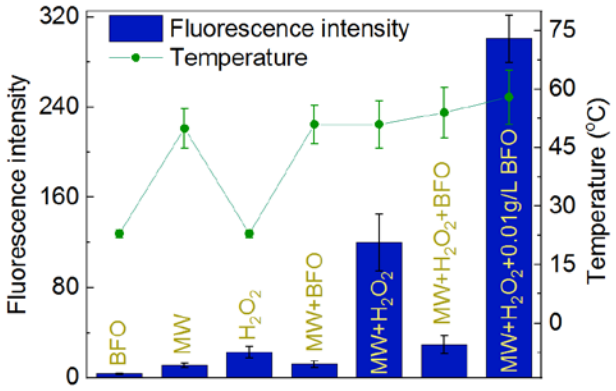

Figure 6.11 Fluorescence intensity changes at 425 nm with excitation wavelength at 315 nm observed from 30 mL 5×10^{-4} M terephthalic acid solution in 2×10^{-3} M NaOH under different experimental conditions. (MW 125 W, 60 s irradiation, 10 mg L^{-1} 1,4-dioxane, 30 mM H_2O_2, 1 g L^{-1} catalyst). All error bars represent standard deviation from triplicate experiments.

6.3.4 Filtration Experiments with Pure Water and Simulated Foulant Solutions

Water permeation of the modified membranes was monitored and compared with the pristine ceramic membrane. Figure 6.12a shows that the pure water permeability for both the pristine and BFO-coated ceramic membranes was enhanced almost twice under MW irradiation. However, no significant difference in water permeability was found between pristine and modified membranes. The elevated water permeability could be primarily attributed to the increasing water temperature (from 23±2 °C to 56±4 °C), which may alter the liquid viscosity and enhance the membrane flux. The increased flux under high temperatures was also reported in previous studies [604, 617, 618]. We did the control experiment with mildly heated water (60±5 °C) as the feed. The results (Figure 6.13) show that the water permeability was higher than that with the feed of room temperature (23±2 °C). Thus, a normalized flux at 25 °C was calculated to eliminate the influence of temperature on the membrane flux. Figure 6.12b shows that the normalized fluxes were similar under different MW power levels, confirming that the increased water permeability was solely due to the elevated temperature caused by MW irradiation.

On other hand, the temperature of the water passing through the heated membrane depends on MW irradiation intensity and filtration flux. As shown in Figure 6.12b, the permeate solution temperature increased up to 55 ^{o}C when passing through the irradiated membranes at ~380 LMH under 125 W MW irradiation. To avoid water heating that may increase energy loss, controlling proper levels of MW irradiation and membrane flux is critical. Our results indicate that the temperature of permeate water decreased with the increase of permeate flux. For example, the permeate temperature changed from 23.8 to 30.4 ^{o}C when the permeate flux was ~772 LMH under 125 W MW irradiation (Figure 6.13).

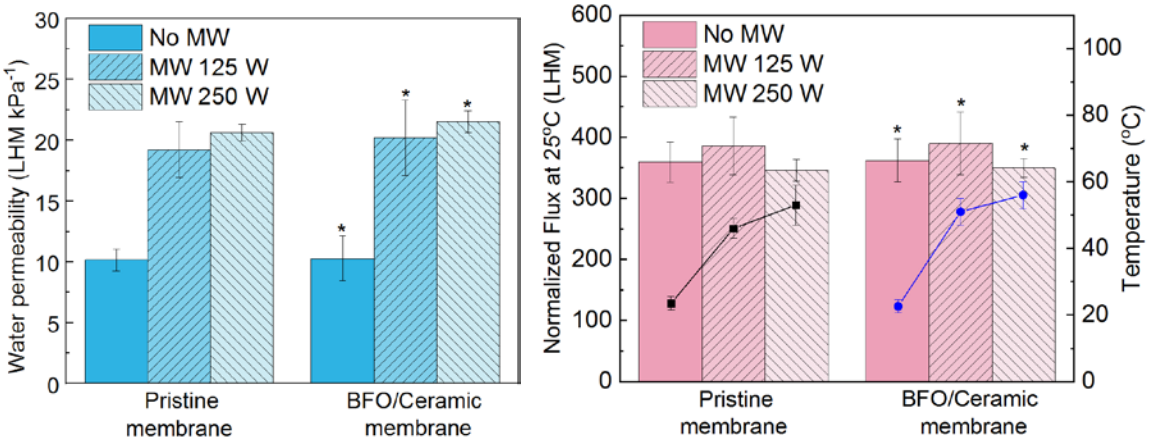

Figure 6.12 Pure water permeability, and normalized flux at 25°C of pristine membrane and BFO-coated ceramic membrane. The membrane filtration area was 10.2 cm^2 and the normalized flux was calculated under 35 kPa. All error bars represent standard deviation from triplicate experiments. * No significant difference was observed between the pristine and BFO-coated ceramic membranes.

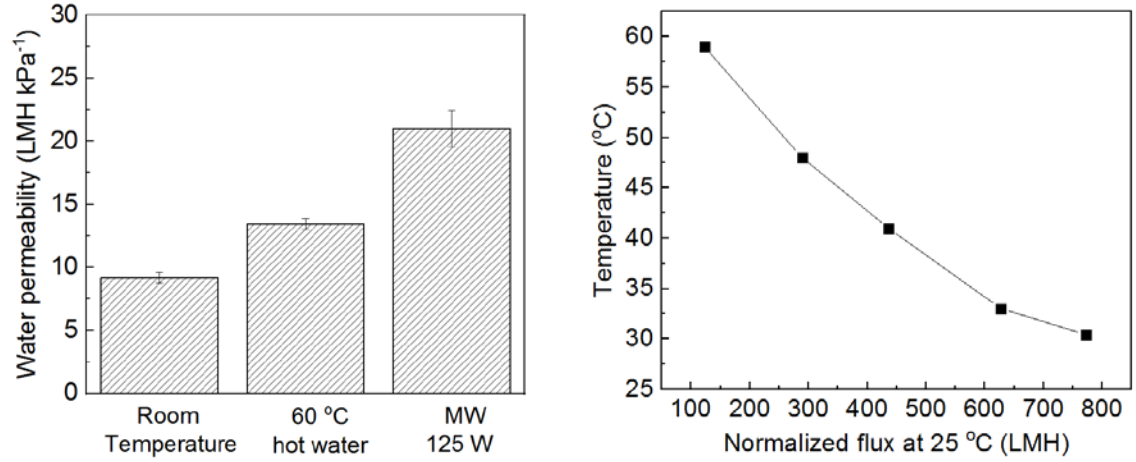

Figure 6.13 (a) Pure water permeability of pristine membrane under different conditions; and (b) Temperature changes of permeate with different permeate flux under MW irradiation of 125 W. The initial feed solution temperature was 24 ± 0.5 °C.

Without MW irradiation, the pure water permeability of membranes before and after the modification had no significant difference (see Figure 6.12a). Table 6.1 shows the overall membrane porosity and mean pore sizes of the BFO-coated membrane increased slightly, probably because the coating layer of the BFO catalysts increased the overall membrane porosity. However, Figure 6.14 shows the surface pores of the BFO-coated

membranes were apparently blocked by the deposited BFO catalysts, which slightly reduced the surface pore size distribution according to the ImageJ analysis in Figure 6.14c.

Table 6.1 Properties of the Membranes: Overall Porosity and Mean Pore Radius

Membrane	Porosity (%)	Mean pore radius (nm)
Pristine	50.9%	258
BFO-Coated	53.2%	272

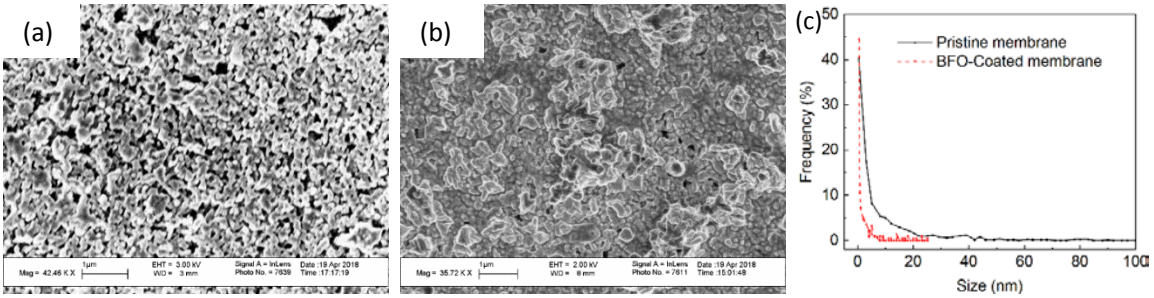

Figure 6.14 Membrane top surface image (a) before and (b) after modification and (c) membrane pore size distribution analyzed with ImageJ.

The variation in permeate flux of the membranes was monitored under various experimental conditions and compared by evaluating variations of the permeability coefficient (K_w), calculated by Equation 6.3. Figure 6.15 shows that the pure water permeability was enhanced almost two times by 125 W and 250 W MW irradiation. Since temperature changes may alter liquid viscosity and influences membrane flux, Equation 6.4 was used to eliminate the influence of temperature on membrane flux. It shows that the normalized flux at 25 ^{o}C was similar with higher MW power level, indicating that the increased water permeability was solely due to the higher temperature (23.5 ^{o}C for no MW, 46 ^{o}C for 125 W MW, and 53 ^{o}C for 250 W MW) caused by MW irradiation.

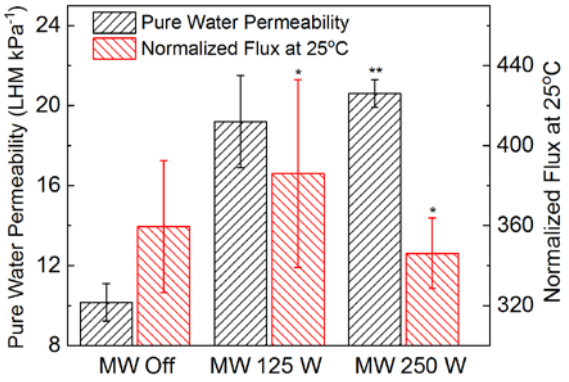

Figure 6.15 Pure water permeability (K_w) and normalized flux at 25°C (J_{25}) using ceramic membrane under different MW power levels. The membrane filtration area was 10.3 cm^2 and the normalized flux was calculated under 5 psi.

* No significant difference observed over the control group (MW Off).
** No significant difference observed over the parallel group (MW 125 W).

Figure 6.16 is the results for the filtration experiments and it shows that the fouling could be mitigated greatly with 250 W microwave irradiation while 125 W MW irradiation did not help much on flux maintenance or neither on the HA rejection during the filtration. With increasing MW irradiation time, the temperature of the filtration cell increased fast during the beginning 10-20 minutes and then kept stable for different irradiation power levels. Under 250 W MW irradiation, the temperature increased to a much higher level than that under 125 W MW irradiation. It indicated that the thermal effect is likely to be the dominant mechanism for the antifouling results.

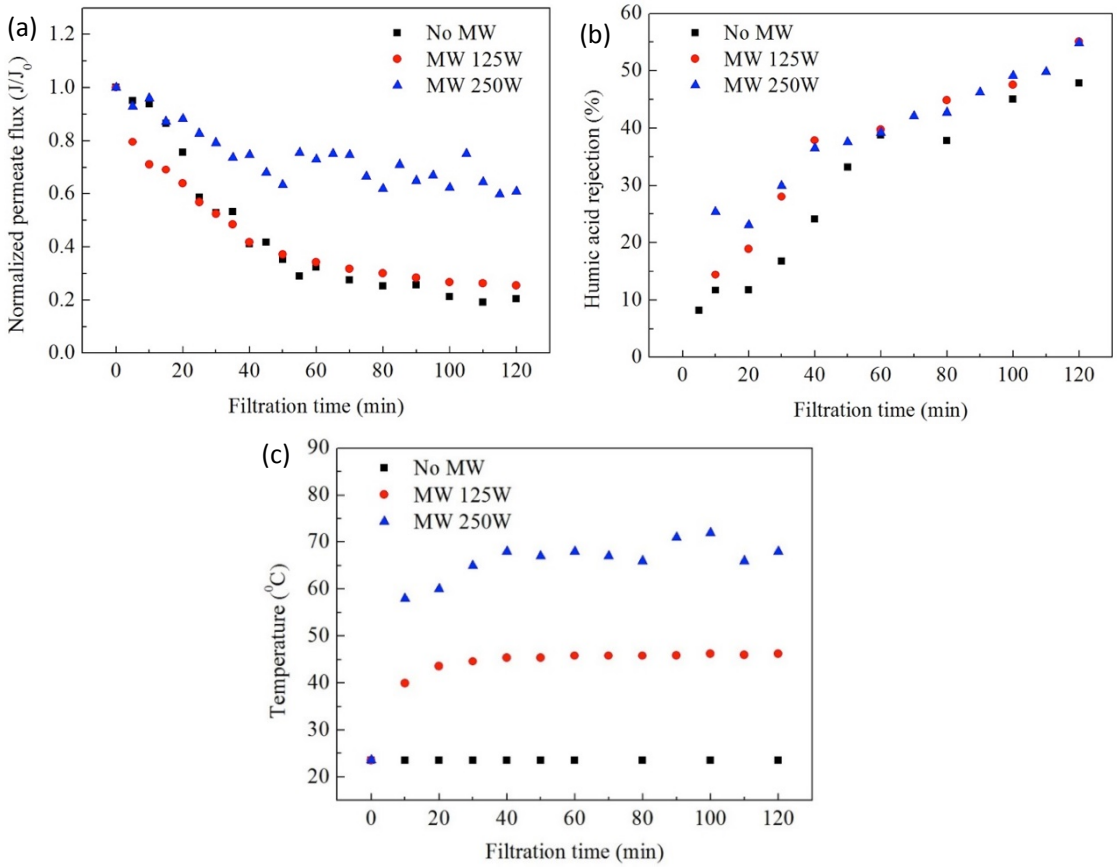

Figure 6.16 Permeate flux (a), humic acid rejection (b) and temperatures (c) during the 2 h HA filtration under different MW power levels. The HA solution concentration was 10 mg L^{-1}. The filtration pressure was 5 psi.

6.3.5 MW/H_2O_2 Degradation of MB Solutions

6.3.5.1 Effect of Variables on the Decomposition of MB. To determine the influences of microwave (MW) irradiation, hydrogen peroxide (H_2O_2) and their synergistic effects, experiments were conducted to compare the MB decomposition under MW irradiation alone, H_2O_2 alone, and MW irradiation with H_2O_2 for different exposure times. Our preliminary results show that microwave irradiation significantly enhanced the oxidation of MB, which was bleached faster than H_2O_2 without MW irradiation and the microwave irradiation alone (Figure 6.17). This indicates that in the MW-H_2O_2 system, H_2O_2 had the capacity to generate more radicals under stimulation by MW irradiation and

degraded the pollutants with hydroxyl radicals (•OH, 2.8 V of redox potential).[630] The mechanism involved in the MW-H_2O_2 system is shown in reaction equations below:

$$H_2O_2 \xrightarrow{MW} 2 \bullet OH \tag{6.16}$$

$$\bullet OH + Dye \rightarrow Products \tag{6.17}$$

Furthermore, the temperature under MW irradiation can rise rapidly compared with conventional heating due to the polarization effect of the water molecules and H_2O_2 molecules. And high temperature is beneficial for the degradation reaction in a short time period because of the increase in the reaction rate constant according to the Arrhenius equation.[631, 632]

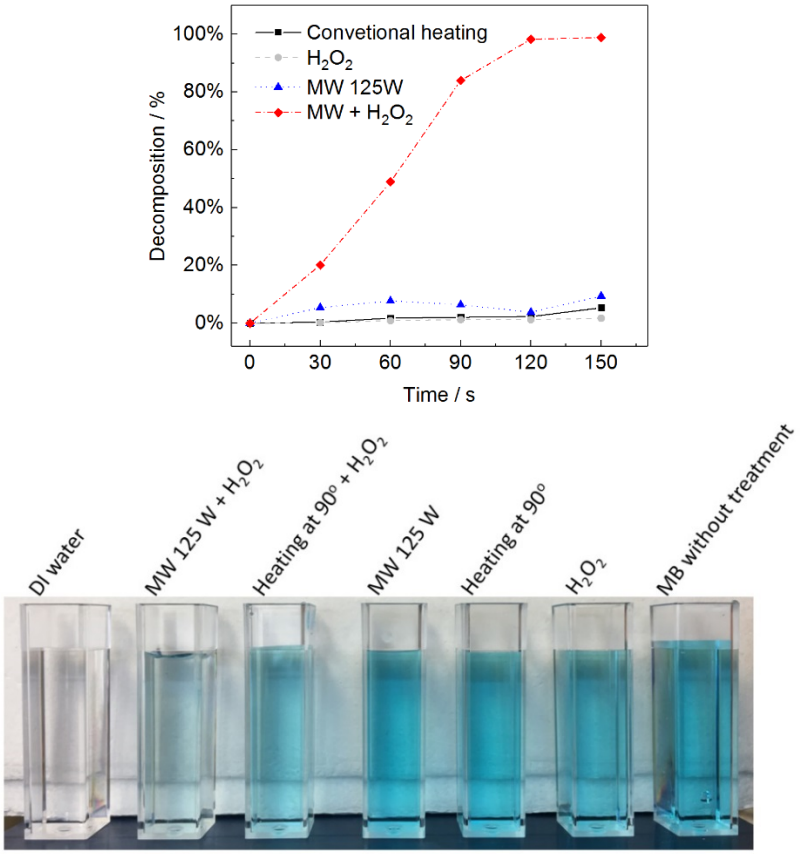

Figure 6.17 Effect of microwave irradiation on MB decomposition (microwave power 125 W, initial MB concentration 1 mg L^{-1}, 90 s).

Figure 6.18a show the influence of microwave power 125, 250 and 375 W respectively on MB decomposition for different irradiation times. The figures show that as the power increases the efficiency of MB removal increases. The hydroxyl radicals formed from H_2O_2 in the presence of microwave energy react preferentially by addition to aromatic moieties. The addition of hydroxyl radicals leads to the formation of hydroxycyclohexadienyl radicals, which may undergo a variety of reactions, the most important being hydroxylation.[631] To assess the influence of the initial concentration on MB degradation, experiments were conducted at varying MB concentrations (1, 3, and 5 mg L^{-1}). From Figure 6.181b, it can be seen that the degradation of MB declines with an increase in the initial concentration, due to the higher requirement of hydroxyl radicals for the decomposition process. The calculated consumption values were 6.25 W h at 125 W, 5.56 kW h at 250 W, and 5.21 W h at 375 W, respectively, when the decomposition rate was reaching 80%. It shows that the electrical energy consumed at 125 W microwave power was the lowest power consumption, which indicated the most efficient microwave power setting.

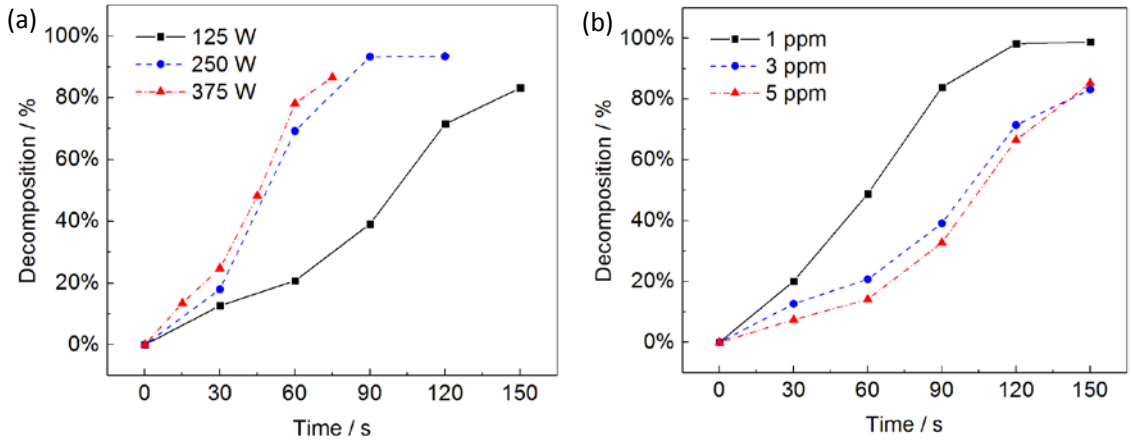

Figure 6.18 (a) Effect of microwave irradiation power level on MB decomposition (initial MB concentration 3 mg L^{-1}, H_2O_2 100 µL); (b) Effect of initial MB concentration on MB decomposition (MW power 125 W, H_2O_2 100 µL).

In order to study the thermal effect on the decomposition of MB, experiments were conducted, with and without MW irradiation. Initially the degradation processes were conducted at various MW power inputs for different time intervals and the final solution temperature was measured at the specified time (Figure 6.19a). Then by fixing the temperature, the degradation experiments were once again conducted using conventional heating for each experimental condition. Figure 6.19b compares the reduction in MB concentration with and without MW irradiation for different time intervals. It can be observed from the figure that the decomposition of MB was always higher for MW irradiation conditions than for conventional heating.

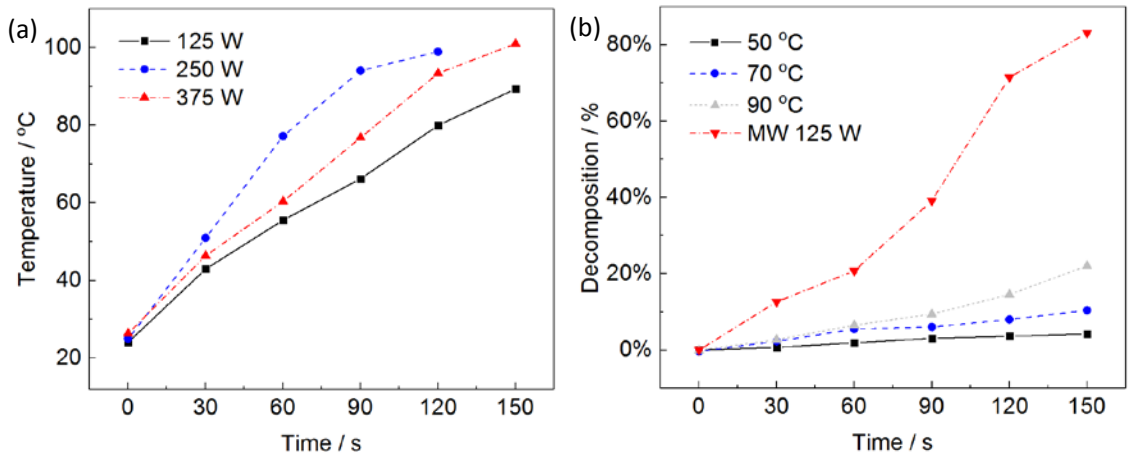

Figure 6.19 (a) Temperature changes with different MW irradiation power levels and times; (b) Comparison of conventional heating at several temperatures with of MW irradiation on MB decomposition (intial MB concentration 3 mg L^{-1}, H_2O_2 100 µL).

The rate of the decomposition process was analyzed using the experimental data obtained with various initial concentrations of MB (1, 3 and 5 mg L^{-1}). Since it was difficult to assess the degradation rate at high microwave power, the lower microwave power (125 W) was chosen for the kinetic study. During the decomposition process, a number of reactions occur and so difficulties arise in predicting the individual rate constants of the reactions, which leads the way to finding the overall rate constant of the decomposition

process. The experimental data were fitted with a zero-order and first-order kinetic model as shown below:

$$\text{Zero-order:} \quad -(C - C_0)/C_0 = Kt \tag{6.18}$$

$$\text{First-order:} \quad -\ln(C/C_0) = Kt \tag{6.19}$$

where C_0 is initial concentration, C final concentration, K rate constant and t irradiation time.

The microwave-Fenton-like degrdation of other pollutants (*i.e.*, BPA, RhB, PFOA) mostly follows pseudo first order kinetcs.[625, 627, 633] However, the present experimental data fitted indeed better with the zero-order kinetic model better with R^2 values higher than 0.95 (Figure 6.20a). It might because no catalyst was used in this study. The slope of the graph $-(C - C_0)/C_0$ vs irradiation time (t) represents the rate constant of the overall decomposition process for the zero-order reaction. The K values for 1, 3, and 5 mg L^{-1} were 0.0076, 0.0053 and 0.0050 mg L^{-1} s^{-1} respectively. The slope of the graph $-\ln(C/C_0)$ vs irradiation time (t) represents the rate constant of the overall decomposition process for the first-order reaction. The K values for 1, 3, and 5 mg L^{-1} were 0.0276, 0.0097 and 0.0094 s^{-1} respectively. From the graph (Figure 6.18b), it was observed that the rate of decomposition decreased with increase in initial concentration of MB but the decomposition rate for 1 and 3 mg L^{-1} were almost the same, which was also confirmed by the K value.

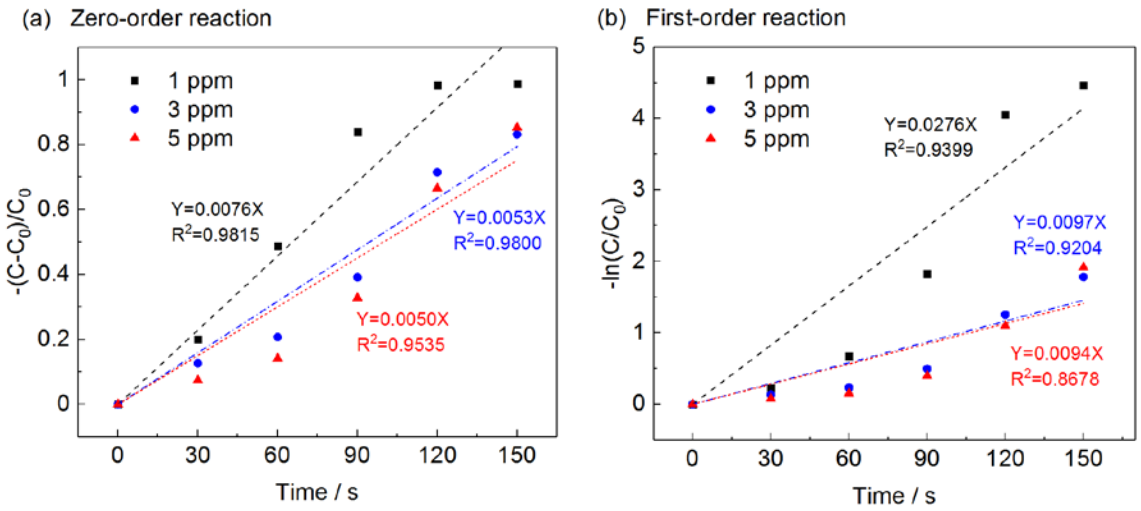

Figure 6.20 (a) Zero-order kinetics for MB decomposition and (b) first-order kinetics for MB decompostion.

6.3.5.2 Quantum Yield Efficiency Calculation. The rate of molecules decomposition for MB in Figure 6.18b was calculated with Equation 6.9.

$$\#\ \text{molecules decomposed per second} = \frac{N_A \cdot V \cdot (C_0 - C_t)}{t} = 6.4\times10^{14}\ \text{s}^{-1}$$

where N_A is Avogadro constant (6.02×10^{23} mol^{-1}), V is the solution volume (25 mL), t is the reaction time (150 s), C_o is the initial molecules concentration (3 mg L^{-1}, 8×10^{-6} mol L^{-1}) and C_t is the molecules concentration after the reaction (20% of C_o, 1.6×10^{-6} mol L^{-1}).

If the energy loss due to heating water is ignored, the total flux of MW photons absorbed can be calculated by Equation 6.10:

$$\#\ \text{photons absorbed per second} = \frac{Q}{E_P} = 7.7\times10^{25}\ \text{s}^{-1}$$

where Q is the microwave power used in the experiment (125 W), and E_P is the energy in joules per photon for the microwave (1.62×10^{-24} J photon^{-1}).

The apparent quantum yield, ϕ, is equal to:

$$\phi = \frac{\#\text{ molecules decomposed per second}}{\#\text{ photons absorbed per second}} = \frac{6.4\times10^{14}\ \text{s}^{-1}}{7.7\times10^{25}\ \text{s}^{-1}} = 8.3\times10^{-12}$$

If considering the heat loss, the microwave power converted to heat can be calculated by Equation 6.20.

$$Q_H = \frac{m\cdot C_p\cdot(T_f - T_s)}{t} = 45.5\ \text{W} \tag{6.20}$$

where Q_H is the energy converted to heat (W), m is the mass of the solution (25 g), C_p is the specific heat of the object material (4.2 kJ kg^{-1} $^{o}\text{C}^{-1}$), T_s is the starting temperature (25 ^{o}C), T_f is the final temperature (90 ^{o}C), t is the time the microwave oven was turned on (150 s). Thus,

$$\#\text{ photons absorbed per second} = \frac{Q - Q_H}{E_P} = \frac{125 - 45.5}{1.62\times10^{-24}} = 4.9\times10^{25}$$

where Q is the microwave power used in the experiment (125 W), Q_H is the energy converted to heat (45.5 W), and E_P is the energy in joules per photon for the microwave (1.62×10^{-24} J photon^{-1}).

The revised quantum yield will be:

$$\phi = \frac{\#\text{ molecules decomposed per second}}{\#\text{ photons absorbed per second}} = \frac{6.4\times10^{14}\ \text{s}^{-1}}{4.9\times10^{25}\ \text{s}^{-1}} = 1.3\times10^{-11}$$

Further considering the energy loss for water vaporization, the microwave power converted to heat can be calculated by Equation 6.21.

$$Q_H = \frac{(m - m_v)\cdot C_p\cdot(T_f - T_s)}{t} + \frac{m_v\cdot C_p\cdot(100 - T_s) + m_v\cdot H_{vap}}{t} = 76.2\ \text{W} \tag{6.21}$$

where m_v is the mass of the water vapor (for this microwave test, 2 g of water vaporized as calculated by the loss of solution weight after the reaction), H_{vap} is the vaporization heat of water (2.26 kJ g^{-1}), t is the time the microwave oven was turned on for (150 s).

The effective available MW energy is reduced to:

$$\#\text{ photons absorbed per second} = \frac{Q - Q_H}{E_P} = \frac{125 - 76.2}{1.62 \times 10^{-24}} = 3 \times 10^{25}$$

Thus, the revised quantum yield is:

$$\phi = \frac{\#\text{ molecules decomposed per second}}{\#\text{ photons absorbed per second}} = \frac{6.4 \times 10^{14}\ \text{s}^{-1}}{3 \times 10^{25}\ \text{s}^{-1}} = 2.1 \times 10^{-11}$$

6.3.5.3 Energy Loss from Heating Water. The membrane filtration system was specially designed such that water is of a small mass portion among all membrane module components (*e.g.*, membranes, holders, supports), which aims to avoid absorption of MW energy by water while maximizing the absorption by solid catalyst on membrane. In our laboratory filtration module, the water volume in the filtration cell is ~2 mL and the filtration flow was constant at ~6.75 mL min^{-1} (flux: ~380 LMH), which resulted in a hydraulic retention time (HRT) of ~24 s. Thus, water heating during such a short HRT is very limited and can be negligible. We calculated the energy loss from heating water below:

$$Q_H = \frac{m \cdot C_p \cdot (T_f - T_s)}{t} = 11.5\ \text{W}$$

where Q_H is the energy converted to heat (W), m is the mass of the water in the filtration cell (2 g), C_p is the specific heat of water (4.2 kJ kg^{-1} $^oC^{-1}$), T_s is the starting temperature (23 ^oC), T_f is the final temperature (56 ^oC), t is the hydraulic retention time of water in the

filtration cell (24 s). Thus, the heat loss due to the water heating was around 11.5 W, which was less than 10% of the total energy of MW irradiation (125 W).

To further reduce the water heating issue, we may potentially decrease the HRT by increasing the flux as shown in Figure 6.13b while not compromising the desirable degradation rates of target pollutants. The focus of this study was to test the feasibility of this novel MW-assisted membrane filtration process and to share new insight into reactive membrane filtration processes with enhanced degradation and antifouling features. A comprehensive and reasonable techno-economic analysis could be done on a scaled-up system with considerations of potential cost reduction from the improved filtration flux, reduced backwashing frequency and reduced chemical cleaning, which is a focus in future studies.

6.3.6 Degradation and Removal Performances of Emerging Organic Pollutants by MW-assisted Membrane Filtration with/without H_2O_2

6.3.6.1 Decomposition of 1,4-dioxane in a Batch Mode. Before the degradation experiment, the adsorption–desorption equilibrium of 1,4-dioxane on the catalyst surface was achieved. The catalysts (BFO, 1.0 g L^{-1}) were dispersed into 30 mL of 1,4-dioxane aqueous solution (10.0 mg L^{-1}) with agitation for 30.0 min. Samples were taken at given time intervals (5.0 min) and the adsorption curve of the 1,4-dioxane in the presence of BFO catalysts were shown in the Figure 6.21a. It shows that BFO had an adsorption capacity of 0.01 g-1,4-dioxane g-BFO^{-1}, which was attributed to its large surface area and small pore diameter.[634] The adsorption capacity was not high, it might because that the low concentration of 1,4-dioxane caused low mas transfer rate of the pollutants (*i.e.*, the pollutant cannot approach the active sites on the absorbents).

Since microwave irradiation increases molecular motion, collision and possibly •OH generation, we expect that microwave irradiation will also facilitate the degradation of 1,4-dioxane. Figure 6.21b shows that the removal rate of 1,4-dioxane increased with the increasing MW irradiation time. Besides, as a source of •OH, H_2O_2 play a joint role with microwave irradiation and catalyst dose in the degradation of 1,4-dioxane. Compared with H_2O_2 alone (7% removal rate, which is not shown in the graph), the removal rate of 1,4-dioxane was enhanced much more with the addition of BFO. It is reported that the formation of standing waves during MW irradiation leads to the overheating of some spots on the MW absorbent (BFO catalyst in this study).The temperature of this kind of spots on the catalyst could be as high as 1000 ^oC or more, referred to as "hot spots",[635, 636] which was proven to have the capacity to promote the degradation of organic pollutants due to its high temperature.[637] 1,4-dioxane was reported to be unstable at elevated temperatures and pressures.[638] The high temperature caused by the superheating effect of MW irradiation and the localized high pressure caused by the burst of nanobubbles contributed to the degradation of 1,4-dioxane as well. Based on these findings, a microwave-assisted functionalized membrane filtration system was tested for 1,4-dioxane in the following section.

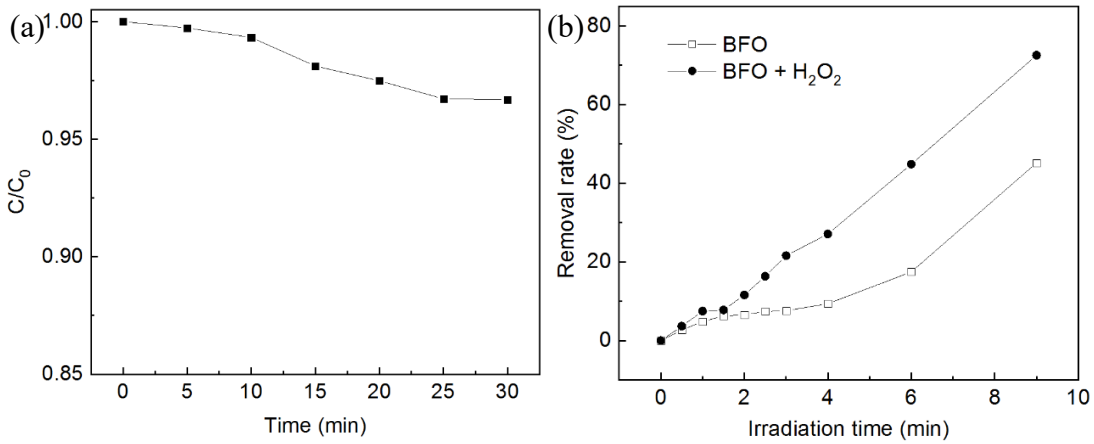

Figure 6.21 (a) Adsorption curves of the 1,4-dioxane using BFO catalysts; (b) Effect of H_2O_2 dose on removal rate of 1,4-dioxane. (Reaction conditions: MW 125 W, 1,4-dioxane 10 mg L^{-1}, H_2O_2 dosage 3 mg L^{-1}, catalyst dosage 0.1 g L^{-1}).

Since MW irradiation enhances nanobubbles/•OH generation, we expect that the degradation of 1,4-dioxane or other organic pollutants can be enhanced when water passes through the catalyst layer of membranes. Figure 6.22a shows that the removal rate of 1,4-dioxane was enhanced under MW irradiation. MW alone removed about 3% of the 1,4-dioxane perhaps due to the increased temperature of ceramic membrane surface via the localized heating, as 1,4-dioxane has been reported to be unstable at elevated temperatures and pressures.[638] Similarly, the water bath heating at 70 ^{o}C caused ~3% removal of 1,4-dioxane from water. On the other hand, the H_2O_2 alone resulted in a removal rate of only 7%, which was increased to 18% under MW irradiation. Thus, MW irradiation obviously enhanced the •OH generation from H_2O_2 according to Figure 6.22b. The non-thermal effect of MW irradiation on the formation of •OH is due to the excitation of H_2O_2 molecules to higher vibrational and rotational energy levels, which weakens the chemical bond of H_2O_2 molecules and facilitate the generation of •OH.[599]

Compared with BFO alone, the MW irradiation enhanced the 1,4-dioxane removal by BFO from 3% to 24%. Figure 6.22b shows that the hydroxyl radical generation was not

significantly enhanced in the MW/BFO system, which indicated that the enhanced removal could be caused by the local heating on the MW absorbent (BFO catalyst) rather than radical oxidation reactions. It was reported that MW-absorbents could generate "hot spots" (local temperature as high as 1000 ^{o}C) on the surface of absorbents.[635] For example, granular activated carbon under MW irradiation can promote the degradation of organic pollutants through the high-temperature oxidation.[637] This could also explain the enhanced degradation of 1,4-dioxane under BFO+MW condition in our study.

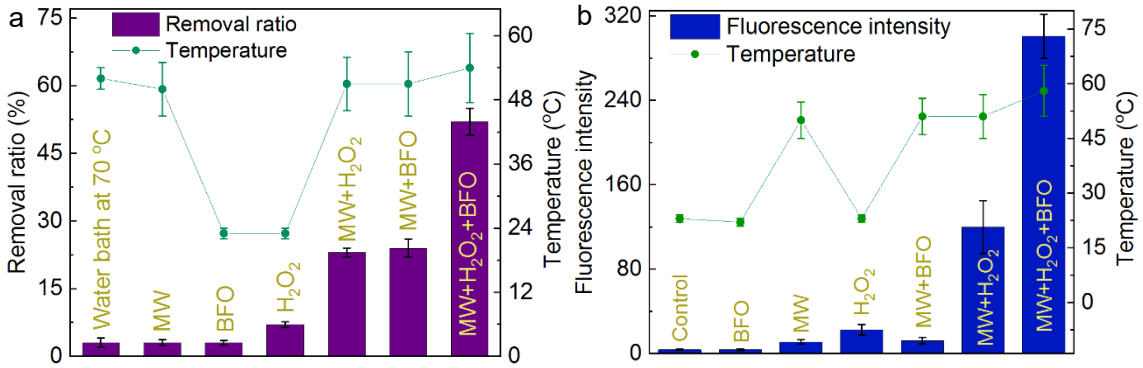

Figure 6.22 Degradation of 1.4-dioxane, ·OH radical generation and temperature changes under microwave irradiation. a. Removal rate of 1,4-dioxane under different reaction conditions. (MW 125 W, 60 s irradiation, 10 mg L^{-1} 1,4-dioxane, 30 mM H_2O_2, 1 g L^{-1} catalyst). b. Fluorescence intensity changes at 425 nm with excitation wavelength at 315 nm observed from 30 mL 5×10^{-4} M terephthalic acid solution in 2×10^{-3} M NaOH under different experimental conditions. All error bars represent standard deviation from triplicate experiments.

6.3.6.2 Assessment of 1,4-dioxane Mineralization. The mineralization degree of 1,4-dioxane solutions was determined by a total organic carbon (TOC) analyzer (TOC-VCSH, Shimadzu). The incomplete removal of TOC indicated that 1,4-dioxane, although effectively decomposed via this microwave assisted reaction, maybe converted to other organic byproducts as reported elsewhere.

H_2O_2 played a synergistic role with BFO under MW irradiation and further increased the removal rate to 53%. The local "hot spots", hydroxyl radicals and

nanobubbles may cooperatively contribute to enhanced degradation of 1,4-dioxane. To assess the mineralization rate of 1,4-dioxane, and to differentiate the contributions of high temperatures and oxidation by radicals, a total organic carbon (TOC) analysis (Figure 6.23) was performed, which shows that approximately 3% of 1,4-dioxane was removed under 70 ^{o}C water bath with 3% of TOC reduction as well. By contrast, 53% of 1,4-dioxane was degraded under the condition of MW+H_2O_2+BFO with a TOC reduction of 36%. Clearly, the temperature increase had a minor contribution to the removal of 1,4-dioxane, while most of the degradation/mineralization was attributed to the microwave-catalysis reactions.

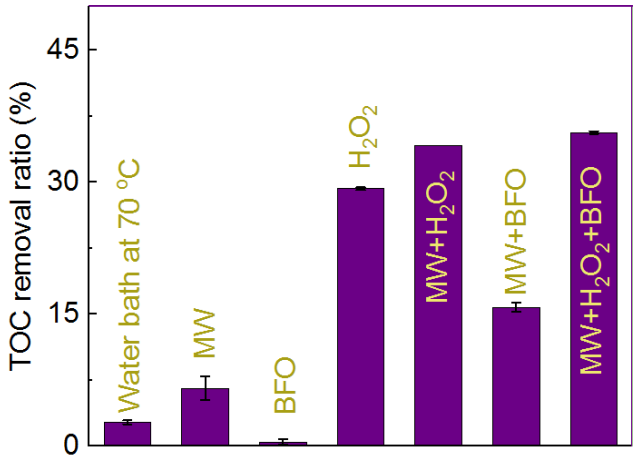

Figure 6.23 Comparison of TOC removal ratio under different reaction conditions. Reaction conditions: MW 125 W, 60 s irradiation, 10 mg L^{-1} 1,4-dioxane, 30 mM H_2O_2, 1 g L^{-1} catalyst.

The identified intermediate products from the 1,4-dioxane degradation by hydroxyl radicals were analyzed with FTIR spectroscopy in previous studies.[639, 640] Those byproducts included formic, oxalic, acetic, glycolic, and methoxyacetic acids, which agrees with previously reported (Figure 6.24).[641] Based on these findings, the MW/BFO/H_2O_2 process of 1,4-dioxane degradation is driven by •OH radicals as well. In the chromatographic study of metabolites, ethylene glycol diformate, ethylene glycol monoformate, and formic acid were identified as major reaction intermediates, and thereby,

the main reaction pathways have been proposed in Figure 6.25.[642] However, the FTIR test was carried out for the 1,4-dioxane solutions before and after treatment but failed to provide any information about intermediates or 1,4-dioxane.

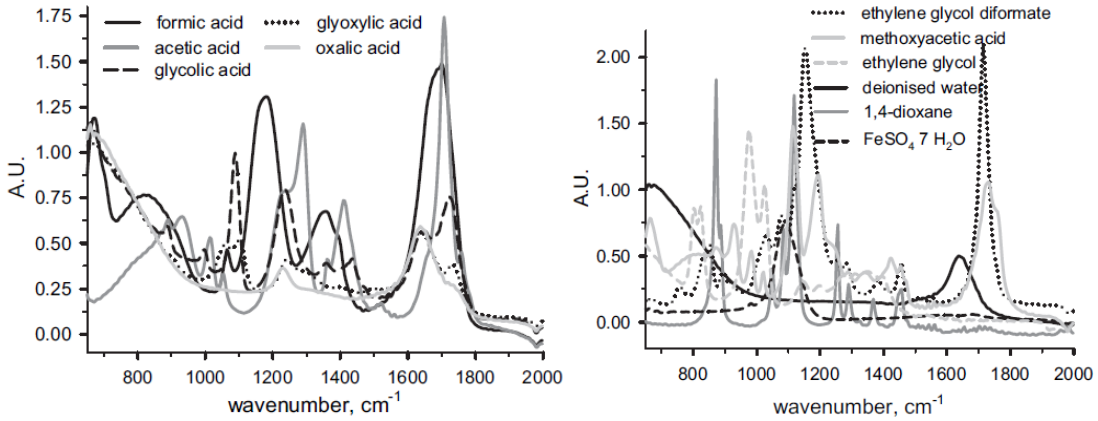

Figure 6.24 Reference spectra for the main chemicals that are expected to be found along the Fenton oxidation treatment of 1,4-dioxane.[640]

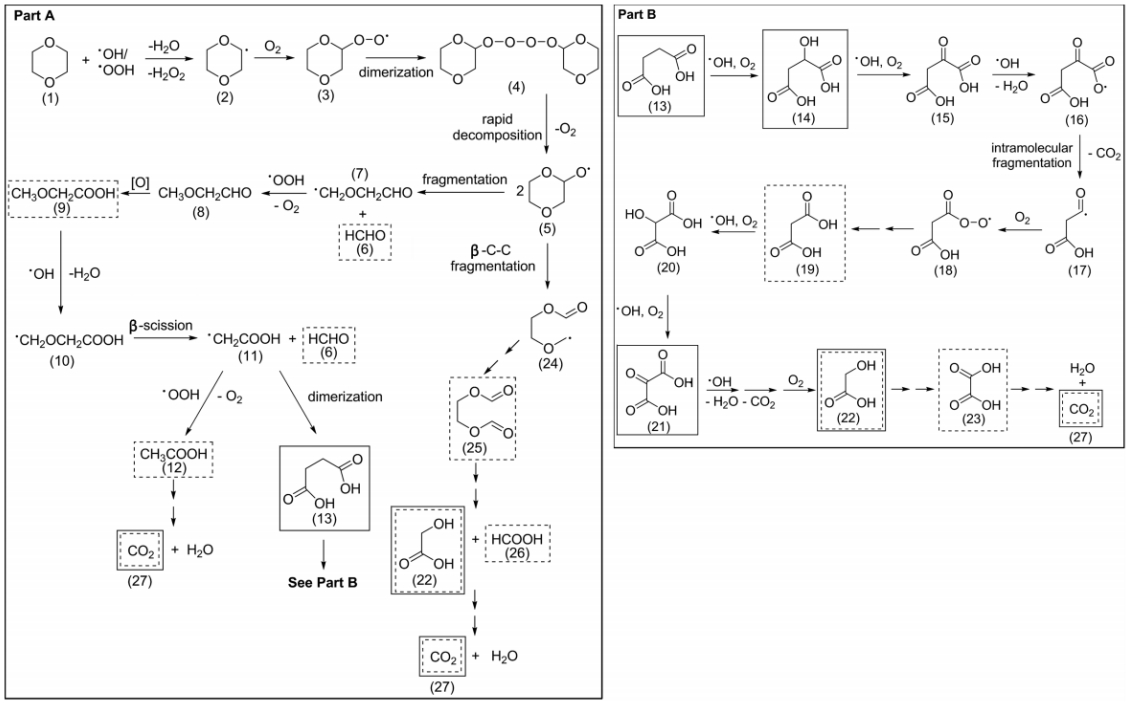

Figure 6.25 Degradation pathway for 1,4-dioxane proposed by Jasmann *et al*. Part A: Reaction pathway for the initial oxidation of 1,4-dioxane to CO_2 or the succinic acid intermediate. Part B: Reaction pathway from succinic acid to CO_2.[643]

6.3.6.3 MW-assisted Membrane Filtration of 1,4-dioxane and Anti-fouling Performance. We also assessed the antifouling performance of functionalized ceramic membrane (TiO_2/Al_2O_3) during filtration of 1,4-dioxane solution. As mentioned above that extremely high temperatures can cause the elimination of the oxidative species, so pulse MW irradiation was applied to mitigate the adverse effects. Figure 6.26a shows that for pristine and BFO-coated ceramic membranes, the transmembrane pressure (TMP) both slightly increased without microwave irradiation. With microwave on, the TMP decreased significantly. When microwave was off the TMP bounced up. This antifouling or defouling behavior might be attributed to the formation and burst of nanobubbles or the local heat under MW, which will be further analyzed.

Figure 6.26b shows that, after spiking H_2O_2 into the filtration system, the TMP appeared to increase more appreciably than without spiking H_2O_2 under no microwave irradiation, indicating that H_2O_2 may result in certain degradation byproduct formation of 1,4-dioxane or changed the solution characteristics that promoted membrane fouling. H_2O_2 addition seemed to suppress fouling in the long term, as the TMP did not progressively increase under microwave irradiation. Clearly, under microwave irradiation, the BFO coating on ceramic membrane and H_2O_2 dosage improved anti-fouling performance.

Figure 6.26a showed that the overall TMP of the pristine membrane decreased around 8.5% while the BFO-coated membrane increased about 3.5% once the MW was off at 120 min. This indicated that the temperature increasing might be reason for TMP drop. However, it should be noted that the TMP increased immediately when the MW was off, while the temperature should not be decreased immediately. If the TMP drops were caused by the high temperature, the author assumed that the local temperature of the membrane

surface inside the filtration cell might be much higher than the temperature of the water during the MW-on periods. This extreme-high temperature might be caused by the burst of nanobubbles or the local heat caused by the MW. Once the MW was off, the local extreme-high temperature would decrease immediately. But it was not possible to measure the temperature when the MW was on. On the other hand, the foulants might not be degraded efficiently, that's why the TMP kept increasing when the MW was off.

On the other side, for the BFO coated membrane filtration with the addition of H_2O_2, the flux increased slightly during the MW-OFF stage. It needs to be noted that at the last MW-OFF stage, the flux was almost constant for 25 minutes. Meanwhile, the pristine membrane with the addition of H_2O_2 demonstrated increasing TMP during the last MW-OFF stage. Besides, the decreased flux might be caused by the local temperature instead of the high bulk temperature. Because during the MW-OFF stages, the temperature did not decrease immediately once the MW was off, however, the TMP increased immediately. It indicated that the local high temperature or pressures caused by the nanobubbles and the microwave non-thermal effects might be the contributors. That's why the TMP changed immediately with the switch ON-OFF of microwave. In Figure 6.26b, we compared the TMP change behavior of BFO coated membrane and pristine membrane during the last MW-OFF stage, and it should be noted that the BFO-coated membrane had controlled the TMP to a low and constant level. Meanwhile the overall TMP of the pristine membrane decreased around 18% but kept increasing. It indicated that the membrane fouling was controlled due to the potential degradation of pollutants and the BFO enhanced the degradation efficiency and better anti-fouling performance.

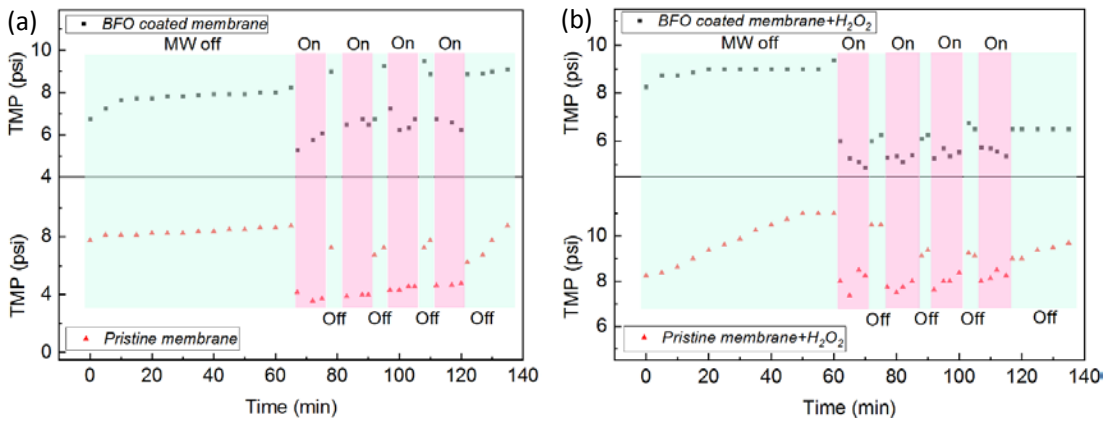

Figure 6.26 Flux resistance of pristine membrane and BFO-coated membrane (a) without and (b) with H_2O_2 as indicated by transmembrane pressure (TMP) versus filtration time (min). The flow rate was 6.75 ml·min^{-1}, initial 1,4-Dioxane loading rate: 10 mg·L^{-1}. MW power level: 125 W and H_2O_2 concentration: 30 mM.

Furthermore, other effects from MW irradiation also contributed to the anti-fouling behavior from the aspect of water surface tension in two folds. First, it was reported that the surface tension of solutions containing large numbers of air nanobubbles could be reduced by up to about 15%.[644] And nanobubbles generation via microwave irradiation was verified in a previous study.[626] It showed that the thermal and non-thermal effects of microwave radiation made contributions to decreasing the gas solubility, thus facilitating nanobubbles nucleation. In our study, MW irradiation might induce the generation of nanobubbles in the solution and lead to decreased solution surface tension, which facilitate the removal or detachment of pollutants from the membrane surface. Since the natural gas (air) concentration in the feed solution was low, the nanobubbles number after the microwave irradiation might not be high enough to induce significant decreased water surface tension. Thus, the influence of microwave-irradiated water on membrane filtration performance was studied.

Actually, nanobubbles mixture solutions have been applied for surface cleaning and contamination prevention.[278, 591, 645, 646] The possible mechanisms for cleaning by

nanobubbles in these studies were mostly three categories: (1) nanobubbles can pick up nanoparticles by new bubble nucleation as well as collision; (2) nanobubbles bind preferentially to small hydrophobic particles causing them to merge to form larger agglomerates due to the large capillary forces that develop; (3) the negatively charged nanobubbles attached on the pollutants and detached them from the solid surfaces. For example, a mixture of air nanobubbles and microbubbles has been shown to clean the concentration polarization that builds up on reverse osmosis membranes and both permeate flux and the solute rejection were improved with the presence of nanobubbles in the feed solution.[645] It indicated that the application of nanobubbles water could make a cleaning-in-place (CIP) operation possible. Similarly, our study applied MW irradiation to improve the pollutant removal and membrane fouling mitigation, which means this process is able to maintain or recover the flux without stopping, which reduced the cost and energy consumption.

Second, water surface tension decreases with increasing temperature, microwave irradiation expectedly lowers the surface tension during heating.[647] However, MW irradiation was reported to decrease the water surface tension for an extended period of time after the irradiation even the water returned to its original temperature. This lasting effect can be attributed to the unique hydrogen bonds of interfacial water molecules.[648] The H-bond network at the interface depends on the dynamics of H-bond forming and breaking, which is directly related to the rotational motion of the water molecules.[649] Thus, the surface tension could be lower because the dynamic switching of H bonds at the interface is faster after microwave treatment. As discussed above, the lower surface tension could

lead to lower affinity of pollutants to the membrane surface, which is in a similar manner to that of surfactant or detergent solutions.

Figure 6.27 shows that under the same permeate flux (~380 LMH) and the same initial concentration (10 mg L^{-1}) of 1,4-dioxane, the removal rate of 1,4-dioxane was 53±2% on the ceramic membrane with BFO/MW/H_2O_2 and 34±5% on the pristine ceramic membrane with MW/H_2O_2. Without MW, the removal rate was approximately 25% for both BFO-coated and pristine membranes, in the presence of H_2O_2. Similarly, a much lower removal rate of 10% was observed on the two types of membranes indicating that 1,4-dioxane could not be physically rejected by the membrane filtration. The removal is primarily due to the oxidation by H_2O_2 or MW-catalyzed Fenton-like reactions as demonstrated in the following section.

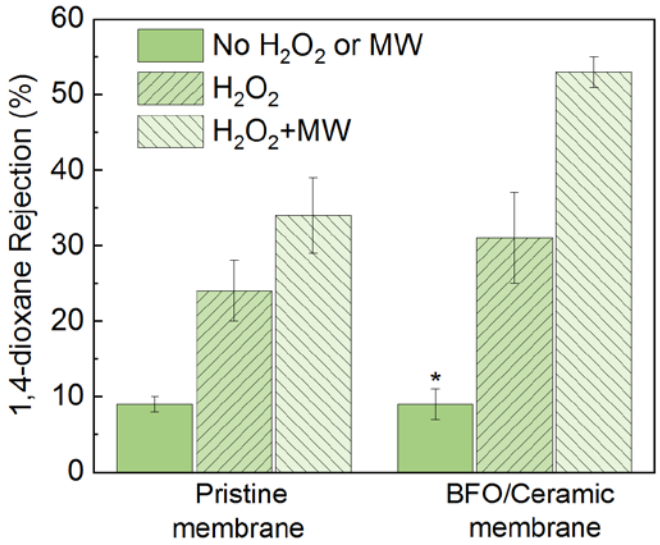

Figure 6.27 1,4-dioxiane rejection of pristine membrane and BFO/Ceramic membrane.

The molecular weight of 1,4-dioxane is 88.11 g mol^{-1} and the pore size of membrane is 140 nm. Therefore, the accumulation of 1,4-dioxane on membrane surface was unlikely to happen significantly. However, we suspect that the pore blockage or pore

narrowing could be caused by 1,4-dioxane and its degradation intermediates. The hypothetical oxidation degradation pathway for 1,4-dioxane has been reported in literature [641, 650]. As shown in Figure 6.25, the oxidation of 1,4-dioxane generated organic aldehyde and carboxylic acid intermediates (*e.g.*, succinic acid, malic acid, mesoxalic acid, glycolic acid, formaldehyde and methoxyacetaldehyde), which could induce membrane fouling in the similar way as dissolved organic matters [643]. Figure 6.26a shows that for the pristine and BFO-coated ceramic membranes, the transmembrane pressure (TMP) both slightly increased without MW irradiation, probably because of the pore blockage or pore narrowing caused by the 1,4-dioxane and/or its degradation intermediates [643, 650].

The potential chemical mechanisms of this MW-enhanced membrane filtration system are outlined in Figure 6.28. The combination of MW irradiation, MW catalysts and oxidants leads to a MW-induced catalytic oxidation (MICO) process [626]. MW irradiation can enhance the catalytic capacity of a metal catalyst or the generation of "hot spots" on MW absorbent and improve the performance of water treatment processes. In this MW-Fenton-like system, the following reactions occur between the transition metal ion (Fe^{3+}) in BFO and H_2O_2 [633]:

$$Fe\ (III) + H_2O_2 \rightarrow Fe\ (II) + H^+ + \bullet OOH \quad (6.22)$$

$$Fe\ (II) + H_2O_2 \rightarrow Fe\ (III) + OH^- + \bullet OH \quad (6.23)$$

This MW-Fenton-like process was reported to a pronounced generation rate of •OH, effective under a wide pH range [651]. In this study, the MICO process was performed on a porous ceramic membrane as a support, which integrated the advantages of the MICO process and membrane filtration process. The ceramic membranes may prevent

aggregation of catalytic nanoparticles and avoids the need to separate catalysts from the reaction mixture. The filtration process may also enhance the convective mass transport of reactants on the immobilized catalyst nanoparticles and improve the reaction kinetics.

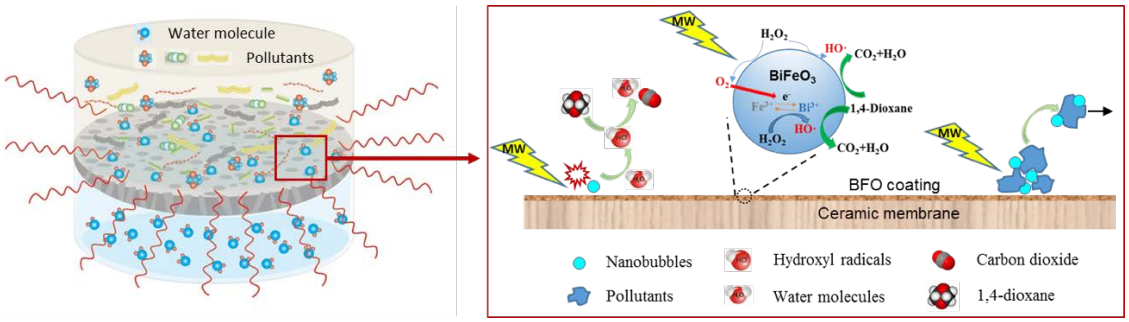

Figure 6.28 Schematic representation of hypothesized mechanism in the MW-enhanced membrane filtration system.

6.3.6.4 Comparison of 1,4-dioxane Degradation with Other Treatment Techniques. Various advanced oxidation processes (AOP) such as electro-chemical degradation, photo-Fenton, photocatalytic degradation, or other catalytic degradation have been studied for 1,4-dioxane degradation [643, 652-655]. Here we compared the 1,4-dioxane removal rates (g-1,4-dioxane g-catalyst^{-1} min^{-1}) by different treatment techniques as shown in Table 6.2. Clearly, MW-Fenton-like process in our study had a shorter reaction time and a higher removal rate (5.2 g-1,4-dioxane g-catalyst^{-1} min^{-1}). Moreover, MW-assisted catalytic process with BFO performs well under a natural pH, which may be advantageous over traditional Fenton or Fenton-like catalytic processes that require low or narrow pHs. More importantly, none of these previous AOPs were conducted concurrently with membrane filtration, where pollutant degradation must be achieved in a short reaction time.

Furthermore, the treatment efficiency was affected by the transmittance of the polluted water during the practical application. For example, the low transmittance of the wastewater, particularly the dye or printing wastewater, would lead to a severe reduction

in the UV light intensity. Besides, with the passage of treatment time, the catalysts could be deactivated by the adsorption of pollutants or intermediates on the surfaces, leading to partial or complete blocking of the active sites. The MW irradiation would not have this kind of adverse conditions to some extent. This is mainly because that MW could penetrate and apply on the catalyst surface and also the absorbed pollutants or intermediates would be removed from the surface due to the localized superheating effect.[656]

Table 6.2 Comparison of Treatment Performances of Different Treatment Techniques

Degradation methods	Catalysts/ reagents used	Initial concentration of 1,4-dioxane	pH	Reaction Time	1,4-dioxane removal rate (g-1,4-dioxane g-catalyst^{-1} min^{-1})*	Refs.
Electrochemical oxidation	TiO_2/Na_2SO_4	300 μg L^{-1}	7.2±1.0	1.5 day	N.A.	Jasmann *et al.*[643]
Photo-Fenton	$Fe(II)/H_2O_2$	0.1 M	3.0	4 h	0.165	Chitra *et al.*[652]
Fe^0/UV	None/Fe^0	10 mg L^{-1}	3.0	4 h	N.A.	Son *et al.*[653]
Photocatalytic/ H_2O_2/UV	TiO_2/H_2O_2	360 μg L^{-1}	3.0	10 min	0.035	Coleman *et al.*[654]
H_2O_2/O_3	None/H_2O_2+O_3	160 mg L^{-1}	5.8	60 min	N.A.	Suh *et al.*[655]
MW/BFO/H_2O_2	$BiFeO_3/H_2O_2$	10 mg L^{-1}	7.5±0.5	1 min	5.2	Present study

* The 1,4-dioxane removal rate was calculated based on the experimental data under optimum conditions reported in literature. N.A. indicated that the reference did not provide relevant data for the calculation.

6.3.7 Microbial Inactivation by MW-assisted Membrane Filtration with/without H_2O_2

H_2O_2 promotes the formation of HO•, which can also be accelerated by ultrasound,[657] or microwave irradiation due to cavitation and bubble collapse. H_2O_2 is a well-established and commonly used disinfectant that finds its antibacterial value in the fact that it is a strong oxidizing agent. H_2O_2 may not only help reduce the MW dose, but also produces dissolved oxygen during microbial disinfection. BFO is a catalyst and when paired with microwave heating is reported to provide a synergistic antibacterial effect. Through the magnetic resonance produced within the BFO catalyst (by way of the microwave) BFO has been linked to enhance the heating rate and thus may improve the ability to disinfect a sample. In this experiment, we qualitatively assessed HO• generation from H_2O_2 activated by a microwave unit and investigated the bactericidal effect of this HO• generation on *E. coli*.

6.3.7.1 Antibacterial Activity. To evaluate disinfection effects of microwave irradiation against *E. coli*, bacteria in the PSB solutions were treated with different conditions. As shown in Figure 6.29, the treatment with H_2O_2/MW was the most effective one but the overall removal rate was not high. The possible reason might because of the low dosage of H_2O_2 and short microwave irradiation time. However, the results showed that bacteria can be killed to a certain extent by only MW irradiation, only BFO and BFO/MW.

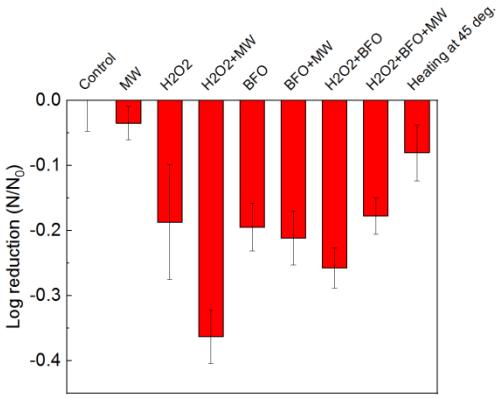

Figure 6.29 Bacterial inactivation of *E. coli* cells exposed to MW irradaition, H_2O_2, BFO and approparite controls. Samples (30 mL 7×10^5 CFU mL^{-1}) were irradiated in petri dish for 30 s at 125 W using a conventional MW oven, H_2O_2 dosage 25 mM and BFO dosage 0.5 g L^{-1}.

Next, higher H_2O_2 dosage and longer MW irradiation was carried out for the antibacterial experiments. Figure 6.30 showed that BFO/MW/ H_2O_2 demonstrated high removal of bacteria and H_2O_2 solely had obvious disinfection effect. It indicated that MW irradiation with BFO can enhance the disinfection effect. However, H_2O_2/MW process showed lower removal rate than only H_2O_2 process. Thus, another antibacterial experiments were carried out to verify the results.

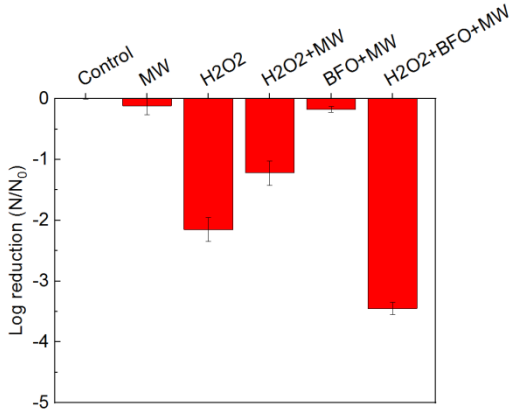

Figure 6.30 Bacterial inactivation of *E. coli* cells exposed to MW irradaition, H_2O_2, BFO and approparite controls. Samples (30 mL 6×10^3 CFU mL^{-1}) were irradiated in petri dish for 60 s at 125 W using a conventional MW oven, H_2O_2 dosage 100 mM and BFO dosage 0.1 g L^{-1}.

The repeated results were shown in Figure 6.31, it indicated that H_2O_2/MW had higher bacterial removal rate than only H_2O_2 process. The H_2O_2/MW/BFO demonstrated much higher removal rate that H_2O_2/MW, which indicated that BFO enhanced the disinfection effects. It needs to be noted that the BFO/MW process demonstrated the similar removal efficiency as only H_2O_2. This findings indicated that BFO/MW could work as a substitute for the H_2O_2 disinfection process, which was commonly used. Besides, the BFO/H_2O_2/MW process with 50 mM H_2O_2 dosage demonstrated similar disinfection efficiency as H_2O_2/MW with 100 mM H_2O_2 dosage, and higher than only H_2O_2 with with 100 mM H_2O_2 dosage. As discussed above for the organic polutatns degradation exeperiments, the MW-Fenton-like process which combined MW irradaiton, MW catalyst and oxidants, showed accelerated generation rate of •OH by the localized MW superheating effect. The reaction activation energy was reduced under MW irradation and H_2O_2 dosage could be reduced as well. This result indicated that the addition of BFO could help reduce the H_2O_2 dosage for disinfection process during the application.

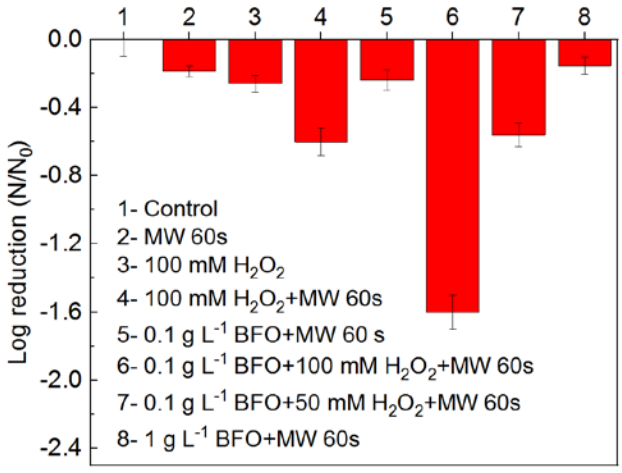

Figure 6.31 Bacterial inactivation of *E. coli* exposed to MW irradiation, H_2O_2, BFO and appropriate controls. Samples (30 mL 8×10^5 CFU mL^{-1}) were irradiated in petri dish for 60 s at 125 W using a conventional MW oven.

6.3.8 Effect of MW on Membrane Surface Integrity/Catalyst Stability

The stability and durability of the prepared membranes are important properties for a sustainable filtration process. The stability and durability research typically involves the comparison of the crystallinity changes of catalyst, the catalytic activity changes, metal leaching after consecutive filtration cycles or longer operation periods, the impacts of the catalyst layer thickness, detachment risk, and other engineering issues.

The stability of the BFO-coated ceramic membranes was also indicated by the changes of TMP and 1,4-dioxane removal rate. Figure 6.32 shows that the 1,4-dixoane removal slightly decreased from 48.8%±3.5% to 40.6%±2.3% after five consecutive filtration cycles. TMP slightly increased during the last three cycles, increasing by ~23% at the 4th filtration cycle, because of membrane fouling. Figure 6.33 indicated that BFO coating remained well on the membrane surface after the repeated filtration experiments. Our previous study also examined the stability of catalytic activity and dissolution potential of BFO, showing that BFO catalysts exhibited high catalytic activity and low metal leaching after six cycles of microwave-enhanced Fenton-like reactions for degradation of perfluorooctanoic acid (PFOA).[627]

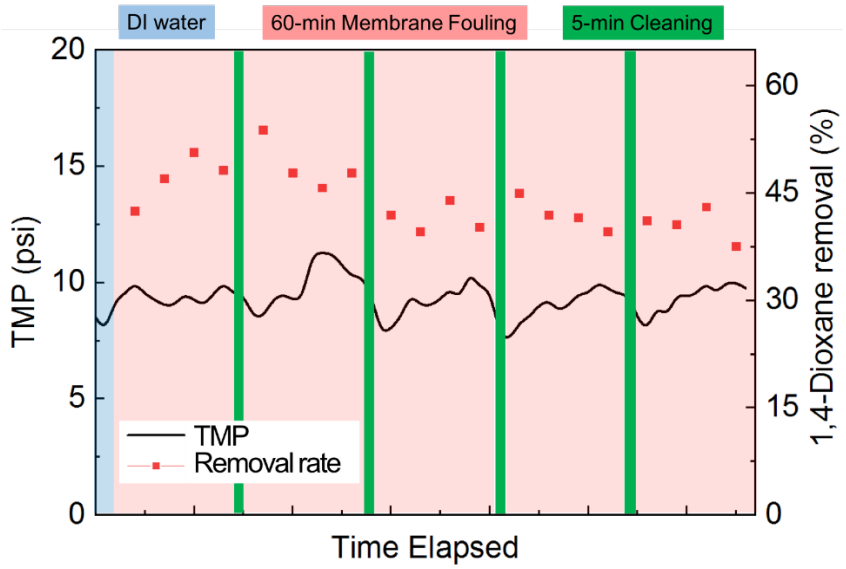

Figure 6.32 Repeated filtration cycles showing transmembrane pressure (TMP) and 1,4-dixoane removal rate with hydraulic cleaning. Each filtration cycle comprised of membrane filtration with 10 ppm 1,4-dioxane solution for 60 min followed by hydraulic cleaning for 5 min. The flow rate was 6.75 ml·min^{-1}, MW power level: 125 W, pulsed MW irradiation (10 min-ON/5min-OFF) and H_2O_2 concentration: 30 mM.

Figure 6.33 The photos of pristine membrane, BFO coated membrane before and after filtration experiments.

Besides, the stability or dissolution potential of BFO was investigated in separate studies that published recently.[627, 658] As shown in Figure 6.34, after six consecutive reaction cycles in microwave-enhanced Fenton-like process (MW-Fenton-like), the removal rate of BPA, the crystal, and hydroxyl radical (·OH) were also used to demonstrate the high catalytic activity of BFO with low metal leaching ratio, indicating that BFO were

successfully prepared with high stability and provide an efficient catalyst for MW-Fenton-like reactions.[658]

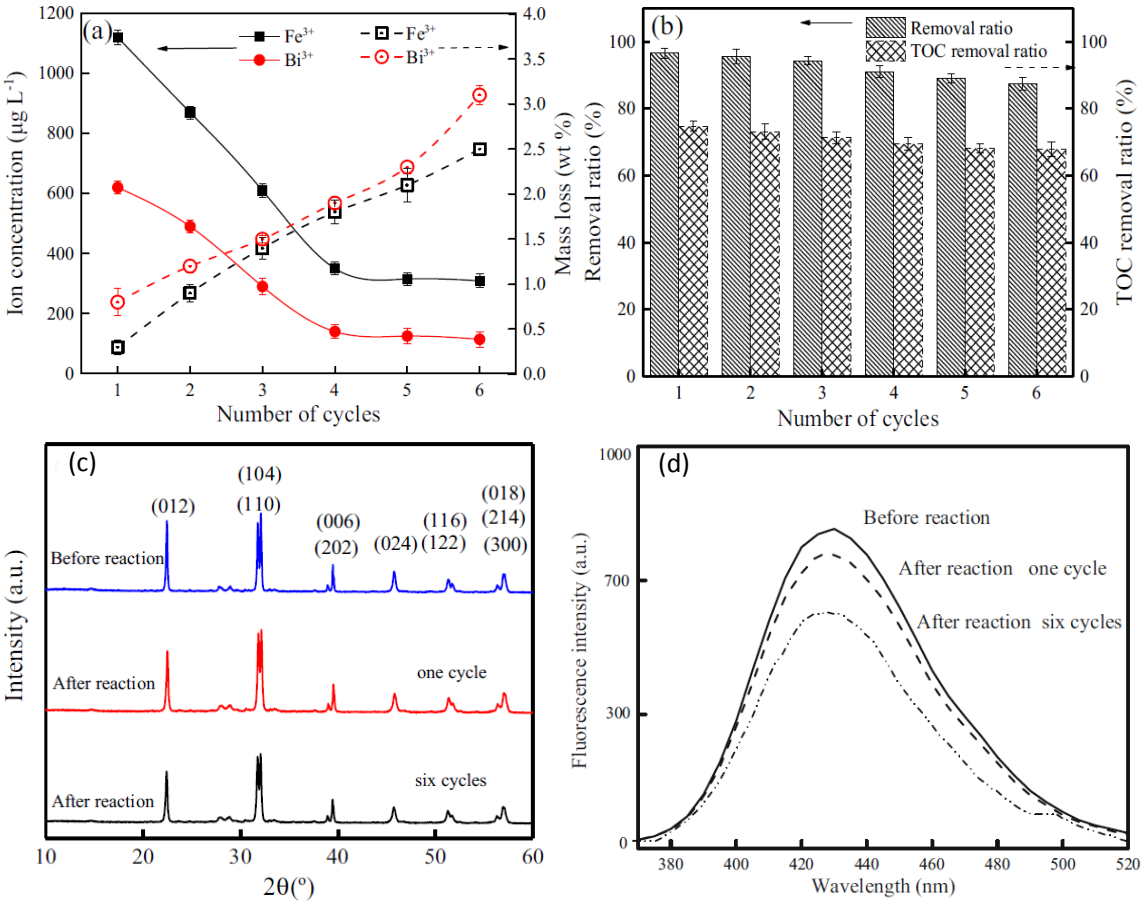

Figure 6.34 The metal leaching rate of BFO (a) and removal rate of BPA (b) in six batch reaction cycles; (c) XRD patterns of BFO changes before and after the catalytic degradation reaction; and (d) ·OH generated with number of cycles. (Conditions: BPA concentration = 20 mg L^{-1}, terephthalic acid concentration = 20.0 mg L^{-1}, microwave power = 200 W, H_2O_2 dosage = 24 mg L^{-1}, catalyst dosage = 1.2 g L^{-1}). Cited from Ref. [658].

6.3.9 Discussion About the Microwave Penetration Depth and Scale-up Feasibility of MW-assisted Filtration System

6.3.9.1 Theory of the Microwave Penetration Depth. The depth of penetration can be calculated by skin depth as follows:[635]

$$D_p = \sqrt{\frac{2}{\omega \mu_0 \sigma}} \tag{6.24}$$

where D_p is the skin depth, ω is the angular frequency, μ_0 is the permeability of free space ($\mu_0 = 4\pi\times10^{-7}$ H m^{-1}) and σ is the electric conductivity. For water, σ is 1.82×10^5 Ω^{-1} m^{-1}, and microwave frequency 2450 MHz, so the skin depth of water is calculated to be 1.9 mm. In the lab-scale experiment, the frequency that is used frequently is 2450 MHz, while 915 MHz is always used in the industrial scale equipment due to its increased penetration depth.[659]

The penetration depth of microwave irradiation in industrial membrane separation systems is critical to warrant the effective reactions on membranes. The penetration depth (D_p) depends on the microwave frequency or wavelength as well as dielectric properties of materials (*e.g.*, water or membrane) as described by the following equation:[609-611]

$$D_p = \frac{\lambda_0}{2\pi(2\varepsilon')^{1/2}}\left\{\left[1+\left(\frac{\varepsilon''}{\varepsilon'}\right)^2\right]-1\right\}^{-1/2} \quad (6.25)$$

where, λ_0 – wavelength for a given frequency [m], ε'– real component of the relative complex electrical permittivity, ε''– imaginary component of the relative complex electrical permittivity, which is defined as: $\varepsilon_r = \varepsilon' - j\varepsilon''$. The real component ε' of the relative complex electrical permittivity represents the ability of a material to store energy, whereas the imaginary component ε'' represents the ability of a dielectric to disperse the energy stored in the electrical field, *i.e.,* to generate losses.[660] The relative dielectric permittivity is not constant as it changes depending on the electrical parameters and the frequency of the electromagnetic wave.

6.3.9.2 Scale-up Feasibility of MW-assisted Filtration System. Figure 6.35 illustrates a transition of this laboratory scale microwave membrane technology to large

scale processes. Ceramic flat-sheet or hollow fiber membranes are incased in nonpolar modular housing materials, which are directly irradiated by microwave sources. Superior to other stimuli such as light illumination or ultrasonication, microwave irradiation can penetrate membrane housing and other cover materials without energy loss as only polar materials such as the coated oxides membranes, metals and the flowing water absorb microwave energy.[661] This will largely increase reaction specificity and lower energy cost. In industrial applications, microwave irradiation could be introduced as Figure 6.35 shows. For instance, microwave injectors can be used to directly irradiate membrane modules from different angles to allow sufficient exposure of ceramic membranes to microwave energy.

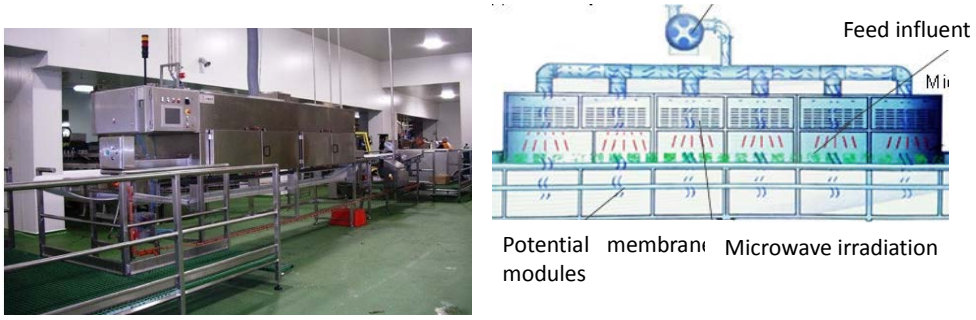

Figure 6.35 Industrial scale microwave reactor for large-scale applications.

Typically, microwave wavelengths range from 1 m to 1 mm with the corresponding frequencies between 300 MHz and 300 GHz. High power or low frequency (long wavelength) microwave generally have greater penetration power. For example, the penetration depth at 2450 MHz is in the order of a few centimeters, depending on the dielectric properties of the absorbing materials. In industry low frequency microwaves (915 MHz) are generally used at high powers (hundreds of Watts) to ensure the effective penetration into treated samples. In membrane filtration, since there are no published demonstrations or reports on microwave penetration for membrane filters, let's look at an example in Figure 6.36 below, where potato starch samples with the moisture content of

37.6% w.b. were heated by microwave at different temperatures and over the frequency range of 20–4,500 MHz. The result shows that the microwave penetration depth could reach up to 1~1.5 m for starch at room temperature for low frequencies. The penetration depth decreases with the increasing frequency, which was also found on other organic materials, such as peanut kernels,[662] fruits,[663] and legume flour.[664] Although polymer or ceramic membrane filtration systems are not the same as these biomass materials, the microwave energy decay across the membrane modules should follow similar patterns, which deserves comprehensive research. Figure 6.37 shows two kinds of membrane module configurations (*e.g.*, hollow fiber and flat sheet) commonly applied in industry. The dimension of these membrane modules ranges from 0.25 m to 3 m, which would fall into the penetration depth of microwave or could be achieved with multiple MW irradiation sources.

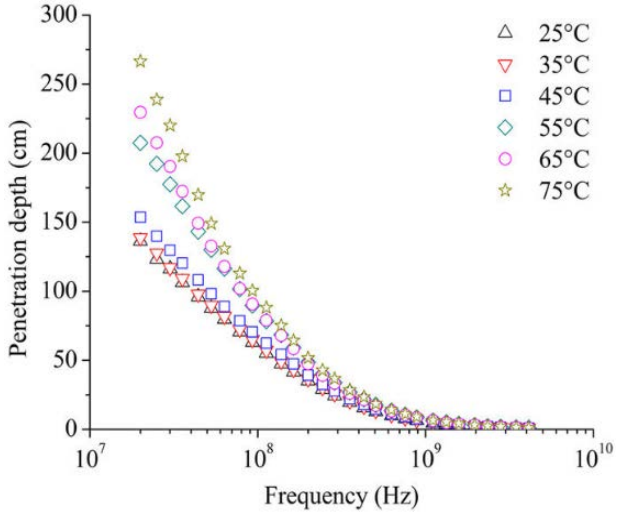

Figure 6.36 Calculated penetration depth of potato starch samples with the moisture content of 37.6% w.b. at 25 (Δ), 35 (∇), 45 (□), 55(◇), 65 (○), and 75 °C (☆) and over the frequency range of 20–4,500 MHz. Cited from ref. [665]

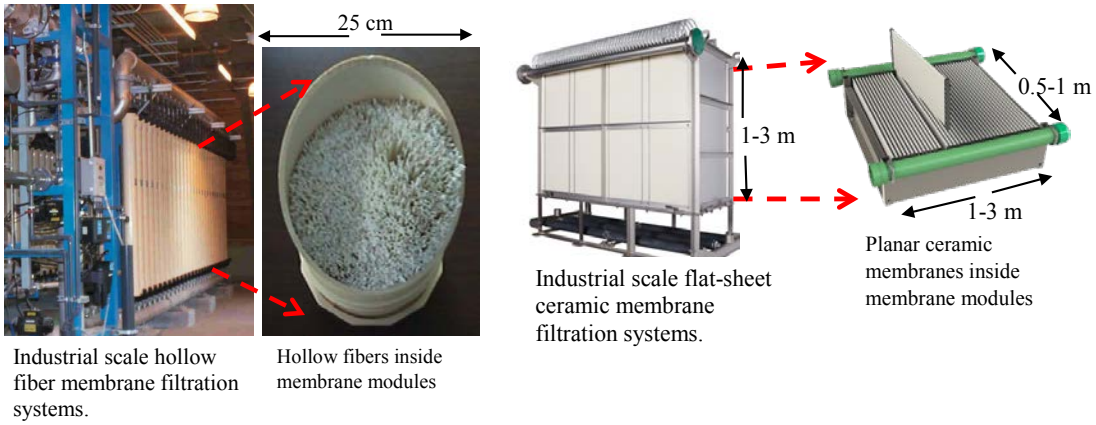

Figure 6.37 Two kinds of membrane module configurations commonly used in industry.

The common hollow fiber membrane modules have sizes of 25 cm or greater in diameter with a high packing density that allow the feed water to pass through the module. Typically, the water content (void space allowing water to pass through divided by the total volume of the membrane module) is less than 10%. As the plastic modular materials and polymer membrane fibers are transparent to microwave, the microwave energy at low frequencies such as to 300 MHz, there is no doubt that microwave energy can thoroughly penetrate the membrane modules greater than 1 m in diameter or length. In our future research, we will prepare or purchase membrane modules of different dimensions and geometries and determine the effective microwave penetration depth in realistic membrane filtration configurations in addition to laboratory scale flat-sheet membrane modules.

Furthermore, heat recovery is also recommended because it is beneficial for reducing the treatment costs and avoiding the heat pollution to protect the environment. For example, recovering the heat from the heated effluent or retentate using heat exchangers would be preferred to avoid heat pollution of environment and facilitate commercialization of MW-assisted filtration technology to some extent.

6.3.9.3 Assessment of Penetration Depth under MW Irradiation. In order to determine the effective microwave penetration depth and direction in realistic membrane filtration configurations, we assembled two bundles of PTFE tubes to simulate the hollow fiber membrane modules in different configurations (Figure 6.38). The first bundle was consisted of 80 pieces of PTFE tubes with inner diameter of 4 mm and length of 5 cm. The second kind of bundle is consisted of 40 pieces of PTFE tubes. After being filled with DI water and sealed with PTFE tapes, the bundles were placed in the center of an anti-node point (maximum heating location) which was confirmed with cheese powder, as shown in Figure 6.3. After being irradiated with 1250W MW for certain seconds at 2.45 GHz, the temperature of water in these tubes were measured with a Raytek MiniTemp MT4 non-contact infrared thermometer. It should be noted that the plastic support and the PTFE tubes are transparent to microwave and allow MW irradiation penetrate them to the water directly without loss.

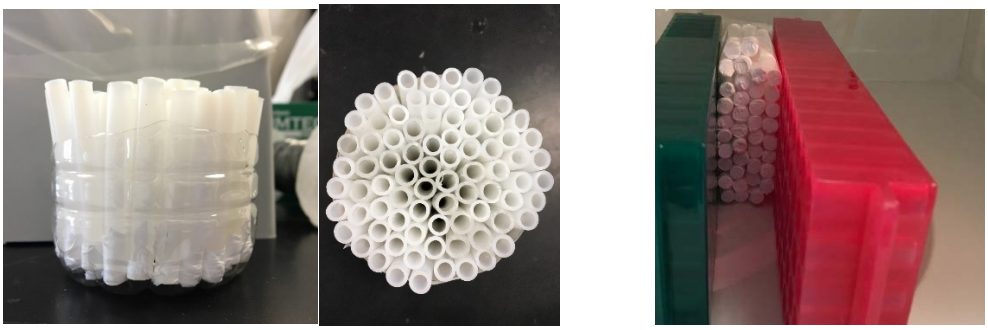

Figure 6.38 Two different bundles of PTFE tubes to assemble the hollow fiber membranes during MW irradiation for assessement of penetration depth.

As shown in Figure 6.39, the tubes in the middle of the bundle were heated to the highest temperature after the MW irradiation. The reason is that the bundle was placed in the middle of an anti-node location, where the maximum heating happened. In a microwave oven, the microwaves reflect from the walls and form a standing wave pattern in the oven.

From the anti-node to the node locations, the microwave power decreases as a sine-shape wave. That is why the heating was not evenly without rotation. Meanwhile, Figure 6.40 shows that the tubes on the top layers were heated to the higher temperature than those in the low layers. Since the irradiation time was as short as 10 s or 25 s, the temperature increased due to heat conduction could be ignored. The bundle was placed in the anti-node location and the MW penetrated the water from top to bottom. That is why the MW irradiation power decreased gradually along with the depth and the water in the bottom was heated slightly.

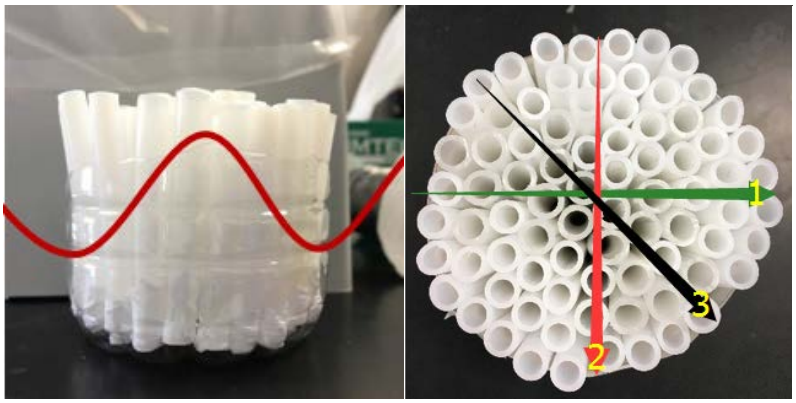

Direction		
1	2	3
43	40	50
54	52	52
51	58	57
57	57	59
55	51	53
40	36	33
27	30	27

Figure 6.39 Measured temperature of water in PTFE tubes after MW irradiation at 1250 W for 20s and frequency 2.45 GHz, room temperature 20.8 ºC.

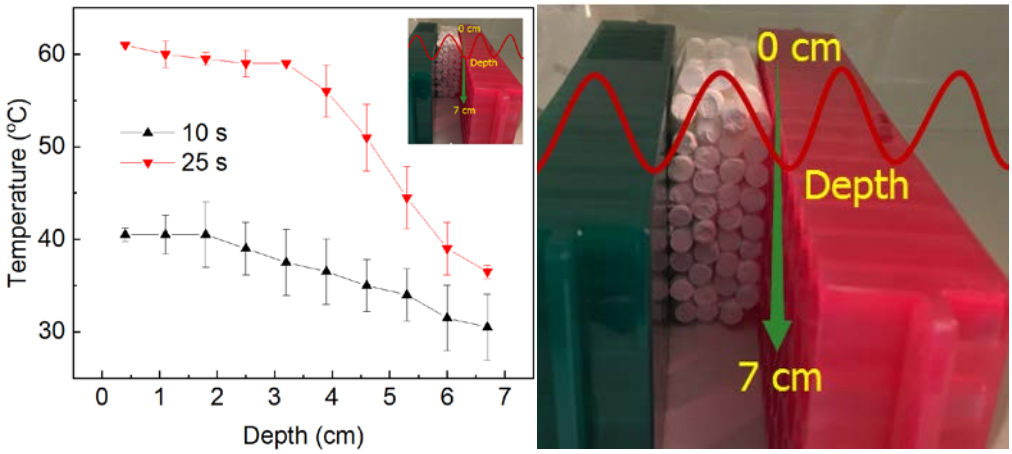

Figure 6.40 Measured penetration depth of water in the tube after MW irradiation at 1250 W and frequency of 2.45 GHz, room temperature 25.8 ºC.

6.4 Conclusions

Prior to membrane filtration experiment, the batch experiments showed that high degradation ratio of methylene blue dye (>95%, initial concentration 1 ppm), excellent antibacterial activity (3.5 log reduction, initial bacterial concentration 10^4 CFU mL^{-1}) and high 1,4-dioxane degradation rate (72%, initial concentration 10 ppm), under the reaction condition of 125 W MW power, 30 mM H_2O_2, 1 g L^{-1} catalyst ($BiFeO_3$), and 2 min irradiation time. With the self-synthesized catalyst ($BiFeO_3$)-coated ceramic membranes, our microwave-assisted membrane filtration system could achieve high 1,4-dixane removal rate (54%) and significant fouling mitigation effect (slower flux decline rate than the process without microwave). The measurement results of particles size distribution and zeta potential of DI water with and without microwave irradiation show that there might have nanobubbles (size peak: 70 nm, 200 nm, 300 nm) produced. And the analysis of hydroxyl radicals also proved that radicals might be the main mechanism for the enhanced removal of pollutants and mitigation of membrane fouling. The results proved that this novel membrane filtration system enables diverse membrane applications such as pollutant removal and disinfection for water reuse and decentralized point-of-use (POU) devices in small drinking water systems.

A novel microwave-enhanced membrane filtration processes has been demonstrated to have antifouling properties and efficient degradation of pollutants during filtration. This microwave-assisted antifouling membrane system opens the possibility to exploring MW-responsive membrane filtration systems using diverse MW-absorbing catalysts such as solid binary oxides (*e.g.*, ZrO_2), ternary oxides (*e.g.*, $BiFeO_3$, $CaTiO_3$), and carbon-based materials for water treatment or chemical processes. Compared to

photocatalytic or sonochemical reactions, MW irradiation can penetrate membrane filtration housing and enable selective absorption onto MW absorbents or catalysts, which can potentially permit efficient surface reactions, leading to diverse environmental or industrial applications. For example, the MW-responsive catalyst, BFO or others may facilitate the local heating, radical generation and nanobubbles formation on ceramic membrane due to the thermal and non-thermal catalytic effects of MW irradiation. Moreover, synergism between H_2O_2 and catalyst-impregnated membrane under MW irradiation leads to the MW-Fenton-like reactions, which promote antifouling and defouling processes, as well as degradation of refractory pollutants.

Additionally, our next-generation membrane filtration system represents a potentially game-changing technology that may transform current physical filtration processes to chemically reactive systems. There has been no research of coupling microwave irradiation with membrane filtration processes, although microwave-assisted flow-through reactors have been designed and utilized in chemical synthesis or conversion. Our hybrid membrane system possesses a great potential to achieve an all-in-one treatment performance equivalent to the current suite of traditional treatment processes (*e.g.*, coagulation, flocculation, sedimentation, granular filtration, microfiltration, and UV disinfection). As such, this work lays groundwork for the development of sustainable decentralized or point-of-use (POU) water purification systems.

6.5 Future Work and Recommendations

6.5.1 AFM Characterization of Nanobubbles and BSA Desorption by MW

Microwave irradiation will be used to prepare nanobubbles on ceramic membranes. The clean ceramic membrane is immersed in DI water. Then pure oxygen is used to aerate degassed DI water at a flow rate of 160 mL min^{-1}. A dissolved oxygen meter (JPSJ605, Shanghai REX Instrument Factory) is used to detect the concentration of dissolved oxygen (DO). To obtain in situ nanobubble images, clean ceramic membrane is fixed on an iron stub with tape and placed into a petri dish with 30 mL DI water before the microwave treatment (OTG Motor Co. Ltd. After this process, ceramic membrane covered with microwave-treated water is carefully and quickly transferred to the AFM sample stage and measured with AFM. The AFM used in the experiment is a Dimension Icon (Bruker) equipped with a liquid cell and an O-ring that sealed the cell and the substrate to prevent liquid leakage during the measurement. During scanning, silicon nitride cantilevers with a spring constant of around 0.32 N m^{-1} were used.[666]

When investigating antifouling by MW, a piece of 1 cm^2 membrane is immersed in the BSA solution (10 mg L^{-1}, 4 mL) for 30 min with microwave irradiation. Then four milliliters of pure water is injected to rinse away any remaining BSA from the membrane surface. The sample is imaged by tapping mode AFM. If the amount of adsorption is reduced than without microwave, it would indicate the effective prevention of deposition of the BSA from solutions to membrane surfaces by microwave.

For defouling experiments, BSA solution (10 mg L^{-1}, 4 mL) is injected into the fluid cell, a piece of 1 cm^2 membrane is immersed in the solution, and allowed to adsorb for 30 min. Then four milliliters of pure water is injected to rinse away any remaining BSA

from the membrane surface. The sample is imaged by tapping mode AFM. After imaging the BSA film, the same membrane sample is applied under MW irradiation for 30 s. Then the same region of the BSA film is again imaged by tapping mode AFM.[277] It is expected that, the coverage of BSA is found to decrease from 100% to 82% after 50 s of microwave treatment via AFM images. The defouling effect of nanobubbles is also investigated using radioactively labeled BSA.[591]

6.5.2 Removal of Antibiotic Resistance Bacteria/Genes (ARB/ARGs) in Drinking Water

Although current conventional disinfectants (*e.g.*, chlorine, chlorine dioxide, or ozone) can eliminate majority of undesirable microorganisms; however, they also render the rise of more than 600 different disinfection byproducts (DBP)[568] and increase microbial resistance to disinfectant chemicals.[571] In addition, the intensive use of antibiotics for human, veterinary and agricultural purposes, results in their continuous release into the environment and the evolution of antibiotic resistance bacteria (ARB) and genes (ARGs).[667] Consequently, conventional disinfection methods are becoming less efficient.[573] UV irradiation is an effective, safe, and environmentally friendly disinfection method but the lack of persistent antibacterial capacity generally causes high risk of bacterial regrowth, particularly in poor sanitation. Thus, drinking water utilities may need to implement alternative disinfection technologies to remain in full regulatory compliance.

Our MW-assisted membrane filtration system is also promising to demonstrate antibacterial features for ARB/ARGs as well as biofouling resistance. Both MW and H_2O_2 have been applied for disinfection widely. However, the high MW power consumption and H_2O_2 usage pose economic challenges and safety concerns. It is anticipated that the functionalized membrane filtration with MW will be a novel disinfection method and

reduce or eliminate the use of H_2O_2 dosage and the MW power consumption, compared with the H_2O_2 or MW treatment alone.

In the future work, removal efficiency and degradation mechanisms of ARB and ARGs will be investigated by filtration of 250 mL bacterial suspension at a pressure of 20 psi. For DNA extraction, each sample (40 mL) collected before and after the filtration experiments is centrifuged for 10 min at 10 000 rpm. Plasmid and genomic DNA are then extracted from the precipitates using the TIANpure Mini Plasmid Kit and TIANamp Bacteria DNA Kit, respectively, following the instructions from the manufacturer (TIANGEN). Bacteria abundance is determined by a plate count.[668] Dilutions of the cell suspension are plated on Luria broth (LB) selective plates containing different antibiotics to select the bacteria resistant to the corresponding antibiotic. Chloramphenicol, tetracycline, and sulfadiazine are the most commonly used antibiotics globally.[669] The concentrations of chloramphenicol, tetracycline, and sulfadiazine employed in the LB selective plates are 32, 16, and 512 mg/L, respectively.[670] After incubation for 24 h at 37 °C, the ARB are quantified via a plate count. Quantitative PCR (qPCR) is performed to determine the abundances of various ARGs using a real-time PCR System (LightCycler480, Applied Science). In order to observe the morphology of bacteria before and after the filtration, cells are stained with the dyes of LIVE/DEAD BacLight bacterial viability kit (L7012, Molecular Probes) following the procedure from the manufacturer. After being incubated at 25 °C in the dark for 15 min, the samples are transferred to the coverslip and examined using a confocal laser scanning microscopy (CLSM, FV1000-IX81, Olympus).[671] The outcome of this future work will provide quantitative insights in the

disinfection potential of MW-enhanced membrane filtration and guide strategy development to minimize the bacterial risk in the drinking water.

6.5.3 Scale-up of Microwave-assisted Flow Processes

The scale-up of microwave-assisted organic syntheses can be classified in terms of the mode of operation, that is, semi-batch or continuous.[672] In most cases, the choice is based on the benefits and limitations associated with the respective mode of operation. Batch scale-up literature mostly reported scaling small reaction volumes of 5 mL conducted in single-mode type of microwave cavities to 1 L multimode microwave ovens.[673] Most of the studies evaluated the limitations related to the volumetric scale-up using standard microwave reactors available commercially.[674] However, a few studies looked into the possibility of designing a microwave setup that satisfied the requirements of large batch processes assuring homogeneous heating.[675, 676] Patil *et al*. presented the following important functionalities that are a must in a microwave setup for development of microwave-integrated reactor systems: (i) a predictable electric field pattern, (ii) a tunable cavity, (iii) reflected power measurements, and (iv) unitized scale-up.[677]

6.5.4 Pilot Plant for Continuous Flow Microwave-Assisted Chemical Reactions

Figure 6.41 outlines the basic structure of the apparatus. It consists of a microwave generator that generates microwaves at 2.45 GHz (HPP121A-INV-02, Hitachi Power Solutions Co., Ltd), a power monitor that measures the power of incident and reflected waves, a three-stub tuner that matches impedance in the apparatus, an applicator that the reactor tube penetrates vertically. It is possible to control the impedance in the apparatus by controlling the insertion length of the stub tuners and the position of the short-circuit plane. Therefore, it is possible to optimize the efficiency of microwave energy absorbed

by the reactant solution in the reactor tube. Since the amount of microwave energy absorbed by a heated material is proportional to the square of electric intensity, the reactor tube needs to be placed in the area where the electric intensity is strong in order for the reactant solution to absorb microwaves efficiently.[678]

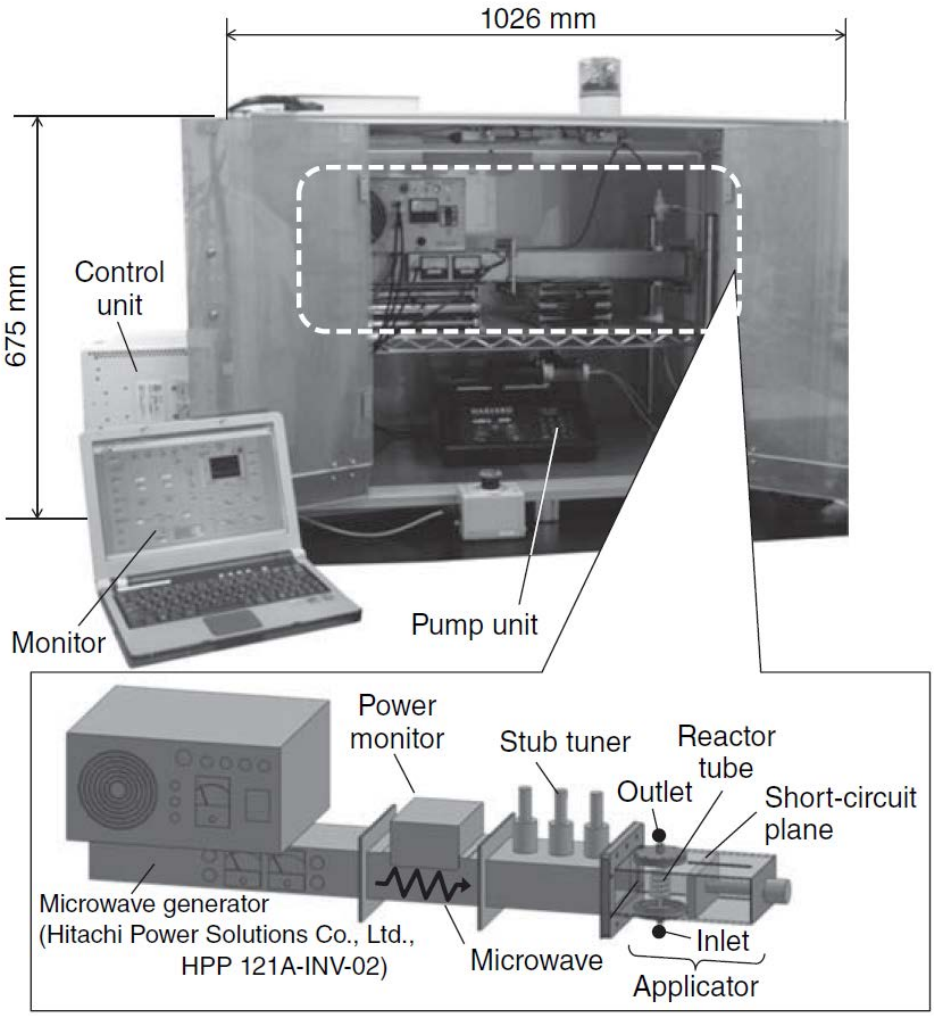

Figure 6.41 Basic structure of the continuous flow microwave-assisted chemical reactor.

APPENDIX

MATLAB CODE FOR CALCULATIONS

The Matlab code used for the calculation of collision efficiency, collision frequency and QSAR models.

A.1 Matlab Code for Calculation of Collision Efficiency and Collision Frequency

A.1.1 Collision Efficiency

The collision efficiency (α) can be calculated with Equation 4.18 and the Matlab code of alpha function is saved as an M file named CollisionEfficiency.M and the codes are shown below:

```
function alpha=CollisionEfficiency(E,delta)
        syms x;
        alpha= double(delta*int(exp(-x)*x^0.5,E,inf));
end
```

Save this function code as CollisionEfficiency.M file. Open this file in Matlab software and put:

```
alpha = CollisionEfficiency("energy barrier value", 1)
```

Press Enter. Then, the result of alpha is the collision efficiency.

For example, for the collision efficiency between the foulant BSA and PVC membrane, the energy barrier value is 210.4 (k_BT). Open the CollisionEfficiency.M file in Matlab and put:

```
alpha = CollisionEfficiency(210.4, 1)
```

Press Enter. Then, the result would be 6.12E-91, which is the collision efficiency.

A.1.2 Collision Frequency

The collision frequency (β) is calculated with Equation 4.19 and the Matlab code of beta function is:

```
function Beta = CollisionFrequency(style, A, r)
        syms h;
        k_b=1.38E-23;
        T=298;
%A=4.3E-18;
%r=133;
        mu=1E-3;
        lambda_c=100;
        u=h./r;
if style == 131
      U = -A./1000*r./12./h.*(1./(1+11.12.*h./lambda_c));
else
        U = -A/1000/6*(1/u+1/(u+2)+log(u/(u+2)));
end
        lambda = (6.*u.^2+13.*u+2)./(6.*u.^2+4.*u);
        test = lambda.*exp(U./k_b./T)./(2+u).^2;
%t = test;
        test = matlabFunction(test);
        res = quadgk(test,0,inf);
        Beta = (8.*k_b.*T./(3.*mu)./(2./r.*res));
end
```

Save this function code as CollisionFrequency.M file. Open this file in Matlab software and put:

```
Beta = CollisionFrequency("style", A, r)
```

Press Enter. Then, the result of Beta is the collision frequency.

For example, for the collision frequency between the foulant BSA and PVC membrane, the style is 132, A is 4.3E-18, and r is 133. Open the CollisionFrequency.M file in Matlab and put:

```
Beta = CollisionFrequency(132, 4.3E-18, 133)
```

Press Enter. Then, the result would be 6.60E-18, which is the collision frequency.

A.2 Matlab Code for QSAR Models

A.2.1 QSAR Model for the Water Permeability and Membrane Characteristics

The QSAR model for the water permeability and membrane characteristics is developed using the MATLAB code below.

```
t = [34.8 72.9 0.00 -42.5 1 75.4 70.1 85.38;
36.5 136.3 0.00 -49.4 0.85294 68.3 43.3 38.5;
37.9 130.3 0.00 -62.4 0.7268 61.7 30.8 36.28;
38.2 159.0 7.95 -64.2 0.61016 60.0 28.3 30.15;
40.4 136.5 11.67 -64.1 0.46333 51.3 22.1 23.61;
34.8 72.9 0.00 -40.2 1 75.4 70.1 85.38;
39.6 112.4 23.40 -63.5 0.75587 70.7 63.2 57.63;
40.2 119.2 42.67 -53.7 0.60011 65.9 62.3 57.5;
40.9 118.0 84.00 -64.4 0.4713 62.1 56.0 55.1;
45.1 123.8 100.75 -66.4 0.37066 57.5 42.7 56.3;
34.8 72.9 0.00 -42.5 1 75.4 70.1 85.38;
38.2 136.3 0.00 -42.0 0.84982 70.5 50.4 64.5;
38.6 152.5 0.00 -44.4 0.72412 68.7 58.1 64.6;
38.9 144.0 0.00 -48.5 0.52218 71.9 55.9 65;
38.9 134.8 0.00 -40.1 0.46627 69.1 60.3 60];
poro = t(:,1);
rou = t(:,2);
hyd = t(:,3);
cha = t(:,4);
inten = t(:,5);
ten = t(:,6);
elo = t(:,7);
perm = t(:,8);
tbl =
    table(poro,rou,hyd,cha,inten,ten,elo,perm,'VariableNames',{'poro','rou',
    'hyd','cha','inten','ten','elo','perm'});
lm = fitlm(tbl,'perm~poro+rou+hyd+cha+inten+ten+elo') % Model 1
```

Detailed explanations for each line in the code are provided below:

Line 1-15: Put in the raw data from Table A.1.

Line 16-23: Define each column with the variable names. For example, column 1 is the surface porosity values.

Line 24: Create the data table with the data in Line 1-15

Line 25: Use fitlm function to build the linear model between water permeability and other seven properties.

Save this function code as an M file named qsar1.M file. Put the data in the Table A.1 to replace the bold texts above. Then press “Run”. Then, the result of QSAR model shows up as shown below.

```
1 -  Linear regression model:
2 -  perm ~ 1 + poro + rou + hyd + cha + inten + ten + elo
3 -  Estimated Coefficients:
                        Estimate          SE
                        ________    ________

4 -  (Intercept)        -55.705         109.31
5 -  poro               2.2717          2.3529
6 -  rou                -0.26925        0.14739
7 -  hyd                0.072444        0.15478
8 -  cha                0.70522         0.36951
9 -  inten              3.1303          23.847
10 - ten                1.2489          1.1016
11 - elo                0.16435         0.45804
```

Detailed explanations for each line in the code are provided below:

Line 1: the model type is linear regression model.

Line 2: the linear equation that include the variables fitting the model.

Line 3: the coefficients for each variables will be show below.

Line 4: the value for the intercept in the linear equation.

Line 5-11: the coefficients and standard error for each variables.

Thus, the QSAR model for the water permeability and membrane characteristics is expressed in Equation 5.1.

A.2.2 QSAR Model for the HA Rejection and Membrane Characteristics

The QSAR model for the HA rejection and membrane characteristics is developed using the MATLAB code below.

```
1 -  t = [35.01  91.5   92.4   -53.8  1.0  66.79  49.1  41;
2 -  35.1  87.8  86.8  -55.7  1.0  56.46  41.8  36;
3 -  37.9  99.6  67.4  -56.7  1.0  57.94  38.5  32;
4 -  40.1  138.8  64.9  -57.1  1.0  53.30  27.4  36;
5 -  41.5  129.2  23.0  -79.7  1.0  37.75  8.9  38;
6 -  35.0  91.5  92.4  -53.8  1.00  66.8  49.1  41;
7 -  36.8  94.2  98.0  -69.1  0.87  64.3  45.8  41;
8 -  38.3  104.3  109.4  -46.8  0.89  56.4  45.0  35;
9 -  40.5  104.7  91.8  -49.3  0.85  53.6  41.1  29;
10 - 45.5  109.5  90.6  -59.9  0.84  46.7  26.2  27;
11 - 35.0  91.5  92.4  -53.8  1.00  66.8  49.1  41;
12 - 36.5  115.5  96.5  -51.2  0.91  63.7  56.0  49;
13 - 38.2  131.8  102.3  -46.3  0.91  62.5  45.5  46;
14 - 38.3  139.0  93.3  -58.8  1.00  68.5  59.7  41;
15 - 38.7  140.5  88.0  -64.9  1.00  64.4  48.7  43];
16 - poro = t(:,1);
17 - rou = t(:,2);
18 - hyd = t(:,3);
19 - cha = t(:,4);
20 - inten = t(:,5);
21 - ten = t(:,6);
22 - elo = t(:,7);
23 - rej = t(:,8);
24 - tbl =
     table(poro,rou,hyd,cha,inten,ten,elo,rej,'VariableNames',{'poro','rou',
     'hyd','cha','inten','ten','elo','rej'});
25 - lm = fitlm(tbl,'rej~poro+rou+hyd+cha+inten+ten+elo') % Model 2
```

Detailed explanations for each line in the code are provided below:

Line 1-15: Put in the raw data from Table A.1.

Line 16-23: Define each column with the variable names. For example, column 1 is the surface porosity values.

Line 24: Create the data table with the data in Line 1-15.

Line 25: Use fitlm function to build the linear model between HA rejection and other seven properties.

Save this function code as an M file named qsar2.M file. Put the data in the Table A.1 to replace the bold texts above. Then press “Run”. Then, the result of QSAR model shows up as shown below.

```
1 -  Linear regression model:
2 -  rej ~ 1 + poro + rou + hyd + cha + inten + ten + elo

3 -  Estimated Coefficients:
                    Estimate        SE
                    ________        _______
4 -  (Intercept)    144.14          54.217
5 -  poro           -2.6579         0.83556
6 -  rou            0.25785         0.076616
7 -  hyd            -0.016964       0.15929
8 -  cha            -0.14521        0.17699
9 -  inten          -49.292         32.093
10 - ten            0.0021455       0.43628
11 - elo            -0.0013342      0.28448
```

Detailed explanations for each line in the code are provided below:

Line 1: the model type is linear regression model.

Line 2: the linear equation that include the variables fitting the model.

Line 3: the coefficients for each variables will be show below.

Line 4: the value for the intercept in the linear equation.

Line 5-11: the coefficients and standard error for each variables.

Thus, the QSAR model for the HA rejection and membrane characteristics is expressed in Equation 5.2.

Table A.1 Experimental Database for QSAR Models

Porosity	Roughness	Hydrophobicity	Surface charge	Intensity	Tensile strength	Elongation	Permeability	HA rejection
34.8	72.9	0.00	-42.5	1.00	75.4	70.1	85.38	41
36.5	136.3	0.00	-49.4	0.85	68.3	43.3	38.5	36
37.9	130.3	0.00	-62.4	0.73	61.7	30.8	36.28	32
38.2	159.0	7.95	-64.2	0.61	60.0	28.3	30.15	36
40.4	136.5	11.67	-64.1	0.46	51.3	22.1	23.61	38
34.8	72.9	0.00	-40.2	1.00	75.4	70.1	85.38	41
39.6	112.4	23.40	-63.5	0.76	70.7	63.2	57.63	41
40.2	119.2	42.67	-53.7	0.60	65.9	62.3	57.5	35
40.9	118.0	84.00	-64.4	0.47	62.1	56.0	55.1	29
45.1	123.8	100.75	-66.4	0.37	57.5	42.7	56.3	27
34.8	72.9	0.00	-42.5	1.00	75.4	70.1	85.38	41
38.2	136.3	0.00	-42.0	0.85	70.5	50.4	64.5	49
38.6	152.5	0.00	-44.4	0.72	68.7	58.1	64.6	46
38.9	144.0	0.00	-48.5	0.52	71.9	55.9	65	41
38.9	134.8	0.00	-40.1	0.47	69.1	60.3	60	43

REFERENCES

1. Van der Bruggen, B.; Vandecasteele, C.; Van Gestel, T.; Doyen, W.; Leysen, R., A review of pressure‐driven membrane processes in wastewater treatment and drinking water production. *Environ. Prog.* **2003,** *22*, 46-56.

2. Qu, X.; Alvarez, P. J.; Li, Q., Applications of nanotechnology in water and wastewater treatment. *Water Res.* **2013,** *47*, 3931-3946.

3. Drioli, E.; Criscuoli, A.; Curcio, E., Integrated membrane operations for seawater desalination. *Desalination* **2002,** *147*, 77-81.

4. Imbrogno, J.; Belfort, G., Membrane desalination: where are we, and what can we learn from fundamentals? *Annu. Rev. Chem. Biomol. Eng.* **2016,** *7*, 29-64.

5. Luján-Facundo, M. J.; Mendoza-Roca, J. A.; Cuartas-Uribe, B.; Álvarez-Blanco, S., Cleaning efficiency enhancement by ultrasounds for membranes used in dairy industries. *Ultrason. Sonochem.* **2016,** *33*, 18-25.

6. Agenson, K. O.; Urase, T., Change in membrane performance due to organic fouling in nanofiltration (NF)/reverse osmosis (RO) applications. *Sep. Purif. Technol.* **2007,** *55*, 147-156.

7. Du, J. R.; Peldszus, S.; Huck, P. M.; Feng, X., Modification of membrane surfaces via microswelling for fouling control in drinking water treatment. *J. Membr. Sci.* **2015,** *475*, 488-495.

8. Matin, A.; Shafi, H.; Wang, M.; Khan, Z.; Gleason, K.; Rahman, F., Reverse osmosis membranes surface-modified using an initiated chemical vapor deposition technique show resistance to alginate fouling under cross-flow conditions: Filtration & subsequent characterization. *Desalination* **2016,** *379*, 108-117.

9. Igbinigun, E.; Fennell, Y.; Malaisamy, R.; Jones, K. L.; Morris, V., Graphene oxide functionalized polyethersulfone membrane to reduce organic fouling. *J. Membr. Sci.* **2016,** *514*, 518-526.

10. Chang, H.; Liang, H.; Qu, F.; Ma, J.; Ren, N.; Li, G., Towards a better hydraulic cleaning strategy for ultrafiltration membrane fouling by humic acid: Effect of backwash water composition. *J. Env. Sci.* **2016,** *43*, 177-186.

11. Jiang, W.; Wei, Y.; Gao, X.; Gao, C.; Wang, Y., An innovative backwash cleaning technique for NF membrane in groundwater desalination: Fouling reversibility and cleaning without chemical detergent. *Desalination* **2015,** *359*, 26-36.

12. Rabuni, M.; Sulaiman, N. N.; Aroua, M.; Chee, C. Y.; Hashim, N. A., Impact of in situ physical and chemical cleaning on PVDF membrane properties and performances. *Chem. Eng. Sci.* **2015,** *122*, 426-435.

13. Jutaporn, P.; Singer, P. C.; Cory, R. M.; Coronell, O., Minimization of short-term low-pressure membrane fouling using a magnetic ion exchange (MIEX®) resin. *Water Res.* **2016,** *98*, 225-234.

14. Yu, W.; Yang, Y.; Graham, N., Evaluation of ferrate as a coagulant aid/oxidant pretreatment for mitigating submerged ultrafiltration membrane fouling in drinking water treatment. *Chem. Eng. J.* **2016,** *298*, 234-242.

15. Ao, L.; Liu, W.; Zhao, L.; Wang, X., Membrane fouling in ultrafiltration of natural water after pretreatment to different extents. *J. Env. Sci.* **2016,** *43*, 234-243.

16. Van der Bruggen, B.; Braeken, L.; Vandecasteele, C., Flux decline in nanofiltration due to adsorption of organic compounds. *Sep. Purif. Technol.* **2002,** *29*, 23-31.

17. Braeken, L.; Boussu, K.; Van der Bruggen, B.; Vandecasteele, C., Modeling of the adsorption of organic compounds on polymeric nanofiltration membranes in solutions containing two compounds. *ChemPhysChem* **2005,** *6*, 1606-1612.

18. Vercellino, T.; Morse, A.; Tran, P.; Hamood, A.; Reid, T.; Song, L.; Moseley, T., The use of covalently attached organo-selenium to inhibit S. aureus and E. coli biofilms on RO membranes and feed spacers. *Desalination* **2013,** *317*, 142-151.

19. Freger, V.; Gilron, J.; Belfer, S., TFC polyamide membranes modified by grafting of hydrophilic polymers: an FTIR/AFM/TEM study. *J. Membr. Sci.* **2002,** *209*, 283-292.

20. Field, R., Fundamentals of fouling. Weinheim, Germany: Wiley-VCH, **2010**.

21. Shi, X.; Tal, G.; Hankins, N. P.; Gitis, V., Fouling and cleaning of ultrafiltration membranes: A review. *J. Water Process Eng.* **2014,** *1*, 121-138.

22. Zondervan, E.; Roffel, B., Evaluation of different cleaning agents used for cleaning ultra filtration membranes fouled by surface water. *J. Membr. Sci.* **2007,** *304*, 40-49.

23. Kyllönen, H.; Pirkonen, P.; Nyström, M.; Nuortila-Jokinen, J.; Grönroos, A., Experimental aspects of ultrasonically enhanced cross-flow membrane filtration of industrial wastewater. *Ultrason. Sonochem.* **2006,** *13*, 295-302.

24. Kyllönen, H. M.; Pirkonen, P.; Nyström, M., Membrane filtration enhanced by ultrasound: a review. *Desalination* **2005,** *181*, 319-335.

25. Enevoldsen, A. D.; Hansen, E. B.; Jonsson, G., Electro-ultrafiltration of industrial enzyme solutions. *J. Membr. Sci.* **2007,** *299*, 28-37.

26. Stawikowska, J.; Livingston, A. G., Assessment of atomic force microscopy for characterisation of nanofiltration membranes. *J. Membr. Sci.* **2013,** *425*, 58-70.

27. Last, J. A.; Russell, P.; Nealey, P. F.; Murphy, C. J., The Applications of Atomic Force Microscopy to Vision Science. *Invest. Ophthalmol. Vis. Sci.* **2010,** *51*, 6083-6094.

28. Webb, H. K.; Truong, V. K.; Hasan, J.; Crawford, R. J.; Ivanova, E. P., Physico-mechanical characterisation of cells using atomic force microscopy—current research and methodologies. *J. Microbiol. Methods* **2011,** *86*, 131-139.

29. Butt, H.-J.; Cappella, B.; Kappl, M., Force measurements with the atomic force microscope: Technique, interpretation and applications. *Surf. Sci. Rep.* **2005,** *59*, 1-152.

30. Cohen, S. R.; Bitler, A., Use of AFM in bio-related systems. *Curr. Opin. Colloid Interface Sci.* **2008,** *13*, 316-325.

31. Franz, C. M.; Puech, P. H., Atomic force microscopy: a versatile tool for studying cell morphology, adhesion and mechanics. *Cell Mol. Bioeng.* **2008,** *1*, 289-300.

32. Bieletzki, M.; Hynninen, T.; Soini, T. M.; Pivetta, M.; Henry, C. R.; Foster, A. S.; Esch, F.; Barth, C.; Heiz, U., Topography and work function measurements of thin MgO(001) films on Ag(001) by nc-AFM and KPFM. *Phys. Chem. Chem. Phys.* **2010,** *12*, 3203-3209.

33. Boussu, K.; Van der Bruggen, B.; Volodin, A.; Snauwaert, J.; Van Haesendonck, C.; Vandecasteele, C., Roughness and hydrophobicity studies of nanofiltration membranes using different modes of AFM. *J. Colloid Interface Sci.* **2005,** *286*, 632-638.

34. Hayashi, K.; Iwata, M., Stiffness of cancer cells measured with an AFM indentation method. *J. Mech. Behav. Biomed. Mater.* **2015,** *49*, 105-111.

35. Zhang, W.; Hughes, J.; Chen, Y., Impacts of hematite nanoparticle exposure on biomechanical, adhesive, and surface electrical properties of Escherichia coli cells. *Appl. Environ. Microbiol.* **2012,** *78*, 3905-3915.

36. Wang, C.; Zhao, Y.; Zheng, S.; Xue, J.; Zhou, J.; Tang, Y.; Jiang, L.; Li, W., Effect of enamel morphology on nanoscale adhesion forces of streptococcal bacteria : An AFM study. *Scanning* **2015,** *37*, 313-321.

37. Zhang, W.; Stack, A. G.; Chen, Y., Interaction force measurement between E. coli cells and nanoparticles immobilized surfaces by using AFM. *Colloids Surf. B Biointerfaces* **2011,** *82*, 316-324.

38. Ahmed, N.; Nino, D. F.; Moy, V. T., Measurement of solution viscosity by atomic force microscopy. *Rev. Sci. Instrum.* **2001,** *72*, 2731-2734.

39. Trotsenko, O.; Koestner, R.; Roiter, Y.; Tokarev, A.; Minko, S., Probing rough composite surfaces with atomic force microscopy: Nafion ionomer in fuel cell electrodes. *Polymer* **2016,** *102*, 396-403.

40. Estevez, I.; Chrétien, P.; Schneegans, O.; Houzé, F., Specific methodology for capacitance imaging by atomic force microscopy: A breakthrough towards an elimination of parasitic effects. *Appl. Phys. Lett.* **2014,** *104*, 083108.

41. Jeandupeux, O.; Marsico, V.; Acovic, A.; Fazan, P.; Brune, H.; Kern, K., Use of scanning capacitance microscopy for controlling wafer processing. *Microelectron. Reliab.* **2002,** *42*, 225-231.

42. Middea, A.; Spinelli, L. S.; Souza Junior, F. G.; Neumann, R.; Gomes, O. d. F. M.; Fernandes, T. L. A. P.; de Lima, L. C.; Barthem, V. M. T. S.; de Carvalho, F. V., Synthesis and characterization of magnetic palygorskite nanoparticles and their application on methylene blue remotion from water. *Appl. Surf. Sci.* **2015,** *346*, 232-239.

43. Puntambekar, K. P.; Pesavento, P. V.; Frisbie, C. D., Surface potential profiling and contact resistance measurements on operating pentacene thin-film transistors by Kelvin probe force microscopy. *Appl. Phys. Lett.* **2003,** *83*, 5539-5541.

44. Melitz, W.; Shen, J.; Kummel, A. C.; Lee, S., Kelvin probe force microscopy and its application. *Surf. Sci. Rep.* **2011,** *66*, 1-27.

45. Berger, R.; Butt, H.-J.; Retschke, M. B.; Weber, S. A. L., Electrical modes in scanning probe microscopy. *Macromol. Rapid Commun.* **2009,** *30*, 1167-1178.

46. Sugimura, H.; Ishida, Y.; Hayashi, K.; Takai, O.; Nakagiri, N., Potential shielding by the surface water layer in Kelvin probe force microscopy. *Appl. Phys. Lett.* **2002,** *80*, 1459-1461.

47. Liscio, A.; Palermo, V.; Mullen, K.; Samori, P., Tip-sample interactions in Kelvin probe force microscopy: quantitative measurement of the local surface potential. *J. Phys. Chem. C* **2008,** *112*, 17368-17377.

48. Kaneko, K.; Inoke, K.; Freitag, B.; Hungria, A. B.; Midgley, P. A.; Hansen, T. W.; Zhang, J.; Ohara, S.; Adschiri, T., Structural and Morphological Characterization of Cerium Oxide Nanocrystals Prepared by Hydrothermal Synthesis. *Nano Lett.* **2007,** *7*, 421-425.

49. Porter, A. E.; Gass, M.; Muller, K.; Skepper, J. N.; Midgley, P. A.; Welland, M., Direct imaging of single-walled carbon nanotubes in cells. *Nat Nano* **2007,** *2*, 713-717.

50. Zhang, W.; Yao, Y.; Chen, Y., Imaging and quantifying the morphology and nanoelectrical properties of quantum dot nanoparticles interacting with DNA. *J. Phys. Chem. C* **2010,** *115*, 599-606.

51. Zhang, W.; Chen, Y., Experimental determination of conduction and valence bands of semiconductor nanoparticles using Kelvin probe force microscopy. *J. Nanopart. Res.* **2013,** *15*, 1-7.

52. Shikler, R.; Fried, N.; Meoded, T.; Rosenwaks, Y., Measuring minority-carrier diffusion length using a Kelvin probe force microscope. *Phys. Rev. B: Condens. Matter* **2000,** *61*, 11041.

53. Palermo, V.; Palma, M.; Tomović, Ž.; Watson, M. D.; Friedlein, R.; Müllen, K.; Samorì, P., Influence of Molecular Order on the Local Work Function of Nanographene Architectures: A Kelvin-Probe Force Microscopy Study. *Chemphyschem* **2005,** *6*, 2371-2375.

54. Hayashi, K.; Saito, N.; Sugimura, H.; Takai, O.; Nakagiri, N., Regulation of the Surface Potential of Silicon Substrates in Micrometer Scale with Organosilane Self-Assembled Monolayers. *Langmuir* **2002,** *18*, 7469-7472.

55. Sun, L.; Wang, J.; Bonaccurso, E., Nanoelectronic Properties of a Model System and of a Conjugated Polymer: A Study by Kelvin Probe Force Microscopy and Scanning Conductive Torsion Mode Microscopy. *J. Phys. Chem. C* **2010,** *114*, 7161-7168.

56. Alexander, J.; Magonov, S.; Moeller, M., Topography and surface potential in Kelvin force microscopy of perfluoroalkyl alkanes self-assemblies. *J. Vac. Sci. Technol. B* **2009,** *27*, 903-911.

57. Zhang, W.; Yao, Y.; Chen, Y., Imaging and quantifying the morphology and nanoelectrical properties of quantum dot nanoparticles interacting with DNA. *J. Phys. Chem. C* **2011,** *115*, 599–606.

58. Muller, E. A.; Pollard, B.; Raschke, M. B., Infrared Chemical Nano-Imaging: Accessing Structure, Coupling, and Dynamics on Molecular Length Scales. *J. Phys. Chem. Lett.* **2015,** *6*, 1275-1284.

59. Dazzi, A.; Prater, C. B.; Hu, Q.; Chase, D. B.; Rabolt, J. F.; Marcott, C., AFM-IR: Combining Atomic Force Microscopy and Infrared Spectroscopy for Nanoscale Chemical Characterization. *Appl. Spectrosc.* **2012,** *66*, 1365-1384.

60. Hung, P. Y.; O'Loughlin, T. E.; Lewis, A.; Dechter, R.; Samayoa, M.; Banerjee, S.; Wood, E. L.; Hight Walker, A. R. In *Potential application of tip-enhanced Raman spectroscopy (TERS) in semiconductor manufacturing*, SPIE Advanced Lithography. International Society for Optics and Photonics, San Jose, California, USA, March, 2015; San Jose, California, USA, March, 2015; pp 94241S-94241S-13.

61. Biagi, M. C.; Fabregas, R.; Gramse, G.; Van Der Hofstadt, M.; Juárez, A.; Kienberger, F.; Fumagalli, L.; Gomila, G., Nanoscale Electric Permittivity of Single Bacterial Cells at Gigahertz Frequencies by Scanning Microwave Microscopy. *ACS Nano* **2016,** *10*, 280-288.

62. Humer, I.; Bethge, O.; Bodnarchuk, M.; Kovalenko, M.; Yarema, M.; Heiss, W.; Huber, H. P.; Hochleitner, M.; Hinterdorfer, P.; Kienberger, F.; Smoliner, J., Scanning microwave microscopy and scanning capacitance microscopy on colloidal nanocrystals. *J. Appl. Phys.* **2011,** *109*, 064313.

63. Vitry, P.; Bourillot, E.; Plassard, C.; Lacroute, Y.; Calkins, E.; Tetard, L.; Lesniewska, E., Mode-synthesizing atomic force microscopy for 3D reconstruction of embedded low-density dielectric nanostructures. *Nano Res.* **2015,** *8*, 2199-2205.

64. Macpherson, J. V.; Unwin, P. R., Combined Scanning Electrochemical−Atomic Force Microscopy. *Anal. Chem.* **2000,** *72*, 276-285.

65. Dazzi, A.; Saunier, J.; Kjoller, K.; Yagoubi, N., Resonance enhanced AFM-IR: A new powerful way to characterize blooming on polymers used in medical devices. *Int. J. Pharm.* **2015,** *484*, 109-114.

66. Lo, M.; Prater, C.; Dazzi, A.; Shetty, R.; Kjoller, K. In *Nanoscale chemical composition mapping of polymers at 100nm spatial resolution with AFM-based IR spectroscopy*, SPIE Defense, Security, and Sensing. International Society for Optics and Photonics, Baltimore, Maryland, USA, May, May; Baltimore, Maryland, USA, May, 2012; pp 83730L-83730L-4.

67. Morsch, S.; Lyon, S.; Greensmith, P.; Smith, S. D.; Gibbon, S. R., Mapping water uptake in organic coatings using AFM-IR. *Faraday Discuss.* **2015,** *180*, 527-542.

68. Dazzi, A.; Prazeres, R.; Glotin, F.; Ortega, J., Subwavelength infrared spectromicroscopy using an AFM as a local absorption sensor. *Infrared phys. & technol.* **2006,** *49*, 113-121.

69. Resonance enhanced AFM-IR. http://www.anasysinstruments.com/resonance-enhanced-afm-ir-2/, Anasys Instruments, Santa Barbara, CA.: (accessed 12, 2016).

70. Marcott, C.; Lo, M.; Kjoller, K.; Prater, C.; Noda, I., Spatial Differentiation of Sub-Micrometer Domains in a Poly(hydroxyalkanoate) Copolymer Using Instrumentation that Combines Atomic Force Microscopy (AFM) and Infrared (IR) Spectroscopy. *Appl. Spectrosc.* **2011,** *65*, 1145-1150.

71. Ghosh, S.; Ramos, L.; Remita, S.; Dazzi, A.; Deniset-Besseau, A.; Beaunier, P.; Goubard, F.; Aubert, P.-H.; Remita, H., Conducting polymer nanofibers with controlled diameters synthesized in hexagonal mesophases. *New J. Chem.* **2015,** *39*, 8311-8320.

72. Tang, F.; Bao, P.; Su, Z., Analysis of Nanodomain Composition in High-Impact Polypropylene by Atomic Force Microscopy-Infrared. *Anal. Chem.* **2016,** *88*, 4926-4930.

73. Lu, F.; Jin, M.; Belkin, M. A., Tip-enhanced infrared nanospectroscopy via molecular expansion force detection. *Nat. Phot.* **2014,** *8*, 307-312.

74. Dillon, E.; Lo, M.; Kjoller, K.; Hu, Q.; Shetty, R., Nanoscale Infrared Spectroscopy of Biological Systems. *Biophys. J.* **2015,** *108*, 492a.

75. Miller, L. M.; Dumas, P., From structure to cellular mechanism with infrared microspectroscopy. *Curr. Opin. Struct. Biol.* **2010,** *20*, 649-656.

76. Hanna, C.; Jonathan, R. F.; Min-Feng, Y.; Lawrence, A. B.; Alexander, F. V.; William, P. K., Improved atomic force microscope infrared spectroscopy for rapid nanometer-scale chemical identification. *Nanotechnology* **2013,** *24*, 444007.

77. Van Eerdenbrugh, B.; Lo, M.; Kjoller, K.; Marcott, C.; Taylor, L. S., Nanoscale Mid-Infrared Evaluation of the Miscibility Behavior of Blends of Dextran or Maltodextrin with Poly(vinylpyrrolidone). *Mol. Pharm.* **2012,** *9*, 1459-1469.

78. Purohit, H. S.; Taylor, L. S., Miscibility of Itraconazole–Hydroxypropyl Methylcellulose Blends: Insights with High Resolution Analytical Methodologies. *Mol. Pharm.* **2015,** *12*, 4542-4553.

79. Miller, L. M.; Bourassa, M. W.; Smith, R. J., FTIR spectroscopic imaging of protein aggregation in living cells. *BBA Biomembr.* **2013,** *1828*, 2339-2346.

80. Kennedy, E.; Al-Majmaie, R.; Al-Rubeai, M.; Zerulla, D.; Rice, J. H., Quantifying nanoscale biochemical heterogeneity in human epithelial cancer cells using combined AFM and PTIR absorption nanoimaging. *J. Biophotonics* **2015,** *8*, 133-141.

81. Vitry, P.; Rebois, R.; Bourillot, E.; Deniset-Besseau, A.; Virolle, M.-J.; Lesniewska, E.; Dazzi, A., Combining infrared and mode synthesizing atomic force microscopy: Application to the study of lipid vesicles inside Streptomyces bacteria. *Nano Res.* **2016,** *9*, 1674-1681.

82. Mayet, C.; Dazzi, A.; Prazeres, R.; Ortega, J.-M.; Jaillard, D., In situ identification and imaging of bacterial polymer nanogranules by infrared nanospectroscopy. *Analyst* **2010,** *135*, 2540-2545.

83. Gunatillake, P.; Mayadunne, R.; Adhikari, R., Recent developments in biodegradable synthetic polymers. *Biotechnol. Annu. Rev.* **2006,** *12*, 301-347.

84. Baldassarre, L.; Giliberti, V.; Rosa, A.; Ortolani, M.; Bonamore, A.; Baiocco, P.; Kjoller, K.; Calvani, P.; Nucara, A., Mapping the amide I absorption in single bacteria and mammalian cells with resonant infrared nanospectroscopy. *Nanotechnology* **2016,** *27*, 075101.

85. Prater, C.; Kjoller, K.; Cook, D.; Shetty, R.; Meyers, G.; Reinhardt, C.; Felts, J.; King, W.; Vodopyanov, K.; Dazzi, A., Nanoscale infrared spectroscopy of materials by atomic force microscopy. *Microsc. Anal.* **2010,** *24*, 5-8.

86. Lahiri, B.; Holland, G.; Centrone, A., Chemical imaging beyond the diffraction limit: experimental validation of the PTIR technique. *Small* **2013,** *9*, 439-445.

87. Mukherjee, S.; Gowen, A., A review of recent trends in polymer characterization using non-destructive vibrational spectroscopic modalities and chemical imaging. *Anal. Chim. Acta* **2015,** *895*, 12-34.

88. Eby, T.; Gundusharma, U.; Lo, M.; Sahagian, K.; Marcott, C.; Kjoller, K., Reverse engineering of polymeric multilayers using AFM-based nanoscale IR spectroscopy and thermal analysis. *Spectrosc. Eur.* **2012,** *24*, 18.

89. Centrone, A., Infrared Imaging and Spectroscopy Beyond the Diffraction Limit. *Annu. Rev. Anal. Chem.* **2015,** *8*, 101-126.

90. Dazzi, A.; Glotin, F.; Carminati, R., Theory of infrared nanospectroscopy by photothermal induced resonance. *J. Appl. Phys.* **2010,** *107*, 124519.

91. Instruments, A. Tapping AFM-IR: Highest performance nanoIR chemical imaging to 10nm resolution. http://www.anasysinstruments.com/wp-content/uploads/Tapping-AFM-IR.pdf (accessed 12, 2016).

92. Kjoller, K.; Felts, J.; Cook, D.; Prater, C.; King, W., High-sensitivity nanometer-scale infrared spectroscopy using a contact mode microcantilever with an internal resonator paddle. *Nanotechnology* **2010,** *21*, 185705.

93. Livneh, T.; Zhang, J.; Cheng, G.; Moskovits, M., Polarized Raman scattering from single GaN nanowires. *Phys. Rev. B* **2006,** *74*, 035320.

94. Zhong, H.; Wang, J.; Chen, X.; Li, Z.; Xu, W.; Lu, W., Effect of Mn+ ion implantation on the Raman spectra of ZnO. *J. Appl. Phys.* **2006,** *99*, 3905.

95. Calizo, I.; Balandin, A.; Bao, W.; Miao, F.; Lau, C., Temperature dependence of the Raman spectra of graphene and graphene multilayers. *Nano Lett.* **2007,** *7*, 2645-2649.

96. Lucas, M.; Young, R., Effect of uniaxial strain deformation upon the Raman radial breathing modes of single-wall carbon nanotubes in composites. *Phys. Rev. B* **2004,** *69*, 085405.

97. Jiang, N.; Kurouski, D.; Pozzi, E. A.; Chiang, N.; Hersam, M. C.; Van Duyne, R. P., Tip-enhanced Raman spectroscopy: From concepts to practical applications. *Chem. Phys. Lett.* **2016,** *659*, 16-24.

98. Raman, C. V.; Krishnan, K. S., A new type of secondary radiation. *Nature* **1928,** *121*, 501-502.

99. Domke, K. F.; Pettinger, B., Studying surface chemistry beyond the diffraction limit: 10 years of TERS. *ChemPhysChem* **2010,** *11*, 1365-1373.

100. Kaemmer, S. B.; Ruiter, T.; Pittenger, B., Atomic force microscopy with Raman and tip-enhanced Raman spectroscopy. *Microsc. Today* **2012,** *20*, 22-27.

101. Nacken, T.; Damm, C.; Walter, J.; Rüger, A.; Peukert, W., Delamination of graphite in a high pressure homogenizer. *RSC Adv.* **2015,** *5*, 57328-57338.

102. Lindberg, G.; O'Loughlin, T.; Gross, N.; Reznik, A.; Abbaszadeh, S.; Karim, K.; Belev, G.; Hunter, D.; Weinstein, B., Raman and AFM mapping studies of photo-induced crystallization in a-Se films: substrate strain and thermal effects 1. *Can. J. Phys.* **2013,** *92*, 728-731.

103. O'Loughlin, T. E.; Depner, S. W.; Schultz, B. J.; Banerjee, S., Microwave-induced nucleation of conducting graphitic domains on silicon carbide surfaces. *J. Vac. Sci. Technol. B* **2014,** *32*, 011215.

104. Saito, R.; Hofmann, M.; Dresselhaus, G.; Jorio, A.; Dresselhaus, M., Raman spectroscopy of graphene and carbon nanotubes. *Advances in Physics* **2011,** *60*, 413-550.

105. Fleischmann, M.; Hendra, P. J.; McQuillan, A. J., Raman spectra from electrode surfaces. *J. Chem. Soc., Chem. Commun.* **1973**, 80-81.

106. Campos, A. R.; Gao, Z.; Blaber, M. G.; Huang, R.; Schatz, G. C.; Van Duyne, R. P.; Haynes, C. L., Surface-Enhanced Raman Spectroscopy Detection of Ricin B Chain in Human Blood. *J. Phys. Chem. C* **2016,** *120*, 20961-20969.

107. Ma, C.; Harris, J. M., Surface-Enhanced Raman Spectroscopy Investigation of the Potential-Dependent Acid−Base Chemistry of Silver-Immobilized 2-Mercaptobenzoic Acid. *Langmuir* **2011,** *27*, 3527-3533.

108. Zaleski, S.; Wilson, A. J.; Mattei, M.; Chen, X.; Goubert, G.; Cardinal, M. F.; Willets, K. A.; Van Duyne, R. P., Investigating Nanoscale Electrochemistry with Surface- and Tip-Enhanced Raman Spectroscopy. *Acc. Chem. Res.* **2016,** *49*, 2023-2030.

109. Masango, S. S.; Hackler, R. A.; Henry, A.-I.; McAnally, M. O.; Schatz, G. C.; Stair, P. C.; Van Duyne, R. P., Probing the Chemistry of Alumina Atomic Layer Deposition Using Operando Surface-Enhanced Raman Spectroscopy. *J. Phys. Chem. C* **2016,** *120*, 3822-3833.

110. van Schrojenstein Lantman, E.; de Peinder, P.; Mank, A.; Weckhuysen, B., Separation of Time‐Resolved Phenomena in Surface‐Enhanced Raman Scattering of the Photocatalytic Reduction of p‐Nitrothiophenol. *ChemPhysChem* **2015,** *16*, 547-554.

111. Markel, V.; Shalaev, V.; Zhang, P.; Huynh, W.; Tay, L.; Haslett, T.; Moskovits, M., Near-field optical spectroscopy of individual surface-plasmon modes in colloid clusters. *Phys. Rev. B* **1999,** *59*, 10903.

112. Stockman, M. I.; Shalaev, V. M.; Moskovits, M.; Botet, R.; George, T. F., Enhanced Raman scattering by fractal clusters: Scale-invariant theory. *Phys. Rev. B* **1992,** *46*, 2821.

113. Erol, M.; Han, Y.; Stanley, S. K.; Stafford, C. M.; Du, H.; Sukhishvili, S., SERS not to be taken for granted in the presence of oxygen. *JACS* **2009,** *131*, 7480-7481.

114. Ikeda, K.; Sato, J.; Uosaki, K., Surface-enhanced Raman scattering at well-defined single crystalline faces of platinum-group metals induced by gap-mode plasmon excitation. *J. Photochem. Photobiol. A Chem.* **2011,** *221*, 175-180.

115. Cialla, D.; Deckert‐Gaudig, T.; Budich, C.; Laue, M.; Möller, R.; Naumann, D.; Deckert, V.; Popp, J., Raman to the limit: tip‐enhanced Raman spectroscopic investigations of a single tobacco mosaic virus. *J. Raman Spectrosc.* **2009,** *40*, 240-243.

116. Yeo, B.-S.; Stadler, J.; Schmid, T.; Zenobi, R.; Zhang, W., Tip-enhanced Raman Spectroscopy–Its status, challenges and future directions. *Chem. Phys. Lett.* **2009,** *472*, 1-13.

117. Vannier, C.; Yeo, B.-S.; Melanson, J.; Zenobi, R., Multifunctional microscope for far-field and tip-enhanced Raman spectroscopy. *Rev. Sci. Instrum.* **2006,** *77*, 023104.

118. Zhang, W.; Yeo, B. S.; Schmid, T.; Zenobi, R., Single Molecule Tip-Enhanced Raman Spectroscopy with Silver Tips. *J. Phys. Chem. C* **2007,** *111*, 1733-1738.

119. Steidtner, J.; Pettinger, B., High-resolution microscope for tip-enhanced optical processes in ultrahigh vacuum. *Rev. Sci. Instrum.* **2007,** *78*, 103104.

120. Yeo, B.-S.; Amstad, E.; Schmid, T.; Stadler, J.; Zenobi, R., Nanoscale Probing of a Polymer-Blend Thin Film with Tip-Enhanced Raman Spectroscopy. *Small* **2009,** *5*, 952-960.

121. Yano, T.-a.; Verma, P.; Saito, Y.; Ichimura, T.; Kawata, S., Pressure-assisted tip-enhanced Raman imaging at a resolution of a few nanometres. *Nature Photon.* **2009,** *3*, 473-477.

122. Neugebauer, U.; Rösch, P.; Schmitt, M.; Popp, J.; Julien, C.; Rasmussen, A.; Budich, C.; Deckert, V., On the Way to Nanometer-Sized Information of the Bacterial Surface by Tip-Enhanced Raman Spectroscopy. *ChemPhysChem* **2006,** *7*, 1428-1430.

123. Bailo, E.; Deckert, V., Tip‐Enhanced Raman Spectroscopy of Single RNA Strands: Towards a Novel Direct‐Sequencing Method. *Angew. Chem. Int. Ed.* **2008,** *47*, 1658-1661.

124. Böhme, R.; Cialla, D.; Richter, M.; Rösch, P.; Popp, J.; Deckert, V., Biochemical imaging below the diffraction limit‐probing cellular membrane related structures by tip‐enhanced Raman spectroscopy (TERS). *J.biophoton.* **2010,** *3*, 455-461.

125. Sweetenham, C. S.; Larraona-Puy, M.; Notingher, I., Simultaneous Surface-Enhanced Raman Spectroscopy (SERS) and Atomic Force Microscopy (AFM) for Label-Free Physicochemical Analysis of Lipid Bilayers. *Appl. Spectrosc.* **2011,** *65*, 1387-1392.

126. Treffer, R.; Böhme, R.; Deckert-Gaudig, T.; Lau, K.; Tiede, S.; Lin, X.; Deckert, V., Advances in TERS (tip-enhanced Raman scattering) for biochemical applications. *Biochem. Soc. Trans.* **2012,** *40*, 609-614.

127. Wood, B. R.; Bailo, E.; Khiavi, M. A.; Tilley, L.; Deed, S.; Deckert-Gaudig, T.; McNaughton, D.; Deckert, V., Tip-enhanced Raman scattering (TERS) from hemozoin crystals within a sectioned erythrocyte. *Nano Lett.* **2011,** *11*, 1868-1873.

128. Schmid, T.; Yeo, B.-S.; Leong, G.; Stadler, J.; Zenobi, R., Performing tip-enhanced Raman spectroscopy in liquids. *J. Raman Spectrosc.* **2009,** *40*, 1392-1399.

129. Steidtner, J.; Pettinger, B., Tip-enhanced Raman spectroscopy and microscopy on single dye molecules with 15 nm resolution. *Phys. Rev. Lett.* **2008,** *100*, 236101.

130. van Schrojenstein Lantman, E. M.; Deckert-Gaudig, T.; Mank, A. J.; Deckert, V.; Weckhuysen, B. M., Catalytic processes monitored at the nanoscale with tip-enhanced Raman spectroscopy. *Nat. Nano.* **2012,** *7*, 583-586.

131. Harvey, C. E.; van Schrojenstein Lantman, E. M.; Mank, A. J. G.; Weckhuysen, B. M., An integrated AFM-Raman instrument for studying heterogeneous catalytic systems: a first showcase. *Chem. Commun.* **2012,** *48*, 1742-1744.

132. Harvey, C. E.; Weckhuysen, B. M., Surface- and Tip-Enhanced Raman Spectroscopy as Operando Probes for Monitoring and Understanding Heterogeneous Catalysis. *Catal. Lett.* **2015,** *145*, 40-57.

133. Kumar, N.; Stephanidis, B.; Zenobi, R.; Wain, A.; Roy, D., Nanoscale mapping of catalytic activity using tip-enhanced Raman spectroscopy. *Nanoscale* **2015,** *7*, 7133-7137.

134. Zhong, J.-H.; Jin, X.; Meng, L.; Wang, X.; Su, H.-S.; Yang, Z.-L.; Williams, C. T.; Ren, B., Probing the electronic and catalytic properties of a bimetallic surface with 3 nm resolution. *Nat. Nano.* **2016,** *12,* 132.

135. Hartman, T.; Wondergem, C. S.; Kumar, N.; van den Berg, A.; Weckhuysen, B. M., Surface-and Tip-Enhanced Raman Spectroscopy in Catalysis. *J. Phys. Chem. Lett.* **2016,** *7*, 1570-1584.

136. Berweger, S.; Neacsu, C. C.; Mao, Y.; Zhou, H.; Wong, S. S.; Raschke, M. B., Optical nanocrystallography with tip-enhanced phonon Raman spectroscopy. *Nat. Nano.* **2009,** *4*, 496-499.

137. Schmid, T.; Opilik, L.; Blum, C.; Zenobi, R., Nanoscale Chemical Imaging Using Tip-Enhanced Raman Spectroscopy: A Critical Review. *Angew. Chem. Int. Ed.* **2013,** *52*, 5940-5954.

138. Nieman, L. T.; Krampert, G. M.; Martinez, R. E., An apertureless near-field scanning optical microscope and its application to surface-enhanced Raman spectroscopy and multiphoton fluorescence imaging. *Rev. Sci. Instrum.* **2001,** *72*, 1691-1699.

139. Opilik, L.; Dogan, Ü.; Li, C.-Y.; Stephanidis, B.; Li, J.-F.; Zenobi, R., Chemical Production of Thin Protective Coatings on Optical Nanotips for Tip-Enhanced Raman Spectroscopy. *J. Phys. Chem. C* **2016,** *120*, 20828-20832.

140. Domke, K. F.; Zhang, D.; Pettinger, B., Enhanced Raman spectroscopy: single molecules or carbon? *J. Phys. Chem. C* **2007,** *111*, 8611-8616.

141. Blum, C.; Schmid, T.; Opilik, L.; Weidmann, S.; Fagerer, S. R.; Zenobi, R., Understanding tip‐enhanced Raman spectra of biological molecules: a combined Raman, SERS and TERS study. *J. Raman Spectrosc.* **2012,** *43*, 1895-1904.

142. Blum, C.; Opilik, L.; Atkin, J. M.; Braun, K.; Kämmer, S. B.; Kravtsov, V.; Kumar, N.; Lemeshko, S.; Li, J. F.; Luszcz, K., Tip‐enhanced Raman spectroscopy‐an interlaboratory reproducibility and comparison study. *J. Raman Spectrosc.* **2014,** *45*, 22-31.

143. Peica, N.; Thomsen, C.; Maultzsch, J., Studying the local character of Raman features of single-walled carbon nanotubes along a bundle using TERS. *Nano. Res. Lett.* **2011,** *6*, 174.

144. Snitka, V.; Rodrigues, R. D.; Lendraitis, V., Novel gold cantilever for nano-Raman spectroscopy of graphene. *Microelectron. Eng.* **2011,** *88*, 2759-2762.

145. Wang, P.; Zhang, D.; Li, L.; Li, Z.; Zhang, L.; Fang, Y., Reversible defect in graphene investigated by Tip-enhanced Raman spectroscopy. *Plasmonics* **2012,** *7*, 555-561.

146. Lee, N.; Hartschuh, R.; Mehtani, D.; Kisliuk, A.; Maguire, J.; Green, M.; Foster, M.; Sokolov, A., High contrast scanning nano‐Raman spectroscopy of silicon. *J. Raman Spectrosc.* **2007,** *38*, 789-796.

147. Zhang, W.; Cui, X.; Yeo, B.-S.; Schmid, T.; Hafner, C.; Zenobi, R., Nanoscale roughness on metal surfaces can increase tip-enhanced Raman scattering by an order of magnitude. *Nano Lett.* **2007,** *7*, 1401-1405.

148. Downes, A.; Salter, D.; Elfick, A., Heating effects in tip-enhanced optical microscopy. *Opt. Express* **2006,** *14*, 5216-5222.

149. Lee, C.; Bain, C. D., Raman spectra of planar supported lipid bilayers. *Biochim. Biophys. Acta* **2005,** *1711*, 59-71.

150. Chan, K. L. A.; Sergei, G. K., Finding a needle in a chemical haystack: tip-enhanced Raman scattering for studying carbon nanotubes mixtures. *Nanotechnology* **2010,** *21*, 445704.

151. Shiotari, A.; Kumagai, T.; Wolf, M., Tip-Enhanced Raman Spectroscopy of Graphene Nanoribbons on Au(111). *J. Phys. Chem. C* **2014,** *118*, 11806-11812.

152. Ghislandi, M.; Hoffmann, G. G.; Tkalya, E.; Xue, L.; With, G. D., Tip-Enhanced Raman Spectroscopy and Mapping of Graphene Sheets. *Appl. Spectrosc. Rev.* **2012,** *47*, 371-381.

153. Das, I.; Sharma, A.; Agrawal, N. R., *An Introduction to Physical Chemistry*. New Age International: New Delhi, India, **2005**.

154. Wang, H.; Park, M.; Liang, H.; Wu, S.; Lopez, I. J.; Ji, W.; Li, G.; Snyder, S. A., Reducing ultrafiltration membrane fouling during potable water reuse using pre-ozonation. *Water Res.* **2017,** *125*, 42-51.

155. Yu, W.; Graham, N. J.; Fowler, G. D., Coagulation and oxidation for controlling ultrafiltration membrane fouling in drinking water treatment: application of ozone at low dose in submerged membrane tank. *Water Res.* **2016,** *95*, 1-10.

156. Li, L.; Wang, Z.; Rietveld, L. C.; Gao, N.; Hu, J.; Yin, D.; Yu, S., Comparison of the effects of extracellular and intracellular organic matter extracted from Microcystis aeruginosa on ultrafiltration membrane fouling: dynamics and mechanisms. *Environ. Sci. Technol.* **2014,** *48*, 14549-14557.

157. Li, K.; Huang, T.; Qu, F.; Du, X.; Ding, A.; Li, G.; Liang, H., Performance of adsorption pretreatment in mitigating humic acid fouling of ultrafiltration membrane under environmentally relevant ionic conditions. *Desalination* **2016,** *377*, 91-98.

158. Qu, F.; Liang, H.; Zhou, J.; Nan, J.; Shao, S.; Zhang, J.; Li, G., Ultrafiltration membrane fouling caused by extracellular organic matter (EOM) from Microcystis aeruginosa: effects of membrane pore size and surface hydrophobicity. *J. Membr. Sci.* **2014,** *449*, 58-66.

159. Li, K.; Qu, F.; Liang, H.; Shao, S.; Han, Z.-s.; Chang, H.; Du, X.; Li, G., Performance of mesoporous adsorbent resin and powdered activated carbon in mitigating ultrafiltration membrane fouling caused by algal extracellular organic matter. *Desalination* **2014,** *336*, 129-137.

160. Meng, X.; Tang, W.; Wang, L.; Wang, X.; Huang, D.; Chen, H.; Zhang, N., Mechanism analysis of membrane fouling behavior by humic acid using atomic force microscopy: Effect of solution pH and hydrophilicity of PVDF ultrafiltration membrane interface. *J. Membr. Sci.* **2015,** *487*, 180-188.

161. Wang, L.; Miao, R.; Wang, X.; Lv, Y.; Meng, X.; Yang, Y.; Huang, D.; Feng, L.; Liu, Z.; Ju, K., Fouling behavior of typical organic foulants in polyvinylidene fluoride ultrafiltration membranes: characterization from microforces. *Environ. Sci. Technol.* **2013,** *47*, 3708-3714.

162. Zamani, F.; Ullah, A.; Akhondi, E.; Tanudjaja, H. J.; Cornelissen, E. R.; Honciuc, A.; Fane, A. G.; Chew, J. W., Impact of the surface energy of particulate foulants on membrane fouling. *J. Membr. Sci.* **2016,** *510*, 101-111.

163. Myat, D. T.; Stewart, M. B.; Mergen, M.; Zhao, O.; Orbell, J. D.; Gray, S., Experimental and computational investigations of the interactions between model organic compounds and subsequent membrane fouling. *Water Res.* **2014,** *48*, 108-118.

164. Cao, H.; Habimana, O.; Semião, A. J.; Allen, A.; Heffernan, R.; Casey, E., Understanding particle deposition kinetics on NF membranes: A focus on micro-beads and membrane interactions at different environmental conditions. *J. Membr. Sci.* **2015,** *475*, 367-375.

165. Wang, X.; Zhou, M.; Meng, X.; Wang, L.; Huang, D., Effect of protein on PVDF ultrafiltration membrane fouling behavior under different pH conditions: interface adhesion force and XDLVO theory analysis. *Front. of Env. Sci. Eng.* **2016,** *10*, 12.

166. Zhang, M.; Liao, B.-q.; Zhou, X.; He, Y.; Hong, H.; Lin, H.; Chen, J., Effects of hydrophilicity/hydrophobicity of membrane on membrane fouling in a submerged membrane bioreactor. *Bioresour. Technol.* **2015,** *175*, 59-67.

167. Lin, T.; Lu, Z.; Chen, W., Interaction mechanisms of humic acid combined with calcium ions on membrane fouling at different conditions in an ultrafiltration system. *Desalination* **2015,** *357*, 26-35.

168. Fu, W.; Hua, L.; Zhang, W., Experimental and Modeling Assessment of the Roles of Hydrophobicity and Zeta Potential in Chemically Modified Polyethersulfone Membrane Fouling Kinetics. *Ind. Eng. Chem. Res.* **2017**.

169. Cheng, X.; Liang, H.; Ding, A.; Qu, F.; Shao, S.; Liu, B.; Wang, H.; Wu, D.; Li, G., Effects of pre-ozonation on the ultrafiltration of different natural organic matter (NOM) fractions: membrane fouling mitigation, prediction and mechanism. *J. Membr. Sci.* **2016,** *505*, 15-25.

170. Huang, W.; Wang, L.; Zhou, W.; Lv, W.; Hu, M.; Chu, H.; Dong, B., Effects of combined ozone and PAC pretreatment on ultrafiltration membrane fouling control and mechanisms. *J. Membr. Sci.* **2017,** *533*, 378-389.

171. Tian, J.-y.; Ernst, M.; Cui, F.; Jekel, M., Effect of particle size and concentration on the synergistic UF membrane fouling by particles and NOM fractions. *J. Membr. Sci.* **2013,** *446*, 1-9.

172. Yunos, M. Z.; Harun, Z.; Basri, H.; Ismail, A. F., Studies on fouling by natural organic matter (NOM) on polysulfone membranes: effect of polyethylene glycol (PEG). *Desalination* **2014,** *333*, 36-44.

173. Ma, B.; Hu, C.; Wang, X.; Xie, Y.; Jefferson, W. A.; Liu, H.; Qu, J., Effect of aluminum speciation on ultrafiltration membrane fouling by low dose aluminum coagulation with bovine serum albumin (BSA). *J. Membr. Sci.* **2015,** *492*, 88-94.

174. Hou, L.; Wang, Z.; Song, P., A precise combined complete blocking and cake filtration model for describing the flux variation in membrane filtration process with BSA solution. *J. Membr. Sci.* **2017,** *542*, 186-194.

175. Chen, J.; Zhang, M.; Li, F.; Qian, L.; Lin, H.; Yang, L.; Wu, X.; Zhou, X.; He, Y.; Liao, B.-Q., Membrane fouling in a membrane bioreactor: high filtration resistance of gel layer and its underlying mechanism. *Water Res.* **2016,** *102*, 82-89.

176. Tansel, B.; Dizge, N.; Tansel, I. N., Analysis of high resolution flux data to characterize fouling profiles of membranes with different MWCO under different filtration modes. *Sep. Purif. Technol.* **2017,** *173*, 200-208.

177. Sun, Y.; Qin, Z.; Zhao, L.; Chen, Q.; Hou, Q.; Lin, H.; Jiang, L.; Liu, J.; Du, Z., Membrane fouling mechanisms and permeate flux decline model in soy sauce microfiltration. *J. Food Process Eng.* **2017**.

178. Liu, B.; Qu, F.; Liang, H.; Van der Bruggen, B.; Cheng, X.; Yu, H.; Xu, G.; Li, G., Microcystis aeruginosa-laden surface water treatment using ultrafiltration: Membrane fouling, cell integrity and extracellular organic matter rejection. *Water Res.* **2017,** *112*, 83-92.

179. Meng, F.; Chae, S. R.; Drews, A.; Kraume, M.; Shin, H. S.; Yang, F., Recent advances in membrane bioreactors (MBRs): Membrane fouling and membrane material. *Water Res.* **2009,** *43*, 1489-1512.

180. Hwang, K. J.; Chiang, Y. C., Comparisons of membrane fouling and separation efficiency in protein/polysaccharide cross-flow microfiltration using membranes with different morphologies. *Sep. Purif. Technol.* **2014,** *125*, 74-82.

181. Mollahosseini, A.; Rahimpour, A., Interfacially polymerized thin film nanofiltration membranes on TiO2 coated polysulfone substrate. *J.Ind. Eng. Chem.* **2014,** *20*, 1261-1268.

182. Weis, A.; Bird, M. R.; Nyström, M.; Wright, C., The influence of morphology, hydrophobicity and charge upon the long-term performance of ultrafiltration membranes fouled with spent sulphite liquor. *Desalination* **2005,** *175*, 73-85.

183. He, Z.; Kasemset, S.; Kirschner, A. Y.; Cheng, Y.-H.; Paul, D. R.; Freeman, B. D., The effects of salt concentration and foulant surface charge on hydrocarbon fouling of a poly(vinylidene fluoride) microfiltration membrane. *Water Res.* **2017,** *117*, 230-241.

184. Childress, A. E.; Elimelech, M., Effect of solution chemistry on the surface charge of polymeric reverse osmosis and nanofiltration membranes. *J. Membr. Sci.* **1996,** *119*, 253-268.

185. Han, M. J.; Baroña, G. N. B.; Jung, B., Effect of surface charge on hydrophilically modified poly(vinylidene fluoride) membrane for microfiltration. *Desalination* **2011,** *270*, 76-83.

186. Xiao, K.; Wang, X.; Huang, X.; Waite, T. D.; Wen, X., Combined effect of membrane and foulant hydrophobicity and surface charge on adsorptive fouling during microfiltration. *J. Membr. Sci.* **2011,** *373*, 140-151.

187. Lee, S.; Kim, S.; Cho, J.; Hoek, E. M. V., Natural organic matter fouling due to foulant–membrane physicochemical interactions. *Desalination* **2007,** *202*, 377-384.

188. Brant, J. A.; Childress, A. E., Assessing short-range membrane–colloid interactions using surface energetics. *J. Membr. Sci.* **2002,** *203*, 257-273.

189. Powell, L. C.; Hilal, N.; Wright, C. J., Atomic force microscopy study of the biofouling and mechanical properties of virgin and industrially fouled reverse osmosis membranes. *Desalination* **2017,** *404*, 313-321.

190. Johnson, D.; Hilal, N., Characterisation and quantification of membrane surface properties using atomic force microscopy: A comprehensive review. *Desalination* **2015,** *356*, 149-164.

191. Wang, X.; Zhou, M.; Meng, X.; Wang, L.; Huang, D.; Xia, S., Adhesion force analysis of protein fouling of PVDF ultrafiltration membrane using atomic force microscope. *Huan jing ke xue* **2015,** *36*, 2900-2905.

192. Donose, B.; Birkett, G.; Pratt, S., Insight in to the Initial Stages of Silica Scaling Employing a Scanning Electron and Atomic Force Microscopy Approach. *J Membra Sci Technol* **2016,** *6*, 2.

193. Hashino, M.; Hirami, K.; Ishigami, T.; Ohmukai, Y.; Maruyama, T.; Kubota, N.; Matsuyama, H., Effect of kinds of membrane materials on membrane fouling with BSA. *J. Membr. Sci.* **2011,** *384*, 157-165.

194. Gao, F.; Sheng, Y.; Li, Y.; Cao, H.; Su, C., Mechanism analysis of nanofiltration membrane fouling behavior by mixed BSA-HA using AFM with modified polyamide-probe. *Desalin. Water Treat.* **2017,** *59*, 55-64.

195. Bowen, W. R.; Hilal, N.; Lovitt, R. W.; Wright, C. J., Direct measurement of interactions between adsorbed protein layers using an atomic force microscope. *J. Colloid Interface Sci.* **1998,** *197*, 348-352.

196. Bowen, W. R.; Doneva, T. A.; Stoton, J. A. G., Protein deposition during cross-flow membrane filtration: AFM studies and flux loss. *Colloids Surf. B: Biointerfaces* **2003,** *27*, 103-113.

197. Li, Q.; Elimelech, M., Organic fouling and chemical cleaning of nanofiltration membranes: measurements and mechanisms. *Environ. Sci. Technol.* **2004,** *38*, 4683-4693.

198. Yamamura, H.; Kimura, K.; Okajima, T.; Tokumoto, H.; Watanabe, Y., Affinity of functional groups for membrane surfaces: implications for physically irreversible fouling. *Environ. Sci. Technol.* **2008,** *42*, 5310-5315.

199. Bowen, W. R.; Hilal, N.; Lovitt, R. W.; Wright, C. J., A new technique for membrane characterisation: direct measurement of the force of adhesion of a single particle using an atomic force microscope. *J. Membr. Sci.* **1998,** *139*, 269-274.

200. Mi, B.; Elimelech, M., Chemical and physical aspects of organic fouling of forward osmosis membranes. *J. Membr. Sci.* **2008,** *320*, 292-302.

201. Otitoju, T. A.; Ahmad, A. L.; Ooi, B. S., Influence of ethanol as bore fluid component on the morphological structure and performance of PES hollow fiber membrane for oil in water separation. *Korean J. Chem. Eng.* **2017,** *34*, 2703-2709.

202. Susan, L.; Ismail, S.; Ooi, B.; Mustapa, H., Surface morphology of pvdf membrane and its fouling phenomenon by crude oil emulsion. *Journal of Water Process Engineering* **2017,** *15*, 55-61.

203. Mustafa, G.; Wyns, K.; Vandezande, P.; Buekenhoudt, A.; Meynen, V., Novel grafting method efficiently decreases irreversible fouling of ceramic nanofiltration membranes. *J. Membr. Sci.* **2014,** *470*, 369-377.

204. Kimura, K.; Tanaka, K.; Watanabe, Y., Microfiltration of different surface waters with/without coagulation: Clear correlations between membrane fouling and hydrophilic biopolymers. *Water Res.* **2014,** *49*, 434-443.

205. Gitis, V.; Haught, R. C.; Clark, R. M.; Gun, J.; Lev, O., Application of nanoscale probes for the evaluation of the integrity of ultrafiltration membranes. *J. Membr. Sci.* **2006,** *276*, 185-192.

206. Nyström, M.; Zhu, H., Characterization of cleaning results using combined flux and streaming potential methods. *J. Membr. Sci.* **1997,** *131*, 195-205.

207. Wienk, I.; Meuleman, E.; Borneman, Z.; Van Den Boomgaard, T.; Smolders, C., Chemical treatment of membranes of a polymer blend: mechanism of the reaction of hypochlorite with poly (vinyl pyrrolidone). *J. Polym. Sci., Part A: Polym. Chem.* **1995,** *33*, 49-54.

208. Wolff, S. H.; Zydney, A. L., Effect of bleach on the transport characteristics of polysulfone hemodialyzers. *J. Membr. Sci.* **2004,** *243*, 389-399.

209. Qin, J. J.; Cao, Y. M.; Li, Y., Effect of hypochlorite concentration on properties of posttreated outer‐skin ultrafiltration membranes spun from cellulose acetate/poly (vinyl pyrrolidone) blends. *J. Appl. Polym. Sci.* **2005,** *97*, 227-231.

210. Pabby, A. K.; Rizvi, S. S.; Requena, A. M. S., *Handbook of membrane separations: chemical, pharmaceutical, food, and biotechnological applications*. CRC press: **2015**.

211. Wyart, Y.; Nitsche, S.; Chaudanson, D.; Glucina, K.; Moulin, P., The use of HRSEM to characterize new and aged membranes in drinking water production. *Membr. Water Treat.* **2011,** *2*, 251-266.

212. Zhang, Y.; Tian, J.; Liang, H.; Nan, J.; Chen, Z.; Li, G., Chemical cleaning of fouled PVC membrane during ultrafiltration of algal-rich water. *J. Environ. Sci.* **2011,** *23*, 529-536.

213. Antón, E.; Álvarez, J. R.; Palacio, L.; Prádanos, P.; Hernández, A.; Pihlajamäki, A.; Luque, S., Ageing of polyethersulfone ultrafiltration membranes under long-term exposures to alkaline and acidic cleaning solutions. *Chem. Eng. Sci.* **2015,** *134*, 178-195.

214. Regula, C.; Carretier, E.; Wyart, Y.; Sergent, M.; Gésan-Guiziou, G.; Ferry, D.; Vincent, A.; Boudot, D.; Moulin, P., Ageing of ultrafiltration membranes in

contact with sodium hypochlorite and commercial oxidant: Experimental designs as a new ageing protocol. *Sep. Purif. Technol.* **2013,** *103*, 119-138.

215. Awanis Hashim, N.; Liu, Y.; Li, K., Stability of PVDF hollow fibre membranes in sodium hydroxide aqueous solution. *Chem. Eng. Sci.* **2011,** *66*, 1565-1575.

216. Begoin, L. Analysis of industrial spiral modules for ultrafiltration of dairy fluids. Physico-chemistry of the cleaning of polyethersulfone membranes of ultrafiltration of skimmed milk. Rennes 1, 2004.

217. Antony, A.; Fudianto, R.; Cox, S.; Leslie, G., Assessing the oxidative degradation of polyamide reverse osmosis membrane—Accelerated ageing with hypochlorite exposure. *J. Membr. Sci.* **2010,** *347*, 159-164.

218. Nyström, M.; Järvinen, P., Modification of polysulfone ultrafiltration membranes with UV irradiation and hydrophilicity increasing agents. *J. Membr. Sci.* **1991,** *60*, 275-296.

219. Zhu, H.; Nyström, M., Cleaning results characterized by flux, streaming potential and FTIR measurements. *Colloids Surf. A Physicochem. Eng. Asp.* **1998,** *138*, 309-321.

220. Zhang, S.; Shen, J.; Qiu, X.; Weng, D.; Zhu, W., ESR and vibrational spectroscopy study on poly(vinylidene fluoride) membranes with alkaline treatment. *J. Power Sources* **2006,** *153*, 234-238.

221. D'Souza, N. M.; Mawson, A. J., Membrane Cleaning in the Dairy Industry: A Review. *Crit. Rev. Food Sci. Nutr.* **2005,** *45*, 125-134.

222. Susanto, H.; Ulbricht, M., Characteristics, performance and stability of polyethersulfone ultrafiltration membranes prepared by phase separation method using different macromolecular additives. *J. Membr. Sci.* **2009,** *327*, 125-135.

223. Zhang, Y.; Wang, J.; Gao, F.; Chen, Y.; Zhang, H., A comparison study: The different impacts of sodium hypochlorite on PVDF and PSF ultrafiltration (UF) membranes. *Water Res.* **2017,** *109*, 227-236.

224. Kuhn, K. J.; Hahn, B.; Percec, V.; Urban, M. W., Structural and Quantitative Analysis of Surface Modified Poly(vinylidene fluoride) Films Using ATR FT-IR Spectroscopy. *Appl. Spectrosc.* **1987,** *41*, 843-847.

225. Marchand-Brynaert, J.; Jongen, N.; Dewez, J.-L., Surface hydroxylation of poly(vinylidene fluoride) (PVDF) film. *J. Polym. Sci. A Polym. Chem.* **1997,** *35*, 1227-1235.

226. Kise, H.; Ogata, H., Phase transfer catalysis in dehydrofluorination of poly(vinylidene fluoride) by aqueous sodium hydroxide solutions. *J. Sci. Polym. Chem.* **1983,** *21*, 3443-3451.

227. Regula, C.; Carretier, E.; Wyart, Y.; Gésan-Guiziou, G.; Vincent, A.; Boudot, D.; Moulin, P., Chemical cleaning/disinfection and ageing of organic UF membranes: A review. *Water Res.* **2014,** *56*, 325-365.

228. Roesink, H. D. W.; Beerlage, M. A. M.; Potman, W.; van den Boomgaard, T.; Mulder, M. H. V.; Smolders, C. A., Characterization of new membrane materials by means of fouling experiments Adsorption of bsa on polyetherimide—polyvinylpyrrolidone membranes. *Colloids Surf.* **1991,** *55*, 231-243.

229. Yadav, K.; Morison, K. R., Effects of hypochlorite damage on flux through polyethersulphone ultrafiltration membranes. *Fouling and Cleaning in Food Processing, Cambridge* **2010**.

230. Yadav, K.; Morison, K.; Staiger, M. P., Effects of hypochlorite treatment on the surface morphology and mechanical properties of polyethersulfone ultrafiltration membranes. *Polym. Degrad. Stab.* **2009,** *94*, 1955-1961.

231. Bégoin, L.; Rabiller-Baudry, M.; Chaufer, B.; Faille, C.; Blanpain-Avet, P.; Bénézech, T.; Doneva, T., Methodology of analysis of a spiral-wound module. Application to PES membrane for ultrafiltration of skimmed milk. *Desalination* **2006,** *192*, 40-53.

232. Bégoin, L.; Rabiller-Baudry, M.; Chaufer, B.; Hautbois, M.-C.; Doneva, T., Ageing of PES industrial spiral-wound membranes in acid whey ultrafiltration. *Desalination* **2006,** *192*, 25-39.

233. Gaudichet-Maurin, E.; Thominette, F., Ageing of polysulfone ultrafiltration membranes in contact with bleach solutions. *J. Membr. Sci.* **2006,** *282*, 198-204.

234. Arkhangelsky, E.; Kuzmenko, D.; Gitis, V., Impact of chemical cleaning on properties and functioning of polyethersulfone membranes. *J. Membr. Sci.* **2007,** *305*, 176-184.

235. Grant, E.; Halstead, B. J., Dielectric parameters relevant to microwave dielectric heating. *Chem. Soc. Rev.* **1998,** *27*, 213-224.

236. Tai, H.-S.; Jou, C.-J. G., Application of granular activated carbon packed-bed reactor in microwave radiation field to treat phenol. *Chemosphere* **1999,** *38*, 2667-2680.

237. Kunlan, L.; Lixin, X.; Jun, L.; Jun, P.; Guoying, C.; Zuwei, X., Salt-assisted acid hydrolysis of starch to D-glucose under microwave irradiation. *Carbohydr. Res.* **2001,** *331*, 9-12.

238. Cheng, H.; Hu, E., Method to remove organic pollutants through coupling microwave degradation based on microporous mineral adsorption. Google Patents: 2015.

239. Cravotto, G.; Di Carlo, S.; Ondruschka, B.; Tumiatti, V.; Roggero, C. M., Decontamination of soil containing POPs by the combined action of solid Fenton-like reagents and microwaves. *Chemosphere* **2007,** *69*, 1326-1329.

240. Liu, X.; Quan, X.; Bo, L.; Chen, S.; Zhao, Y., Simultaneous pentachlorophenol decomposition and granular activated carbon regeneration assisted by microwave irradiation. *Carbon* **2004,** *42*, 415-422.

241. Lin, L.; Yuan, S.; Chen, J.; Xu, Z.; Lu, X., Removal of ammonia nitrogen in wastewater by microwave radiation. *J. Hazard. Mater.* **2009,** *161*, 1063-1068.

242. Lin, L.; Chen, J.; Xu, Z.; Yuan, S.; Cao, M.; Liu, H.; Lu, X., Removal of ammonia nitrogen in wastewater by microwave radiation: a pilot-scale study. *J. Hazard. Mater.* **2009,** *168*, 862-867.

243. Yuan, S.; Tian, M.; Lu, X., Microwave remediation of soil contaminated with hexachlorobenzene. *J. Hazard. Mater.* **2006,** *137*, 878-885.

244. Abramovitch, R. A.; Bangzhou, H.; Abramovitch, D. A.; Jiangao, S., In situ decomposition of PAHs in soil and desorption of organic solvents using microwave energy. *Chemosphere* **1999,** *39*, 81-87.

245. Abramovitch, R. A.; Bangzhou, H.; Abramovitch, D. A.; Jiangao, S., In situ decomposition of PCBs in soil using microwave energy. *Chemosphere* **1999,** *38*, 2227-2236.

246. Abramovitch, R. A.; Bangzhou, H.; Davis, M.; Peters, L., Decomposition of PCB's and other polychlorinated aromatics in soil using microwave energy. *Chemosphere* **1998,** *37*, 1427-1436.

247. Tai, H.-S.; Jou, C.-J. G., Immobilization of chromium-contaminated soil by means of microwave energy. *J. Hazard. Mater.* **1999,** *65*, 267-275.

248. Ji, Z.; Wang, J.; Hou, D.; Yin, Z.; Luan, Z., Effect of microwave irradiation on vacuum membrane distillation. *J. Membr. Sci.* **2013,** *429*, 473-479.

249. Huang, K.; Yang, X., Advanced of non-thermal effect of microwave accelerating chemical reaction. *Prog Nat Sci* **2006,** *16*, 273-279.

250. Tuziuti, T.; Yasui, K.; Kanematsu, W. In *Measurement of the Change in the Number of Ultrafine Bubbles through Pressurization*, International Conference on Optical Particle Characterization (OPC 2014), International Society for Optics and Photonics: 2014; pp 92320T-92320T-4.

251. Kobayashi, H.; Maeda, S.; Kashiwa, M.; Fujita, T. In *Measurement and identification of ultrafine bubbles by resonant mass measurement method*, International Conference on Optical Particle Characterization (OPC 2014), International Society for Optics and Photonics: 2014; pp 92320S-92320S-5.

252. Kobayashi, H.; Maeda, S.; Kashiwa, M.; Fujita, T. In *Measurements of ultrafine bubbles using different types of particle size measuring instruments*, International Conference on Optical Particle Characterization (OPC 2014), International Society for Optics and Photonics: 2014; pp 92320U-92320U-5.

253. Maeda, S.; Kobayashi, H.; Ida, K.; Kashiwa, M.; Nishihara, I.; Fujita, T. In *The effect of dilution on the quantitative measurement of bubbles in high-density ultrafine bubble-filled water using the light scattering method*, International Conference on Optical Particle Characterization (OPC 2014), International Society for Optics and Photonics: 2014; pp 92320V-92320V-5.

254. Lou, S.-T.; Ouyang, Z.-Q.; Zhang, Y.; Li, X.-J.; Hu, J.; Li, M.-Q.; Yang, F.-J., Nanobubbles on solid surface imaged by atomic force microscopy. *J. Vac. Sci. Technol. B* **2000,** *18*, 2573-2575.

255. Carambassis, A.; Jonker, L. C.; Attard, P.; Rutland, M. W., Forces measured between hydrophobic surfaces due to a submicroscopic bridging bubble. *Phys. Rev. Lett.* **1998,** *80*, 5357.

256. Ishida, N.; Sakamoto, M.; Miyahara, M.; Higashitani, K., Optical observation of gas bridging between hydrophobic surfaces in water. *J. Colloid Interface Sci.* **2002,** *253*, 112-116.

257. Miller, J.; Hu, Y.; Veeramasuneni, S.; Lu, Y., In-situ detection of butane gas at a hydrophobic silicon surface. *Colloids Surf. A Physicochem. Eng. Asp.* **1999,** *154*, 137-147.

258. Holmberg, M.; Kühle, A.; Mørch, K. A.; Boisen, A., Nanobubble Trouble on Gold Surfaces. *Langmuir* **2003,** *19*, 10510-10513.

259. Pashley, R. M.; Rzechowicz, M.; Pashley, L. R.; Francis, M. J., De-Gassed Water Is a Better Cleaning Agent. *J. Phys. Chem. B* **2005,** *109*, 1231-1238.

260. Paxton, W. F.; Kistler, K. C.; Olmeda, C. C.; Sen, A.; St. Angelo, S. K.; Cao, Y.; Mallouk, T. E.; Lammert, P. E.; Crespi, V. H., Catalytic Nanomotors: Autonomous Movement of Striped Nanorods. *JACS* **2004,** *126*, 13424-13431.

261. Takahashi, M., Base and technological application of micro-bubble and nano-bubble. *Mater. Integr* **2009,** *22*, 2-19.

262. N., M. J.; Shaini, A. H.; H., B. J., Stability of Nanobubbles. *Env. Eng. Sci.* **2018,** *35*, 1216-1227.

263. Demangeat, J.-L., Gas nanobubbles and aqueous nanostructures: the crucial role of dynamization. *Homeopathy* **2015,** *104*, 101-115.

264. Uchida, T.; Oshita, S.; Ohmori, M.; Tsuno, T.; Soejima, K.; Shinozaki, S.; Take, Y.; Mitsuda, K., Transmission electron microscopic observations of nanobubbles and their capture of impurities in wastewater. *Nano. Res. Lett.* **2011,** *6*, 1.

265. Zimmerman, W. B.; Tesař, V.; Bandulasena, H. H., Towards energy efficient nanobubble generation with fluidic oscillation. *Curr. Opin. Colloid Interface Sci.* **2011,** *16*, 350-356.

266. Takahashi, M.; Chiba, K.; Li, P., Free-radical generation from collapsing microbubbles in the absence of a dynamic stimulus. *J. Phys. Chem. B* **2007,** *111*, 1343-1347.

267. Ushikubo, F. Y.; Furukawa, T.; Nakagawa, R.; Enari, M.; Makino, Y.; Kawagoe, Y.; Shiina, T.; Oshita, S., Evidence of the existence and the stability of nano-bubbles in water. *Colloids Surf. A Physicochem. Eng. Asp.* **2010,** *361*, 31-37.

268. Liu, S.; Kawagoe, Y.; Makino, Y.; Oshita, S., Effects of nanobubbles on the physicochemical properties of water: The basis for peculiar properties of water containing nanobubbles. *Chem. Eng. Sci.* **2013,** *93*, 250-256.

269. Ohgaki, K.; Khanh, N. Q.; Joden, Y.; Tsuji, A.; Nakagawa, T., Physicochemical approach to nanobubble solutions. *Chem. Eng. Sci.* **2010,** *65*, 1296-1300.

270. Duval, E.; Adichtchev, S.; Sirotkin, S.; Mermet, A., Long-lived submicrometric bubbles in very diluted alkali halide water solutions. *PCCP* **2012,** *14*, 4125-4132.

271. Bowley, W. W.; Hammond, G. L., Controlling factors for oxygen transfer through bubbles. *Ind. Eng. Chem. Process. Des. Dev.* **1978,** *17*, 2-8.

272. Agarwal, A.; Ng, W. J.; Liu, Y., Principle and applications of microbubble and nanobubble technology for water treatment. *Chemosphere* **2011,** *84*, 1175-1180.

273. Li, P.; Takahashi, M.; Chiba, K., Enhanced free-radical generation by shrinking microbubbles using a copper catalyst. *Chemosphere* **2009,** *77*, 1157-1160.

274. Oshita, S.; Liu, S. In *Nanobubbles characteristics and its application to agriculture and foods*, International Symposium on Agri-Foods for Health and Wealth, August, 2013; pp 5-8.

275. Takahashi, M.; Kawamura, T.; Yamamoto, Y.; Ohnari, H.; Himuro, S.; Shakutsui, H., Effect of shrinking microbubble on gas hydrate formation. *J. Phys. Chem. B* **2003,** *107*, 2171-2173.

276. Kimura, T.; Ando, T., Physical control of chemical reaction by ultrasonic waves. *Ultranson. Technol.* **2002,** *14*, 7-8.

277. Wu, Z.; Chen, H.; Dong, Y.; Mao, H.; Sun, J.; Chen, S.; Craig, V. S.; Hu, J., Cleaning using nanobubbles: defouling by electrochemical generation of bubbles. *J. Colloid Interface Sci.* **2008,** *328*, 10-14.

278. Zhu, J.; An, H.; Alheshibri, M.; Liu, L.; Terpstra, P. M. J.; Liu, G.; Craig, V. S. J., Cleaning with Bulk Nanobubbles. *Langmuir* **2016**.

279. Yabe, A.; Goto, M., Nanobubble utilization method and device. Google Patents: 2003.

280. Sang-Ryul, R., Method and apparatus for generating nano-bubbles in liquid. Google Patents: 2014.

281. Yano, H.; Sakai, A., System and method for generating nanobubbles. Google Patents: 2012.

282. Chiba, K.; Takahashi, M., Method of forming nanobubbles. Google Patents: 2005.

283. Chiba, K.; Takahashi, M., Oxygen nanobubble water and method of producing the same. Google Patents: 2005.

284. Sato, K., Recent Patents on Micro- and Nano-Bubble Applications and Potential Application of a Swirl-type Generator. *Recent Pat. .Mechan. Eng.* **2011,** *4*, 202-211.

285. Hielscher, T., Ultrasonic production of nano-size dispersions and emulsions. *arXiv preprint arXiv:0708.1831* **2007**.

286. Zimmerman, W. B.; Tesar, V.; Butler, S.; Bandulasena, H. C., Microbubble generation. *Recent Pat. Eng.* **2008,** *2*, 1-8.

287. Najafi, A. S.; Drelich, J.; Yeung, A.; Xu, Z.; Masliyah, J., A novel method of measuring electrophoretic mobility of gas bubbles. *J. Colloid Interface Sci.* **2007,** *308*, 344-350.

288. Yang, S.; Dammer, S. M.; Bremond, N.; Zandvliet, H. J.; Kooij, E. S.; Lohse, D., Characterization of nanobubbles on hydrophobic surfaces in water. *Langmuir* **2007,** *23*, 7072-7077.

289. Yang, S.; Tsai, P.; Kooij, E. S.; Prosperetti, A.; Zandvliet, H. J. W.; Lohse, D., Electrolytically Generated Nanobubbles on Highly Orientated Pyrolytic Graphite Surfaces. *Langmuir* **2009,** *25*, 1466-1474.

290. Wang, L.; Miao, X.; Pan, G., Microwave-Induced Interfacial Nanobubbles. *Langmuir* **2016,** *32*, 11147-11154.

291. Jin, F.; Ye, X.; Wu, C., Observation of kinetic and structural scalings during slow coalescence of nanobubbles in an aqueous solution. *J. Phys. Chem. B* **2007,** *111*, 13143-13146.

292. Shang, R.; Goulas, A.; Tang, C. Y.; de Frias Serra, X.; Rietveld, L. C.; Heijman, S. G., Atmospheric pressure atomic layer deposition for tight ceramic nanofiltration membranes: Synthesis and application in water purification. *J. Membr. Sci.* **2017,** *528*, 163-170.

293. Govardhan, B.; Chandrasekhar, S. S.; Sridhar, S., Purification of surface water using novel hollow fiber membranes prepared from polyetherimide/polyethersulfone blends. *J. Environ. Chem. Eng.* **2017,** *5*, 1068-1078.

294. Ang, W.; Nordin, D.; Mohammad, A.; Benamor, A.; Hilal, N., Effect of membrane performance including fouling on cost optimization in brackish water desalination process. *Chem. Eng. Res. Des.* **2017,** *117*, 401-413.

295. Sørensen, I.; Jensen, S.; Ottosen, N.; Neve, T.; Wiking, L., Chemical Quality of Raw Milk Retentate processed by Ultra‐filtration or Reverse Osmosis at the Dairy Farm. *Int. J. Dairy Technol.* **2016,** *69*, 31-37.

296. Issaoui, M.; Limousy, L.; Lebeau, B.; Bouaziz, J.; Fourati, M., Manufacture and optimization of low-cost tubular ceramic supports for membrane filtration: application to algal solution concentration. *Environ. Sci. Pollut. Res.* **2017**, 1-13.

297. Xie, M.; Shon, H. K.; Gray, S. R.; Elimelech, M., Membrane-based processes for wastewater nutrient recovery: technology, challenges, and future direction. *Water Res.* **2016,** *89*, 210-221.

298. Cheng, W. P.; Chen, P. H.; Tian, D. R.; Yu, R. F.; Fu, C. H., Use of nanofiltration membranes to concentrate and recover leached aluminum from acidified water treatment sludge. *Environ. Prot. Eng.* **2016,** *42*.

299. Noor, S. M.; Ahmad, N.; Khattak, M.; Khan, M.; Mukhtar, A.; Kazi, S.; Badshah, S.; Khan, R., Application of Sayong Ball Clay Membrane Filtration for Ni (II) Removal from Industrial Wastewater. *J. Taibah Univ. Sci.* **2017**.

300. Wei, L.; Wang, K.; Kong, X.; Liu, G.; Cui, S.; Zhao, Q.; Cui, F., Application of ultra-sonication, acid precipitation and membrane filtration for co-recovery of protein and humic acid from sewage sludge. *Fron. Environ. Sci. Eng.* **2016,** *10*, 327-335.

301. Zhang, C. H.; Yang, F. L.; Wang, W. J.; Chen, B., Preparation and characterization of hydrophilic modification of polypropylene non-woven fabric by dip-coating PVA (polyvinyl alcohol). *Sep. Purif. Technol.* **2008,** *61*, 276-286.

302. Yang, Y.; Zhang, H.; Wang, P.; Zheng, Q.; Li, J., The influence of nano-sized TiO 2 fillers on the morphologies and properties of PSF UF membrane. *J. Membr. Sci.* **2007,** *288*, 231-238.

303. Luo, M.; Tang, W.; Zhao, J.; Pu, C., Hydrophilic modification of poly (ether sulfone) used TiO 2 nanoparticles by a sol–gel process. *J. Mater. Process. Technol.* **2006,** *172*, 431-436.

304. Du, J. R.; Peldszus, S.; Huck, P. M.; Feng, X., Modification of poly(vinylidene fluoride) ultrafiltration membranes with poly(vinyl alcohol) for fouling control in drinking water treatment. *Water Res.* **2009,** *43*, 4559-4568.

305. Chae, S. R.; Yamamura, H.; Ikeda, K.; Watanabe, Y., Comparison of fouling characteristics of two different poly-vinylidene fluoride microfiltration membranes in a pilot-scale drinking water treatment system using pre-coagulation/sedimentation, sand filtration, and chlorination. *Water Res.* **2008,** *42*, 2029-2042.

306. Wu, X.; Shertok, J.; Konstantin, P. Hydrophilic membrane. Patent #6,039,872, Mar 21, 2000.

307. Uragami, T.; Naito, Y.; Sugihara, M., Studies on synthesis and permeability of special polymer membranes. *Polym. Bull.* **1981,** *4*, 617-622.

308. Abed, M. R. M.; Kumbharkar, S. C.; Groth, A. M.; Li, K., Ultrafiltration PVDF hollow fibre membranes with interconnected bicontinuous structures produced via a single-step phase inversion technique. *J. Membr. Sci.* **2012,** *407–408*, 145-154.

309. Susanto, H.; Ulbricht, M., Characteristics, performance and stability of polyethersulfone ultrafiltration membranes prepared by phase separation method using different macromolecular additives. *J. Membr. Sci.* **2009,** *327*, 125-135.

310. Wang, D.; Li, K.; Teo, W. K., Preparation and characterization of polyvinylidene fluoride (PVDF) hollow fiber membranes. *J. Membr. Sci.* **1999,** *163*, 211-220.

311. Fontananova, E.; Jansen, J. C.; Cristiano, A.; Curcio, E.; Drioli, E., Effect of additives in the casting solution on the formation of PVDF membranes. *Desalination* **2006,** *192*, 190-197.

312. Geng, Z.; Yang, X.; Boo, C.; Zhu, S.; Lu, Y.; Fan, W.; Huo, M.; Elimelech, M.; Yang, X., Self-cleaning anti-fouling hybrid ultrafiltration membranes via side chain grafting of poly (aryl ether sulfone) and titanium dioxide. *J. Membr. Sci.* **2017,** *529*, 1-10.

313. Ma, W.; Rajabzadeh, S.; Shaikh, A. R.; Kakihana, Y.; Sun, Y.; Matsuyama, H., Effect of type of poly(ethylene glycol) (PEG) based amphiphilic copolymer on antifouling properties of copolymer/poly(vinylidene fluoride) (PVDF) blend membranes. *J. Membr. Sci.* **2016,** *514*, 429-439.

314. Yeo, H. T.; Lee, S. T.; Han, M. J., Role of a Polymer Additive in Casting Solution in Preparation of Phase Inversion Polysulfone Membranes. *J. Chem. Eng. Jpn.* **2000,** *33*, 180-184.

315. Zhu, J.; Zhang, Q.; Zheng, J.; Hou, S.; Zhang, S.; Li, S., Correlation of the polymer hydrophilicity and membrane fabrication process on the properties of asymmetric membranes in a vapor-induced phase-inversion process. *J. Appl. Polym. Sci.* **2017,** *134*, 44701.

316. Du, C.; Ma, X.; Li, J.; Wu, C., Improving the charged and antifouling properties of PVDF ultrafiltration membranes by blending with polymerized ionic liquid copolymer P. *J. Appl. Polym. Sci.* **2017**.

317. Nie, C.; Yang, Y.; Peng, Z.; Cheng, C.; Ma, L.; Zhao, C., Aramid nanofiber as an emerging nanofibrous modifier to enhance ultrafiltration and biological performances of polymeric membranes. *J. Membr. Sci.* **2017,** *528*, 251-263.

318. Wong, P. C. Y.; Kwon, Y.-N.; Criddle, C. S., Use of atomic force microscopy and fractal geometry to characterize the roughness of nano-, micro-, and ultrafiltration membranes. *J. Membr. Sci.* **2009,** *340*, 117-132.

319. Torrestiana-Sanchez, B.; Ortiz-Basurto, R.; Brito-De La Fuente, E., Effect of nonsolvents on properties of spinning solutions and polyethersulfone hollow fiber ultrafiltration membranes. *J. Membr. Sci.* **1999,** *152*, 19-28.

320. Mosqueda-Jimenez, D. B.; Narbaitz, R. M.; Matsuura, T.; Chowdhury, G.; Pleizier, G.; Santerre, J. P., Influence of processing conditions on the properties of ultrafiltration membranes. *J. Membr. Sci.* **2004,** *231*, 209-224.

321. Jalili, N.; Laxminarayana, K., A review of atomic force microscopy imaging systems: application to molecular metrology and biological sciences. *Mechatronics* **2004,** *14*, 907-945.

322. Butt, H. J.; Cappella, B.; Kappl, M., Force measurements with the atomic force microscope: Technique, interpretation and applications. *Surf. Sci. Rep.* **2005,** *59*, 1-152.

323. Fu, W.; Zhang, W., Hybrid AFM for Nanoscale Physicochemical Characterization: Recent Development and Emerging Applications. *Small* **2017,** *13*, 1603525.

324. Hołda, A. K.; Vankelecom, I. F. J., Understanding and guiding the phase inversion process for synthesis of solvent resistant nanofiltration membranes. *J. Appl. Polym. Sci.* **2015,** *132*.

325. Vats, K.; Marsh, G.; Harding, K.; Zampetakis, I.; Waugh, R. E.; Benoit, D. S. W., Nanoscale physicochemical properties of chain- and step-growth polymerized PEG hydrogels affect cell-material interactions. *J. Biomed. Mater. Res. B* **2017**, 1112–1122.

326. Zhu, J.; Wang, Q.; Zhou, S.; Li, Q.; Gan, M.; Jiang, H.; Qin, W.; Liu, X.; Hu, Y.; Qiu, G., Insights into the relation between adhesion force and chalcopyrite-bioleaching by Acidithiobacillus ferrooxidans. *Colloids Surf. B Biointerfaces* **2015,** *126*, 351-357.

327. Islam, N.; Tuli, R. A.; George, G. A.; Dargaville, T. R., Colloidal drug probe: Method development and validation for adhesion force measurement using Atomic Force Microscopy. *Adv. Powder Technol.* **2014,** *25*, 1240-1248.

328. Alsteens, D.; Dague, E.; Rouxhet, P. G.; Baulard, A. R.; Dufrêne, Y. F., Direct Measurement of Hydrophobic Forces on Cell Surfaces Using AFM. *Langmuir* **2007,** *23*, 11977-11979.

329. Vadillo-Rodríguez, V.; Busscher, H. J.; van der Mei, H. C.; de Vries, J.; Norde, W., Role of lactobacillus cell surface hydrophobicity as probed by AFM in adhesion to surfaces at low and high ionic strength. *Colloids Surf. B Biointerfaces* **2005,** *41*, 33-41.

330. Dufrêne, Y. F., Direct Characterization of the Physicochemical Properties of Fungal Spores Using Functionalized AFM Probes. *Biophys. J.* **2000,** *78*, 3286-3291.

331. Vezenov, D. V.; Noy, A.; Rozsnyai, L. F.; Lieber, C. M., Force Titrations and Ionization State Sensitive Imaging of Functional Groups in Aqueous Solutions by Chemical Force Microscopy. *JACS* **1997,** *119*, 2006-2015.

332. Sinniah, S. K.; Steel, A. B.; Miller, C. J.; Reutt-Robey, J. E., Solvent Exclusion and Chemical Contrast in Scanning Force Microscopy. *JACS* **1996,** *118*, 8925-8931.

333. van der Vegte, E. W.; Hadziioannou, G., Scanning Force Microscopy with Chemical Specificity: An Extensive Study of Chemically Specific Tip−Surface Interactions and the Chemical Imaging of Surface Functional Groups. *Langmuir* **1997,** *13*, 4357-4368.

334. Shahin, V.; Hafezi, W.; Oberleithner, H.; Ludwig, Y.; Windoffer, B.; Schillers, H.; Kühn, J. E., The genome of HSV-1 translocates through the nuclear pore as a condensed rod-like structure. *J. Cell Sci.* **2006,** *119*, 23-30.

335. Burnham, N.; Chen, X.; Hodges, C.; Matei, G.; Thoreson, E.; Roberts, C.; Davies, M.; Tendler, S., Comparison of calibration methods for atomic-force microscopy cantilevers. *Nanotechnology* **2002,** *14*, 1.

336. Eaton, P.; Smith, J. R.; Graham, P.; Smart, J. D.; Nevell, T. G.; Tsibouklis, J., Adhesion force mapping of polymer surfaces: factors influencing force of adhesion. *Langmuir* **2002,** *18*, 3387-3389.

337. Tournadre, G. d.; Reisdorffer, F.; Rödel, R.; Simonetti, O.; Klauk, H.; Giraudet, L., High voltage surface potential measurements in ambient conditions: Application to organic thin-film transistor injection and transport characterization. *J. Appl. Phys.* **2016,** *119*, 125501.

338. Palermo, V.; Palma, M.; Samorì, P., Electronic characterization of organic thin films by Kelvin probe force microscopy. *Adv. Mater.* **2006,** *18*, 145-164.

339. Morsch, S.; Liu, Y.; Greensmith, P.; Lyon, S. B.; Gibbon, S. R., Molecularly controlled epoxy network nanostructures. *Polymer* **2017,** *108*, 146-153.

340. Kelchtermans, M.; Lo, M.; Dillon, E.; Kjoller, K.; Marcott, C., Characterization of a polyethylene–polyamide multilayer film using nanoscale infrared spectroscopy and imaging. *Vib. Spectrosc* **2016,** *82*, 10-15.

341. Zhang, H.; Ding, C.; Cao, J.; Xu, W.; Li, X.; Zhang, H., A novel solvent-template method to manufacture nano-scale porous membranes for vanadium flow battery applications. *J. Mater. Chem. A* **2014,** *2*, 9524-9531.

342. Borodko, Y.; Habas, S. E.; Koebel, M.; Yang, P.; Frei, H.; Somorjai, G. A., Probing the interaction of poly (vinylpyrrolidone) with platinum nanocrystals by UV-Raman and FTIR. *J. Phys. Chem. B* **2006,** *110*, 23052-23059.

343. Shahbaziniaz, M.; Foroutan, S. M.; Bolourchian, N., Dissolution rate enhancement of clarithromycin using ternary ground mixtures: Nanocrystal formation. *Iranian journal of pharmaceutical research: IJPR* **2013,** *12*, 587.

344. Castillo, P. M.; de la Mata, M.; Casula, M. F.; Sánchez-Alcázar, J. A.; Zaderenko, A. P., PEGylated versus non-PEGylated magnetic nanoparticles as camptothecin delivery system. *Beilstein J. Nanotechnol.* **2014,** *5*, 1312-1319.

345. Rao, S.; Bálint, Š.; Cossins, B.; Guallar, V.; Petrov, D., Raman Study of Mechanically Induced Oxygenation State Transition of Red Blood Cells Using Optical Tweezers. *Biophys. J.* **2009,** *96*, 209-216.

346. Cauberg, E. C.; de Bruin, D. M.; Faber, D. J.; van Leeuwen, T. G.; de la Rosette, J. J.; de Reijke, T. M., A new generation of optical diagnostics for bladder cancer: technology, diagnostic accuracy, and future applications. *Eur. Urol.* **2009,** *56*, 287-297.

347. Sharma, M.; Bijwe, J., Influence of molecular weight on performance properties of polyethersulphone and its composites with carbon fabric. *Wear* **2012,** *274*, 388-394.

348. Djaoued, Y.; Robichaud, J.; Brüning, R.; Albert, A.-S.; Ashrit, P. V., The effect of poly (ethylene glycol) on the crystallisation and phase transitions of nanocrystalline TiO2 thin films. *Mater. Sci. Poland* **2005,** *23*, 15-27.

349. Stylianou, S. K.; Katsoyiannis, I. A.; Ernst, M.; Zouboulis, A. I., Impact of O3 or O3/H2O2 treatment via a membrane contacting system on the composition and characteristics of the natural organic matter of surface waters. *Environ. Sci. Pollut. Res.* **2018,** *25*, 12246-12255.

350. Stylianou, S. K.; Katsoyiannis, I. A.; Ernst, M.; Zouboulis, A. I., Impact of O3 or O3/H2O2 treatment via a membrane contacting system on the composition and characteristics of the natural organic matter of surface waters. *Environ. Sci. Pollut. Res.* **2017**.

351. Zhang, S.; Shao, T.; Karanfil, T., The effects of dissolved natural organic matter on the adsorption of synthetic organic chemicals by activated carbons and carbon nanotubes. *Water Res.* **2011,** *45*, 1378-1386.

352. Tian, J.-y.; Ernst, M.; Cui, F.; Jekel, M., Correlations of relevant membrane foulants with UF membrane fouling in different waters. *Water Res.* **2013,** *47*, 1218-1228.

353. Boyer, T. H.; Singer, P. C.; Aiken, G. R., Removal of Dissolved Organic Matter by Anion Exchange: Effect of Dissolved Organic Matter Properties. *Environ. Sci. Technol.* **2008,** *42*, 7431-7437.

354. Sharp, E. L.; Parsons, S. A.; Jefferson, B., Seasonal variations in natural organic matter and its impact on coagulation in water treatment. *Sci. Total Environ.* **2006,** *363*, 183-194.

355. Katsoyiannis, I. A.; Canonica, S.; von Gunten, U., Efficiency and energy requirements for the transformation of organic micropollutants by ozone, O3/H2O2 and UV/H2O2. *Water Res.* **2011,** *45*, 3811-3822.

356. Papageorgiou, A.; Stylianou, S. K.; Kaffes, P.; Zouboulis, A. I.; Voutsa, D., Effects of ozonation pretreatment on natural organic matter and wastewater derived organic matter – Possible implications on the formation of ozonation by-products. *Chemosphere* **2017,** *170*, 33-40.

357. Hunter, R. J., *Zeta potential in colloid science: principles and applications*. Academic press: New York/London, **2013**, Vol. 2.

358. Rajabzadeh, S.; Sano, R.; Ishigami, T.; Kakihana, Y.; Ohmukai, Y.; Matsuyama, H., Preparation of hydrophilic vinyl chloride copolymer hollow fiber membranes with antifouling properties. *Appl. Surf. Sci.* **2015,** *324*, 718-724.

359. Xie, M.; Nghiem, L. D.; Price, W. E.; Elimelech, M., Impact of humic acid fouling on membrane performance and transport of pharmaceutically active compounds in forward osmosis. *Water Res.* **2013,** *47*, 4567-4575.

360. Mozes, N.; Rouxhet, P. G., Methods for measuring hydrophobicity of microorganisms. *J. Microbiol. Methods* **1987,** *6*, 99-112.

361. Alias, N. H.; Jaafar, J.; Samitsu, S.; Matsuura, T.; Ismail, A. F.; Othman, M. H. D.; Rahman, M. A.; Othman, N. H.; Abdullah, N.; Paiman, S. H.; Yusof, N.; Aziz, F., Photocatalytic nanofiber-coated alumina hollow fiber membranes for highly efficient oilfield produced water treatment. *Chem. Eng. J.* **2018**.

362. Cassie, A.; Baxter, S., Wettability of porous surfaces. *Trans. Faraday Soc.* **1944,** *40*, 546-551.

363. Liscio, A.; Palermo, V.; Müllen, K.; Samorì, P., Tip− sample interactions in Kelvin probe force microscopy: quantitative measurement of the local surface potential. *J. Phys. Chem. C* **2008,** *112*, 17368-17377.

364. Berger, R.; Butt, H. J.; Retschke, M. B.; Weber, S. A., Electrical modes in scanning probe microscopy. *Macromol. Rapid Commun.* **2009,** *30*, 1167-1178.

365. Dalrymple, O. K.; Halfhide, T.; Udom, I.; Gilles, B.; Wolan, J.; Zhang, Q.; Ergas, S., Wastewater Use in Algae Production for Generation of Renewable Resources: A Review and Preliminary Results. *Aquat. Biosyst.* **2013,** *9*, 2-2.

366. Winger, M.; de Vries, A. H.; van Gunsteren, W. F., Force-field dependence of the conformational properties of α, ω-dimethoxypolyethylene glycol. *Mol. Phys.* **2009,** *107*, 1313-1321.

367. Pollack, K. A. Multiply Complex, Non-Toxic, Anti-Fouling Surfaces Designed for Marine and Biomedical Applications. Texas A&M University, 2014.

368. Havenstrite, K. L.; McCray, V. W.; Felkins, B. M.; Cook, P. A., Contact lens with a hydrophilic layer. Google Patents: 2016.

369. Cole, E. T.; Scott, R. A.; Connor, A. L.; Wilding, I. R.; Petereit, H.-U.; Schminke, C.; Beckert, T.; Cadé, D., Enteric coated HPMC capsules designed to achieve intestinal targeting. *Int. J. Pharm.* **2002,** *231*, 83-95.

370. Wei, J.; Zhang, X.; Song, F., Deformation of Surface Nanobubbles Induced by Substrate Hydrophobicity. *Langmuir* **2016,** *32*, 13003-13008.

371. Barish, J. A.; Goddard, J. M., Anti-fouling surface modified stainless steel for food processing. *Food Bioprod. Process.* **2013,** *91*, 352-361.

372. Alsteens, D.; Müller, D. J.; Dufrêne, Y. F., Multiparametric Atomic Force Microscopy Imaging of Biomolecular and Cellular Systems. *Acc. Chem. Res.* **2017**.

373. Birkenhauer, E.; Neethirajan, S., Prevention and Control of Biofilms in the Food Industry and Bio‐Nanotechnology Approaches. *Biofilms Food Environ.* **2015**, 84.

374. Zhang, G.; Ji, S.; Gao, X.; Liu, Z., Adsorptive fouling of extracellular polymeric substances with polymeric ultrafiltration membranes. *J. Membr. Sci.* **2008,** *309*, 28-35.

375. Shirazi, S.; Lin, C. J.; Chen, D., Inorganic fouling of pressure-driven membrane processes — A critical review. *Desalination* **2010,** *250*, 236-248.

376. Lafreniere, L. Y.; Talbot, F. D.; Matsuura, T.; Sourirajan, S., Effect of poly (vinylpyrrolidone) additive on the performance of poly (ether sulfone) ultrafiltration membranes. *Ind. Eng. Chem. Res.* **1987,** *26*, 2385-2389.

377. Ochoa, N.; Pradanos, P.; Palacio, L.; Pagliero, C.; Marchese, J.; Hernandez, A., Pore size distributions based on AFM imaging and retention of multidisperse polymer solutes: characterisation of polyethersulfone UF membranes with dopes containing different PVP. *J. Membr. Sci.* **2001,** *187*, 227-237.

378. Wu, J.; Huang, X., Effect of mixed liquor properties on fouling propensity in membrane bioreactors. *J. Membr. Sci.* **2009,** *342*, 88-96.

379. Zhan, J.; Liu, Z.; Wang, B.; Ding, F., Modification of a membrane surface charge by a low temperature plasma induced grafting reaction and its application to reduce membrane fouling. *Sep. Sci. Technol.* **2004,** *39*, 2977-2995.

380. van der Marel, P.; Zwijnenburg, A.; Kemperman, A.; Wessling, M.; Temmink, H.; van der Meer, W., Influence of membrane properties on fouling in submerged membrane bioreactors. *J. Membr. Sci.* **2010,** *348*, 66-74.

381. Kim, D. S.; Kang, J. S.; Lee, Y. M., The Influence of Membrane Surface Properties on Fouling in a Membrane Bioreactor for Wastewater Treatment. *Sep. Sci. Technol.* **2004,** *39*, 833-854.

382. Nakamura, K.; Matsumoto, K., Properties of protein adsorption onto pore surface during microfiltration: Effects of solution environment and membrane hydrophobicity. *J. Membr. Sci.* **2006,** *280*, 363-374.

383. Fan, L.; Harris, J. L.; Roddick, F. A.; Booker, N. A., Influence of the characteristics of natural organic matter on the fouling of microfiltration membranes. *Water Res.* **2001,** *35*, 4455-4463.

384. Nakamura, K.; Matsumoto, K., Protein adsorption properties on a microfiltration membrane: A comparison between static and dynamic adsorption methods. *J. Membr. Sci.* **2006,** *285*, 126-136.

385. Wang, Q.; Wang, Z.; Wu, Z., Effects of solvent compositions on physicochemical properties and anti-fouling ability of PVDF microfiltration membranes for wastewater treatment. *Desalination* **2012,** *297*, 79-86.

386. Chang, H.; Qu, F.; Liu, B.; Yu, H.; Li, K.; Shao, S.; Li, G.; Liang, H., Hydraulic irreversibility of ultrafiltration membrane fouling by humic acid: Effects of membrane properties and backwash water composition. *J. Membr. Sci.* **2015,** *493*, 723-733.

387. van Oss, C. J., Hydrophobicity of biosurfaces — Origin, quantitative determination and interaction energies. *Colloids Surf. B: Biointerfaces* **1995,** *5*, 91-110.

388. Van Oss, C.; Good, R.; Chaudhury, M., The role of van der Waals forces and hydrogen bonds in "hydrophobic interactions" between biopolymers and low energy surfaces. *J. Colloid Interface Sci.* **1986,** *111*, 378-390.

389. Oss, C. v.; Good, R.; Busscher, R., Estimation of the polar surface tension parameters of glycerol and formamide, for use in contact angle measurements on polar solids. *J. Dispers. Sci. Technol.* **1990,** *11*, 75-81.

390. Van Oss, C. J., Acid—base interfacial interactions in aqueous media. *Colloids Surf. A Physicochem. Eng. Asp.* **1993,** *78*, 1-49.

391. Susanto, H.; Ulbricht, M., Influence of ultrafiltration membrane characteristics on adsorptive fouling with dextrans. *J. Membr. Sci.* **2005,** *266*, 132-142.

392. Corbett, J. C. W.; McNeil-Watson, F.; Jack, R. O.; Howarth, M., Measuring surface zeta potential using phase analysis light scattering in a simple dip cell arrangement. *Colloids Surf. A Physicochem. Eng. Asp.* **2012,** *396*, 169-176.

393. Thomas, T. E.; Aani, S. A.; Oatley-Radcliffe, D. L.; Williams, P. M.; Hilal, N., Laser Doppler Electrophoresis and electro-osmotic flow mapping: A novel methodology for the determination of membrane surface zeta potential. *J. Membr. Sci.* **2017,** *523*, 524-532.

394. Corbett, J. C.; McNeil-Watson, F.; Jack, R. O.; Howarth, M., Measuring surface zeta potential using phase analysis light scattering in a simple dip cell arrangement. *Colloids Surf. A Physicochem. Eng. Asp.* **2012,** *396*, 169-176.

395. Swan, J. W.; Furst, E. M., A simpler expression for Henry's function describing the electrophoretic mobility of spherical colloids. *J. Colloid Interface Sci.* **2012,** *388*, 92-94.

396. Tanyolaç, D.; Sönmezışık, H.; Özdural, A. R., A low cost porous polyvinylbutyral membrane for BSA adsorption. *Biochem. Eng. J.* **2005,** *22*, 221-228.

397. Meng, X.; Tang, W.; Wang, L.; Wang, X.; Huang, D.; Chen, H.; Zhang, N., Mechanism analysis of membrane fouling behavior by humic acid using atomic force microscopy: Effect of solution pH and hydrophilicity of PVDF ultrafiltration membrane interface. *J. Membr. Sci.* **2015,** *487*, 180-188.

398. Toh, P. Y.; Ng, B. W.; Ahmad, A. L.; Chieh, D. C. J.; Lim, J., The role of particle-to-cell interactions in dictating nanoparticle aided magnetophoretic separation of microalgal cells. *Nanoscale* **2014**.

399. Ge, S.; Agbakpe, M.; Wu, Z.; Kuang, L.; Zhang, W.; Wang, X., Influences of surface coating, UV irradiation and magnetic field on the algae removal using magnetite nanoparticles. *Environ. Sci. Technol.* **2014,** *49*, 1190-1196.

400. Tang, C. Y.; Chong, T. H.; Fane, A. G., Colloidal interactions and fouling of NF and RO membranes: A review. *Adv. Colloid Interface Sci.* **2011,** *164*, 126-143.

401. Zhang, W.; Zhang, X., Adsorption of MS2 on oxide nanoparticles affects chlorine disinfection and solar inactivation. *Water Res.* **2015,** *69*, 59-67.

402. Grasso, D.; Subramaniam, K.; Butkus, M.; Strevett, K.; Bergendahl, J., A review of non-DLVO interactions in environmental colloidal systems. *Rev. Environ. Sci. Biotechnol.* **2002,** *1*, 17-38.

403. Yoon, R.-H.; Flinn, D. H.; Rabinovich, Y. I., Hydrophobic interactions between dissimilar surfaces. *J. Colloid Interface Sci.* **1997,** *185*, 363-370.

404. Park, B.-J.; Abu-Lail, N. I., The role of the pH conditions of growth on the bioadhesion of individual and lawns of pathogenic Listeria monocytogenes cells. *J. Colloid Interface Sci.* **2011,** *358*, 611-620.

405. Meagher, L.; Klauber, C.; Pashley, R. M., The influence of surface forces on the fouling of polypropylene microfiltration membranes. *Colloids Surf. A Physicochem. Eng. Asp.* **1996,** *106*, 63-81.

406. Song, L., Flux decline in crossflow microfiltration and ultrafiltration: mechanisms and modeling of membrane fouling. *J. Membr. Sci.* **1998,** *139*, 183-200.

407. Elimelech, M.; Gregory, J.; Jia, X., *Particle deposition and aggregation: measurement, modelling and simulation*. Butterworth-Heinemann: **2013**.

408. Stamatakis, K.; Tien, C., A simple model of cross-flow filtration based on particle adhesion. *AlChE J.* **1993,** *39*, 1292-1302.

409. Suki, A.; Fane, A. G.; Fell, C. J. D., Flux decline in protein ultrafiltration. *J. Membr. Sci.* **1984,** *21*, 269-283.

410. Bouchard, C. R.; Jolicoeur, J.; Kouadio, P.; Britten, M., Study of humic acid adsorption on nanofiltration membranes by contact angle measurements. *Can. J. Chem. Eng.* **1997,** *75*, 339-345.

411. Gourley, L.; Britten, M.; Gauthier, S. F.; Pouliot, Y., Characterization of adsorptive fouling on ultrafiltration membranes by peptides mixtures using contact angle measurements. *J. Membr. Sci.* **1994,** *97*, 283-289.

412. Salgin, S.; Salgin, U.; Soyer, N., Streaming potential measurements of polyethersulfone ultrafiltration membranes to determine salt effects on membrane zeta potential. *Int. J. Electrochem. Sci.* **2013,** *8*, 4073-4084.

413. Wang, Y. N.; Tang, C. Y., Fouling of Nanofiltration, Reverse Osmosis, and Ultrafiltration Membranes by Protein Mixtures: The Role of Inter-Foulant-Species Interaction. *Environ. Sci. Technol.* **2011,** *45*, 6373-6379.

414. Luo, J.; Chan, W. B.; Wang, L.; Zhong, C. J., Probing interfacial interactions of bacteria on metal nanoparticles and substrates with different surface properties. *Int. J. Antimicrob. Agents* **2010,** *36*, 549-556.

415. Reinsch, V. E.; Greenberg, A. R.; Kelley, S. S.; Peterson, R.; Bond, L. J., A new technique for the simultaneous, real-time measurement of membrane compaction and performance during exposure to high-pressure gas. *J. Membr. Sci.* **2000,** *171*, 217-228.

416. Brinkert, L.; Abidine, N.; Aptel, P., On the relation between compaction and mechanical properties for ultrafiltration hollow fibers. *J. Membr. Sci.* **1993,** *77*, 123-131.

417. Wang, Y.; Combe, C.; Clark, M. M., The effects of pH and calcium on the diffusion coefficient of humic acid. *J. Membr. Sci.* **2001,** *183*, 49-60.

418. Phillies, G. D., Diffusion of bovine serum albumin in a neutral polymer solution. *Biopolymers* **1985,** *24*, 379-386.

419. Van Oss, C. J., *The properties of water and their role in colloidal and biological systems*. Academic Press: **2008**, Vol. 16.

420. Meechai, N.; Jamieson, A. M.; Blackwell, J., Translational Diffusion Coefficients of Bovine Serum Albumin in Aqueous Solution at High Ionic Strength. *J. Colloid Interface Sci.* **1999,** *218*, 167-175.

421. Milcent, S.; Carrère, H., Clarification of lactic acid fermentation broths. *Sep. Purif. Technol.* **2001,** *22-23*, 393-401.

422. Maruyama, T.; Katoh, S.; Nakajima, M.; Nabetani, H.; Abbott, T. P.; Shono, A.; Satoh, K., FT-IR analysis of BSA fouled on ultrafiltration and microfiltration membranes. *J. Membr. Sci.* **2001,** *192*, 201-207.

423. Ang, W. S.; Elimelech, M., Protein (BSA) fouling of reverse osmosis membranes: Implications for wastewater reclamation. *J. Membr. Sci.* **2007,** *296*, 83-92.

424. Hashino, M.; Hirami, K.; Katagiri, T.; Kubota, N.; Ohmukai, Y.; Ishigami, T.; Maruyama, T.; Matsuyama, H., Effects of three natural organic matter types on cellulose acetate butyrate microfiltration membrane fouling. *J. Membr. Sci.* **2011,** *379*, 233-238.

425. Xiao, F.; Xiao, P.; Zhang, W. J.; Wang, D. S., Identification of key factors affecting the organic fouling on low-pressure ultrafiltration membranes. *J. Membr. Sci.* **2013,** *447*, 144-152.

426. Tian, J.; Ernst, M.; Cui, F.; Jekel, M., Effect of different cations on UF membrane fouling by NOM fractions. *Chem. Eng. J.* **2013,** *223*, 547-555.

427. Zhang, W.; Crittenden, J.; Li, K.; Chen, Y., Attachment efficiency of nanoparticle aggregation in aqueous dispersions: modeling and experimental validation. *Environ. Sci. Technol.* **2012,** *46*, 7054-7062.

428. Lin, T.; Shen, B.; Chen, W.; Zhang, X., Interaction mechanisms associated with organic colloid fouling of ultrafiltration membrane in a drinking water treatment system. *Desalination* **2014,** *332*, 100-108.

429. Hungerford, G.; Benesch, J.; Mano, J. F.; Reis, R. L., Effect of the labelling ratio on the photophysics of fluorescein isothiocyanate (FITC) conjugated to bovine serum albumin. *Photochem. Photobiol. Sci.* **2007,** *6*, 152-158.

430. Braga, J.; Desterro, J. M.; Carmo-Fonseca, M., Intracellular macromolecular mobility measured by fluorescence recovery after photobleaching with confocal laser scanning microscopes. *Mol. Biol. Cell* **2004,** *15*, 4749-4760.

431. Ferrando, M.; Rŏžek, A.; Zator, M.; Lopez, F.; Güell, C., An approach to membrane fouling characterization by confocal scanning laser microscopy. *J. Membr. Sci.* **2005,** *250*, 283-293.

432. Chen, M.; Lee, D.; Tay, J., Distribution of extracellular polymeric substances in aerobic granules. *Appl. Microbiol. Biotechnol.* **2007,** *73*, 1463-1469.

433. Toh, P. Y.; Ng, B. W.; Ahmad, A. L.; Chieh, D. C. J.; Lim, J., The role of particle-to-cell interactions in dictating nanoparticle aided magnetophoretic separation of microalgal cells. *Nanoscale* **2014,** *6*, 12838-12848.

434. Ohler, B., Cantilever spring constant calibration using laser Doppler vibrometry. *Rev. Sci. Instrum.* **2007,** *78*, 063701.

435. Subhi, N.; Verliefde, A. R. D.; Chen, V.; Le-Clech, P., Assessment of physicochemical interactions in hollow fibre ultrafiltration membrane by contact angle analysis. *J. Membr. Sci.* **2012,** *403-404*, 32-40.

436. Brant, J. A.; Childress, A. E., Assessing short-range membrane–colloid interactions using surface energetics. *J. Membr. Sci.* **2002,** *203*, 257-273.

437. Chin, Y.-P.; Aiken, G.; O'Loughlin, E., Molecular Weight, Polydispersity, and Spectroscopic Properties of Aquatic Humic Substances. *Environ. Sci. Technol.* **1994,** *28*, 1853-1858.

438. Shao, J.; Hou, J.; Song, H., Comparison of humic acid rejection and flux decline during filtration with negatively charged and uncharged ultrafiltration membranes. *Water Res.* **2011,** *45*, 473-482.

439. Evanko, C. R.; Dzombak, D. A., Influence of structural features on sorption of NOM-analogue organic acids to goethite. *Environ. Sci. Technol.* **1998,** *32*, 2846-2855.

440. El-Rehaili, A. M.; Weber, W. J., Correlation of humic substance trihalomethane formation potential and adsorption behavior to molecular weight distribution in raw and chemically treated waters. *Water Res.* **1987,** *21*, 573-582.

441. Parsons, J., Humus Chemistry-Genesis, Composition, Reactions. *Soil Science* **1983,** *135*, 129-130.

442. Turhan, Y.; Doğan, M.; Alkan, M., Poly(vinyl chloride)/Kaolinite Nanocomposites: Characterization and Thermal and Optical Properties. *Ind. Eng. Chem. Res.* **2010,** *49*, 1503-1513.

443. Giordano, M.; Kansiz, M.; Heraud, P.; Beardall, J.; Wood, B.; McNaughton, D., Fourier transform infrared spectroscopy as a novel tool to investigate changes in intracellular macromolecular pools in the marine microalga Chaetoceros muellerii (Bacillariophyceae). *J. Phycol.* **2001,** *37*, 271-279.

444. Kontrec, J.; Kralj, D.; Brečević, L.; Falini, G., Influence of some polysaccharides on the production of calcium carbonate filler particles. *J. Cryst. Growth* **2008,** *310*, 4554-4560.

445. Ubaldini, A. L.; Baesso, M. L.; Sehn, E.; Sato, F.; Benetti, A. R.; Pascotto, R. C., Fourier transform infrared photoacoustic spectroscopy study of physicochemical interaction between human dentin and etch-&-rinse adhesives in a simulated moist bond technique. *J. Biomed. Opt.* **2012,** *17*, 0650021-0650025.

446. Corbatón-Báguena, M.-J.; Gugliuzza, A.; Cassano, A.; Mazzei, R.; Giorno, L., Destabilization and removal of immobilized enzymes adsorbed onto polyethersulfone ultrafiltration membranes by salt solutions. *J. Membr. Sci.* **2015,** *486*, 207-214.

447. Yu, C.-H.; Fang, L.-C.; Lateef, S. K.; Wu, C.-H.; Lin, C.-F., Enzymatic treatment for controlling irreversible membrane fouling in cross-flow humic acid-fed ultrafiltration. *J. Hazard. Mater.* **2010,** *177*, 1153-1158.

448. Susanto, H.; Arafat, H.; Janssen, E. M. L.; Ulbricht, M., Ultrafiltration of polysaccharide–protein mixtures: Elucidation of fouling mechanisms and fouling control by membrane surface modification. *Sep. Purif. Technol.* **2008,** *63*, 558-565.

449. Duclos-Orsello, C.; Li, W.; Ho, C.-C., A three mechanism model to describe fouling of microfiltration membranes. *J. Membr. Sci.* **2006,** *280*, 856-866.

450. Lu, X.; Arias Chavez, L. H.; Romero-Vargas Castrillón, S.; Ma, J.; Elimelech, M., Influence of active layer and support layer surface structures on organic fouling propensity of thin-film composite forward osmosis membranes. *Environ. Sci. Technol.* **2015,** *49*, 1436-1444.

451. Tijing, L. D.; Woo, Y. C.; Choi, J.-S.; Lee, S.; Kim, S.-H.; Shon, H. K., Fouling and its control in membrane distillation—a review. *J. Membr. Sci.* **2015,** *475*, 215-244.

452. Miao, R.; Wang, L.; Lv, Y.; Wang, X.; Feng, L.; Liu, Z.; Huang, D.; Yang, Y., Identifying polyvinylidene fluoride ultrafiltration membrane fouling behavior of different effluent organic matter fractions using colloidal probes. *Water Res.* **2014,** *55*, 313-322.

453. Wu, S.-E.; Lin, N.-J.; Chou, C.-Y.; Hu, C.-C.; Tung, K.-L., Biofouling mechanism of polysaccharide–protein–humic acid mixtures on polyvinylidene fluoride microfiltration membranes. *J. Taiwan Inst. Chem. Eng.* **2017,** *94*, 2-9.

454. Castaing, J.-B.; Massé, A.; Pontié, M.; Séchet, V.; Haure, J.; Jaouen, P., Investigating submerged ultrafiltration (UF) and microfiltration (MF) membranes for seawater pre-treatment dedicated to total removal of undesirable micro-algae. *Desalination* **2010,** *253*, 71-77.

455. Zhang, W.; Zhang, W.; Zhang, X.; Amendola, P.; Hu, Q.; Chen, Y., Characterization of dissolved organic matters responsible for ultrafiltration membrane fouling in algal harvesting. *Algal Res.* **2013,** *2*, 223-229.

456. Zhang, W., Nanoparticle Aggregation: Principles and Modeling. In *Nanomaterial: Impacts on Cell Biology and Medicine*, Capco, D. G., et al., Eds. Springer Netherlands: Dordrecht, **2014**, pp 19-43.

457. Holthoff, H.; Egelhaaf, S. U.; Borkovec, M.; Schurtenberger, P.; Sticher, H., Coagulation rate measurements of colloidal particles by simultaneous static and dynamic light scattering. *Langmuir* **1996,** *12*, 5541-5549.

458. Honig, E.; Roebersen, G.; Wiersema, P., Effect of hydrodynamic interaction on the coagulation rate of hydrophobic colloids. *J. Colloid Interface Sci.* **1971,** *36*, 97-109.

459. Chang, H.; Liang, H.; Qu, F.; Liu, B.; Yu, H.; Du, X.; Li, G.; Snyder, S. A., Hydraulic backwashing for low-pressure membranes in drinking water treatment: A review. *J. Membr. Sci.* **2017,** *540*, 362-380.

460. Jezowska, A.; Bottino, A.; Capannelli, G.; Fabbri, C.; Migliorini, G., Ultrafiltration as direct pre-treatment of seawater – a case study. *Desalination* **2009,** *245*, 723-729.

461. Li, L.; Wray, H. E.; Andrews, R. C.; Bérubé, P. R., Ultrafiltration Fouling: Impact of Backwash Frequency and Air Sparging. *Sep. Sci. Technol.* **2014,** *49*, 2814-2823.

462. Hwang, K.-J.; Chan, C.-S.; Tung, K.-L., Effect of backwash on the performance of submerged membrane filtration. *J. Membr. Sci.* **2009,** *330*, 349-356.

463. Akhondi, E.; Wicaksana, F.; Fane, A. G., Evaluation of fouling deposition, fouling reversibility and energy consumption of submerged hollow fiber membrane systems with periodic backwash. *J. Membr. Sci.* **2014,** *452*, 319-331.

464. Nakanishi, K.; Sakiyama, T.; Imamura, K., On the adsorption of proteins on solid surfaces, a common but very complicated phenomenon. *J. Biosci. Bioeng.* **2001,** *91*, 233-244.

465. Katsoufidou, K.; Yiantsios, S.; Karabelas, A., An experimental study of UF membrane fouling by humic acid and sodium alginate solutions: the effect of backwashing on flux recovery. *Desalination* **2008,** *220*, 214-227.

466. Vatanpour, V.; Madaeni, S. S.; Rajabi, L.; Zinadini, S.; Derakhshan, A. A., Boehmite nanoparticles as a new nanofiller for preparation of antifouling mixed matrix membranes. *J. Membr. Sci.* **2012,** *401–402*, 132-143.

467. Zinadini, S.; Zinatizadeh, A. A.; Rahimi, M.; Vatanpour, V.; Zangeneh, H., Preparation of a novel antifouling mixed matrix PES membrane by embedding graphene oxide nanoplates. *J. Membr. Sci.* **2014,** *453*, 292-301.

468. Arkhangelsky, E.; Kuzmenko, D.; Gitis, N. V.; Vinogradov, M.; Kuiry, S.; Gitis, V., Hypochlorite Cleaning Causes Degradation of Polymer Membranes. *Tribology Lett.* **2007,** *28*, 109-116.

469. Arkhangelsky, E.; Kuzmenko, D.; Gitis, V., Impact of chemical cleaning on properties and functioning of polyethersulfone membranes. *J. Membr. Sci.* **2007,** *305*, 176-184.

470. Gitis, V.; Haught, R. C.; Clark, R. M.; Gun, J.; Lev, O., Application of nanoscale probes for the evaluation of the integrity of ultrafiltration membranes. *J. Membr. Sci.* **2006,** *276*, 185-192.

471. Jung, B.; Yoon, J. K.; Kim, B.; Rhee, H.-W., Effect of molecular weight of polymeric additives on formation, permeation properties and hypochlorite treatment of asymmetric polyacrylonitrile membranes. *J. Membr. Sci.* **2004,** *243*, 45-57.

472. Pellegrin, B.; Prulho, R.; Rivaton, A.; Thérias, S.; Gardette, J.-L.; Gaudichet-Maurin, E.; Causserand, C., Multi-scale analysis of hypochlorite induced PES/PVP ultrafiltration membranes degradation. *J. Membr. Sci.* **2013,** *447*, 287-296.

473. Gijsbertsen-Abrahamse, A. J.; Cornelissen, E. R.; Hofman, J. A. M. H., Fiber failure frequency and causes of hollow fiber integrity loss. *Desalination* **2006,** *194*, 251-258.

474. Zhu, Y.; Wang, F.; Liu, L.; Xiao, S.; Chang, Z.; Wu, Y., Composite of a nonwoven fabric with poly (vinylidene fluoride) as a gel membrane of high safety for lithium ion battery. *Energ. Environ. Sci.* **2013,** *6*, 618-624.

475. Shi, S.; Dursch, T. J.; Blake, C.; Mukundan, R.; Borup, R. L.; Weber, A. Z.; Kusoglu, A., Impact of hygrothermal aging on structure/function relationship of perfluorosulfonic‐acid membrane. *J. Polym. Sci. B Polym. Phys.* **2016,** *54*, 570-581.

476. Eddington, D. T.; Puccinelli, J. P.; Beebe, D. J., Thermal aging and reduced hydrophobic recovery of polydimethylsiloxane. *Sensors Actuat. B Chem.* **2006,** *114*, 170-172.

477. Kwapiszewska, K.; Żukowski, K.; Kwapiszewski, R.; Brzózka, Z., Double casting prototyping with a thermal aging step for fabrication of 3D microstructures in poly (dimethylsiloxane). *AIMS Biophysics* **2016,** *3*, 553-562.

478. Jo, B.-H.; Van Lerberghe, L. M.; Motsegood, K. M.; Beebe, D. J., Three-dimensional micro-channel fabrication in polydimethylsiloxane (PDMS) elastomer. *J. Microelectromech. Syst.* **2000,** *9*, 76-81.

479. Kwon, Y.-N.; Leckie, J. O., Hypochlorite degradation of crosslinked polyamide membranes: II. Changes in hydrogen bonding behavior and performance. *J. Membr. Sci.* **2006,** *282*, 456-464.

480. Abdullah, S. Z.; Bérubé, P. R., Filtration and cleaning performances of PVDF membranes aged with exposure to sodium hypochlorite. *Sep. Purif. Technol.* **2018,** *195*, 253-259.

481. Wu, Q.; Zhang, X.; Cao, G., Impacts of sodium hydroxide and sodium hypochlorite aging on polyvinylidene fluoride membranes fabricated with different methods. *J. Environ. Sci.* **2018,** *67*, 294-308.

482. Robinson, S.; Abdullah, S. Z.; Bérubé, P.; Le-Clech, P., Ageing of membranes for water treatment: Linking changes to performance. *J. Membr. Sci.* **2016,** *503*, 177-187.

483. Yadav, K.; Morison, K. R., Effects of hypochlorite exposure on flux through polyethersulphone ultrafiltration membranes. *Food Bioprod. Process.* **2010,** *88*, 419-424.

484. Pellegrin, B.; Mezzari, F.; Hanafi, Y.; Szymczyk, A.; Remigy, J.-C.; Causserand, C., Filtration performance and pore size distribution of hypochlorite aged PES/PVP ultrafiltration membranes. *J. Membr. Sci.* **2015,** *474*, 175-186.

485. Abdullah, S. Z.; Bérubé, P. R., Assessing the effects of sodium hypochlorite exposure on the characteristics of PVDF based membranes. *Water Res.* **2013,** *47*, 5392-5399.

486. Levitsky, I.; Duek, A.; Arkhangelsky, E.; Pinchev, D.; Kadoshian, T.; Shetrit, H.; Naim, R.; Gitis, V., Understanding the oxidative cleaning of UF membranes. *J. Membr. Sci.* **2011,** *377*, 206-213.

487. Arkhangelsky, E.; Goren, U.; Gitis, V., Retention of organic matter by cellulose acetate membranes cleaned with hypochlorite. *Desalination* **2008,** *223*, 97-105.

488. Alkmin, A. R.; Amaral, M. C. S.; de França Neta, L. S.; Cerqueira, A. C.; Santiago, V. M. J., Ageing effect on chlorinated polyethylene membrane of an MBR caused by chemical cleaning procedures AU - da Costa, Paula Rocha. *Desalin. Water Treat.* **2015,** *53*, 1460-1470.

489. Rouaix, S.; Causserand, C.; Aimar, P., Experimental study of the effects of hypochlorite on polysulfone membrane properties. *J. Membr. Sci.* **2006,** *277*, 137-147.

490. Hassouna, F.; Therias, S.; Mailhot, G.; Gardette, J.-L., Photooxidation of poly(N-vinylpyrrolidone) (PVP) in the solid state and in aqueous solution. *Polym. Degrad. Stab.* **2009,** *94*, 2257-2266.

491. Kaeselev, B.; Pieracci, J.; Belfort, G., Photoinduced grafting of ultrafiltration membranes: comparison of poly(ether sulfone) and poly(sulfone). *J. Membr. Sci.* **2001,** *194*, 245-261.

492. Y. Ho, J.; Matsuura, T.; P. Santerre, J., The effect of fluorinated surface modifying macromolecules on the surface morphology of polyethersulfone membranes. *Journal of Biomaterials Science, Polymer Edition* **2000,** *11*, 1085-1104.

493. Causserand, C.; Pellegrin, B.; Rouch, J.-C., Effects of sodium hypochlorite exposure mode on PES/PVP ultrafiltration membrane degradation. *Water Res.* **2015,** *85*, 316-326.

494. Hashim, N. A.; Liu, Y.; Li, K., Stability of PVDF hollow fibre membranes in sodium hydroxide aqueous solution. *Chem. Eng. Sci.* **2011,** *66*, 1565-1575.

495. Touffet, A.; Baron, J.; Welte, B.; Joyeux, M.; Teychene, B.; Gallard, H., Impact of pretreatment conditions and chemical ageing on ultrafiltration membrane performances. Diagnostic of a coagulation/adsorption/filtration process. *J. Membr. Sci.* **2015,** *489*, 284-291.

496. Singh, S.; Khulbe, K.; Matsuura, T.; Ramamurthy, P., Membrane characterization by solute transport and atomic force microscopy. *J. Membr. Sci.* **1998,** *142*, 111-127.

497. Koyuncu, I.; Brant, J.; Lüttge, A.; Wiesner, M. R., A comparison of vertical scanning interferometry (VSI) and atomic force microscopy (AFM) for characterizing membrane surface topography. *J. Membr. Sci.* **2006,** *278*, 410-417.

498. Fu, W.; Hua, L.; Zhang, W., Experimental and Modeling Assessment of the Roles of Hydrophobicity and Zeta Potential in Chemically Modified Poly (ether sulfone) Membrane Fouling Kinetics. *Ind. Eng. Chem. Res.* **2017,** *56*, 8580-8589.

499. Fu, W.; Wang, L.; Chen, F.; Zhang, X.; Zhang, W., Polyvinyl chloride (PVC) ultrafiltration membrane fouling and defouling behavior: EDLVO theory and interface adhesion force analysis. *J. Membr. Sci.* **2018,** *564*, 204-210.

500. Belfer, S.; Fainchtain, R.; Purinson, Y.; Kedem, O., Surface characterization by FTIR-ATR spectroscopy of polyethersulfone membranes-unmodified, modified and protein fouled. *J. Membr. Sci.* **2000,** *172*, 113-124.

501. Kazarian, S. G.; Chan, K. A., ATR-FTIR spectroscopic imaging: recent advances and applications to biological systems. *Analyst* **2013,** *138*, 1940-1951.

502. Thygesen, O.; Hedegaard, M. A. B.; Zarebska, A.; Beleites, C.; Krafft, C., Membrane fouling from ammonia recovery analyzed by ATR-FTIR imaging. *Vib. Spectrosc* **2014,** *72*, 119-123.

503. Fu, W.; Carbrello, C.; Wu, X.; Zhang, W., Visualizing and quantifying the nanoscale hydrophobicity and chemical distribution of surface modified polyethersulfone (PES) membranes. *Nanoscale* **2017,** *9*, 15550-15557.

504. Pellegrin, B.; Gaudichet-Maurin, E.; Causserand, C., Mechano-chemical ageing of PES/PVP ultrafiltration membranes used in drinking water production. *Water Science and Technology: Water Supply* **2013,** *13*, 541-551.

505. Lee, J.; Bartelt-Hunt, S. L.; Li, Y., Development of Quantitative Structure–Activity Relationships for Nanoparticle Titanium Dioxide Aggregation in the Presence of Organic Contaminants. *Environ. Eng. Sci.* **2018,** *35*, 918-926.

506. Thominette, F.; Farnault, O.; Gaudichet-Maurin, E.; Machinal, C.; Schrotter, J.-C., Ageing of polyethersulfone ultrafiltration membranes in hypochlorite treatment. *Desalination* **2006,** *200*, 7-8.

507. Prulho, R.; Therias, S.; Rivaton, A.; Gardette, J.-L., Ageing of polyethersulfone/polyvinylpyrrolidone blends in contact with bleach water. *Polym. Degrad. Stab.* **2013,** *98*, 1164-1172.

508. Rahimpour, A.; Madaeni, S.; Amirinejad, M.; Mansourpanah, Y.; Zereshki, S., The effect of heat treatment of PES and PVDF ultrafiltration membranes on morphology and performance for milk filtration. *J. Membr. Sci.* **2009,** *330*, 189-204.

509. Middleton, W. J.; Lindsey, R. V., Hydrogen Bonding in Fluoro Alcohols. *JACS* **1964,** *86*, 4948-4952.

510. Gao, F.; Wang, J.; Zhang, H.; Hang, M. A.; Cui, Z.; Yang, G., Interaction energy and competitive adsorption evaluation of different NOM fractions on aged membrane surfaces. *J. Membr. Sci.* **2017,** *542*, 195-207.

511. Hanafi, Y.; Loulergue, P.; Ababou-Girard, S.; Meriadec, C.; Rabiller-Baudry, M.; Baddari, K.; Szymczyk, A., Electrokinetic analysis of PES/PVP membranes aged by sodium hypochlorite solutions at different pH. *J. Membr. Sci.* **2016,** *501*, 24-32.

512. Alenazi, N. A.; Hussein, M. A.; Alamry, K. A.; Asiri, A. M., Modified polyether-sulfone membrane: a mini review. *Des. Monomers Polym.* **2017,** *20*, 532-546.

513. Tsehaye, M. T.; Velizarov, S.; Van der Bruggen, B., Stability of polyethersulfone membranes to oxidative agents: A review. *Polym. Degrad. Stab.* **2018,** *157*, 15-33.

514. Roesink, H. D. W.; Beerlage, M.; Potman, W.; Van den Boomgaard, T.; Mulder, M.; Smolders, C., Characterization of new membrane materials by means of fouling experiments adsorption of bsa on polyetherimide—polyvinylpyrrolidone membranes. *Colloids Surf.* **1991,** *55*, 231-243.

515. Deborde, M.; von Gunten, U., Reactions of chlorine with inorganic and organic compounds during water treatment—Kinetics and mechanisms: A critical review. *Water Res.* **2008,** *42*, 13-51.

516. Zhu, X.; Zheng, W.-R.; Tang, X.-F.; Zhang, W.-B.; Zha, L.-S., Experimental and theoretical investigations of thermal degradation behaviors of poly (aryl ether sulfone) s. *J. Sulfur Chem.* **2018,** *39*, 64-75.

517. Loría-Bastarrachea, M.; Herrera-Kao, W.; Cauich-Rodríguez, J.; Cervantes-Uc, J.; Vázquez-Torres, H.; Ávila-Ortega, A., A TG/FTIR study on the thermal degradation of poly (vinyl pyrrolidone). *J. Therm. Anal. Calorim.* **2011,** *104*, 737-742.

518. Peniche, C.; Zaldívar, D.; Pazos, M.; Páz, S.; Bulay, A.; Román, J. S., Study of the thermal degradation of poly (N‐vinyl‐2‐pyrrolidone) by thermogravimetry‐FTIR. *J. Appl. Polym. Sci.* **1993,** *50*, 485-493.

519. Bianco, G.; Soldi, M.; Pinheiro, E.; Pires, A.; Gehlen, M.; Soldi, V., Thermal stability of poly (N-vinyl-2-pyrrolidone-co-methacrylic acid) copolymers in inert atmosphere. *Polym. Degrad. Stabl.* **2003,** *80*, 567-574.

520. Wienk, I. M.; Meuleman, E. E. B.; Borneman, Z.; van den Boomgaard, T.; Smolders, C. A., Chemical treatment of membranes of a polymer blend: Mechanism of the reaction of hypochlorite with poly(vinyl pyrrolidone). *J. Polym. Sci., Part A: Polym. Chem.* **1995,** *33*, 49-54.

521. Qin, J.-J.; Oo, M. H.; Li, Y., Development of high flux polyethersulfone hollow fiber ultrafiltration membranes from a low critical solution temperature dope via hypochlorite treatment. *J. Membr. Sci.* **2005,** *247*, 137-142.

522. Hanafi, Y.; Szymczyk, A.; Rabiller-Baudry, M.; Baddari, K., Degradation of Poly(Ether Sulfone)/Polyvinylpyrrolidone Membranes by Sodium Hypochlorite: Insight from Advanced Electrokinetic Characterizations. *Environ. Sci. Technol.* **2014,** *48*, 13419-13426.

523. Prasetya, A.; Mursiti, S.; Maryan, S.; Jati, N. In *Isolation and Identification of Active Compounds from Papaya Plants and Activities as Antimicrobial*, IOP

Conference Series: Materials Science and Engineering, IOP Publishing: 2018; p 012007.

524. Zhang, Y.; Wang, J.; Gao, F.; Chen, Y.; Zhang, H., A comparison study: The different impacts of sodium hypochlorite on PVDF and PSF ultrafiltration (UF) membranes. *Water Res.* **2017,** *109*, 227-236.

525. Yuan, W.; Zydney, A. L., Humic acid fouling during ultrafiltration. *Environ. Sci. Technol.* **2000,** *34*, 5043-5050.

526. Guo, W.; Ngo, H.-H.; Li, J., A mini-review on membrane fouling. *Bioresour. Technol.* **2012,** *122*, 27-34.

527. Gao, W.; Liang, H.; Ma, J.; Han, M.; Chen, Z.-l.; Han, Z.-s.; Li, G.-b., Membrane fouling control in ultrafiltration technology for drinking water production: a review. *Desalination* **2011,** *272*, 1-8.

528. Kimura, K.; Hane, Y.; Watanabe, Y.; Amy, G.; Ohkuma, N., Irreversible membrane fouling during ultrafiltration of surface water. *Water Res.* **2004,** *38*, 3431-3441.

529. Katsoufidou, K.; Yiantsios, S.; Karabelas, A., A study of ultrafiltration membrane fouling by humic acids and flux recovery by backwashing: experiments and modeling. *J. Membr. Sci.* **2005,** *266*, 40-50.

530. Mohammadi, T.; Madaeni, S.; Moghadam, M., Investigation of membrane fouling. *Desalination* **2003,** *153*, 155-160.

531. Smith, P. J.; Shon, H. K.; Vigneswaran, S.; Ngo, H. H.; Nguyen, H., Productivity enhancement in a cross-flow ultrafiltration membrane system through automated de-clogging operations. *J. Membr. Sci.* **2006,** *280*, 82-88.

532. Sun, M.; Su, Y.; Mu, C.; Jiang, Z., Improved antifouling property of PES ultrafiltration membranes using additive of silica− PVP nanocomposite. *Ind. Eng. Chem. Res.* **2009,** *49*, 790-796.

533. Marchese, J.; Ponce, M.; Ochoa, N.; Prádanos, P.; Palacio, L.; Hernández, A., Fouling behaviour of polyethersulfone UF membranes made with different PVP. *J. Membr. Sci.* **2003,** *211*, 1-11.

534. Sun, J.; Hu, C.; Tong, T.; Zhao, K.; Qu, J.; Liu, H.; Elimelech, M., Performance and Mechanisms of Ultrafiltration Membrane Fouling Mitigation by Coupling Coagulation and Applied Electric Field in a Novel Electrocoagulation Membrane Reactor. *Environ. Sci. Technol.* **2017,** *51*, 8544-8551.

535. Xing, J.; Wang, H.; Cheng, X.; Tang, X.; Luo, X.; Wang, J.; Wang, T.; Li, G.; Liang, H., Application of low-dosage UV/chlorine pre-oxidation for mitigating ultrafiltration (UF) membrane fouling in natural surface water treatment. *Chem. Eng. J.* **2018**.

536. Tang, S.; Zhang, Z.; Zhang, X., Coupling in-situ ozonation with ferric chloride addition for ceramic ultrafiltration membrane fouling mitigation in wastewater treatment: Quantitative fouling analysis. *J. Membr. Sci.* **2018**.

537. Wang, J.; Wu, B.; Yang, S.; Liu, Y.; Fane, A. G.; Chew, J. W., Characterizing the scouring efficiency of Granular Activated Carbon (GAC) particles in membrane fouling mitigation via wavelet decomposition of accelerometer signals. *J. Membr. Sci.* **2016,** *498*, 105-115.

538. Wu, B.; Zamani, F.; Lim, W.; Liao, D.; Wang, Y.; Liu, Y.; Chew, J. W.; Fane, A. G., Effect of mechanical scouring by granular activated carbon (GAC) on membrane fouling mitigation. *Desalination* **2017,** *403*, 80-87.

539. Fan, X.; Zhao, H.; Quan, X.; Liu, Y.; Chen, S., Nanocarbon-based membrane filtration integrated with electric field driving for effective membrane fouling mitigation. *Water Res.* **2016,** *88*, 285-292.

540. Ding, A.; Fan, Q.; Cheng, R.; Sun, G.; Zhang, M.; Wu, D., Impacts of applied voltage on microbial electrolysis cell-anaerobic membrane bioreactor (MEC-AnMBR) and its membrane fouling mitigation mechanism. *Chem. Eng. J.* **2018,** *333*, 630-635.

541. Xie, M.; Luo, W.; Gray, S. R., Surface pattern by nanoimprint for membrane fouling mitigation: Design, performance and mechanisms. *Water Res.* **2017,** *124*, 238-243.

542. Wang, Z.; Jin, J.; Hou, D.; Lin, S., Tailoring surface charge and wetting property for robust oil-fouling mitigation in membrane distillation. *J. Membr. Sci.* **2016,** *516*, 113-122.

543. Wang, Z.; Lin, S., Membrane fouling and wetting in membrane distillation and their mitigation by novel membranes with special wettability. *Water Res.* **2017,** *112*, 38-47.

544. Ho, K.; Teow, Y.; Mohammad, A.; Ang, W.; Lee, P., Development of graphene oxide (GO)/multi-walled carbon nanotubes (MWCNTs) nanocomposite conductive membranes for electrically enhanced fouling mitigation. *J. Membr. Sci.* **2018,** *552*, 189-201.

545. Kano, H.; Umeda, Y.; Kasai, T.; Sasaki, T.; Matsumoto, M.; Yamazaki, K.; Nagano, K.; Arito, H.; Fukushima, S., Carcinogenicity studies of 1,4-dioxane administered in drinking-water to rats and mice for 2years. *Food Chem. Toxicol.* **2009,** *47*, 2776-2784.

546. Dickenson, E. R.; Higgins, C., Treatment Mitigation Strategies for Poly-and Perfluoroalkyl Substances [Project# 4322]. **2016**.

547. Jiang, C. R.; Xu, Z. C.; Guo, Q. W.; Zhuo, Q. F., Degradation of bisphenol A in water by the heterogeneous photo-Fenton. *Environ. Technol.* **2014,** *35*, 966-972.

548. Staples, C. A.; Dorn, P. B.; Klecka, G. M.; O'Block, S. T.; Harris, L. R., A review of the environmental fate, effects, and exposures of bisphenol A. *Chemosphere* **1998,** *36*, 2149-2173.

549. Fassi, S.; Djebbar, K.; Bousnoubra, I.; Chenini, H.; Sehili, T., Oxidation of bromocresol green by different advanced oxidation processes: Fenton, Fenton-like, photo-Fenton, photo-Fenton-like and solar light. Comparative study. *Desalin. Water Treat.* **2014,** *52*, 4982-4989.

550. Song, J. M.; Wang, H.; Hu, G.; Zhao, S. J.; Hu, H. Q.; Jin, B. K., $ZnWO_4$–Cu system with enhanced photocatalytic activity by photo-Fenton-like synergistic reaction. *Mater. Res. Bulletin* **2012,** *47*, 3296-3300.

551. Devi, L.; Kumar, S.; Reddy, K., Photo fenton like process Fe3+/(NH4) 2S2O8/UV for the degradation of Di azo dye congo red using low iron concentration. *Open Chem.* **2009,** *7*, 468-477.

552. Rivero, M.; Parsons, S.; Jeffrey, P.; Pidou, M.; Jefferson, B., Membrane chemical reactor (MCR) combining photocatalysis and microfiltration for grey water treatment. *Water Sci. Techno.* **2006,** *53*, 173-180.

553. Augugliaro, V.; Litter, M.; Palmisano, L.; Soria, J., The combination of heterogeneous photocatalysis with chemical and physical operations: A tool for improving the photoprocess performance. *J. Photochem. Photobiol. C Photochem. Rev.* **2006,** *7*, 127-144.

554. Fu, J.; Ji, M.; Wang, Z.; Jin, L.; An, D., A new submerged membrane photocatalysis reactor (SMPR) for fulvic acid removal using a nano-structured photocatalyst. *J. Hazard. Mater.* **2006,** *131*, 238-242.

555. Fu, J.; Ji, M.; Zhao, Y.; Wang, L., Kinetics of aqueous photocatalytic oxidation of fulvic acids in a photocatalysis–ultrafiltration reactor (PUR). *Sep. Purif. Technol.* **2006,** *50*, 107-113.

556. Mozia, S., Photocatalytic membrane reactors (PMRs) in water and wastewater treatment. A review. *Sep. Purif. Technol.* **2010,** *73*, 71-91.

557. Harman, B. I.; Koseoglu, H.; Yigit, N. O.; Beyhan, M.; Kitis, M., The use of iron oxide-coated ceramic membranes in removing natural organic matter and phenol from waters. *Desalination* **2010,** *261*, 27-33.

558. Byun, S.; Davies, S. H.; Alpatova, A. L.; Corneal, L. M.; Baumann, M. J.; Tarabara, V. V.; Masten, S. J., Mn oxide coated catalytic membranes for a hybrid ozonation–membrane filtration: Comparison of Ti, Fe and Mn oxide coated membranes for water quality. *Water Res.* **2011,** *45*, 163-170.

559. Mansourpanah, Y.; Madaeni, S. S.; Rahimpour, A.; Farhadian, A.; Taheri, A. H., Formation of appropriate sites on nanofiltration membrane surface for binding TiO2 photo-catalyst: Performance, characterization and fouling-resistant capability. *J. Membr. Sci.* **2009,** *330*, 297-306.

560. Zakersalehi, A.; Choi, H.; Andersen, J.; Dionysiou, D. D., Photocatalytic ceramic membranes. *Membr. Sci. Technol.* **2013**.

561. Sabate, J.; Anderson, M.; Kikkawa, H.; Xu, Q.; Cervera-March, S.; Hill, C., Nature and properties of pure and nb-doped Ti02 ceramic membranes affecting the photocatalytic degradation of 3-chlorosalicylic acid as a model of halogenated organic compounds. *J. Catal.* **1992,** *134*, 36-46.

562. Song, L.; Zhu, B.; Gray, S.; Duke, M.; Muthukumaran, S., Performance of Hybrid Photocatalytic-Ceramic Membrane System for the Treatment of Secondary Effluent. *Membranes* **2017,** *7*, 20.

563. Lim, T.-T.; Goei, R., Combined Photocatalysis–Separation Processes for Water Treatment Using Hybrid Photocatalytic Membrane Reactors. In *Photocatalysis*, **2016**, pp 130-156.

564. Athanasekou, C. P.; Moustakas, N. G.; Morales-Torres, S.; Pastrana-Martínez, L. M.; Figueiredo, J. L.; Faria, J. L.; Silva, A. M.; Dona-Rodriguez, J. M.; Romanos, G. E.; Falaras, P., Ceramic photocatalytic membranes for water filtration under UV and visible light. *Appl. Cat. B Environ.* **2015,** *178*, 12-19.

565. Lavonen, E. E.; Gonsior, M.; Tranvik, L. J.; Schmitt-Kopplin, P.; Köhler, S. J., Selective Chlorination of Natural Organic Matter: Identification of Previously Unknown Disinfection Byproducts. *Environ. Sci. Technol.* **2013,** *47*, 2264-2271.

566. Daiber, E. J.; DeMarini, D. M.; Ravuri, S. A.; Liberatore, H. K.; Cuthbertson, A. A.; Thompson-Klemish, A.; Byer, J. D.; Schmid, J. E.; Afifi, M. Z.; Blatchley, E. R.; Richardson, S. D., Progressive Increase in Disinfection Byproducts and Mutagenicity from Source to Tap to Swimming Pool and Spa Water: Impact of Human Inputs. *Environ. Sci. Technol.* **2016,** *50*, 6652-6662.

567. Jeong, C. H.; Postigo, C.; Richardson, S. D.; Simmons, J. E.; Kimura, S. Y.; Mariñas, B. J.; Barcelo, D.; Liang, P.; Wagner, E. D.; Plewa, M. J., Occurrence and Comparative Toxicity of Haloacetaldehyde Disinfection Byproducts in Drinking Water. *Environ. Sci. Technol.* **2015,** *49*, 13749-13759.

568. Zhai, H.; Zhang, X.; Zhu, X.; Liu, J.; Ji, M., Formation of Brominated Disinfection Byproducts during Chloramination of Drinking Water: New Polar Species and Overall Kinetics. *Environ. Sci. Technol.* **2014,** *48*, 2579-2588.

569. Shi, P.; Jia, S.; Zhang, X.-X.; Zhang, T.; Cheng, S.; Li, A., Metagenomic insights into chlorination effects on microbial antibiotic resistance in drinking water. *Water Res.* **2013,** *47*, 111-120.

570. Loo, S.-L.; Fane, A. G.; Lim, T.-T.; Krantz, W. B.; Liang, Y.-N.; Liu, X.; Hu, X., Superabsorbent Cryogels Decorated with Silver Nanoparticles as a Novel Water Technology for Point-of-Use Disinfection. *Environ. Sci. Technol.* **2013,** *47*, 9363-9371.

571. Chiao, T.-H.; Clancy, T. M.; Pinto, A.; Xi, C.; Raskin, L., Differential Resistance of Drinking Water Bacterial Populations to Monochloramine Disinfection. *Environ. Sci. Technol.* **2014,** *48*, 4038-4047.

572. Krasner, S. W.; Weinberg, H. S.; Richardson, S. D.; Pastor, S. J.; Chinn, R.; Sclimenti, M. J.; Onstad, G. D.; Thruston, A. D., Occurrence of a New Generation of Disinfection Byproducts†. *Environ Sci Technol* **2006,** *40*, 7175-7185.

573. Mahmoudi, M.; Serpooshan, V., Silver-Coated Engineered Magnetic Nanoparticles Are Promising for the Success in the Fight against Antibacterial Resistance Threat. *ACS NANO* **2012,** *6*, 2656-2664.

574. Wu, M.-C.; Deokar, A. R.; Liao, J.-H.; Shih, P.-Y.; Ling, Y.-C., Graphene-Based Photothermal Agent for Rapid and Effective Killing of Bacteria. *ACS NANO* **2013,** *7*, 1281-1290.

575. Hlavsa, M. C., Outbreaks Associated with Treated Recreational Water—United States, 2000–2014. *MMWR. Morbidity and mortality weekly report* **2018,** *67*.

576. Cao, Z.; Ge, H.; Lai, S., Studies on synthesis and adsorption properties of chitosan cross-linked by glutaraldehyde and Cu(II) as template under microwave irradiation. *Eur. Polym. J.* **2001,** *37*, 2141-2143.

577. Shao, J.; Yang, Y.; Zhong, Q., Studies on preparation of oligoglucosamine by oxidative degradation under microwave irradiation. *Polym. Degrad. Stab.* **2003,** *82*, 395-398.

578. Ku, H. S.; Siores, E.; Taube, A.; Ball, J. A. R., Productivity improvement through the use of industrial microwave technologies. *Compt. Ind. Eng.* **2002,** *42*, 281-290.

579. Wang, Y.; Zhang, P., Photocatalytic decomposition of perfluorooctanoic acid (PFOA) by TiO_2 in the presence of oxalic acid. *J. Hazard. Mater.* **2011,** *192*, 1869-75.

580. Zhang, Z.; Xu, Y.; Shen, M.; Dionysiou, D. D.; Wu, D.; Chen, Z.; Li, F.; Liu, D.; Zhang, F., Assisted activated carbon‐microwave degradation of the sodium dodecyl benzene sulfonate by nano‐ or micro‐Fe3O4 and comparison of their catalytic activity. *Environ. Prog. Sustain. Energy* **2013,** *32*, 181-186.

581. Moholkar, V.; Choudhury, H. A.; Singh, S.; Khanna, S.; Ranjan, A.; Chakma, S.; Bhasarkar, J., Physical and chemical mechanisms of ultrasound in biofuel synthesis. In *Production of Biofuels and Chemicals with Ultrasound*, Springer: **2015**, pp 35-86.

582. Liu, S.; Oshita, S.; Kawabata, S.; Makino, Y.; Yoshimoto, T., Identification of ROS Produced by Nanobubbles and Their Positive and Negative Effects on Vegetable Seed Germination. *Langmuir* **2016,** *32*, 11295-11302.

583. Mezule, L.; Tsyfansky, S.; Yakushevich, V.; Juhna, T., A simple technique for water disinfection with hydrodynamic cavitation: Effect on survival of Escherichia coli. *Desalination* **2009,** *248*, 152-159.

584. Jyoti, K.; Pandit, A. B., Water disinfection by acoustic and hydrodynamic cavitation. *BioChem. Eng. J.* **2001,** *7*, 201-212.

585. Kalumuck, K. M.; Chahine, G. L., The use of cavitating jets to oxidize organic compounds in water. *J. Fluids Eng.* **2000,** *122*, 465-470.

586. Wang, X.; Zhang, Y., Degradation of alachlor in aqueous solution by using hydrodynamic cavitation. *J. Hazard. Mater.* **2009,** *161*, 202-207.

587. Takenouchi, T., Behavior of hydrogen nanobubbles in alkaline electrolyzed water and its rinse effect for sulfate ion remained on nickel-plated surface. *J. Appl. Electrochem.* **2010,** *40*, 849-854.

588. Zhang, M.; Seddon, J. R. T., Nanobubble–Nanoparticle Interactions in Bulk Solutions. *Langmuir* **2016,** *32*, 11280-11286.

589. Liu, G.; Wu, Z.; Craig, V. S., Cleaning of protein-coated surfaces using nanobubbles: an investigation using a quartz crystal microbalance. *J. Phys. Chem. C* **2008,** *112*, 16748-16753.

590. Liu, G.; Craig, V. S., Improved cleaning of hydrophilic protein-coated surfaces using the combination of nanobubbles and SDS. *ACS Appl. Mater. Interfaces* **2009,** *1*, 481-487.

591. Wu, Z.; Chen, H.; Dong, Y.; Mao, H.; Sun, J.; Chen, S.; Craig, V. S. J.; Hu, J., Cleaning using nanobubbles: Defouling by electrochemical generation of bubbles. *J. Colloid Interface Sci.* **2008,** *328*, 10-14.

592. Qi, X.; Li, Z., Efficiency optimization of a microwave-assisted Fenton-like process for the pretreatment of chemical synthetic pharmaceutical wastewater. *Desalin. Water Treat.* **2015,** *57*, 11756-11764.

593. Einaga, H.; Nasu, Y.; Oda, M.; Saito, H., Catalytic performances of perovskite oxides for CO oxidation under microwave irradiation. *Chem. Eng. J.* **2016,** *283*, 97-104.

594. Yang, Y.; Wang, P.; Shi, S.; Liu, Y., Microwave enhanced Fenton-like process for the treatment of high concentration pharmaceutical wastewater. *J. Hazard. Mater.* **2009,** *168*, 238-245.

595. Qi, X. D.; Li, Z. H. In *Efficiency optimization of organic pollutant removal in pharmaceutical wastewater by microwave-assisted Fenton-like technology*, Applied Mechanics and Materials, Trans Tech Publ: 2014; pp 406-410.

596. Iboukhoulef, H.; Amrane, A.; Kadi, H., Microwave-enhanced Fenton-like system, Cu(II)/H2O2, for olive mill wastewater treatment. *Environ. Technol.* **2013,** *34*, 853-860.

597. Yan, P.; Gao, L. B.; Li, W. T. In *Microwave-Enhanced Fenton-Like System, Fe3O4/H2O2 for Rhodamine B Wastewater Degradation*, Applied Mechanics and Materials, Trans Tech Publ: 2014; pp 834-837.

598. Atta, A. Y.; Jibril, B. Y.; Al-Waheibi, T. K.; Al-Waheibi, Y. M., Microwave-enhanced catalytic degradation of 2-nitrophenol on alumina-supported copper oxides. *Catal. Commun.* **2012,** *26*, 112-116.

599. Wang, N.; Wang, P., Study and application status of microwave in organic wastewater treatment – A review. *Chem. Eng. J.* **2016,** *283*, 193-214.

600. Li, S.; Zhang, W.; Zhang, G.; Zheng, H.; Zhu, W.; Wang, P.; Zheng, Y.; Xu, Z.; Lv, G.; Bai, X.; Wu, Y., Microwave enhanced Fenton-like process for degradation of perfluorooctanoic acid (PFOA) using Pb-BiFeO3/rGO as a highly active heterogeneous catalyst. *Environ Sc.Tech.* **2016,** *Under Review*.

601. Ma, N.; Fan, X.; Quan, X.; Zhang, Y., Ag–TiO2/HAP/Al2O3 bioceramic composite membrane: Fabrication, characterization and bactericidal activity. *J. Membr. Sci.* **2009,** *336*, 109-117.

602. Lv, Y.; Liu, H.; Wang, Z.; Liu, S.; Hao, L.; Sang, Y.; Liu, D.; Wang, J.; Boughton, R. I., Silver nanoparticle-decorated porous ceramic composite for water treatment. *J. Membr. Sci.* **2009,** *331*, 50-56.

603. Karnik, B. S.; Baumann, M. J.; Masten, S. J.; Davies, S. H., AFM and SEM characterization of iron oxide coated ceramic membranes. *J. Mater. Sci.* **2006,** *41*, 6861-6870.

604. Xiangli, F.; Chen, Y.; Jin, W.; Xu, N., Polydimethylsiloxane (PDMS)/Ceramic Composite Membrane with High Flux for Pervaporation of Ethanol−Water Mixtures. *Ind. Eng. Chem. Res.* **2007,** *46*, 2224-2230.

605. Acquisto, B. A.; Reimers, R. S.; Smith, J. E.; Pillai, S. D., Factors affecting disinfection and stabilization of sewage sludge. *Proceedings of the Water Environment Federation* **2006,** 5345-5361.

606. Remya, N.; Lin, J.-G., Current status of microwave application in wastewater treatment—a review. *Chem. Eng. J.* **2011,** *166*, 797-813.

607. Nascimento, U. M.; Azevedo, E. B., Microwaves and their coupling to advanced oxidation processes: Enhanced performance in pollutants degradation. *J. Environ. Sci. Health A* **2013,** *48*, 1056-1072.

608. NYSERDA, *Feasibility of Using Microwave Radiation to Facilitate the Dewatering, Anaerobic Digestion and Disinfection of Wastewater Treatment Plant Sludge*; Report 10881. 11-05, April, **2011**.

609. Schmink, J. R.; Leadbeater, N. E., Microwave heating as a tool for sustainable chemistry. *Microwave heating as a tool for sustainable chemistry. CRC Press, Boca Raton, FL* **2010**, 1-24.

610. Kappe, C. O., Controlled Microwave Heating in Modern Organic Synthesis. *Angew. Chem. Int. Ed.* **2004,** *43*, 6250-6284.

611. de la Hoz, A., Microwave Heating as a Tool for Sustainable Chemistry. Edited by Nicholas E. Leadbeater. Wiley Online Library: 2011.

612. Tripathi, B. P.; Dubey, N. C.; Choudhury, S.; Stamm, M., Antifouling and tunable amino functionalized porous membranes for filtration applications. *J. Mater. Chem.* **2012,** *22*, 19981-19992.

613. Calgaroto, S.; Wilberg, K. Q.; Rubio, J., On the nanobubbles interfacial properties and future applications in flotation. *Miner. Eng.* **2014,** *60*, 33-40.

614. Ishibashi, K.-i.; Fujishima, A.; Watanabe, T.; Hashimoto, K., Detection of active oxidative species in TiO2 photocatalysis using the fluorescence technique. *Electrochem. Commun.* **2000,** *2*, 207-210.

615. Xiao, Q.; Si, Z.; Zhang, J.; Xiao, C.; Tan, X., Photoinduced hydroxyl radical and photocatalytic activity of samarium-doped TiO_2 nanocrystalline. *J. Hazard. Mater.* **2008,** *150*, 62-67.

616. Yu, J.; Wang, W.; Cheng, B.; Su, B.-L., Enhancement of photocatalytic activity of mesporous TiO2 powders by hydrothermal surface fluorination treatment. *J. Phys. Chem. C* **2009,** *113*, 6743-6750.

617. Chae, S.-R.; Yamamura, H.; Ikeda, K.; Watanabe, Y., Comparison of fouling characteristics of two different poly-vinylidene fluoride microfiltration membranes in a pilot-scale drinking water treatment system using pre-coagulation/sedimentation, sand filtration, and chlorination. *Water Res.* **2008,** *42*, 2029-2042.

618. Suzuki, T.; Watanabe, Y.; Ozawa, G.; Ikeda, S., Removal of soluble organics and manganese by a hybrid MF hollow fiber membrane system. *Desalination* **1998,** *117*, 119-129.

619. Huang, X.; Liu, R.; Qian, Y., Behaviour of soluble microbial products in a membrane bioreactor. *Process Biochem.* **2000,** *36*, 401-406.

620. Deng, D.; Li, F.; Li, M., A novel propane monooxygenase initiating degradation of 1, 4-dioxane by Mycobacterium dioxanotrophicus PH-06. *Environ. Sci. Technol. Lett.* **2017,** *5*, 86-91.

621. Sun, M.; Zucker, I.; Davenport, D. M.; Zhou, X.; Qu, J.; Elimelech, M., Reactive, Self-Cleaning Ultrafiltration Membrane Functionalized with Iron Oxychloride Nanocatalysts. *Environ. Sci. Technol.* **2018,** *52*, 8674-8683.

622. Nocker, A.; Cheung, C.-Y.; Camper, A. K., Comparison of propidium monoazide with ethidium monoazide for differentiation of live vs. dead bacteria by selective removal of DNA from dead cells. *J. Microbiol. Methods* **2006,** *67*, 310-320.

623. Sun, L.; Bolton, J. R., Determination of the quantum yield for the photochemical generation of hydroxyl radicals in TiO2 suspensions. *J. Phys. Chem.* **1996,** *100*, 4127-4134.

624. Asakuma, Y., Transport Phenomena and Thermal Property under Microwave Irradiation. *Microwaves in Catalysis: Methodology and Applications* **2015**.

625. Li, S.; Zhang, G.; Zheng, H.; Wang, N.; Zheng, Y.; Wang, P., Microwave-assisted synthesis of $BiFeO_3$ nanoparticles with high catalytic performance in microwave-enhanced Fenton-like process. *RSC Adv.* **2016,** *6*, 82439-82446.

626. He, H.; Yang, S.; Yu, K.; Ju, Y.; Sun, C.; Wang, L., Microwave induced catalytic degradation of crystal violet in nano-nickel dioxide suspensions. *J. Hazard. Mater.* **2010,** *173*, 393-400.

627. Li, S.; Zhang, G.; Zhang, W.; Zheng, H.; Zhu, W.; Sun, N.; Zheng, Y.; Wang, P., Microwave enhanced Fenton-like process for degradation of perfluorooctanoic acid (PFOA) using Pb-BiFeO3/rGO as heterogeneous catalyst. *Chem. Eng. J.* **2017,** *326*, 756-764.

628. Luo, W.; Li, Y.-S.; Yuan, J.; Zhu, L.; Liu, Z.; Tang, H.; Liu, S., Ultrasensitive fluorometric determination of hydrogen peroxide and glucose by using multiferroic BiFeO3 nanoparticles as a catalyst. *Talanta* **2010,** *81*, 901-907.

629. Huang, J.; Tan, G.; Yang, W.; Zhang, L.; Ren, H.; Xia, A., Microwave hydrothermal synthesis of BiFeO3: Impact of different surfactants on the morphology and photocatalytic properties. *Mater. Sci. Semicond. Process.* **2014,** *25*, 84-88.

630. Ravera, M.; Buico, A.; Gosetti, F.; Cassino, C.; Musso, D.; Osella, D., Oxidative degradation of 1,5-naphthalenedisulfonic acid in aqueous solutions by microwave irradiation in the presence of H2O2. *Chemosphere* **2009,** *74*, 1309-1314.

631. Prasannakumar, B. R.; Regupathi, I.; Murugesan, T., An optimization study on microwave irradiated decomposition of phenol in the presence of H2O2. *J. Chem. Technol. Biotechnol.* **2009,** *84*, 83-91.

632. Hong, J.; Yuan, N.; Wang, Y.; Qi, S., Efficient degradation of Rhodamine B in microwave-H2O2 system at alkaline pH. *Chem. Eng. J.* **2012,** *191*, 364-368.

633. Li, S.; Zhang, G.; Zheng, H.; Zheng, Y.; Wang, P., Application of BiFeO3-based on nickel foam composites with a highly efficient catalytic activity and easily recyclable in Fenton-like process under microwave irradiation. *J. Power Sources* **2018,** *386*, 21-27.

634. Li, S.; Zhang, G.; Zheng, H.; Wang, N.; Zheng, Y.; Wang, P., Microwave-assisted synthesis of BiFeO 3 nanoparticles with high catalytic performance in microwave-enhanced Fenton-like process. *RSC Adv.* **2016,** *6*, 82439-82446.

635. Bo, L. L.; Zhang, Y. B.; Quan, X.; Zhao, B., Microwave assisted catalytic oxidation of p-nitrophenol in aqueous solution using carbon-supported copper catalyst. *J. Hazard. Mater.* **2008,** *153*, 1201-1206.

636. Dankovich, T. A., Microwave-assisted incorporation of silver nanoparticles in paper for point-of-use water purification. *Environ. Sci. Nano* **2014,** *1*, 367-378.

637. Xu, D.; Cheng, F.; Zhang, Y.; Song, Z., Degradation of methyl orange in aqueous solution by microwave irradiation in the presence of granular-activated carbon. *Water Air Soil Pollut.* **2014,** *225*, 1983.

638. Calvo-Flores, F. G.; Isac-Garcia, J.; Jiménez, J. A. D.; Dobado, J. A., *Emerging Pollutants: Origin, Structure, and Properties*. John Wiley & Sons: **2018**.

639. Barndõk, H.; Merayo, N.; Blanco, L.; Hermosilla, D.; Blanco, Á., Application of on-line FTIR methodology to study the mechanisms of heterogeneous advanced oxidation processes. *App. Cat. B Environ.* **2016,** *185*, 344-352.

640. Merayo, N.; Hermosilla, D.; Cortijo, L.; Blanco, Á., Optimization of the Fenton treatment of 1,4-dioxane and on-line FTIR monitoring of the reaction. *J. Hazard. Mater.* **2014,** *268*, 102-109.

641. Stefan, M. I.; Bolton, J. R., Mechanism of the degradation of 1, 4-dioxane in dilute aqueous solution using the UV/hydrogen peroxide process. *Environ. Sci. Technol.* **1998,** *32*, 1588-1595.

642. Barndõk, H.; Hermosilla, D.; Han, C.; Dionysiou, D. D.; Negro, C.; Blanco, Á., Degradation of 1,4-dioxane from industrial wastewater by solar photocatalysis using immobilized NF-TiO2 composite with monodisperse TiO2 nanoparticles. *App. Cat. B Environ.* **2016,** *180*, 44-52.

643. Jasmann, J. R.; Borch, T.; Sale, T. C.; Blotevogel, J., Advanced Electrochemical Oxidation of 1,4-Dioxane via Dark Catalysis by Novel Titanium Dioxide (TiO2) Pellets. *Environ. Sci. Technol.* **2016,** *50*, 8817-8826.

644. Ushida, A.; Hasegawa, T.; Narumi, T.; Nakajima, T., Flow properties of nanobubble mixtures passing through micro-orifices. *Int. J. Heat Fluid Flow* **2013,** *40*, 106-115.

645. Dayarathne, H. N. P.; Choi, J.; Jang, A., Enhancement of cleaning-in-place (CIP) of a reverse osmosis desalination process with air micro-nano bubbles. *Desalination* **2017,** *422*, 1-4.

646. Uchida, T.; Oshita, S.; Ohmori, M.; Tsuno, T.; Soejima, K.; Shinozaki, S.; Take, Y.; Mitsuda, K., Transmission electron microscopic observations of nanobubbles and their capture of impurities in wastewater. *Nano. Res. Lett.* **2011,** *6*, 295.

647. Gittens, G., Variation of surface tension of water with temperature. *J. Colloid Interface Sci.* **1969,** *30*, 406-412.

648. Parmar, H.; Asada, M.; Kanazawa, Y.; Asakuma, Y.; Phan, C. M.; Pareek, V.; Evans, G. M., Influence of microwaves on the water surface tension. *Langmuir* **2014,** *30*, 9875-9879.

649. Park, S.; Fayer, M. D., Hydrogen bond dynamics in aqueous NaBr solutions. *PNAS* **2007,** *104*, 16731-16738.

650. Beckett, M. A.; Hua, I., Elucidation of the 1, 4-dioxane decomposition pathway at discrete ultrasonic frequencies. *Environ. Sci. Technol.* **2000,** *34*, 3944-3953.

651. Wang, N.; Zheng, T.; Jiang, J.; Lung, W.-s.; Miao, X.; Wang, P., Pilot-scale treatment of p-Nitrophenol wastewater by microwave-enhanced Fenton oxidation process: Effects of system parameters and kinetics study. *Chem. Eng. J.* **2014,** *239*, 351-359.

652. Chitra, S.; Paramasivan, K.; Cheralathan, M.; Sinha, P. K., Degradation of 1,4-dioxane using advanced oxidation processes. *Environ. Sci. Pollut. Res.* **2012,** *19*, 871-878.

653. Son, H.-S.; Im, J.-K.; Zoh, K.-D., A Fenton-like degradation mechanism for 1,4-dioxane using zero-valent iron (Fe0) and UV light. *Water Res.* **2009,** *43*, 1457-1463.

654. Coleman, H. M.; Vimonses, V.; Leslie, G.; Amal, R., Degradation of 1,4-dioxane in water using TiO2 based photocatalytic and H2O2/UV processes. *J. Hazard. Mater.* **2007,** *146*, 496-501.

655. Suh, J. H.; Mohseni, M., A study on the relationship between biodegradability enhancement and oxidation of 1,4-dioxane using ozone and hydrogen peroxide. *Water Res.* **2004,** *38*, 2596-2604.

656. Zhao, G.; Gao, J.; Shi, W.; Liu, M.; Li, D., Electrochemical incineration of high concentration azo dye wastewater on the in situ activated platinum electrode with sustained microwave radiation. *Chemosphere* **2009,** *77*, 188-193.

657. Hu, Y.; Zhang, Z.; Yang, C., Measurement of hydroxyl radical production in ultrasonic aqueous solutions by a novel chemiluminescence method. *Ultrason. Sonochem.* **2008,** *15*, 665-672.

658. Li, S.; Zhang, G.; Zheng, H.; Zheng, Y.; Wang, P., Stability of BiFeO3 nanoparticles via microwave-assisted hydrothermal synthesis in Fenton-like process. *Environ. Sci. Pollut. Res.* **2017,** *24*, 24400-24408.

659. Wang, P., Environmental microwave chemistry technology. *Chem. Ind. Press, Beijing* **2003**.

660. Nowak, D., The Impact of Microwave Penetration Depth on the Process of Heating the Moulding Sand with Sodium Silicate. *Arch. of Foundry Eng.* **2017,** *17*, 115-118.

661. Peng, Z.; Hwang, J.-Y.; Mouris, J.; Hutcheon, R.; Huang, X., Microwave penetration depth in materials with non-zero magnetic susceptibility. *ISIJ Int.***2010,** *50*, 1590-1596.

662. Zhang, S.; Zhou, L.; Ling, B.; Wang, S., Dielectric properties of peanut kernels associated with microwave and radio frequency drying. *Biosyst. Eng.* **2016,** *145*, 108-117.

663. Wang, S.; Tang, J.; Johnson, J.; Mitcham, E.; Hansen, J. D.; Hallman, G.; Drake, S.; Wang, Y., Dielectric properties of fruits and insect pests as related to radio frequency and microwave treatments. *Biosyst. Eng.* **2003,** *85*, 201-212.

664. Guo, W.; Wang, S.; Tiwari, G.; Johnson, J. A.; Tang, J., Temperature and moisture dependent dielectric properties of legume flour associated with dielectric heating. *LWT-Food Sci. Technol.* **2010,** *43*, 193-201.

665. Zhu, Z.; Guo, W., Frequency, moisture content, and temperature dependent dielectric properties of potato starch related to drying with radio-frequency/microwave energy. *Sci. Rep.* **2017,** *7*, 9311.

666. Chen, J.; Xue, S.; Song, Y.; Shen, M.; Zhang, Z.; Yuan, T.; Tian, F.; Dionysiou, D. D., Microwave-induced carbon nanotubes catalytic degradation of organic pollutants in aqueous solution. *J. Hazard. Mater.* **2016,** *310*, 226-234.

667. Ren, S.; Boo, C.; Guo, N.; Wang, S.; Elimelech, M.; Wang, Y., Photocatalytic Reactive Ultrafiltration Membrane for Removal of Antibiotic Resistant Bacteria and Antibiotic Resistance Genes from Wastewater Effluent. *Environ. Sci. Technol.* **2018,** *52*, 8666-8673.

668. Pei, R.; Kim, S.-C.; Carlson, K. H.; Pruden, A., Effect of River Landscape on the sediment concentrations of antibiotics and corresponding antibiotic resistance genes (ARG). *Water Res.* **2006,** *40*, 2427-2435.

669. Luo, Y.; Mao, D.; Rysz, M.; Zhou, Q.; Zhang, H.; Xu, L.; J. J. Alvarez, P., Trends in Antibiotic Resistance Genes Occurrence in the Haihe River, China. *Environ. Sci. Technol.* **2010,** *44*, 7220-7225.

670. Guo, M.-T.; Yuan, Q.-B.; Yang, J., Microbial selectivity of UV treatment on antibiotic-resistant heterotrophic bacteria in secondary effluents of a municipal wastewater treatment plant. *Water Res.* **2013,** *47*, 6388-6394.

671. Xia, D.; Ng, T. W.; An, T.; Li, G.; Li, Y.; Lu, A.; Wong, P.-K., A Recyclable Mineral Catalyst for Visible-Light-Driven Photocatalytic Inactivation of Bacteria: Natural Magnetic Sphalerite. *Environ. Sci. Technol.* **2013,** *47*, 11166-11173.

672. Benaskar, F.; Patil, N.; Rebrov, V.; Schouten, J.; Hessel, V., Microwaves in cu-catalyzed organic synthesis in batch and flow mode. *Microwaves in Catalysis: Methodology and Applications* **2015**.

673. He, P.; Haswell, S. J.; I. Fletcher, P. D., Efficiency, monitoring and control of microwave heating within a continuous flow capillary reactor. *Sensors Actuat. B Chem.* **2005,** *105*, 516-520.

674. Marafie, J. A.; Moseley, J. D., The application of stop-flow microwave technology to scaling-out SNAr reactions using a soluble organic base. *Org. Biomol. Chem.* **2010,** *8*, 2219-2227.

675. Amore, K. M.; Leadbeater, N. E., Microwave‐Promoted Esterification Reactions: Optimization and Scale‐Up. *Macromol. Rapid Commun.* **2007,** *28*, 473-477.

676. Kremsner, J. M.; Stadler, A.; Kappe, C. O., The scale-up of microwave-assisted organic synthesis. In *Microwave Methods in Organic Synthesis*, Springer: **2006**, pp 233-278.

677. Patil, N. G.; Benaskar, F.; Meuldijk, J.; Hulshof, L. A.; Hessel, V.; Schouten, J. C.; Esveld, E. D.; Rebrov, E. V., Microwave assisted flow synthesis: coupling of electromagnetic and hydrodynamic phenomena. *AlChE J.* **2014,** *60*, 3824-3832.

678. Matsuzawa, M.; Togashi, S., Pilot Plant for Continuous Flow Microwave-Assisted Chemical Reactions. *Microwaves in Catalysis: Methodology and Applications* **2015**.